Operando chemical tomography of packed bed and membrane reactors for methane processing

Antonios Vamvakeros

Department of Chemistry

University College London

Thesis submitted for the degree of Doctor of Philosophy

2017

Declaration

I, Antonios Vamvakeros confirm that the work presented in this thesis is my own. Where information has been derived from other sources, I can confirm that this has been indicated in the thesis.

……

Abstract

Heterogeneous functional materials, like catalytic solids, batteries and fuel cells tend to usually possess complex structures where the 3D spatial distribution of the various components of these materials is rarely uniform. Such materials are known to change with time under operating conditions. In order to gain an insight into the structure-function relationships, it is essential to study them *in situ* with spatially-resolved techniques. The work presented in this thesis focuses on the development and application of synchrotron X-ray tomographic imaging methods to study various catalytic materials in real time and under real process conditions.

The main X-ray tomographic imaging technique used in this study is X-ray diffraction computed tomography (XRD-CT) which couples powder diffraction with "pencil" beam computed tomography. Chapters 3 and 4 of this thesis outline some of the technical achievements accomplished in this work. More specifically, Chapter 3 outlines the development of a new data processing strategy used to remove line or "streak" artefacts generated in reconstructed XRD-CT images due to the presence of large crystallites in the sample; a common problem in XRD-CT measurements. Chapter 4 introduces a new data collection strategy, termed interlaced XRD-CT, which allows, post experiment, choice between temporal and spatial resolution. This data collection strategy can in principle be applied to all pencil beam CT techniques.

The results from the first multi-length scale chemical imaging experiments of an unpromoted and a La-promoted Mn-Na-W/SiO_2 catalyst for the oxidative coupling of methane are presented in Chapter 5. The spatially-resolved chemical signals obtained from these *operando* experiments provided new chemical information that can lead to the rational design of improved OCM catalysts. In Chapter 6, the results from, the first ever reported, XRD-CT experiments of working catalytic membrane reactors are presented. It is shown that the pertinent changes in the physicochemical state of these integrated reactor systems can be spatially-resolved. The results from Rietveld analysis of a 5D diffraction imaging (>10^6 diffraction patterns) redox experiment of a Ni-Pd/CeO_2-ZrO_2/Al_2O_3 catalyst and the first XRD-CT study of this catalyst during partial oxidation of methane are presented in Chapter 7.

Acknowledgments

I would like to thank my supervisor, Professor Andy Beale, for giving me the opportunity to work on this project. He both guided me throughout the project and also encouraged me to pursue my personal research interests, attend several scientific workshops and present my work at numerous international conferences. He kept me motivated and helped me to not lose focus and was always available when I needed his advice.

I would also like to thank Dr. Simon Jacques for his continuous support during this project. I have to acknowledge that he was very patient with me, always eager to answer my questions, no matter how simple they were. We had countless discussions not only about chemical imaging but also numerous debates about arts and politics.

Many thanks to Dr. Ilias Ismagilov and especially to Dr. Vesna Middelkoop for providing the materials I used in this project. During the past couple of years, I had the pleasure of doing most of the night shifts during the beamtime experiments with Dr. Pierre Senecal and Dr. Steve Price. I thank them both for their help and encouragement. I also had the honour of working with the scientist in charge of the ID15 beamline, Dr. Marco Di Michiel, during the beamtime experiments at the ESRF. His passion for the chemical imaging synchrotron experiments motivated me to become a better scientist.

I would also like to thank my co-supervisor Dr. Paul Shearing for all the discussions we had during this project. Being my supervisor during my Masters project, he inspired me to continue my studies and pursue a PhD.

I would also like to thank all my colleagues and friends at the Research Complex at Harwell, especially Alex O'Malley, Anna Gould, Miren Agote, Scott Rogers and Wilm (Vinnie) Jones, for making my PhD a great experience. I leave with memories that I will always cherish. Also special thanks to two of my Greek friends also living abroad, Kostas Papanikolaou and Kostas Gounaropoulos, for always being there when I needed them during my PhD.

Last but not least, I would like to thank all my friends in Greece and my family, especially my parents, Xenofon Vamvakeros and Peggy Miliou for their continuous support in all my endeavors.

This PhD thesis is dedicated to my grandparents.

Publications

- “Chemical imaging of Fischer-Tropsch catalysts under operating conditions”, S.W.T. Price *et al.*, **2017**, Science Advances
- “Real-Time Scattering-Contrast Imaging of a Supported Cobalt-Based Catalyst Body during Activation and Fischer–Tropsch Synthesis Revealing Spatial Dependence of Particle Size and Phase on Catalytic Properties”, P. Senecal *et al.*, **2017**, *ACS Catalysis*, 7, 2284–2293.
- “Interlaced X-ray diffraction computed tomography”, A. Vamvakeros *et al.*, **2016**, *Journal of Applied Crystallography,* 49, 485-496.
- “Catching catalysis in action”, A. Vamvakeros and S. D. M. Jacques, March **2016**, *ESRF News*, No. 73.
- “Removing multiple outliers and single-crystal artefacts from X-ray diffraction computed tomography data”, A. Vamvakeros *et al.*, **2015**, *Journal of Applied Crystallography,* 48, 1943-1955.
- “Real time chemical imaging of a working catalytic membrane reactor during oxidative coupling of methane”, A. Vamvakeros *et al.*, **2015**, *Chemical Communications,* 51, 12752-12755.

Conferences

Invited speaker

- 24th Congress and General Assembly of the International Union of Crystallography (21-28/08/2017, Hyderabad, India)
- 65th Annual Conference on Applications of X-ray Analysis (01-05/08/2016, Chicago, USA)
- Sino-German Workshop on "In situ Spectroscopy on Catalysts and Membranes" (28-29/08/2015 in Karlsruhe Institute of Technology, Germany)

Oral presentations

- ESRF User Meeting 2017, Operando structural studies in Materials Science (06-08/02/2017, Grenoble, France)
- 16th International Congress on Catalysis (03-08/07/2016, Beijing, China)
- 12th International Conference on Catalysis in Membrane Reactors (22-25/06/15, Szczecin, Poland)
- 5th International Conference On Operando Spectroscopy (17-21/05/2015, Deauville, France)
- 1st UK Catalysis Conference (08-09/01/2015, Loughborough, United Kingdom)

Table of Contents

Chapter 1: Introduction

Chapter 2: Methodology

Chapter 3: Removing multiple outliers and single crystal artefacts from X-ray diffraction computed tomography data

Chapter 4: Interlaced X-ray Diffraction Computed Tomography

Chapter 5: *Operando* studies of fixed bed reactors for the oxidative coupling of methane Introduction

Conclusions & Future Work

Appendix

CHAPTER 1: Introduction

Introduction

In almost every field of the chemical industry, varying from pharmaceuticals to petrochemicals, catalysts are used to produce the desired chemical products. It is estimated that 80-90% of the chemical industrial products are manufactured through catalytic processes.[1] Catalytic converters used for emission control by the automotive industry is probably the most well-known example for the general public.

A catalyst is a substance that accelerates the kinetics of a chemical reaction by decreasing its activation energy. This is done by providing alternative reaction pathways which are energetically more favourable. The catalyst forms bonds with the reactant molecules allowing them to interact and form the product(s) which then leave the catalyst. This means that at the end of every reaction cycle, the state of the catalyst is the same as before the reaction took place.[2] In other words, a catalyst provides a convenient place for the reactant molecules to meet and the catalyst itself emerges from the process unaltered. It should be emphasized that catalysts therefore change only the reaction rates and not the chemical equilibrium which is defined by thermodynamics.[3] To clarify, the overall change in free energy for both reactions (catalytic and uncatalyzed) is the same.[4]

There are three main types of catalytic processes: biocatalysis, homogeneous catalysis and heterogeneous catalysis. In biocatalysis, natural catalysts, like enzymes, are used to chemically transform mainly organic compounds at low temperatures (body temperatures). In homogeneous catalysis, both the catalyst and the reactants are in the same phase state. Such reactions typically involve soluble catalysts being in a solution (catalyst and reactants being in liquid phase). On the other hand, in heterogeneous catalysis, the catalyst is in a different phase state to the reactants. In most cases, the catalyst is in the solid state and the reactants are in the gas and/or liquid phase. In this work, heterogeneous catalysis processes were investigated where the catalysts are in the solid state and the reactants are in the gas state.

Catalytic solids

The main advantage of catalysts is that they allow the operation of chemical reactors at lower temperatures and/or pressures leading to a decrease of the energy demands and overall cost of the chemical processes. It is equally important to note that catalysts can also provide enhanced selectivity for a desired chemical product (apart from higher conversion of the reactants for given operating conditions). The performance of a catalyst is therefore determined by its activity (conversion of reactants), selectivity (towards a desired chemical) and stability. The stability of a catalyst describes its performance as a function of time.

Unfortunately, the deactivation of catalysts over time (loss of activity and/or selectivity) cannot be fully prevented and consequently catalysts must occasionally be replaced with fresh batches; this costs industry billions of dollars per year.[5] It is of no wonder that understanding the mechanisms leading to catalyst deactivation is one the key aspects of catalysis research.[6-8] A recent review study by Argyle and Bartholomew covers this topic in detail.[5] Such a thorough discussion is beyond the scope of this work but it should be mentioned that the main types of catalyst deactivation can be classified as: chemical, thermal and mechanical. There are several catalyst deactivation mechanisms which belong to these categories. For example, catalysts can be poisoned (chemical deactivation) when chemical species originating from the reactants (or products) are strongly chemisorbed on the catalyst active sites (active sites are blocked for the chemical reaction). Another characteristic example is the thermal degradation and sintering of catalysts (thermal/chemical) which decreases the catalytically active surface area. High temperature treatment of solid catalysts can also lead to the formation of undesired solid phases in the catalyst.

There are several types of catalytic solids, varying from microporous (e.g. derived from natural substances, like certain types of clays and zeolites, or synthetic ones like aluminosilicates) to nonporous materials (e.g. metals). Metals and metal alloys can be supported or unsupported catalysts. A characteristic example of a supported catalyst is Ni/Al_2O_3 (Ni metal particles dispersed on an Al_2O_3 support) which is used for methane reforming reactions. Such catalysts are discussed in more detail in Chapter 7. It should also be mentioned that metal oxides can also be active catalysts.

For example, a Mn_2O_3-Na_2WO_4/SiO_2 catalyst for the oxidative coupling of methane reaction was also investigated in this work (Chapters 5-6).

3D imaging of catalytic solids and functional materials

The keystone of catalysis research is understanding how catalysts work. More specifically, understanding how the structure of a catalyst is related to its performance (activity/selectivity). Such knowledge is essential in order to rationally design optimized catalytic materials.[9] However, catalytic solids usually comprise complex three-dimensional structures which show heterogeneities. This means that different 'chemical sites' may be present some of which may be catalytically active and others may not.[10] It is therefore crucial to be able to obtain information not only about the nature of the active components of a catalyst but also information about their distribution (e.g. uniform, egg-shell, egg-yolk and egg-white) and their accessibility.[11] It is of no wonder then that in the past decade there has been a lot of effort in developing and applying X-ray tomographic imaging techniques to study solid catalysts and other functional materials. X-rays can penetrate solid materials and probe their internal structure without destroying them and the combination of X-rays with the computed tomography (CT) method allows for multi-dimensional (>1D) spatial information. X-ray tomographic imaging techniques can provide information at the atomic to nano scale across micro and millimetre domains and it is this information that governs the likely final application/properties of the functional materials. One can argue that these techniques are essential to bridge the technical challenge of scale-up of these materials from laboratory to industrial scale and everyday life applications.

For example, X-ray absorption CT has been widely used to study solid oxide fuel cells (SOFCs).[12, 13] These are high temperature fuel cells (electrochemical energy devices) where the electrolyte is in the solid state; typically the oxygen ion conductor yttria-stabilised zirconia (YSZ) is used in this role.[14] The oxygen molecules are reduced at the cathode (perovskite-type mixed ionic and electronic conducting materials are typically used) and oxygen ions travel through the electrolyte to the anode where the fuel (e.g. hydrogen or hydrocarbons) is electrochemically burned. X-ray absorption

CT (micro-CT) can be applied to investigate whole SOFC stacks providing spatially-resolved information at the µm to mm/cm level (e.g. the presence and/or behaviour of cracks or pores under operation), but the main advantages of this technique are exploited when this technique is coupled with microscopy.[12, 13] More specifically, full-field X-ray microscopy or nano-CT is now widely used to investigate the microstructure of SOFCs with most studies focusing on the Ni (electro-)catalyst at the anode. Imaging with full-field X-ray microscopy can yield reconstructed data with sub 50 nm spatial resolution and it is possible to not only quantify physical properties like porosity, tortuosity and pore size distribution but also to study the connectivity, the triple phase boundary and the volume fraction of the various phases present in the sample (e.g. Ni/YSZ/void in the case of a SOFC anode).[15-23] As expected, nano-CT has been employed to study not only SOFCs but functional materials in general. In their extensive review, Cocco *et al.* discuss the applications of X-ray micro/nano CT to study proton exchange membrane fuel cells (PEMFCs), also known as polymer electrolyte membrane fuel cells, solar cells and catalytic solids.[22] In PEMFCs, micro-CT has been usually employed to study the water distribution during operation of the fuel cell while nano-CT has been used to study the morphology of the various layers present at the electrodes.[24, 25] These typically include a gas diffusion layer (GDL), a microporous layer (MPL) and a catalyst layer (CL). In batteries, it has been shown that it is not only possible to study the microstructure of the electrodes and their evolution (e.g. formation/growth of dendrites) but also to capture/image the whole device during operation (e.g. during thermal runaway).[26, 27] In the case of catalytic solids, X-ray micro/nano CT is often used to study the gas transport through the catalyst porous media and assess the systems for possible mass transport limitations. For the interested reader, this topic is thoroughly discussed in a recent review paper by Novák *et al*.[28] It has also proven to be a useful tool to investigate the degradation/ageing effects of exhaust gas catalysts (Pt/Al_2O_3 coated on different monoliths).[29, 30] Finally, it should be mentioned that X-ray phase contrast CT and the recently developed ptychographic X-ray CT technique have also been used to study the pore structure/network of catalytic solids.[31, 32]

In situ / *operando* multi-dimensional chemical imaging of functional materials

As mentioned previously, functional materials tend to change under operating conditions. This means that in order to fully understand the structure-function relationships, it is essential to study them under real process conditions.[9, 10, 33-35] The term *operando* (first introduced in 2002 by Miguel A. Banares, Eric M. Gaigneaux, Gerhard Mestl and Bert M. Weckhuysen) is used to distinguish between traditional *in situ* experiments and *in situ* experiments where there is direct proof that the system is captured in its active state.[36] In catalysis, this is achieved by simultaneous *in situ* characterisation of the catalyst and analysis of the reaction products (e.g. with IR spectroscopy, mass spectrometry or gas chromatography).

In the past three decades, a lot of effort has been made to create complex reactor cells and operando set-ups to study catalysts under working conditions. Such developments are essential in order to close the "operando gap" and obtain information about the active state of catalysts operating at temperatures and/or pressures similar to the ones applied in industries.[10, 37] X-rays produced at synchrotrons have high brilliance, high flux and are tuneable (i.e. there is a wide range of available photon energies).[38] These characteristics make synchrotron X-rays ideal for catalytic studies as it is possible to conduct time-resolved experiments with second to sub-second time resolution.[38] This means that X-ray based techniques at synchrotron facilities have the potential to provide invaluable information about the catalytic materials under working conditions; information that is not available with lab-based instruments.[10]

Chemical tomography

In most cases X-ray absorption micro/nano CT offers limited, if any, chemical information regarding the state of functional materials. This is due to the fact that it is based on differences in the attenuation of X-rays passing through the sample (X-ray absorption contrast) and as a result it cannot differentiate between elements with similar atomic numbers (or components with similar density) or chemical species. However, it is possible to obtain the desired spatially-resolved chemical

information by combining X-ray scattering and spectroscopic techniques with computed tomography. Such techniques are considered to fall under the umbrella of "chemical tomography" as each pixel (or more precisely voxel) in the reconstructed images corresponds to a chemical signal. For example, in X-ray diffraction computed tomography (XRD-CT) each pixel corresponds to a diffraction pattern while in X-ray fluorescence computed tomography (XRF-CT) each pixels corresponds to an XRF spectrum.[39, 40] As a result, chemical tomographic techniques yield either 3D (cross sections or "slices" with 2D spatial and 1D spectral) or 4D data (3D spatial and 1D spectral). Tracking the chemical changes taking place in a functional material under operating conditions as a function of time and/or chemical environment (e.g. different reaction mixtures in catalysis) and/or temperature/pressure and/or potential (i.e. in electrochemical systems) leads to minimum 5D data.[41] Some key studies in the field of chemical tomography are reported in Table 1.

Table 1: Firsts in chemical tomography with emphasis given on applications in catalysis

Description	Year	Ref
Demonstration of XRD-CT in the laboratory (*ex situ*)	1987	[40]
Demonstration of XRF-CT (*ex situ*)	1987	[39]
Demonstration of synchrotron XRD-CT (*ex situ*)	1998	[42]
XAFS-CT of a solid catalyst (*ex situ*)	2003	[43]
XRF-CT of a solid catalyst (*ex situ*)	2005	[44]
Demonstration of SAXS-CT	2006	[45]
Demonstration of multi-modal CT (*ex situ*)	2008	[46]
Demonstration of full-field XANES nanotomography applied to battery electrodes (*ex situ*)	2011	[47]
3D-XRD-CT of a catalyst (*in situ*)	2011	[48]
Full-field XANES nanotomography of a solid catalyst (*in situ*)	2012	[49]
Demonstration of PDF-CT (*in situ*)	2013	[50]
Multi-modal CT of catalytic system where one of the reactants is in the liquid phase (*in situ*)	2015	[51]
XRD-CT of dense ceramic catalytic membrane reactors (*in situ*)	2015	[52]
Combined XRD-CT/PDF-CT of an industrial catalyst pellet (*in situ*)	2017	[53]

XANES-CT and XRF-CT

Schroer *et al*. were the first to couple X-ray absorption fine structure spectroscopy (XAFS) with CT and study a catalytic material.[43] More specifically, X-ray absorption near-edge structure (XANES) spectroscopy was combined with first generation ("pencil"/narrow beam scanning approach) CT (XANES-CT) to image a 30% CuO/ZnO catalyst. Linear combination fitting of the spatially-resolved XANES spectra yielded different maps of metallic, monovalent (Cu_2O) and divalent Cu (CuO).[54] This feasibility study showed that it is possible to create "chemical" maps which correspond to different oxidation states of a target element using XANES-CT.

The first 3D-XANES-CT measurements were performed in 2011 by Meier *et al.* who showed that it is possible to combine full-field X-ray microscopy and XANES spectroscopy.[47] *Ex situ* characterisation of battery electrodes with 3D-XANES-CT yielded 3D maps of different Ni chemical species (varying from metallic Ni to NiO). Similarly, Nelson *et al.* studied the microstructure of Ni-YSZ SOFC anodes (several samples were taken from SOFCs that had been operating for different periods of time) by performing full-field X-ray nano-CT measurements below and above the Ni K-edge.[20] This approach allowed to have better contrast in the reconstructed absorption CT images which simplified the image segmentation process. Nano-3D-XANES-CT, also known as XANES spectroscopic nanotomography, as also applied by Shearing *et al*. and Karen Chen-Wiegart *et al*. to study the microstructure of Ni-YSZ SOFC anodes.[55, 56] Full-field XANES nanotomography was employed by Boesenberg *et al*. to study the Li deintercalation in a $LiFePO_4$ single particle ($LiFePO_4$ is commonly used as the cathode in Li ion batteries).[57] Saida *et al*. applied a very similar technique, termed 3D-laminography-XANES, to image the cathode electrode (Pt/C) of a fresh and a degraded PEMFC and managed to obtain 3D maps of the Pt catalyst particles (3D distribution maps) at the PEMFC cathode for the first time.[58]

Full-field XANES nanotomography has been also used to study fluid catalytic cracking (FCC) catalysts focusing on the intrusion/incorporation of metals (Ni, Fe) in the catalyst particles (zeolite Y based catalysts).[59, 60] Full-field XANES nanotomography also proved to be a useful tool to study the dealumination of industrial FCC catalysts.[61] XRF-CT has been also employed by the same group to map the

distribution of numerous metals, including Ni, Fe, V, Ca, La and Ti, in aged FCC catalyst particles.[62] The advantage of XRF-CT over XANES-CT is that it allows the creation of multiple chemical maps corresponding to the different elements present in the sample. However, XRF-CT is a scanning tomographic technique (first generation CT approach) and as a result requires significant amount of time to image 3D volumes. It should be noted that Jones *et al*. were the first to demonstrate the feasibility of XRF-CT to investigate catalytic solids by studying an Fe-based Fischer–Tropsch synthesis catalyst.[44] Price *et al*. employed μ-XRF-CT and μ-XANES-CT (scanning mode) to study a Mo-promoted colloidal Pt/C industrial catalyst used for the selective hydrogenation of (non)functionalised nitroarenes.[63] A whole catalyst particle (ca. 12 × 15 × 20 μm^3) was imaged with μ-XRF-CT, yielding 3D maps of the Pt and Mo species present in the particle. It should finally be mentioned that Liu *et al.* studied an FCC catalyst at different length scales by combining (scanning) μ-3D-XRF-CT and (full-field) nano-CT. [64]

It should be noted though that all the aforementioned XANES-CT measurements were performed *ex situ*. Gonzalez-Jimenez *et al*. were the first to investigate a working catalytic solid with full-field XANES nanotomography.[49] An $Fe_2O_3/TiO_2/ZnO/K_2O$ catalyst was studied during the Fischer–Tropsch-to-Olefins synthesis (FTO) reaction at 350 °C and 10 bar in synthesis gas (H_2/CO=1). By targeting the Fe and Zn K-edges it was possible to create 3D chemical maps and observe the chemical evolution of a catalyst particle (21 × 21 mm^2) as a function of time with spatial resolution at the nm scale (pixel size of 28 × 28 nm^2). Cats *et al*. used the same reactor setup to investigate a Co/TiO_2 Fischer–Tropsch synthesis (FTS) catalyst particle with full-field XANES nanotomography (the term X-ray nanoscopy was used in the study) by targeting the Co K-edge.[65] It was shown that the evolution of the Co species could be efficiently tracked during calcination, reduction and real FTS reaction conditions. This Co/TiO_2 FTS catalyst was further investigated by the same group focusing on the distribution of the Co species using multiple X-ray microscopy-based techniques.[66] Unfortunately, the drawback of most X-ray microscopy (nanoscopy) studies is that a single catalyst particle (or a very small region of the electrodes in the case of electrochemical devices) is investigated which may not be

representative of the catalyst bed (or electrodes). It is generally accepted that such complex materials should ideally be characterised using a multi-length scale approach.

XRD-CT and PDF-CT

XRD-CT was first demonstrated in 1987 by Harding *et al*. using a laboratory diffractometer.[40] However, in the past decade, it has been realised that its full potential as a materials characterisation technique can be exploited using synchrotron light.[41, 42] Jacques *et al.* performed the first *in situ* XRD-CT experiments by investigating a hydrogenation Ni/Al_2O_3 catalyst during its preparation.[48] Dynamic XRD-CT scans were performed during temperature ramping from ambient conditions to 500 °C under He flow (22 XRD-CT scans in total, acquisition time of ca. 10 min per XRD-CT). It was shown that the dynamic XRD-CT scans allowed to track the evolution of the Ni species ($[NiCl_2(en)(H_2O)_4]$, where en=ethylenediamine, is the Ni precursor) during this calcination experiment. In this study, 3D-XRD-CT was also demonstrated for the first time. This was achieved by collecting 10 XRD-CT scans along the catalyst bed before and after the *in situ* experiment (i.e. two 3D-XRD-CT scans were collected). This system was further investigated by the same group by studying the Ni/Al_2O_3 catalyst with combined XRD-CT and micro-CT not only during its preparation (calcination under N_2 followed by an oxidation and a reduction step) but also under methanation reaction conditions (CO/H_2 in N_2).[67] The 3D-XRD-CT data revealed that in the active catalyst, the crystalline Ni-containing species are found in the metallic Ni form and follow an egg-shell distribution. These observations were also supported by the micro-CT measurements. It should be noted that this was the first time XRD-CT was employed to study a catalyst under working conditions.

Beale *et al*. used the XRD-CT technique to investigate the effects of sulphur (S) on commercial $Cu/ZnO/Al_2O_3$ catalysts used for the Water Gas Shift (WGS) reaction.[68] As mentioned previously, one common (chemical) deactivation mechanism for catalysts is by poisoning the active metal sites. Various concentrations of H_2S were used in order to study the S poisoning of the $Cu/ZnO/Al_2O_3$ catalysts. The spatially-resolved diffraction signals obtained from the XRD-CT measurements revealed that Cu and Zn sulphides (i.e. CuS, Cu_2S and ZnS) formed during the H_2S treatment and

that these phases followed predominantly an egg-shell distribution. It was also shown that the CuS and ZnS shells became thicker with increasing H_2S concentration.

PDF-CT is a technique that couples X-ray atomic pair distribution function analysis with CT. PDF-CT can be considered to be a complementary technique to XRD-CT as it allows to identify and quantify amorphous and nanocrystalline components present in a sample (XRD-CT being blind to such components). From an experimental point of view, PDF-CT measurements are identical to XRD-CT ones with the only difference being the *Q* range sampled. More specifically, typically in XRD-CT scans the Q_{max} sampled is ca. 10 $Å^{-1}$ while in PDF-CT scans Q_{max} is ca. 25-30 $Å^{-1}$. The PDF data are then obtained by Fourier transform processing of the recorded 2D diffraction patterns taking into account the diffuse scattering underneath Bragg scattering signal. Jacques *et al*. were the first to not only demonstrate the feasibility of PDF-CT experiments but also to study a Pd/Al_2O_3 catalyst *in situ* during its preparation (calcination and reduction steps) with both XRD-CT and PDF-CT.[50] The XRD-CT and PDF-CT data yielded almost identical phase distribution maps of crystalline Pd and PdO. However, it was shown that nanocrystalline Pd and PdO (<2 nm crystallite size) present closer to the core of the catalyst could only be identified by PDF-CT.

Senecal *et al*. recently also showed that combined XRD-CT/PDF-CT measurements can provide unprecedented information regarding the state of catalysts during their activation and under reaction conditions.[53] More specifically, an industrial 10 wt. % Co/Al_2O_3 catalyst (3 mm cylindrical pellet) was investigated during its activation under H_2 flow (reduction step) and during the FTS reaction (CO/H_2 in He). It was shown that there were two different Co_3O_4 species present in the fresh catalyst; well dispersed Co_3O_4 exhibiting strong metal-support interaction (SMSI) and aggregated/poorly dispersed Co_3O_4 not interacting strongly with the Al_2O_3 support. The small well dispersed Co_3O_4 nanoparticles (≤6.5 nm) did not fully reduce to the active Co metallic phase but remained as CoO by the end of the activation (reduction) process. On the other hand, the larger Co_3O_4 nanoparticles are seen to reduce to Co, especially those closer to the catalyst surface. However, the most important result was related to the behaviour of the small Co-containing nanoparticles near the surface of the catalyst pellet. It was shown that these species reduce to metallic Co

during the activation of the catalyst (reduction step) but are more prone to re-oxidize to the inactive CoO phase under FTS reaction conditions (due to water formation during the FTS reaction).

Finally, it should be noted that it is possible to combine XRD/PDF-CT with other chemical tomographic techniques. Bleuet *et al*. were the first to introduce this multi-modal CT approach by demonstrating the feasibility to simultaneously perform an X-ray diffraction/fluorescence/absorption CT scan (μ-XRD/XRF/absorption CT).[46] Basile *et al*. were the first to simultaneously collect XRF-CT and XRD-CT scans to perform *ex situ* characterisation of Ni-based catalyst coating FeCrAlY foams (structured catalysts used for the steam reforming of methane reaction).[69] The combined XRF/XRD-CT data allowed to correlate the elemental distribution maps obtained from XRF-CT (e.g. Ni, Fe, Cr and Y) with the phase distribution maps obtained from the XRD-CT data (e.g. Ni, NiO, $NiAl_2O_4$ and Al_2O_3). Price *et al*. were the first to use combined XRF/XRD-CT to study *in situ* a Mo-promoted Pt/C catalyst for the hydrogenation of nitrobenzene.[51] It should be noted that this was also the first XRF/XRD-CT study of a catalytic system where one of the reactants is in the liquid phase (nitrobenzene in ethanol solution). The XRF-CT data revealed that the Pt followed an egg-shell distribution (Pt being predominantly located at the surface of the catalyst) while the Mo was uniformly distributed over the catalyst particle. The XRD-CT data proved to be less useful in this study as there was absence of crystalline Pt species in most regions of this catalyst. Recently, Price *et al*. also employed combined XRF/XRD-CT to investigate the behaviour of two 10% Co – 1% Re – 5% TiO_2/SiO_2 FTS catalysts during activation and under reaction conditions (2 and 4 bar pressure).[70] The difference between the two catalysts was the order of addition of the metal precursors and promoters. It was shown that such changes can have a big impact not only on the spatial distribution of the various elements but also on physicochemical properties of these catalyst (i.e. crystalline phases and crystallite sizes during catalyst activation and operation).

It should finally be mentioned that small angle X-ray scattering CT (SAXS-CT), first demonstrated in 2006 by Schroer *et al*., is another chemical tomographic technique which can provide information regarding the shape and size of nanoparticles.[45]

Schaff *et al*. recently showed that it is possible to obtain full 3D scattering distribution in reciprocal space for each voxel of the 3D object in real space by using virtual tomography axes (6D SAXT-CT).[71] To date, SAXS-CT has not been used to study catalysts but it is expected to become a powerful tool for characterisation of functional materials in general. Similar is the case for other synchrotron X-ray imaging techniques developed in the past decade including three-dimensional X-ray diffraction microscopy (3DXRD), X-ray diffraction contrast tomography (DCT), three-dimensional coherent X-Ray diffraction imaging (CDI) and X-ray ptychographic computed tomography.[72-75]

Outlook and future prospects

In this chapter, it was discussed why it is essential to characterise functional materials, like catalysts, fuel cells and batteries, during their operation. In the case of catalytic systems, it is highly desirable to look at the catalyst behaviour under industrially relevant conditions (i.e. chemical environment, temperatures and/or pressures) and ideally to study them in their intact industrial form. Such experiments, although technically challenging, are essential to gain a better understanding of the structure-activity relationships and the behaviour of functional materials under real process conditions. Synchrotrons provide an invaluable tool to perform these *in situ*/ *operando* experiments due to the nature of the X-rays (e.g. brilliance, brightness and penetration) produced at these facilities (see Chapter 2 for more details). A review of the various state-of-the-art synchrotron X-ray tomographic techniques used to characterise functional materials was also provided. It was shown that in the past decade, there has been a continuous effort to combine X-ray scattering and spectroscopic techniques with computed tomography in order to obtain spatially-resolved chemical information about these systems. As discussed in the literature review, full field and scanning transmission X-ray microscopy (in many cases coupled with XRF mapping or XRF-CT) have already proven to be very useful tools to study single catalyst particles and the electrodes in batteries and fuel cells. It was also shown that the XRD/PDF-CT techniques have been mainly exploited to study catalytic systems and in several cases under real reaction conditions. There are only two reported examples where these techniques have been applied to investigate

batteries and fuel cells and in both cases these are *ex situ* studies.[76, 77] However, one can easily foresee that XRD/PDF-CT and multimodal XRF/XRD-PDF/absorption-CT will gain a lot of attraction in the near future as techniques to study electrochemical energy devices under operating conditions too. Finally, it should be noted that the XRD/PDF-CT techniques are still under development. A characteristic example is related to the data processing of XRD-CT data. More specifically, the feasibility to perform Rietveld analysis of the reconstructed XRD-CT data was only recently demonstrated by Wragg *et al*. who investigated (*ex situ*) a SAPO-34 zeolite catalyst used for the methanol-to-olefins reaction.[78] One can envision chemical CT techniques (XAFS/XRF/XRD/PDF/SAXS-CT) becoming the preferred techniques to characterise heterogeneous materials and even replacing traditional bulk *in situ* techniques (e.g. PXRD) and X-ray (absorption contrast) imaging in the not too distant future.

References

1. Chorkendorff, I. and J.W. Niemantsverdriet, *Concepts of Modern Catalysis and Kinetics*. 2006: Wiley.
2. Berzelius, J.J., *Årsberättelsen om framsteg i fysik och kemi.* Royal Swedish Academy of Sciences, 1835.
3. Fogler, H.S., *Elements of Chemical Reaction Engineering*. 2006: Prentice Hall PTR.
4. Niemantsverdriet, J.W., *Spectroscopy in Catalysis*. 2007: Wiley.
5. Argyle, M.D. and C.H. Bartholomew, *Heterogeneous catalyst deactivation and regeneration: A review.* Catalysts, 2015. **5**(1): p. 145-269.
6. Denny, P.J. and M.V. Twigg, *Factors Determining the Life of Industrial Heterogeneous Catalysts*, in *Studies in Surface Science and Catalysis*. 1980. p. 577-599.
7. Bartholomew, C.H., *CATALYST DEACTIVATION.* Chemical Engineering (New York), 1984. **91**(23): p. 96-112.
8. Butt, J.B., *CATALYST DEACTIVATION AND REGENERATION*. Catalysis: Science and Technology. Vol. 6. 1984. 1-63.
9. Weckhuysen, B.M., *Chemical imaging of spatial heterogeneities in catalytic solids at different length and time scales.* Angewandte Chemie - International Edition, 2009. **48**(27): p. 4910-4943.
10. Beale, A.M., S.D. Jacques, and B.M. Weckhuysen, *Chemical imaging of catalytic solids with synchrotron radiation.* Chem Soc Rev, 2010. **39**(12): p. 4656-72.
11. Buurmans, I.L.C. and B.M. Weckhuysen, *Heterogeneities of individual catalyst particles in space and time as monitored by spectroscopy.* Nat Chem, 2012. **4**(11): p. 873-886.
12. Malzbender, J., R.W. Steinbrech, and L. Singheiser, *A review of advanced techniques for characterising SOFC behaviour.* Fuel Cells, 2009. **9**(6): p. 785-793.

13. Shearing, P.R., D.J.L. Brett, and N.P. Brandon, *Towards intelligent engineering of SOFC electrodes: a review of advanced microstructural characterisation techniques.* International Materials Reviews, 2010. **55**(6): p. 347-363.
14. Mahato, N., et al., *Progress in material selection for solid oxide fuel cell technology: A review.* Progress in Materials Science, 2015. **72**: p. 141-337.
15. Grew, K.N., et al., *Nondestructive nanoscale 3D elemental mapping and analysis of a solid oxide fuel cell anode.* Journal of the Electrochemical Society, 2010. **157**(6): p. B783-B792.
16. Guan, Y., et al., *Analysis of the three-dimensional microstructure of a solid-oxide fuel cell anode using nano X-ray tomography.* Journal of Power Sources, 2011. **196**(4): p. 1915-1919.
17. Shearing, P.R., et al., *Exploring microstructural changes associated with oxidation in Ni–YSZ SOFC electrodes using high resolution X-ray computed tomography.* Solid State Ionics, 2012. **216**: p. 69-72.
18. Laurencin, J., et al., *Characterisation of Solid Oxide Fuel Cell Ni–8YSZ substrate by synchrotron X-ray nano-tomography: from 3D reconstruction to microstructure quantification.* Journal of Power Sources, 2012. **198**: p. 182-189.
19. Chen-Wiegart, Y.-c.K., et al., *Oxidation states study of nickel in solid oxide fuel cell anode using x-ray full-field spectroscopic nano-tomography.* Applied Physics Letters, 2012. **101**(25): p. 253901.
20. Nelson, G.J., et al., *Three-dimensional microstructural changes in the Ni–YSZ solid oxide fuel cell anode during operation.* Acta Materialia, 2012. **60**(8): p. 3491-3500.
21. Cronin, J.S., et al., *Three-dimensional reconstruction and analysis of an entire solid oxide fuel cell by full-field transmission X-ray microscopy.* Journal of Power Sources, 2013. **233**: p. 174-179.
22. Cocco, A.P., et al., *Three-dimensional microstructural imaging methods for energy materials.* Physical Chemistry Chemical Physics, 2013. **15**(39): p. 16377-16407.
23. Shearing, P.R., et al., *Analysis of triple phase contact in Ni–YSZ microstructures using non-destructive X-ray tomography with synchrotron radiation.* Electrochemistry Communications, 2010. **12**(8): p. 1021-1024.
24. Kim, S.-G. and S.-J. Lee, *A review on experimental evaluation of water management in a polymer electrolyte fuel cell using X-ray imaging technique.* Journal of Power Sources, 2013. **230**: p. 101-108.
25. Shojaeefard, M.H., et al., *A review on microstructure reconstruction of PEM fuel cells porous electrodes for pore scale simulation.* International Journal of Hydrogen Energy, 2016. **41**(44): p. 20276-20293.
26. Finegan, D.P., et al., *In-operando high-speed tomography of lithium-ion batteries during thermal runaway.* Nature Communications, 2015. **6**: p. 6924.
27. Schröder, D., et al., *In operando x-ray tomography for next-generation batteries: A systematic approach to monitor reaction product distribution and transport processes.* Journal of Physics D: Applied Physics, 2016. **49**(40).
28. Novák, V., et al., *Understanding the gas transport in porous catalyst layers by using digital reconstruction techniques.* Current Opinion in Chemical Engineering, 2015. **9**: p. 16-26.
29. Hofmann, G., et al., *Ageing effects on exhaust gas catalysts: Microscopic changes captured by x-ray tomography.* Journal of Physics: Conference Series, 2014. **499**(1).
30. Hofmann, G., et al., *Aging of a Pt/Al2O3 exhaust gas catalyst monitored by quasi in situ X-ray micro computed tomography.* RSC Advances, 2015. **5**(9): p. 6893-6905.
31. Dasilva, J.C., et al., *Assessment of the 3-D pore structure and individual components of preshaped catalyst bodies by X-ray imaging.* ChemCatChem, 2015. **7**(3): p. 413-416.

32. Han, T., et al., *3 D Imaging and Structural Analysis of a Mesoporous-Silica-Body-Supported Eggshell Cobalt Catalyst for Fischer–Tropsch Synthesis.* ChemCatChem, 2016. **8**(18): p. 2860.
33. Grunwaldt, J.D. and C.G. Schroer, *Hard and soft X-ray microscopy and tomography in catalysis: bridging the different time and length scales.* Chem Soc Rev, 2010. **39**(12): p. 4741-53.
34. Grunwaldt, J.-D., J.B. Wagner, and R.E. Dunin-Borkowski, *Imaging Catalysts at Work: A Hierarchical Approach from the Macro- to the Meso- and Nano-scale.* ChemCatChem, 2013. **5**(1): p. 62-80.
35. Andrews, J.C. and B.M. Weckhuysen, *Hard X-ray spectroscopic nano-imaging of hierarchical functional materials at work.* ChemPhysChem, 2013. **14**(16): p. 3655-3666.
36. Urakawa, A., *Trends and advances in Operando methodology.* Current Opinion in Chemical Engineering, 2016. **12**: p. 31-36.
37. O'Brien, M.G., et al., *Closing the operando gap: The application of high energy photons for studying catalytic solids at work.* Applied Catalysis A: General, 2011. **391**(1–2): p. 468-476.
38. Jacques, S.D.M., et al., *Recent progress in the use of in situ X-ray methods for the study of heterogeneous catalysts in packed-bed capillary reactors.* Catalysis Today, 2009. **145**(3-4): p. 204-212.
39. Boisseau, P. and L. Grodzins, *Fluorescence tomography using synchrotron radiation at the NSLS.* Hyperfine Interactions, 1987. **33**(1-4): p. 283-292.
40. Harding, G., J. Kosanetzky, and U. Neitzel, *X-ray diffraction computed tomography.* Medical Physics, 1987. **14**(4): p. 515-525.
41. Beale, A.M., et al., *Progress towards five dimensional diffraction imaging of functional materials under process conditions.* Coordination Chemistry Reviews, 2014. **277**: p. 208-223.
42. Kleuker, U., et al., *Feasibility study of x-ray diffraction computed tomography for medical imaging.* Physics in Medicine and Biology, 1998. **43**(10): p. 2911-2923.
43. Schroer, C.G., et al., *Mapping the chemical states of an element inside a sample using tomographic x-ray absorption spectroscopy.* Applied Physics Letters, 2003. **82**(19): p. 3360-3362.
44. Jones, K.W., et al., *Synchrotron X-ray microprobe and computed microtomography for characterization of nanocatalysts.* Nuclear Instruments and Methods in Physics Research, Section B: Beam Interactions with Materials and Atoms, 2005. **241**(1-4): p. 331-334.
45. Schroer, C.G., et al., *Mapping the local nanostructure inside a specimen by tomographic small-angle x-ray scattering.* Applied Physics Letters, 2006. **88**(16).
46. Bleuet, P., et al., *Probing the structure of heterogeneous diluted materials by diffraction tomography.* Nature Materials, 2008. **7**(6): p. 468-472.
47. Meirer, F., et al., *Three-dimensional imaging of chemical phase transformations at the nanoscale with full-field transmission X-ray microscopy.* Journal of Synchrotron Radiation, 2011. **18**(5): p. 773-781.
48. Jacques, S.D.M., et al., *Dynamic x-ray diffraction computed tomography reveals real-time insight into catalyst active phase evolution.* Angewandte Chemie - International Edition, 2011. **50**(43): p. 10148-10152.
49. Gonzalez-Jimenez, I.D., et al., *Hard X-ray nanotomography of catalytic solids at work.* Angewandte Chemie - International Edition, 2012. **51**(48): p. 11986-11990.
50. Jacques, S.D., et al., *Pair distribution function computed tomography.* Nature Communications, 2013. **4**: p. 2536.

51. Price, S.W.T., et al., *In Situ Microfocus Chemical Computed Tomography of the Composition of a Single Catalyst Particle During Hydrogenation of Nitrobenzene in the Liquid Phase.* Angewandte Chemie, 2015. **127**(34): p. 10024-10027.
52. Vamvakeros, A., et al., *Real time chemical imaging of a working catalytic membrane reactor during oxidative coupling of methane.* Chemical Communications, 2015. **51**(64): p. 12752-12755.
53. Senecal, P., et al., *Real-Time Scattering-Contrast Imaging of a Supported Cobalt-Based Catalyst Body during Activation and Fischer–Tropsch Synthesis Revealing Spatial Dependence of Particle Size and Phase on Catalytic Properties.* ACS Catalysis, 2017: p. 2284-2293.
54. Schroer, C.G., et al., *Tomographic x-ray absorption spectroscopy.* Physica Scripta, 2005. **2005**(T115): p. 1026.
55. Shearing, P.R., et al., *Exploring microstructural changes associated with oxidation in Ni-YSZ SOFC electrodes using high resolution X-ray computed tomography.* Solid State Ionics, 2012. **216**: p. 69-72.
56. Karen Chen-Wiegart, Y.C., et al., *Oxidation states study of nickel in solid oxide fuel cell anode using x-ray full-field spectroscopic nano-tomography.* Applied Physics Letters, 2012. **101**(25).
57. Boesenberg, U., et al., *Mesoscale Phase Distribution in Single Particles of LiFePO4 following Lithium Deintercalation.* Chemistry of Materials, 2013. **25**(9): p. 1664-1672.
58. Saida, T., et al., *4D visualization of a cathode catalyst layer in a polymer electrolyte fuel cell by 3D laminography-XAFS.* Angewandte Chemie - International Edition, 2012. **51**(41): p. 10311-10314.
59. Meirer, F., et al., *Agglutination of single catalyst particles during fluid catalytic cracking as observed by X-ray nanotomography.* Chemical Communications, 2015. **51**(38): p. 8097-8100.
60. Meirer, F., et al., *Mapping metals incorporation of a whole single catalyst particle using element specific X-ray nanotomography.* Journal of the American Chemical Society, 2015. **137**(1): p. 102-105.
61. Kalirai, S., et al., *Visualizing Dealumination of a Single Zeolite Domain in a Real-Life Catalytic Cracking Particle.* Angewandte Chemie - International Edition, 2016. **55**(37): p. 11134-11138.
62. Kalirai, S., et al., *X-ray Fluorescence Tomography of Aged Fluid-Catalytic-Cracking Catalyst Particles Reveals Insight into Metal Deposition Processes.* ChemCatChem, 2015. **7**(22): p. 3674-3682.
63. Price, S.W.T., et al., *Chemical imaging of single catalyst particles with scanning μ-XANES-CT and μ-XRF-CT.* Physical Chemistry Chemical Physics, 2015. **17**(1): p. 521-529.
64. Liu, Y., et al., *Relating structure and composition with accessibility of a single catalyst particle using correlative 3-dimensional micro-spectroscopy.* Nature Communications, 2016. **7**.
65. Cats, K.H., et al., *X-ray nanoscopy of cobalt Fischer-Tropsch catalysts at work.* Chemical Communications, 2013. **49**(41): p. 4622-4624.
66. Cats, K.H., et al., *Active phase distribution changes within a catalyst particle during Fischer-Tropsch synthesis as revealed by multi-scale microscopy.* Catalysis Science and Technology, 2016. **6**(12): p. 4438-4449.
67. O'Brien, M.G., et al., *Active phase evolution in single Ni/Al2O3 methanation catalyst bodies studied in real time using combined [small mu]-XRD-CT and [small mu]-absorption-CT.* Chemical Science, 2012. **3**(2): p. 509-523.

68. Beale, A.M., et al., *Chemical imaging of the sulfur-induced deactivation of Cu/ZnO catalyst bodies.* Journal of Catalysis, 2014. **314**: p. 94-100.
69. Basile, F., et al., *Combined Use of Synchrotron-Radiation-Based Imaging Techniques for the Characterization of Structured Catalysts.* Advanced Functional Materials, 2010. **20**(23): p. 4117-4126.
70. Price, S.W.T., et al., *Chemical imaging of Fischer-Tropsch catalysts under operating conditions.* Science Advances, 2017. **3**(3).
71. Schaff, F., et al., *Six-dimensional real and reciprocal space small-angle X-ray scattering tomography.* Nature, 2015. **527**(7578): p. 353-356.
72. Poulsen, H., *An introduction to three-dimensional X-ray diffraction microscopyThis article forms part of a special issue dedicated to advanced diffraction imaging methods of materials, which will be published as a virtual special issue of the journal in 2013.* Journal of Applied Crystallography, 2012. **45**(6): p. 1084-1097.
73. Ludwig, W., et al., *X-ray diffraction contrast tomography: a novel technique for three-dimensional grain mapping of polycrystals. I. Direct beam case.* Journal of Applied Crystallography, 2008. **41**(2): p. 302-309.
74. Barty, A., et al., *Three-Dimensional Coherent X-Ray Diffraction Imaging of a Ceramic Nanofoam: Determination of Structural Deformation Mechanisms.* Physical Review Letters, 2008. **101**(5): p. 055501.
75. Holler, M., et al., *X-ray ptychographic computed tomography at 16 nm isotropic 3D resolution.* Scientific Reports, 2014. **4**: p. 3857.
76. Jensen, K.M.O., et al., *X-Ray Diffraction Computed Tomography for Structural Analysis of Electrode Materials in Batteries.* Journal of the Electrochemical Society, 2015. **162**(7): p. A1310-A1314.
77. Sanchez, D.F., et al., *A 2D and 3D X-ray μ-diffraction and μ-fluorescence study of a mixed ionic electronic conductor.* International Journal of Hydrogen Energy, 2017. **42**(2): p. 1203-1211.
78. Wragg, D.S., et al., *Rietveld analysis of computed tomography and its application to methanol to olefin reactor beds.* Journal of Applied Crystallography, 2015. **48**(6): p. 1719-1728.

CHAPTER 2: Methodology

Introduction

The main characterisation techniques used in this study are reviewed in this section with the major emphasis given to X-ray Diffraction Computed Tomography (XRD-CT) as this project focuses on the application and development of this technique.

Generation of X-rays

In 1895, Wilhelm Röntgen, a German physicist, was the first to discover X-rays and was subsequently awarded the first Nobel Prize in Physics (in 1901).[1] X-rays are electromagnetic waves with wavelengths in the Ångstrøm range (1 Å = 10^{-10} m) which can penetrate solid materials and probe their internal structure non-destructively. These amazing properties of X-rays make them an invaluable tool in numerous fields, varying from medicine to materials science and engineering.

Laboratory X-ray sources

In laboratory instruments, X-rays are generated after accelerated electrons interact with a metal target. Electrons are emitted from an electrically heated filament (thermionic emission) acting as the cathode (typically W) and are accelerated by the application of a potential difference (typically up to 60 kV) to strike a metal anode target all within an evacuated chamber. The electromagnetic radiation produced by the rapidly decelerated electrons (as a result of their collision with the metal target atoms) is referred to as Bremsstrahlung (literally meaning “breaking radiation”) and has a continuous spectrum (so called “white” radiation). If the energy of the electrons is higher than a specific value, which depends only on the metal used as the anode, then a second spectrum is generated which is superimposed on top of the continuous spectrum. This new spectrum is known as “characteristic radiation” and consists of discrete peaks whose energy depends only on the metal used as the anode. Electrons from inner electron shells (1s and 2p) of the (metal) atom are ejected and their replacement from other electrons from higher atomic levels gives rise to characteristic emission of X-ray photons with specific energy (i.e. equal to the energy

difference between the higher and the vacant atomic level). In most cases, Cu or Mo are commonly used as the metal target elements but also Cr, Fe, Co, Ag and W anodes are available for more specialized applications. A typical X-ray spectrum obtained from a Cu metal target is shown in Figure 1. The energy of both types of radiation can be increased (smaller wavelength) by increasing the potential difference (accelerating voltage). However, most of the energy of the electron beam is lost as heat (the anode typically needs to be water cooled) and only a small fraction is converted to X-ray radiation.

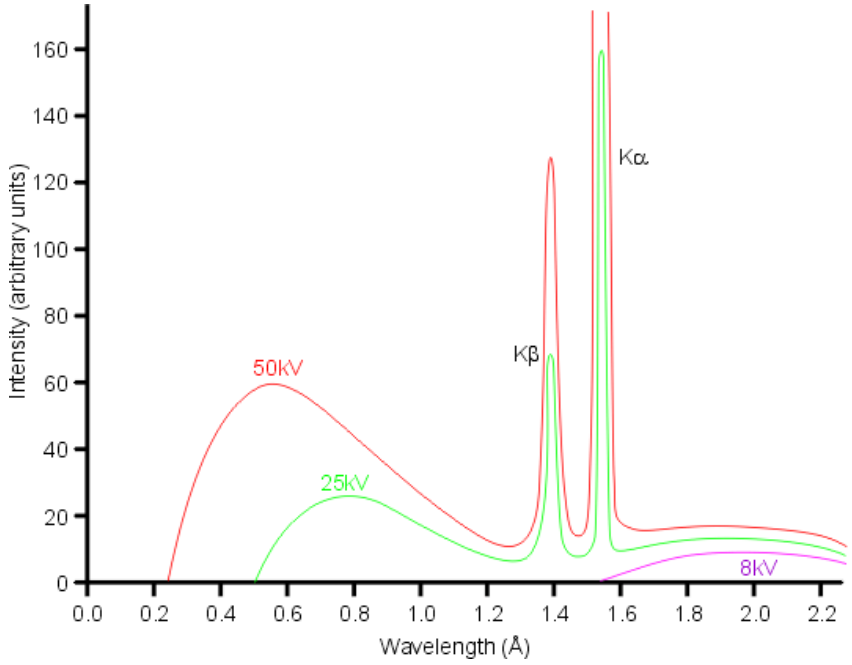

Figure 1: A typical X-ray spectrum obtained from a Cu metal target. The image was taken from: http://pd.chem.ucl.ac.uk/pdnn/inst1/xrays.htm

Synchrotron X-ray sources

X-rays can also be generated in synchrotrons where charged particles, typically electrons, are accelerated to relativistic velocities. These high energy particles are then periodically forced to change direction leading to the emittance of electromagnetic radiation so called synchrotron radiation. An illustration of a synchrotron in provided in Figure 2. The electrons are initially generated by an electron gun. As with laboratory instruments, a high voltage cathode is heated under vacuum and electrons are produced by thermionic emission. These electrons are then accelerated to relativistic velocities using electric fields. This part of the synchrotron is called the linear accelerator, or “linac” (A in Figure 2).

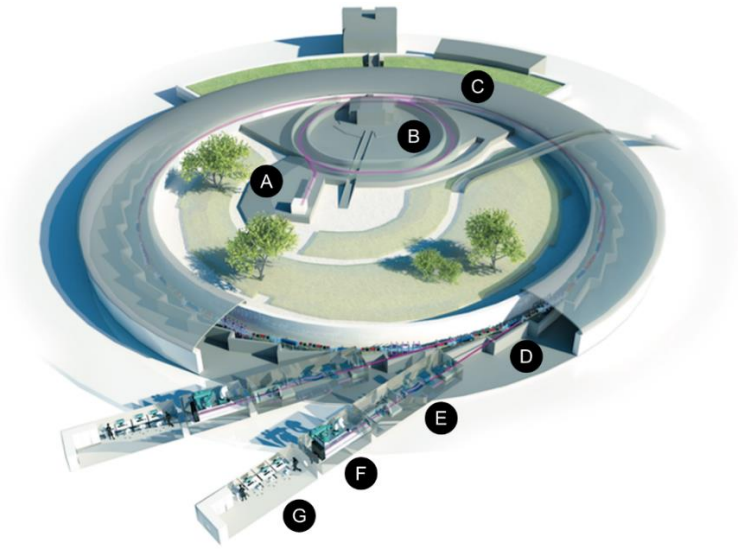

Figure 2: Illustration of a synchrotron. A: Linear accelerator (linac), B: Booster synchrotron, C: Storage ring, D: Optics hutch, E: Experimental hutch, F: Control hutch. The image was taken from: http://www.esrf.eu/about/synchrotron-science/synchrotron

The electrons are then injected into the booster synchrotron (B in Figure 2). As the name implies, the electrons are further accelerated in this part of the synchrotron before being injected into the storage ring. Although it might also be implied from Figure 2 that the booster synchrotron and the storage ring are circular, this is not entirely true. Dipole magnets, also known as bending magnets, are used to curve the electrons around the bends in the booster synchrotron while a radio frequency (RF) voltage source accelerates them in the straight sections. The (final) energy of the electrons leaving the booster is an important characteristic of the synchrotron machine. For example, the electrons leaving the booster part of the Diamond light source (DLS) have energy of 3 GeV while the energy of the electrons at the ESRF is 6 GeV. As a general rule of thumb, the greater the energy of the electrons in the storage ring, the higher is the energy of the emitted X-ray radiation.

The electron beam is then injected into the storage ring of the synchrotron (C in Figure 2) which consists of several straight and curved sections combined together to form a closed loop. The storage ring is kept under vacuum in order to minimize the interactions of the electron beam with molecules. Electromagnets, known as bending magnets, are placed at the curved sections and are used to curve the electron beam and allow the electrons to maintain their orbital path around the storage ring. Every time the electrons pass through an electromagnet, they lose

energy by emitting electromagnetic radiation. Therefore, bending magnets are also a source of synchrotron radiation (emitted tangentially to the electron beam path as shown on the left side of Figure 3). This synchrotron radiation is used as the X-ray source for experiments performed at the various beamlines (D to G in Figure 2). The energy of the electrons is replenished by RF cavities also present around the storage ring. Apart from bending magnets, insertion devices, such as wigglers and undulators, are also used in synchrotrons (typically in 3rd generation synchrotrons) to produce X-rays. Insertion devices are composed of arrays of small magnets with alternating polarity and their main advantage is that more collimated and brilliant X-rays are generated compared to bending magnets (as illustrated on the right side of Figure 3). The brilliance of a source is defined as the number of photons produced per second (photon flux) per unit solid angle per unit area of the beam per unit energy bandwidth (ph × s^{-1} × $mrad^{-2}$ × mm^{-2} × 0.1% BW). In other words, brilliance defines the number of photons of a given wavelength and direction present on a spot per unit of time. Brilliance is typically used to compare different X-ray sources.

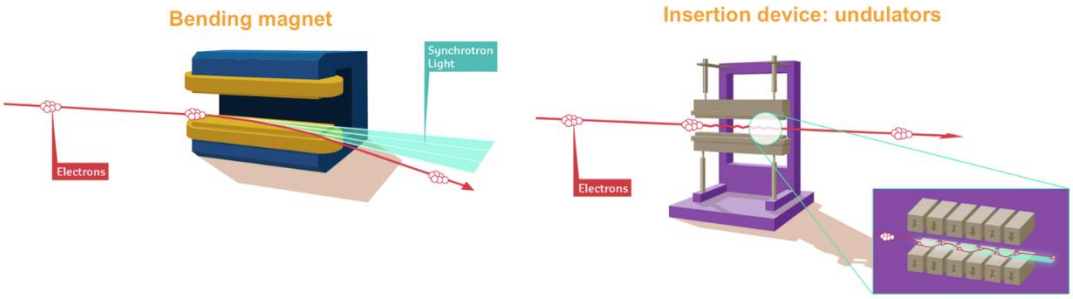

Figure 3: Left: Bending magnet. Right: Undulator. The image was taken from: http://www.esrf.eu/about/synchrotron-science/synchrotron

Each beamline is directly connected to the storage ring by a front end (D in Figure 2). The front end also serves to monitor the position of the synchrotron light and to protect the storage ring in case there are leaks in the beamline. When the front end is closed, the optics hutch can be accessed (E in Figure 2), where most of the beamline X-ray optics can be found (e.g. X-ray mirrors and monochromators) typically used to filter and/or focus the X-ray beam and accessed by the beamline personnel. The experimental hutch (F in Figure 2) is the part of the beamline accessed by the synchrotron facility users as it is the part of the beamline that houses the experiment.

The experiment is monitored through the control hutch where in many cases it is possible to remotely perform sample/detector alignments and position the samples, control the various instruments, etc.

The main advantages of X-rays generated at synchrotrons compared to laboratory instruments can be summarised as the following:

1. In most cases, several orders of magnitude higher brilliance compared to laboratory instruments
2. Highly collimated (more collimated vertically than horizontally) X-ray beam (divergence of the X-ray beam in the order of mrads).
3. Synchrotron radiation generates a smooth continuous spectrum which allows for wide tunability in energy/wavelength. Depending on the experiment, "white" or highly monochromatic and radiation can be used.
4. Horizontally polarised X-ray beam

It is therefore no wonder that synchrotron light has become an invaluable tool for materials characterisation studies. However, its main advantages compared to laboratory instruments are mainly exploited in dynamic experiments which require a large number of photons of a specific wavelength arriving at a small region of the sample per unit of time. Such are dynamic experiments involving functional materials like catalytic reactors and electrochemical devices (e.g. fuel cells and batteries).

X-ray diffraction

In 1912, Max von Laue, a German physicist, discovered that X-rays can be diffracted, verifying the wave nature of X-rays for the first time and for this work he was awarded the Nobel Prize in Physics in 1914. X-ray diffraction (XRD) is used to determine the crystal structure of single crystals; a technique also known as X-ray crystallography. This is achieved by analysing the intensity and the directions of the diffracted X-ray beam. The basic principle behind X-ray diffraction lies on the fact that the wavelength of X-rays is of the same order of magnitude as the distances between the atoms in the crystals (approximately 1 Å). This means that one can calculate the positions of the atoms in the unit cell of a single crystal (therefore bond angles and interatomic distances) by studying the diffraction pattern; the unit cell being the

"building block" of a crystal (a single crystal is simply a repetition of a unit cell in three-dimensional space). William Henry Bragg and William Lawrence Bragg (father and son) were the first to conduct XRD experiments and managed to derive information about the structure of crystals for which they were awarded the Nobel Prize in Physics in 1915. Bragg's Law states that:

$$n\lambda = 2d \sin\theta$$

λ is the wavelength of the illuminating X-ray beam, d is the inter-planar spacing involved and ϑ is the angle between the incident (or diffracted) ray and the relevant crystal planes; n is an integer referred to as the order of diffraction (n = 1, 2, 3, …).

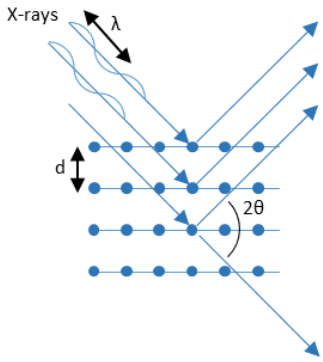

Figure 4: Schematic representation of X-ray diffraction from part of a single crystal.

When Bragg's Law is satisfied, X-ray waves scattered from successive planes in the crystal will travel distances differing by exactly one wavelength (n = 1 because n^{th} order of diffraction from (hkl) planes can be treated as 1st order of diffraction from (nh, nknl) planes with spacing d/n). XRD is therefore the result of constructive and destructive interference of elastically scattered X-ray waves. A schematic representation of X-ray diffraction from part of a single crystal is shown Figure 4.

Powder diffraction

An ideal power consists of a very large number of randomly oriented crystallites. When the powder sample is illuminated with a monochromatic X-ray beam, diffraction will take place from the planes in those crystallites that are oriented at an angle that fulfils Bragg's law (Figure 5). Powder X-ray diffraction, usually mentioned

as powder diffraction, can also be used to determine the crystal structure of materials, but the lower the symmetry of the unit cell, the more challenging it becomes. The difficulty in indexing the peaks and measuring the different reflections increases with increasing complexity of the crystal structure. The reason why this happens is that the number of lines in the diffraction patterns increases as the structure becomes more complex and overlapping of the reflections cannot be avoided (i.e. with decreasing unit cell symmetry). On the other hand, single crystal diffraction reflections can be separated using a 2D detector. Consequently, powder diffraction is predominantly used to fingerprint materials and detect the presence of a known compound or phase in a pure or mixed material.[2] This is done by comparing the diffraction pattern from the experiment with diffraction patterns of known compounds. There are various different databases that contain either measured powder diffraction patterns or corresponding crystal structures for many thousands of materials.

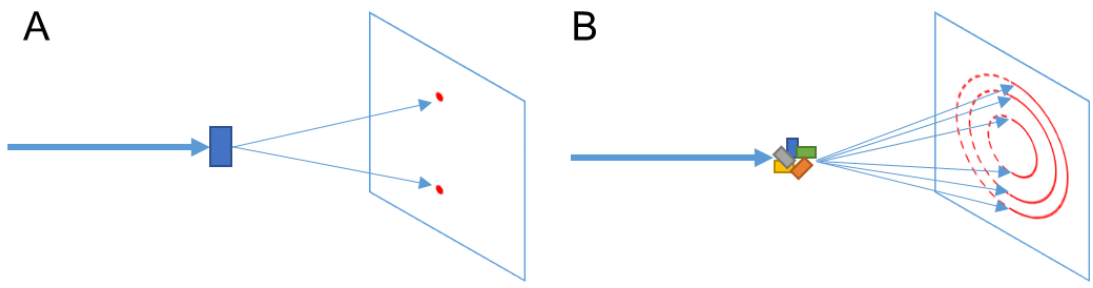

Figure 5: A: X-ray diffraction from a single crystal, B: X-ray diffraction from a polycrystalline (powder) sample

In the field of heterogeneous catalysis, powder XRD is often used to identify the different phases that are present in the catalyst, to observe the possible evolution of these phases during the catalyst lifetime or even to estimate average crystallite sizes of crystalline phases.[3] It can also be used to check for impurities in the sample.[2] In order to obtain useful results from a powder XRD experiment, the sample has to possess certain characteristics. These can be summarised as the following:[4]

- The individual crystallites composing the specimen must be highly crystalline. This means that the size of the crystallites must be large enough such that poor diffraction is avoided.

- The crystallites must be randomly oriented to represent all possible crystal orientations.
- The size of the crystallites must be small enough such that a sufficiently large statistical number can be present within a powder specimen to represent all possible orientations.

Rietveld refinement

As mentioned previously, it becomes more and more difficult to index the peaks and to measure the different reflections with increasing complexity of a crystal structure due to peak overlap. However, it is possible to solve the crystal structure by analysing a powder diffraction pattern. The breakthrough in powder diffraction analysis for structure determination was made by Hugo Rietveld.[5] It has to be emphasized though that Rietveld refinement is used to refine a structure model, not to directly solve a crystal structure.

Initially, the peaks need to be indexed in order to obtain the (possible) unit cell and the space group. Unit cell refinement should be performed to get the best unit cell candidate before taking the next steps towards the structure solution. Le Bail (or Pawley) whole powder profile (structure-less) fit can be performed to extract the unit cell parameters and the peak shapes.[6, 7] In a Le Bail analysis, the peak intensities are allowed to fit the experimental values; the intensity of the peaks is not bound by the chemistry of the unit cell (e.g. types and number of atoms). Real-space or reciprocal-space methods can be used to obtain an initial the structure model but if there is *a priori* knowledge of the crystal structure model, then Rietveld refinement can be performed directly after the structure-less whole powder profile analysis.

The Rietveld refinement method is a least-squares based minimisation algorithm that tries to minimise the difference between a calculated profile (model) and the observed (experimental) data. The Rietveld method takes into account the positions, the intensities and the shape of the powder diffraction peaks. The lattice parameters and the space group of the unit cell define the peak positions while the atom types, positions and vibrations define the peak intensities. Importantly, it allows the refinement of the atomic coordinates in the unit cell, the atomic displacement

parameters and the occupancies of the atoms. The aim of the Rietveld refinement is to minimise the residual function:

$$\sum_{i}^{n} w_i (y_i^{obs} - y_i^{calc})^2$$

where y_i^{obs} is the observed intensity at observation point *i*, y_i^{calc} is the calculated intensity at observation point *i* and w_i is the weight at observation point *i* (typically $w_i = 1 / y_i^{obs}$). The total powder diffraction intensity, Y_c, can be expressed as:

$$Y_c = Y_b + S_h \sum_{n}^{nphases} S_n I_n$$

Where Y_b is the background intensity, S_h is the histogram scale factor, S_n is the scale factor corresponding to each *n* phase (if there are several phases present in the sample) and I_n is the intensity contribution of each *n* phase. This intensity contribution, I_n, depends on numerous factors:

$$I_n = LPAm_{hkl} F_{hkl}^2 S(2\theta - 2\theta_{hkl})$$

Where *L* is the Lorentz-Polarization factor, *P* is the preferred orientation, *A* is the X-ray absorption, *m* is the (hkl) reflection multiplicity, F_{hkl} is the structure factor and $S(2\theta\text{-}2\theta_{hkl})$ is the value of the profile peak shape function for a (hkl) reflection at position 2θ, displaced from its expected position, $2\theta_{hkl}$. The structure factor (assuming isotropic thermal motion) can be calculated as following:

$$F_{hkl} = \sum_{j=1}^{m} O_j f_j e^{[2\pi i(hx_j + ky_j + lz_j)]} e^{(\frac{-B(sin\theta)^2}{\lambda})}$$

where O_j is the occupancy of atom *j*, f_j is the scattering factor of atom *j*, x_j, y_j and z_j are the coordinates of atom *j*, *B* is the Debye-Waller factor and *λ* is the wavelength of the X-ray beam. The scattering factor of an atom f_j describes the effectives of that atom in scattering X-rays and is a function not only on the atomic number but also the scattering angle 2θ (the values of the scattering factors decrease with increasing angle 2θ).

As it is implied from the previous formulas, the Rietveld method is a whole power pattern fitting technique which can be used not only for structure refinement but also for quantitative phase analysis of samples consisting of multiple crystalline phases. Various statistics factors (known as *R* factors) are used to assess the quality of the fit (or the validity of a crystal structure model). The most important being the following:

$$R_p = \frac{\sum_i^N |y_i^{obs} - y_i^{calc}|}{\sum_i^n |y_i^{obs}|}$$

$$R_{wp} = \left(\frac{\sum_i^N w_i \left|y_i^{obs} - y_i^{calc}\right|^2}{\sum_i^n w_i \left|y_i^{obs}\right|^2}\right)^{\frac{1}{2}}$$

$$R_{exp} = \left(\frac{(N - P + C)}{\sum_i^n \left|y_i^{obs}\right|}\right)^{\frac{1}{2}}$$

Where *N* is the number of observation points, *P* is the number of refined parameters and *C* is the number of constraints applied to the model. However, visual inspection of the raw and fitted data is always the preferred way to evaluate the quality of the Rietveld refinement. This is the reason why the difference between the two profile patterns, observed and calculated one, is always plotted in the same figure as the aforementioned patterns. The difference plot should ideally be a flat line.

Neutron powder diffraction

It should finally be mentioned that neutron powder diffraction is another very powerful characterisation technique for materials. In fact, in some cases this technique can provide information about a material that is otherwise unavailable with X-ray powder diffraction. This is because X-rays are scattered by the electron cloud around the nucleus of an atom while neutrons are scattered directly by the nucleus of an atom. As it will be described below, this phenomenon has direct implications to the values of the scattering factors and as a result to the intensities of the peaks in the powder diffraction data.

According to the de Broglie relationship matter exhibits wave properties. So for a neutron beam the de Broglie relationship is expressed as:

$$\lambda = \frac{h}{p} = \frac{h}{m_n v}$$

where *h* is Planck's constant, *p* is the momentum of the neutron, m_n is the neutron mass and *v* is the velocity of the neutron particle. Neutrons that have wavelengths in the Å range can be used for materials studies. The main sources of neutrons for materials studies have been nuclear reactors where neutrons are generated by atomic fission from uranium. Neutrons can also be generated in spallation sources which are synchrotrons but the accelerated particles are not electrons but protons. The neutrons are produced by bombarding a W target with high energy protons.

As mentioned previously, the values of the X-ray scattering factors depend on the number of electrons present in the atom and the X-ray scattering angle 2θ. More specifically, the X-ray scattering factors increase with increasing atomic number (heavy elements scatter X-rays more strongly than lighter elements) and decrease with increasing angle 2θ ($sin\theta/\lambda$ dependence). This decrease in scattering power is explained by the fact that at large angles the scattered X-rays from different parts of the electron cloud of an atom are no longer in phase. On the contrary, neutrons are scattered from the nucleus of an atom and since the nucleus is significantly smaller compared to the electron cloud, the neutron scattering factors are almost independent of the scattering angle. The neutron scattering factors do not decrease with decreasing atomic number (as the X-ray scattering factors) but depend on the structure of the nucleus of an atom which means that they can vary significantly between isotopes of an element.

As a result, neutron powder diffraction data contain more information for large *Q* ranges compared to X-ray powder diffraction data and allow the calculation of more precise values for the unit cell parameters and atomic positions and occupancies. For the reasons explained previously, neutron powder diffraction data are also preferred to X-ray ones when both very heavy and very light atoms are present in the unit cell. In this work, neutron powder diffraction data were used to solve the crystal structure of the $BaCo_{0.4}Fe_{0.4}Zr_{0.2}O_{3-\delta}$ perovskite which contains both very heavy (Ba) and light (O) atoms (results presented in Chapter 6).

X-ray absorption computed tomography

Almost 120 years have passed since Wilhelm Röntgen performed the first X-ray imaging experiment using a photographic plate. The classic radiograph depicts the bones of his wife's hand also showing her wedding ring on her fourth finger. X-ray radiography has since then become an invaluable tool not only for medical applications but also in materials science. Nowadays, ultra-fast radiographs can be captured at synchrotron facilities where both brilliant X-ray sources and efficient X-ray detectors are available (typically charge coupled devices (CCD) are used). The basic principle of X-ray radiography lies on illuminating an object with an X-ray beam and measuring the intensities of the transmitted X-rays through the sample with a detector. According to the Beer-Lambert law, X-rays of a given wavelength λ are attenuated as they pass through a homogenous object:

$$I_t = I_o e^{-\mu x}$$

where I_t is the intensity of the transmitted X-rays through the sample, I_o is the intensity of the illuminating X-ray beam, μ is a linear attenuation coefficient (typically given in cm^{-1} units) and x is the sample thickness (length of X-ray beam path through the sample). In some cases, the mass attenuation coefficient is used:

$$\mu = \frac{A}{d}$$

where μ is the linear attenuation coefficient, A is the mass attenuation coefficient and d is the density of the sample.

X-ray absorption computed tomography (aka X-ray CT) is an X-ray based imaging technique that is used to study the internal structure of objects. The first CT scanner was built for medical applications by Hounsfield.[8] Hounsfield and Cormack shared the 1979 Nobel Prize in Medicine for their individual efforts in developing X-ray CT. Nowadays, X-ray CT scanners are widely used not only in hospitals (aka medical-CT scanners) but also in industries to characterise materials systems. The main advantage of this technique is that it is non-destructive and the same sample can be tested several times and/or be retrieved for further analysis after the tomographic experiment. The first incarnation of X-ray CT relied on the use of a narrow ("pencil")

X-ray beam. This type of CT scan is described in details in a later section in this chapter where the technique X-ray diffraction computed tomography is discussed.

Parallel beam geometry

Currently in synchrotrons, the parallel beam geometry is typically used to perform X-ray absorption CT scans. The sample is illuminated with a monochromatic X-ray beam and a number of individual radiographs (projections) are recorded while the sample is being rotated, typically covering an angular range of 0 – 180°. This is illustrated on the left side of Figure 6. The X-ray beam size is typically is larger than the sample but there are ways to perform an X-ray CT scan when this is not the case.

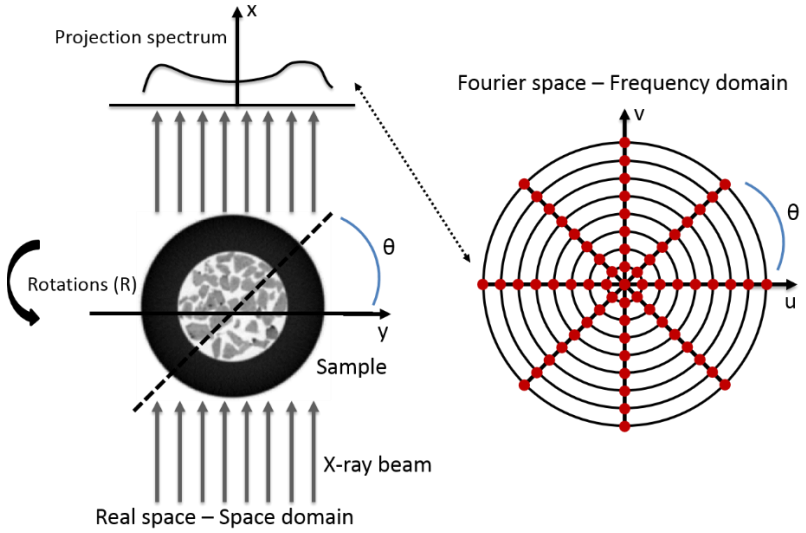

Figure 6: The sampling in the real space (left) and frequency (discrete points at multiple angles) domain (right) during a parallel beam X-ray absorption CT scan.

Each projection dataset composes a 2D matrix (image) where the value of each element (pixel) corresponds to the intensity of X-rays transmitted through the sample. The measured intensity can be expressed as:

$$I_t = I_o e^{\iiint -\mu(x,y,z)dxdydz}$$

where $\mu(x,y,z)$ is the linear absorption coefficient of every sample voxel (volume element). Of course, a 3D object can be also described as a series of 2D objects. So, for every row in the projection datasets, the measured intensity can be expressed as:

$$I_t = I_o e^{\iint -\mu(x,y)dxdy} <=> \ln\left(\frac{I_o}{I_t}\right) = \iint \mu(x,y)dxdy$$

It is therefore possible, from the ratio of the intensities of the X-rays (illuminating and transmitted), to calculate the line integral of the absorption coefficient along the propagation direction of the X-rays. However, this is in fact the radon transform of the absorption coefficients which can be used to reconstruct a 2D image of the object (cross section or "slice") as described by Radon (inverse radon transform).[9] There are several types of algorithms available to perform the image reconstruction; the two most well-known ones being iterative algebraic algorithms and algorithms based on Fourier analysis of the projection data. All these algorithms are called tomographic reconstruction algorithms.

Common tomographic reconstruction algorithms

Some of the most widely used iterative tomographic reconstruction algorithms are the algebraic reconstruction technique (ART), the simultaneous iterative reconstruction technique (SIRT) and the simultaneous algebraic reconstruction technique (SART).[10-12] For example, in the ART algorithm all the pixels of the reconstructed image (2D matrix) are initially set to an arbitrary value. The values of the matrix change during every iteration cycle as it is attempted to create an image whose radon transform matches the (experimental) projection data. Algebraic iterative algorithms offer the advantage of applying constraints during the image reconstruction process (e.g. force the pixels to only have non-negative values) but they are significantly slower compared to the ones based on Fourier analysis of the projection data. It should be noted though that there is continuous effort by the scientific community to develop new tomographic reconstruction algorithms that are both more efficient and more robust.[13]

The back-projection algorithm is the simplest of all tomographic reconstruction algorithms. As the name implies, the reconstructed image, it initially being an empty matrix, acts as a canvas on which the projection spectra (Figure 6) are painted. This means that each projection spectrum is smeared back through the image in the direction they were collected during the tomographic scan (tomographic angle). As a result, the reconstructed image is the result of the sum of the back-projected projection spectra. However, the back-projection algorithm, although conceptually simple, always yields blurred images. This is because the sampling in the frequency

domain during a CT scan is inhomogeneous (oversampling closer to the centre of the sample – the density of the radial points decreases with increasing distance from the centre of the sample). This is clearly demonstrated on the right side of Figure 6.

The Fourier slice theorem states that the Fourier transform of a projection spectrum of a 2D function *f(x,y)* is equal to a slice through the Fourier transform of *f(x,y)* taken along a line passing the origin in the propagation direction.[9, 14] This means that the Fourier transform projection spectra can be used to create the Fourier transform of the (reconstructed) image (2D frequency spectrum of the image) and then reconstruct the image by taking the inverse Fourier transform. This algorithm is called the direct Fourier reconstruction algorithm. However, as described previously, the sampling in the frequency domain is not homogeneous (as a result from changing from Cartesian to polar coordinates) which means that an interpolation step is required.

The most commonly used tomographic reconstruction algorithm is the filtered back projection algorithm. It can be considered a hybrid of the back projection and the direct Fourier reconstruction algorithms. In the filtered back projection algorithm, the projection spectra are convoluted with a sharpening filter (e.g. ramp filter) before they are back projected. More specifically, the Fourier transform of every projection spectrum is calculated and multiplied by the appropriate filter (the convolution of two functions is equivalent to simple multiplication of their Fourier Transforms). Then the inverse Fourier transform is calculated and back projected in the direction it was collected (the original projection spectrum) during the tomographic scan (tomographic angle). The application of the sharpening filter is used to overcome the blurring of the reconstructed images. This is clearly demonstrated in Figure 7 where the radon transform of a (phantom) image is created and two reconstructed images using the back projection and the filtered back projection are shown. It can be seen that the highly absorbing regions (in the case of X-ray absorption CT) in the sample result follow sinusoidal trajectories in the radon transform and this is the reason why this construction (radon transform) in referred to as a sinogram.

Indeed, the filtered back projection is not only an effective algorithm (dealing with the image blurring) but also a lot faster compared to iterative ones. However, it does

not allow for any constraints to be applied and it is prone to creating artefacts in the reconstructed images if there is angular undersampling (not enough projections) during the acquisition of the tomographic scan.

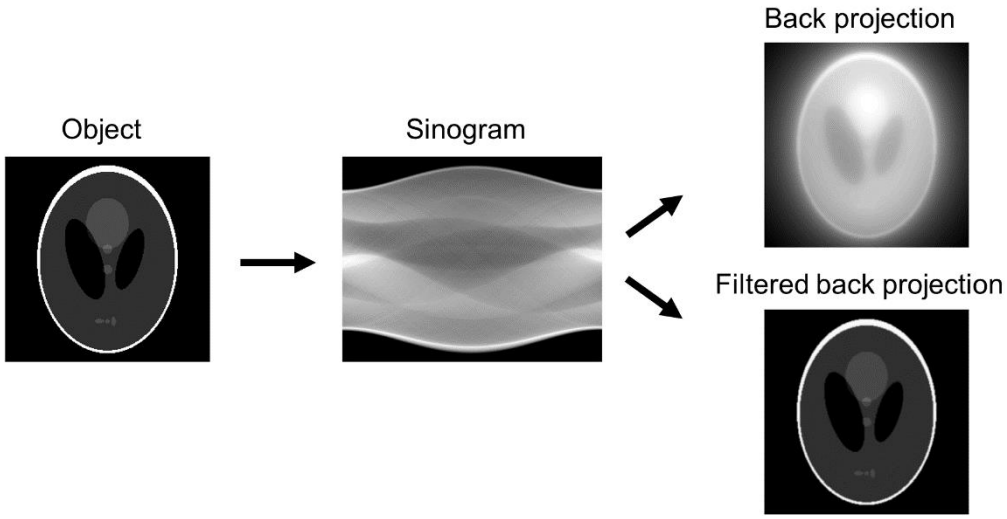

Figure 7: The sinogram of an object (phantom image) is created by calculating the radon transform. The reconstructed images using the back projection and the filtered back projection algorithms are also shown.

X-ray absorption CT is also called micro-CT (also known as MicroComputed Tomography, X-ray tomographic microscopy, computerized microtomography, or just μ-CT) when the pixel size of the reconstructed images is in the μm scale (nowadays typically 1-10 μm).[15] The results from a micro-CT measurement performed in synchrotrons using parallel beam geometry consist a 3D matrix (three spatial dimensions). The raw reconstructed data volume can be used for local characterisation (e.g. morphological features in specific sample regions) or even as a template (after segmenting and generating meshes) for modelling the transport properties of the material. It should finally be mentioned that recent advances in full-field X-ray microscopy or nano-CT, have made possible the acquisition of data volumes with voxel sizes in the nm scale (10s to 100s of nm). Such high resolution X-ray CT data allow to investigate the microstructure of the sample under study and directly quantify physical properties of the sample (e.g. porosity, tortuosity and pore size distribution).[16]

X-ray diffraction computed tomography

The technique of X-ray diffraction computed tomography (XRD-CT) for materials applications was first demonstrated by Harding *et al*. using a laboratory diffractometer.[17] XRD-CT is a non-destructive and non-invasive technique which can provide local structure information with high spatial resolution and resolve microstructure heterogeneities. This chemical tomographic technique, like X-ray fluorescence computed tomography (XRF-CT), X-ray absorption fine structure spectroscopy computed tomography (XAFS-CT) and Pair distribution function computed tomography (PDF-CT), is sensitive to both the chemical state and physical form of the species present in the system, making it an invaluable tool for heterogeneous materials characterisation.[18, 19]

In contrast to X-ray absorption CT, which is based on differences in the attenuation of X-rays passing through materials, XRD-CT exploits differences in the diffraction signal of the crystalline phases present in the sample and the corresponding solid-state chemical species can be separated even if they possess similar densities. In the reconstructed XRD-CT images, each pixel corresponds to a single diffraction pattern allowing the creation of maps corresponding to the different chemical species present in the sample (chemical imaging). It is even possible to obtain three-dimensional (3D) spatial resolution by scanning along the sample height (i.e. by combining XRD-CT data in a 3D 'stack'). This means that the XRD-CT method can provide us with information in 5 dimensions (e.g. 3D spatial and 1D spectral information tracked as a function of time).[19]

XRD-CT is mainly applied at synchrotron facilities where the combination of the brilliant X-rays produced coupled with state-of-the-art detectors allow for dynamic XRD-CT scans with fast acquisition times (i.e. acquisition time of less 100 ms per 2D diffraction pattern).[20] The spatial resolution of the XRD-CT images is determined by the size of the illuminating X-ray beam. One can reduce the beam size down to a few microns (or even below) by using slits but this also decreases the brightness of the X-ray beam and increase the required time to acquire data of decent quality.[21] However, the continuous effort to develop and use more efficient detectors and sophisticated X-ray optics (e.g. use of X-ray refractive lenses to focus the X-ray beam

instead of slits) is bound to not only reduce the acquisition time to perform an XRD-CT scan but also to improve the spatial resolution of the reconstructed images.[19]

Data acquisition

A schematic representation of an XRD-CT experiment is provided in Figure 8. The method relies on a "pencil" beam scanning approach (as in the 1st generation X-ray absorption CT experiments) using a highly collimated or focussed monochromatic beam with, for best counting statistics/speed, scattered X-rays recorded on an area detector. This is typically normal to and centred with respect to the beam.

Typically, the object is translated across the X-ray beam (i.e. perpendicular to the beam axis) with a step size close/same as the horizontal size of the incoming X-ray beam and for every translational step *t*, diffraction patterns are collected using an area detector. The length of the translational scan can be the same as the width of the sample but in practice the value for the length *s* used is higher (i.e. number of translational steps $n = s / t$). This is because one should take into account the imperfection of the sample alignment and also the fact that the sample may move during successive tomographic collections. After a translational scan is completed, the sample is rotated (angular step) and the translational scan is repeated. The angular range usually covered is from 0 to π and the number of angles scanned *m* should be, as in the case of the first generation X-ray absorption CT, equal to the number of translational measurements times π/2 (i.e. $m = n \times \pi/2$). However, in practice, the number of angular steps can be decreased without significant changes in the quality of the collected data.[22]

This type of data acquisition is the simplest one. The various data collection strategies available for the XRD-CT technique are thoroughly discussed in Chapter 4 where a new data collection strategy, termed as interlaced XRD-CT, is also introduced and demonstrated. Last but not least, another data collection strategy is introduced in Chapter 7 which was used to collect ultra-fast XRD-CT scans. This data collection strategy allowed the acquisition of not only the largest 3D-XRD-CT data volume ever reported in literature, at least at the time of writing, but also the fastest single XRD-CT scan.

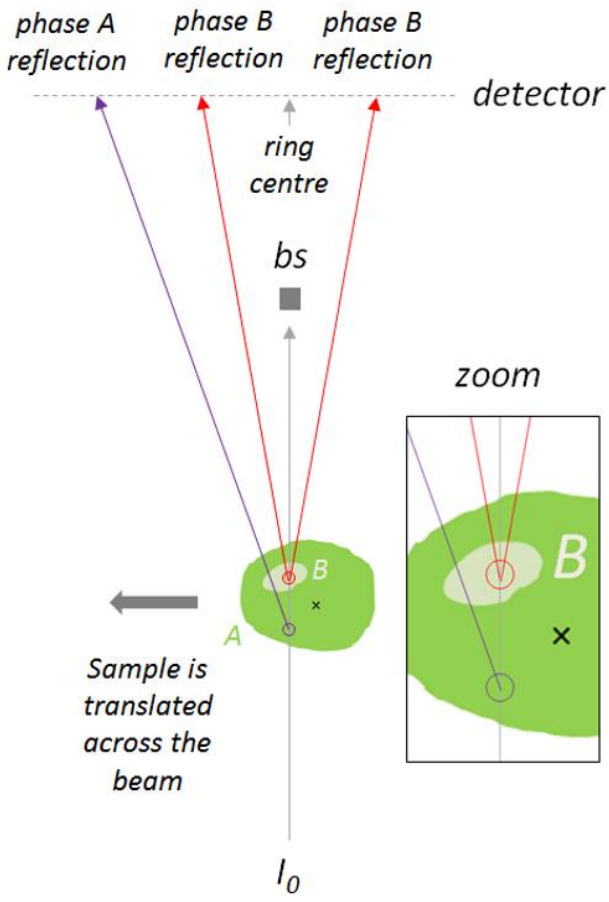

Figure 8: Tomographic plane schematics of XRD-CT experiment. In the schematic the green object consists primarily of phases A (coloured green) with an inclusion of a small amount of phase B (coloured light grey/green). The incident beam is denoted I_0, the detector is protected from the incident beam by use of a beamstop (denoted bs in the schematics). As the object is translated across the beam, diffraction is recorded from the entire path of the incident beam. If A and B are powders, characteristic Bragg reflections from both phases will be recorded on the detector manifesting as diffraction rings on the detector. This is illustrated in the figure where purple ray path indicates a reflection at high 2θ *angles from phase A, and the red paths indicate a single reflection from phase B recorded at low* 2θ *angles on different sides of the detector ring centre.*

Data processing

As mentioned previously, XRD-CT experiments are performed mainly at synchrotron facilities by illuminating a sample with a monochromatic pencil beam and collecting two dimensional diffraction patterns with an area detector. The main steps during the processing of the XRD-CT data can be summarized as the following: [21, 23, 24]

- 2D diffraction patterns are retrieved for every tomographic angle ω (rotation axis) and position *y* (translation axis perpendicular to the beam axis) of the sample.
- The 2D diffraction patterns are converted into 1D diffraction patterns by azimuthal integration.

- A stack of sinograms is created for every observation point in the 1D diffraction patterns. Each sinogram shows the intensity of a single observation point as a function of translation (position *y*) and rotation (angle *ω*) of the sample.
- The XRD-CT images are reconstructed from the sinograms by applying computed tomography techniques (e.g. filtered back projection algorithm or algebraic reconstruction techniques). In these raw XRD-CT images each pixel corresponds to a single diffraction pattern (reconstructed data volume).
- The analysis is performed using the XRD-CT reconstructed data volume. The various options for the analysis are discussed in a following section.

Another option is to perform peak fitting in the projection data and reconstruct features that contain physical/chemical information (e.g. phase distribution maps). However, one has to be careful about this approach as there can be areas in the sample where a specific phase is nanocrystalline, therefore generating very broad diffraction peaks while in other areas the same phase may be highly crystalline leading to the formation of very sharp diffraction peaks. In such a case, the peaks should be probably treated as a two phase problem otherwise it is impossible to apply a correct peak shape function to fit the data. However, if there is a distribution of crystallite sizes, then the peak fitting process becomes more challenging.

In this study, the reconstructed images were obtained using the *reverse analysis* method where the whole projection dataset volume is reconstructed leading to a 3D matrix. In this case, every pixel in the reconstructed XRD-CT image contains/corresponds to a single diffraction pattern.[23]

Line or "streak" artefacts

The most often encountered artefacts in XRD-CT experiments are related to the saturation of pixels in the raw 2D diffraction patterns obtained during the tomographic scans. Artefacts can be generated in the image reconstruction process if the crystallite/domain size of the materials is similar to the size of the X-ray beam.[24] The presence of large crystallites in the sample can lead to single-crystal-like spots in the 2D diffraction patterns and not smooth Debye-Scherrer rings. When a pixel in the

sinograms possesses a significantly higher intensity compared to the surrounding pixels, the reconstructed image will have artefacts. These artefacts have the form of lines or "streaks". This problem is thoroughly discussed in the Chapter 3 where a new filtering strategy is presented that allows the suppression/removal of such artefacts from XRD-CT data.

Physico-chemical information from XRD-CT

XRD-CT is essentially a powder XRD experiment with high spatial resolution. This means that it is possible to extract all the information typically available in a powder diffraction pattern. In the case of XRD-CT, the reconstructed data compose a 3D matrix where two dimensions are spatial and one dimension is spectral (diffraction patterns in the case of XRD-CT, spectra in the case of spectroscopic-CT techniques like XRF-CT and XAFS-CT). Therefore, it is possible, depending of course on the quality of the collected diffraction patterns, to:

- Create phase distribution maps of the various crystalline phases present in the sample. These maps can be created either by:
    1. Calculating the summed image over a specific $2\theta/d/Q$ region (3^{rd} dimension of the reconstructed 3D matrix) where a diffraction peak of interest is present. This is not the preferred way as it does not involve background subtraction but it is a quick way to obtain some information regarding the location the crystalline phases (e.g. if a phase of interest is uniformly distributed in the sample under study or if it is mainly present at specific regions of the sample).
    2. Batch-fitting of a single or multiple peaks. Diffraction peaks of interest are chosen (typically the highest intensity peaks of each crystalline phase) and batch-fitting of the reconstructed XRD-CT data is performed. The background is modelled usually by using a polynomial and the diffraction peaks are fitted using a peak shape function (e.g. Gaussian, Lorentzian and Pseudo-Voigt). The phase distribution maps correspond to the obtained areas of the fitted peaks.
    3. Performing full profile analysis of the reconstructed XRD-CT data. This is the most challenging approach as it requires data with decent

signal-to-noise ratio. To clarify, this approach typically involves (quantitative) Rietveld analysis of 10s of thousands of diffraction patterns (i.e. per XRD-CT dataset). The phase scale factors obtained from Rietveld analysis of XRD-CT data can be used to create phase distribution maps. Maps corresponding to weight fraction of each crystalline phase can also be created.

- Perform phase identification of unknown phases (even minor ones) which can sometimes be challenging in traditional bulk powder XRD measurements. For example, a summed diffraction pattern extracted from a sample region where an unknown phase is in high concentration (strong diffraction signal) can make the phase identification significantly easier. Similarly, minor unknown phases which can missed in bulk powder XRD measurements (average chemical signal) can be identified with XRD-CT. Examples appear throughout this work, (Chapters 3-7) where localized phases have been identified which would otherwise have been unobservable. Although this is a major advantage it also means that the reconstructed data have to be rigorously inspected and there is a need for the development of algorithms to aid this process.
- Estimate crystallite size and strain and create 2D images where the intensity of each pixel corresponds to a specific value of the former physical properties.
- Create maps corresponding to the unit cell parameters of the various crystalline phases present in the sample which can provide not only chemical but also physical information about the system under study (requires full profile analysis of the XRD-CT data). For example, in case of high temperature XRD-CT experiments, it is possible to observe if the temperature distribution is uniform (uniform distribution of the unit cell volume maps) in the sample under investigation or not (uneven distribution of the unit cell volume maps).
- Rietveld analysis of the XRD-CT data can also provide maps of the atomic displacement parameters (thermal parameters) and the occupancies of the atoms present in the unit cell. Rietveld refinement of the reconstructed XRD-CT data was first demonstrated by Wragg *et al*. using SAPO-34 zeolite catalyst.[25]

In this study, almost all the previous approaches were used to process and analyze the XRD-CT data obtained from the *in situ* and *operando* experiments presented in Chapters 5-7. Batch-fitting of a single or multiple peaks was performed when the quality of the diffraction patterns did not allow Rietveld analysis of the reconstructed XRD-CT data volumes. In Chapter 5, Rietveld analysis of XRD-CT data was performed using the MultiRef framework.[26] The MultiRef code is written in MATLAB and it allows the use of parallel computing to perform Rietveld analysis with GSAS.[27] Unfortunately, as it will be discussed in more details in the respective chapter, GSAS is not robust enough for the Rietveld analysis of XRD-CT data. Of course, this is to be expected as it was not designed for the analysis of tomographic data. The Rietveld analysis of the XRD-CT data presented in Chapters 6 and 7 was performed using the TOPAS software package which proved to be very robust but is also an expensive commercial software package.[28]

References

1. Röntgen, W.C., *On a new kind of rays.* Science, 1896. **3**(59): p. 227-231.
2. Smart, L.E. and E.A. Moore, *Solid State Chemistry: An Introduction*. 2012: CRC Press, Talor & Francis group.
3. Niemantsverdriet, J.W., *Spectroscopy in Catalysis: An Introduction*. 2007: Wiley-VCH.
4. Cockcroft, J.K. and P. Barnes, *Advanced Certificate in Powder Diffraction on the Web*. Birkbeck College, University of London.
5. Rietveld, H., *A profile refinement method for nuclear and magnetic structures.* Journal of Applied Crystallography, 1969. **2**(2): p. 65-71.
6. Pawley, G., *Unit-cell refinement from powder diffraction scans.* Journal of Applied Crystallography, 1981. **14**(6): p. 357-361.
7. Le Bail, A., H. Duroy, and J.L. Fourquet, *Ab-initio structure determination of LiSbWO6 by X-ray powder diffraction.* Materials Research Bulletin, 1988. **23**(3): p. 447-452.
8. Hounsfield, G.N., *Computerized transverse axial scanning (tomography): I. Description of system.* British Journal of Radiology, 1973. **46**(552): p. 1016-1022.
9. Radon, J., *ON THE DETERMINATION OF FUNCTIONS FROM THEIR INTEGRAL VALUES ALONG CERTAIN MANIFOLDS.* IEEE Transactions on Medical Imaging, 1986. **MI-5**(4): p. 170-176.
10. Gordon, R., R. Bender, and G.T. Herman, *Algebraic Reconstruction Techniques (ART) for three-dimensional electron microscopy and X-ray photography.* Journal of Theoretical Biology, 1970. **29**(3): p. 471-476,IN1-IN2,477-481.
11. Andersen, A.H. and A.C. Kak, *Simultaneous Algebraic Reconstruction Technique (SART): A superior implementation of the ART algorithm.* Ultrasonic Imaging, 1984. **6**(1): p. 81-94.
12. Gilbert, P., *Iterative methods for the three-dimensional reconstruction of an object from projections.* Journal of Theoretical Biology, 1972. **36**(1): p. 105-117.

13. Beister, M., D. Kolditz, and W.A. Kalender, *Iterative reconstruction methods in X-ray CT.* Physica Medica, 2012. **28**(2): p. 94-108.
14. Als-Nielsen, J. and D. McMorrow, *Imaging*, in *Elements of Modern X-ray Physics*. 2011, John Wiley & Sons, Inc. p. 305-342.
15. Stock, S.R., *MicroComputed Tomography: Methodology and Applications*. 2008: CRC Press.
16. Liu, Y., et al., *To get the most out of high resolution X-ray tomography: A review of the post-reconstruction analysis.* Spectrochimica Acta Part B: Atomic Spectroscopy, 2016. **117**: p. 29-41.
17. Harding, G., J. Kosanetzky, and U. Neitzel, *X-ray diffraction computed tomography.* Medical Physics, 1987. **14**: p. 515-525.
18. Grunwaldt, J.-D., J.B. Wagner, and R.E. Dunin-Borkowski, *Imaging Catalysts at Work: A Hierarchical Approach from the Macro- to the Meso- and Nano-scale.* ChemCatChem, 2013. **5**(1): p. 62-80.
19. Beale, A.M., et al., *Progress towards five dimensional diffraction imaging of functional materials unders process conditions.* Coordination Chemistry Reviews, 2014.
20. Kleuker, U., et al., *Feasibility study of x-ray diffraction computed tomography for medical imaging.* Physics in Medicine and Biology, 1998. **43**(10): p. 2911-2923.
21. O'Brien, M.G., et al., *Active phase evolution in single Ni/Al2O3 methanation catalyst bodies studied in real time using combined μ-XRD-CT and μ-absorption-CT.* Chemical Science, 2012. **3**(2): p. 509.
22. Álvarez-Murga, M., P. Bleuet, and J.L. Hodeau, *Diffraction/scattering computed tomography for three-dimensional characterization of multi-phase crystalline and amorphous materials.* Journal of Applied Crystallography, 2012. **45**(6): p. 1109-1124.
23. Bleuet, P., et al., *Probing the structure of heterogeneous diluted materials by diffraction tomography.* Nature Materials, 2008. **7**(6): p. 468-472.
24. Alvarex-Murga, M., et al., *Microstructural mapping of C60 phase transformation into disordered graphite at high pressure, using X-ray diffraction microtomography.* Journal of Applied Crystallography, 2011(44): p. 163-171.
25. Wragg, D.S., et al., *Rietveld analysis of computed tomography and its application to methanol to olefin reactor beds.* Journal of Applied Crystallography, 2015. **48**(6): p. 1719-1728.
26. Frolich, S. and H. Birkedal, *MultiRef: software platform for Rietveld refinement of multiple powder diffractograms from in situ, scanning or diffraction tomography experiments.* Journal of Applied Crystallography, 2015. **48**(6): p. 2019-2025.
27. Dreele, A.C.L.R.B.V., *General Structure Analysis System (GSAS)*. 2000: USA. p. 86-748.
28. *TOPAS Version 5.0*. Bruker AXS: Karlsruhe, Germany.

CHAPTER 3: Removing multiple outliers and single crystal artefacts from X-ray diffraction computed tomography data

Abstract

In this chapter, a simple but effective filtering approach to deal with single crystal artefacts in X-ray diffraction computed tomography (XRD-CT) is reported. In XRD-CT, large crystallites can produce spots on top of the powder diffraction rings, which after azimuthal integration and tomographic reconstruction, lead to line/streak artefacts in the tomograms. In the simple approach presented here, the polar transform of collected 2D diffraction patterns is calculated followed by directional median/mean filtering prior to integration. Reconstruction of 1D diffraction projection datasets treated in such a way leads to very significant improvement in reconstructed image quality for systems that exhibit powder spottiness arising from large crystallites. This approach is not computationally heavy which is an important consideration with big datasets and such as is the case with XRD-CT. The method should have application to 2D X-ray diffraction data in general where such spottiness arises. This work was published at the peer reviewed Journal of Applied Crystallography: *Vamvakeros, A., Jacques, S. D. M., Di Michiel, M., Middelkoop, V., Egan, C. K., Cernik, R. J. & Beale, A. M. (2015), Journal of Applied Crystallography 48, 1943-1955.*

Introduction

XRD-CT marries traditional computed tomography with conventional powder XRD offering a powerful chemical imaging method.[1-3] It was first demonstrated using laboratory X-ray radiation but its potential has been more fully realised using synchrotron radiation.[4] Local diffraction signals can be extracted that allow not only

the observation and identification of materials that conventional methods such as powder XRD may be blind to, but also the extraction of local chemical and physical information.[5, 6] Obtaining this spatially resolved information is essential in materials science. For example, the distribution of different crystallographic phases and/or elements in a heterogeneous catalyst is expected to directly affect its performance.[7, 8] One can readily make the argument that such methods will become standard methods to characterise materials, like conventional X-ray imaging (μCT) and classical in situ X-ray powder diffraction. Indeed, this is reflected in the gaining popularity of XRD-CT and there is now a number of material studies and developmental publications in this area.[5, 9-20] Especially in the field of heterogeneous catalysis, XRD-CT has already proven to be a powerful characterization tool used for spatially resolved studies as it allows catalytic reactors to be studied intact and under real process conditions.[6, 21-24]

Despite this interest, there are several issues that need to be addressed before the technique can be more widely adopted and these are mostly associated with treatment and processing of collected data. Included in this are problems associated with crystallite size of materials composing the scanned object. The issues of small crystallites leading to the loss of Bragg diffraction has been addressed by the development of pair distribution function computed tomography (PDF-CT), but to date, there is no adequate procedure for dealing with or preventing the artefacts caused by large crystallites.[25] The problem faced becomes a greater issue with higher resolution XRD-CT scans where the use of smaller beams can lead to substantial deviations from the ideal powder condition.

X-ray Diffraction Computed Tomography

Before elaborating further on this specific problem and the attempts to date to address this, the XRD-CT principle and experiment are briefly described. The method relies on a pencil beam scanning approach using a highly collimated or focussed monochromatic beam with, for best counting statistics/speed, scattered X-rays recorded on an area detector. This is typically normal to and centred with respect to the beam. If the object under study behaves as a powder, the images obtained will be 2D powder patterns containing powder diffraction rings. Each pattern contains

the integral diffraction contributions seen by the detector from the entire length of the beam, so for a 5 mm diameter sample centred on the beam, ignoring the air scatter from outside the sample, the detector will see diffraction contributions from the entire 5mm length the beam is passing through.

There are several existing approaches to the collection but in all cases the translational scan should be of sufficient size that the object is totally scanned for all measured angles. In many cases though, one may need to perform a translational scan smaller than the cross section of the sample (e.g. avoid scanning the whole *in situ* cell in case of a fixed bed reactor). However, this means that the diffracting/scattering contribution from these parts of the sample cannot be easily separated/removed from the acquired data. Regarding the angular scan, in most cases it is sufficient to scan angles from 0 to π.

The raw data is thus a 4D projection dataset of size $n \times m \times p \times q$ where n is translational sampling, m is rotational sampling and $p \times q$ is the area detector size. As in the case of the first generation X-ray computed tomography, according to the Nyquist sampling theorem, the number of angles scanned should be equal to the number of translational measurements times $\pi/2$ (i.e. $m = n \times \pi/2$). However, in practice, the number of angular steps can be decreased without significant changes in the quality of the collected data.[26] Most typically, the raw 4D dataset is reduced by azimuthal integration such that diffraction intensity is stored as a 3D projection dataset of size $n \times m \times r$ where r is the number of radial steps, and this 3rd dimension represents the scattering angle 2θ. Features can be extracted from the projection dataset and reconstructed to real space images (of size $n \times n$) using filtered back projection or algebraic reconstruction methods.[27, 28] An alternative approach, termed *the reverse analysis method*, is to reconstruct each of the r sinograms to real space images to produce an $n \times n \times r$ image set which represents reconstructed diffraction patterns for all of the pixels in the measured slice.[4]

The single crystal artefact problem

For objects composed of small randomly orientated crystals the projected diffraction patterns contain 'powder' rings. Where the crystal size is large with respect to the

size of the incident beam this moves towards a more single-crystal behaviour and spots appear in the recorded diffraction patterns.[29] This phenomena is well understood but it is important to highlight some points. By large crystallites, here we mean those which represent a large number of repeat crystallographic units. As such, they tend to give rise to strong diffraction signals when lying in a position to satisfy the Bragg condition leading to high intensity spots on the detector.

When the incident X-ray beam is small, there is a smaller number of crystallites in the diffracting volume and as such a larger number of spots appear in the recorded diffraction pattern. More specifically, the spottiness arises from the combination of strong diffraction of favoured orientations and accentuated by a lower population of crystallites which are, by statistical consequence, less randomly orientated. As a result, the diffraction signal generated by each sample volume element (voxel) consists of two components: one which is independent on the voxel orientation (i.e. signal produced by the small crystallites randomly oriented) and one which is dependent on the orientation (i.e. signal produced by the large crystallites). Panel A of Figure 1 shows an example 2D diffraction image exhibiting such spottiness. When radially integrating spotty powder patterns, the integral intensity can deviate significantly from that which would arise from an ideal powder sample.

This can be further exacerbated in XRD-CT where, by the nature of the tomographic collection procedure, the orientation of the studied object favours the measurement of some planes at the expense of others. XRD-CT produces artefact-free images only when the scattering power of every scanned sample volume element (voxel) is independent from the sample orientation. If this condition is not met, then the spotty powder patterns will cause spottiness within the sinogram constructions, as is shown in Panel B of Figure 1, leading to streak artefacts in the reconstructed images, as is shown in Panel C of Figure 1. This phenomenon can be a major problem in XRD-CT data as if the artefacts are severe, then the desired spatial information will be lost.

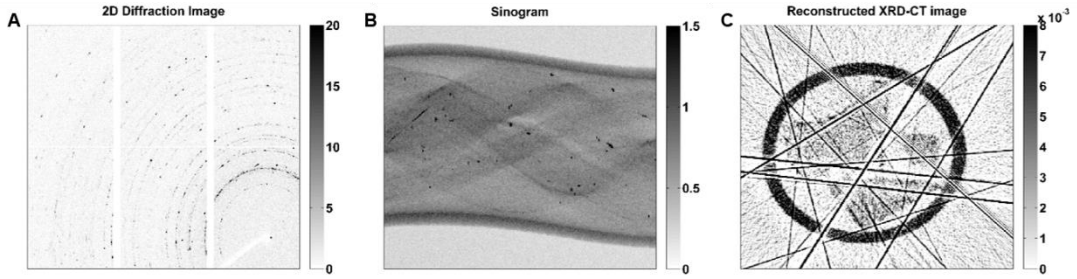

Figure 1: Panel A: A raw 2D diffraction image of 2 % La-2 % Mn-1.6 % Na-3.1 % W/SiO_2 catalyst collected during an XRD-CT scan using a 46 keV monochromatic pencil beam with a spot size of 2.5 x 2.5 µm. Panel B: Sinogram of scattering angle 5.3° 2ϑ corresponding to a SiO_2 cristobalite peak. Panel C: The respective reconstructed XRD-CT image using the Filtered Back Projection algorithm. Color bars indicate intensity in arbitrary units.

Existing strategies for treatment of single-crystal-diffraction artefacts

The ideal filter would remove the spots from the raw powder diffraction images while maintain the intensities of the powder diffraction rings. In XRD-CT, a good approach to mitigate the spottiness problem is to use a continuous angle scanning approach. Here, the data collection is conducted so that the object is rotated at fixed speed about the tomographic axis and diffraction patterns are accumulated over a fixed angular range (equivalent to the angular step in a stop-start approach). This means that during collection crystallites are swept into the diffracting volume and their orientations are constantly changed and with respect to the axis of rotation all angles are equally sampled. This requires continuous rotation in the range 0 to ~ π for each translation. Whilst continuous scanning does not necessarily fully eradicate the streak artefact problem, in practice this is the best approach if circumstances permit. However, there are collection strategies and measurement constraints that preclude such measurement and for such one must look for other ways to deal with spotty data.

A simple approach to deal with spottiness is by applying image filtering techniques to the recorded 2D diffraction images.[26] An image threshold approach has been previously proposed and generally applied in the past. In this method, the pixels that have intensities above the threshold value are excluded in the azimuthal integration [30]. It is important to note here that replacing pixels above the threshold value with zero should be avoided as this would certainly lead to distortion of Bragg intensity after azimuthal integration. The image threshold approach has also been

implemented in recently developed software programs.[31-34] Unfortunately, there are potential problems with this approach. Firstly, the threshold is arbitrary since it must be chosen by the user; for individual or a small number of diffraction patterns a 'satisfactory' result can be obtained by eye but for XRD-CT where the datasets can contain several thousand images it would be obviously unrealistic to check each treated image. One could use a harsh threshold to be fairly confident that spots at a specific 2θ angle were removed but this brings us to a second problem; harsh thresholds reduce acquisition statistics. Finally, such methods do not deal with relatively difference in intensities at different 2θ values: both strong and weak diffraction peaks may exhibit spottiness and obviously a single threshold cannot deal with this and preserve the required information.

Voltolini et al. also reported the limitations of the threshold method to remove spottiness from the raw 2D diffraction images collected during an XRD-CT experiment.[16] The authors proposed a different approach where the contributions from single crystals and powder are separated in XRD-CT data. This is achieved by (1) applying a median filter for each angle projection set, (2) subtracting the filtered images from the raw 2D diffraction images to get a spot pattern, (3) creating masks by setting a threshold using the difference images (involving some image dilation), (4) removing diffraction spots from the raw diffraction images using the masks, (5) replacing the spots in the raw diffraction images with values from the median filtered images; it is claimed that this is better than replacing with zero values), (6) subtracting the images created in step (5) from the raw diffraction images to obtain the large grain images. This approach has some good advantages as it is possible to obtain information about the signal generated from both the large crystallites and the powder. Nevertheless, this method is computationally heavy, the image dilation in step (3) does not guarantee complete removal of the spots and the powder intensities are not maintained because the intensities are based on in-filled values.

Another potential approach is to apply image filtering techniques directly to the sinogram after azimuthal integration. However, in our experience, standard 1D or 2D median filtering is often not effective at removing these artefacts and leads to loss/blurring of information. A better approach may be to employ a sinusoidal

median filter specifically designed for sinogram treatment but this has yet to be investigated. This is probably not worthwhile though as again the median will lead to blurring, though at least in a desired direction.

A different way to deal with streak artefacts in the reconstructed XRD-CT images is to use a method sometimes applied in conventional X-ray tomography.[35] The intersection of the streaks in the reconstructed images are first found and segmented. This segmented image is then forward projected to arrive at a sinogram which is then subtracted from the original sinogram. This updated sinogram is then back projected to arrive, hopefully, at a streak free image. Although this is a tried and tested method, it requires several computational steps and may not be easily automated or practicable for XRD-CT data.

Herein, we report an alternative approach, which requires minimum user input, to deal with multiple outliers and spottiness in 2D diffraction images. We compare the effect of different filters applied directly to the raw 2D diffraction images collected during an XRD-CT experiments. Data from two experiments on studying the *in situ* chemistry of working catalytic reactors are presented, one with using a monochromatic pencil beam with a spot size of 25 x 25 µm and one with a spot size of 2.5 x 2.5 µm demonstrating the efficacy of this simple filtering approach even with high resolution XRD-CT data. This is important as the assumption of an ideal powder can become less valid with decreasing beam size relative to the average crystallite size of the sample, thus leading to spotty diffraction images.

Materials and Methods

Two different catalytic reactors were tested at beamline station ID15A of the ESRF. In each case, the reactor was mounted into a gas delivery stub, itself mounted to a standard goniometer. The goniometer was fixed to a rotation stage set upon a translation stage to facilitate the movements required for the CT measurement. Heating was achieved by virtue of two hot air blowers heating each side of the catalytic membrane reactor. A state-of-the-art PILATUS3 X CdTe 300K hybrid photon counting area detector, which uses cadmium telluride (CdTe) as the semiconducting direct conversion layer, was used to record the 2D diffraction patterns. Tomographic

reconstruction was performed using filtered back projection (FBP). The MATLAB (The MathWorks Inc., Natick, MA, USA) scripts used in this work are provided in the Appendix.[36]

The first reactor tested was a catalytic membrane reactor (CMR) for the oxidative coupling of methane (OCM) to produce C2 molecules. The 2 % Mn-1.6 % Na-3.1 % W/SiO_2 catalyst bed was packed inside a $BaCo_{0.4}Fe_{0.4}Zr_{0.2}O_{3-\delta}$ (BCFZ) hollow-fibre BCFZ membrane (2.4 mm diameter and 180 µm wall thickness). The catalyst bed was supported with glass wool. Details of the preparation of catalyst and membranes are given in Chapters 5 and 7 respectively. XRD-CT measurements were performed using a 93 keV monochromatic pencil beam with a spot size of 25 x 25 µm. The XRD-CT measurements were made with 140 translations over 180° in 1.8° steps covering a physical area of 3.5 x 3.5 mm. Reconstruction of these data yielded XRD-CT images with 140 x 140 pixels and 25 µm resolution.

The second reactor was a fixed bed reactor consisting of a 2 % La-2 % Mn-1.6 % Na-3.1 % W/SiO_2 catalyst bed supported with glass wool. Details of the preparation of catalyst are given in Chapter 5. XRD-CT measurements were performed using a 46 keV monochromatic pencil beam with a spot size of 2.5 x 2.5 µm. The XRD-CT measurements were made with 300 translations over 180° in 0.75° steps covering a physical area of 750 x 750 µm. Reconstruction of these data yielded XRD-CT images with 300 x 300 pixels and 2.5 µm resolution.

Results & Discussion

A simple method is proposed that treats the original 2D diffraction data collected from an XRD-CT experiment (e.g. Panel A of Figure 2). Firstly, the raw 2D diffraction images are polar transformed to arrive at images illustrated in Panel B of Figure 2. In the polar transformed image, there are zero elements which were generated as a result of binning the data because only part of the powder diffraction rings were collected (i.e. azimuthal range smaller than 0 to 2π). A mask has to be applied to set the values of these pixels to NaN (not a number) values so that these elements are not taken into account during the image reconstruction process. The mask can be created by using either a 2D diffraction image acquired by testing a standard (e.g.

CeO_2 NIST standard) or any 2D diffraction image acquired during the actual XRD-CT experiment. The pixels with zero intensity generated by binning the data have to be separated from the pixels with zero intensity in the raw 2D images. This is done by: a) setting the value of the pixels in the raw 2D image that have zero intensity to an arbitrary positive value (e.g. one), b) performing the polar transformation and c) setting the zero values to NaN and the rest to one. In cases where there are pixels in the raw 2D images with negative or extreme values, these are set to zero before the polar transformation and are then converted to NaN values. The mask that was created for processing the XRD-CT data is presented in Panel C of Figure 2.

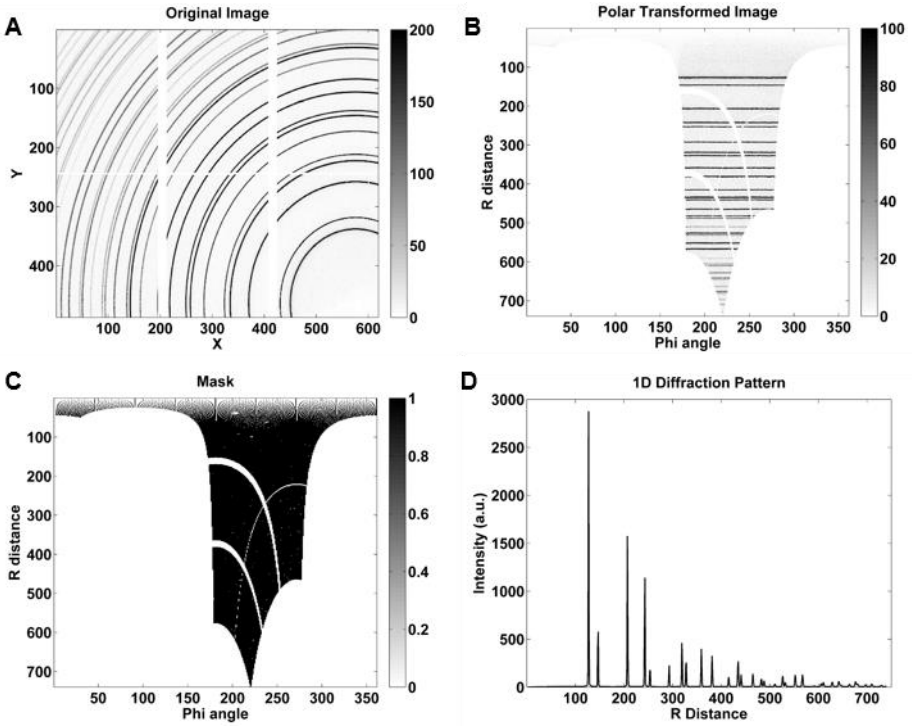

Figure 2: Panel A: Original 2D diffraction data of CeO_2 standard. Panel B: The transformed image in polar coordinates. Panel C: The binary mask containing ones and NaN values. Panel D: The derived 1D diffraction pattern is a vector whose elements are the mean values of each row in the polar transformed image after the application of the mask. Color bars indicate intensity in arbitrary units.

It is important to note that this mask needs to be created only once per XRD-CT experiment, it does not require any user input and is then used for processing all the raw 2D diffraction data. More specifically, this is done by multiplying the polar transformed image with the binary mask (i.e. a mask that contains ones and NaN values) and the mean value for each row can be calculated (the developed in-house MATLAB code uses the nanmean function which excludes the NaN values) which generates a vector that represents the respective 1D diffraction pattern (Panel D of

Figure 2). Note, this process yields the same 1D diffraction patterns as the standard azimuthal integration and is also computationally cost equivalent to standard azimuthal integration.

In our recent study, we showed that the crystalline phases present in the 2 % Mn-1.6 % Na-3.1 % W/SiO2 catalyst at ambient conditions are Na_2WO_4, Mn_2O_3, SiO_2 cristobalite and SiO_2 tridymite (see Chapter 6 for more details).[6] We also reported a chemical interaction between the catalyst particles and the BCFZ membrane at the high temperatures required for the OCM reaction which led to the formation of a new stable phase, identified as $BaWO_4$. This solid-state chemical interaction is a thermal effect as it takes place during temperature ramping without the presence of any reactive gases (i.e. before switching to OCM conditions). Unfortunately, the formation of $BaWO_4$, leads also to the formation of large crystallites, themselves giving rise to single-crystal-like diffraction and therefore spottiness in the raw 2D diffraction images. On the other hand, these XRD-CT data present a great opportunity to investigate the effect of different filters during the image reconstruction process. Furthermore, the quality of the sinograms and the reconstructed XRD-CT images corresponding to $BaWO_4$ can serve as a benchmarking tool for the different filters.

In this study, we are presenting the results from a high temperature XRD-CT scan of the CMR (775 °C). The sinograms being presented here are derived from the highest intensity peaks of SiO_2 cristobalite, $BaWO_4$ and Mn_2O_3 phases. More specifically, these sinograms correspond to scattering angles 1.87, 2.26 and 2.80° 2θ respectively (Figure A1 in Appendix). Regarding the BCFZ sinograms, the intensity of the (111) reflection is used (scattering angle 3.22° 2θ). In all the figures presented in this section, a mask has been applied to the reconstructed XRD-CT images setting the value of the pixels outside the sample to zero.

As mentioned previously, when no filter is applied (i.e. equivalent to standard azimuthal integration), the spottiness in the original 2D diffraction images is not suppressed and the reconstructed XRD-CT images contain streak artefacts. In the case of the XRD-CT data presented here, it can be seen in Figure 3 that the reconstructed image corresponding to the $BaWO_4$ phase is full of streak artefacts and useful information cannot be readily extracted concerning this phase. These artefacts

are present to a lesser extent in the image corresponding to the Mn_2O_3 phase and are absent in the images corresponding to the cristobalite and BCFZ phases. Figure 3 is the template which should be used to compare and assess the effectiveness of the different filters presented in this study. At this point, it should be noted that different reconstruction algorithms (i.e. apart from FBP) have also been implemented but the line artefacts remain in the reconstructed images (Figure A2 in Appendix). As a result, in this study, the FBP algorithm was chosen to reconstruct the sinograms after applying the various filters in the polar transformed images as it is a very fast and easy to implement algorithm.

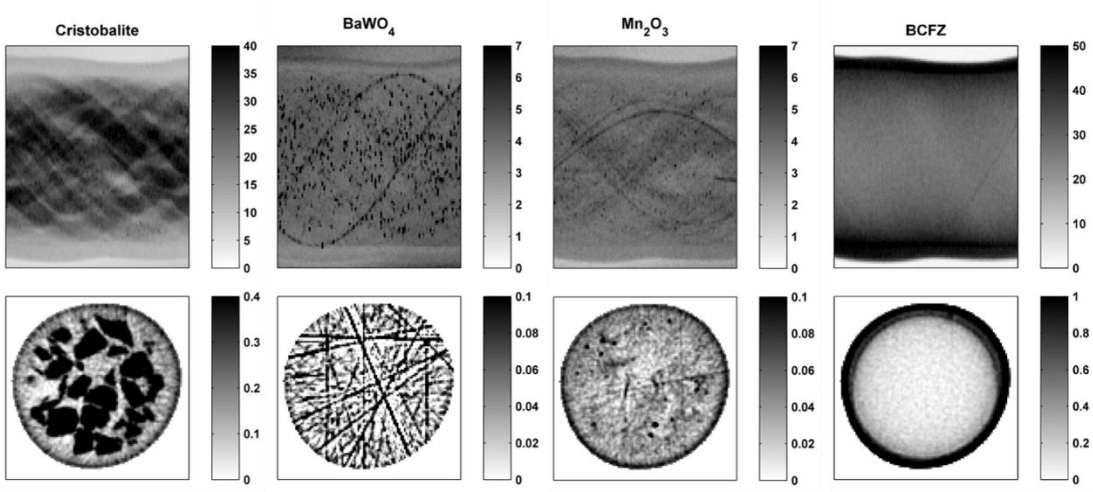

Figure 3: The sinograms of SiO_2 cristobalite, $BaWO_4$, Mn_2O_3, BCFZ and the corresponding reconstructed XRD-CT images are shown when no filter is used (i.e. equivalent to standard azimuthal integration). Color bars indicate intensity in arbitrary units.

The advantage of using the polar transformed images to apply potential filters instead of the raw 2D diffraction images is that a variety of different matrix operations can be easily performed to treat the spottiness. Several different approaches are discussed in the following section.

Median filter

The simplest operation that can be applied is a row-wise median operation. The median value of each row is calculated which is different from the application of a standard median filter to the polar transformed image. Essentially, this means that the values of each row are sorted and the middle value of the population is stored in a vector. The results are presented in Figure 4. The streak artefacts are indeed

removed but this process leads to distorted images due to the crude nature of this filtering operation.

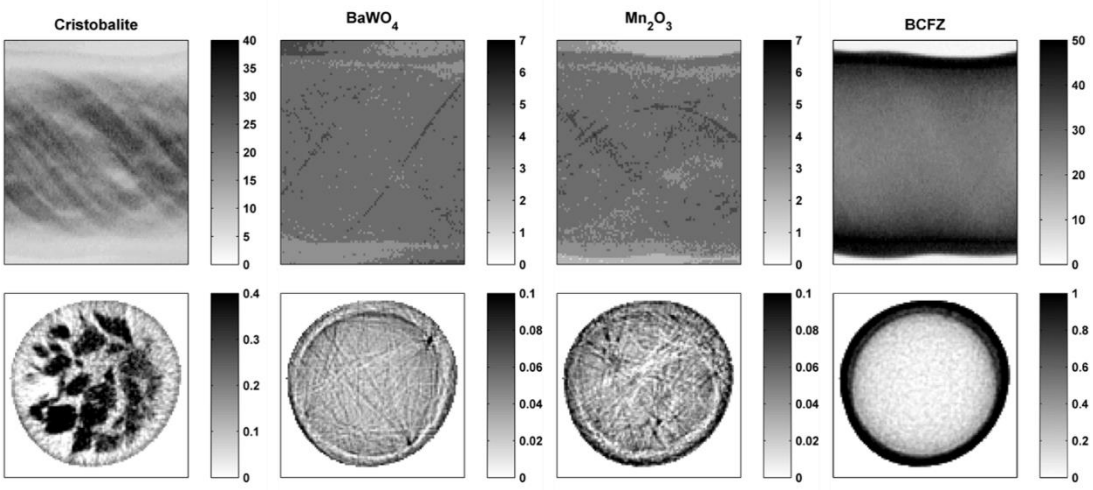

Figure 4: The sinograms of SiO_2 cristobalite, $BaWO_4$, Mn_2O_3, BCFZ and the corresponding reconstructed XRD-CT images are shown when the median value of each row in the polar transformed images is used. Color bars indicate intensity in arbitrary units.

Alpha-trimmed mean filter

Another approach is to apply an alpha-trimmed mean to each row of the polar transformed image.[37] The user is requested to provide a percentage for the trimmed mean. This percentage corresponds to a specific number of pixels p for each row in the polar transformed images. The number p is row dependant as a different number of pixels describe different diffraction peaks in the 2D diffraction images. The values of each row in the polar transformed images are then sorted and the mean value of each row is calculated after excluding the p pixels. The extreme values are removed from both the high and low end (p/2 values respectively) for every row of the polar transformed images and reliable intensities without significant loss of information can be obtained. This is shown in Figure A3 in the Appendix where the CeO_2 1D diffraction pattern has been calculated using different values for the alpha-trimmed mean filter. It is essential to note here that the desired filter should avoid significant decrease in intensity in the obtained 1D diffraction patterns as this would directly alter the chemical information. Although phase distribution maps can still be created when loss of intensity takes place, this should be prevented. If the XRD-CT data are of high enough quality, then sequential whole powder pattern fitting can be performed to create maps showing the change of unit cell parameters, average

crystallite size and in the case of preferred orientation, texture distribution maps.[5] However, reliable intensities are needed if sequential/parametric Rietveld refinement is to be performed. Therefore, the desired filter should be able to remove outliers and deal with single-crystal-diffraction artefacts but at the same time not radically alter the intensities of the other peaks in the derived 1D diffraction patterns.

The effect of the alpha-trimmed mean filters using different percentages (i.e. 0, 1, 2 and 3 %) is shown in Figure 5 where the sinograms and respective images corresponding to $BaWO_4$ are presented; the reason for this choice of display is that the impact of the filters can be readily observed. Indeed, it is impressive that only 2 % trimmed mean is enough to eradicate most of the hotspots in the sinogram while maintaining the main features. The new reconstructed image now reveals the important spatial information that could not be extracted before; the formation of $BaWO_4$ takes place at the interface between the catalyst particles and the inner side of the BCFZ membrane. The effect of a 5, 10, 25 and 50 % alpha-trimmed mean filter has also been investigated but the quality of the reconstructed XRD-CT images does not further improve or deteriorate compared to the 3 % alpha-trimmed mean filter therefore these results are not presented here.

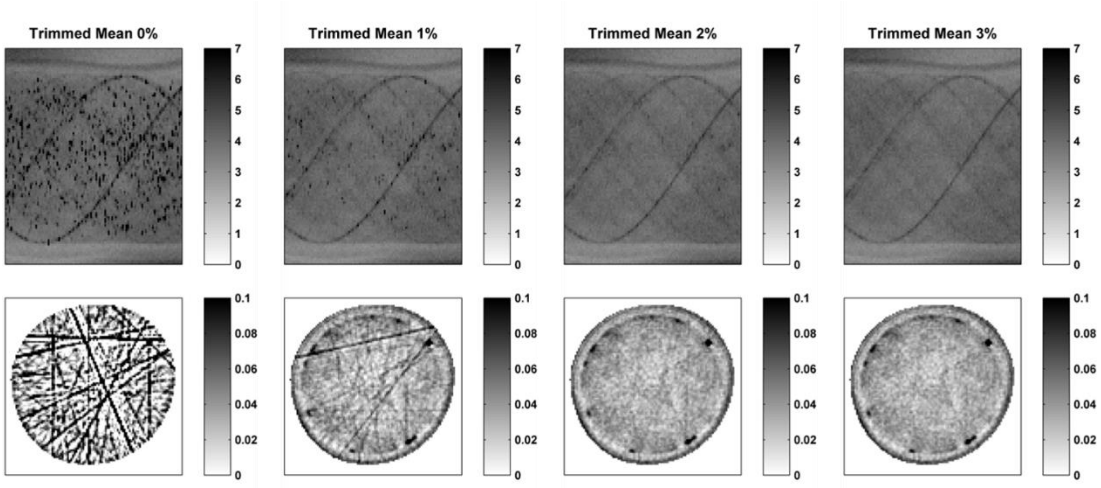

Figure 5: The effect of alpha-trimmed mean filters using different percentages (i.e. 0, 1, 2 and 3%) is shown. The sinograms and respective images correspond to the $BaWO_4$ phase. Color bars indicate intensity in arbitrary units.

In Figure 6, the effect of the 3 % trimmed mean filter is shown. It is important to note that this filter not only removed the artefacts from the $BaWO_4$ XRD-CT image but also improved the quality of the reconstructed images corresponding to the other phases.

This improvement is also observable in the Mn_2O_3 XRD-CT image where minor streak artefacts have been removed, yielding a clearer image.

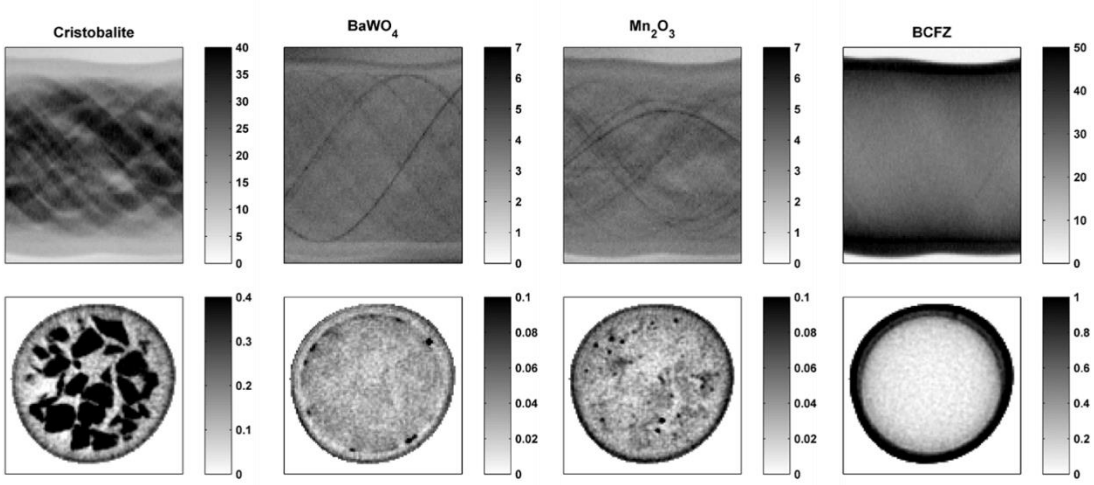

Figure 6: The sinograms of SiO_2 cristobalite, $BaWO_4$, Mn_2O_3, BCFZ and the corresponding reconstructed XRD-CT images are shown when the 3% alpha-trimmed mean filter is used. Color bars indicate intensity in arbitrary units.

Standard Deviation based Trimmed Mean filter

A similar approach to the alpha-trimmed mean one is the application of a trimmed mean that trims values based on the calculated value of the standard deviation of the each row in the polar transformed images. It works as follows: the absolute value of the difference of the between the intensity of every pixel of each row and the mean intensity of that row is calculated. If this calculated value is higher than the value of the standard deviation of that row, then the intensity of the pixels that satisfy this condition is set to NaN value. By replacing the values of these pixels with NaNs, these pixels do not contribute to the statistical result. This means that this filter works in a similar way to an alpha-trimmed mean filter as it removes pixels from both the high and low end (i.e. due to the presence of the absolute in previous condition). However, in the case of the standard deviation based trimmed mean (SDTM) filter, the number of elements excluded in each row of the polar transformed images is not a fixed number but depends on the value of the standard deviation of each row. The user has to specify how many times the standard deviation should be selected as the criterion for the filter to operate.

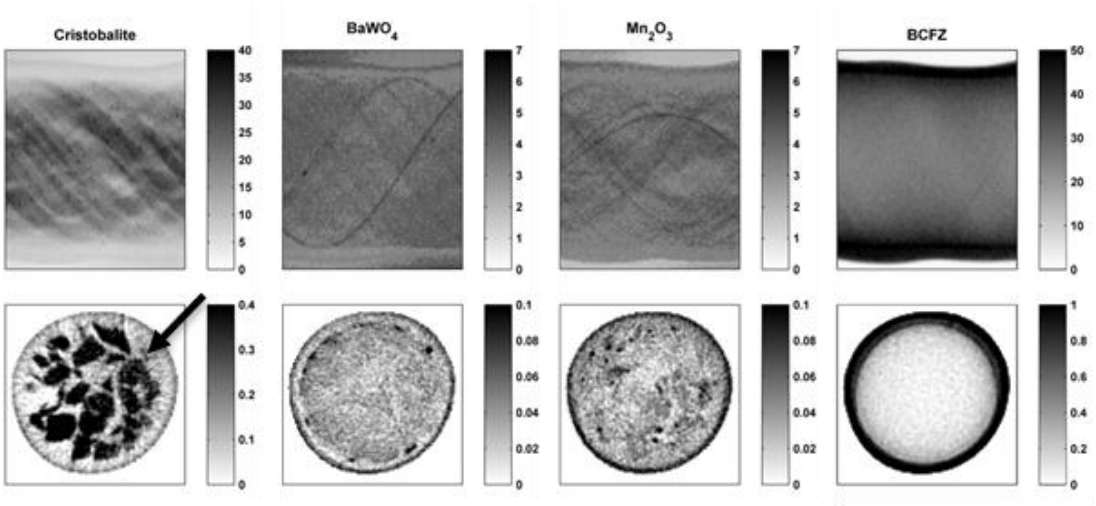

Figure 7: The sinograms of SiO_2 cristobalite, $BaWO_4$, Mn_2O_3, BCFZ and the corresponding reconstructed XRD-CT images are shown when the SDTM filter, using one standard deviation, is applied. Color bars indicate intensity in arbitrary units.

The effect of the adaptive trimmed mean filter using one and three times the standard deviation is shown in Figures 7 and 8 respectively. Where one standard deviation has been applied, most of the artefacts have been removed from the $BaWO_4$ XRD-CT image (Figure 7). However, there is loss of intensity in the cristobalite phase, as highlighted by the arrow in Figure 7. On the other hand, when using three standard deviations, it is shown that the intensity of the cristobalite XRD-CT image is maintained but there are still streak artefacts in the $BaWO_4$ XRD-CT image (Figure 8). This can also be observed by inspecting the $BaWO_4$ sinogram where a significant number of hotspots have not been removed, as highlighted by the arrows in Figure 8. The behaviour of this filter can be rationalised as follows: when there are spotty powder diffraction rings in the raw 2D diffraction images, the value of the calculated standard deviation for the respective row in the polar transformed image can be high enough that not enough pixels are rejected during filtering. Similarly, in cases where the calculated standard deviation is too low, a significant number of pixels may end up being rejected. An alternative approach to the SDTM filter would be to perform the trimming based on a more robust statistical measure, like the median absolute deviation (MAD) estimator, similarly to the Hampel identifier, instead of the value of the standard deviation for each row of the polar transformed images.[38] The Hampel identifier is used to identify outliers which may not be appropriate in the case of very

spotty 2D diffraction images but this remains to be investigated. Unfortunately, it also requires the user to choose a threshold value.

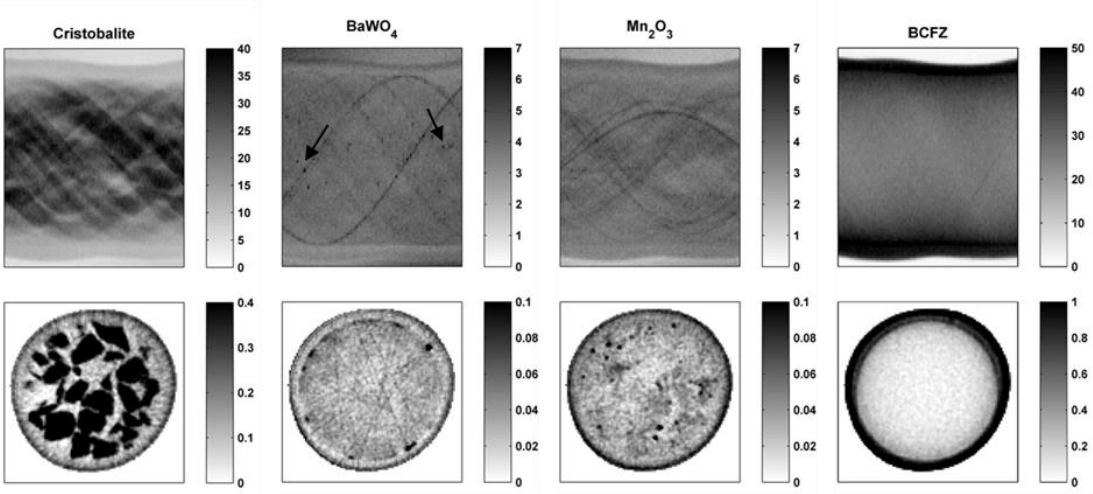

Figure 8: The sinograms of SiO_2 cristobalite, $BaWO_4$, Mn_2O_3, BCFZ and the corresponding reconstructed XRD-CT images are shown when the SDTM filter, using three times the standard deviation, is applied. Color bars indicate intensity in arbitrary units.

2-D Order Statistic Median filters

Finally, an alternative method to deal with spottiness in the raw 2D diffraction images is to apply local order statistic filters to the polar transformed images.[39] The three filters presented here are *n*th rank-order filters.[40] This local filtering process requires a few extra steps as certain software programs may not be able to handle correctly the NaN values present in the polar transformed images after the application of the binary mask (Panel C of Figure 2). For example, the developed MATLAB in-house script uses the *ordfilt2* function that allows the user to create custom 2-D order-statistic filters but fails if there are NaN values present in the image to be processed. Fortunately, there is a quick way to overcome this problem. For every row in the polar transformed images, the pixels that have NaN values are moved to the end of the row (Panel A of Figure 9). It is important to note here that this matrix operation is not equivalent to sorting the values because the application of a filter (e.g. local median filter) to a row with sorted values will radically alter the results. The next step is to create another binary image containing ones and NaN values which will be used as a mask later on (Panel B of Figure 9). Finally, the NaN values in the transformed image are set to zero, the desired filter is applied to the transformed image and the new image is multiplied with the new mask. As before, the respective 1D diffraction

pattern is a vector whose elements are the mean values of each row (Panel C of Figure 9). Also it should be noted that these local filters can be combined very easily with the ones previously mentioned in this study (e.g. first apply the local median filter and then a trimmed mean filter).

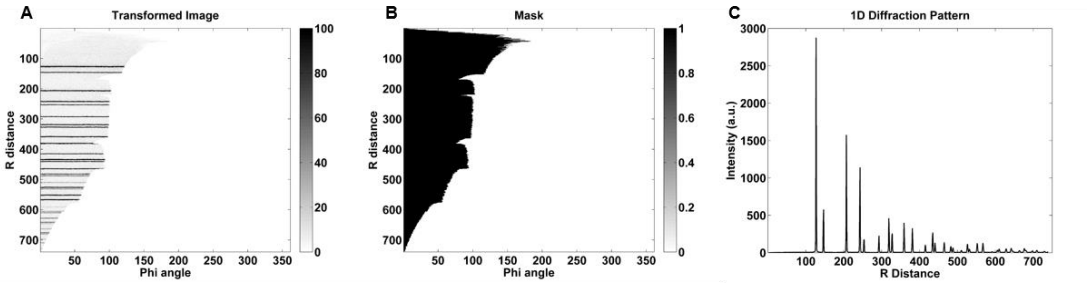

Figure 9: Panel A: The transformed image in polar coordinates. Panel B: The binary mask containing ones and NaN values. Panel C: The derived 1D diffraction pattern is a vector whose elements are the mean values of each row in the polar transformed image after the application of the mask. The 2D diffraction image using the CeO_2 presented in Figure 2 is used. Color bars indicate intensity in arbitrary units.

The effect of local median filters is shown in Figure 10, where the sinograms and respective images corresponding to $BaWO_4$ are presented. A simple filter that can be applied is the traditional median filter where the domain of operation is a three by three matrix (i.e. eight neighbouring pixels). As can be seen in Figure 10, although most of the hotspots have been removed in the sinograms not all have been eradicated which leads to the formation of a few streak artefacts in the reconstructed images. The next filter is a cross median filter where the domain of operation is again a three by three matrix but only the north, east, west and south neighbouring pixels are taken into account. This filter eradicates the hotspots in the sinogram but at the expense of losing intensity which can be easily observed in the respective reconstructed image. Last but not least, a median row filter [1 1 1 1 1] is applied which blurs information only in the horizontal direction. The domain of operation for this filter is a five by one matrix where the first and second, east and west, neighbouring pixels are taken into account. This filter shows promising results as it eradicates the hotspots in the sinogram without any significant loss of intensity.

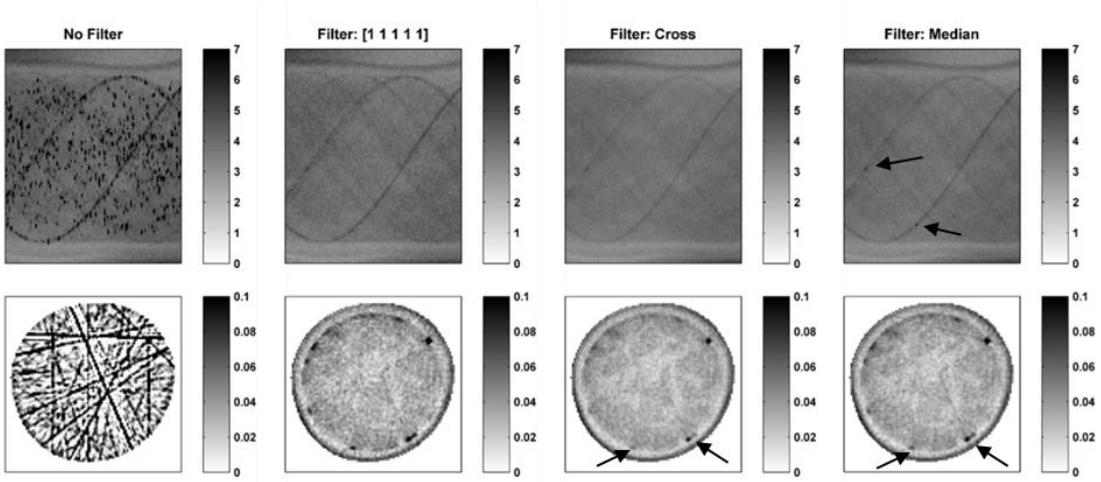

Figure 10: The effect of different local median filters (i.e. a 1 x 5 row, a cross and a 3 x 3 median filter) is shown. The sinograms and respective reconstructed images correspond to the BaWO4 phase. Color bars indicate intensity in arbitrary units.

In Figure 11, the effect of the median row filter [1 1 1 1 1] is shown. It shown that this filter did not only eradicate the artefacts associated with the $BaWO_4$ images but it also improved the Mn_2O_3 images. Unfortunately, there is loss of intensity in the SiO_2 cristobalite images (i.e. both in the sinogram and the corresponding reconstructed image as highlighted by the arrow in Figure 11) compared to images created with standard azimuthal integration (Figure 3) and the 3% trimmed mean filter (Figure 6).

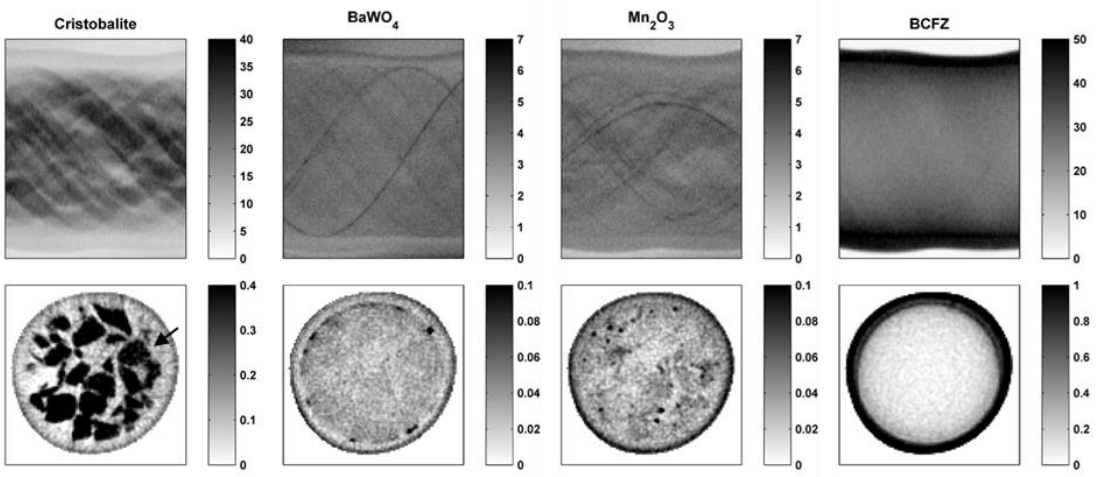

Figure 11: The sinograms of SiO_2 cristobalite, $BaWO_4$, Mn_2O_3, BCFZ and the corresponding reconstructed XRD-CT images are shown when the median row filter [1 1 1 1 1] is used. Color bars indicate intensity in arbitrary units.

High Resolution XRD-CT Data

The results from a high resolution XRD-CT scan of a 2 % La-2 % Mn-1.6 % Na-3.1 % W/SiO_2 catalyst at ambient conditions are shown in Figure 12. The sinograms being

presented here are derived from raw scattering intensity of SiO_2 cristobalite, SiO_2 tridymite, SiO_2 quartz and Na_2WO_4 phases. More specifically, these sinograms correspond to scattering angles 4.86, 4.04, 4.56 and 2.87° 2θ respectively. As expected, when no filter is applied, the spottiness in the original 2D diffraction images is not suppressed and the reconstructed XRD-CT images contain streak artefacts (Figure 1). As it is shown in Figure 12, all four reconstructed XRD-CT images contain streak artefacts and the desired spatial information is lost.

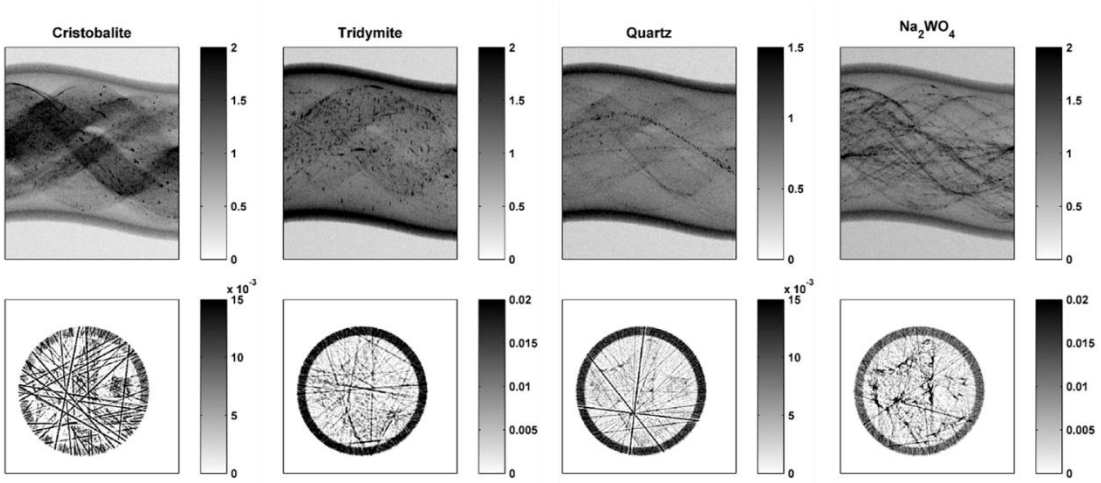

Figure 12: The sinograms of SiO_2 cristobalite, SiO_2 tridymite, SiO_2 quartz, Na_2WO_4 and the corresponding reconstructed XRD-CT images are shown when no filter is used (i.e. equivalent to standard azimuthal integration). Color bars indicate intensity in arbitrary units.

As the 3% alpha-trimmed mean filter showed the best performance for removing the single-crystal-diffraction artefacts from the XRD-CT data collected with the CMR, this filter was chosen to be tested with the spotty 2D diffraction images of the high resolution XRD-CT scan too. The results after the application of the 3% alpha-trimmed mean filter are presented in Figure 13. It can be seen that this filter efficiently removed the artefacts from the all the SiO_2 phases and it improved the quality of the reconstructed images corresponding to the Na_2WO_4 phase. The SiO_2 cristobalite and tridymite phases are homogeneously distributed in the three 2 % La-2 % Mn-1.6 % Na-3.1 % W/SiO_2 catalyst particles while there are hotspots of the SiO_2 quartz phase. More importantly, the Na_2WO_4 phase is preferentially located near the edge of the catalyst particles.

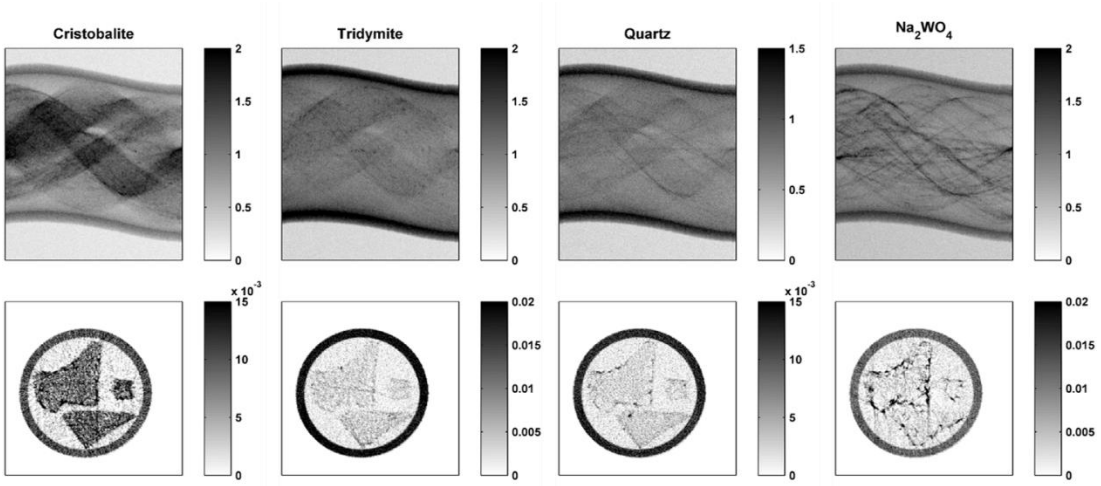

Figure 13: The sinograms of SiO_2 cristobalite, SiO_2 tridymite, SiO_2 quartz, Na_2WO_4 and the corresponding reconstructed XRD-CT images are shown when the 3% alpha-trimmed mean filter is used. Color bars indicate intensity in arbitrary units.

Future Work

The new filtering approach demonstrated here opens new pathways to improve the quality of the reconstructed XRD-CT images as a variety of different filters can be applied to the polar transformed images. Filters including the Winsorised mean, the Hampel filter, the modified trimmed mean filter (MTM), local min and max filters by applying appropriate rank-order filters, local trimmed mean filters (i.e. instead of calculating a single trimmed mean value for each row in the polar transformed images) and local mean filters can be tested.[37, 41] The effect of adaptive filters, like the adaptive median filter, the adaptive trimmed mean filter (both symmetrical and unsymmetrical) and their variations can also be explored.[42-47] The potential of recently developed arithmetic filters, which avoid the slow process of sorting the values, like the iterative truncated mean (ITM), the weighted iterative truncated mean (WITM) and the iterative trimmed and truncated mean (ITTM) should also be investigated.[48-50] However, it is essential to note here that all the filters should fulfil another criterion too; the filtering process must be computationally efficient. This criterion should not be treated lightly as a single XRD-CT scan can easily yield tens of thousands of powder diffraction images.

Towards high quality XRD-CT images

The advent of novel, more efficient detectors (e.g. the PILATUS3 X CdTe 300K hybrid photon counting area detector introduced here) along with the continuous effort to

achieve more brilliant and intense hard X-rays produced at third generation synchrotrons (e.g. the Upgrade Programme at the ESRF) is expected to set the XRD-CT technique at the forefront of materials science research.[51] XRD-CT has the potential to be used not only for spatially resolved studies but also for dynamic, time resolved studies leading to five dimensional (i.e. 3D spatial and 1D spectral as a function of time) diffraction imaging.[8] However, this will also lead to a radical increase in the amount of data being collected during a single beam time experiment and efficient, fast and user friendly routes to yield high quality, artefact-free, XRD-CT images will be needed.

Conclusions

We have reported a fast and easy image filtering approach to deal with a common image based problem during the analysis of XRD-CT data. The formation of spots in the raw 2D diffraction images due to single-crystal effects leads also to hotspots in the sinograms and to line/streak artefacts in the reconstructed XRD-CT images. A potential way to overcome this problem is to apply filters to the original 2D diffraction images after transforming them to polar coordinates. In the future, this simple filtering strategy could also be easily implemented in the Python scripts of GSAS-II and PyFAI (which can also be used in combination with the DAWN software), but also in other software programs used for analysis of XRD-CT data, like the XRDUA. We compared different filters and showed that the most promising results are generated with a simple alpha-trimmed mean filter as the streak artefacts can be removed without significant loss of information. This filtering method requires the user to choose a percentage for the trimmed mean and this value is expected to be sample dependant. However, we have shown that the 3% alpha-trimmed mean shows promising result even with high resolution XRD-CT data (i.e. beam with a spot size of 2.5 x 2.5 µm). Future work will focus on the development of a script that can process a single XRD-CT dataset efficiently, using several values so that the user can first inspect the quality of the reconstructed XRD-CT images and then choose the correct value and apply it to the rest of the XRD-CT data collected during an experiment.

References

1. Hounsfield, G.N., *Computerized transverse axial scanning (tomography): I. Description of system.* British Journal of Radiology, 1973. **46**(552): p. 1016-1022.
2. Elliott, J.C. and S.D. Dover, *X-ray microtomography.* Journal of Microscopy, 1982. **126**(2): p. 211-213.
3. Harding, G., J. Kosanetzky, and U. Neitzel, *X-ray diffraction computed tomography.* Medical Physics, 1987. **14**(4): p. 515-525.
4. Bleuet, P., et al., *Probing the structure of heterogeneous diluted materials by diffraction tomography.* Nature Materials, 2008. **7**(6): p. 468-472.
5. Egan, C.K., et al., *Non-invasive imaging of the crystalline structure within a human tooth.* Acta Biomaterialia, 2013. **9**(9): p. 8337-8345.
6. Vamvakeros, A., et al., *Real time chemical imaging of a working catalytic membrane reactor during oxidative coupling of methane.* Chemical Communications, 2015. **51**(64): p. 12752-12755.
7. Grunwaldt, J.-D., J.B. Wagner, and R.E. Dunin-Borkowski, *Imaging Catalysts at Work: A Hierarchical Approach from the Macro- to the Meso- and Nano-scale.* ChemCatChem, 2013. **5**(1): p. 62-80.
8. Beale, A.M., et al., *Progress towards five dimensional diffraction imaging of functional materials under process conditions.* Coordination Chemistry Reviews, 2014. **277–278**: p. 208-223.
9. Stock, S.R., F. De Carlo, and J.D. Almer, *High energy X-ray scattering tomography applied to bone.* J Struct Biol, 2008. **161**(2): p. 144-50.
10. Álvarez-Murga, M., et al., *Microstructural mapping of C60 phase transformation into disordered graphite at high pressure, using X-ray diffraction microtomography.* Journal of Applied Crystallography, 2010. **44**(1): p. 163-171.
11. De Nolf, W. and K. Janssens, *Micro X-ray diffraction and fluorescence tomography for the study of multilayered automotive paints.* Surface and Interface Analysis, 2010. **42**(5): p. 411-418.
12. Palancher, H., et al., *Hard X-ray diffraction scanning tomography with sub-micrometre spatial resolution: application to an annealed γ-U0.85Mo0.15particle.* Journal of Applied Crystallography, 2011. **44**(5): p. 1111-1119.
13. Valentini, L., et al., *Towards three-dimensional quantitative reconstruction of cement microstructure by X-ray diffraction microtomography.* Journal of Applied Crystallography, 2011. **44**(2): p. 272-280.
14. Stock, S.R. and J.D. Almer, *Diffraction microcomputed tomography of an Al-matrix SiC-monofilament composite.* Journal of Applied Crystallography, 2012. **45**(6): p. 1077-1083.
15. Valentini, L., et al., *Multifractal Analysis of Calcium Silicate Hydrate (C-S-H) Mapped by X-ray Diffraction Microtomography.* Journal of the American Ceramic Society, 2012. **95**(8): p. 2647-2652.
16. Voltolini, M., et al., *Understanding cement hydration at the microscale: new opportunities from `pencil-beam' synchrotron X-ray diffraction tomography.* Journal of Applied Crystallography, 2013. **46**(1): p. 142-152.
17. Bonnin, A., et al., *Impurity precipitation in atomized particles evidenced by nano x-ray diffraction computed tomography.* Applied Physics Letters, 2014. **105**(8): p. 084103.
18. Cedola, A., et al., *Three dimensional visualization of engineered bone and soft tissue by combined x-ray micro-diffraction and phase contrast tomography.* Phys Med Biol, 2014. **59**(1): p. 189-201.

19. Jensen, K.M.O., et al., *X-Ray Diffraction Computed Tomography for Structural Analysis of Electrode Materials in Batteries.* Journal of the Electrochemical Society, 2015. **162**(7): p. A1310-A1314.
20. Vanmeert, F., G. Van der Snickt, and K. Janssens, *Plumbonacrite identified by X-ray powder diffraction tomography as a missing link during degradation of red lead in a Van Gogh painting.* Angew Chem Int Ed Engl, 2015. **54**(12): p. 3607-10.
21. Jacques, S.D., et al., *Dynamic X-ray diffraction computed tomography reveals real-time insight into catalyst active phase evolution.* Angew Chem Int Ed Engl, 2011. **50**(43): p. 10148-52.
22. O'Brien, M.G., et al., *Active phase evolution in single Ni/Al2O3 methanation catalyst bodies studied in real time using combined μ-XRD-CT and μ-absorption-CT.* Chemical Science, 2012. **3**(2): p. 509.
23. Beale, A.M., et al., *Chemical imaging of the sulfur-induced deactivation of Cu/ZnO catalyst bodies.* Journal of Catalysis, 2014. **314**: p. 94-100.
24. Price, S.W.T., et al., *In Situ Microfocus Chemical Computed Tomography of the Composition of a Single Catalyst Particle During Hydrogenation of Nitrobenzene in the Liquid Phase.* Angewandte Chemie, 2015. **127**(34): p. 10024-10027.
25. Jacques, S.D., et al., *Pair distribution function computed tomography.* Nature Communications, 2013. **4**: p. 2536.
26. Álvarez-Murga, M., P. Bleuet, and J.L. Hodeau, *Diffraction/scattering computed tomography for three-dimensional characterization of multi-phase crystalline and amorphous materials.* Journal of Applied Crystallography, 2012. **45**(6): p. 1109-1124.
27. Gordon, R., R. Bender, and G.T. Herman, *Algebraic Reconstruction Techniques (ART) for three-dimensional electron microscopy and X-ray photography.* Journal of Theoretical Biology, 1970. **29**(3): p. 471-476,IN1-IN2,477-481.
28. Kak, A.C., *Computerized tomography with X-ray, emission, and ultrasound sources.* Proceedings of the IEEE, 1979. **67**(9): p. 1245-1272.
29. Wilchinsky, Z.W., *Effect of crystal, grain, and particle size on X-ray power diffracted from powders.* Acta Crystallographica, 1951. **4**(1): p. 1-9.
30. Hammersley, A.P., *ESRF Internal Report*. Vol. ESRF98HA01T. 1998.
31. Toby, B.H. and R.B. Von Dreele, *GSAS-II: The genesis of a modern open-source all purpose crystallography software package.* Journal of Applied Crystallography, 2013. **46**(2): p. 544-549.
32. De Nolf, W., F. Vanmeert, and K. Janssens, *XRDUA: Crystalline phase distribution maps by two-dimensional scanning and tomographic (micro) X-ray powder diffraction.* Journal of Applied Crystallography, 2014. **47**(3): p. 1107-1117.
33. Basham, M., et al., *Data Analysis WorkbeNch (DAWN).* Journal of Synchrotron Radiation, 2015. **22**: p. 853-858.
34. Ashiotis, G., et al., *The fast azimuthal integration Python library: PyFAI.* Journal of Applied Crystallography, 2015. **48**: p. 510-519.
35. Kak, A.C., et al., *Principles of Computerized Tomographic Imaging*. 1988: IEEE Press.
36. *MATLAB*. 2010, The MathWorks Inc.: Natick, Massachusetts.
37. Bednar, J.B. and T.L. Watt, *ALPHA-TRIMMED MEANS AND THEIR RELATIONSHIP TO MEDIAN FILTERS.* IEEE Transactions on Acoustics, Speech, and Signal Processing, 1984. **ASSP-32**(1): p. 145-153.
38. Davies, L. and U. Gather, *The Identification of Multiple Outliers.* Journal of the American Statistical Association, 1993. **88**(423): p. 782-792.
39. Bovik, A.C., T.S. Huang, and D.C. Munson Jr, *GENERALIZATION OF MEDIAN FILTERING USING LINEAR COMBINATIONS OF ORDER STATISTICS.* IEEE Transactions on Acoustics, Speech, and Signal Processing, 1983. **ASSP-31**(6): p. 1342-1350.

40. Nodes, T.A. and N.C. Gallagher, Jr., *Median Filters: Some Modifications and Their Properties.* IEEE Transactions on Acoustics, Speech, and Signal Processing, 1982. **30**(5): p. 739-746.
41. Lee, Y.H. and S.A. Kassam, *GENERALIZED MEDIAN FILTERING AND RELATED NONLINEAR FILTERING TECHNIQUES.* IEEE Transactions on Acoustics, Speech, and Signal Processing, 1985. **ASSP-33**(3): p. 672-683.
42. Restrepo, A. and A.C. Bovik, *Adaptive trimmed mean filters for image restoration.* IEEE Transactions on Acoustics, Speech, and Signal Processing, 1988. **36**(8): p. 1326-1337.
43. Hsieh, J., *Adaptive trimmed mean filter for computed tomographic imaging.* Proceedings of SPIE - The International Society for Optical Engineering, 1994. **2299**: p. 316-324.
44. Taguchi, A., *Adaptive α-trimmed mean filter with excellent detail-preservation and evaluation of its performance.* Electronics and Communications in Japan, Part III: Fundamental Electronic Science (English translation of Denshi Tsushin Gakkai Ronbunshi), 1995. **78**(10): p. 46-56.
45. Hwang, H. and R.A. Haddad, *Adaptive median filters: new algorithms and results.* IEEE Transactions on Image Processing, 1995. **4**(4): p. 499-502.
46. Marazzi, A. and C. Ruffieux, *The truncated mean of an asymmetric distribution.* Computational Statistics and Data Analysis, 1999. **32**(1): p. 79-100.
47. Li, S., Y. Li, and J. Jin, *Adaptive trimmed mean as a location estimate.* Journal of Systems Science and Complexity, 2012. **25**(5): p. 973-986.
48. Jiang, X., *Iterative truncated arithmetic mean filter and its properties.* IEEE Transactions on Image Processing, 2012. **21**(4): p. 1537-1547.
49. Miao, Z. and X. Jiang, *Weighted iterative truncated mean filter.* IEEE Transactions on Signal Processing, 2013. **61**(16): p. 4149-4160.
50. Miao, Z. and X. Jiang, *Additive and exclusive noise suppression by iterative trimmed and truncated mean algorithm.* Signal Processing, 2014. **99**: p. 147-158.
51. *ESRF*. Available from: http://www.esrf.eu/about/upgrade.

CHAPTER 4: Interlaced X-ray Diffraction Computed Tomography

Abstract

In this Chapter, an X-ray diffraction computed tomography (XRD-CT) data collection strategy that allows, post experiment, choice between temporal and spatial resolution is reported. This strategy enables time resolved studies on comparatively short time scales, alternatively allowing for improved spatial resolution if the system under study, or components within, appear to be unchanging. The application of the method for studying a Mn-Na-W/SiO_2 packed bed reactor in situ is demonstrated. Additionally, the opportunities to further improve the data collection strategy enabling post collection tuning between statistical, temporal and spatial resolutions are also discussed. In principle, the interlaced scanning approach can be also applied to other pencil beam tomographic techniques, like X-ray fluorescence computed tomography (XRF-CT), X-ray Absorption Fine Structure computed tomography (XAFS-CT) and tomographic Scanning Transmission X-ray Microscopy (STXM). This work was published at the peer reviewed Journal of Applied Crystallography: *Vamvakeros, A., Jacques, S. D. M., Di Michiel, M., Senecal, P., Middelkoop, V., Cernik, R. J. & Beale, A. M. (2016). Journal of Applied Crystallography 49, 485-496.*

Introduction

X-ray diffraction computed tomography (XRD-CT) is an emerging technique that can provide spatially resolved physico-chemical information from within the interiors of intact objects. Originally demonstrated as a laboratory technique, this method has been most usefully applied when using synchrotron X-ray radiation coupled with large area 2D detectors.[1, 2] Indeed, in the past decade, synchrotron XRD-CT has been employed in several studies and has proven to be a powerful characterisation tool to investigate a wide range of inhomogeneous materials.[3-19] Furthermore, the nature of the X-rays generated by third generation synchrotrons (i.e. high intensity and

brilliance) allow for relatively fast acquisition times enabling dynamic XRD-CT experiments.[20-24] In the field of heterogeneous catalysis, such dynamic tomographic experiments are of great importance, as catalytic solids can evolve under operating conditions.[25, 26]

X-ray Diffraction Computed Tomography

As the name suggests, the XRD-CT technique is a marriage of powder X-ray diffraction (PXRD) with computed tomography (CT). Comparable to the first incarnation of traditional X-ray computed tomography (X-ray CT), a pencil beam scanning approach is used, but instead of recording the absorption of X-rays, the diffraction signal is collected to yield a diffraction projection data set.[27, 28] More specifically, the sample is translated along an axis which is perpendicular to the beam axis while being illuminated with a highly collimated or focussed monochromatic X-ray beam and the scattered X-rays are recorded with an area detector (i.e. for best counting statistics/speed). In most cases, the size of the translational scan is chosen to be larger than the sample size to ensure that the whole sample is scanned for all measured angles, while the size of the translation step is typically chosen to be the same as the horizontal size of the illuminating X-ray beam. Ideally, as in the case of every pencil beam scanning tomographic technique, the number of angles measured should be equal to the number of translation steps times $\pi/2$ (i.e. Nyquist sampling theorem) but in practice, this number can be decreased without significant loss of the quality in the reconstructed images and typically the angular range covered is from 0 to π.[29]

As shown in Figure 1, the raw XRD-CT data collected from a single tomographic scan can be interpreted as a $X \times Y \times R \times T$ matrix (i.e. 4D matrix) where $X \times Y$ is the size of the acquired 2D diffraction images, T is the number of translation steps and R is the number of rotation steps. After performing azimuthal integration of the 2D diffraction images, the size of the matrix is reduced to $R \times T \times d$ (i.e. 3D matrix), where d is the number of observation points in the derived 1D diffraction patterns. The sinograms (i.e. the projection data) therefore represent a volume, similarly to the case of traditional X-ray CT but in the case of XRD-CT data, the third dimension is not

spatial but spectral. If 3D-XRD-CT is performed (i.e. by acquiring multiple XRD-CT datasets at different positions along the third spatial dimension), then the projection data are stored as a 4D matrix (i.e. 3D spatial and 1D spectral dimensions). Five dimensional diffraction imaging can also be achieved by performing successive 3D-XRD-CT scans [26]. In this case, the solid state changes taking place during the experiment are monitored as a function of time or pressure or temperature and the data are stored as a 5D matrix. Finally, the reconstructed real-space images are obtained by applying tomographic reconstruction algorithms (e.g. algebraic reconstruction techniques or filtered back projection algorithms) to the projection data.[30-33] In this study, the reconstructed images were obtained using the *reverse analysis* method where the whole projection dataset volume is reconstructed leading to a $T \times T \times d$ (i.e. 3D matrix).

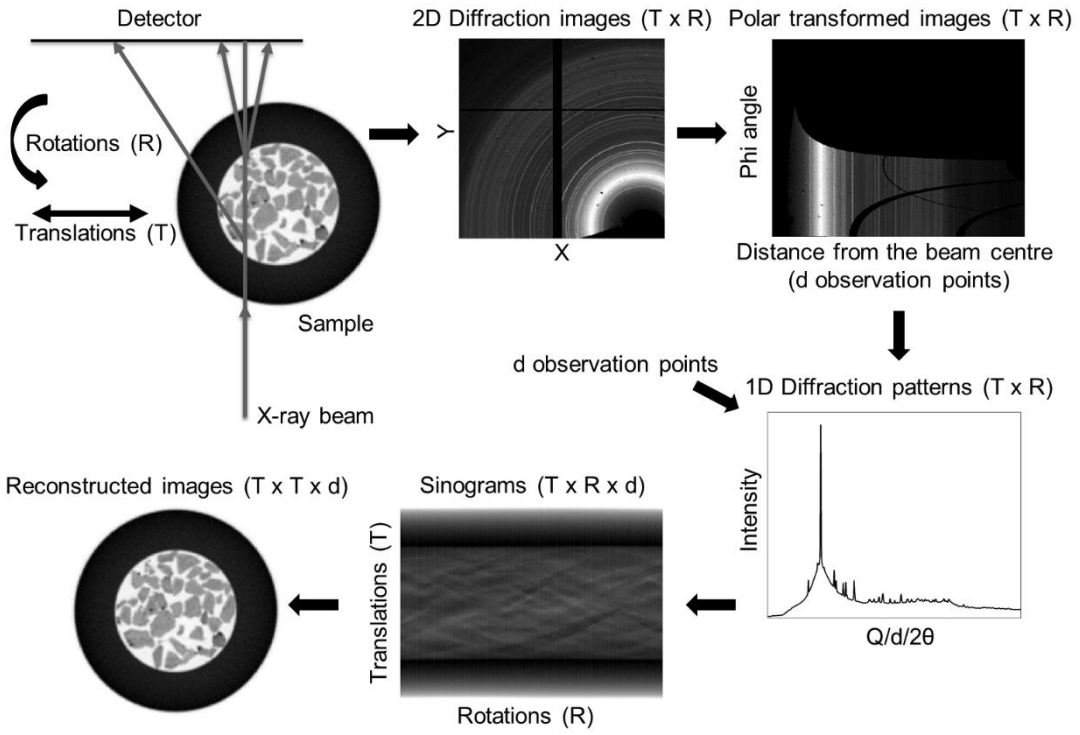

Figure 1 The sample is translated along an axis which is perpendicular to the beam axis while being illuminated with an X-ray beam and rotated, typically covering an angular range of 0 to π, while 2D diffraction patterns (size of X × Y) are recorded with an area detector. The total number of 2D diffraction patterns collected is equal to T x R, where T is the number of translation steps and R is the number of rotation steps. The 2D diffraction patterns are then azimuthally integrated to give 1D diffraction patterns (containing d observation points) which are plotted as a function of translations and rotations, yielding the sinogram volume (T × R × d matrix). The reconstructed volume (T × T × d matrix) is derived by applying a tomographic reconstruction algorithm to the sinogram volume. The images shown in this figure were derived from the XRD-CT data presented later in this Chapter.

In dynamic XRD-CT, a number of collections is carried out to yield a series of XRD-CT slices showing the spatial changes in chemistry/physical form within a sample over time. To date, the spatial and temporal resolutions in such experiments were fixed during collection by choice of acquisition parameters and these resolutions were traded off against one another. High spatial resolution could be obtained but with low temporal resolution and vice-versa. The risk here is that chemical / physical changes could occur during the collection of a single XRD-CT slice yielding only a partial understanding of the relationship between spatial composition and time.

Data collection strategies

In this section, a review of the existing data collection strategies to perform an XRD-CT scan is provided (Table 1) and the advantages/disadvantages of each method are discussed in detail. The main aim of this short review is to find the scanning approach/approaches that minimise the dead time in an XRD-CT scan. This dead time is mainly associated with the mechanical movements (i.e. how the sample moves during the tomographic scan). Optimising the sample movement is essential as it can lead to significant decrease of the overall acquisition time of an XRD-CT scan.

Stepped scans

In the simplest approach, the sample is traversed in fixed steps across the beam and diffraction patterns are collected at each step. The process is then repeated at a number of fixed sample angular rotations, typically covering an angular range from 0 to π. However, this approach is slow and alternative scanning strategies should be used. The reduction of the required time to perform an XRD-CT scan does not depend only on the properties of the X-ray beam and the efficiency of the detector but also on the data collection strategy. The optimization of the XRD-CT data collection process is essential as it not only leads to more efficient use of beamtime but it may also be highly desired for specific experiments. An example for the latter case is the application of XRD-CT to track the evolving solid state chemistry of functional materials. In such dynamic XRD-CT experiments, the solid state changes taking place in the sample can be faster than the overall time of the tomographic scan.

Continuous scans

In another approach, the sample is continuously traversed across the beam and diffraction patterns are collected at a fixed interval with the process then being repeated at a number of fixed angular rotations (i.e. step angular scan). This collection strategy can significantly reduce the required time to perform a single XRD-CT scan. A similar approach is the continuous angular scan. In this case, the sample is continuously rotated and diffraction patterns are collected at a fixed interval with the process then repeated at a number of fixed sample traverse steps. The object is rotated at fixed speed about the tomographic axis and diffraction patterns are accumulated over a fixed angular range. This scanning approach requires continuous rotation in the range 0 to ~ π for each translation. The continuous angular scan approach should be the preferred option as a much bigger portion of reciprocal space is collected compared to the continuous traverse scan approach. More specifically, the crystallites are swept into the diffracting volume, so their orientations are constantly changed and all angles are equally sampled with respect to the axis of rotation. This is important as the formation of outliers and spots in the raw 2D diffraction images generated by large crystallites can potentially be mitigated. This is a frequently encountered problem in XRD-CT experiments as such single-crystal artefacts (i.e. spots) in the raw 2D diffraction images lead to hotspots in the sinograms and streak artefacts in the reconstructed images (i.e. yielding distorted XRD-CT images). The continuous angular scan approach does not guarantee the eradication of the single-crystal artefacts but there are available strategies to remove them during the processing of the collected data, post experiment, by applying appropriate filters to the raw 2D diffraction images [34].

Infinite continuous rotation scan

An alternative collection strategy is the infinite continuous rotation approach. It is identical to the continuous angular scan approach but in this case the sample is rotated from 0 to $c \times \pi$ instead of 0 to π, where c is a large integer number. More specifically, the new angular position of the sample after every traverse scan is not 0 but $c \times \pi$. For example, the angular position is π after the 1st traverse scan, 2π after the 2nd traverse scan, 3π after the 3rd traverse scan, etc. This means that the dead

time of the tomographic scan is reduced as the sample does not need to be rotated back to 0 after every traverse scan. However, the infinite continuous rotation approach may not always be feasible to implement experimentally. For example, *in situ* catalytic experiments require gas lines, therefore more sophisticated reactor cells would be needed in order to use the infinite continuous rotation approach (e.g. a reactor in which the gas connections allow for free rotation).

Zigzag scan

A zigzag scanning approach can also significantly reduce the dead time of the tomographic measurement without the need for specially designed reactors (in contrast to the infinite continuous rotation approach). The zigzag approach can be easily combined with all the previously mentioned collection strategies (i.e. stepped and continuous scans). For example, when continuous traverse scan is used, the sample is returned to the initial position after every angular step. It is possible to avoid the dead time associated with this movement by performing the scan at the next angle but setting the new starting position (i.e. for the traverse scan) as the final position of the previous scan (i.e. the starting positions of the sample will be alternately 0 and π for every traverse step). As expected, the values in the 3D matrix of the projection data (i.e the sinograms) need to be sorted appropriately before a reconstruction tomographic algorithm is used. This is shown in Figure 2 where a global sinogram from a continuous traverse zigzag XRD-CT scan (left) and the new sinogram after sorting the values appropriately (right) are shown.

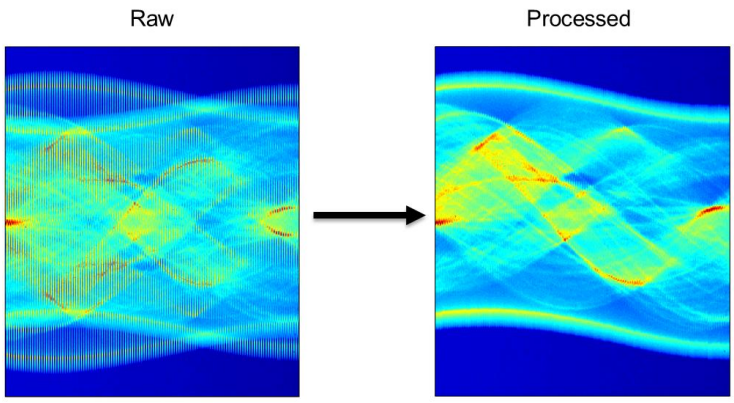

Figure 2: Global sinograms of a 2 % La-2 % Mn-1.6 % Na-3.1 % W/SiO2 catalyst collected during an XRD-CT scan at ambient conditions using a 46 keV monochromatic pencil beam with a spot size of 2.5 × 2.5 µm. Left: raw data using the zigzag approach. Right: The new global sinogram after sorting the values appropriately.

Interlaced X-ray Diffraction Computed Tomography

In this study, we report a new data collection strategy, Interlaced XRD-CT (IXRD-CT), which allows, post experiment, to choose between temporal and spatial resolution. In a typical XRD-CT experiment, the number of translation and rotation steps (or equivalently the total length and the angular range to be covered) and the values of these steps define the spatial and temporal resolution of the tomographic measurement. Unfortunately, although both high spatial and temporal resolution is desired, there is always a trade-off between the two when conventional data collection strategies are employed. This means that high spatial resolution scans have low temporal resolution while high temporal resolution scans have low spatial resolution. IXRD-CT offers a way to bridge this gap by providing temporal resolution inside a high spatial resolution XRD-CT scan. The basic principle of this method consists of performing subsequent XRD-CT scans with low spatial but high temporal resolution, which can be then easily combined, post experiment, to yield the same results as the equivalent high spatial resolution XRD-CT scan. In an XRD-CT scan, the spatial resolution is defined by the traverse step size which is typically, but not necessarily, the same as the horizontal size of the illuminating X-ray beam. In an IXRD-CT scan, the time resolution is chosen before the tomographic measurement begins. There are two types of IXRD-CT scans: a) continuous traverse IXRD-CT scan and b) continuous angular IXRD-CT scan. Both methods are explained in the following sections. The work presented herein demonstrates the feasibility to perform IXRD-CT scans and the advantages of applying such a scanning approach in XRD-CT experiments. However, it should be highlighted that the interlaced scanning approach can, in principle, be applied to other pencil beam chemical (i.e. hyperspectral) tomographic techniques, like X-ray fluorescence computed tomography (XRF-CT), X-ray Absorption Fine Structure computed tomography (XAFS-CT) and tomographic Scanning Transmission X-ray Microscopy (STXM) [35-39].

Continuous traverse IXRD-CT scan

In the case of the continuous traverse IXRD-CT scan, the value of the angular step size (*Sa*) corresponding to a desired high spatial resolution XRD-CT scan is initially chosen (e.g. angular step size of 1.5°). The next step is to choose the temporal

resolution (*Rt*) of the IXRD-CT scan. This is defined as an integer value which represents how many times the temporal resolution is increased compared to the high spatial resolution XRD-CT scan. For example, if the value of *Rt* is 8, then the temporal resolution of the IXRD-CT will be eight times higher than the high spatial resolution XRD-CT scan. The IXRD-CT will therefore consist of *Rt* XRD-CT scans with angular step size of $Sa \times Rt$. For example, if *Sa* is 1.5° and *Rt* is 8, then the new angular step size will be 12°.

As mentioned previously, the angular range typically covered in an XRD-CT scan is 0 to 180°. The *Rt* XRD-CT scans composing the IXRD-CT scan cover the same angular range (i.e. 180° in total) and have the same angular step size but the starting angular positions are different. These angles can be easily calculated: 0, *Sa*, $2 \times Sa$, $3 \times Sa$, …, $(Rt - 1) \times Sa$. An example, where *Sa* is 1.5° and *Rt* is 8, is provided in Figure 3. The starting angles of the eight tomographic scans are 0, 1.5, 3, 4.5, 6, 7.5, 9 and 10.5°. As one can easily understand, combining these eight tomographic datasets, post experiment, will give results identical to a high spatial resolution XRD-CT of 1.5° angular step size covering an angular range of 0 to 180°. At the same time, each one of the *Rt* XRD-CT scans has *Rt* times lower spatial and *Rt* times higher temporal resolution compared to an IXRD-CT scan.

The final step is to decide the order of the *Rt* XRD-CT scans. This step is crucial and should be not treated lightly as it determines whether the temporal resolution will be directly linked to the spatial one or not. In the case of previously mentioned example, the optimal order of the individual *Rt* XRD-CT scans is shown in Panel C of Figure 3. These *Rt* tomographic scans are referred to as “tomo” numbers in Figure 3 (i.e. tomo number 1 to 8). Furthermore, combining tomo pairs *k* and $k + 1$, where *k* is 1, 3, 5 and 7 (i.e. tomo 1 & 2, 3 & 4, 5 & 6, 7 & 8), lead to XRD-CT datasets with four times higher temporal resolution and four times lower spatial resolution compared to the complete IXRD-CT scan. Similarly, combining tomo pairs *k* to $k + 3$, where *k* is 1 and 5 (i.e. tomo 1 to 4 and tomo 5 to 8), lead to XRD-CT datasets with two times higher temporal resolution and two times lower spatial resolution compared to the complete IXRD-CT scan. It should also be noted that the results from successive IXRD-CT scans can be combined to yield new datasets (e.g. new IXRD-CT shown in panel C

of Figure 3). This can be essential in dynamic experiment where solid state changes can take place during a single tomographic scan.

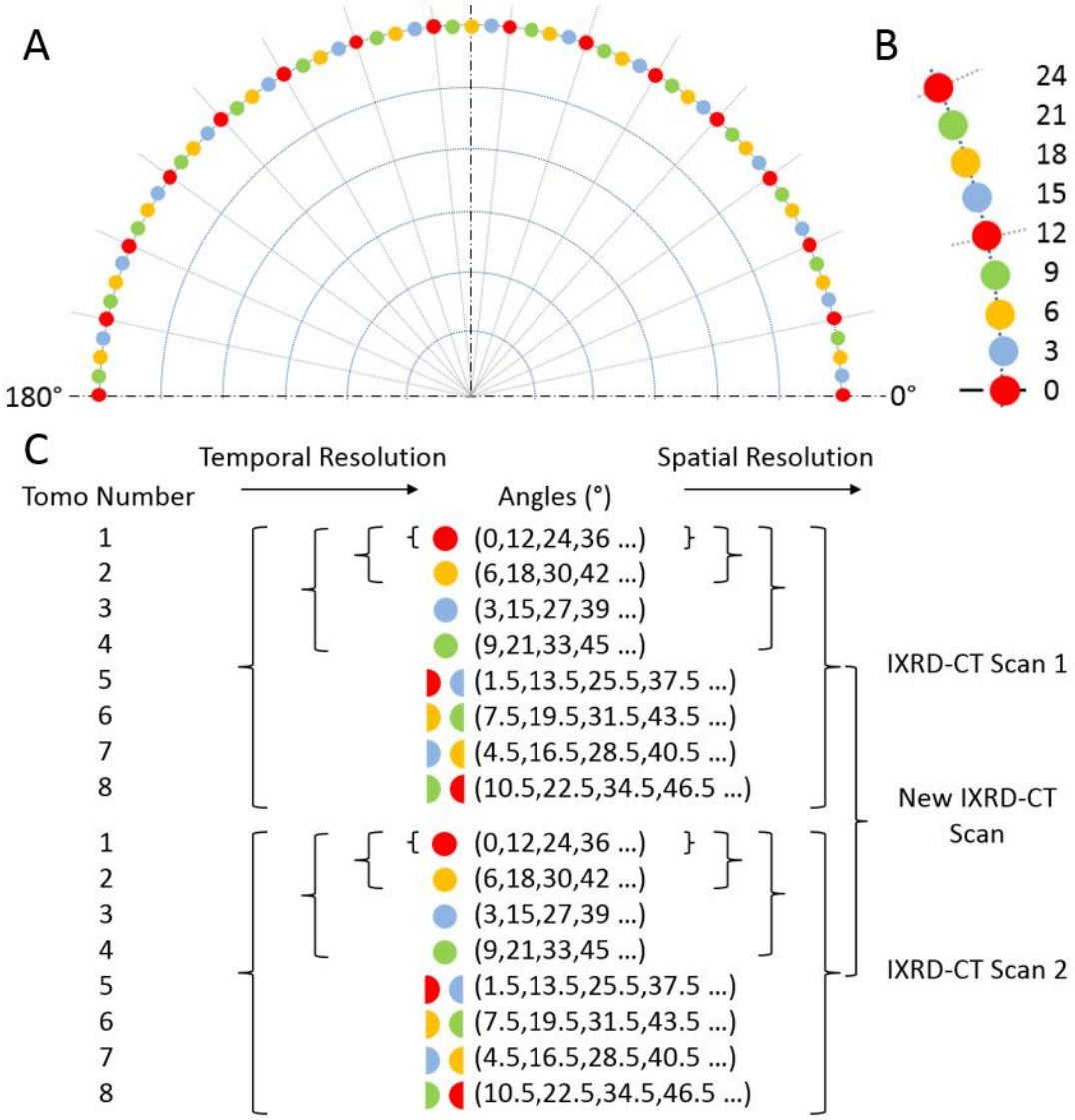

Figure 3: Panel A: Schematic representation of a continuous traverse IXRD-CT scan consisting of eight XRD-CT scans. Panel B: Expanded section of panel A, showing the angular positions of the individual XRD-CT scans. Panel C: Demonstration of how the spatiotemporal resolution changes in the IXRD-CT scan and the possible combinations of individual datasets.

However, if the order of the eight XRD-CT scans composing the complete IXRD-CT scan is different than those previously mentioned, then the spatial and the temporal resolution cannot be linked appropriately. For example, an alternative order to perform these scans is presented in panel A of Figure 4. In this case, half the spatial resolution (i.e. by combining tomo scans 1, 3, 5 and 7) does not lead to double temporal resolution but to 7/8 the temporal resolution of the complete IXRD-CT scan. Similarly, 1/4 the spatial resolution (i.e. by combining tomo scans 1 & 5) does not

lead to four times higher temporal resolution but only 5/8 of the complete IXRD-CT scan. As a result, the full potential of this IXRD-CT measurement (i.e. eight XRD-CT scans with an angular step of 12°) is not reached.

At this point, it should be noted that the number *Rt* of the tomographic scans composing the IXRD-CT scan should not be an odd number as the same problem arises. Although any even number can be used, ideally *Rt* should be a power of 2 (e.g. 2, 4 and 8). In panel B of Figure 4, an example is given when the IXRD-CT scan consists of six XRD-CT scans. In this case, the angular step is 9° and the optimal order to perform the individual scans is shown in panel B of Figure 4. However, it can be seen that the spatial and temporal resolution cannot be perfectly linked even when the optimal order is chosen. More specifically, combining tomo scans 1, 3 and 4 gives half the spatial but 1.5 times the temporal resolution of the complete IXRD-CT scan (instead of double). This happens because the time to perform tomo scan 2 has to be taken into account too.

A

8 XRD-CT Scans

Tomo Number	Angles (°)
1	(0,12,…)
2	(1.5,13.5,…)
3	(3,15,…)
4	(4.5,16.5,…)
5	(6,18,…)
6	(7.5,19.5,…)
7	(9,21,…)
8	(10.5,22.5,…)

B

6 XRD-CT Scans

Tomo Number	Angles (°)	Tomo Scans Combination	Temporal Resolution	Spatial Resolution
1	(0,7.5,…)	1	6*x*	1*x*
2	(4.5,12,…)			
3	(3,10.5,…)	1,2	3*x*	2*x*
4	(6,13.5,…)	1,3,4	1.5*x*	3*x*
5	(1.5,9,…)			
6	(7.5,15,…)	1 to 6	1*x*	6*x*

Figure 4: Panel A: A potential order to perform an IXRD-CT scan consisting of eight XRD-CT scans. Panel B: Demonstration of how the spatiotemporal resolution changes in an IXRD-CT scan consisting of six XRD-CT scans and the possible combinations of individual datasets are presented.

Continuous angular IXRD-CT scan

The basic principle of the continuous angular IXRD-CT scan is the same as the continuous traverse IXRD-CT scan. The only difference is that now the fast tomographic axis is the rotation axis and the slow tomographic axis is the translation axis. For example, if the slow axis step size (i.e. translational step) is a number *l* corresponding to a specific length (e.g. the horizontal size of the X-ray beam) and *Rt* is chosen to be 8, then the spatial and temporal resolution of the complete IXRD-CT scan will be identical to the previous continuous traverse IXRD-CT example. More

specifically, in both types of IXRD-CT, the angular range covered is 0 to 180° with a step of 1.5° and the same length is covered with a step of *l*. However, the sinograms are changing in a different way. In the case of a continuous traverse IXRD-CT scan, as will be shown later on, combining different XRD-CT scans increases the number of limits of the axis corresponding to rotations. For clarity, the XRD-CT scans composing the complete IXRD-CT scan will be referred as tomo scans for the rest of the Chapter.

Demonstration and comparison of the IXRD-CT methods

A demonstration using the previous continuous traverse IXRD-CT example is provided in Figure 5 where the presented sinogram corresponds to the global sinogram (i.e. the sinogram volume summed along the 3rd dimension, which is the spectral dimension) of an IXRD-CT experiment of a fixed bed reactor. More details about the experiment are provided in the next section. The filtered back projection (FBP) algorithm was chosen to reconstruct the sinograms as it is a very fast and easy-to-implement algorithm. It can be seen in Figure 5 that the direct reconstruction of the sinograms leads to artefacts in the reconstructed images. This is apparent in the high temporal/low spatial resolution scan (i.e. *1x* in Figure 5) where there are intensity variations present in the reconstructed images suggesting that the sample is highly inhomogeneous. Furthermore, it there are regions in the images where the intensity is higher than the background implying that there is sample present in these areas. However, both these phenomena are artefacts being generated due to the angular undersampling (Figure A8 in Appendix). The artefacts due to undersampling (i.e. limited number of projections) are a well-known problem in traditional X-ray CT [40]. Herein, these artefacts have been mitigated by convoluting the sinograms with an appropriate window function prior to reconstruction (i.e. by changing the width of the Hann window accordingly). As expected, reconstructing the filtered sinograms leads to the lower spatial resolution images shown in Figure 5 but the previously mentioned artefacts have been removed. There are options one can explore in order to optimize the quality of the reconstructed images of the high temporal tomo scans. For example, the effect of different reconstruction algorithms can be investigated (Figures A9 and A10 in the Appendix). However, this is beyond the scope of the work presented here.

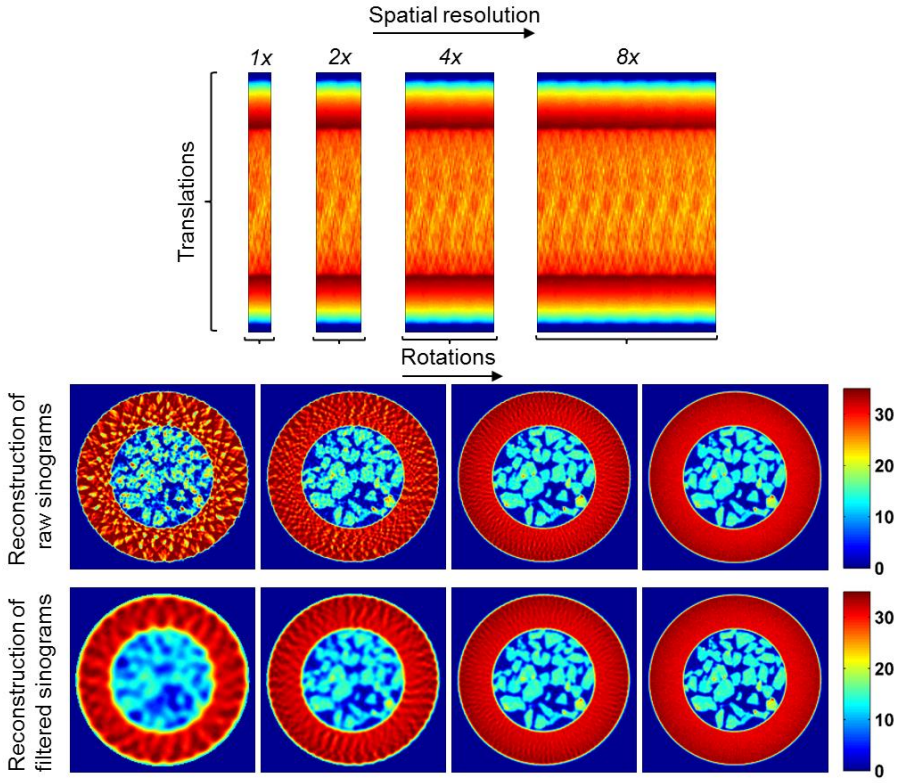

Figure 5: Continuous traverse IXRD-CT scan: the spatial resolution can be increased by combining different XRD-CT scans. The limits of the sinogram axis corresponding to translations remain constant while the limits of the sinogram axis corresponding to rotations gradually increases, increasing the spatial resolution of the respective reconstructed images. Color bars indicate intensity in arbitrary units.

On the contrary, in the case of the continuous angular IXRD-CT method, it is the sinogram axis corresponding to translations that is changing while the sinogram axis corresponding to rotations remains the same. As a result, in a continuous angular IXRD-CT scan, the resolution of the reconstructed XRD-CT images is changing during the IXRD-CT. This is clearly shown in the simulation presented in Figure 6 (using the complete sinogram presented in Figure 5) where the sinograms and the corresponding reconstructed images are presented. In a continuous angular IXRD-CT, the traverse step size is multiple times larger than the horizontal size of the illuminating X-ray beam meaning that there are parts of the sample that are not scanned leading to loss of information. Furthermore, in case of a problem during acquisition of the tomo scans (e.g. beam refill, significant intensity variations of the X-ray beam) the sinograms cannot be easily corrected by applying a simple scale factor as in the case of the continuous traverse IXRD-CT scan (i.e. if there are no solid state changes during acquisition, then the total scattering intensity for every line scan should be the same). In summary, the problems that need to be faced with a

continuous angular IXRD-CT scan can be summarised as the following: 1) the sinograms of the corresponding tomo scans have to be independently centred, 2) the size of the reconstructed images changes when sinograms from different tomo scans are combined, 3) there is potentially loss of information due to the fact that the whole sample is not scanned in every tomo scan; information that requires further data processing to be gained back (if possible) and 4) the requirement for a stable X-ray beam. Taking into account the previous reasons and the increased the complexity of data acquisition and processing without evident gain in information or image quality, it was decided to perform the experiments using the continuous traverse IXRD-CT approach.

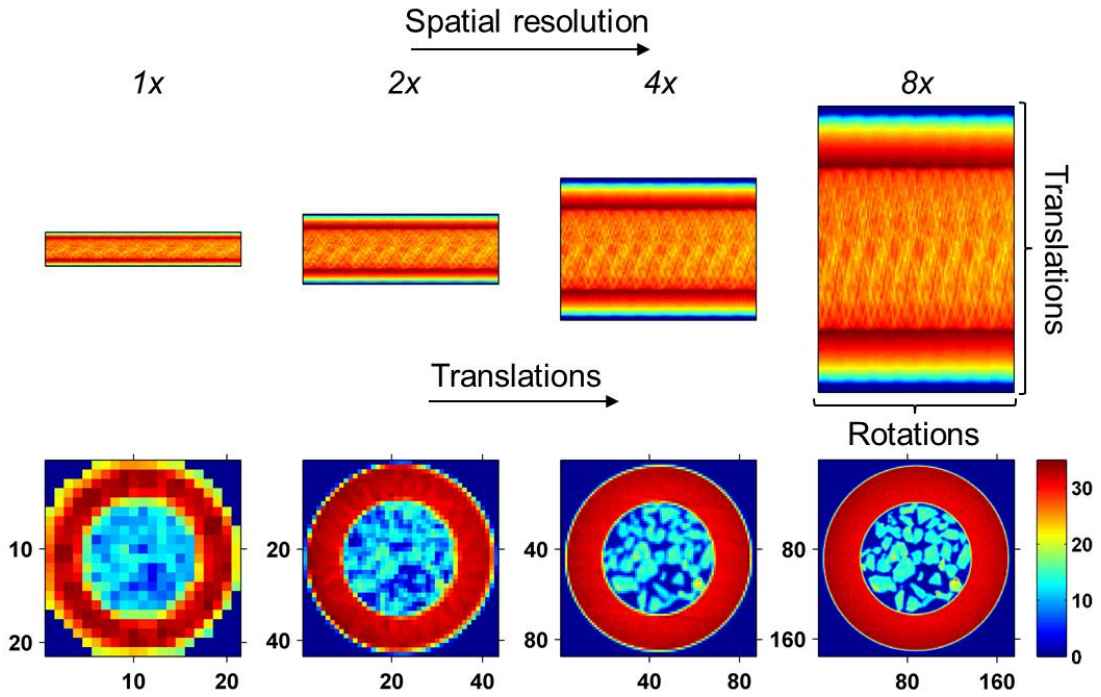

Figure 6: Continuous angular IXRD-CT scan: the spatial resolution can be increased by combining different XRD-CT scans. The limits of the sinogram axis corresponding to the angles sampled remain constant while the limits of the sinogram axis corresponding to translations gradually increases, increasing not just the spatial resolution but also the size of the reconstructed images. Color bar indicates intensity in arbitrary units.

Materials and Methods

Catalyst preparation

The 2 wt. % La – 2 wt. % Mn – 1.6 wt. % Na – 3.1 wt. %W/SiO_2 and the 2 wt. % Mn – 1.6 wt. % Na – 3.1 wt. % W/SiO_2 catalysts were prepared by the sequential incipient wetness impregnation method. At first a SiO_2 support (commercial Silica gel Davisil

646) was impregnated by an aqueous solution of sodium tungstate dehydrate $Na_2WO_4 \cdot 2H_2O$ and sodium oxalate $Na_2C_2O_4$ taken in appropriate amounts. The Na-W/SiO_2 was dried at 120 °C for 6 h and was then impregnated by an aqueous solution of manganese (II) acetate tetrahydrate $Mn(CH3COO)_2 \cdot 4H_2O$ and lanthanum nitrate hexahydrate $La(NO_3)_3 \cdot 6H_2O$ salts, taken in appropriate concentrations. The catalysts were then dried at 120 °C for 6 h and calcined in air at 850 for 6 h with a heating rate of 2 °C min^{-1}. The catalysts used in this study were kindly provided by the Boreskov Institute of Catalysis (BIC).

XRD-CT measurements at ID15, ESRF

XRD-CT measurements were made at beamline station ID15A of the ESRF using a 92.8 keV monochromatic X-ray beam focused to have a spot size of 25 µm x 25 µm. 2D powder diffraction patterns were collected using a Pilatus3 X CdTe 300K (487 × 619 pixels, pixel size of 172 µm) hybrid photon counting area detector which uses cadmium telluride (CdTe) as the semiconducting direct conversion layer. The acquisition time per point was 50 ms. The reactor was mounted into a gas delivery stub, itself mounted to a standard goniometer. The goniometer was fixed to a rotation stage set upon a translation stage to facilitate the movements required for the CT measurement. Heating was achieved by virtue of two hot air blowers heating each side of the catalytic membrane reactor.

The tomographic measurements were made with 180 translation steps (translation step size of 25 µm) covering 0 - 180° angular range, in steps of 1.5° (i.e. 120 line scans). The detector calibration was performed using a CeO_2 NIST standard. Every 2D diffraction image was converted to a 1D powder diffraction pattern after applying an appropriate filter (i.e. 10% trimmed mean filter) to remove outliers using in-house developed MATLAB scripts.[34] The final XRD-CT images (i.e. reconstructed data volume) were reconstructed using the filtered back projection algorithm. Each IXRD-CT scan consisted of eight XRD-CT scans. The angular step of the individual XRD-CT scans was 12° and the order of these scans was the same as the one presented in Figure 3.

Results & Discussion

The data collection strategy used in this tomographic experiment is the continuous traverse IXRD-CT scanning approach. The results from two successive IXRD-CT scans of the 2 % Mn-1.6 % Na-3.1 % W/SiO_2 catalyst during temperature ramping from 455 to 765 °C with a ramp rate of 4.5 °C min^{-1} under He flow (30 mL min^{-1}) are presented in this section. In the interest of brevity, the two complete IXRD-CT scans will be referred to as IXRD-CT scan 1 and IXRD-CT scan 2 respectively. Each complete IXRD-CT scan is composed of eight XRD-CT scans which will be referred to as tomo scans 1 to 8. We have recently reported that the main crystalline phases present in this catalyst at ambient conditions are cristobalite, tridymite (both SiO_2 polymorphs), Mn_2O_3 and Na_2WO_4.[24] This catalyst is a well-established catalyst for the oxidative coupling of methane (OCM) to produce ethylene [41]. The melting point of Na_2WO_4 in 1 bar pressure is 695 °C which is significantly lower than the required temperatures for the OCM reaction.[42, 43] This means that Na_2WO_4 is expected to be present in a molten state under OCM conditions.[24, 44] Therefore, this catalyst was considered to be an ideal system to test the feasibility of IXRD-CT measurements as there are solid state changes taking place during temperature ramping even under the flow of inert gases. Herein, we will be mainly focusing on the evolution of the Na_2WO_4 phase.

Space series

An appropriate mask, as shown in Figure 7, has been applied to all the reconstructed images presented in this work in order to remove the contribution from the capillary and show only the sample of interest. This mask was created using the reconstructed image of the global sinogram shown in Figure 5. Also in the Figures where parts of the complete IXRD-CT sinograms are used (i.e. less than eight tomo scans), the respective sinograms were convolved with an appropriate Hann window function prior to reconstruction as discussed previously.

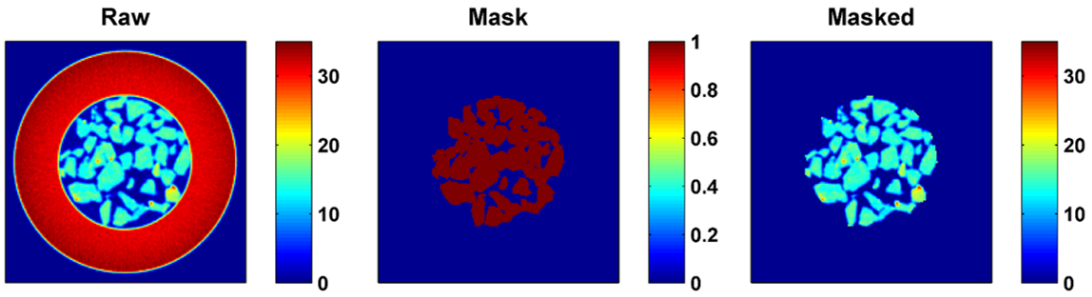

Figure 7: Left: The reconstructed image of the global sinogram of the IXRD-CT scan 1 shown in Figure 5. Middle: The mask created to separate the catalyst particles from the capillary (glassware). Right: The reconstructed image after applying the mask. Color bars indicate intensity in arbitrary units.

In Figure 8, the summed diffraction patterns of the two IXRD-CT scans are presented (i.e. by summing the reconstructed volume along the two spatial dimensions). Also shown are the main diffraction peaks generated by two crystalline SiO_2 polymorphs (i.e. cristobalite and tridymite), Mn_2O_3 and two Na_2WO_4 phases. Minor peaks corresponding to SiO_2 quartz were also identified. It can be clearly seen that the peaks corresponding to the high symmetry (cubic) Na_2WO_4 phase are not present in the IXRD-CT scan 2 diffractogram. The transformation of the cubic Na_2WO_4 phase to a lower symmetry orthorhombic Na_2WO_4 phase will be discussed in more detail in the following section.

In the 1930s, it was suggested that two phase transitions of the anhydrous Na_2WO_4 (phase I) take place above 585 °C, the first (phase II) being stable for only a few degrees and the second (phase III) being stable up to the melting point of Na_2WO_4.[43, 45] Later studies showed that the high symmetry, cubic *Fd-3m*, Na_2WO_4 (phase I) changes to a lower symmetry (phase III) and the orthorhombic *Pnam* space group was suggested after peak indexing.[46] It has to be noted though that the high temperature PXRD measurement was performed at 628 °C which is significantly lower than the melting point of Na_2WO_4. Further studies the binary Na_2WO_4-Na_2MoO_4 system by Bottelberghs and Van Vuren suggested that different structural changes take place: cubic *Fd-3m* to orthorhombic $Pbn2_1$ at 588 °C, $Pbn2_1$ to orthorhombic *Fddd* at 590 °C and *Fddd* to hexagonal $P6_3/mmc$ above 640 °C [47]. Recent high temperature Raman studies showed that there is a transition from the high symmetry cubic Na_2WO_4 phase to a lower symmetry above 560 °C.[48] In that study, the Na_2WO_4 system was studied up to 645 °C. To our knowledge, there are no

high temperature PXRD studies in literature showing a crystalline Na_2WO_4 phase being present above 650 °C. More specifically, two high temperature PXRD studies of a $NaWO_4$ containing catalyst (i.e. a Mn-Na-W/SiO_2 and a NaCl-Mn-Na-W/SiO_2 catalyst respectively) have shown that there are no crystalline Na_2WO_4 or other W containing phases present above 700 °C.[49, 50] In this experiment, the cubic Na_2WO_4 phase disappears completely at approximately 600 °C. The new Na_2WO_4 phase starts appearing above 565 °C as suggested by Lima et al., but only one peak can be observed from the diffraction patterns.[48] The summed diffraction patterns for every translational scan for the two IXRD-CT scans (240 in total) are plotted in Figure A12 of the Appendix. The new phase is apparent above 585 °C, where all the peaks are clearly visible and this phase disappears completely at approximately 660 °C. No Na_2WO_4 peaks are observed up to the final temperature of 765 °C. Peak indexing can be very challenging as there are numerous phases present in the catalyst and there are peaks overlapping. For this reason, the space groups suggested by the previous studies were used. The published crystallographic information file (CIF) after Pistorius (*Pnam* space group, PDF ref.: 00-020-1163) does not predict all the peaks associated with the new Na_2WO_4 phase.[46] Similar results are obtained when the hexagonal *$P6_3/mmc$* space group is used. However, when the orthorhombic *Fddd* space group is used, all the peaks in the diffractograms are predicted; a symmetry which has been suggested in the literature in the past.[47] This is clearly shown at the right side of Figure 8. As shown in Figure A13 in the Appendix, Pawley whole powder pattern fitting was also performed with the GSASII software using the appropriate unit cells to ensure that no peaks were neglected after the phase identification.[51] The summed diffraction from tomo scan 1 of IXRD-CT scan 2 was used for the Pawley analysis, corresponding to a temperature range of 620 to 640 °C, as there is only the low symmetry Na_2WO_4 phase present and no cubic Na_2WO_4.

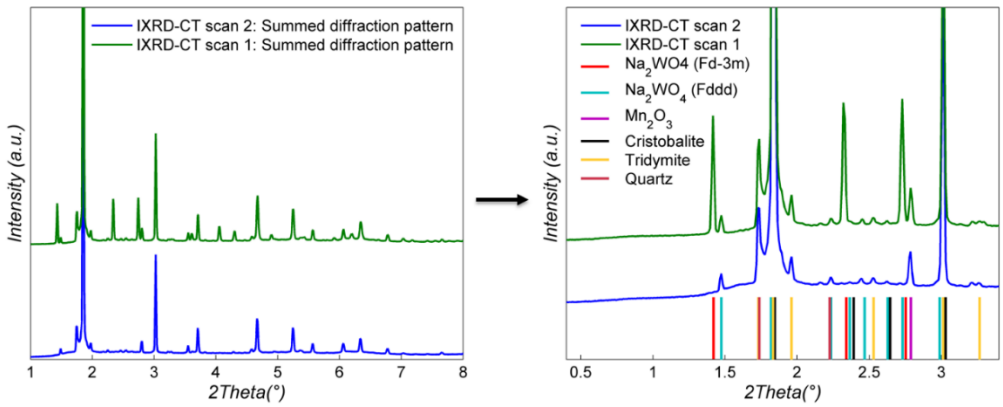

Figure 8: Left: IXRD-CT scan 1 and 2 summed diffraction patterns. Right: A region of interest (ROI) of the two diffraction patterns, showing the main diffraction peaks generated by the two Na_2WO_4 phases, Mn_2O_3, cristobalite, tridymite and quartz.

First, the results from the IXRD-CT scan 1 are presented. In Figure 9, reconstructed images of cristobalite corresponding to scattering 2θ angle of 1.85° (reflection (111)) are shown. The reconstructed images corresponding to cristobalite define well the shape and size of the catalyst particles as it is the main crystalline phase of the catalyst support. As discussed previously, it is possible to combine the different tomo scans composing the IXRD-CT scan post experiment. Such an example is presented in Figure 9, where it is shown how the spatial resolution is gradually increases when different tomo scans are combined.

At this point, another major advantage of the IXRD-CT method should be highlighted; the diffraction peaks present in the IXRD-CT data can be treated independently. More specifically, observation points in the reconstructed data corresponding to diffraction peaks generated by a crystalline phase that is not changing during an experiment can be accumulated over time (i.e. using different/successive IXRD-CT datasets) improving the statistics. One may therefore argue that in fact there are not two but three resolutions that can be directly linked in IXRD-CT experiments: spatial, temporal and statistical.

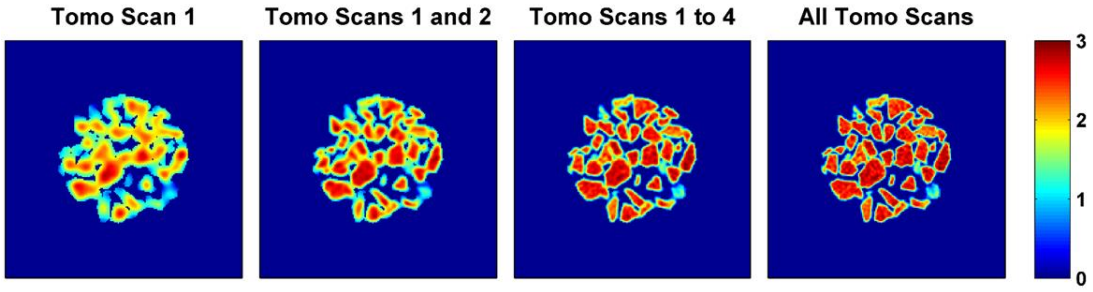

Figure 9: Reconstructed images corresponding to the main diffraction peak of cristobalite (i.e. reflection (111)) from the IXRD-CT scan 1 dataset. It is shown that combining multiple tomo scans leads to significant increase in spatial resolution. Color bar indicates intensity in arbitrary units.

In Figure 10, reconstructed images of cristobalite, Mn_2O_3 and two Na_2WO_4 phases corresponding to scattering 2θ angle of 1.85 (reflection (111)), 2.79 (reflection (222)), 1.42 (reflection (111)) and 1.48 ° (reflection (111)) respectively are shown. These 2θ angles correspond to the highest intensity diffraction peaks generated by these phases. An inspection of the sinograms reveals that there is a Na_2WO_4 phase transition taking place during the IXRD-CT scan 1. It should be noted here that it is fundamentally wrong to reconstruct the sinograms corresponding to the two Na_2WO_4 phases as the sample is not present in some parts of these two sinograms (Na_2WO_4 cubic and Na_2WO_4 orthorhombic in Figure 10). Here exactly lies the advantage of an IXRD-CT scan; it allows the tracking of solid-state changes taking place during a tomographic scan and the reconstruction of the respective sinograms does not violate the principles of computed tomography. This will be demonstrated in the next section. In Figure 10, it can also be seen that the Mn_2O_3 is not co-located with the cubic Na_2WO_4 which is in agreement with our previous study.[24] This is important as it simplifies the interpretation of the results. More specifically, it can be seen in Figure 10 that the new phase that appears is co-located with the cubic Na_2WO_4 phase suggesting that this is another Na-W-O phase.

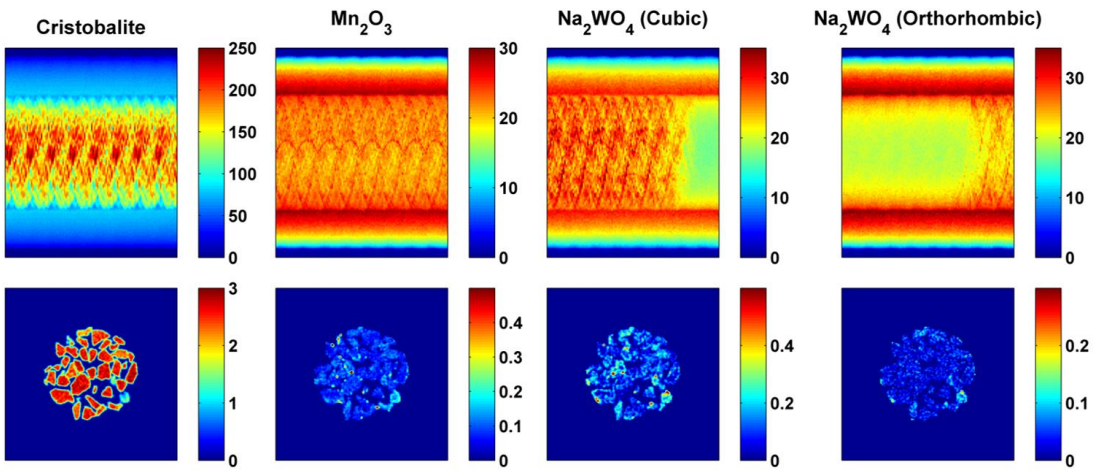

Figure 10: The sinograms from IXRD-CT scan 1 corresponding to cristobalite, Mn_2O_3, two Na_2WO_4 phases and the respective reconstructed images are shown (temperature range of 455 to 610 °C). The sinograms correspond to scattering angles 1.85, 2.79, 1.42 and 1.48° respectively. Color bars indicate intensity in arbitrary units.

The results from the IXRD-CT scan 2 are presented in Figure 11 where the sinograms and the corresponding reconstructed images of cristobalite, Mn_2O_3 and Na_2WO_4 (orthorhombic) are shown. The cubic Na_2WO_4 phase is no longer present and the orthorhombic Na_2WO_4 phase disappears at approximately 660 °C. No other Na-W-O phases were observed at higher temperatures. This is in agreement with our previous study of a catalytic membrane reactor containing this catalyst.[24]

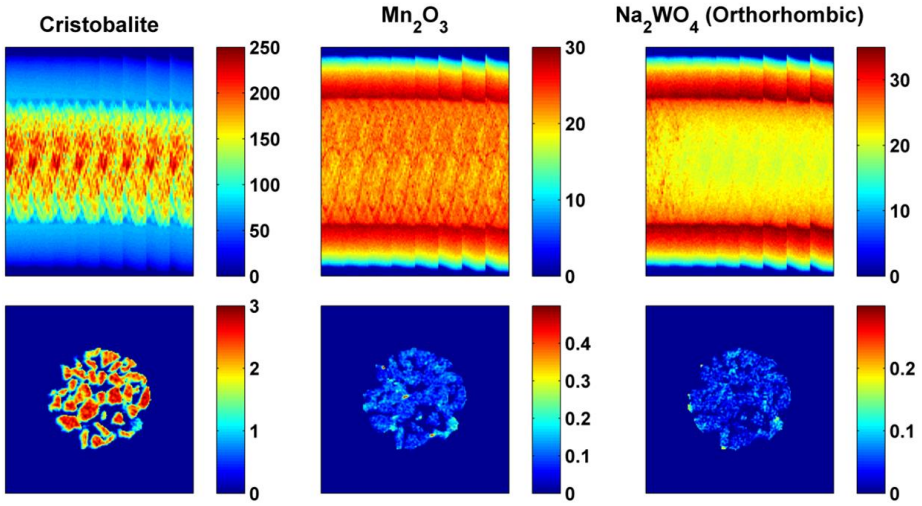

Figure 11: The sinograms from IXRD-CT scan 2 corresponding to cristobalite, Mn_2O_3, Na_2WO_4 (low symmetry) phases and the respective reconstructed images are shown (temperature range of 610 to 765 °C). The sinograms correspond to scattering angles 1.85, 2.79 and 1.48° respectively. Color bars indicate intensity in arbitrary units.

Time series

An example of the temporal resolution that an IXRD-CT scan can provide, is demonstrated in Figure 12. The reconstructed images presented correspond to the two Na_2WO_4 phases (scattering 2θ angles 1.42 and 1.48° respectively) present in the catalyst. The acquisition time of the complete IXRD-CT scan was approximately 35 min, therefore the reconstructed images shown in Figure 12 correspond to ¼ of the overall time (i.e. approximately 8.75 min). It can be clearly seen that the orthorhombic Na_2WO_4 phase forms/grows when the cubic Na_2WO_4 phase disappears.

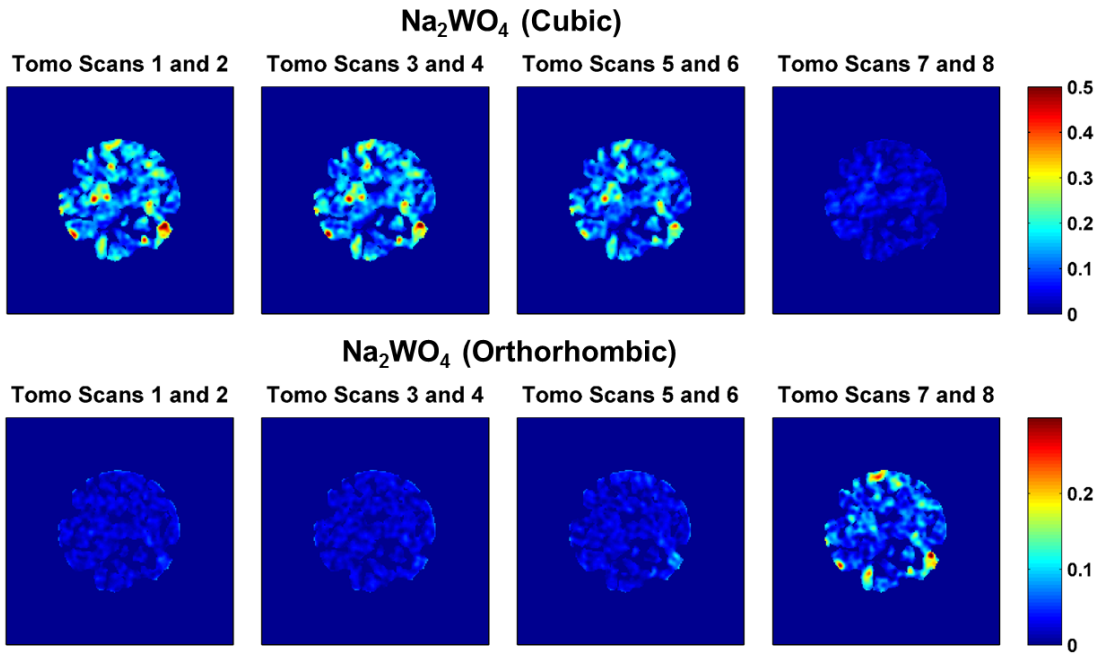

Figure 12: Top row: Reconstructed images corresponding to the high symmetry Na_2WO_4 phase. Bottom row: Reconstructed images corresponding to the low symmetry Na_2WO_4 phase. Temperature range: 455 to 494 °C for tomo scans 1 and 2, 494 to 533 °C for tomo scans 3 and 4, 533 to 571 °C for tomo scans 5 and 6, 571 to 610 °C for tomo scans 7 and 8. Color bars indicate intensity in arbitrary units.

In Figure 13, the summed diffraction patterns from two tomo scans (i.e. tomo scan 1 and 8) are presented. Both these tomo scans belong to the IXRD-CT scan 1. At the right side of Figure 13, a region of interest of these two diffraction patterns is selected showing the high intensity peaks corresponding to the cubic and orthorhombic Na_2WO_4 phases (red and cyan lines respectively).

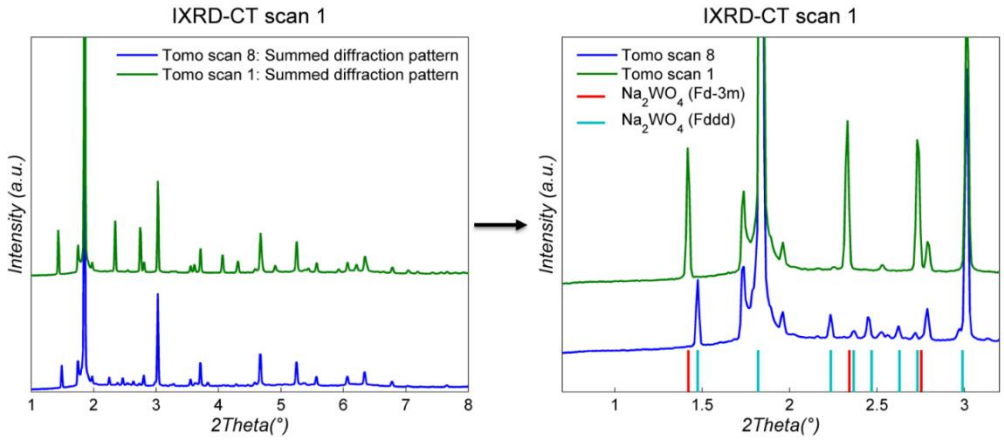

Figure 13: Left: Tomo scan 1 and 8 summed diffraction patterns (IXRD-CT scan 1). Right: A region of interest (ROI) of the two diffraction patterns, showing the main diffraction peaks generated by the two Na_2WO_4 phases.

Finally, as discussed previously, it is possible to combine tomo scans from successive IXRD-CT scans (Figure 3). An example is provided in Figure 14 where is it shown that by combining tomo scans 7 and 8 from IXRD-CT scan 1 with tomo scans 1 and 2 from IXRD-CT scan 2, a new IXRD-CT dataset is created. Another possibility, also shown in Figure 14, is to combine tomo scan 8 from IXRD-CT scan 1 and tomo scan 1 from IXRD-CT scan 2.

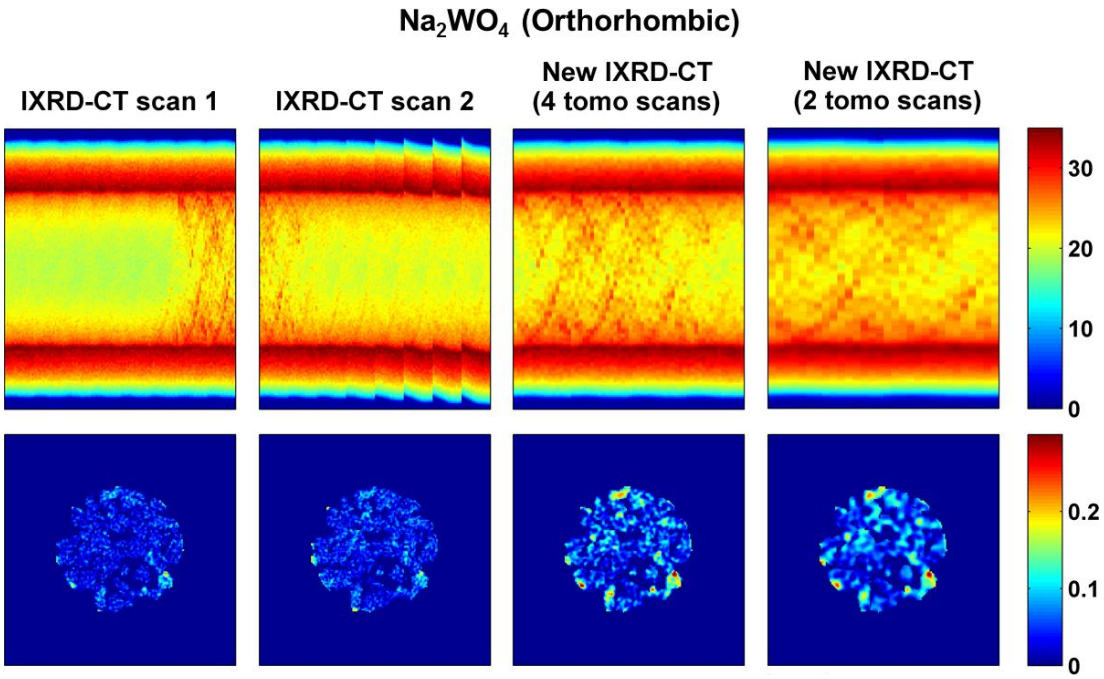

Figure 14: Sinograms and reconstructed images of the orthorhombic Na_2WO_4 phase using different IXRD-CT datasets. First column: IXRD-CT scan 1. Second column: IXRD-CT scan 2, Third column: New IXRD-CT dataset derived by combining tomo scans 7-8 from IXRD-CT scan 1 and tomo scans 1-2 from IXRD-CT scan 2. Fourth column: New IXRD-CT dataset derived by combining tomo scan 8 from IXRD-CT scan 1 and tomo scan 1 from IXRD-CT scan 2. Color bars indicate intensity in arbitrary units.

This is important as it can be seen that the reconstructed image of the new sinogram corresponding to the low symmetry Na_2WO_4 phase yields higher quality images. In this case, higher quality simply means that it is easier to identify the high concentration areas of this phase in the catalyst particles compared to the complete IXRD-CT scans.

Conclusions

We have presented a short review of the existing data collection strategies during an XRD-CT measurement and discussed the advantages/disadvantages of each method. However, a superior data collection strategy, interlaced XRD-CT (IXRD-CT), has been suggested as a method that allows, post experiment, choice between temporal and spatial resolution. The main advantages of the IXRD-CT method can be summarised as the following:

1. High spatial resolution can be chosen when the system is not changing
2. High temporal resolution can be chosen when the system is changing
3. Data from successive XRD-CT can be combined
4. Different Bragg reflections can be treated independently

This method not only enables dynamic XRD-CT studies on comparatively short time scales but also allows for improved spatial resolution if the system under study, or components within, appear to be unchanging. In this study, the feasibility to perform an IXRD-CT experiment was demonstrated using an OCM catalyst that was studied during temperature ramping under inert conditions. It was shown that increased time resolution can be achieved and solid state changes taking place inside a complete IXRD-CT could be tracked accurately. The real power in XRD-CT experiments is to be found when employed in time-resolved mode and that the interlaced scanning approach is the best method to retain the option of time *versus* spatial resolution without suffering the consequence of 'incorrect' choice when measuring unknown samples whose behaviour may be less predictable. In principle, the interlaced scanning approach can be also applied to other pencil beam chemical (i.e. hyperspectral) tomographic techniques, like XRF-CT, XAFS-CT and tomographic STXM.

References

1. Harding, G., J. Kosanetzky, and U. Neitzel, *X-ray diffraction computed tomography.* Medical Physics, 1987. **14**(4): p. 515-525.
2. Bleuet, P., et al., *Probing the structure of heterogeneous diluted materials by diffraction tomography.* Nature Materials, 2008. **7**(6): p. 468-472.
3. Stock, S.R., F. De Carlo, and J.D. Almer, *High energy X-ray scattering tomography applied to bone.* J Struct Biol, 2008. **161**(2): p. 144-50.
4. Álvarez-Murga, M., et al., *Microstructural mapping of C60 phase transformation into disordered graphite at high pressure, using X-ray diffraction microtomography.* Journal of Applied Crystallography, 2010. **44**(1): p. 163-171.
5. De Nolf, W. and K. Janssens, *Micro X-ray diffraction and fluorescence tomography for the study of multilayered automotive paints.* Surface and Interface Analysis, 2010. **42**(5): p. 411-418.
6. Basile, F., et al., *Combined Use of Synchrotron-Radiation-Based Imaging Techniques for the Characterization of Structured Catalysts.* Advanced Functional Materials, 2010. **20**(23): p. 4117-4126.
7. Artioli, G., et al., *X-ray diffraction microtomography (XRD-CT), a novel tool for non-invasive mapping of phase development in cement materials.* Analytical and Bioanalytical Chemistry, 2010. **397**(6): p. 2131-2136.
8. Palancher, H., et al., *Hard X-ray diffraction scanning tomography with sub-micrometre spatial resolution: application to an annealed γ-U0.85Mo0.15particle.* Journal of Applied Crystallography, 2011. **44**(5): p. 1111-1119.
9. Valentini, L., et al., *Towards three-dimensional quantitative reconstruction of cement microstructure by X-ray diffraction microtomography.* Journal of Applied Crystallography, 2011. **44**(2): p. 272-280.
10. Stock, S.R. and J.D. Almer, *Diffraction microcomputed tomography of an Al-matrix SiC-monofilament composite.* Journal of Applied Crystallography, 2012. **45**(6): p. 1077-1083.
11. Valentini, L., et al., *Multifractal Analysis of Calcium Silicate Hydrate (C-S-H) Mapped by X-ray Diffraction Microtomography.* Journal of the American Ceramic Society, 2012. **95**(8): p. 2647-2652.
12. Voltolini, M., et al., *Understanding cement hydration at the microscale: new opportunities from `pencil-beam' synchrotron X-ray diffraction tomography.* Journal of Applied Crystallography, 2013. **46**(1): p. 142-152.
13. Egan, C.K., et al., *Non-invasive imaging of the crystalline structure within a human tooth.* Acta Biomaterialia, 2013. **9**(9): p. 8337-8345.
14. Ruiz-Martínez, J., et al., *Correlating Metal Poisoning with Zeolite Deactivation in an Individual Catalyst Particle by Chemical and Phase-Sensitive X-ray Microscopy.* Angewandte Chemie International Edition, 2013. **52**(23): p. 5983-5987.
15. Bonnin, A., et al., *Impurity precipitation in atomized particles evidenced by nano x-ray diffraction computed tomography.* Applied Physics Letters, 2014. **105**(8): p. 084103.
16. Cedola, A., et al., *Three dimensional visualization of engineered bone and soft tissue by combined x-ray micro-diffraction and phase contrast tomography.* Phys Med Biol, 2014. **59**(1): p. 189-201.
17. Jensen, K.M.O., et al., *X-Ray Diffraction Computed Tomography for Structural Analysis of Electrode Materials in Batteries.* Journal of the Electrochemical Society, 2015. **162**(7): p. A1310-A1314.

18. Vanmeert, F., G. Van der Snickt, and K. Janssens, *Plumbonacrite identified by X-ray powder diffraction tomography as a missing link during degradation of red lead in a Van Gogh painting.* Angew Chem Int Ed Engl, 2015. **54**(12): p. 3607-10.
19. Wragg, D.S., et al., *Rietveld analysis of computed tomography and its application to methanol to olefin reactor beds.* Journal of Applied Crystallography, 2015. **48**(6): p. 1719-1728.
20. Jacques, S.D., et al., *Dynamic X-ray diffraction computed tomography reveals real-time insight into catalyst active phase evolution.* Angew Chem Int Ed Engl, 2011. **50**(43): p. 10148-52.
21. O'Brien, M.G., et al., *Active phase evolution in single Ni/Al2O3 methanation catalyst bodies studied in real time using combined μ-XRD-CT and μ-absorption-CT.* Chemical Science, 2012. **3**(2): p. 509.
22. Beale, A.M., et al., *Chemical imaging of the sulfur-induced deactivation of Cu/ZnO catalyst bodies.* Journal of Catalysis, 2014. **314**: p. 94-100.
23. Price, S.W.T., et al., *In Situ Microfocus Chemical Computed Tomography of the Composition of a Single Catalyst Particle During Hydrogenation of Nitrobenzene in the Liquid Phase.* Angewandte Chemie, 2015. **127**(34): p. 10024-10027.
24. Vamvakeros, A., et al., *Real time chemical imaging of a working catalytic membrane reactor during oxidative coupling of methane.* Chemical Communications, 2015. **51**(64): p. 12752-12755.
25. Grunwaldt, J.-D., J.B. Wagner, and R.E. Dunin-Borkowski, *Imaging Catalysts at Work: A Hierarchical Approach from the Macro- to the Meso- and Nano-scale.* ChemCatChem, 2013. **5**(1): p. 62-80.
26. Beale, A.M., et al., *Progress towards five dimensional diffraction imaging of functional materials under process conditions.* Coordination Chemistry Reviews, 2014. **277–278**: p. 208-223.
27. Hounsfield, G.N., *Computerized transverse axial scanning (tomography): I. Description of system.* British Journal of Radiology, 1973. **46**(552): p. 1016-1022.
28. Elliott, J.C. and S.D. Dover, *X-ray microtomography.* Journal of Microscopy, 1982. **126**(2): p. 211-213.
29. Álvarez-Murga, M., P. Bleuet, and J.L. Hodeau, *Diffraction/scattering computed tomography for three-dimensional characterization of multi-phase crystalline and amorphous materials.* Journal of Applied Crystallography, 2012. **45**(6): p. 1109-1124.
30. Gordon, R., R. Bender, and G.T. Herman, *Algebraic Reconstruction Techniques (ART) for three-dimensional electron microscopy and X-ray photography.* Journal of Theoretical Biology, 1970. **29**(3): p. 471-476,IN1-IN2,477-481.
31. Kak, A.C., *Computerized tomography with X-ray, emission, and ultrasound sources.* Proceedings of the IEEE, 1979. **67**(9): p. 1245-1272.
32. Beister, M., D. Kolditz, and W.A. Kalender, *Iterative reconstruction methods in X-ray CT.* Physica Medica, 2012. **28**(2): p. 94-108.
33. Liu, L., *Model-based Iterative Reconstruction: A Promising Algorithm for Today's Computed Tomography Imaging.* Journal of Medical Imaging and Radiation Sciences, 2014. **45**(2): p. 131-136.
34. Vamvakeros, A., et al., *Removing multiple outliers and single-crystal artefacts from X-ray diffraction computed tomography data.* Journal of Applied Crystallography, 2015. **48**(6): p. 1943-1955.
35. Boisseau, P., *Determination of Three Dimensional Trace Element Distributions by the Use of Monochromatic X-ray Microbeams*. 1986: Massachusetts Institute of Technology, Department of Physics.

36. Boisseau, P. and L. Grodzins, *Fluorescence tomography using synchrotron radiation at the NSLS.* Hyperfine Interactions, 1987. **33**(1-4): p. 283-292.
37. Schroer, C.G., et al., *Mapping the chemical states of an element inside a sample using tomographic x-ray absorption spectroscopy.* Applied Physics Letters, 2003. **82**(19): p. 3360-3362.
38. Wang, et al., *Soft X-ray microscopy with a cryo scanning transmission X-ray microscope: II. Tomography.* Journal of Microscopy, 2000. **197**(1): p. 80-93.
39. Johansson, G.A., et al., *Three-dimensional chemical mapping by scanning transmission X-ray spectromicroscopy.* Journal of Synchrotron Radiation, 2007. **14**(5): p. 395-402.
40. Kak, A.C., et al., *Principles of Computerized Tomographic Imaging*. 1988: IEEE Press.
41. Arndt, S., et al., *Mn–Na2WO4/SiO2 as catalyst for the oxidative coupling of methane. What is really known?* Applied Catalysis A: General, 2012. **425-426**: p. 53-61.
42. Haynes, W.M., *CRC Handbook of Chemistry and Physics, 95th Edition*. 2014: CRC Press.
43. Goranson, R.W. and F.C. Kracek, *An experimental investigation of the effect of pressure on phase equilibria of sodium tungstate and of related thermodynamic properties.* The Journal of Chemical Physics, 1935. **3**(2): p. 107-115.
44. Sadjadi, S., et al., *Feasibility study of the Mn-Na2WO4/SiO2 catalytic system for the oxidative coupling of methane in a fluidized-bed reactor.* Catalysis Science and Technology, 2015. **5**(2): p. 942-952.
45. Austin, J.B. and R.H.H. Pierce Jr, *The linear thermal expansion of sodium tungstate between 20° and 600°.* The Journal of Chemical Physics, 1935. **3**(11): p. 683-686.
46. Pistorius, C.W.F.T., *Phase diagrams of sodium tungstate and sodium molybdate to 45 kbar.* The Journal of Chemical Physics, 1966. **44**(12): p. 4532-4537.
47. Bottelberghs, P.H. and F.R. van Buren, *Phase relations, dopant effects, structure, and high electrical conductivity in the Na2WO4Na2MoO4 system.* Journal of Solid State Chemistry, 1975. **13**(3): p. 182-191.
48. Lima, C.L., et al., *Temperature-induced phase transformations in Na2WO4 and Na2MoO4 crystals.* Journal of Raman Spectroscopy, 2011. **42**(4): p. 799-802.
49. Hou, S., et al., *Site requirements for the oxidative coupling of methane on SiO 2-supported Mn catalysts.* Industrial and Engineering Chemistry Research, 2006. **45**(21): p. 7077-7083.
50. Hiyoshi, N. and T. Ikeda, *Oxidative coupling of methane over alkali chloride-Mn-Na2WO4/SiO2 catalysts: Promoting effect of molten alkali chloride.* Fuel Processing Technology, 2015. **133**: p. 29-34.
51. Toby, B.H. and R.B. Von Dreele, *GSAS-II: The genesis of a modern open-source all purpose crystallography software package.* Journal of Applied Crystallography, 2013. **46**(2): p. 544-549.

CHAPTER 5: *Operando* studies of fixed bed reactors for the oxidative coupling of methane

Abstract

Mn-Na-W/SiO_2-based materials are considered to be the most promising catalysts for the oxidative coupling of methane (OCM) to light olefins reaction. Such catalysts have been extensively studied over the past 25 years but there is still ongoing debate regarding the active state of these catalysts and the reasons behind their deactivation over time. In this work, we present the first multi-length-scale studies of a Mn-Na-W/SiO_2 and a La-promoted Mn-Na-W/SiO_2 catalyst under real reaction conditions. The catalysts were investigated from the reactor level (mm scale) down to the single catalyst particle level (μm scale) with different synchrotron X-ray based computed tomography techniques (multimodal CT experiments). These *in situ* spatially-resolved studies performed with XRD-CT (catalytic reactor) and multimodal μ-XRF/XRD/absorption CT (single catalyst particle) revealed that the unpromoted Mn-Na-W/SiO_2 catalyst is chemically unstable at high temperatures and there is loss of active components. One of the main catalyst components, Na_2WO_4, is seen to melt before reaching the desired operating reactor temperature of 800 °C and the Na^+ and WO_2^{2-} species become not only mobile but also volatile, even chemically interacting with the reactor vessel. Furthermore, the SiO_2 support of the catalyst is seen to evolve with time at high temperatures gradually changing from cristobalite to the tridymite and quartz phases. Importantly, it is shown that the presence of highly crystalline Mn_2O_3/Mn_7SiO_{12} and/or $MnWO_4$ is not required to yield an active catalyst. Last but not least, the higher stability of the La-promoted Mn-Na-W/SiO_2 catalyst compared to the unpromoted one is also explained for the first time and it is mainly attributed to the formation and growth of a new phase at high temperatures, identified as $NaLa(WO_4)_2$, which acts as a chemical trap for the mobile/volatile Na^+

and WO_2^{2-} species. This knowledge opens new pathways to rationally designing improved catalysts for the OCM reaction.

Literature Review

Introduction

The exploitation of shale gas, by hydraulic fracturing or fracking, along with the continuous global effort to reduce/ban gas flaring due to air pollution, have already led to a dramatic increase in the availability of methane.[1, 2] Nowadays, methane, which is the main component of natural gas, shale gas and renewable biogas, is considered to be an abundant hydrocarbon source compared to crude oil and there is a lot of ongoing interest in producing higher value bulk chemicals from it.[3, 4] Environmentally-friendly and cost-effective processing technologies of direct conversion of methane to light olefins (e.g. ethylene), alternative to the highly energy consuming steam cracking of crude oil, are needed.[4, 5]

Traditionally, the methane upgrading to higher hydrocarbon molecules is achieved indirectly. At industrial scale, in gas-to-liquids (GTL) plants, the methane is first reformed (i.e. steam, partial or autothermal reforming) to produce "synthesis gas" (i.e. a mixture of CO and H_2) which is then used in a second catalytic reactor to produce synthetic fuels (liquids and/or gases) via the Fischer–Tropsch reaction.[6] However, alternative technologies that require a single catalytic reactor allowing the direct conversion of methane to industrially useful chemicals are desired and such technologies have recently gained a lot of attention.[7-11] A characteristic example is the oxidative coupling of methane (OCM) reaction which can potentially provide an economically viable route for ethylene production:[12-14]

$$2CH_4 + O_2 \rightarrow C_2H_4 + 2H_2O \qquad \Delta H°_{298K} = -282 \text{ kJ mol}^{-1}$$

In general, high temperatures (i.e. typically above 750 °C) are required for the OCM reaction due to the chemical stability of the methane molecule (energy of ca. 438 KJ mol^{-1} is required to break the C-H bond).[15] In order for the OCM reaction to be an economically viable technology for industrial applications, the solid catalyst should exhibit not only high methane activity and selectivity to C_2 molecules but also long-

term chemical stability under the required high temperatures. This is the main reason why research is still focusing on the development of new OCM catalysts.

The Mn-Na-W/SiO_2 catalyst

Since the early work of Keller and Bhasin, who first screened numerous materials as catalysts for the OCM reaction (i.e. various metal oxides on α-Al_2O_3 support), there have been thousands of reports in literature regarding active OCM catalysts; a Web of Science search for "oxidative coupling of methane" (i.e. title only search) gives more than 1000 results (1982-2017 time period).[16] However, it is generally accepted that the most promising OCM catalysts are the Mn-Na-W/SiO_2 based catalysts as such catalysts exhibit high performance under OCM reaction conditions (>20 % yield for C_2 molecules at 800 °C).[15, 17] Although this family of catalysts has been extensively investigated over the past 25 years, there is still much debate in literature regarding the active phases/species, chemical stability, role of promoters, preferred method of preparation, optimal weight loading of the different elements and even the reasons behind the deactivation of these catalysts.[18, 19]

Looking for the best combination of materials

Sofranko *et al.* examined the performance of various transition metal oxides (i.e. 5 wt. % metal loadings) in a cyclic redox mode.[20] The methane first reacted with the catalyst in the absence of oxygen to form coupling products and then the reduced catalyst was re-oxidized with air in a separate step. Manganese oxide on silica was found to be the best catalyst in terms of stability and productivity. The species responsible for the high selectivity to C_2 were considered to be manganese oxide or manganese silicate species. Jones *et al.* investigated the effect of the addition of alkali and alkali earth metals to the manganese oxide on silica catalyst; sodium pyrophosphate (i.e. 15 wt. % Mn – 5 wt. % $Na_4P_2O_7$ / SiO_2 catalysts) showed the most promising results (with an increase of 40 % for C_2 selectivity compared to the alkali free catalyst).[21] It was suggested that the role of the pyrophosphate ion is to increase the stability of the catalyst, while the sodium ion increases the selectivity to C_2 molecules by increasing the basicity at the surface of the catalyst. It was also suggested that a sodium-manganese interaction may prevent the full oxidation of the methane. It was later tested in a fixed bed reactor where methane and air were

co-fed into the reactor and it was reported that activity was higher in this mode.[22] Ji *et al.* showed that the addition of transition metals to a Mn-W/SiO_2 catalyst does not improve the catalytic performance and that the positive effect of the addition of alkali metals ions (Na and K) is greater than the effect of alkali earth ions Ba and Ca.[23] Malekzadeh *et al.* used different transition metal oxides (Mn, V, Cr, Mn, Fe, Co and Zn) on Na_2WO_4/SiO_2 catalysts and it was shown that the Mn-Na-W/SiO_2 catalysts showed the best performance.[24] Both Mahmoodi *et al.* and Hou *et al.*, studied the effect of using different oxo-anions (e.g. V, Cr, Nb, W, Mo, P, S) in the Na-Mn/SiO_2 catalyst and it was shown that the Mn-Na-W/SiO_2 catalyst exhibited the best performance in terms of both activity (methane conversion) and selectivity (to C_2 molecules).[25, 26] Yildiz *et al.* tried different supports for the Mn-Na-W catalyst and the SiO_2 supported catalyst showed the best results.[27] Later studies by the same group showed that when ordered mesoporous silicas are used as support materials, the performance (activity and C_2 selectivity) of the Mn-Na-W/SiO_2 is increased.[28] It should be mentioned though that the catalysts were tested under OCM reaction conditions for ca. 16 h so the long-term beneficial effect of the microporous SiO_2 remains to be seen.

Why is it the most promising OCM catalyst?

Fang *et al.* were the first to develop the Mn-Na_2WO_4/SiO_2 as a catalyst for the OCM reaction.[29, 30] This catalyst is considered to be one of the best catalysts for the OCM reaction mainly due to its stability and productivity under high temperatures (i.e. > 20 % methane conversion and 80 % C_2 selectivity at ca. 800 °C).[31, 32] Jiang *et al.* investigated the interaction between the metal oxides and the support of this catalyst.[33] The results showed a strong interaction between Na_2WO_4 and SiO_2 as the transformation of amorphous silica to the crystalline α-cristobalite phase is directly related to the presence of Na_2WO_4. More specifically, the addition of 1 wt. % Na_2WO_4 led to the formation of cristobalite and complete transformation of amorphous silica was achieved when 4 wt. % Na_2WO_4 was used. It was later suggested by Palermo *et al.* that sodium has a dual role; it acts both as a structural (by inducing the phase transformation of amorphous silica to α-cristobalite) and as a chemical promoter (by dispersing the tungsten surface species).[34] It is interesting to note that in the work

of Jiang *et al.*, the XRD peaks corresponding to a Mn_2O_3 phase (1.9 wt. % Mn) appeared only when Na_2WO_4 was also used.[33] According to the authors, this implied both high dispersion on the manganese oxide on the SiO_2 support and a strong interaction with it. XPS measurements suggested the presence of oxygen species that did not belong to Na_2WO_4, Mn_2O_3 or SiO_2. A surface $Si_3WO_{8.5}$ cluster, in which a W=O and three surface W-O-Si bonds are present, was suggested as the active centre for the OCM reaction. In contrast to the work of Sofranko *et al.*, Jiang *et al.* suggested that tungsten silicate at the surface of the catalyst must be responsible for the selective oxidation of methane and not a manganese silicate species.[20, 33] It was also suggested that the role of Mn in the Mn_2O_3 phase is to enhance the lattice oxygen transport and the oxygen exchange between the gas phase and the lattice oxygen.[33] It has to be noted though that the 1.9 wt. % Mn – 5 wt % Na_2WO_4/SiO_2 gave higher C_2 yield compared to the Mn free catalyst (i.e. 5 wt. % Na_2WO_4/SiO_2).

Wang *et al.* investigated the performance of 2 wt. % Mn – 5 wt. % Na_2WO_4/SiO_2, 2 wt. % Mn – 5 wt. % Na_2WO_4/MgO, 5 wt. % $NaMnO_4$/MgO, 5 wt. % Na_2WO_4/MgO, 5 wt. % Na_2WO_4/SiO_2, and 5 wt. % $NaMnO_4/SiO_2$ in a pulse mode reactor and in a continuous flow reactor.[32] The first three catalysts exhibited high activity and selectivity for C_2 molecules (20 % conversion of methane and 80 % selectivity for C_2 at 800 ^oC with a CH_4/O_2 ratio of 7.4). The Mn-Na_2WO_4/SiO_2 and the Mn-Na_2WO_4/MgO also showed high stability, as the performance of these catalysts did not decrease for more than 30 h of time on stream. In a later study by Pak and Lunsford, the Mn-Na_2WO_4/MgO catalyst gradually deactivated over time due to the formation of hot spots as large as 150 °C (with respect to the temperature of the bed) while the Mn-Na_2WO_4/SiO_2 remained stable for 97 h of operation.[35] The cause of the reduction in activity for the Mn-Na_2WO_4/MgO was suggested to be the decrease in Mn concentration at the catalyst surface. In a similar study by the same group, the deactivation of the Mn-Na_2WO_4/SiO_2 catalyst was also observed and it was suggested that the formation of hot spots in large catalyst beds mask the deactivation of the catalyst as the initial performance of the catalyst could be recovered by increasing the temperature.[36] The formation of hot spots under OCM reaction conditions and their negative effect on the catalyst performance have been recently investigated by

Lee *et al.*[37] The performance of the $NaMnO_4$/MgO and the $NaMnO_4/SiO_2$ decreased over time, and it was concluded that W plays an important role in the stability of the catalyst by preventing loss of the alkali metal (Na). The same explanation was given by Jones *et al.* regarding the high stability of the Mn-$Na_4P_2O_7/SiO_2$ catalyst (i.e. the pyrophosphate ion increased the stability by preventing loss of Na).[21] Wang *et al.* suggested that the formation of sodium and manganese silicates is prevented by WO_4^{2-} ions and that this is indicated by XRD patterns.[32] Unfortunately, the diffraction patterns are not presented in the paper. The catalysts that did not contain Mn exhibited inferior performance (i.e. both in activity and selectivity) indicating that Mn is directly related to the active phase of the catalyst. Also, the performance of the Na_2WO_4/MgO catalyst increased significantly with the addition of Mn (above 1 wt. % Mn no additional improvement took place) which further supports the authors' suggestion. Furthermore, the fact that the addition of Na_2WO_4 to Mn/MgO enhanced its poor catalytic performance and that the $NaMnO_4$/MgO catalyst shows good performance indicates that Na is also directly related to the active phase of the catalyst. Also, the $MnWO_4$ phase was detected with XRD in all catalysts but it was suggested that this is not the active phase because the $NaMnO_4$/MgO catalyst shows high catalytic activity and does not contain W.[32] The results from XPS measurements indicated that the concentration of Na is significantly higher in the surface than in the bulk and that probably different Na-containing phases are present (i.e. apart from the crystalline Na_2WO_4 phase). These conclusions are not in agreement with the work of Jiang *et al*.[33] It has to be noted however, that the catalytic activity data for several catalysts are not presented in the paper.[32]

The results from the pulse reaction experiments performed by Wang *et al*. are in agreement with those reported from Sofranko *et al.*, suggesting that the performance of the catalysts was higher in the co-feed mode than the pulse mode.[22, 32] This means that oxygen in the gas phase is essential in order to achieve high methane conversion and that the contribution of bulk lattice oxygen is negligible. This is also in agreement with later studies by Pak, Qiu and Lunsford.[36] It was suggested that the active sites might be created by interaction between the oxygen from the gas phase and manganese ions at the catalyst surface. It was further pointed

out that while Na enhances the selectivity to C_2, it does not contribute to the activity of the catalyst. However, it was suggested that the role of Na is to disperse the Mn ions.

Wang *et al.* claimed that the main Mn-containing phases in their Mn-Na_2WO_4/SiO_2 catalyst were $MnWO_4$ and Mn_2O_3.[32] However, the XRD patterns were not presented in the paper. When W was not used, the only Mn-containing phase detected was Mn_7SiO_{12} and Na was found in the form of sodium silicates. The addition of Na_2CO_3 led to a decrease in $MnWO_4$ and α-cristobalite phases but also to an increase in Na_2WO_4 and tridymite phases. The XPS results showed that the surface composition of the Mn-Na_2WO_4/SiO_2 varies significantly from that of the bulk and that manganese is present as Mn^{3+} and/or Mn^{2+}. This transition from Mn^{3+} to Mn^{2+} has also been claimed by Kou *et al.*[38]

The group of Li *et al.* also performed long-term stability tests of the Mn-Na_2WO_4/SiO_2 and XRD results showed that the cristobalite phase of the support gradually converts to tridymite and α-quartz phases.[39, 40] The same SiO_2 phase transition has been verified by Wang *et al.* and Ahari *et al.* and it was shown that the activity of the catalyst was not affected by it.[41, 42] In contrast to the study of Wang *et al.* (catalyst prepared by the incipient wetness impregnation method), the crystalline Na_2WO_4 and Mn_2O_3 phases were not present in the XRD patterns collected at room temperature after a 500 h stability test under OCM conditions as presented in the work of Li *et al.* (catalyst prepared by the mixture slurry method).[39-41] The activity of the catalyst did not change significantly but the CO selectivity increased and the C_2 selectivity decreased over time. It was claimed that there was loss of active components during the operation of the catalyst. However, it is essential to note that there are peaks present in the diffraction pattern after the OCM experiment that have not been indexed. These diffraction peaks are probably generated by a crystalline $MnWO_4$ phase. It should also be noted that decrease in the performance of Na-Mn-W/SiO_2 catalysts over time under OCM reaction conditions has been reported in other studies.[35, 36, 43-45] In contrast, Mn-Na-W/SiO_2 catalysts prepared by fluidized bed processing and the solution combustion method have shown high stability at high temperatures.[46, 47]

Kou *et al.* characterised three Mn-Na_2WO_4/SiO_2 catalyst samples (i.e. fresh catalyst, after 100 h of operation and at the end of the OCM experiment after 450 h of operation) with X-ray absorption fine structure spectroscopy (XAFS) and XPS measurements.[38] It was suggested that discretely distributed oxygen-enriched amorphous phases are present at the surface of the catalyst (i.e. tetrahedral WO_4 and octahedral MnO_6). The formation of tetrahedral coordinated Mn^{2+} species takes place after long runs under OCM conditions while the WO_4 species disappear from the surface. The W in the tetrahedral WO_4 was claimed to be responsible for the activation of methane and the Mn in the octahedral MnO_6 for the oxygen transformation and transport. It has to be noted that this was not an *in situ* XAFS study as the catalyst samples were taken from the OCM reactor (i.e. quenched samples) and the measurements were performed at room temperature. It should also be noted that the OCM reaction mixture used in this study contained steam too (CH_4 : O_2 :H_2O = 6 : 1 : 3). Wang *et al.* concluded that W contributes to the stability of the catalyst emphasising though that it is not a component of the active phase/species and that highly dispersed Mn is responsible for the catalytic activity.[32] It was also suggested that high selectivity to C_2 molecules is achieved in the presence of Na and that the active phase exists only in the presence of gas phase oxygen and only for a short period of time.

Ji *et al.* prepared numerous Mn-Na_2WO_4/SiO_2 catalysts by varying the contents (wt. %) of Mn, Na and W in order to investigate the relationship between the structure and the performance of these catalysts.[48] XRD, XPS and Raman spectroscopy measurements revealed valuable information about the properties of the Mn-Na_2WO_4/SiO_2 catalyst. The optimal composition was found to be: 0.4-2.3 % Na, 2.2-8.9 % W and 0.5-3 % Mn. The surface concentration of Mn was shown to be directly related to the activity of the catalyst and the selectivity to C_2 molecules. It was suggested that the role of Na is to enhance the migration of Mn and W to the surface of the catalyst, therefore improving the methane conversion and selectivity to C_2 molecules, as well as to moderate the formation of CO. The activity and selectivity of the tetrahedral WO_4 were higher when compared to the octahedral WO_6. It was concluded that the active sites should include Na-O-Mn and Na-O-W species.

La-promoted Mn-Na-W/SiO_2 catalysts

There are only a few studies available in literature where the effects of promoting the Mn-Na-W/SiO_2 catalyst with La have been investigated.[44, 45, 49, 50] Wu *et al.* were the first to study the La-Na-W/SiO_2 catalysts and it was shown that the catalytic performance is significantly enhanced compared to the La-free catalyst (i.e. approximately 25 % C_2 yield - 45 % increase compared to the unpromoted catalyst) regardless of the amount of La loading (i.e. 0.05, 0.25, 2 and 10 wt. % La).[49] Ghose *et al.* achieved 27 % C_2 yield, one of the highest reported values for fixed bed reactors in literature, using a 5 % La-10 % Na_2WO_4-5 % Mn/SiO_2 catalyst.[50] More importantly, the La promoted Mn-Na-W/SiO_2 catalysts show not only higher performance under OCM reaction conditions but also exhibit higher stability.[44, 45] However, to date, La-Mn-Na-W/SiO_2 catalysts have not been investigated with any scattering or spectroscopic technique under reaction conditions.

Summary

In conclusion, it is evident that there is much disagreement in literature regarding the structure-activity relationships for the Mn-Na_2WO_4/SiO_2 catalyst and only a handful of results are consistent (e.g. the phase transformation of amorphous silica to the inert α-cristobalite phase). In a recent review paper by Arndt *et al.*, it was suggested that a synergistic effect between Mn, Na and W must be responsible for the catalyst activity but it is still not clear how these catalysts behave under reaction conditions as there is a lack of *in situ* or *operando* studies in literature regarding these materials.[31] The following study aims to rationalise the diversity of observations reported in the literature to date by investigating the behaviour of an unpromoted and a La-promoted Mn-Na-W/SiO_2 catalyst under *operando* conditions and to discover the roles of the various catalyst components.

Materials and Methods

Catalyst preparation

The 2 wt. % La – 2 wt. % Mn – 1.6 wt. % Na – 3.1 wt. %W/SiO_2 and the 2 wt. % Mn – 1.6 wt. % Na – 3.1 wt. % W/SiO_2 catalysts were prepared by the sequential incipient wetness impregnation method. At first a SiO_2 support (commercial Silica gel Davisil

646) was impregnated by an aqueous solution of sodium tungstate dehydrate $Na_2WO_4 \cdot 2H_2O$ and sodium oxalate $Na_2C_2O_4$ taken in appropriate amounts. The Na-W/SiO_2 was dried at 120 °C for 6 h and was then impregnated by an aqueous solution of manganese (II) acetate tetrahydrate $Mn(CH3COO)_2 \cdot 4H_2O$ and lanthanum nitrate hexahydrate $La(NO_3)_3 \cdot 6H_2O$ salts, taken in appropriate concentrations. The catalysts were then dried at 120 °C for 6 h and calcined in air at 850 for 6 h with a heating rate of 2 °C min^{-1}. The catalysts used in this study were kindly provided by the Boreskov Institute of Catalysis (BIC).

Operando XRD-CT measurements at ID15, ESRF

XRD-CT measurements were made at beamline station ID15A of the ESRF using a 92.8 keV monochromatic X-ray beam focused to have a spot size of 25 µm x 25 µm. 2D powder diffraction patterns were collected using a Pilatus3 X CdTe 300K (487 × 619 pixels, pixel size of 172 µm) hybrid photon counting area detector which uses cadmium telluride (CdTe) as the semiconducting direct conversion layer. The acquisition time per point was 50 ms. The tomographic measurements were made with 180 translation steps covering 0 - 180° angular range, in steps of 1.5° (i.e. 120 line scans). In total, 21600 2D powder diffraction patterns were collected for each XRD-CT scan. The calibration was performed using a CeO_2 NIST standard. Every 2D diffraction image was converted to a 1D powder diffraction pattern after applying an appropriate filter to remove outliers or single-crystal diffraction artefacts using in-house developed MATLAB scripts.[51] The data were then reshaped to form a 3D matrix (i.e. 180 × 120 × 1500 matrix) where the 1st dimension corresponds to the translation steps, the 2nd dimension to the rotation steps and the 3rd dimension to the channels in the 1D powder diffraction patterns. Each sinogram (in total 1500 sinograms) was reconstructed using the SART algorithm from the ASTRA Toolbox.[52] In order to decrease the required computational time to reconstruct the data, the image obtained using the filtered back projection algorithm was used as the matrix for the first iteration of the SART algorithm (instead of an empty matrix). Each sinogram was reconstructed independently and the reconstructed data yielded a 180 × 180 × 1500 matrix). The voxel size was 25 μm^3 and the physical area covered was 4.5 x 4.5 mm.

The two fixed bed reactors tested comprised 2 % Mn-1.6 % Na-3.1 % W/SiO_2 and 2 % La-2 % Mn-1.6 % Na-3.1 % W/SiO_2 catalysts respectively (within 4 mm outer diameter quartz capillary fixed bed reactors supported by glass wool). In both cases the catalyst loading was 35 mg. The reactor was mounted into a gas delivery stub, itself mounted to a standard goniometer (to enable alignment). The goniometer was fixed to a rotation stage set upon a translation stage to facilitate the movements required for the CT measurement. Heating was achieved by virtue of two Eurotherm controlled hot air blowers heating each side of the catalytic reactor. XRD-CT measurements were made at nominal temperatures, ambient up to 1000 °C equating to actual temperatures (i.e. after temperature calibration) of ambient and 800 °C with a nominal ramp rate of 5 °C min^{-1}. During the *in situ* XRD-CT measurements, the outflow gasses were monitored by mass spectrometry using an Ecosys portable mass spectrometer. The mass spec line was inserted inside the capillary from the top. The experimental sample setup is shown in Figure 1.

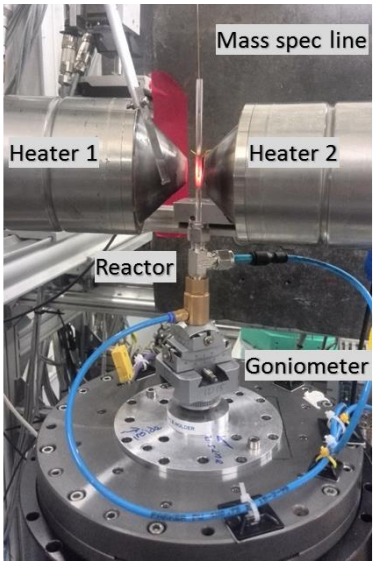

Figure 1: Photograph of the experimental setup used for the operando XRD-CT measurements at the ID15A beamline of the ESRF; indicated are the main parts of the experimental apparatus.

Rietveld analysis of XRD-CT data

Quantitative Rietveld refinement was performed using the reconstructed diffraction patterns, on a voxel by voxel basis. The MultiRef MATLAB framework was chosen for the Rietveld analysis as MATLAB allows for parallel computing using multicore processors. Such a feature is essential when full power profile analysis of XRD-CT data

is attempted due to the very large number of datasets.[53] The Multiref framework reads/writes the required files and the Rietveld refinement is performed by the GSAS software.[54] The results from the refinements can be imported into MALTAB and create the various images (e.g. phase distribution maps based on the scale factors, lattice parameters etc.).

However, at this point it should be noted that there are some problems/limitations/bugs with this approach as GSAS/EXPGUI was not designed for the analysis of XRD-CT data:

- As always, the starting model for the quantitative Rietveld refinement needs to take into account all the different crystalline phases that are present in the sample. However, if the sample is inhomogeneous (which is usually the reason why an XRD-CT experiment is performed in the first place), then there will be regions in the sample where one or more phases may be absent. Although this should not be a problem for the Rietveld refinement (as the scale factors for these phases should be set to/close to zero), in many cases GSAS fails to properly deal with this issue and the intensities for the corresponding phases can take arbitrary values. Thankfully, the scale factors corresponding to these phases take on a negative value so it is trivial to remove these pixels from the results just by setting the negative values to zero (i.e. scale factor maps).
- Refining the Lorentzian component (LX in GSAS) in order to have an estimate of the average crystallite size also proved to yield unstable refinements so the peak shape was kept constant during the Rietveld refinement.
- GSAS is also unable to handle irregular 2θ step sizes. This means that the data need to be interpolated prior to the refinement. This is not a problem when high resolution powder diffraction data are collected. However, in synchrotron XRD-CT experiments, area detectors are used and the 2θ resolution is not comparable with even laboratory data (unless a short *Q* range is chosen). This means that if possible, interpolation should be avoided in cases the peak intensities change (i.e. when there are not many observation points describing a diffraction peak).

As a result, the Rietveld refinement analysis of the XRD-CT data presented herein was based on the intensity of the scale factors and as such it is treated as a semi-quantitative analysis. In order to have a good starting model, the summed diffraction pattern of each XRD-CT dataset (i.e. reconstructed data volume) was exported and then quantitative Rietveld analysis was performed.

Ex situ X-ray micro-CT and SEM/WDS measurements

The μ-absorption-CT (micro-CT) measurements were performed at room temperature before and after the OCM experiments at beamline station ID15A of the ESRF using a 92.8 keV monochromatic X-ray beam. Radiographs were recorded with an X-ray imaging camera (CCD) and the pixel resolution was 5.8 μm. Each micro-CT scan consisted of 900 projections (radiographs) covering an angular range of 0-180 ° (i.e. angular step size of 0.2°). Flat-field and dark current images were also collected prior to the micro-CT measurements and were used to normalize the acquired radiographs before the tomographic reconstruction. The tomographic data were reconstructed using the filtered back projection algorithm. The reconstructed data volume, after cropping, corresponded to a 751 × 751 × 501 matrix (X × Y × Z).

The spent Mn-Na-W/SiO_2 catalyst after the *operando* XRD-CT experiment was sent to the Flemish Institute for Technological Research (VITO) for SEM/WDS characterisation. SEM micrographs and elemental mapping data were collected for locations of interest at the catalyst-capillary interface on a JEOL JXA8530F in-lens Schottky FEG-EPMA instrument (Field Emission Gun Electron Probe Micro-Analyser) operated at an accelerating voltage of 15 keV with a probe current of 50 nA and equipped with five vertical crystal WDS (wavelength-dispersive spectrometer) detectors.

Operando multimodal μ-XRF/XRD/absorption-CT measurements at I18, DLS

Combined μ-XRF-CT and μ-XRD-CT measurements were performed at beamline station I18 of the Diamond Light Source using a 13 keV monochromatic X-ray beam with a spot size of 2.3 μm (V) × 3.5 μm (H). 2D powder diffraction patterns and XRF spectra were collected at 5 μm intervals with a collection time of ca. 350 ms/point. The 2D powder diffraction patterns were recorded with a Photonic Sciences CMOS-

based X-ray imaging detector. The calibration was performed using a LaB_6 reference material. Typically, a total of 125 translation steps were performed for each tomographic angle and in total 55 angles were used. The angular step size was 3.5 ° and the angular range covered was 0-189 °. This was necessary due to the complex experimental setup which is shown in Figure 2. During the tomographic scans, at specific angles, the quartz support rod of the reactor cell blocked the XRD and/or the XRF signal. The solution to this problem was to increase the angular range cover to 0-189 ° (typically 0-180 ° angular range is covered). The temperature of the reactors was controlled with the Thermo Riko's GA198 - 1kW Atmospheric Quartz guided Infrared (IR) heater. The IR heater was placed on a motorised stage in order to maintain the sample to IR heater distance constant during the tomographic measurements. The IR heater was positioned within 2.0 mm of the sample and it was operated at the maximum stable temperature to ensure maximum heating. Prior to the beamtime experiment, temperature calibration experiments were performed to ensure that the operating temperature of 800 °C can be reached with this heating system.

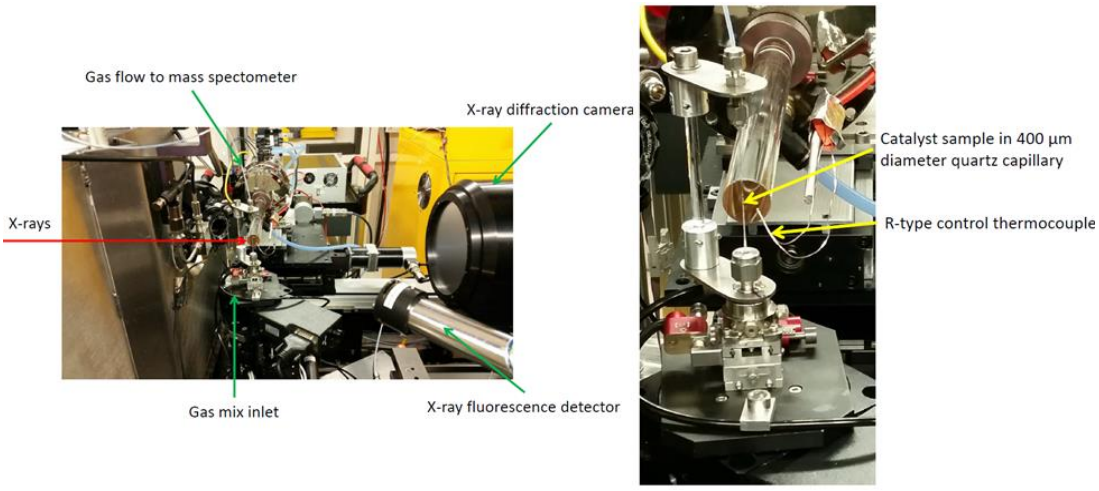

Figure 2: Experimental setup for the combined µ-XRD-CT, µ-XRF-CT and µ-absorption-CT operando measurements at beamline I18, DLS.

High temperature and *ex situ* PXRD measurements

The powder diffraction measurements were performed in Bragg-Brentano geometry with a Rigaku Smartlab diffractometer (Cu $K_{\alpha 1}$ radiation wavelength 0.154 nm) using a D/tex Ultra 250 1D silicon strip detector and a 2-bounce Ge monochromator (220). An Anton Parr HTK hot stage was used for the measurements from ambient

temperature to 800 °C under He flow (30 ml min^{-1}). The angular range covered was 10-90 °2θ with a step size of 0.01 ° (acquisition speed of 0.7 ° min^{-1}). The temperature ramping rate was 10 °C min^{-1} and a time period of 10 min was allowed for temperature stabilisation before the acquisition of each powder diffraction pattern was initialised.

Ex situ XRD-CT measurements at ID11 and ID31, ESRF

The 2 % Mn-1.6 % Na-3.1 % W/SiO_2 catalyst after high temperature heat treatment under He flow and the 2 % La-2 % Mn-1.6 % Na-3.1 % W/SiO_2 catalyst after performing a second calcination step were investigated with *ex situ* XRD-CT measurements. XRD-CT measurements were made at station ID31 of the ESRF using a 70 keV monochromatic X-ray beam focused to have a spot size of 20 µm x 20 µm. 2D powder diffraction patterns were collected using the state-of-the-art Pilatus3 X CdTe 2M (1475 × 1679pixels, pixel size of 172 µm) hybrid photon counting area detector which uses Cadmium Telluride (CdTe) as the semiconducting direct conversion layer. The acquisition time per point was 20 ms. The tomographic measurements were made with 180 translation steps covering 0-180 ° angular range, in steps of 1.5° (i.e. 120 line scans). The calibration was performed using a CeO_2 NIST standard. Every 2D diffraction image was converted to a 1D powder diffraction pattern after applying an appropriate filter to remove outliers or single-crystal diffraction artefacts using in-house developed MATLAB scripts. The same data processing strategy was followed as in the case of the *operando* XRD-CT measurements. The final XRD-CT images (i.e. reconstructed volume) were reconstructed using the filtered back projection algorithm.

The 2 % La-2 % Mn-1.6 % Na-3.1 % W/SiO_2 catalyst after high temperature heat treatment under chemical environment (i.e. He flow) was investigated with *ex situ* XRD-CT measurements .These XRD-CT measurements were made at station ID11 of the ESRF using a 65.35 keV monochromatic X-ray beam focused to have a spot size of 10 µm x 10 µm. 2D powder diffraction patterns were collected using a FReLoN camera. The acquisition time per point was 25 ms (rapid readout was achieved after pixel binning and yielding images with 2048 x 512 pixels). The tomographic measurements were made with 150 translation steps covering 0-180 ° angular range,

in steps of 1.8 ° (i.e. 100 line scans). The calibration was performed using a CeO_2 NIST standard. Every 2D diffraction image was converted to a 1D powder diffraction pattern after applying an appropriate filter to remove outliers or single-crystal diffraction artefacts using in-house developed MATLAB scripts. The same data processing strategy was followed as in the case of the *operando* XRD-CT measurements. The final XRD-CT images were reconstructed using the filtered back projection algorithm.

Results & Discussion

Operando XRD-CT experiments during OCM

The 2 % Mn-1.6 % Na-3.1 % W/SiO_2 catalyst

The phase identification of the fresh 2 % Mn-1.6 % Na-3.1 % W/SiO_2 catalyst was performed using the summed diffraction pattern from a room temperature XRD-CT scan before the OCM experiment. The crystalline phases identified were: Cristobalite-low (ICSD: 9327), Tridymite-low (ICSD: 413210), Quartz-low (ICSD: 16331), Na_2WO_4 (ICSD: 2133), Mn_2O_3 (ICSD: 159865) and/or Mn_7SiO_{12} (ICSD: 71793). The results of the phase identification are presented in Figure 3 where a region of interest of the summed diffraction pattern is shown.

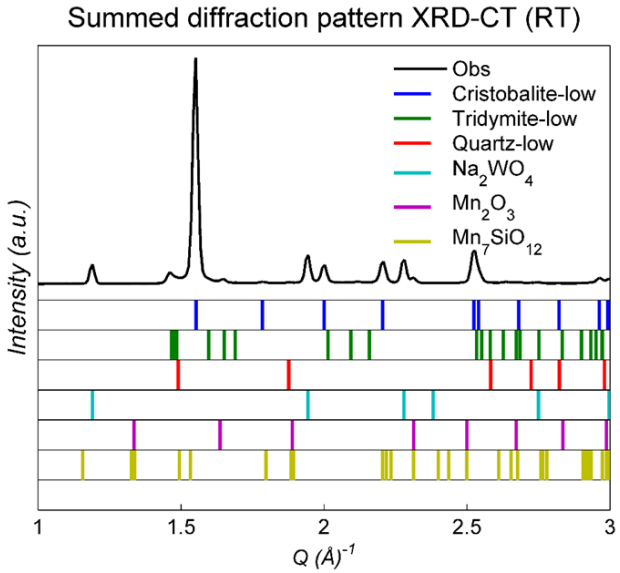

Figure 3: Phase identification of the 2 % Mn-1.6 % Na-3.1 % W/SiO_2 catalyst. Black line: the summed diffraction patterns from the room temperature XRD-CT scan (i.e. after applying a binary mask to the reconstructed data in order to extract the diffraction patterns generated only by the sample), Blue ticks: Cristobalite, Green ticks: Tridymite, Red ticks: Quartz, Cyan ticks: Na_2WO_4, Magenta ticks: Mn_2O_3, Yellow ticks: Mn_7SiO_{12}.

A schematic representation of the experimental protocol followed for the OCM experiment with the 2 % Mn-1.6 % Na-3.1 % W/SiO_2 catalyst is shown in Figure 4 and in more details in Table 1. Initially, an XRD-CT scan (1) of the fresh catalyst was collected at room temperature as mentioned previously. The temperature of the reactor was then increased to 800 °C with a ramp rate of 5 °C min^{-1} under the flow of He (i.e. 30 ml min^{-1}). Four interlaced XRD-CT (IXRD-CT) scans were collected during temperature ramping (2-5).[55] Once the required temperature was reached, another XRD-CT scan was performed (6). The inlet gas was then switched to air (i.e. 50 ml min^{-1}) and an XRD-CT scan was collected (7). The catalyst bed was then exposed to various OCM reaction gas mixtures (i.e. gas mixtures of CH_4/He/Air). The mass spectrometry data are presented in a later section and serve to illustrate that the catalyst was active under the imposed conditions (i.e. temperature and reaction mixtures). Since there is a lot of debate in literature regarding the long term stability and reasons behind the deactivation of this family of catalysts (i.e. Mn-Na-W/SiO_2 catalysts), it was considered essential to investigate the behaviour of the catalyst under CH_4 rich environments (i.e. very reducing environments). The inlet gas mixture was switched to CH_4 / Air with a molar ratio of 10:1 (total flow rate of 110 ml min^{-1}) and an XRD-CT scan was performed (8). This gas mixture was maintained during cooling to room temperature, till the end of the experiment. Two IXRD-CT scans were collected during cooling (9-10) and a final XRD-CT scan was performed at room temperature after the OCM experiment (11).

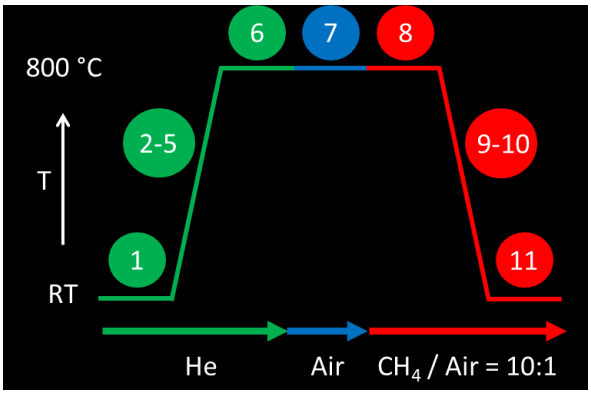

Figure 4: Schematic representation of the protocol followed during the OCM experiment with the Mn – Na – W/SiO_2 catalyst.

Table 1: Conditions applied for the OCM experiment with the Mn – Na – W/SiO_2 catalyst.

		Interlaced XRD-CT							Interlaced XRD-CT		
XRD-CT scans	**1**	**2**	**3**	**4**	**5**	**6**	**7**	**8**	**9**	**10**	**11**
Nominal T (°C)	**RT**	**RT-265**	**265-500**	**500-740**	**750-979**	**979-1000**	**1000**	**1000**	**1000-250**	**250-75**	**RT**
Gas mixture	**He**	**He**	**He**	**He**	**He**	**He**	**Air**	**CH_4/Air**	**CH_4/Air**	**CH_4/Air**	**CH_4/Air**
Flowrate (mL min^{-1})	**30**	**30**	**30**	**30**	**30**	**30**	**50**	**100/10**	**100/10**	**100/10**	**100/10**

In order to efficiently track the evolving solid-state chemistry of functional materials, like catalysts, fuel cells and batteries, it is desired to have both high spatial and temporal resolution. Typically, the temporal resolution of an X-ray tomographic scan is equal to the total acquisition time to perform that measurement. It has been recently shown that by developing new data collection strategies, like the interlaced approach, it is feasible to bridge the gap between the spatial and temporal resolution.[55] Additionally, in the case of dynamic XRD-CT experiments, it is also possible to treat the acquired data as a series of line scans. This means that relatively fast solid-state changes can be tracked as a function of time but without any spatial resolution (i.e. no spatially resolved information). An example is provided below.

As mentioned previously, four IXRD-CT scans were performed during temperature ramping for room temperature to 800 °C. Post experiment, it is trivial to export the summed diffraction pattern per tomographic angle (i.e. summed diffraction pattern per line scan). In total, these data correspond to 480 diffraction patterns (4 × 120 line scans). In contrast to typical PXRD data collected in transmission geometry at synchrotrons (i.e. point - bulk PXRD or line - PXRD mapping), the contribution of the amorphous silica capillary (or any other containing vessel) can be removed from the diffraction patterns. This is very important as data interpretation can become significantly easier (i.e. modelling/fitting the background in case of full powder profile analysis). This is demonstrated in Figure 5.

Initially, a crude binary mask is created by segmenting the glass (i.e. scattering signal originating from the capillary) from the sample (Panel B in Figure 5). In this case, the summed image of the reconstructed data volume was used (XRD-CT scan 1). The new

mask is then applied to the data volume (Panel C in Figure 5) and then the data are forward projected using the appropriate tomographic angles (i.e. simulation of a tomographic scan). The new projection data volume actually corresponds to air and glass X-ray scattering (Panel D in Figure 5). The summed diffraction pattern of the raw projection data volume and the scattering pattern of the new projection data volume are shown in Panel E of Figure 5 (blue and green line respectively). A simple subtraction of the air/glass X-ray scattering pattern from the raw data leads to a new diffraction pattern with a smoothed and easy to fit/model background.

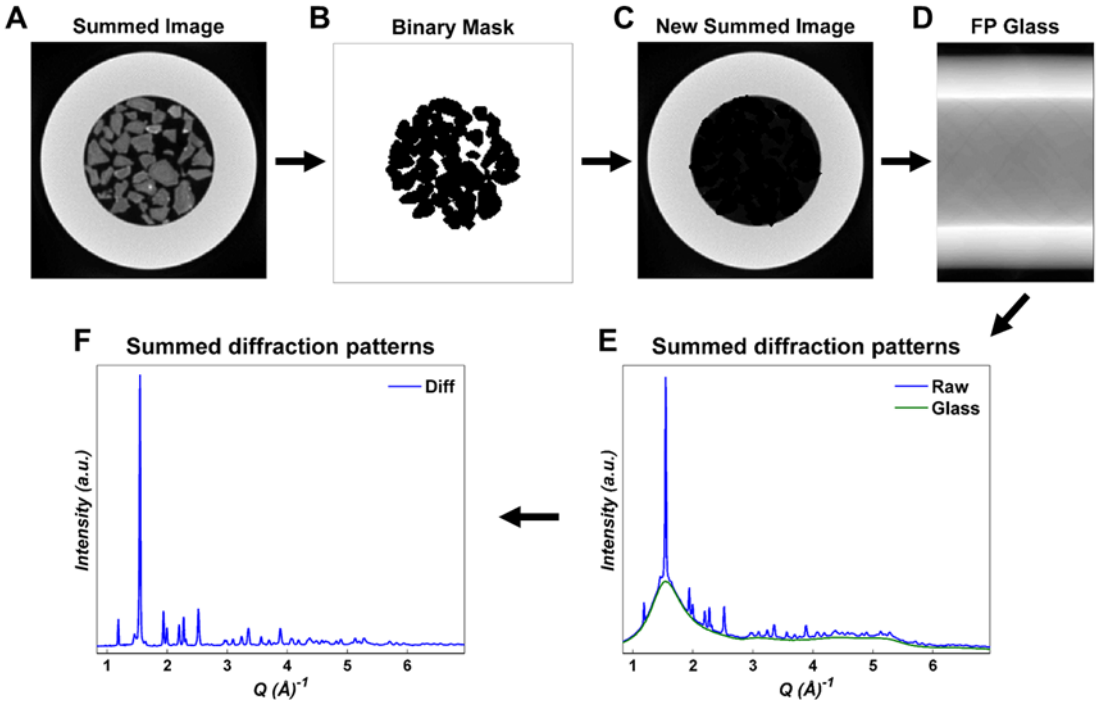

Figure 5: Panel A: Summed image of the reconstructed data volume, Panel B: Binary mask created after applying an appropriate threshold value to the summed image, Panel C: New summed image after applying the mask to the reconstructed data volume, Panel D: Summed image of the new forward projected data volume, Panel E: Summed diffraction pattern of the raw projection data volume and the new forward projected data volume, Panel F: Difference between the two diffraction patterns

This data processing strategy for suppressing the background intensity in the diffraction patterns was applied to the 480 diffraction patterns collected during the temperature ramping (i.e. summed diffraction patterns per line scan). In Figure 6, the new diffraction patterns for the catalyst are plotted as a function of temperature and the results are shown from two different points of view. There is a transition of the crystalline SiO_2 cristobalite phase from tetragonal (characteristic peaks at Q = 2.0 and 2.2 $Å^{-1}$, reflections (111) and (102)) to cubic symmetry (aka. low-to-high or alpha-to-

beta transition) at ca. 250-260 °C, which is a well-known temperature effect.[56] More importantly, it can be seen that the peaks corresponding to cubic (Fd-3m) Na_2WO_4 (characteristic peak at Q = 1.18 $Å^{-1}$, reflection (111)) disappear at ca. 600 °C and also the lower symmetry orthorhombic (Fddd) Na_2WO_4 phase disappears before reaching 680 °C.

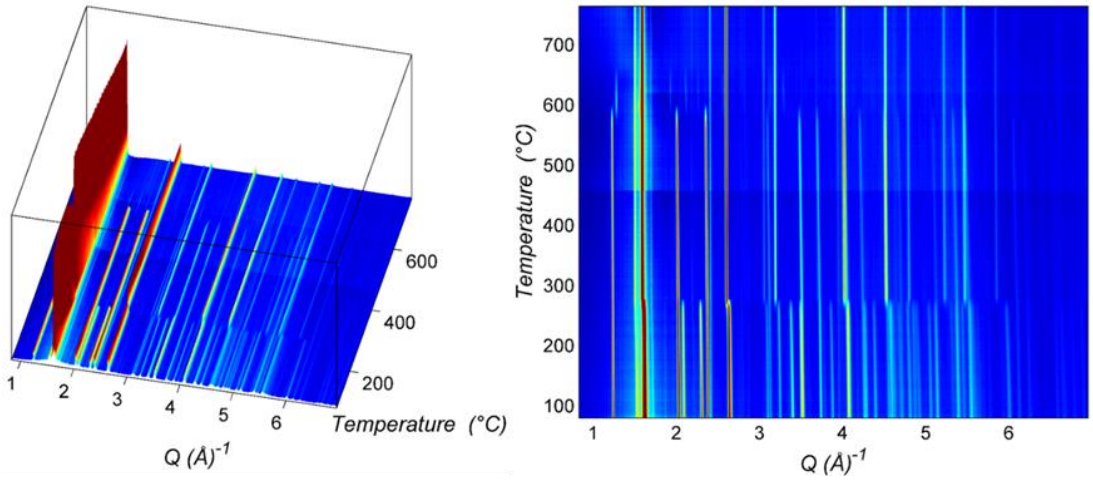

Figure 6: The summed diffraction patterns per line scan acquired during the temperature ramping (4 IXRD-CT scans) after background subtraction are plotted as a function of temperature.

An instrument parameter file was created using information extracted from the Rietveld analysis of the CeO_2 NIST standard diffraction pattern recorded for calibration purposes. A Chebyshev polynomial was used to fit the background and a pseudo-Voigt profile function to fit the diffraction peaks.[57] A CeO_2 CIF file was obtained from the ICSD database to be used for the Rietveld refinement (ICSD: 72155). The results from the refinement are presented in Figure 7.

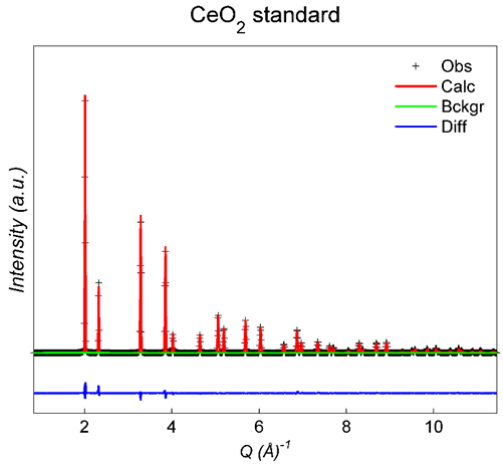

Figure 7: Rietveld refinement of CeO_2 diffraction pattern collected with a CeO_2 NIST standard during the beamtime experiment at beamline ID15 of the ESRF.

The summed diffraction pattern of every XRD-CT dataset was exported and quantitative Rietveld refinement was performed prior to the Rietveld analysis of the XRD-CT data. This is a necessary step in order to obtain a good starting model before processing the ca. 30,000 diffraction patterns of each XRD-CT dataset. The main aim of the Rietveld analysis of the summed diffraction patterns of each XRD-CT dataset was to obtain proper values for the unit cell parameters of each crystalline phase (i.e. for the high temperature XRD-CT scans).

It should also be noted here that, as previously stated in literature, it is very challenging to reach a conclusion whether the Mn_2O_3 (Bixbyite) or the Mn_7SiO_{12} (Braunite) or both phases are present in the Mn-W-Na/SiO_2 catalysts.[58, 59] The highest intensity peak generated by these phases is at approximately Q = 2.31 $Å^{-1}$ ((222) reflection for Mn_2O_3 and (224) reflection for Mn_7SiO_{12}). However, as it is clearly shown in Figure 3, this is a minor peak even when the summed diffraction pattern is used (small peak at the right side of a Na_2WO_4 peak). As these two phases generate very similar diffraction patterns and mainly one diffraction peak can be observed, the Rietveld analysis of the XRD-CT data was performed using only the Mn_2O_3 structure in the model (higher symmetry). The results from the quantitative Rietveld refinement using the summed diffraction pattern of the XRD-CT data collected at room temperature are shown in Figure 8 (Rw = 0.11 on 750 observations).

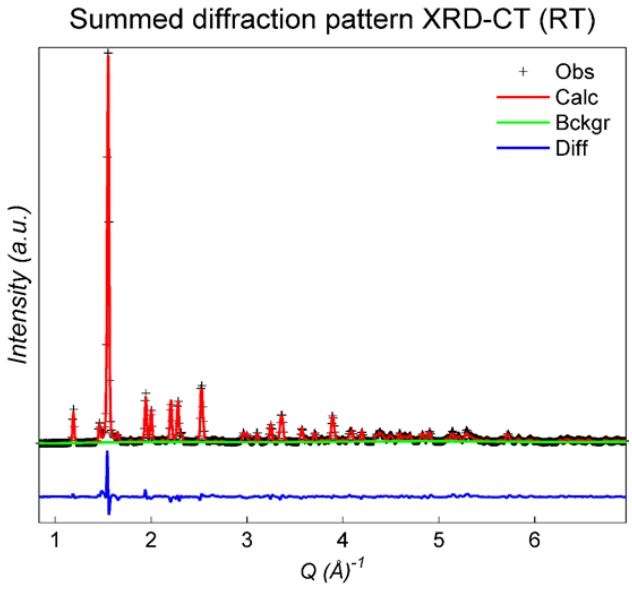

Figure 8: Quantitative Rietveld refinement using the summed diffraction pattern of the room temperature XRD-CT dataset.

The same data processing strategy was followed for the Rietveld analysis of all XRD-CT data. More specifically, two refinement cycles were performed and a sufficient large number of iterations was used (i.e. 30) per refinement cycle. In the first refinement cycle, the background and the scale factors of the crystalline phases were refined. In the second refinement cycle, the unit cell parameters of the cristobalite phase were also refined apart from the scale factors and the background. The main results from the multiphase Rietveld of the XRD-CT data is presented in Figure 9 which represents the analysis of ca. 150,000 diffraction patterns.

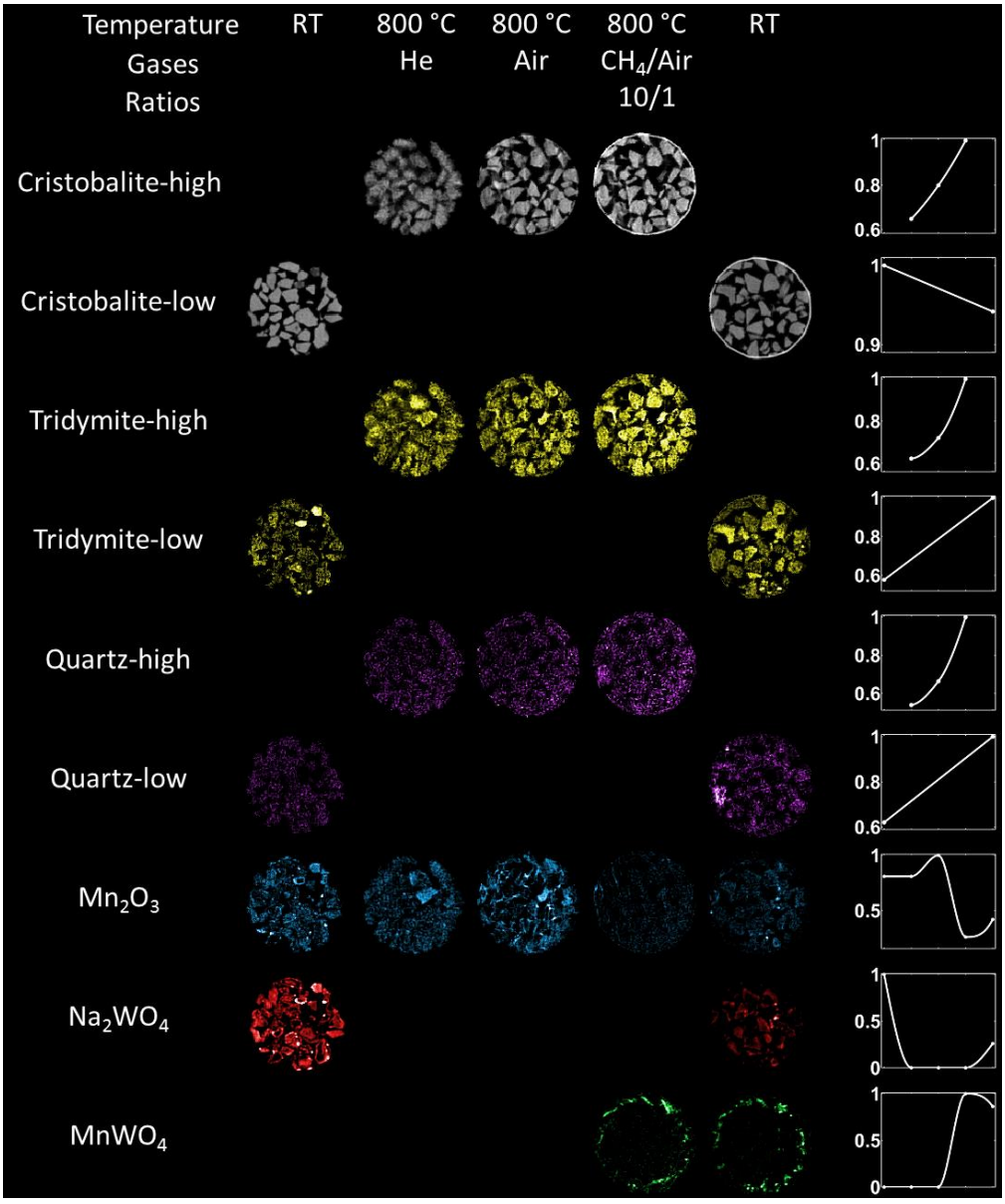

Figure 9: Phase distribution maps created based on the intensities of the scale factors of each crystalline phase. Right: Relative changes of each component during the OCM experiment with the Mn – Na – W/SiO_2 catalyst.

These phase distribution maps represent the values of the scale factors of each crystalline phase (XRD-CT scans 1, 6, 7, 8 and 11 as shown previously in Figure 4). The summed intensity of the scale factors over each XRD-CT scan was calculated and these values were then normalised with respect to the maximum value. These results are plotted at the right side of Figure 9 and show the relative change of each crystalline phase during the OCM experiment.

Looking at the results obtained from the fresh 2 % Mn-1.6 % Na-3.1 % W/SiO_2 catalyst (i.e. room temperature XRD-CT scan), it can be seen there a few catalyst particles rich in tridymite but, in general, it is the cristobalite phase distribution map that describes very well the catalyst particles in terms of both shape and size. As shown previously, in the summed diffraction pattern presented in Figure 3, there are only minor amounts of quartz in the fresh catalyst. The $NaWO_4$ and the Mn_2O_3 / Mn_7SiO_{12} phases are not perfectly co-located which is to be expected as the catalyst was prepared by the sequential incipient wetness impregnation method. This is clearly demonstrated in Panel A of Figure 10.

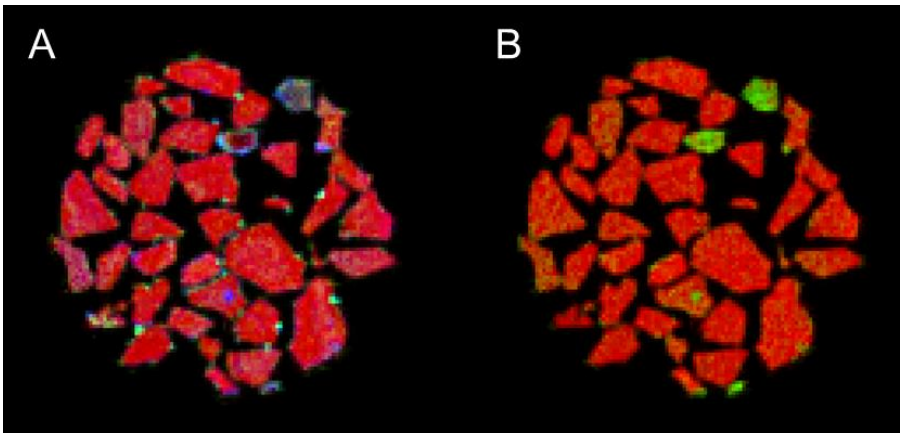

Figure 10: RGB images produced after the Rietveld analysis of the XRD-CT scan collected at room temperature before the OCM experiment (XRD-CT scan 1). Panel A: Red: Cristobalite, Green: Mn_2O_3 / Mn_7SiO_{12}, Blue: Na_2WO_4. Panel B: Red: Cristobalite, Green: Tridymite.

In this RGB image, the green colour corresponds to the Mn_2O_3 / Mn_7SiO_{12} map, the blue colour to the Na_2WO_4 map and the red colour to the cristobalite map. It can also be seen that Mn_2O_3 / Mn_7SiO_{12} is mainly present at the catalyst surface (green hotspots). Additionally, it is very interesting to note that there are some particles rich in tridymite. This is shown in the RGB image in Panel B of Figure 10, where the red colour corresponds to the cristobalite map and the green to the tridymite map. This

phenomenon may imply that these particles where exposed to different conditions compared to the rest during the preparation of this catalyst (e.g. calcination step).

Upon reaching the required high temperatures for the OCM reaction, the crystalline Na_2WO_4 phase has disappeared. As shown previously in Figure 6, the cubic Na_2WO_4 first transforms into a lower symmetry orthorhombic Na_2WO_4 phase and then this new phase disappears too. At 800 °C, no Na-W-O phase is observed in the XRD-CT data. During temperature ramping to 800 °C, there was sample movement and as a result the data acquired from XRD-CT scan 6 yielded blurred images. As it will be shown in the following section, this sample movement was a result of a chemical interaction of the catalyst with the capillary and not of just thermal expansion of the sample. The phase identification of the 2 % Mn-1.6 % Na-3.1 % W/SiO_2 catalyst at 800 °C (He flow) was performed using the summed diffraction pattern (XRD-CT dataset 6). The results from the phase identification are presented in Figure 11 where a region of interest of the summed diffraction pattern is shown.

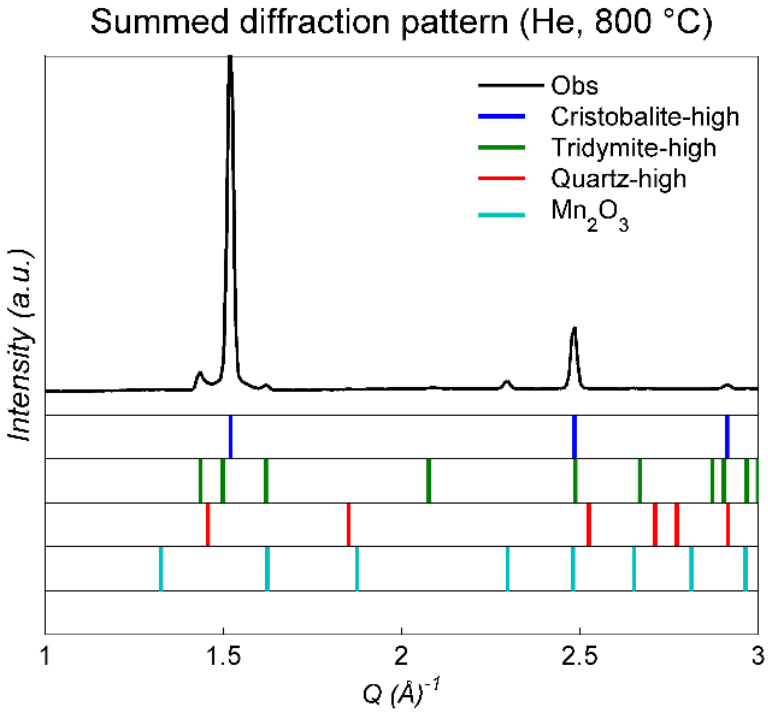

Figure 11 Phase identification of the 2 % Mn-1.6 % Na-3.1 % W/SiO_2 catalyst at 800 °C under He flow. Black line: the summed diffraction patterns from the XRD-CT dataset 6 (i.e. after applying a binary mask to the reconstructed data in order to extract the diffraction patterns generated only by the sample), Blue ticks: Cristobalite-high, Green ticks: Tridymite-high, Red ticks: Quartz-high, Cyan ticks: Mn_2O_3 (Mn_7SiO_{12} is not presented here as it was not used for the Rietveld analysis of the XRD-CT data).

The following CIF files were used for the Rietveld analysis of the XRD-CT data collected at 800 °C: Cristobalite-high (ICSD: 9327), Tridymite-high (ICSD: 200479), Quartz-high (ICSD: 42498) and Mn_2O_3 (ICSD: 159865). The results from the quantitative Rietveld refinement using the summed diffraction pattern of the XRD-CT data collected at 800 °C under He flow (XRD-CT scan 6) are shown in Figure 12 (Rw = 0.098 on 900 observations).

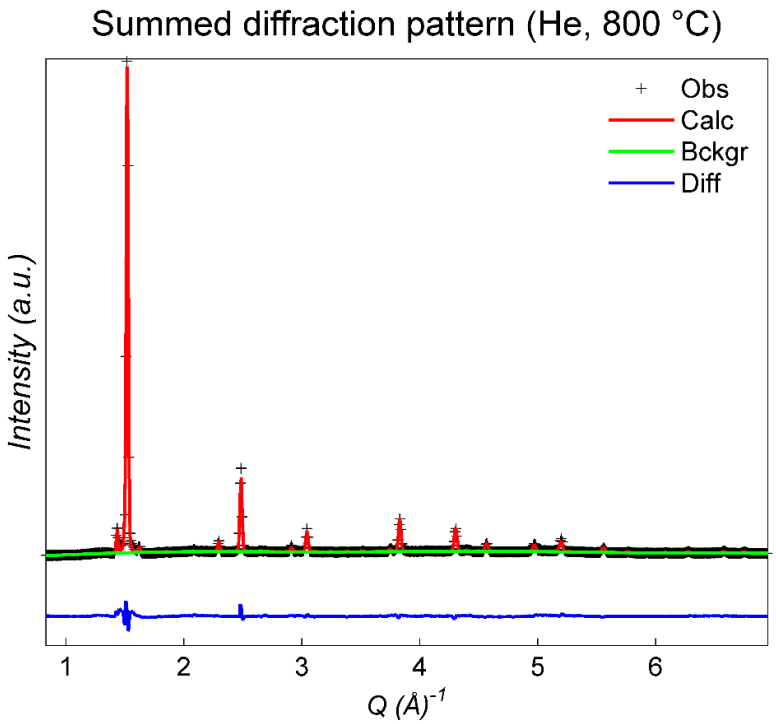

Figure 12: Quantitative Rietveld refinement using the summed diffraction pattern of the XRD-CT dataset 6 (He flow, 800 °C).

The sample stabilized with time at 800 °C. However, the subsequent XRD-CT scans (i.e. XRD-CT scans 7 and 8) were collected at a different height (i.e. vertical position) of the catalyst bed compared to XRD-CT scan 6 due to the sample movement. This means that the result obtained from the Rietveld analysis showing the crystalline Mn_2O_3 / Mn_7SiO_{12} phases growing during the activation step (i.e. air flow of 50 ml min^{-1}) should be treated with caution. On the other hand, there are significant solid-state changes taking place under reducing conditions (XRD-CT scan 8). At this point it should be noted that five different reaction mixtures were introduced to the catalyst bed prior to XRD-CT scan 8 in order to validate that the reactor was operating under real OCM conditions. The reaction mixtures used for the OCM experiment are shown in Table 2.

Table 2: Summary of reaction mixtures tested during the OCM experiment with the 2 % Mn-1.6 % Na-3.1 % W/SiO_2 catalyst

	Flowrate (mL min^{-1})		
	CH_4	He	Air
Reaction mixture 1	5	95	5
Reaction mixture 2	20	80	5
Reaction mixture 3	50	50	5
Reaction mixture 4	20	10	24
Reaction mixture 5	100	-	10

As mentioned previously, the outflow gasses were monitored for the duration of the whole experiment by mass spectrometry using an Ecosys portable mass spectrometer. The mass spectrometry data are presented in Figure 13 where the signals from specific masses of interest are shown.

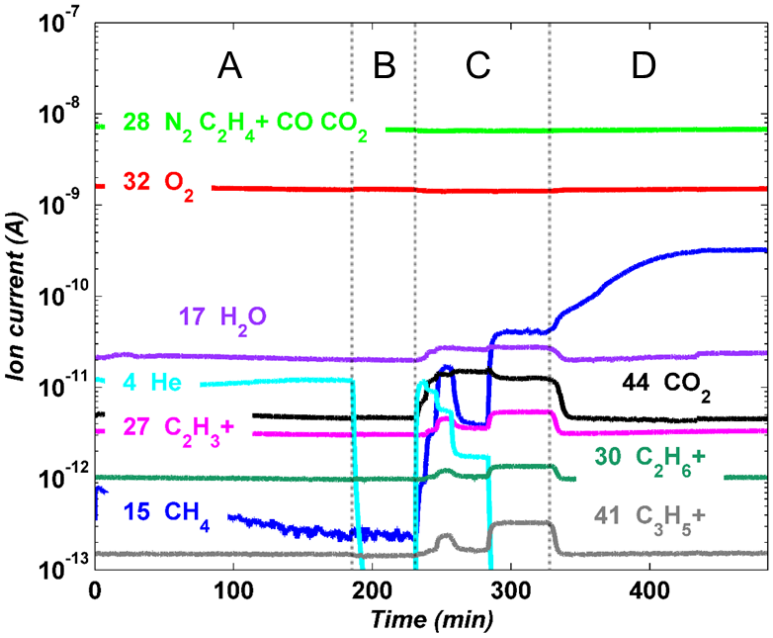

Figure 13 Mass spectrometry data corresponding to the following m/z ratios (possible species and respective line colour in parentheses): 4 (He - cyan), 15 (CH_4+ - blue), 17 (H_2O - purple), 27 (C_2H_2+ - magenta), 28 (N_2, CO, C_2H_4+ - green), 30 (C_2H_6+ - dark green), 32 (O_2 - red), 41 (C_3H_5+ - grey) and 44 (CO_2 - black). Panel A: Temperature ramping to 800 °C under He flow and dwelling for the duration of XRD-CT scan 6 (ca. 45 min), Panel B: Air flow (50 ml min^{-1}), Panel C: OCM reaction conditions using different reaction mixtures, Panel D: Cooling to room temperature while keeping the last reaction gas mixture (i.e. CH_4 : Air = 10:1)

It can be clearly seen that upon switching to OCM reaction conditions (i.e. from Panel B to Panel C in Figure 13), the signal from masses 27, 30 and 41 appeared which correspond to fractions from higher hydrocarbon molecules than CH_4 (i.e. C_2H_3+,

C_2H_6+ and C_3H_5+ respectively). More importantly, the final reaction mixture (reaction mixture 5 in Table 2) was maintained even during cooling to room temperature (Panel D in Figure 13). It can be seen that the signal from these masses disappeared very quickly during cooling along with the signal from masses 17 and 44 which correspond to H_2O and CO_2; molecules which are also expected to form under reaction conditions.

The most important results from the Rietveld analysis of the collected XRD-CT data were obtained from the XRD-CT scan 8 (Figure 9). The diffraction signal generated by the Mn_2O_3 / Mn_7SiO_{12} phases is seen to be diminished while a new crystalline Mn phase is formed. This new phase was identified as $MnWO_4$. The results from the phase identification are shown in Figure 14 where the summed diffraction pattern of XRD-CT scan 11 is used (room temperature XRD-CT scan after the OCM experiment).

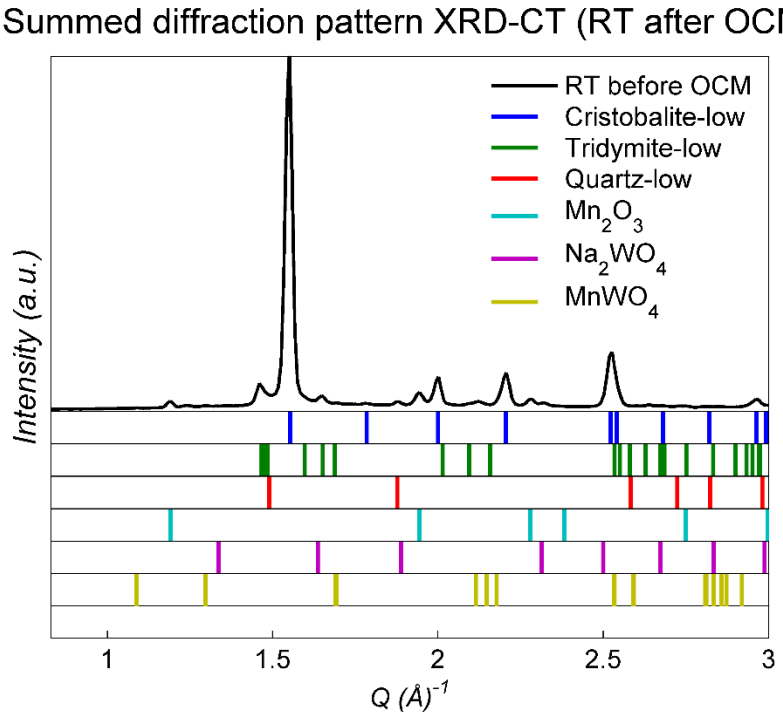

Figure 14 Phase identification of the 2 % Mn-1.6 % Na-3.1 % W/SiO_2 catalyst at room temperature after the OCM experiment. Black line: the summed diffraction patterns from the XRD-CT dataset 11 (i.e. after applying a binary mask to the reconstructed data in order to extract the diffraction patterns generated only by the sample), Blue ticks: Cristobalite-low, Green ticks: Tridymite-low, Red ticks: Quartz-low, Cyan ticks: Mn_2O_3, Magenta ticks: Na_2WO_4, Yellow ticks: $MnWO_4$

This result shows that under very reducing environments (i.e. CH_4 : Air = 10:1), not only the surface Mn^{3+} species reduce to Mn^{2+} species but also the bulk ones do too. The formation of $MnWO_4$ after an OCM experiment has been reported several times

in the literature in the past and very recently from an *in situ* PXRD experiment.[26, 46, 60] However, to our knowledge, this is the first true *operando* experiment of this family of catalysts. The Panel 5 of Figure 15 shows the results from the mass spectrometry data collected during the XRD-CT scan 8. Since there is no change in the mass spectrometry signals during the collection of the XRD-CT scan (no deactivation is implied due to the formation of $MnWO_4$), it is now evident that crystalline Mn_2O_3 / Mn_7SiO_{12} is not required for an active OCM catalyst.

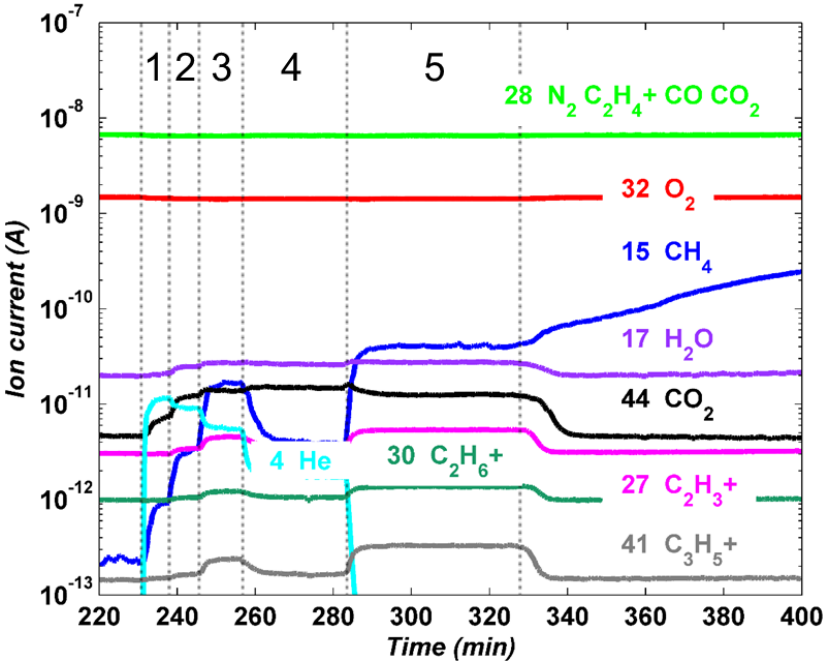

Figure 15: A magnified version of a region of interest of Figure 12. The different regions indicated correspond to the reaction mixtures used during the OCM experiment (presented in Table 2).

More importantly, the spatially-resolved experiments performed with the XRD-CT technique have revealed new information; information that is otherwise lost in bulk measurements. As shown clearly in the phase distribution map of $MnWO_4$, in Figure 9, this new phase is not homogeneously distributed over the catalyst bed. On the contrary, the distribution of the $MnWO_4$ phase is highly heterogeneous as it is seen to preferentially grow close to the capillary wall (but not at it). Additionally, the formation of a crystalline cristobalite ring is observed. It is evident that the crystallization of the amorphous SiO_2 capillary took place at 800 °C. However, as in the case of the Mn-Na-W/SiO_2 catalysts, this phenomenon is only possible at these relatively low temperatures because of the presence of Na^+ ions. It is therefore implied that the Na^+ ions are unstable in this catalyst under OCM reaction conditions

and they become volatile. It has been recently shown that the WO_4^{2-} ions are mobile too (melting point of Na_2WO_4 is 698 °C) and can interact with other materials.[61] However, this new finding shows that another crucial component for a selective OCM catalyst can be lost under reaction conditions and this is bound to be detrimental to the long-term stability of the Mn-Na-W/SiO_2 catalysts.

After cooling to room temperature at the end of the OCM experiment, Na_2WO_4 is seen to reform, albeit to a lesser extent. This is reasonable as the $MnWO_4$ phase is stable and is maintained until the end of the experiment. However, it can be seen in the phase distribution map of Na_2WO_4 in Figure 9 that it is mainly present closer to the centre of the catalyst bed rather than to the capillary. All the previously mentioned heterogeneities are clearly demonstrated in the RGB image shown in Panel A of Figure 16. In this RGB image, the red colour corresponds to the cristobalite map, the green colour to the $MnWO_4$ map and the blue colour to the Na_2WO_4 map. The absence of Na_2WO_4 where $MnWO_4$ is present also indicates the loss of Na from the catalyst particles during the OCM experiment.

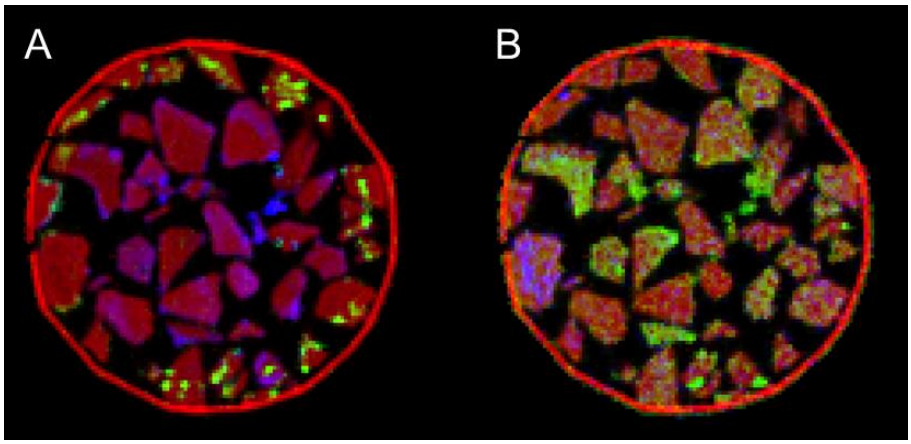

Figure 16: RGB images produced after the Rietveld analysis of the XRD-CT scan collected at room temperature after the OCM experiment (XRD-CT scan 11). Panel A: Red: Cristobalite, Green: $MnWO_4$, Blue: Na_2WO_4. Panel B: Red: Cristobalite, Green: Tridymite, Blue: Quartz.

Furthermore, the results presented in Figure 9 also suggest that there is also an evolution of the SiO_2 support at the high temperatures required for the OCM reaction. It is suggested from the Rietveld analysis that the evolution taking place is the following:

Amorphous silica → Cristobalite → Tridymite → Quartz

The solid-state evolution of SiO_2 at relatively low temperatures (800 °C) when alkali metals are present has been reported and investigated in the literature on several occasions.[62-65] Venezia *et al.* suggested that the alkali ions occupy interstitial sites, collapsing the Si-O-Si bridges and as a results leading to the formation of crystalline forms from amorphous silica.[62] The incorporation of Na species into the silica framework is implied in Figure 17 where the maps of the lattice parameter *a* of the SiO_2 cristobalite-low phase are presented. The values for the unit cell parameters of the cristobalite-low phase were obtained from the Rietveld analysis of the XRD-CT data collected at room temperature (i.e. before and after the OCM experiment).

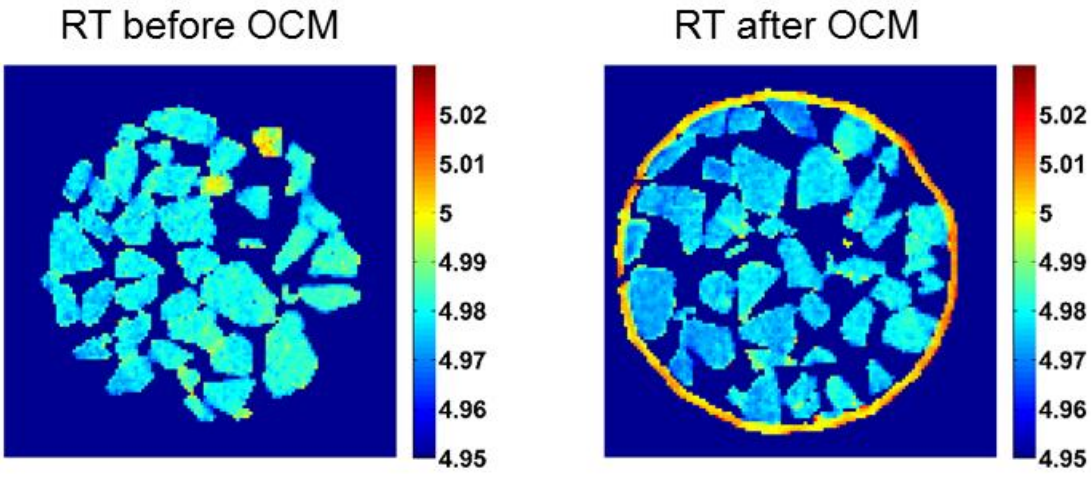

Figure 17: Maps of lattice parameter a of cristobalite-low obtained from the Rietveld analysis of the XRD-CT data collected at room temperature (color bar units in Å).

It has also been previously shown that the transformation to various SiO_2 crystalline phases and from one crystalline phase to another, depends on the temperature, alkali species and alkali loading.[56, 62] It is therefore no wonder there is an evolution of the support as a function of time at high temperatures since there are mobile and volatile Na^+ ions present in this catalyst. In the RGB image shown in Panel B of Figure 16, it can be seen that not only the tridymite signal is strong in several catalyst particles (green colour), but there are also some particles present where there is high concentration of the SiO_2 quartz phase (blue colour).

The 2 % La-2 % Mn-1.6 % Na-3.1 % W/SiO_2 catalyst

As it will be shown in this section, the solid-state chemistry taking place in the 2 % La-2 % Mn-1.6 % Na-3.1 % W/SiO_2 catalyst is significantly different compared to the

unpromoted 2 % Mn-1.6 % Na-3.1 % W/SiO_2 catalyst. A schematic representation of the experimental protocol followed for the OCM experiment with the 2 % La-2 % Mn-1.6 % Na-3.1 % W/SiO_2 catalyst is shown in Figure 18. Initially, an XRD-CT scan (1) of the fresh catalyst was collected at room temperature as mentioned previously. The temperature of the reactor was then increased to 800 °C with a ramp rate of 5 °C min^{-1} under the flow of He (i.e. 30 ml min^{-1}). Four IXRD-CT scans were collected during temperature ramping (2-5). Once the required temperature was reached, two XRD-CT scans were performed (6-7). The inlet gas was then switched to air (i.e. 50 ml min^{-1}) and an XRD-CT scan was collected (8). After this activation step, the catalyst bed was exposed to various OCM reaction gas mixtures (i.e. gas mixtures of CH_4/He/Air) and three XRD-CT scans were performed (9-11). Two IXRD-CT scans were collected during cooling (12-13) and a final XRD-CT scan was performed at room temperature after the OCM experiment (14).

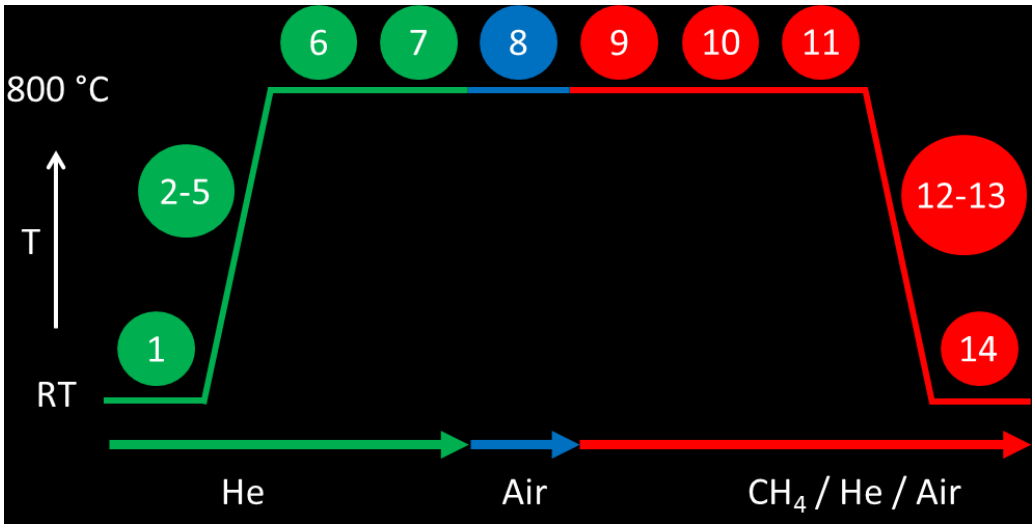

Figure 18: Schematic representation of the protocol followed during the OCM experiment with the La – Mn – Na – W/SiO_2 catalyst.

The phase identification of the fresh 2 % La-2 % Mn-1.6 % Na-3.1 % W/SiO_2 catalyst was performed using the summed diffraction pattern from the room temperature XRD-CT scan. As in the case of the fresh 2 % Mn-1.6 % Na-3.1 % W/SiO_2 catalyst, the main crystalline phases identified were: Cristobalite-low (ICSD: 9327), Tridymite-low (ICSD: 413210), Quartz-low (ICSD: 16331), Na_2WO_4 (ICSD: 2133), Mn_2O_3 (ICSD: 159865) and/or Mn_7SiO_{12} (ICSD: 71793). The only crystalline La-containing phase identified was $La_4Mn_5Si_4O_{22}$ (ICSD: 79811). In a previous study of this catalyst,

TEM/EDX analysis of this catalyst suggested the presence of this La-containing phase although it was not observed with traditional powder XRD.[44] The results of the phase identification are presented in Figure 19. There may be other La-Mn-O or La-W-O species present not observable by XRD, as suggested by TEM/EDX analysis in previous studies of this catalyst, but the observation of this crystalline phase with XRD-CT provides direct evidence that La directly interacts with both the support and the Mn species.

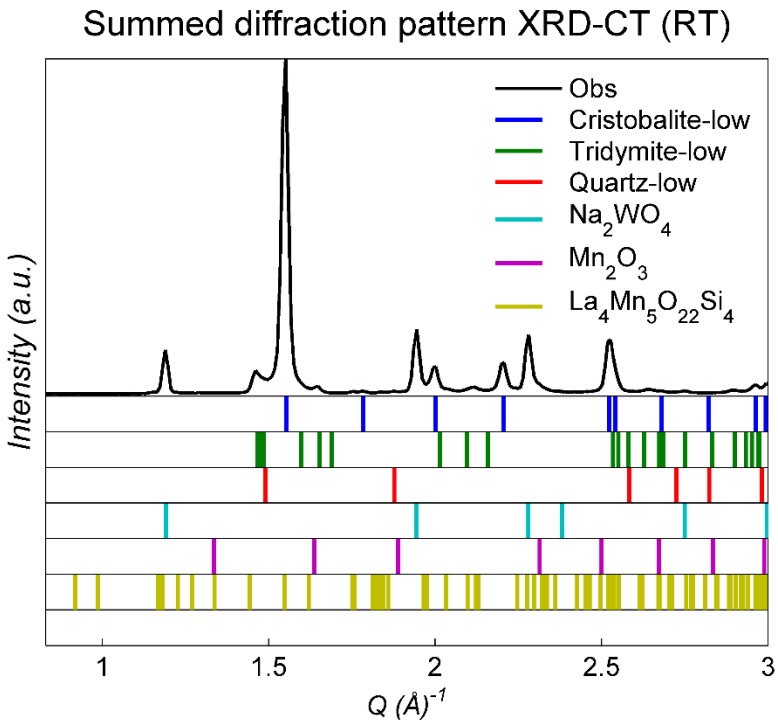

Figure 19: Phase identification of the 2 % La-2 % Mn-1.6 % Na-3.1 % W/SiO_2 catalyst. Black line: the summed diffraction pattern from the room temperature XRD-CT scan (i.e. after applying a binary mask to the reconstructed data in order to extract the diffraction patterns generated only by the sample), Blue ticks: Cristobalite, Green ticks: Tridymite, Red ticks: Quartz, Cyan ticks: Na_2WO_4, Magenta ticks: Mn_2O_3, Yellow ticks: $La_4Mn_5Si_4O_{22}$.

The main results from the Rietveld analysis of the XRD-CT data collected during the OCM experiment with the 2 % La-2 % Mn-1.6 % Na-3.1 % W/SiO_2 catalyst are presented in Figure 20. As in the case of the 2 % Mn-1.6 % Na-3.1 % W/SiO_2 catalyst, these phase distribution maps represent the values of the scale factors of each crystalline phase (XRD-CT scans 1, 6-12 and 15 as shown previously in Figure 18). The summed intensity of the scale factors over each XRD-CT scan was normalised with respect to the maximum value. The results are plotted at the right side of Figure 20 and show the relative change of each crystalline phase during the OCM experiment.

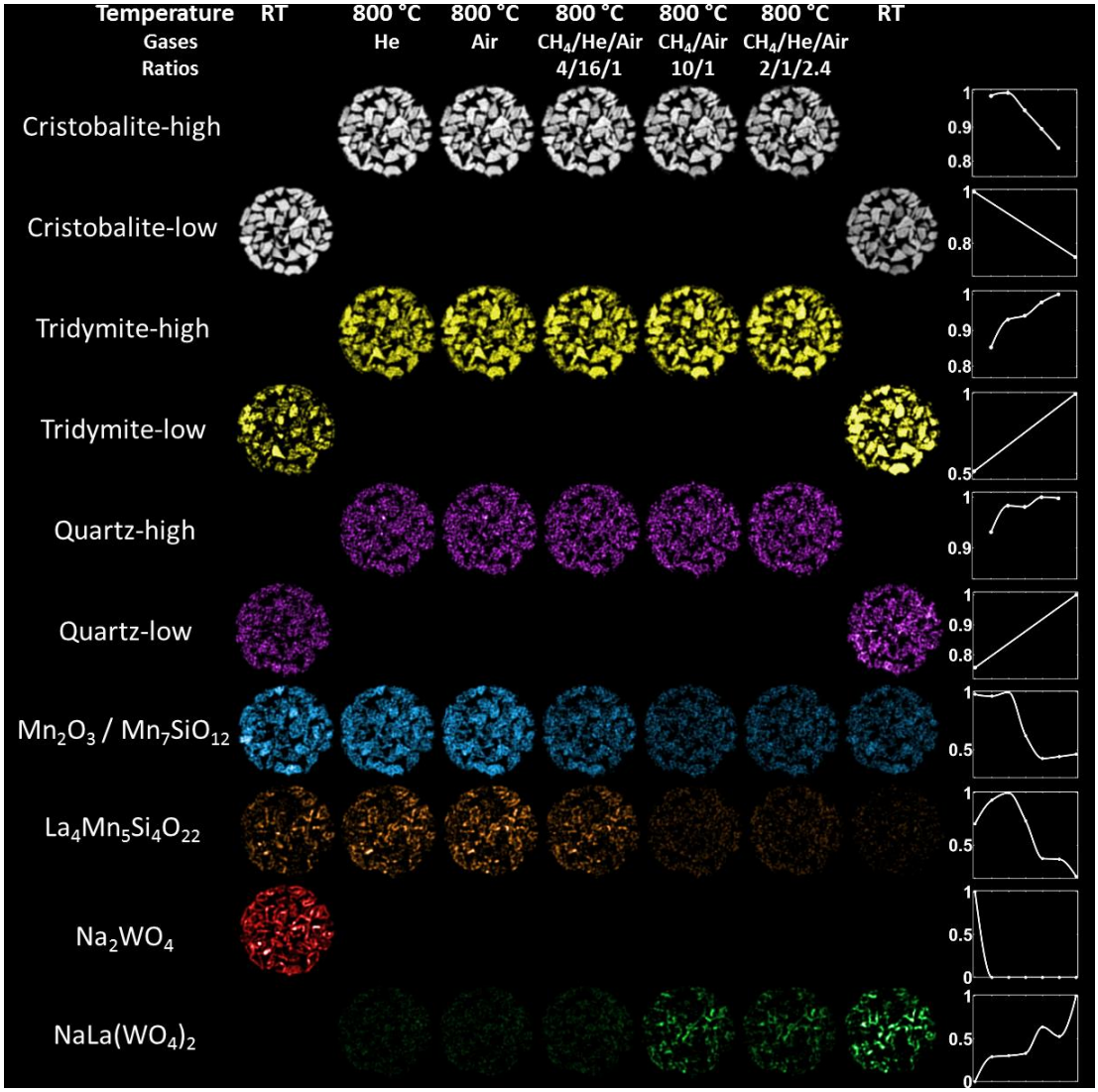

Figure 20: Phase distribution maps created based on the intensities of the scale factors of each crystalline phase. Right: Relative changes of each component during the OCM experiment with the La-Mn-Na-W.SiO_2 catalyst.

As shown in Figure 20 and in contrast to the phase distribution map of Na_2WO_4 of the fresh 2 % Mn-1.6 % Na-3.1 % W/SiO_2 catalyst, the majority of the Na_2WO_4 phase present in the La-promoted catalyst is located near/at the surface of the catalyst particles. This is also the case for the $La_4Mn_5Si_4O_{22}$ phase. On the other hand, the phase distribution map of Mn_2O_3 / Mn_7SiO_{12} shows that it is homogeneously distributed over the catalyst particles which indicates that the presence of La enhances the dispersion of Mn species.

Figure 21 shows magnified versions of selected phase distribution maps of Figures 9 and 20. These phase distribution maps correspond to the cristobalite-low, Na_2WO_4 and Mn_2O_3 / Mn_7SiO_{12} phases and were obtained from the Rietveld analysis of the

La-promoted and unpromoted catalyst XRD-CT data collected at room temperature before the OCM experiments. These results suggest that the presence of La leads to higher dispersion of the Mn_2O_3 / Mn_7SiO_{12} phase and also seems to lead to an egg-shell distribution of the Na_2WO_4 phase (it is predominantly located near the surface of the catalyst particles).

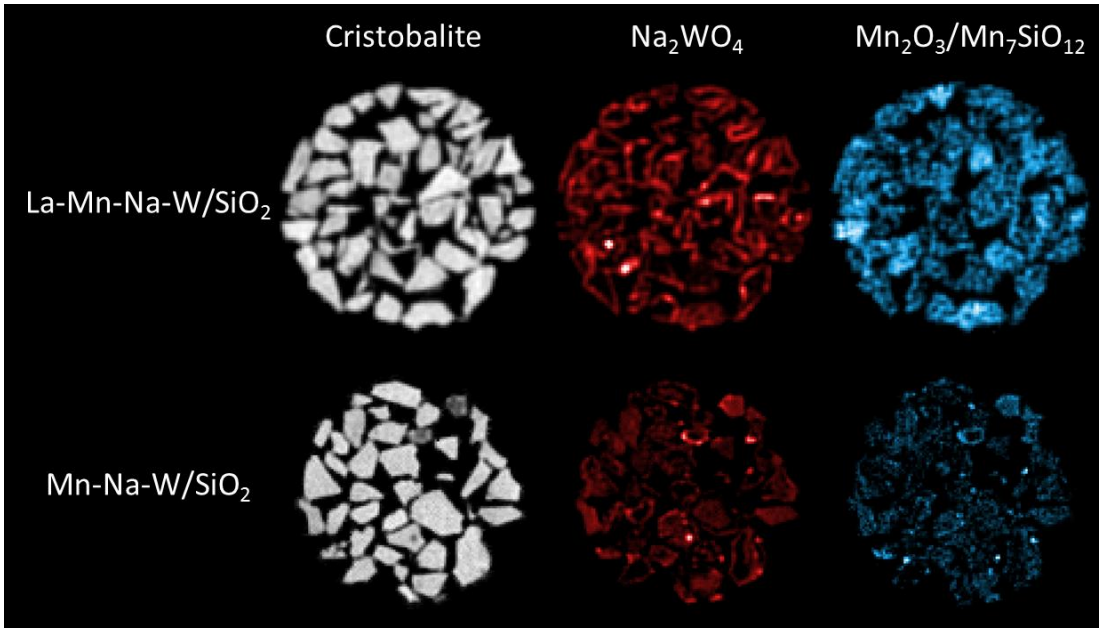

Figure 21: Phase distribution maps of cristobalite (gray), Na_2WO_4 (red) and Mn_2O_3 / Mn_7SiO_{12} as obtained from the Rietveld analysis of the La-promoted and unpromoted catalyst XRD-CT data collected at room temperature before the OCM experiments

The data processing strategy of the four IXRD-CT scans acquired during temperature ramping for room temperature to the operational temperature of 800 °C was the same as described previously (i.e. same as 2 % Mn-1.6 % Na-3.1 % W/SiO_2 catalyst). In Figure 22, the diffraction patterns, after background subtraction, are plotted as a function of temperature and the results are shown from two different points of view. The solid-state chemistry taking place during temperature ramping is identical to the 2 % Mn-1.6 % Na-3.1 % W/SiO_2 catalyst. Cristobalite changes symmetry from tetragonal to cubic at 250-260 °C (low-to-high transition) and cubic Na_2WO_4 transforms to a lower symmetry orthorhombic phase (Fddd) before melting (the Na_2WO_4 diffraction signal disappears before reaching 680 °C).

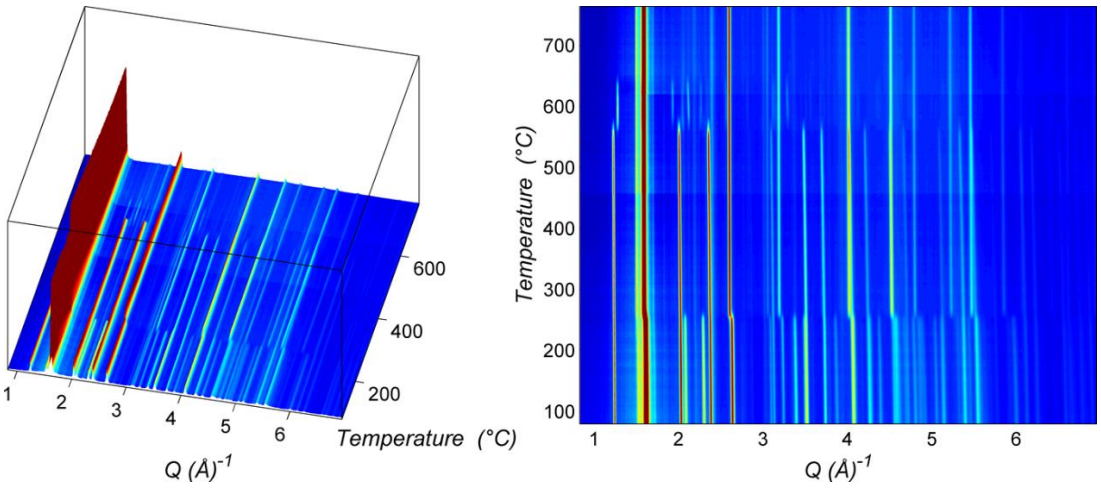

Figure 22: The summed diffraction patterns per line scan acquired during the temperature ramping (four IXRD-CT scans), after background subtraction, are plotted as a function of temperature

Once the required temperature was reached (800 °C), an XRD-CT scan (i.e. XRD-CT scan 6) was performed. However, due to a beam refill during the acquisition of this XRD-CT scan it was decided to acquire a second XRD-CT prior to switching from He to air flow (i.e. XRD-CT scan 7). As there were no solid-state changes during these two XRD-CT scans collected under He flow (i.e. XRD-CT scans 6 and 7), only the results from the second XRD-CT are presented in Figure 20. This is reasonable as the total acquisition time for the two XRD-CT scans was approximately 1h 30min; a relatively short period of time for substantial changes to take place in an inert chemical environment. The next XRD-CT scan (XRD-CT scan 8) was acquired while air flowed through the catalyst bed (50 ml min^{-1}). In Figure 20, it is implied that the diffraction signal from both the Mn_2O_3 / Mn_7SiO_{12} and the $La_4Mn_5Si_4O_{22}$ phases slightly increased. However, the signal generated by these phases significantly decreased once the first CH_4/He/air reaction mixture was used. The four reaction mixtures used in the OCM experiment with the La-promoted catalyst are provided in Table 3.

Table 3: Summary of reaction mixtures tested during the OCM experiment with the 2 % La-2 % Mn-1.6 % Na-3.1 % W/SiO_2 catalyst

	Flowrate (mL min^{-1})		
	CH_4	He	Air
Reaction mixture 1	20	80	5
Reaction mixture 2	100	-	10
Reaction mixture 3	20	10	24
Reaction mixture 4	100	-	10

The mass spectrometry data acquired during the OCM experiment are presented in Figure 23, where the signals from specific masses of interest are shown. It can be clearly seen that upon switching to OCM reaction conditions (i.e. region 1 in Figure 23), the signal from masses 27, 30 and 41 appears which correspond to fractions from higher hydrocarbon molecules other than CH_4 (i.e. C_2H_3+, C_2H_6+ and C_3H_5+ respectively). These signals were present regardless of the reaction mixture used showing the catalyst was captured in its active state during the OCM reaction.

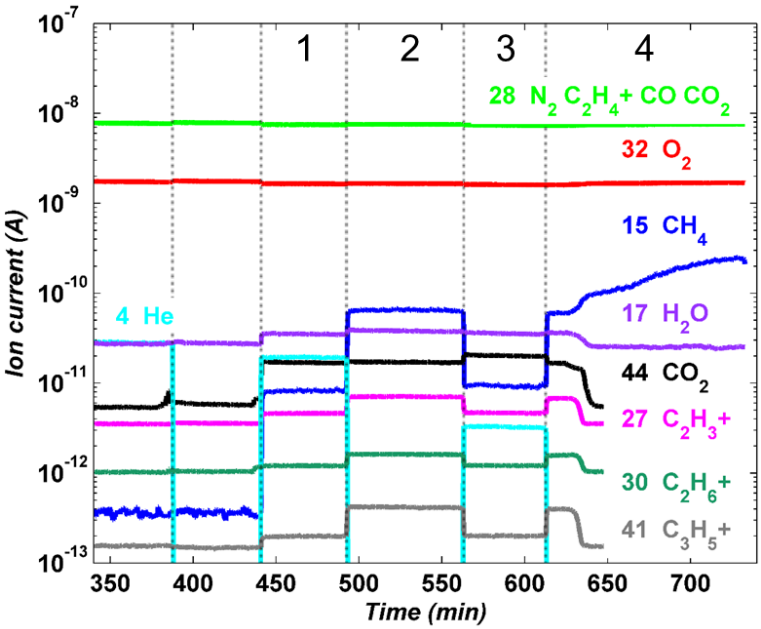

Figure 23: Mass spectrometry data corresponding to the following m/z ratios (possible species and respective line colour in parentheses): 4 (He - cyan), 15 (CH_4+ - blue), 17 (H_2O - purple), 27 (C_2H_2+ - magenta), 28 (N_2, CO, C_2H_4+ - green), 30 (C_2H_6+ - dark green), 32 (O_2 - red), 41 (C_3H_5+ - grey) and 44 (CO_2 - black). The different regions indicated correspond to the reaction mixtures used during the OCM experiment (presented in Table 3).

It is clearly shown in Figure 20 that the diffraction signal from the Mn_2O_3 / Mn_7SiO_{12} and the $La_4Mn_5Si_4O_{22}$ phases ($La_4Mn_5Si_4O_{22}$ has completely disappeared by the end of the OCM experiment) decreased radically when the OCM reaction mixture 2 was used (i.e. CH_4:Air = 10:1). This is expected as the metals in the various metal oxides present in the catalyst will eventually be reduced under these conditions. However, it can be also clearly seen that there are significant differences compared to the La-free catalyst. More specifically, the Mn_2O_3 / Mn_7SiO_{12} signal diminished in the 2 % Mn-1.6 % Na-3.1 % W/SiO_2 catalyst under the same operating conditions (i.e. CH_4:Air = 10:1). As mentioned previously, the Mn species were reduced and a $MnWO_4$ phase

formed. However, in the case of the La-promoted catalyst, the Mn_2O_3 / Mn_7SiO_{12} phases were present for the duration of the whole OCM experiment.

The significance of this result is more apparent when it is taken into account the fact that the La-promoted catalyst was exposed to reducing environments for more than double the time compared to the unpromoted catalyst (ca. 3.5 h for the 2 % La-2 % Mn-1.6 % Na-3.1 % W/SiO_2 catalyst to 1.5 h for the 2 % Mn-1.6 % Na-3.1 % W/SiO_2 catalyst). This result suggests that the La acts as a chemical promoter leading to more stable and difficult-to-reduce Mn species. Furthermore, a new crystalline phase formed at high temperatures which was identified as $NaLa(WO_4)_2$. The results from the phase identification performed using the summed diffraction pattern from the XRD-CT scan collected at room temperature after the OCM experiment is shown in Figure 24. This means that the most important role of La is to stabilise the mobile and volatile Na^+ and WO_4^{2-} species by leading to the formation of this new crystalline phase which is seen to be stable and present until the end of the OCM experiment. As shown in Figure 24, in contrast to the La-free catalyst, there is no crystalline Na_2WO_4 present after cooling to room temperature at the end of the OCM experiment. This proves that the La works efficiently as a trap of the mobile/volatile species present in the catalyst at high temperatures.

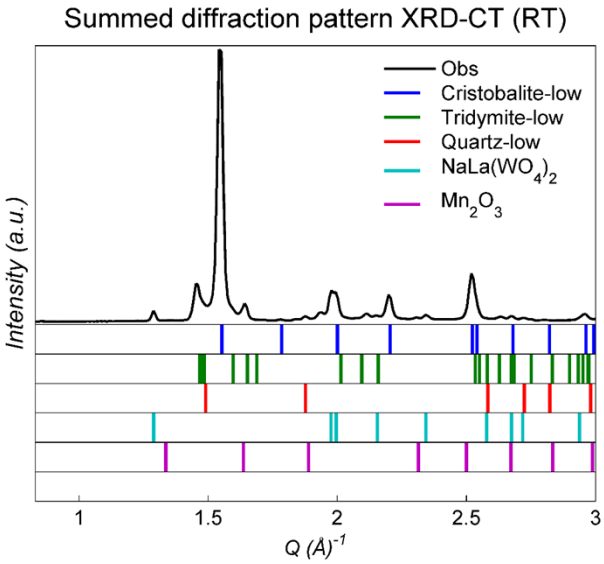

Figure 24: Phase identification of the 2 % La-2 % Mn-1.6 % Na-3.1 % W/SiO_2 catalyst at room temperature after the OCM experiment. Black line: the summed diffraction patterns from the XRD-CT dataset 14 (i.e. after applying a binary mask to the reconstructed data in order to extract the diffraction patterns generated only by the sample), Blue ticks: Cristobalite-low, Green ticks: Tridymite-low, Red ticks: Quartz-low, Cyan ticks: $NaLa(WO_4)_2$ and Magenta ticks: Mn_2O_3.

Further to this, it seems also that La plays a role in supressing the onset of deleterious support changes (Figure 20). Cristobalite is seen again to transform to tridymite at high temperatures as a function of time but the formation and growth of quartz is suppressed. This result was also later verified with *ex situ* PXRD characterisation of the two catalyst (see section starting in page 148 in this Chapter). In Figure 25, the summed diffraction patterns from the XRD-CT scans collected at room temperature before and after the OCM experiment are compared. It is clear that there is a decrease in the cristobalite intensity and increase in the tridymite, no significant growth of quartz and that Na_2WO_4 is not present in the catalyst after cooling to room temperature at the end of the OCM experiment.

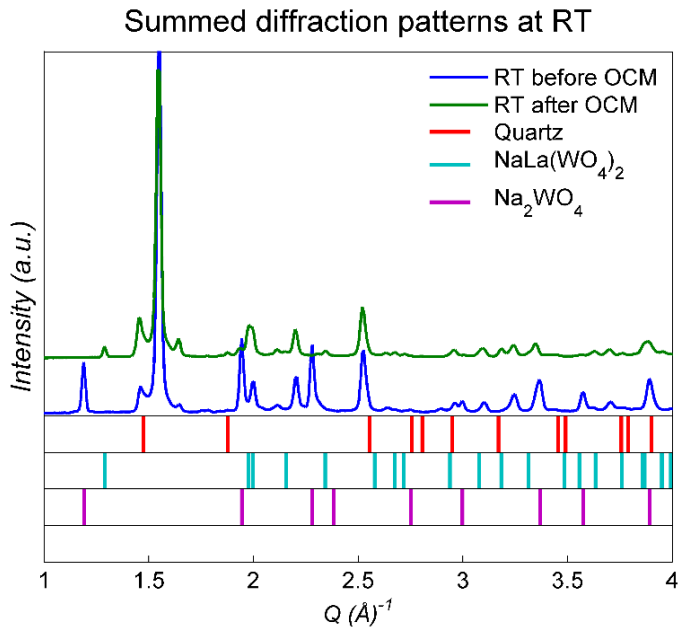

Figure 25: Comparison of summed diffraction patterns from the XRD-CT scans collected at room temperature before and after the OCM experiment (blue and green lines respectively). Also shown are the high intensity reflections of quartz (magenta ticks), $NaLa(WO_4)_2$ (cyan ticks) and Na_2WO_4 ticks.

Ex situ X-ray micro-CT & SEM/WDS measurements

The micro-CT measurements were performed at room temperature before and after each OCM experiment. The results from the micro-CT data of the 2 % La-2 % Mn-1.6 % Na-3.1 % W/SiO_2 catalyst are presented first. In Figure 26, the summed images of the XRD-CT data collected at room temperature before and after the OCM experiment are shown (Panel C and D of Figure 26 respectively) along with the corresponding micro-CT images.

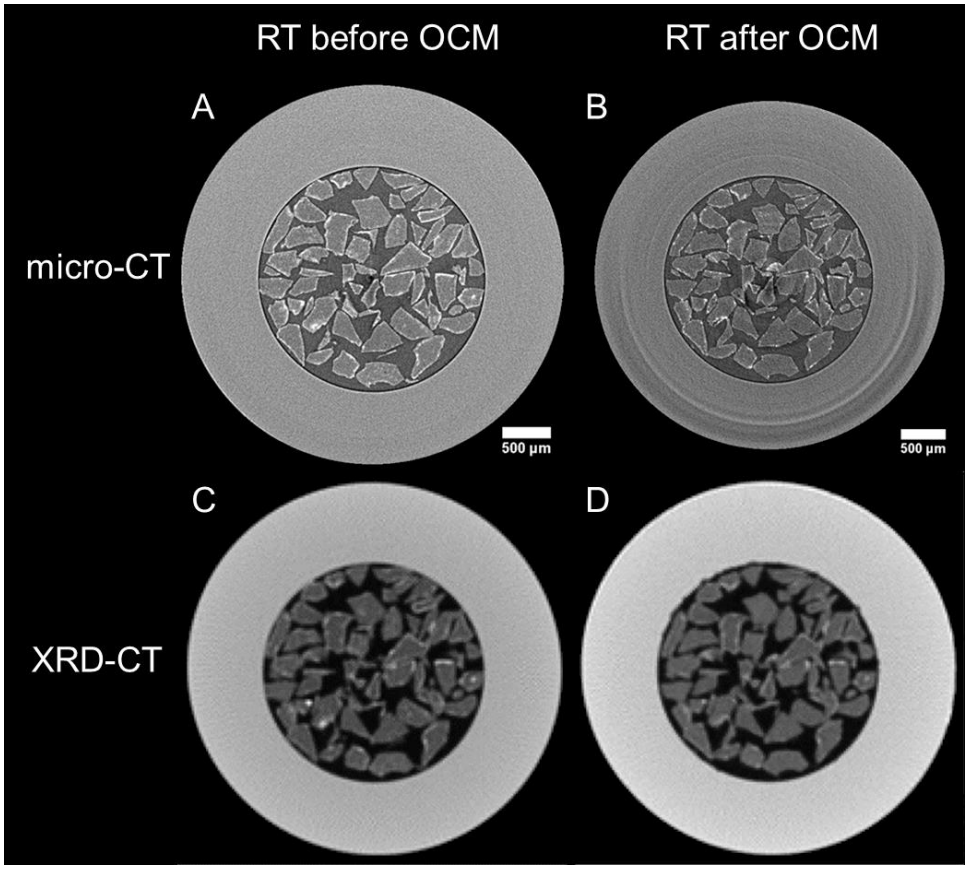

Figure 26: Comparison of summed images of XRD-CT data collected at room temperature before and after the OCM experiment (Panels C and D respectively) and the corresponding micro-CT images (Panels A and B respectively).

The micro-CT data were then cropped (i.e. reconstructed images) in order to remove the capillary and a 3D median filter (3 neighbouring pixels in every direction) was applied to the images using the ImageJ/Fiji software.[66, 67] The filtered images (stack) were then exported as an image sequence (.tiff files). In order to ensure the best possible results, the image segmentation was performed after interactively training a pixel classifier (machine learning algorithms) using the Ilastik software.[68] The segmented volume was then imported to ImageJ/Fiji and used as a binary mask which was then applied to the unfiltered micro-CT data. As a result, the volume rendering (Volume Viewer plugin of ImageJ/Fiji) yielded images where the catalyst particles can be clearly observed. These results are presented in Figure 27. It can be seen that although the La-promoted catalyst was exposed to 800 °C for almost 6 h, the catalyst particles retained their shape and size. This is a very promising result as, at least at the micron-to-mm scale, there are no indications of catalyst particle sintering or thermal degradation.

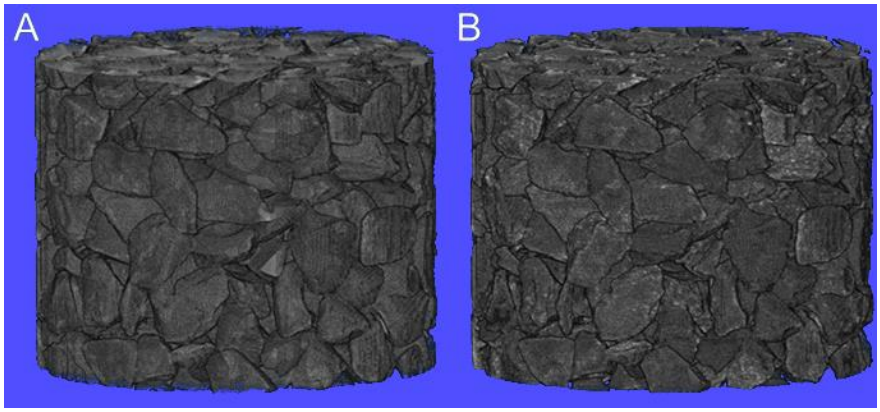

Figure 27: Volume rendering of the micro-CT collected room temperature before and after the OCM experiment (Panels A and B respectively).

In contrast to the results obtained for the La-promoted catalyst, the micro-CT data of the 2 % Mn-1.6 % Na-3.1 % W/SiO_2 catalyst suggest that the unpromoted catalyst is unsuitable for the OCM reaction. These results are in accordance to the respective XRD-CT data. As mentioned in the previous section, the results from the Rietveld analysis of the XRD-CT data collected at room temperature after the OCM experiment suggest that there is migration (loss) of active components from the catalyst particles to the capillary (reactor vessel). Furthermore, the XRD-CT data show that, apart from the loss of Na^+ ions and the crystallisation of the amorphous silica to the crystalline cristobalite phase, the catalyst particles have fused with the capillary (Panel A of Figure 28). The results from the corresponding micro-CT data, as presented in Panel B of Figure 28, are in full agreement with the XRD-CT data. It can be seen that the catalyst particles have not only fused with the capillary but also small cracks have been created (as indicated by the red arrows in Figure 28).

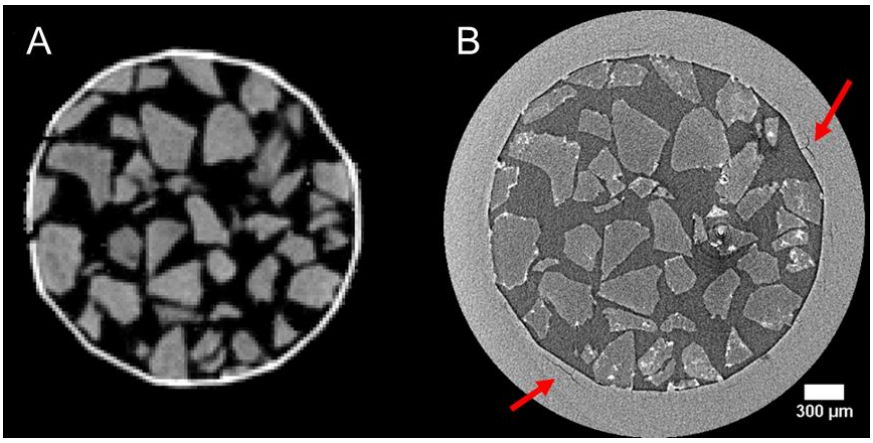

Figure 28: Panel A: Phase distribution map of Cristobalite-low as shown in Figure 9. Panel B: micro-CT image corresponding to the XRD-CT data collected at room temperature after the OCM experiment.

This phenomenon (i.e. catalyst-capillary fusion and cracks formation) can be observed throughout the reactor. This is illustrated in Figure 29 where the reconstructed micro-CT images from eight different positions along the reactor (z direction) are shown. The red arrows indicate catalyst particles fused with the silica capillary while the cyan arrows indicate the presence of cracks in the reactor vessel. These cracks are probably a side effect of the crystallization of the amorphous silica.

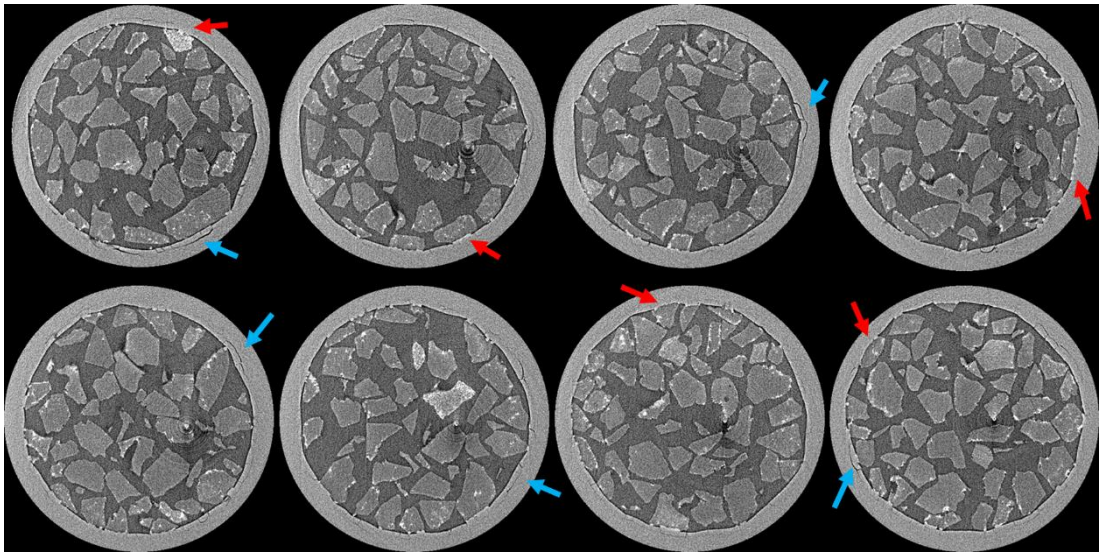

Figure 29: Reconstructed micro-CT images from different positions of the catalytic reactor showing the formation of cracks within the capillary (cyan arrows) and the catalyst bed – capillary interaction (red arrows).

SEM/WDS measurements of the 2 % Mn-1.6 % Na-3.1 % W/SiO_2 catalyst bed were also performed, after the OCM experiment. In Figure 30, an SEM image of the catalytic reactor is presented. As expected, in agreement with the results obtained from the XRD-CT and the micro-CT measurements, there are catalyst particles present that have fused with the capillary (red arrows in Figure 30). A region of interest was chosen (green circle in Figure 30) and then the elemental analysis was performed at a higher magnification level.

In Figure 31, the elemental maps of Si, Na, W, Mn and O along with the corresponding SEM image (bottom left) are presented. Also shown is an SEM image taken at a lower magnification level demonstrating the catalyst-capillary chemical interaction (chosen region of interest for the WDS analysis).

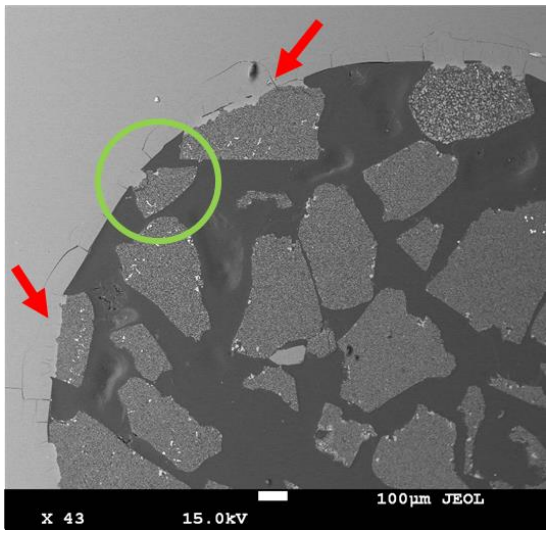

Figure 30: SEM image of the 2 % Mn-1.6 % Na-3.1 % W/SiO_2 catalyst bed after the OCM experiment.

The elemental map of Na clearly shows that Na has left the catalyst particles and moved to the capillary therefore supporting the results obtained from the Rietveld analysis of the XRD-CT data (i.e. larger unit cell of cristobalite present at the inner capillary wall indicating incorporation of Na into the silica framework).

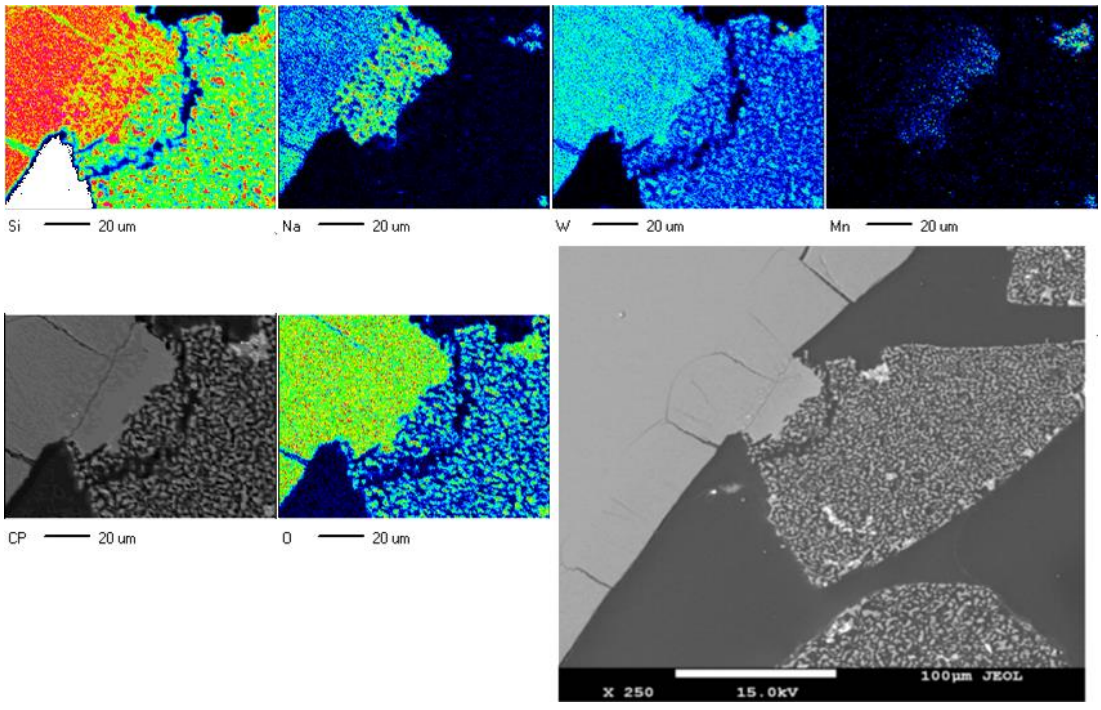

Figure 31: Elemental maps of Si, Na, W, Mn and O along with the corresponding SEM image (bottom left) and an SEM image at a lower magnification level showing the region of interest.

Operando multimodal μ-XRF/XRD/absorption-CT experiments during OCM

In this section the results from the *operando* experiments, with combined μ-XRF/XRD/absorption-CT, of the 2 % Mn-1.6 % Na-3.1 % W/SiO_2 catalyst and the 2 % La-2 % Mn-1.6 % Na-3.1 % W/SiO_2 catalysts are presented. The purpose of these experiments was to investigate the evolution of these catalysts under OCM conditions at a different length scale (i.e. single catalyst particle level). This means that the results obtained from these experiments serve to complement the *operando* XRD-CT experiments presented in the previous section, leading to a true multi-length-scale investigation of these systems (i.e. from the reactor to the single catalyst particle level).

The combined μ-XRF-CT and μ-XRD-CT measurements were made at room temperature, under OCM reaction conditions (ca. 800 °C) and at room temperature at the end of the each experiment. A reaction mixture of 50 % vol. CH_4/Ar and 20 % vol. O_2/He was used keeping the CH_4/O_2 molar ratio equal to 4 in both experiments (i.e. 6 ml min^{-1} of 50 % vol. CH_4/Ar and 3.75 ml min^{-1} of 20 % vol. O_2/He were used). The flow of gases was monitored/controlled with Brooks GF40 mass flow controllers and the gas products were analysed with an Omnistar portable mass spectrometer.

The 2 % Mn-1.6 % Na-3.1 % W/SiO_2 catalyst

A region on interest (4 – 12 keV energy range) of the summed XRF spectra acquired from the μ-XRF-CT scans performed at room temperature for the two catalysts are shown in Figure 32. On the left hand side, the characteristic lines of W (L edges), Mn (K edges) and La (L edges) are shown. On the right hand side, the selected regions of interest for each element are presented. These regions of interest were extracted from the XRF sinograms, creating three sinograms corresponding to the three elements. These sinograms were then reconstructed using the SART algorithm (ASTRA toolbox) yielding elemental maps of the W, Mn (for both catalysts) and La (for the 2 % La-2 % Mn-1.6 % Na-3.1 % W/SiO_2 catalyst).

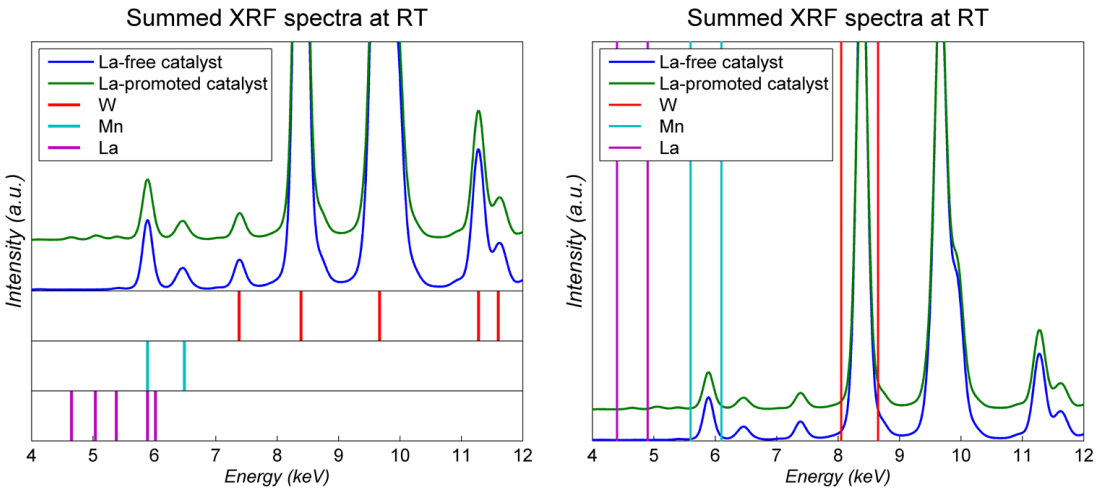

Figure 32 Left: Global XRF spectra for the two catalysts collected at room temperature showing the characteristic lines for each element. Right: The selected regions of interest which were used to create the elemental distribution maps of W, Mn and La.

µ-XRF-CT

The results from the µ-XRF-CT/ µ-absorption-CT scans of the 2 % Mn-1.6 % Na-3.1 % W/SiO_2 catalyst are presented in Figure 34. The µ-XRF-CT scan of the fresh catalyst (i.e. at room temperature) revealed that the W and Mn species are not perfectly co-located in the catalyst particles. This result is in good agreement with the results obtained from the XRD-CT data presented in the previous section (Figures 9 and 10). This is more apparent in Figure 33 where a coloured image is shown. In this image, the blue colour corresponds to the elemental map of W and the green colour corresponds to the elemental map of Mn (i.e. results from the µ-XRF-CT scan of the fresh catalyst).

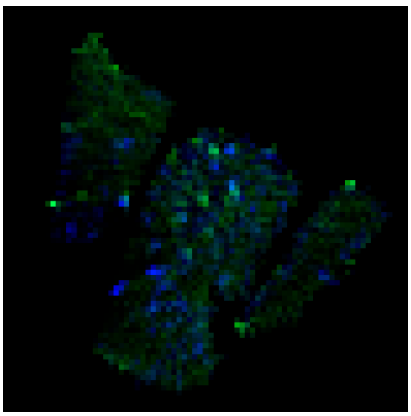

Figure 33: Overlaid elemental maps of W and Mn as obtained from the µ-XRF-CT scan of the fresh 2 % Mn-1.6 % Na-3.1 % W/SiO_2 catalyst. Blue colour: elemental map of W, Green colour: elemental map of Mn.

The high temperature μ-XRF-CT scans were performed at four different vertical positions (Pos 1 to 4 in Figure 34). As it is clearly implied from the μ-absorption-CT maps in Figure 34, different catalyst particles were probed during the tomographic scans at high temperatures compared to the room temperature scans. This is attributed to the thermal expansion of the capillary and not to sample movement as the tomographic scans performed at room temperature before and after the OCM experiment probed the same catalyst particles.

The high temperature μ-XRF-CT scans (ca. 800 °C) revealed new information about this catalyst. The results shown in Figure 34 imply that the Na_2WO_4 phase does not just melt at high temperatures but it also becomes volatile. This is in full agreement with the results from the *operando* XRD-CT experiments of the same catalyst presented in the previous section. However, the results obtained from the μ-XRF-CT scans clearly show that the W containing species also migrate from the catalyst particles to the inner capillary wall. A very thin layer of W containing species is seen to form and grow as a function of time at high temperatures. This "coating" phenomenon is irreversible and this new layer is present even after cooling to room temperature.

It is important to note here that the W XRF signal seems to be dominated by the W species present at the new layer to such an extent that the W species present in the catalyst particles are barely visible in the XRF-CT maps. The migration and volatility of W containing species was also suggested from the *ex situ* SEM/WDS images (elemental map of W) presented earlier in Figure 31. On the other hand, the Mn species are seen to be more stable (i.e. no apparent migration from the catalyst particles to the inner capillary wall).

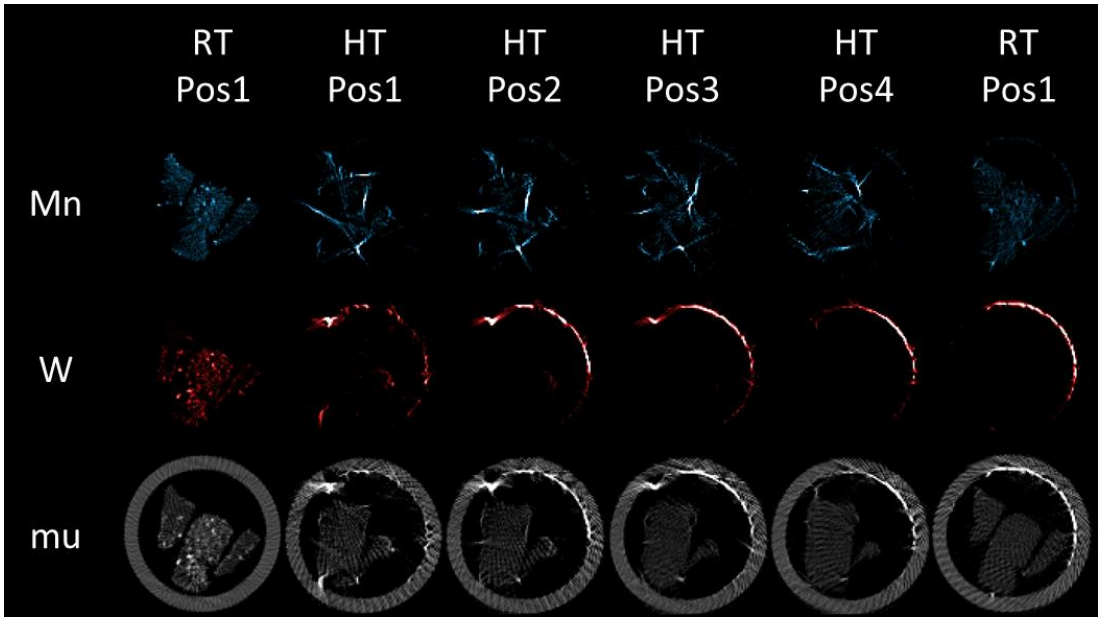

Figure 34: Elemental maps of Mn, W and µ-absorption-CT map (mu) of the 2 % Mn-1.6 % Na-3.1 % W/SiO_2 catalyst – RT for room temperature scans, HT for high temperature scans (ca. 800 °C). The high temperature µ-XRF-CT scans were performed at four different vertical positions (Pos 1 to 4).

µ-XRD-CT

The 2D powder diffraction images acquired during the µ-XRD-CT measurements exhibited spottiness due to the presence of large crystallites in the sample (i.e. large relative to the beam size). A 30% alpha-trimmed mean filter was used to remove outliers and suppress the formation of "streak" artefacts in the reconstructed images.[51] However, as this is a relatively harsh filter and the *Q* range sampled was very narrow (ca. 1-3.4 $Å^{-1}$), the µ-XRD-CT data were processed by fitting specific peaks of interest (i.e. one peak per crystalline phase) rather than performing full profile Rietveld analysis. The results from the phase identification of the fresh 2 % Mn-1.6 % Na-3.1 % W/SiO_2 catalyst are presented in Figure 35. As expected, the same crystalline phases were identified as in the XRD-CT experiments described in the previous section (i.e. cristobalite-low, tridymite-low, Na_2WO_4 and Mn_2O_3 / Mn_7SiO_{12}).

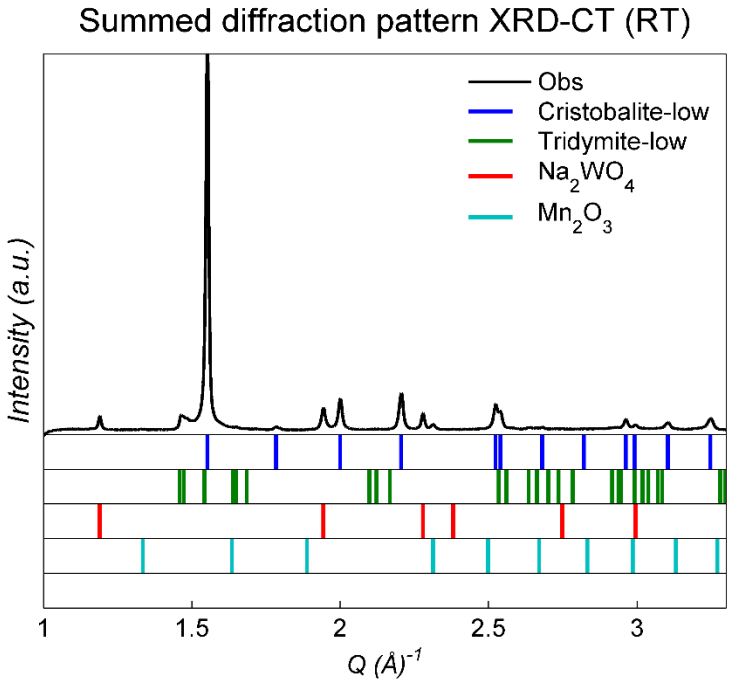

Figure 35: Phase identification of the 2 % Mn-1.6 % Na-3.1 % W/SiO_2 catalyst. Black line: the summed diffraction patterns from the room temperature XRD-CT scan (i.e. after applying a binary mask to the reconstructed data in order to extract the diffraction patterns generated only by the sample), Blue ticks: Cristobalite, Green ticks: Tridymite, Red ticks: : Na_2WO_4, Cyan ticks: Mn_2O_3.

The diffraction peaks of each crystalline phase selected for the peak fitting analysis are summarised in Table 4. A Gaussian peak shape function was used and three refinement cycles were performed allowing for three iterations in each cycle. In the first refinement cycle, the area of the peak and the background (1st degree polynomial) were refined. In the second cycle, the peak position was refined along with the previous parameters and in the final refinement cycle, the full width at half maximum (FWHM) was added to the refinement.

Table 4: Selected diffraction peaks of interest for each crystalline phase

Crystalline phase	**Q ($Å^{-1}$)**	**hkl reflection**	**Temperature**
Cristobalite-low	2.20	(102)	RT
Cristobalite-high	2.48	(220)	HT
Tridymite-low	1.46-1.48	multiple	RT
Tridymite-high	1.43	(100)	HT
Na_2WO_4	2.28	(311)	RT
Mn_2O_3/Mn_7SiO_{12}	2.31	(222)/(224)	All

The results obtained from the peak fitting analysis of the µ-XRD-CT are shown in Figure 36 where the various phase distribution maps, as obtained from the integrated intensities of the respective phases, are presented. In Figure 36, it can be seen that the Na_2WO_4 and the Mn_2O_3/Mn_7SiO_{12} are not perfectly co-located in the fresh catalyst (i.e. room temperature µ-XRD-CT scan) which is in full agreement with the µ-XRF-CT results and the XRD-CT results presented in the previous section. More importantly, it is clearly shown that at high temperatures there is formation and growth of a cristobalite ring at the capillary (reactor vessel). This is important as it proves that the XRD-CT results presented in the previous section are reproducible (Figure 9).

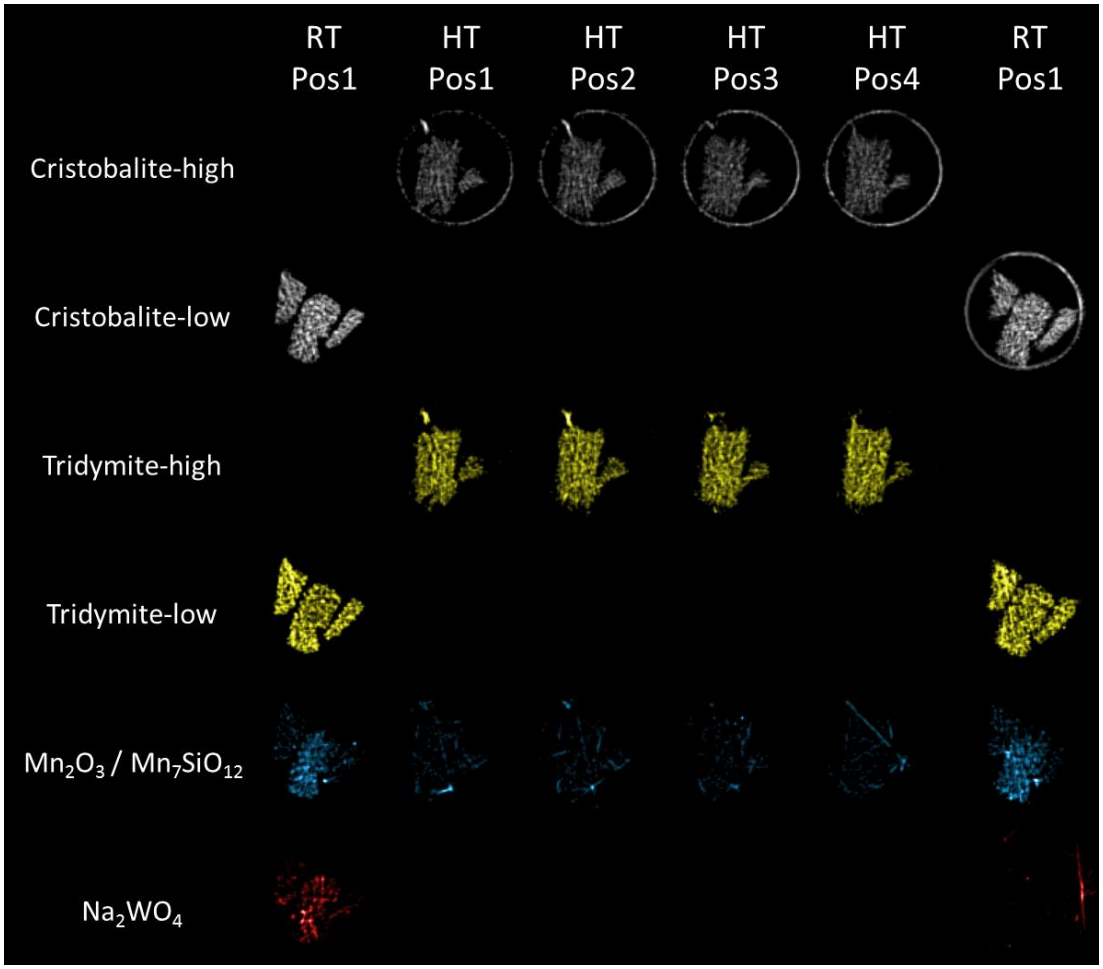

Figure 36: Phase distribution maps of the various crystalline phases present in the 2 % Mn-1.6 % Na-3.1 % W/SiO_2 catalyst during the OCM experiment.

On the other hand, the Mn_2O_3/Mn_7SiO_{12} phases remained present for the duration of this OCM experiment and no $MnWO_4$ was observed. This observation further supports the claim made in the previous section that the formation/growth of

$MnWO_4$ directly depends on the gas environment. In contrast to the previous XRD-CT experiment, where the behaviour of the 2 % Mn-1.6 % Na-3.1 % W/SiO_2 catalyst was investigated under very reducing environments (see Table 2), the CH_4:O_2 ratio was kept constant at 4 for the duration of this OCM experiment. As a result, the majority of the Mn species did not reduce from Mn^{3+} to Mn^{2+}, at least according to the μ-XRD-CT data (i.e. Mn_2O_3/Mn_7SiO_{12} were the only Mn crystalline phases present in the catalyst). Of course, the loss of reactive WO_4^{2-} ions from the catalyst bed to the capillary (as implied from the μ-XRF-CT data) also contributed to the prevention of the $MnWO_4$ formation.

The mass spectrometry data acquired during the OCM experiment with the 2 % Mn-1.6 % Na-3.1 % W/SiO_2 catalyst are presented in Figure 37. It is shown that the signals from masses corresponding to higher than methane hydrocarbon molecules (i.e. 27, 30 and 41) are present under OCM reaction conditions but indeed very weak. This should be expected as there is substantially less catalyst compared to the *operando* experiments presented in the previous section. At the same time, both the μ-XRF-CT and μ-XRD-CT data indicate that there is loss of active components from the catalyst particles to the reactor vessel at high temperatures.

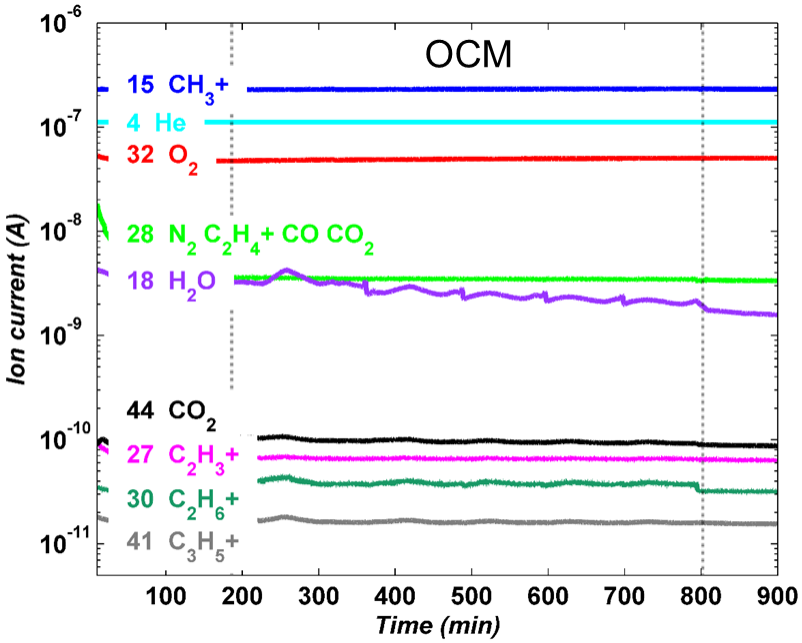

Figure 37: Mass spectrometry data corresponding to the following m/z ratios (possible species and respective line colour in parentheses): 4 (He - cyan), 15 (CH_4+ - blue), 17 (H_2O - purple), 27 (C_2H_2+ - magenta), 28 (N_2, CO, C_2H_4+ - green), 30 (C_2H_6+ - dark green), 32 (O_2 - red), 41 (C_3H_5+ - grey) and 44 (CO_2 - black).

In Figure 36, it can also be seen that the Na_2WO_4 phase reforms after cooling to room temperature at the end of the OCM experiment but it is mainly present at the inner side of the capillary rather than the catalyst particles. In Figure 38, the summed diffraction patterns of all the µ-XRD-CT data acquired from the 2 % Mn-1.6 % Na-3.1 % W/SiO_2 catalyst are presented. These diffraction patterns were exported after applying an appropriate mask to the reconstructed data volume (i.e. signal originating only from the catalyst particles). It can be seen that at high temperatures, the only Mn phase corresponds to Mn_2O_3/Mn_7SiO_{12} (characteristic diffraction peak at ca. 2.3 $Å^{-1}$). Furthermore, only the main peak of Na_2WO_4 can be observed at the summed diffraction pattern of the room temperature µ-XRD-CT data collected at the end of the experiment (highest intensity diffraction peak at ca. 1.94 $Å^{-1}$).

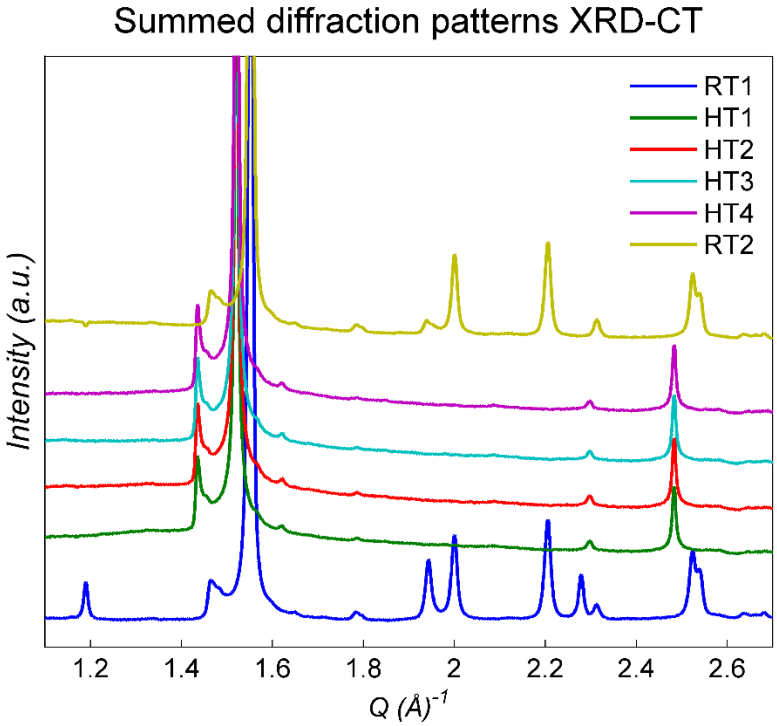

Figure 38: Summed diffraction patterns of the µ-XRD-CT data acquired from the 2 % Mn-1.6 % Na-3.1 % W/SiO_2 catalyst. RT1: room temperature before the OCM experiment, HT1-4: high temperature scans performed at four different vertical positions, RT2: room temperature after the OCM experiment.

The 2 % La-2 % Mn-1.6 % Na-3.1 % W/SiO_2 catalyst

µ-XRF-CT

The µ-XRF-CT scans of the 2 % La-2 % Mn-1.6 % Na-3.1 % W/SiO_2 catalyst are presented in Figure 39. Three µ-XRF-CT scans were performed at 3 different vertical positions by moving the sample in the *z* direction with a step size of 5 µm (Positions

1 to 3 in Figure 39). The µ-XRF-CT scan of the fresh catalyst (i.e. at room temperature) revealed that there are regions in the sample where some elements are co-located and others regions where they are not. More specifically, the Mn species seem to be co-located with the La species at specific regions. On the other hand, in other areas of the sample, separate Mn species are present in the form of Mn_2O_3/Mn_7SiO_{12} (as in the case of the fresh 2 % Mn-1.6 % Na-3.1 % W/SiO_2 catalyst). It should be noted though that in contrast to the 2 % Mn-1.6 % Na-3.1 % W/SiO_2 catalyst, the Mn species in the 2 % La-2 % Mn-1.6 % Na-3.1 % W/SiO_2 catalyst are more homogeneously distributed. Furthermore, the La species are seen to be co-located with the W species at certain regions. As shown in Figure 39, the observations regarding the elemental distribution of Mn, La and W are consistent for all three µ-XRF-CT datasets (i.e. positions 1 to 3).

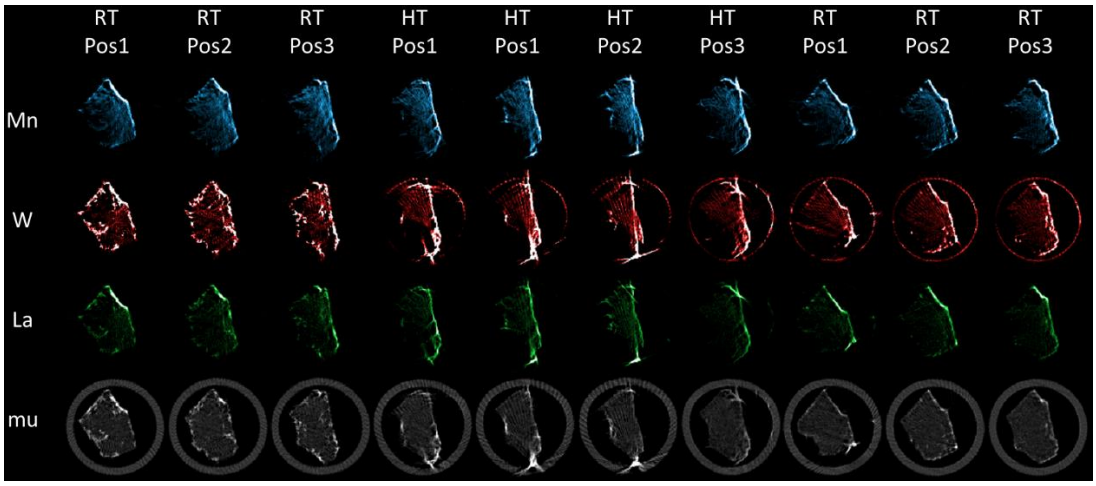

Figure 39: µ-XRF-CT scans of the 2 % La-2 % Mn-1.6 % Na-3.1 % W/SiO_2 catalyst – RT for room temperature scans, HT for high temperature scans (i.e. above 700 °C). µ-XRF-CT scans were performed at three different vertical positions (Position 1 to 3).

At high temperatures, it can be seen that there is again migration of the W containing species, albeit to an impressively lesser extent when compared with the 2 % Mn-1.6 % Na-3.1 % W/SiO_2 catalyst. The difference is apparent when the µ-absorption-CT maps obtained from the two experiments are directly compared (Figures 34 and 39). The Mn species are seen to be stable as there is no indication of Mn species leaving the catalytic particles. However, the µ-XRF-CT maps seem to suggest that there is migration of the Mn species over the catalyst particles. More specifically, after the room temperature scan at the end of the experiment it can be seen that the majority

of the Mn species are present at distinct regions of the catalyst particles (predominantly near the surface of the catalyst particles), probably implying that agglomeration takes place at high temperatures. This is also true for the La-containing species. However, these two results should be treated with caution as the sample volume probed during these µ-XRF-CT scans was not the same (due to the thermal expansion of the capillary during the OCM experiment, as previously discussed).

µ-XRD-CT

The results from the phase identification of the fresh 2 % La-2 % Mn-1.6 % Na-3.1 % W/SiO_2 catalyst are presented in Figure 40. The same crystalline phases were identified as in the XRD-CT experiments described in the previous section (i.e. cristobalite-low, tridymite-low, Na_2WO_4, Mn_2O_3 / Mn_7SiO_{12} and $La_4Mn_5Si_4O_{22}$). The data analysis strategy was identical to the one used for the µ-XRD-CT data of the 2 % Mn-1.6 % Na-3.1 % W/SiO_2 catalyst; a diffraction peak of interest was chosen for each crystalline phase present and then batch peak fitting of the µ-XRD-CT data was performed. These peaks of interest are summarised in Table 5.

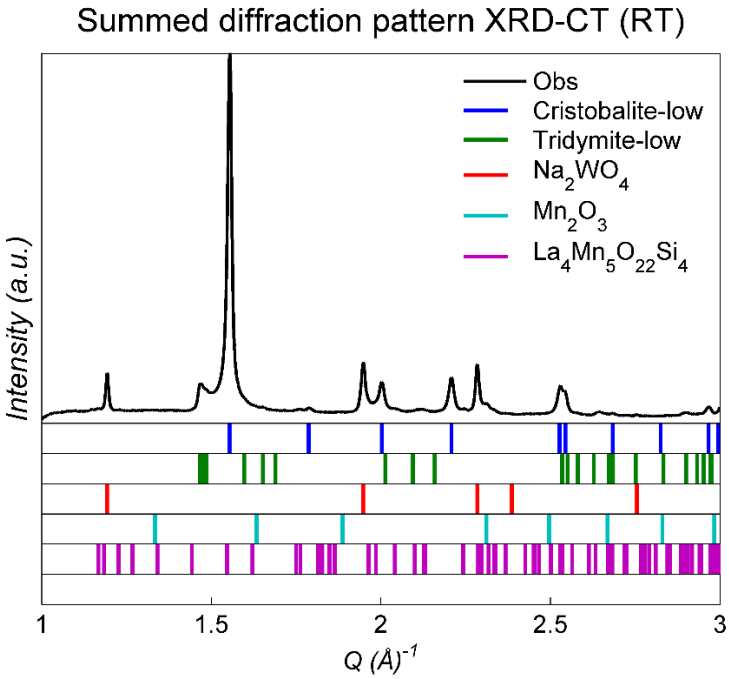

Figure 40: Phase identification of the 2 % La-2 % Mn-1.6 % Na-3.1 % W/SiO_2 catalyst. Black line: the summed diffraction pattern from the room temperature XRD-CT scan (i.e. Position 1 after applying a binary mask to the reconstructed data in order to extract the diffraction patterns generated only by the sample), Blue ticks: Cristobalite, Green ticks: Tridymite, Red ticks: Na_2WO_4, Cyan ticks: Mn_2O_3, Magenta ticks: $La_4Mn_5Si_4O_{22}$.

Table 5: Selected diffraction peaks of interest for each crystalline phase

Crystalline phase	**Q ($Å^{-1}$)**	**hkl reflection**	**Temperature**
Cristobalite-low	2.20	(102)	RT
Cristobalite-high	2.48	(220)	HT
Tridymite-low	1.46-1.48	multiple	RT
Tridymite-high	1.43	(100)	HT
Na_2WO_4	2.28	(311)	RT
Mn_2O_3/Mn_7SiO_{12}	2.31	(222)/(224)	All
$La_4Mn_5Si_4O_{22}$	2.33-2.35	multiple	All
$NaLa(WO_4)_2$	1.96	(112)	All

The results from the peak fitting of the μ-XRD-CT data are presented in Figure 41 where the phase distribution maps of each component are shown. As expected, the crystalline SiO_2 phases (support of the catalyst) are homogeneously distributed and describe very accurately the catalyst particles in terms of both size and shape. This homogeneous distribution of the crystalline SiO_2 phases is consistent for all the μ-XRD-CT datasets (i.e. regardless of *z* position and temperature). More importantly, the Mn_2O_3/Mn_7SiO_{12} phases are also seen to be homogeneously distributed over the catalyst particles which is in full agreement with the XRD-CT data presented in the previous section (Figure 20). This homogeneous distribution of Mn containing species is also suggested from the μ-XRF-CT data presented in Figure 39 as mentioned previously.

On the other hand, the $La_4Mn_5Si_4O_{22}$ phase (i.e. the other crystalline Mn containing phase) is seen to be preferentially located near the surface of the catalyst particles which is also in agreement with the XRD-CT results presented previously in Figure 20. It is therefore consistent that the regions of high intensity in the Mn and La μ-XRF-CT maps presented in Figure 39 are co-located with the $La_4Mn_5Si_4O_{22}$ phase distribution map. The $NaLa(WO_4)_2$ phase is considered to be absent in the fresh catalyst when the summed diffraction pattern is used for the phase identification (Figure 40). However, the μ-XRD-CT data revealed that at certain regions at the surface of the catalyst

particle, there is weak diffraction signal corresponding to the $NaLa(WO_4)_2$ phase. As it is clearly shown in Figures 39 and 41, the combination of the phase distribution maps of Na_2WO_4 and $NaLa(WO_4)_2$ correspond to the W XRF-CT map implying that the W containing species are mainly present in crystalline forms. These observations regarding the distribution of the Mn and Na_2WO_4 species obtained from these high resolution images (Figures 34, 36, 39 and 41) are consistent with previous observations (Figure 21) that La promotion leads to a greater dispersion of the Mn species while Na_2WO_4 is located predominantly near the surface of the catalyst particles (i.e. following an egg shell distribution).

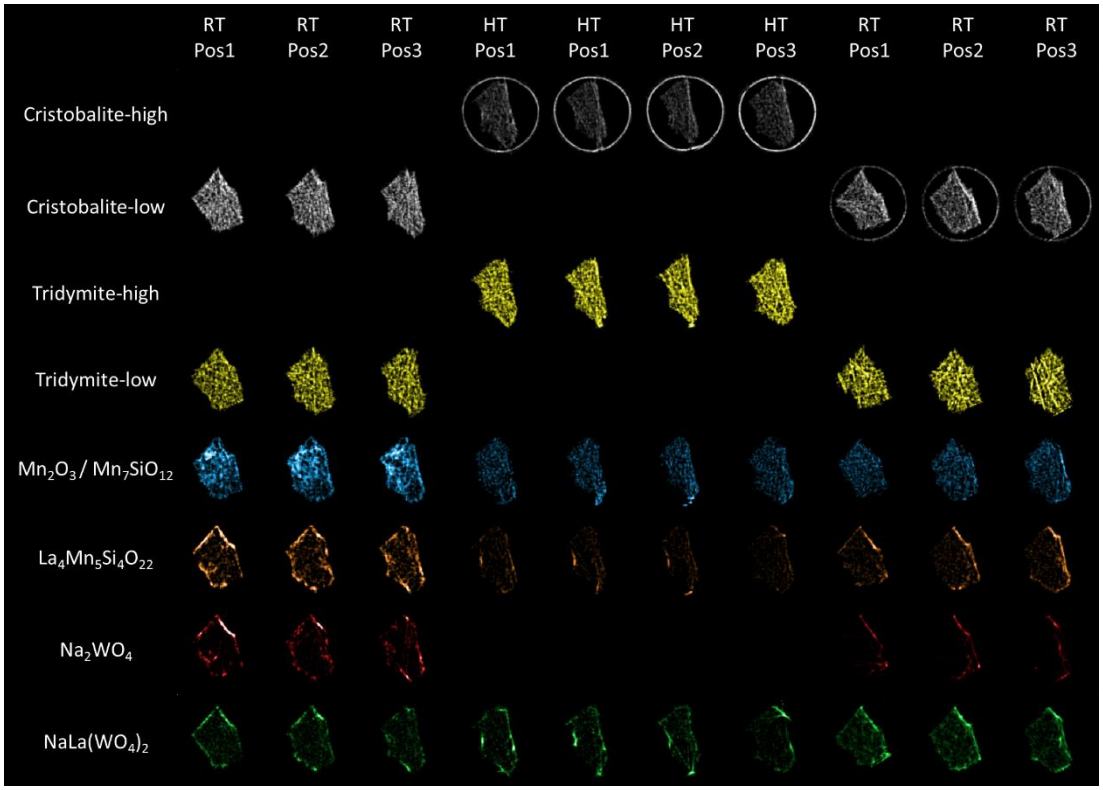

Figure 41: Phase distribution maps of the various crystalline phases present in the 2 % La-2 % Mn-1.6 % Na-3.1 % W/SiO_2 catalyst during the OCM experiment.

At high temperatures, a SiO_2 cristobalite ring is seen to form and grow with time at the inner side of the capillary. As thoroughly discussed in the previous section, this phenomenon is attributed to the loss of Na^+ species from the catalyst to the reactor vessel. It should be noted though that the La-promoted catalyst is seen to be more chemically stable compared to the unpromoted catalyst (more stable Na and W containing species). This is clearly indicated when the W XRF-CT maps of the two catalysts are directly compared (Figures 33 and 38). This claim is also supported from

the fact that at the end of the OCM experiment with the La-promoted catalyst, there is no Na_2WO_4 present at the capillary but only at the catalyst particles (Figures 36 and 41).

As expected, the mass spectrometry data collected during the OCM experiment with the La-promoted catalyst show that the catalyst was captured in its active state. As it is shown in Figure 42, there is signal from masses corresponding to higher than CH_4 hydrocarbon molecules (i.e. m/z of 27 and 30) under reaction conditions (i.e. once the required temperature was reached) and that this signal remains present for the duration of the OCM experiment (i.e. no apparent deactivation of the La-promoted catalyst).

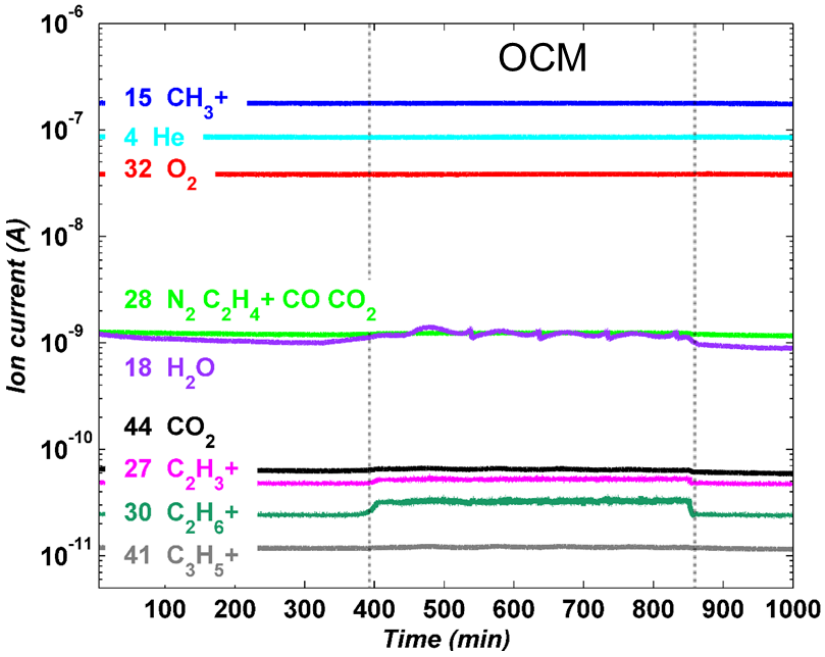

Figure 42: Mass spectrometry data corresponding to the following m/z ratios (possible species and respective line colour in parentheses): 4 (He - cyan), 15 (CH_4+ - blue), 17 (H_2O - purple), 27 (C_2H_2+ - magenta), 28 (N_2, CO, C_2H_4+ - green), 30 (C_2H_6+ - dark green), 32 (O_2 - red), 41 (C_3H_5+ - grey) and 44 (CO_2 - black).

However, the loss of Na and W containing species from the 2 % La-2 % Mn-1.6 % Na-3.1 % W/SiO_2 catalyst (upon reaching the OCM required high temperatures) had an impact on the evolution of the crystalline phases containing these elements. More specifically, in contrast to the XRD-CT experiment presented in the previous section (Figure 35), the growth of the $NaLa(WO_4)_2$ phase was not that significant. In Figure 43, the summed diffraction patterns of all μ-XRD-CT datasets are presented. The

Na_2WO_4 phase is seen to reform upon cooling to room temperature at the end of the OCM experiment but the diffraction signal generated by this phase has been significantly weakened. This also implied from the phase distribution maps of Na_2WO_4 presented in Figure 41. On the other hand, the Mn containing crystalline phases are behaving in accordance to the XRD-CT experiment of the same catalyst presented in the previous section. More specifically, the diffraction signal of both Mn_2O_3/Mn_7SiO_{12} and $La_4Mn_5Si_4O_{22}$ phases decreased under OCM reaction conditions but did not vanish. This should be expected as the Mn_2O_3/Mn_7SiO_{12} phases remained present even in the *operando* XRD-CT experiment presented in the previous section (Figure 20), where the OCM reaction mixtures tested were richer in CH_4 (i.e. very reducing chemical environment).

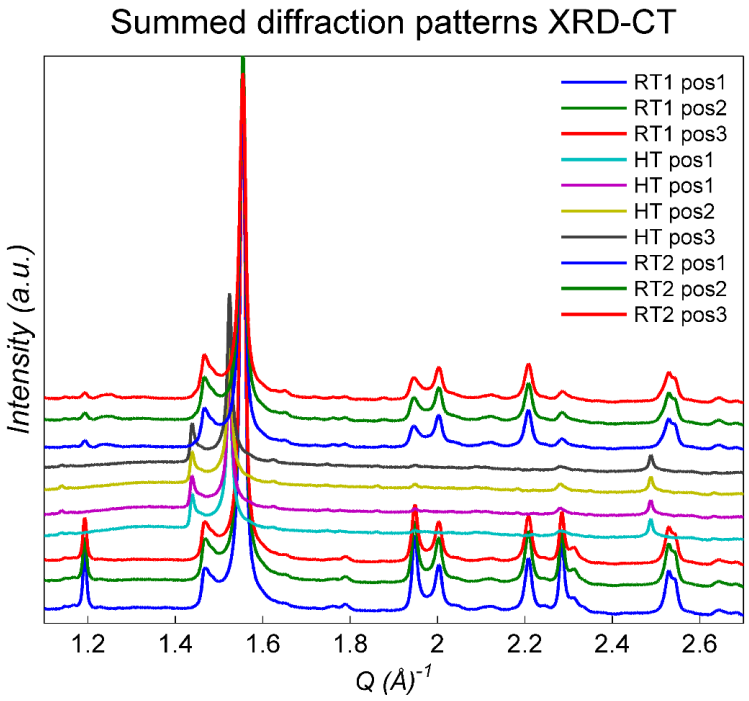

Figure 43: Summed diffraction patterns of the μ-XRD-CT data acquired from the 2 % La-2 % Mn-1.6 % Na-3.1 % W/SiO_2 catalyst.

High temperature PXRD and *ex situ* PXRD and XRD-CT measurements

The behaviour of both the 2 % Mn-1.6 % Na-3.1 % W/SiO_2 and the 2 % La-2 % Mn-1.6 % Na-3.1 % W/SiO_2 catalysts was also investigated with high temperature powder diffraction measurements under chemical environment (i.e. He flow of 30 ml min^{-1}) using a lab diffractometer. The purpose of these experiments was to identify which of the solid-state changes that take place in the catalysts at high temperatures (as

observed from the *operando* X-ray tomographic experiments) are attributed to the chemical environment (i.e. OCM reaction mixtures) and which are attributed to temperature (i.e. thermal effects). The results from the powder diffraction measurements of the 2 % Mn-1.6 % Na-3.1 % W/SiO_2 catalyst are presented in Figure 44.

At 600 °C, the lower symmetry orthorhombic Na_2WO_4 is present (apart from the cubic one) but upon reaching 700 °C there are no diffraction that can be attributed to any Na-W-O phases. This is expected and is in agreement with the results obtained from the IXRD-CT data presented previously (Figure 6). Furthermore, the diffraction signal corresponding to the Mn_2O_3/Mn_7SiO_{12} phases is seen to decrease with time at high temperatures. At this point it should be noted that the acquisition of each powder diffraction pattern lasted for approximately 2 h. This means that the solid-state changes taking place at high temperatures should not be simply tracked/treated as a function of temperature but as a function of both time and temperature (i.e. results of prolonged exposure of the catalyst to high temperatures).

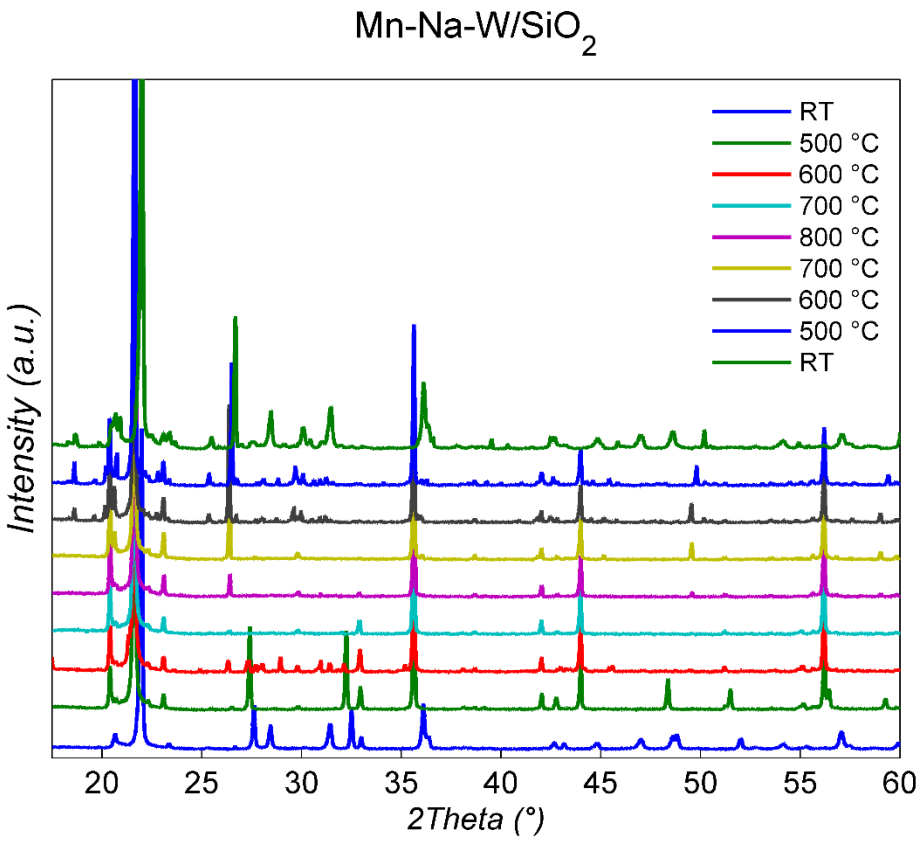

Figure 44: High temperature powder diffraction measurements of the 2 % Mn-1.6 % Na-3.1 % W/SiO_2 catalyst collected under He flow.

It is impressive that no Na_2WO_4 or Mn_2O_3/Mn_7SiO_{12} phases are observed in the catalyst at the end of the experiment. There are no crystalline Na containing phases and the only Mn/W crystalline phase present is $MnWO_4$. This result is crucial as it shows that the Mn species present in the Mn_2O_3/Mn_7SiO_{12} can be reduced from Mn^{3+} to Mn^{2+} at high temperatures even under He flow (thermal effect). This result also implies that the gases used in the calcination step during the preparation of the catalyst can have a strong impact on the state of the catalyst before the actual OCM experiment. To our knowledge this phenomenon has not been reported/investigated in literature in the past. Furthermore, it is seen that that there are significant solid-state changes taking place in the SiO_2 support of the catalyst. Tridymite, as expected, grows during this high temperature treatment of the 2 % Mn-1.6 % Na-3.1 % W/SiO_2 catalyst but it is the increase in the diffraction signal corresponding to quartz that is most significant (2θ = 26.4-26.7°).

The 2 % Mn-1.6 % Na-3.1 % W/SiO_2 catalyst after the high temperature heat treatment under He flow was also examined *ex situ* with XRD-CT. The XRD-CT data were analysed by performing Rietveld analysis of the reconstructed data following the same data processing strategy mentioned in the previous sections. The results from the Rietveld analysis are presented in Figure 45 where the phase distribution maps of each phase are shown. These maps correspond to the values of the scale factors of each crystalline phase as obtained from the Rietveld analysis of the XRD-CT data. As expected, the cristobalite and tridymite phase distribution maps describe very well the sample in terms of both shape and size. As implied in Figure 44, minor quantities of Na_2WO_4 and Mn_2O_3/Mn_7SiO_{12} were detected but the important result is related to the $MnWO_4$ phase. It can be seen that the diffraction signal from the $MnWO_4$ phase is present in all catalyst particles. It is can also be clearly seen that the $MnWO_4$ is not located only at the surface of the catalyst particles but in most cases it is homogeneously distributed over the catalyst particles. Furthermore, the SiO_2 quartz phase is also present and homogeneously distributed in all particles.

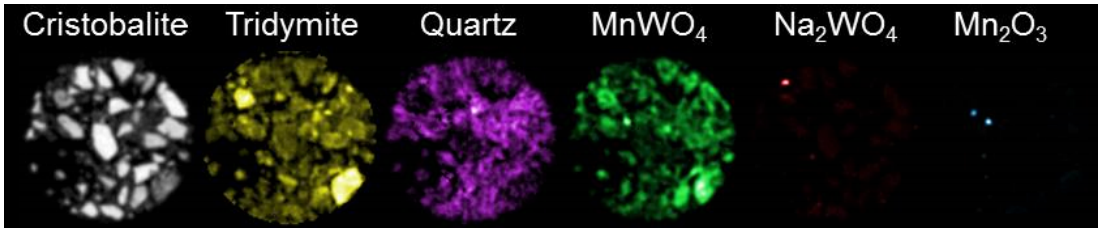

Figure 45: Phase distribution maps of the various crystalline phases present in the 2 % Mn-1.6 % Na-3.1 % W/SiO_2 catalyst (i.e. after high temperature heat treatment under He flow).

A second calcination step was also performed using the 2 % Mn-1.6 % Na-3.1 % W/SiO_2 catalyst. The sample was inserted in a furnace and the temperature was increased from room temperature to 800 °C with a ramping rate of 10 °C min^{-1}. The sample was calcined for 8 h at 800 °C and then the temperature was decreased to room temperature with a cooling rate of 10 °C min^{-1}. The powder diffraction pattern collected after this calcination experiment is presented in Figure 46. As in the case of the high temperature treatment under He flow, there is a large increase in the diffraction signal corresponding to the SiO_2 quartz phase. In contrast to the experiment with the high temperature heat treatment under He flow though, there is still Na_2WO_4 and Mn_2O_3/Mn_7SiO_{12}. There is no $MnWO_4$ present in the catalyst after this calcination experiment further supporting the claim made previously that it is vital to have a source of O_2 in order to prevent the reduction of the Mn species at the high temperatures required for the OCM reaction.

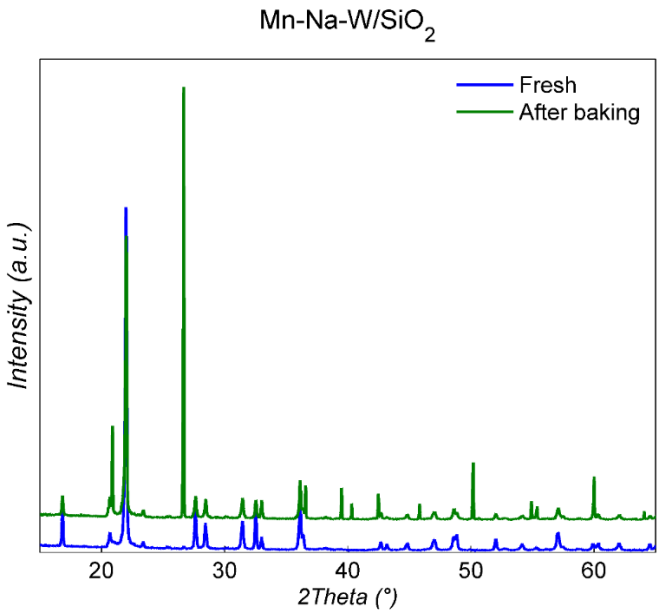

Figure 46: Powder diffraction pattern of the 2 % Mn-1.6 % Na-3.1 % W/SiO_2 catalyst after performing a second calcination step. Main quartz peak is at 2ϑ = 26.4-26.7 °.

A high temperature powder diffraction experiment under He flow was also performed with the 2 % La-2 % Mn-1.6 % Na-3.1 % W/SiO_2 catalyst. The results from these powder diffraction measurements are presented in Figure 47. As in the previous experiment with the unpromoted catalyst, at 600 °C, the lower symmetry orthorhombic Na_2WO_4 is present (apart from the cubic one) but upon reaching 700 °C there are no diffraction that can be attributed to any Na-W-O phases. This result was expected and is in agreement with the results obtained from the IXRD-CT data of the same catalyst presented previously (Figure 22). $NaLa(WO_4)_2$ is seen to be present at 700 °C and continues to grow in successive high temperatures. By the end of the experiment, the diffraction signal generated by the Na_2WO_4, Mn_2O_3/Mn_7SiO_{12} and $La_4Mn_5Si_4O_{22}$ phases has diminished. The only crystalline phase present containing the active components of the catalyst is the $NaLa(WO_4)_2$ phase. Additionally, in contrast to the 2 % Mn-1.6 % Na-3.1 % W/SiO_2 catalyst, the diffraction signal generated by the SiO_2 quartz phase does not significantly change during this experiment. This result further supports the claim made in the previous section that one of the roles of La in this catalyst is to stabilise and supress the solid-state evolution the SiO_2 support.

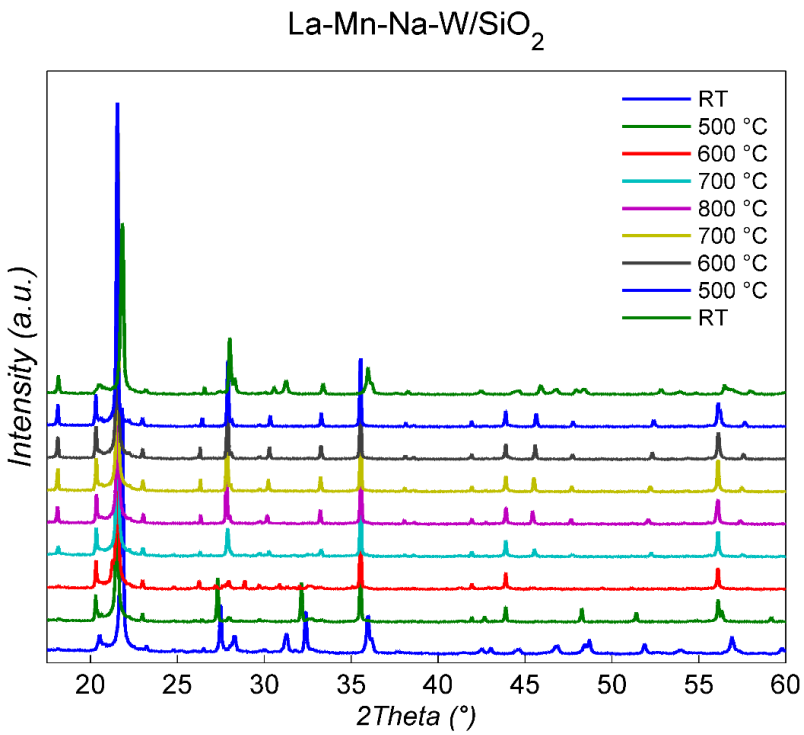

Figure 47 High temperature powder diffraction measurements of the 2 % La-2 % Mn-1.6 % Na-3.1 % W/SiO_2 catalyst collected under He flow.

The 2 % La-2 % Mn-1.6 % Na-3.1 % W/SiO_2 catalyst after the high temperature heat treatment under He flow was also examined *ex situ* with XRD-CT. The XRD-CT data were analysed by performing peak fitting of the reconstructed data following the same data processing strategy mentioned in a previous section (i.e. processing of the *operando* μ-XRD-CT data). The results from the peak fitting analysis are presented in Figure 48 where the phase distribution maps of each phase are shown. Apart from a hotspot corresponding to the SiO_2 quartz phase, it is clearly shown that the main crystalline SiO_2 phases are cristobalite and tridymite. Impressively, there is no indication of the Na_2WO_4, Mn_2O_3/Mn_7SiO_{12} and $La_4Mn_5Si_4O_{22}$ phases even in the XRD-CT data (spatially-resolved information - local diffraction signals).

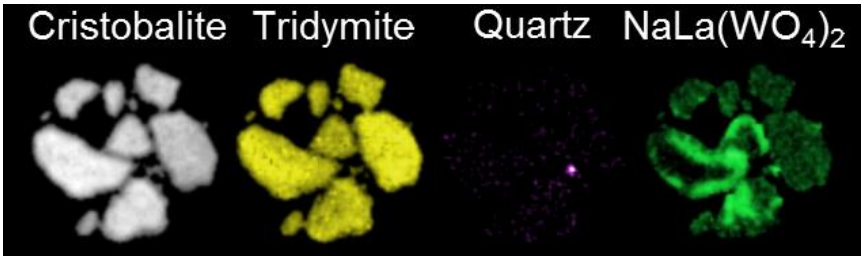

Figure 48: Phase distribution maps of the various crystalline phases present in the 2 % La-2 % Mn-1.6 % Na-3.1 % W/SiO_2 catalyst (i.e. after high temperature heat treatment under He flow).

A second calcination step was performed using also the 2 % La-2 % Mn-1.6 % Na-3.1 % W/SiO_2 catalyst. As in the case of the unpromoted catalyst, the sample was inserted in a furnace and the temperature was increased from room temperature to 800 °C with a ramping rate of 10 °C min^{-1}. The sample was calcined for 8 h at 800 °C and then the temperature was decreased to room temperature with a cooling rate of 10 °C min^{-1}. The sample was then characterised *ex situ* with XRD-CT. The XRD-CT data were analysed by performing Rietveld analysis of the reconstructed data following the same data processing strategy mentioned in a previous sections. The results from the Rietveld analysis are presented in Figure 49 where the phase distribution maps of each phase are shown. These maps represent the values of the scale factors of each crystalline phase. The results are very similar to the ones obtained after the high temperature treatment under He flow. More specifically, the Na_2WO_4, Mn_2O_3/Mn_7SiO_{12} and $La_4Mn_5Si_4O_{22}$ phases are absent in the catalyst after this second calcination step and only $NaLa(WO_4)_2$ is present. This is an important result as it proves that the $NaLa(WO_4)_2$ will form/ grow and eventually be the only

crystalline phase involving the active components of the catalyst regardless of the gases used. The result is the same in all cases: a) if the catalyst is calcination step is prolonged, b) if the catalyst is treated in an inert atmosphere at high temperatures (He), c) if the catalyst is exposed to OCM reaction mixtures (even very reducing environments).

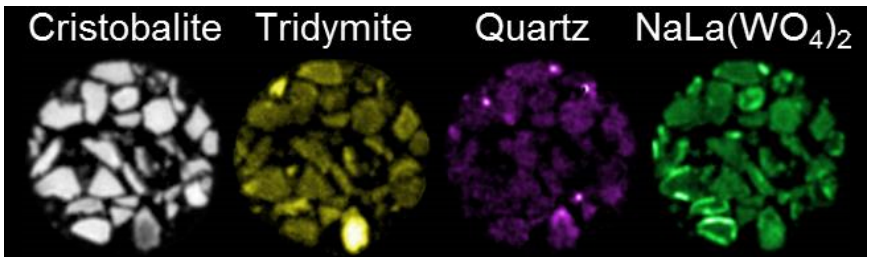

Figure 49: Phase distribution maps of the various crystalline phases present in the 2 % La-2 % Mn-1.6 % Na-3.1 % W/SiO_2 catalyst (after performing a second calcination step).

Conclusions

This is the first multi-length-scale chemical imaging study of unpromoted and La-promoted Mn-Na-W/SiO_2 catalysts under OCM reaction conditions. The catalysts were investigated from the reactor level (mm scale) down to the single catalyst particle level (µm scale) with different synchrotron X-ray based tomographic techniques (multi-modal CT experiments). The *operando* XRD-CT experiments revealed that both catalysts evolve at the high temperatures required for the OCM reaction but also showed that the chemical behaviour of these catalysts is significantly different. The unpromoted Mn-Na-W/SiO_2 catalyst is chemically unstable at high temperatures and there is loss of active components. The XRD-CT data suggested that there is loss of Na^+ from the catalyst particles as formation of cristobalite was observed at the SiO_2 capillary (reactor vessel). This claim was further supported by *ex situ* micro-CT and SEM/WDS measurements; the SEM/WDS measurements also suggested that there is loss of W containing species from the catalyst during the OCM experiment. The loss of active components is attributed to the Na_2WO_4 which melts before reaching the required high temperatures for the OCM reaction and the various Na and W containing species become not only mobile but also volatile. It was also shown that crystalline Mn_2O_3 / Mn_7SiO_{12} is not an essential component to yield an active OCM catalyst as under very reducing

environments the main crystalline phase was $MnWO_4$ and the mass spectrometry data showed that the catalyst was still active (no apparent deactivation). The La-promoted catalyst was shown to be chemically stable and it was shown that this is due to the formation and growth of a new crystalline which was identified as $NaLa(WO_4)_2$.

The *operando* multi-modal CT experiments proved that the results obtained from the XRD-CT experiments presented in the previous section are directly reproducible and also revealed new information regarding the parameters that affect the chemical evolution of both catalysts. It was shown that the behaviour of both catalysts strongly depends on the catalyst pre-treatment (i.e. thermal) and the OCM reaction mixture used. For example, the Mn_2O_3 / Mn_7SiO_{12} crystalline phases can remain stable/present under OCM reaction conditions for a longer period of time if the reaction mixture is not very rich in CH_4 (in very reducing environments the Mn species will be reduced from Mn^{3+} to Mn^{2+} and form the $MnWO_4$ phase). Additionally, the Na and W containing species can become also unstable in the La-promoted catalyst if the temperature of the system is increased rapidly as there is a certain time period needed to for the $NaLa(WO_4)_2$ to form and grow.

Supplementary high temperature PXRD experiments in an inert chemical environment (i.e. He) and *ex situ* PXRD and XRD-CT experiments showed that the formation/growth of the $NaLa(WO_4)_2$ phase is a temperature driven phenomenon. It is a result of thermal treatment of the catalyst and its formation does not depend on the chemical environment present (i.e. purely thermal phenomenon). It can be concluded that in order to have a chemically stable catalyst, it is essential to stabilize the Na^+ and WO_4^{2-} ions at the high temperatures required for the OCM reaction. The multi-length-scale chemical CT experiments presented in this Chapter showed that the La can play this role by trapping the mobile/volatile Na^+ and WO_4^{2-} species by forming this new crystalline phase ($NaLa(WO_4)_2$). The spatially-resolved signal obtained from the chemical CT experiments showed that the La is not only a structural promoter (formation of $NaLa(WO_4)_2$) but also a chemical one as it enhances the Mn interaction of Mn with the SiO_2 support ($La_4Mn_5Si_4O_{22}$ phase present) and the dispersion of the Mn species (homogeneous distribution of the

Mn_2O_3 / Mn_7SiO_{12} phases in the catalyst particles). Last but not least, the La is seen to stabilise the SiO_2 support too by suppressing its evolution at high temperatures. This is probably achieved indirectly by trapping the mobile Na^+ species which are responsible for the transformation of amorphous SiO_2 to various crystalline phases at these relatively low temperatures (ca. 800 °C).

References

1. Kerr, R.A., *Natural Gas From Shale Bursts Onto the Scene.* Science, 2010. **328**(5986): p. 1624-1626.
2. Anejionu, O.C.D., et al., *Contributions of gas flaring to a global air pollution hotspot: Spatial and temporal variations, impacts and alleviation.* Atmospheric Environment, 2015. **118**: p. 184-193.
3. Lunsford, J.H., *Catalytic conversion of methane to more useful chemicals and fuels: a challenge for the 21st century.* Catalysis Today, 2000. **63**(2–4): p. 165–174.
4. McFarland, E., *Unconventional Chemistry for Unconventional Natural Gas.* Science, 2012. **338**(6105): p. 340-342.
5. Tang, P., et al., *Methane activation: the past and future.* Energy & Environmental Science, 2014. **7**(8): p. 2580-2591.
6. Sousa-Aguiar, E.F., F.B. Noronha, and J.A. Faro, *The main catalytic challenges in GTL (gas-to-liquids) processes.* Catalysis Science & Technology, 2011. **1**(5): p. 698-713.
7. Lunsford, J.H., *The Catalytic Oxidative Coupling of Methane.* Angewandte Chemie International Edition in English, 1995. **34**(9): p. 970-980.
8. Zhu, Q., et al., *Sulfur as a selective 'soft' oxidant for catalytic methane conversion probed by experiment and theory.* Nature Chemistry, 2013. **5**(2): p. 104-109.
9. Guo, X., et al., *Direct, Nonoxidative Conversion of Methane to Ethylene, Aromatics, and Hydrogen.* Science, 2014. **344**(6184): p. 616-619.
10. Ruitenbeek, M. and B.M. Weckhuysen, *A Radical Twist to the Versatile Behavior of Iron in Selective Methane Activation.* Angewandte Chemie International Edition, 2014. **53**(42): p. 11137-11139.
11. Schwach, P., et al., *Methane Coupling over Magnesium Oxide: How Doping Can Work.* Angewandte Chemie International Edition, 2013. **52**(43): p. 11381-11384.
12. Godini, H.R., et al., *Techno-economic analysis of integrating the methane oxidative coupling and methane reforming processes.* Fuel Processing Technology, 2013. **106**: p. 684-694.
13. Khojasteh Salkuyeh, Y. and T.A. Adams, II, *A novel polygeneration process to co-produce ethylene and electricity from shale gas with zero CO2 emissions via methane oxidative coupling.* Energy Conversion and Management, 2015. **92**: p. 406-420.
14. Galadima, A. and O. Muraza, *Revisiting the oxidative coupling of methane to ethylene in the golden period of shale gas: A review.* Journal of Industrial and Engineering Chemistry, 2016. **37**: p. 1-13.
15. Karakaya, C. and R.J. Kee, *Progress in the direct catalytic conversion of methane to fuels and chemicals.* Progress in Energy and Combustion Science, 2016. **55**: p. 60-97.
16. Keller, G.E. and M.M. Bhasin, *Synthesis of Ethylene via Oxidative Coupling of Methane. I. Determination of Active Catalysts.* Journal of Catalysis, 1982. **73**(1): p. 9-19.

17. Alvarez-Galvan, M.C., et al., *Direct methane conversion routes to chemicals and fuels.* Catalysis Today, 2011. **171**(1): p. 15-23.
18. Takanabe, K., *Catalytic Conversion of Methane: Carbon Dioxide Reforming and Oxidative Coupling.* Journal of the Japan Petroleum Institute, 2012. **55**(1): p. 1-12.
19. Arndt, S., et al., *Mn–Na2WO4/SiO2 as catalyst for the oxidative coupling of methane. What is really known?* Applied Catalysis A: General, 2012. **425-426**: p. 53-61.
20. Sofranko, J.A., J.J. Leonard, and A.C. Jones, *The Oxidative Conversion of Methane to Higher Hydrocarbons.* Journal of Catalysis, 1987. **103**(2): p. 302-310.
21. Jones, C.A., J.J. Leonard, and J.A. Sofranko, *The Oxidative Conversion of Methane to Higher Hydrocarbons over Alkali-Promoted Mn/Si02.* Journal of Catalysis, 1987. **103**(2): p. 311-319.
22. Sofranko, J.A., et al., *Catalytic oxidative coupling of methane over sodium-promoted Mn/SiO2 and Mn/MgO.* Catalysis Today, 1988. **3**(2-3): p. 127-135.
23. Ji, S., et al., *Surface WO4 tetrahedron: The essence of the oxidative coupling of methane over M-W-Mn/SiO2 catalysts.* Journal of Catalysis, 2003. **220**(1): p. 47-56.
24. Malekzadeh, A., et al., *Structural features of Na2WO4–MOx/SiO2 catalysts in oxidative coupling of methane reaction.* Catalysis Communications, 2008. **9**(5): p. 960-965.
25. Mahmoodi, S., M.R. Ehsani, and S.M. Ghoreishi, *Effect of promoter in the oxidative coupling of methane over synthesized Mn/SiO2 nanocatalysts via incipient wetness impregnation.* Journal of Industrial and Engineering Chemistry, 2010. **16**(6): p. 923-928.
26. Hou, S., et al., *Site requirements for the oxidative coupling of methane on SiO 2-supported Mn catalysts.* Industrial and Engineering Chemistry Research, 2006. **45**(21): p. 7077-7083.
27. Yildiz, M., et al., *Support material variation for the MnxOy-Na 2WO4/SiO2 catalyst.* Catalysis Today, 2014. **228**: p. 5-14.
28. Yildiz, M., et al., *Enhanced catalytic performance of MnxOy-Na2WO4/SiO2 for the oxidative coupling of methane using an ordered mesoporous silica support.* Chemical Communications, 2014. **50**(92): p. 14440-14442.
29. Fang, X., et al., *Oxidative coupling of methane on W-Mn catalysts.* Journal of Molecular Catalysis (China), 1992. **6**: p. 427–433.
30. Fang, X.P., et al., *Preparation and characterization of W-Mn catalyst for oxidative coupling of methane.* Journal of Molecular Catalysis (China), 1992. **6**: p. 255–262.
31. Arndt, S., et al., *Mn-Na2WO4/SiO2 as catalyst for the oxidative coupling of methane. What is really known?* Applied Catalysis A: General, 2012. **425-426**: p. 53-61.
32. Wang, D., M.P. Rosynek, and J.H. Lunsford, *Oxidative Coupling of Methane over Oxide-Supported Sodium-Manganese Catalysts.* Journal of Catalysis, 1995. **155**(2): p. 290-402.
33. Jiang, Z.-C., et al., *Oxide/Support Interaction and Surface Reconstruction in the Na2WO4/SiO2 System.* The Journal of Physical Chemistry, 1993. **97**(49): p. 12870-12875.
34. Palermo, A., et al., *Critical influence of the amorphous silica-to-cristobalite phase transition on the performance of Mn/Na2WO4/SiO2 catalysts for the oxidative coupling of methane.* Journal of Catalysis, 1998. **177**: p. 259-266.
35. Pak, S. and J.H. Lunsford, *Thermal effects during the oxidative coupling of methane over Mn/Na2WO4/SiO2 and Mn/Na2WO4/MgO catalysts.* Applied Catalysis A: General, 1998. **168**: p. 131-137.

36. Pak, S., P. Qiu, and J.H. Lunsford, *Elementary reaction in the oxidative coupling of methane over Mn/Na2WO4/SiO2 and Mn/Na2WO4/MgO catalysts.* Journal of Catalysis, 1998. **179**: p. 222-230.
37. Lee, J.Y., et al., *Scaled-up production of C2 hydrocarbons by the oxidative coupling of methane over pelletized Na2WO4/Mn/SiO2 catalysts: Observing hot spots for the selective process.* Fuel, 2013. **106**: p. 851-857.
38. Kou, Y., et al., *Amorphous features of working catalysts: XAFS and XPS characterization of Mn/Ma2WO4/SiO2 as used for the oxidative coupling of methane.* Journal of Catalysis, 1998. **173**(2): p. 399-408.
39. Li, S., *Reaction Chemistry of W-Mn/SiO2 Catalyst for the Oxidative Coupling of Methane.* Journal of Natural Gas Chemistry, 2003. **12**(1): p. 1-9.
40. Lin, J., et al., *Stability test of W-Mn/SiO2 catalyst for oxidative coupling of methane.* Shiyou Huagong/Petrochemical Technology, 1995. **24**(5): p. 293-298.
41. Wang, J., et al., *Comparative study on oxidation of methane to ethane and ethylene over Na2WO4-Mn/SiO2 catalysts prepared by different methods.* Journal of Molecular Catalysis A: Chemical, 2006. **245**(1-2): p. 272-277.
42. Ahari, J.S., M.T. Sadeghi, and S. Zarrinpashne, *Effects of operating parameters on oxidative coupling of methane over Na-W-Mn/SiO2 catalyst at elevated pressures.* Journal of Natural Gas Chemistry, 2011. **20**(2): p. 204-213.
43. Dedov, A.G., et al., *Oxidative coupling of methane: Influence of the phase composition of silica-based catalysts.* Applied Catalysis A: General, 2011. **406**(1-2): p. 1-12.
44. Ismagilov, I.Z., et al., *Design of highly efficient catalyst for rational way of direct conversion of methane.* Eurasian Chemico-Technological Journal, 2015. **17**(2): p. 105-118.
45. Ismagilov, I.Z., et al., *Oxidative condensation of methane in the presence of modified MnNaW/SiO<inf>2</inf> catalysts.* Kinetics and Catalysis, 2015. **56**(4): p. 456-465.
46. Simon, U., et al., *Fluidized bed processing of sodium tungsten manganese catalysts for the oxidative coupling of methane.* Chemical Engineering Journal, 2011. **168**(3): p. 1352-1359.
47. Ghose, R., H.T. Hwang, and A. Varma, *Oxidative coupling of methane using catalysts synthesized by solution combustion method.* Applied Catalysis A: General, 2013. **452**: p. 147-154.
48. Ji, S.-f., et al., *The relationship between the structure and the performance of Na-W-Mn/SiO2 catalysts for the oxidative coupling of methane.* Applied Catalysis A: General, 2002. **225**(1-2): p. 271-284.
49. Wu, J., et al., *La-promoted Na2WO4/Mn/SiO2 catalysts for the oxidative conversion of methane simultaneously to ethylene and carbon monoxide.* Applied Catalysis A: General, 2007. **323**: p. 126-134.
50. Ghose, R., H.T. Hwang, and A. Varma, *Oxidative coupling of methane using catalysts synthesized by solution combustion method: Catalyst optimization and kinetic studies.* Applied Catalysis A: General, 2014. **472**: p. 39-46.
51. Vamvakeros, A., et al., *Removing multiple outliers and single-crystal artefacts from X-ray diffraction computed tomography data.* Journal of Applied Crystallography, 2015. **48**(6): p. 1943-1955.
52. van Aarle, W., et al., *The ASTRA Toolbox: A platform for advanced algorithm development in electron tomography.* Ultramicroscopy, 2015. **157**: p. 35-47.
53. Frolich, S. and H. Birkedal, *MultiRef: software platform for Rietveld refinement of multiple powder diffractograms from in situ, scanning or diffraction tomography experiments.* Journal of Applied Crystallography, 2015. **48**(6): p. 2019-2025.

54. Dreele, A.C.L.R.B.V., *General Structure Analysis System (GSAS)*. 2000: USA. p. 86-748.
55. Vamvakeros, A., et al., *Interlaced X-ray diffraction computed tomography.* Journal of Applied Crystallography, 2016. **49**(2): p. 485-496.
56. Cole, S.s., *THE CONVERSION OF QUARTZ INTO CRISTOBALITE BELOW 1000°C, AND SOME PROPERTIES OF THE CRISTOBALITE FORMED*.* Journal of the American Ceramic Society, 1935. **18**(1-12): p. 149-154.
57. Thompson, P., D.E. Cox, and J.B. Hastings, *Rietveld refinement of Debye-Scherrer synchrotron X-ray data from Al2O3.* Journal of Applied Crystallography, 1987. **20**(2): p. 79-83.
58. Yildiz, M., et al., *Silica material variation for the MnxOy-Na2WO4/SiO2.* Applied Catalysis A: General, 2016. **525**: p. 168-179.
59. Sadjadi, S., et al., *Feasibility study of the Mn-Na2WO4/SiO2 catalytic system for the oxidative coupling of methane in a fluidized-bed reactor.* Catalysis Science and Technology, 2015. **5**(2): p. 942-952.
60. Salehoun, V., et al., *Dynamics of Mn / Na2 WO4 / SiO2 catalyst in oxidative coupling of methane.* Chemical Engineering Science, 2008. **63**(20): p. 4910-4916.
61. Vamvakeros, A., et al., *Real time chemical imaging of a working catalytic membrane reactor during oxidative coupling of methane.* Chemical Communications, 2015. **51**(64): p. 12752-12755.
62. Venezia, A.M., et al., *Effect of alkali ions on the amorphous to crystalline phase transition of silica.* Journal of Solid State Chemistry, 2001. **161**(2): p. 373-378.
63. Holmquist, S.B., *Conversion of Quartz to Tridymite.* Journal of the American Ceramic Society, 1961. **44**(2): p. 82-86.
64. Shinohara, Y. and N. Kohyama, *Quantitative Analysis of Tridymite and Cristobalite Crystallized in Rice Husk Ash by Heating.* Industrial Health, 2004. **42**(2): p. 277-285.
65. Zhao, L., et al., *Crystallization of amorphous SiO2 microtubes catalyzed by lithium.* Advanced Functional Materials, 2007. **17**(12): p. 1952-1957.
66. Schindelin, J., et al., *The ImageJ ecosystem: An open platform for biomedical image analysis.* Molecular Reproduction and Development, 2015. **82**(7-8): p. 518-529.
67. Schindelin, J., et al., *Fiji: an open-source platform for biological-image analysis.* Nat Meth, 2012. **9**(7): p. 676-682.
68. Sommer, C., et al. *Ilastik: Interactive learning and segmentation toolkit*. in *2011 IEEE International Symposium on Biomedical Imaging: From Nano to Macro*. 2011.

CHAPTER 6: *Operando* studies of catalytic membrane reactors for the oxidative coupling of methane

Abstract

Catalytic membrane reactors have the potential to render the process of oxidative coupling of methane to produce ethylene economically viable. However, a number of questions regarding the true state of the active catalyst/membrane and their stability over time remain unanswered. Here, the results from the first XRD-CT studies of catalytic membrane reactors are reported. The first experiment was an *in situ* XRD-CT experiment of a Mn-Na-W/SiO_2 - $BaCo_xFe_yZr_zO_{3-\delta}$ (BCFZ) catalytic membrane reactor. This feasibility experiment showed that it is possible to spatially resolve the pertinent changes in the chemical/physical state within a working catalytic membrane reactor. Furthermore, the high operating temperature of the reactor led to a redistribution of WO_4^{2-} species over the catalyst (originating from Na_2WO_4) and onto the membrane leading to the formation and growth of a new phase, identified as $BaWO_4$, which is likely in the long term to be inhibitory to the stability and performance of the catalytic membrane reactor. As presented in this work, this feasibility experiment also revealed that there were three main challenges that had to be overcome: a) design of a new reactor cell allowing the use and control of two separate inlet gas streams, b) perform self-absorption correction of the XRD-CT data and c) solve the crystal structure of BCFZ and refine the BCFZ structure per point using Rietveld refinement (Rietveld analysis of the XRD-CT data). As it is shown here, we were able to not only overcome all these issues but also to perform *operando* XRD-CT experiments of the three different catalytic membrane reactors which allowed us to capture them in their active state and track their evolving solid-state chemistry. Part of this work has been published at the peer reviewed Chemical Communications journal: *Vamvakeros, A., Jacques, S. D. M., Middelkoop, V., Di*

Michiel, M., Egan, C. K., Ismagilov, I. Z., Vaughan, G. B. M., Gallucci, F., van Sint Annaland, M., Shearing, P. R., Cernik, R. J. & Beale, A. M. (2015). Chemical Communications 51, 12752-12755.

Introduction

Mixed Ionic and Electronic Conducting Membranes

There are two main types of oxygen separation systems based on dense ceramics membranes: pure oxygen ion conductors and mixed ionic and electronic conducting membranes. Pure oxygen ion conductors, the most well-known being yttria-stabilized zirconia (YSZ), show high thermal, mechanical and chemical stability under different conditions (e.g. high temperatures). However, they show low electronic conductivity and this is the reason why these materials have been mainly used as electrolytes in solid oxide fuel cells and in electrocatalytic reactors in general.[1, 2] Their main advantage is that the oxygen permeation flux can be adjusted by applying an external electrical current (Figure 1).

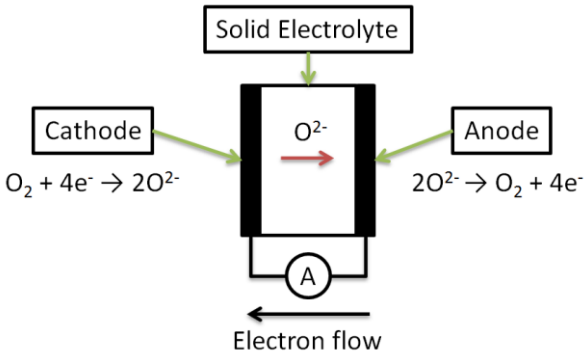

Figure 1: Solid electrolytes as pure oxygen ion conductors in electrocatalytic reactors

On the other hand, mixed ionic and electronic conducting membranes (MIECs) operate without the need for electrodes or an external circuit.[3] The driving force for their operation is the application of a chemical potential gradient (i.e. the presence of an oxygen pressure difference between the two sides of the membrane). The oxygen molecules are adsorbed at the MIEC surface and are reduced to oxygen ions. The oxygen ions permeate through the membrane from the high oxygen partial pressure side to the lower oxygen partial pressure side while a simultaneous counter flux of electrons maintains the charge neutrality of the system (Figure 2).[4]

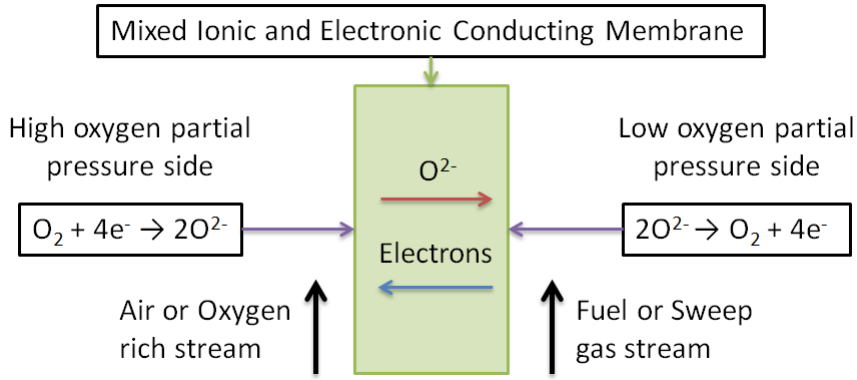

Figure 2: Mixed ionic and electronic conducting (MIECs) dense ceramic membranes for oxygen separation

The applications of MIEC membranes and catalytic membrane reactors for chemical and energy production are discussed thoroughly in two recent review papers by Dong *et al*. and Wei *et al*.[5, 6]

Perovskite-type Ceramics

Perovskite-type ceramics are of great interest as MIEC membrane materials due to their high performance (i.e. high values for oxygen permeation flux).[3] The ideal crystal structure of perovskite-type ceramics is cubic (typically space group 221: Pm-3m) with the formula of $ABO_{3-\delta}$. Large cations (i.e. alkali earth or rare earth metals) are placed in the A site (12-fold coordinated with the oxygen anions) while smaller ones (i.e. transition metals) are placed in the B site (6-fold coordinated).[7] An illustration of the ideal cubic crystal structure of perovskite-type ceramics is presented in Figure 3.

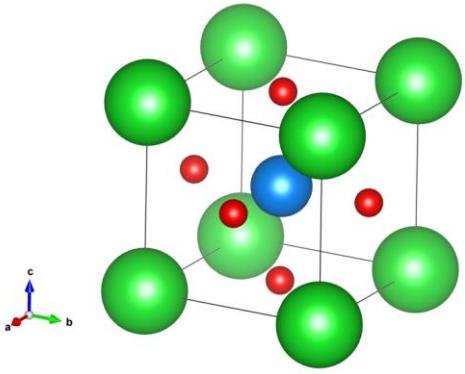

Figure 3: The ideal cubic structure of perovskite-type ceramics with the formula of ABO_3, where the red spheres represent the oxygen sites, the green spheres represent the A sites and the blue sphere represents the B site.

Goldschmidt and Norske suggested a "tolerance factor" (t) as a measure for the stability of the perovskite structure:[8]

$$Tolerance\ factor(t) = \frac{(r_A + r_O)}{\sqrt{2}(r_B + r_O)}$$

Where r_A, r_B and r_O are the ionic radii units of the cation at the A site, the cation at the B site and the oxygen respectively. It is generally accepted that the perovskite structure is preserved if the values of t are between 0.75 and 1.[3, 9] Perovskite-type ceramics can also possess crystal structures of lower symmetry like rhombohedral or orthorhombic crystal structures (t<1).[10]

The ionic conductivity of perovskite-type ceramics is a result of intrinsic defects in the crystal structure. These defects can be vacancies at lattice sites, impurities, ions displaced into interstitial sites or the presence of lattice ions in such a valence state that the total charge of A and B is not equal to +6.[10] In the latter case, the charge neutrality is maintained by the creation of oxygen vacancies which is indicated by the 3-δ oxygen nonstoichiometry. These oxygen vacancies are directly related to the oxygen ion conductivity and this is the reason why materials chemists try to create better materials by doping heterovalent cations into the perovskite crystal structure. However, there is always a trade-off between the oxygen nonstoichiometry and the stability of the perovskite structure.[3]

Teraoka *et al*. were the first to show that perovskite-type ceramics can be used as MIEC membranes for pure oxygen production.[11] The relationship between the oxygen permeability and the structure of the $La_{1-x}Sr_xCo_{1-y}Fe_yO_{3-\delta}$ (LSCF) was investigated. It was shown that the partial substitution of La^{3+} with Sr^{2+} (A site) led to higher values for oxygen permeation flux and this phenomenon was attributed to the creation of oxygen vacancies in the crystal structure. The partial substitution of Fe^{3+} with Co^{3+} also increased the oxygen permeation flux because the smaller ionic radius of Co^{3+} and bonding energy of Co^{3+} to oxide ions helps the oxygen diffusion through the crystal. However, the $SrCo_{2.5+\delta}$ showed low oxygen permeability and it was suggested that this happened because this phase did not possess a perovskite structure.

Since the pioneering work of Teraoka *et al.*, materials scientists have focused on synthesizing new perovskite-type ceramics by partially substituting different elements at the A and B sites of the unit cell in order to produce materials that have the desired properties. The goal is to create materials that show high values for oxygen permeation flux, are mechanically and chemically stable under different operating conditions (i.e. chemically stable in a wide range of temperatures and also under both reducing and oxidizing atmospheres). In a review paper by Sunarso *et al.*, the theory behind the transport mechanisms that take place in MIEC membranes, the different preparation methods and the currently available characterisation methods are presented in detail.[4] It is generally accepted that the large rare-earth or alkaline-earth cations at the A site of the perovskite structure are related to the ionic conductivity (i.e. by controlling the oxygen vacancies) whereas the transition metals at the B site are related to the electronic conductivity.[4, 12] The phase stability of the perovskite structure can be enhanced by substituting the A site with higher valent cations but the ionic conductivity will be decreased (i.e. due to reduced oxygen vacancies). Similarly, the electronic conductivity and therefore the oxygen permeation flux can be increased by substituting the B site with transition cations of lower ionic radius but this can lead to a decrease in phase stability. This means that there is always a trade-off between chemical stability and oxygen permeability for the perovskite-type membranes.

There are numerous synthesis methods for the perovskite-type ceramic powders including solid-state reaction, co-precipitation, the sol-gel method, spray drying and freeze drying, solid-state combustion and hydrothermal methods.[10] All these methods are described in detail in a review paper by Patel *et al*.[13] The main characterisation techniques for the perovskite ceramics are X-ray diffraction (XRD), electron microscopy (SEM/TEM) and thermogravimetric analysis (TGA). XRD is typically used to investigate the phase purity while SEM and TEM are used to study the morphology and the particle size of these materials. TGA is mainly used to obtain information about the oxygen nonstoichiometry (i.e. by measuring the weight loss at a specific temperature and/or oxygen partial pressure).

Die pressing, tape casting and extrusion processes have been the main techniques to produce the dense ceramic membranes from the ceramic powders.[10] Disk and tubular geometries have been used extensively in the past but during the last decade research has mainly focused on fabricating novel hollow-fibre membranes.[14-17] These hollow-fibre membranes are usually prepared by using a polymeric spinning technique based on phase inversion.[18] The performance of the perovskite-type membranes is in most cases examined by measuring the values of the oxygen permeation flux under different conditions. As previously discussed, a chemical potential gradient is applied between the two sides of the membrane (i.e. different oxygen partial pressures) and the oxygen permeation flux is calculated by analysing the products (i.e. the two outlet gas streams) with mass spectrometry or gas chromatography.

Dense Ceramic Membrane Reactors for the Oxidative Coupling of Methane

In practice, the MIEC membranes show considerable oxygen permeation only at relatively high temperatures. The activation of the methane molecule also requires high temperatures as the C-H bonds are strong (methane is the least reactive alkane).[10] This makes MIEC membranes promising materials for chemical reactions that involve the activation/transformation of methane. Most studies have focused on the application of these membranes for syngas production via the partial oxidation of methane but, as it will be discussed below, there are also a considerable number of publications regarding their application for the OCM reaction.

Otsuka *et al*. investigated the performance of a Ag-Bi_2O_3/YSZ/Ag electrocatalytic reactor for the OCM reaction.[19] It was shown that the electrochemically pumped oxygen through the yttria-stabilized zirconia to the Ag-Bi_2O_3 catalyst improved the catalytic activity and the selectivity to C_2 molecules. It was suggested that the catalytically active oxygen species must be different when electrochemically pumped oxygen is used instead of oxygen from the gas phase. Nagamoto *et al*. tested a similar electrocatalytic reactor with Ag as the catalyst/electrode using three different modes: pre-mixed oxygen methane gas mixture, oxygen fed electrochemically and a combination of the previous two.[20] The positive effect of the electrochemically pumped oxygen to the catalytic activity and selectivity to C_2 molecules was observed

again. The phenomenon of altering dramatically and reversibly the catalytic activity and selectivity by supplying or removing oxygen anions at the surface of the catalyst with an oxygen ion conductor (e.g. YSZ) is termed as non-Faradaic electrochemical modification of catalytic activity (NEMCA) or electrochemical promotion of catalysis (EPOC).[21, 22] It is called non-faradaic electrochemical modification of catalytic activity because the changes in the catalytic reaction rates exceed the oxygen ion transport rate to or from the catalyst surface by two to four orders of magnitude.[23] The relationship between the applied external electric current and its effect on the reaction rates has been investigated in several papers.[24, 25] For the interested reader, the theory behind the NEMCA effect is discussed in more detail in a recent review paper by Vayenas and Koutsodontis.[26]

As discussed previously, MIEC membranes provide an alternative way to transport oxygen ions without requiring the application of an external electrical current. A comparison between these two methods for the OCM reaction is discussed in a review paper by Liu *et al*.[27] Elshof *et al*. were the first to test perovskite membranes ($La_{0.6}Sr_{0.4}Co_{0.8}Fe_{0.2}O_3$ and $La_{0.8}Ba_{0.2}Co_{0.8}Fe_{0.2}O_3$) for the OCM reaction.[28] When permeated oxygen was used, the selectivity to C_2 molecules was significantly higher than in the mode whereby methane and oxygen were co-fed into the reactor. This result is in agreement with the previous studies where it was suggested that different active species are present in the two modes of operation.[19, 20] Segregation of Sr to the surface was observed and it was suggested that this might be responsible for the deactivation of the membranes (i.e. possible decomposition of the perovskite structure). This Sr segregation at the membrane surface and also the formation of a $SrCO_3$ phase were observed in a later study by Elshof *et al*.[29] The values of C_2 selectivity were high (67 %) at 1153 K (P_{CH4} = 93 kPa) but the conversion of methane was low (less than 3 %). Similar values for C_2 selectivity (approximately 50 %) were achieved in the work of Xu and Thomson.[30] It was suggested that the rate of the oxygen ion recombination to produce oxygen molecules was high and as a result the total oxidation of methane could not be prevented. It was shown that the OCM reaction rate and the selectivity for C_2 molecules can be increased by increasing the partial pressure of methane. However, the three LSCF materials lost their perovskite

structures at temperatures higher than 1023 K under reducing atmospheres (CH_4 and C_2H_6). These phase transformations, however, did not take place under reaction conditions. In another study by Xu and Thomson, high temperature XRD measurements revealed that the $La_{0.6}Sr_{0.4}Co_{0.2}Fe_{0.8}O_3$ maintains its perovskite structure at high temperatures (850 °C) in the presence of He, Ar and N_2 but phase transformations take place at 750 °C in a reducing atmosphere (i.e. methane).[31] However, no phase transformations occurred under OCM reaction conditions (850 °C) from either side of the LSCF membrane disk.

Zeng *et al*. investigated the performance of a $La_{0.8}Sr_{0.2}Co_{0.6}Fe_{0.4}O_3$ membrane disk as a catalyst for the OCM reaction.[32] New phases appeared at the membrane side exposed to He during the oxygen permeation experiment (O_2/N_2 flow from one side and He flow from the other side of the membrane). It was reported that the XRD patterns show that smaller *d*-spacing values are present in the membrane surface exposed to oxygen but this is not obvious from the data presented in the paper and the change in the lattice parameters is not given. Phase transformations occurred under OCM reaction conditions at the membrane surface exposed to methane, but the new phases were not identified. High C_2 selectivity (> 70 %) and C_2 yield (10-18 %) at temperatures higher than 850 °C were achieved when the He/CH_4 was high (40-90). However, these values decreased significantly when the He/CH_4 was lower than 20 and this was attributed to changes in the catalytic properties of LSCF when the oxygen partial pressure close to the membrane surface exposed to methane is low.

In their analysis of dense ceramic membrane reactors, Wang and Lin emphasized that in order to obtain high values for a C_2 yield it is necessary to use a membrane that is catalytically active for the OCM reaction *per se*.[33] It has to be noted though that high C_2 yield can only be achieved if the values of the oxygen permeation flux, the methane flow rate and the OCM reaction rate are similar, if not the same. Tan and Li investigated the performance of an asymmetric hollow-fibre $La_{0.6}Sr_{0.4}Co_{0.2}Fe_{0.8}O_3$ for the OCM reaction.[34] The main advantage of using this type of membrane structure and geometry is that the membrane surface per unit volume is higher than the disk and tubular membranes. Also, the sealing problems at high temperatures can be dealt with by keeping the two sealing ends away from the heating zone.

XRD analysis showed that the LSCF membrane maintained the perovskite structure after the OCM experiment. After four weeks of operation, no decrease in catalytic activity or mechanical performance was observed. Air was used at the outer side of the membrane (flow rate of 22.96 cm^3 min^{-1}) and a mixture of CH_4-Ar (i.e. 9.22 % CH_4 in Ar and flow rate of 17.2 cm^3 min^{-1}) at the inner side of the membrane. At 950 °C, the C_2 yield was 15.3 %, which is significantly higher than those reported from the previous studies where disk membranes were used. It was shown that the C_2 selectivity can be increased by increasing the methane flow rate. It was concluded that the oxygen concentration in the methane stream, the residence time of methane and the temperature are parameters that can directly affect the C_2 yield.

Hollow-Fibre Catalytic Membrane Reactors

In the past two decades, there has been a lot of attention and growing interest in the application of inorganic membranes in catalytic reactors. This new trend can be justified by the recent progress in producing novel inorganic materials with desired properties (e.g. operation under high temperatures, long-term stability and high values of membrane selectivity for the desired chemical, also known as permselectivity), new fabrication methods and membrane geometries and new membrane architectures (e.g. asymmetric membranes).[16, 17, 35-38]

As discussed in Chapter 5, during the OCM reaction, the selectivity for C_2 molecules is decreased with increasing oxygen concentration in the reaction gas mixture. Therefore, an alternative way to avoid a high oxygen concentration and increase the product yield in an OCM system is to use catalytic membrane reactors (instead of fixed bed reactors).[39] The incorporation of a dense hollow-fibre perovskite-type membrane in the catalytic reactor shows several advantages:[40]

- Maintaining the oxygen partial pressure (pO_2) low and homogeneously distributing the oxygen over the chemical reactor can lead to an increase in C_2 selectivity by preventing the total oxidation of methane. The uniform distribution of oxygen mitigates reaction rate and selectivity gradients along the reactor, both of which cannot be avoided in fixed bed reactors.[41]

- Process Intensification: The oxygen separation unit (i.e. separation of oxygen from air) is no longer needed which increases the energy efficiency and decreases the cost of the overall process. The established technologies for air separation and pure oxygen production can be divided into two main categories: cryogenic and non-cryogenic distillation. The cryogenic distillation is based on the liquefaction of air while non-cryogenic distillation involves the separation of air at ambient temperatures via pressure swing adsorption (PSA) by using molecular sieve adsorbents.[3] However, both of these methods are expensive and energy intensive.

- The formation of NO_x is avoided as the membrane is (permeation) selective only for oxygen.[41] The risk of having explosive mixtures is also reduced and higher productivity can be achieved compared to fixed bed reactors as the ratio of the reactants can be closer to stoichiometry.[42]

- The formation of hot spots (common problem in fixed bed reactors) can be mitigated due to the gradual feeding of oxygen along the reactor.[43]

Tan *et al*. investigated the performance of a catalytic membrane reactor using an $La_{0.6}Sr_{0.4}Co_{0.2}Fe_{0.8}O_3$ (LSCF) hollow-fibre membrane and a $SrTi_{0.9}Li_{0.1}O_3$ catalyst for the OCM reaction.[44] The catalyst was packed bed at the inner side of the membrane. Air was used at the outer side of the membrane (32.9 cm^3 min^{-1}) and a mixture of CH_4-He (i.e. 32.5 % CH_4 in He) at the inner side of the membrane (60 cm^3 min^{-1}). At 1248 K, the C_2 yield was 21 % for the catalytic membrane reactor and 15 % for the membrane reactor (i.e. without the catalyst). The activity was significantly improved with the addition of the catalyst but it has to be noted that the C_2 selectivity was higher for the LSCF membrane reactor and this phenomenon was not explained.

Czuprat *et al*. used a catalytic membrane reactor consisting of a $BaCo_{0.4}Fe_{0.4}Zr_{0.2}O_{3-\delta}$ (BCFZ) hollow-fibre membrane and a 2 wt. % Mn - 5 wt. % Na_2WO_4 / SiO_2 catalyst for the OCM reaction.[45] The catalyst was packed bed at the outer side of the membrane. Contact between the catalyst and the BCFZ membrane was prevented by inserting the BCFZ membrane into a porous alumina tube. XRD analysis showed that *α*-quartz, *α*-cristobalite and tridymite SiO_2 phases are present in the fresh catalyst. XRD analysis

of the catalyst after the OCM experiment showed that the Na_2WO_4 phase decreased and the quartz SiO_2 phase increased during the OCM experiment. The following conclusions were made:

- For a fixed flow rate, reducing the oxygen concentration gives increased values for C_2 selectivity but the CH_4 conversion is decreased.
- Decreasing the CH_4 residence time increases the values for C_2 selectivity but the CH_4 conversion is decreased.
- Diluting CH_4 with an inert gas improves the CH_4 conversion but the C_2 selectivity is decreased.

The maximum C_2 yield achieved in this study was reported to be 17 % (74 % C_2 selectivity) at 800 °C. The catalytic activity of the BCFZ hollow-fibre membranes (i.e. without the Mn-Na_2WO_4/SiO_2 catalyst) was not shown but it was mentioned that similar values for C_2 yield were achieved at 950 °C. These results are similar to those reported by Tan *et al*. with the $La_{0.6}Sr_{0.4}Co_{0.2}Fe_{0.8}O_3$ hollow-fibre membrane.[44] A high membrane area per reactor volume can be achieved when the hollow-fibre membranes are arranged in bundles. Further improvement of the performance of the catalyst and the membrane can make this reactor system economically viable for industrial applications.

Materials and Methods

Catalyst and Membrane preparation

The 2 wt. % La – 2 wt. % Mn – 1.6 wt. % Na – 3.1 wt. %W/SiO_2 and the 2 wt. % Mn – 1.6 wt. % Na – 3.1 wt. % W/SiO_2 catalysts were prepared by the sequential incipient wetness impregnation method. At first a SiO_2 support (commercial Silica gel Davisil 646) was impregnated by an aqueous solution of sodium tungstate dehydrate $Na_2WO_4{\cdot}2H_2O$ and sodium oxalate $Na_2C_2O_4$ taken in appropriate amounts. The Na-W/SiO_2 was dried at 120 °C for 6 h and was then impregnated by an aqueous solution of manganese (II) acetate tetrahydrate $Mn(CH3COO)_2{\cdot}4H_2O$ and lanthanum nitrate hexahydrate $La(NO_3)_3{\cdot}6H_2O$ salts, taken in appropriate concentrations. The catalysts were then dried at 120 °C for 6 h and calcined in air at 850 for 6 h with a heating rate

of 2 °C min^{-1}. The catalysts used in this study were kindly provided by the Boreskov Institute of Catalysis (BIC).

The ceramic powders used for the membrane production were fabricated by spray pyrolysis by CerPoTech AS (Trondheim, Norway). Aqueous solutions of the respective precursors were prepared and mixed in stoichiometric ratios, before the stable solution was sprayed into a furnace for each material. The as-prepared powders were calcined, ball milled in ethanol with YSZ grinding media and sieved, before a final heat treatment was executed to remove organic residues from powder processing. The $BaCo_{0.4}Fe_{0.4}Zr_{0.2}O_{3-\delta}$ (BCFZ) and $La_{0.6}Sr_{0.4}Co_{0.2}Fe_{0.8}O_{3-\delta}$ (LSCF) membranes reported here have been manufactured using the spinning and phase inversion methods.[16, 46] The starting polymer suspension was prepared from cellulose acetate (CA, Mr ~52000, Fluka), dimethylsulphoxide (DMSO, Synthesis grade, Merck) and de-ionised water that were used as a phase-inversion polymer, solvent and non-solvent additive to the polymer solution, respectively. The ceramic hollow-fibre membranes used in this study were kindly provided by the Flemish Institute for Technological Research (VITO).

In situ and *Operando* XRD-CT measurements at ID15, ESRF

The results from two separate beamtime experiments are presented in this study. The first beamtime experiment was an *in situ* study of a single CMR (i.e. BCFZ membrane with Mn-Na-W/SiO_2 catalyst) for the OCM reaction. The second beamtime experiment involved the investigation of three CMRs (see below for more details) under *operando* conditions.

In situ XRD-CT measurements

XRD-CT measurements were made at station ID15A of ESRF using a 93 keV monochromatic beam focused to have a spot size of 20 x 20 µm. The *in situ* XRD-CT experiment was performed with a Perkin Elmer XRD 1621 flat panel detector with a CsI conversion layer. The acquisition time per point was 100 ms. The tomographic measurements were made with 130 translation steps (translation step size of 20 µm) covering 0 – 180 ° angular range, in steps of 1.8 ° (i.e. 100 line scans). Reconstruction of these data yielded diffraction images with 130 x 130 pixels with 20 µm resolution.

Every 2D diffraction image was converted to a 1D powder diffraction pattern using MATLAB scripts and the final XRD-CT images (i.e. reconstructed data volume) were reconstructed using the filtered back projection algorithm.

Operando XRD-CT measurements

XRD-CT measurements were made at beamline station ID15A of the ESRF using a 92.8 keV monochromatic X-ray beam focused to have a spot size of 25 µm x 25 µm. 2D powder diffraction patterns were collected using a Pilatus3 X CdTe 300K (487 × 619 pixels, pixel size of 172 µm) hybrid photon counting area detector which uses Cadmium Telluride (CdTe) as the semiconducting direct conversion layer. The acquisition time per point was 50 ms. The tomographic measurements were made with 140 translation steps (translation step size of 25 µm) covering 0 – 180 ° angular range, in steps of 1.8 ° (i.e. 100 line scans). The detector calibration was performed using a CeO_2 NIST standard. Every 2D diffraction image was converted to a 1D powder diffraction pattern after applying an appropriate filter (i.e. 10 % trimmed mean filter) to remove outliers using in-house developed MATLAB scripts.[47] The final XRD-CT images (i.e. reconstructed data volume) were reconstructed using the filtered back projection algorithm.

Reactor Cells

Three types of catalytic membrane reactors suitable for the oxidative coupling of methane were prepared from hollow-fibre membranes (ca. 2.4 mm Ø and 180 µm wall thickness) packed with a catalyst supported between glass wool. More specifically, the following CMRs were tested: 1) BCFZ membrane with Mn-Na-W/SiO_2 catalyst, 2) BCFZ membrane with La-Mn-Na-W/SiO_2 catalyst and 3) LSCF membrane with La-Mn-Na-W/SiO_2 catalyst. In every experiment, the catalytic membrane reactor was glued on top of an alumina rod. For the *operando* XRD-CT experiments, the reactor cell (i.e. the CMR and the alumina rod) was inserted inside a quartz glass tube and a four-way Swagelok piece was used to allow the use of two different gas streams (see Figure 4). Air was used at the outer side of the membrane and a mixture of CH_4 diluted in He at the inner side of the membrane.

In each experiment, the reactor was mounted into a gas delivery stub, itself mounted to a standard goniometer (to enable alignment). The goniometer was fixed to a rotation stage set upon a translation stage to facilitate the movements required for the CT measurement. Heating was achieved by virtue of two hot air blowers heating each side of the catalytic membrane reactor. During the *operando* XRD-CT measurements, the outflow gasses were monitored by mass spectrometry using an Ecosys portable mass spectrometer. The mass spec line was inserted inside the membrane from the top. The experimental setup is shown in Figure 4.

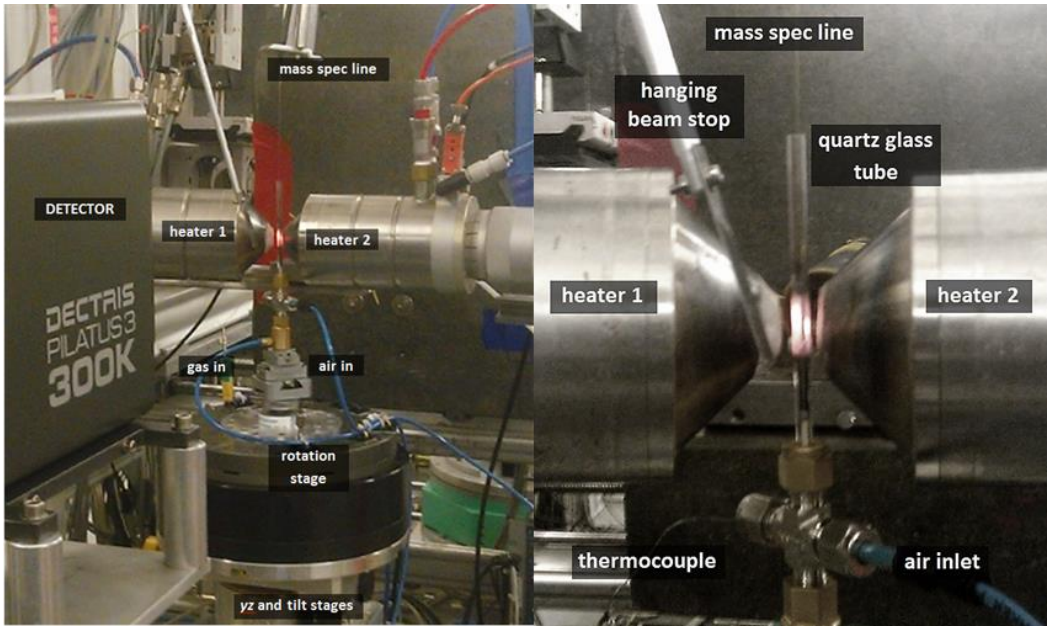

Figure 4 Photographs of the experimental setup used for the operando XRD-CT experiments at the beamline ID15 of the ESRF.

Rietveld analysis of the XRD-CT data

Quantitative Rietveld refinement was performed using the reconstructed diffraction patterns using the TOPAS software, on a voxel by voxel basis.[48] It should be noted that the TOPAS software proved to be a lot more robust compared to the Multiref/GSAS used to process the XRD-CT data presented in Chapter 5. The results from the Rietveld analysis of the XRD-CT data were imported into MALTAB in order to create the figures presented in this chapter (e.g. phase distribution maps based on the scale factors, unit cell parameters maps, etc.).[49] The Rietveld analysis of the XRD-CT data was mainly based on the intensity of the scale factors (unless stated otherwise) and should be treated as a semi-quantitative analysis. In order to have a good starting model, quantitative Rietveld analysis of the summed diffraction pattern

of all XRD-CT datasets was performed prior to the Rietveld analysis of the XRD-CT data.

Ex situ X-ray micro-CT and and SEM/WDS measurements

The μ-absorption-CT (micro-CT) measurements were performed at beamline station ID15 of the ESRF using a 92.8 keV monochromatic X-ray beam. Radiographs were recorded with an X-ray imaging camera (CCD) and the pixel resolution was 5.8 μm. Each micro-CT scan consisted of 900 projections (radiographs) covering an angular range of 0-180 ° (i.e. angular step size of 0.2 °). Flat-field and dark current images were also collected prior to the micro-CT measurements and were used to normalize the acquired radiographs before the tomographic reconstruction. The tomographic data were reconstructed using the filtered back projection algorithm.

The spent CMRs after the *operando* XRD-CT experiments were sent to the Flemish Institute for Technological Research (VITO) for SEM/WDS characterisation. SEM micrographs and elemental mapping data were collected, post experiment, for locations of interest at the catalyst-membrane interface on a JEOL JXA8530F in-lens Schottky FEG-EPMA instrument (Field Emission Gun Electron Probe Micro-Analyser) operated at an accelerating voltage of 15 keV with a probe current of 50 nA and equipped with five vertical crystal WDS (wavelength-dispersive spectrometer) detectors.

Results & Discussion

In situ XRD-CT measurements of a CMR during OCM

As mentioned previously, the first XRD-CT experiment was an *in situ* study of a BCFZ (membrane) – Mn-Na-W/SiO_2 (catalyst) CMR. This experiment should be treated as a feasibility study since it was the first attempt to study these integrated reactor systems *in situ*. It should also be noted that high energy X-rays are a prerequisite in order to investigate such CMR systems. This is due to the presence of the dense ceramic membrane (BCFZ and LSCF membranes were used in these experiments). The experiments reported in this chapter were performed using a ca. 93 keV monochromatic X-ray beam and as a result it was possible for the X-rays to penetrate the CMRs and collect useful diffraction patterns.

A schematic representation of the CMR is shown at the top left of Figure 5; this illustration was actually produced from μ-absorption-CT (micro-CT) data collected during the second beamtime experiment (see respective section for more details). At the bottom right of Figure 5, reconstructed XRD-CT images of raw scattering intensity at the scattering angle ca. 1.75° 2θ (ca. Q = 1.45 Å^{-1}) are presented. These show the growth of the SiO_2 tridymite phase during the operation of the CMR but mainly serve to illustrate that the evolving solid-state chemistry taking place in a CMR can be followed.

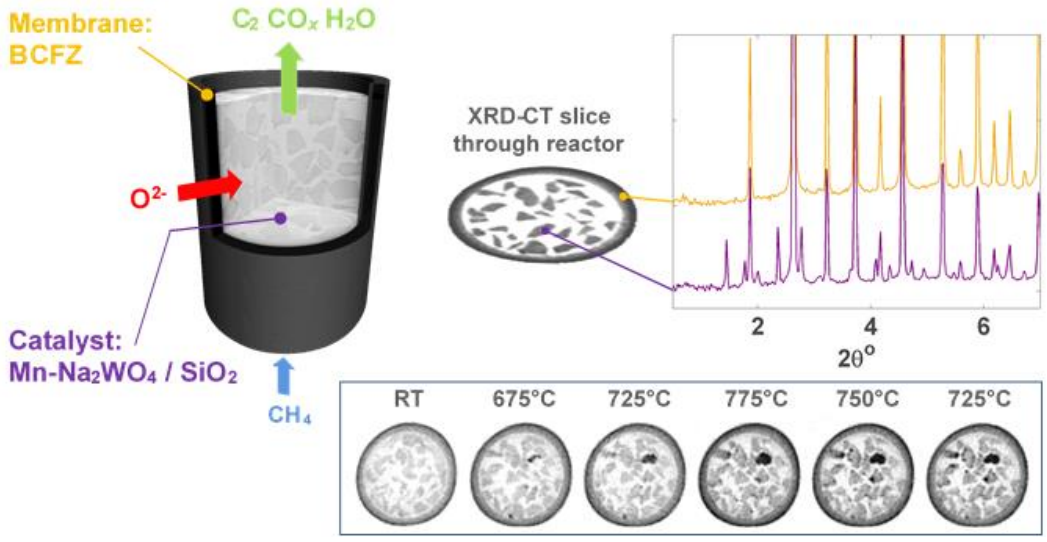

Figure 5: Left: Image showing the CMR. Top right: Within an XRD-CT image each pixel has a corresponding diffraction pattern; the graph inset top right shows two selected diffraction patterns: one from the membrane (yellow trace) and one from the catalyst region (purple trace). Bottom right: Maps of raw scattering intensity at scattering angle ca. 1.75° 2θ (ca. Q = 1.45 Å^{-1}) corresponding to the tridymite phase. Images are displayed with a common intensity scaling.

Each XRD-CT reconstructed slice is actually a data cube where each composing voxel (a three dimensional pixel) contains a reconstructed diffraction pattern. It should be the case that the diffraction observed within each voxel originates only from that part of the sample. Here though, it is important to point out that with these data contain an artefact because an adequate absorption correction was not included in the tomographic reconstruction algorithm. This artefact is apparent in the purple diffraction pattern presented in Figure 5 (top right). This diffraction pattern is from a selected position within the catalyst yet contains some strong peaks which are clearly seen to match the position of the membrane peaks visible in the yellow diffraction pattern. Nevertheless, using knowledge of the BCFZ membrane from post analysis

we are able to know the real bounds of the membrane and the artefact signal can be masked out.

The temperature of the system was increased under the flow of 5 % CH_4/He (volumetric flow rate of 100 ml min^{-1}) and this inlet gas mixture was kept for the duration of the OCM experiment (through the catalyst bed from the inner side of the BCFZ membrane). Figure 6 shows the evolution of the catalyst as the OCM experiment proceeds, presented as phase maps, showing the distributions of five identified crystalline phases and one amorphous phase at all temperatures where XRD-CT data are measured.

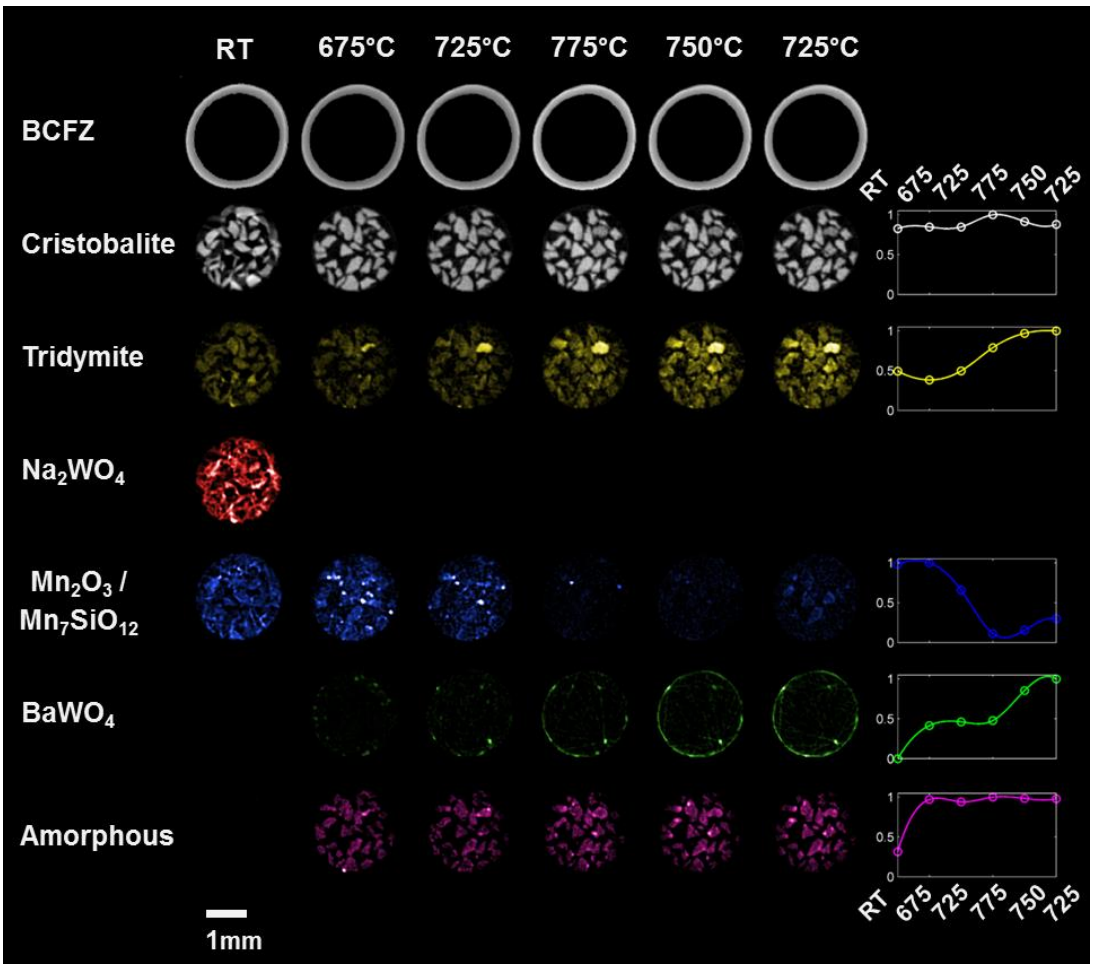

Figure 6: Phase maps for BCFZ, cristobalite and tridymite (crystalline SiO_2 polymorphs), Na_2WO_4, Mn_2O_3/Mn_7SiO_{12}, Ba_2WO_4 and an amorphous phase as determined from the XRD-CT data. These maps have been obtained from the integrated intensities of the respective phases. The graphs show the relative change in each component (normalized to the maximum value (ordinate) vs. temperature in °C (abscissa)), as determined from the integrated intensities.

At room temperature, as expected, both the Mn_2O_3/Mn_7SiO_{12} and Na_2WO_4 phases are present in the catalyst particles. The SiO_2 support is clearly visible principally as

cristobalite-low and secondarily in tridymite-low form. More importantly, the distributions of Mn_2O_3/Mn_7SiO_{12} and Na_2WO_4 show that they are not perfectly co-located. At 675 °C, the Na_2WO_4 phase disappears which is in agreement with the work of Hou *et al*.[15] An amorphous phase (increase of background intensity in the diffraction patterns) appears which is to be expected as the Bragg diffraction signal from one component of the catalyst, i.e. Na_2WO_4, disappears completely. Importantly, a new phase is seen to appear which was identified as $BaWO_4$ (using the ICSD and the ICCD PDF crystallographic databases). Figure 7 shows a selected diffraction pattern at the membrane catalyst interface from the XRD-CT data collected at 725 °C where the entire diffraction pattern can be described by the identified phases $BaWO_4$, cristobalite-high (catalyst support), Mn_2O_3/Mn_7SiO_{12}, tridymite-high (catalyst support) and BCFZ (membrane material). These data were then fitted to obtain semi-quantitative data, thus phase maps showing distributions in space and time can be made. The phase maps were presented in Figure 6. The phase identification process using the ICSD database and the PDF-2013 database showed the same results (i.e. $BaWO_4$ was identified as the new phase that forms during the OCM experiments).

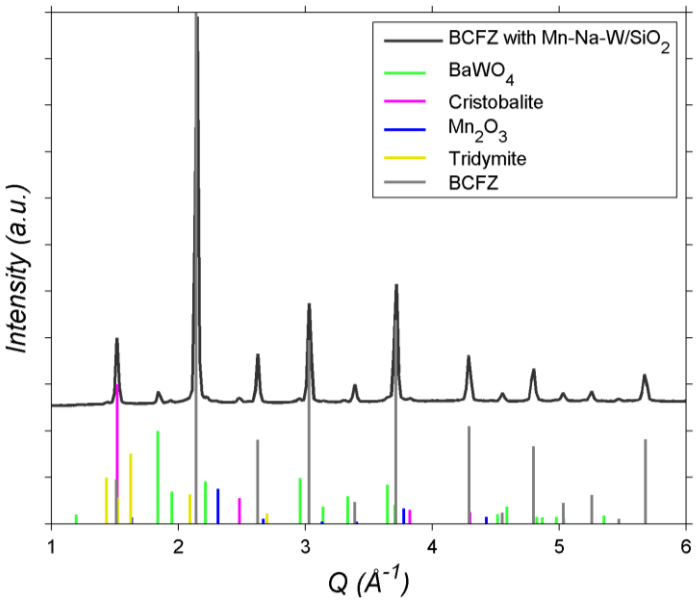

Figure 7: Phase identification of a summed diffraction pattern from pixels of interest (i.e. after applying a mask and taking into account only the pixels where the new $BaWO_4$ phase appears) at 725°C. $BaWO_4$ (01-072-0746), cristobalite-high (01-076-0931), tridymite-high (01-073-0403) and Mn_2O_3 (01-076-0150) were identified using the PDF-2013 database. BCFZ is also shown although the crystal structure of BCFZ is not available in any crystallographic database.

The distribution of the $BaWO_4$ phase does not match the starting distributions of Na_2WO_4 but instead concentrated spots of this phase are forming during the experiment. At 725 °C, Mn_2O_3/Mn_7SiO_{12} decreases but significant amounts of $BaWO_4$ have grown which appears to be migrating towards the inner membrane wall. On reaching 775 °C, Mn_2O_3/Mn_7SiO_{12} is barely detectable yet more $BaWO_4$ forms, lining almost the entirety of the inner membrane wall. We note, Mn-$BaWO_4/SiO_2$ has been tested in the past as an OCM catalyst and it shows a higher selectivity to CO_x than to C_2 molecules.[16] On reducing the temperature to 725 °C, Mn_2O_3/Mn_7SiO_{12} is seen to partially reform. Against the back drop of these changes, the support is seen to also evolve with continuous growth of tridymite (more than doubling in quantity) and less significant initial growth then loss/conversion of cristobalite from tetragonal to cubic forms which is also in agreement with the work of Hou *et al*. (i.e. low-high transition).[15] Also shown is the BCFZ membrane (derived from a map of the intensity of the (100) BCFZ reflection) though its distribution does not change during the course of the experiment; there are however some relative changes observed in the reflection intensities for BCFZ. The intensity distribution maps of the first four peaks of BCFZ from the OCM experiment are presented in Figure 8. These peaks correspond to the (100), (110), (111) and (200) BCFZ reflections respectively.

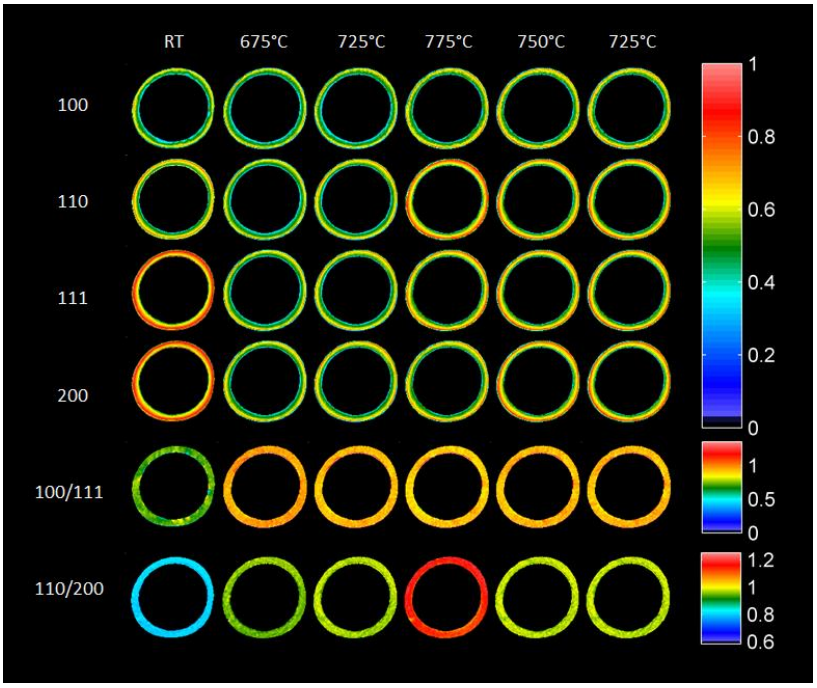

Figure 8: BCFZ normalized intensities for the (100), (110), (111) and (200) BCFZ reflections and reflection intensity ratios (100) / (111) and (110) / (200).

It can be seen that no significant changes in these intensity maps take place during the experiment. However, there is a change for the maps that are generated from the intensity ratio of the (110) over the (200) reflection. Unfortunately, the crystal structure of BCFZ was not available in any crystallographic database and as such it was not possible to refine a BCFZ structure model using the XRD-CT data and rationalize these relative changes in peak intensity (e.g. changes in thermal parameters and/or oxygen occupancy).

The results obtained from the *in situ* study of the BCFZ – Mn-Na-W/SiO_2 CMR showed that XRD-CT can become an invaluable tool to characterise such complex reactor systems under operating conditions and can also be used to track the evolving solid-state chemistry taking place in each reactor component (membrane and catalyst). However, it was also shown that XRD-CT experiments involving CMRs are more challenging compared to fixed bed reactors and after the analysis of the XRD-CT data it was realised that the following issues had to be addressed:

(1) Design of new reactor cell for XRD-CT measurements involving CMRs: For the *operando* CMR XRD-CT experiments, a new reactor cell was designed which serves the following purposes:
    a. Enables controlling gas delivery to the inner side of the follow-fibre membrane.
    b. Enables controlling the gas delivery to the outer of the hollow-fibre; such that air flow can be controlled or inert gasses, such as He, can be imposed.
    c. Enables temperature measurement of the hollow-fibre membrane with a thermocouple (T_c) during the experiment.
    d. Allows for CT alignment by virtue of a goniometer placed below the reactor cell.
    e. Enables CT measurements – not via continuous rotation but oscillation. It is a robust design as it can oscillate many times over many hours of operation.

f. The hollow-fibre membrane can be sealed outside the heating zone and this removes necessity for high temperature glues which would impose a significant additional technical hurdle.
g. This reactor cell also allows for mass spectrometry measurements during the CT measurements.
h. It should also be noted that the heat guns are tied to the y motor above the z stage which enable continuous uniform temperature and allows the CMR to be sampled reliably in z without inducing temperature distortions.

(2) Self-absorption correction of the CMR XRD-CT data: This issue was discussed previously but the BCFZ XRD-CT images presented in Figure 8 also show that there is a gradual loss of intensity from the outer to the inner side of the membrane. In order to correct this absorption artefact, micro-CT data of the various CMRs were also collected. The self-absorption correction strategy used in this study is discussed thoroughly in the next section.

(3) Crystal structure solution of BCFZ: As mentioned previously, changes in the relative intensities of the BCFZ diffraction peaks were observed during the *in situ* XRD-CT experiment of the CMR. In order to rationalise such changes, it is necessary to have a good starting structure model for the BCFZ phase. This was made possible by proposing a crystal structure solution for BCFZ using high resolution neutron powder diffraction data collected at the ISIS neutron source.

Self-absorption correction of XRD-CT data

The strategy followed to perform the self-absorption correction, also known as attenuation correction, of the XRD-CT data collected during the *operando* CMR experiments is discussed in this section. As in the work of Kleuker *et al.*, the attenuation correction was performed using micro-CT data (*ex situ* measurements of the three CMRs acquired at ambient conditions).[50] However, it should be clarified here that there are three distinct methods which can be implemented to perform the self-absorption correction of XRD-CT data using micro-CT data. These methods are the following (ordered with increasing calculation complexity):

(1) Zero order approximation: The same absorption correction is applied to all XRD-CT sinograms (sinogram data volume of an XRD-CT dataset) using the absorption sinogram (micro-CT data). This means this method does not take into account the scattering angles (i.e. same correction for all 2θ/*d*/*Q* values).
(2) First order approximation: The absorption correction varies as a function of 2θ with every XRD-CT sinogram. This means that the absorption correction is different for every 2θ angle and is obtained by ray-tracing by averaging over all the voxels along a given incident ray. As a result, this type of absorption correction is scattering angle dependant but it is also an approximation to the tomographic plane.
(3) Second order approximation: The absorption correction is applied to the raw 2D diffraction images and requires a micro-CT volume of the sample. This method was not explored in this study as it is beyond the scope of this work but it is not expected to significantly alter the data compared to the first order approximation.

In this study, the zero order approximation was used to perform the absorption correction for all the XRD-CT datasets acquired during the *operando* experiments of the CMRs. However, it should be emphasized that MATLAB code was also developed for the first order approximation (see Appendix). This code was tested and compared with the zero order approximation method yielding the same results. This is explained by the fact that the CMR XRD-CT measurements were performed using very hard X-rays (i.e. a 92.8 keV monochromatic X-ray beam) leading to a shift of the diffraction peaks to very small 2θ values. For example, in this study the maximum 2θ value used was ca. 10° 2θ. However, it should be noted that the zero order approximation should be avoided when the XRD-CT data are collected at relatively low energies, as the 2θ values can be relatively large (e.g. >30° 2θ) making this approximation invalid.

Before explaining how the zero order approximation absorption correction strategy was used in this study, there is another issue that should be discussed. The CMR micro-CT data contained an artefact that had to be removed before using them for the absorption correction of the XRD-CT data. This artefact can be easily observed in

the micro-CT image shown in Figure 9 (as indicated by the red arrow) where it can be seen that there is a high intensity "ring" present at the inner side of the BCFZ membrane. This reconstruction artefact is a result of the radical difference in density between the Ba-based BCFZ ceramic membrane and the air and SiO_2 supported catalysts present at the inner side of the membrane.

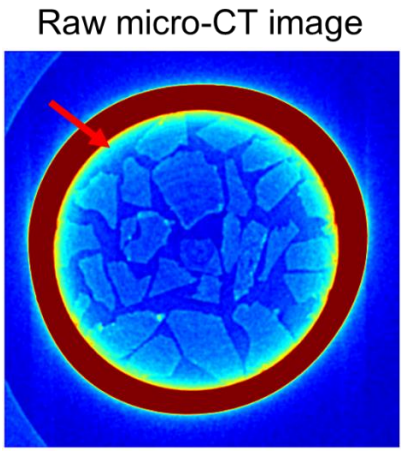

Figure 9: Reconstructed image of interest from the BCFZ – Mn-Na-W/SiO_2 CMR micro-CT data. This image is an attenuation coefficient (μ) map where the blue colour corresponds to low values and the red colour to high values. The BCFZ membrane is a heavily absorbing material especially when compared to the rest of the sample volume probed and as a result a high intensity "ring" artefact is generated (as indicated by the red arrow).

The reason why, in this case, the raw micro-CT data should not be used for the absorption correction of the XRD-CT can be easily understood if one realises how the absorption correction process influences the XRD-CT data. If I_m is the measured intensity of the (radially integrated) diffraction data and A is the absorption, then the absorption corrected diffraction data (I_{xrd}) are derived from the following simple equation:

$$I_{xrd} = \frac{I_m}{A} = \frac{I_m}{\frac{I_t}{I_o}} = \frac{I_m}{\iiint e^{-\mu(x,y,z)\,dx\,dy\,dz}}$$

Where I_o is the intensity of the incident X-rays, I_t is the intensity of the transmitted X-rays through the sample and μ is the attenuation coefficient (Beer-Lambert law). Since the values of the I_t/I_o ratio can be in the 0 – 1 range, it can be easily understood that the absorption correction process leads to XRD-CT data with higher intensity values. This means that after the absorption correction is performed, the diffraction signal generated by the heavily absorbing materials present in the sample will be

increased more compared to the diffraction signal generated by the other materials present in the sample. In the system under study, the absorption correction leads to a substantial increase in the intensity of the BCFZ diffraction peaks (BCFZ is both the most absorbing and best scattering material present in the CMR). As it can be easily understood, if the raw uncorrected micro-CT data are used for the absorption correction of the XRD-CT, then the intensity would increase in the regions where the "ring" artefact is present, leading to wrong results. Unfortunately, to the author's knowledge, there is no global solution to remove such micro-CT artefacts. The strategy chosen, which efficiently removed this artefact without distorting the micro-CT images is illustrated in Figure 10.

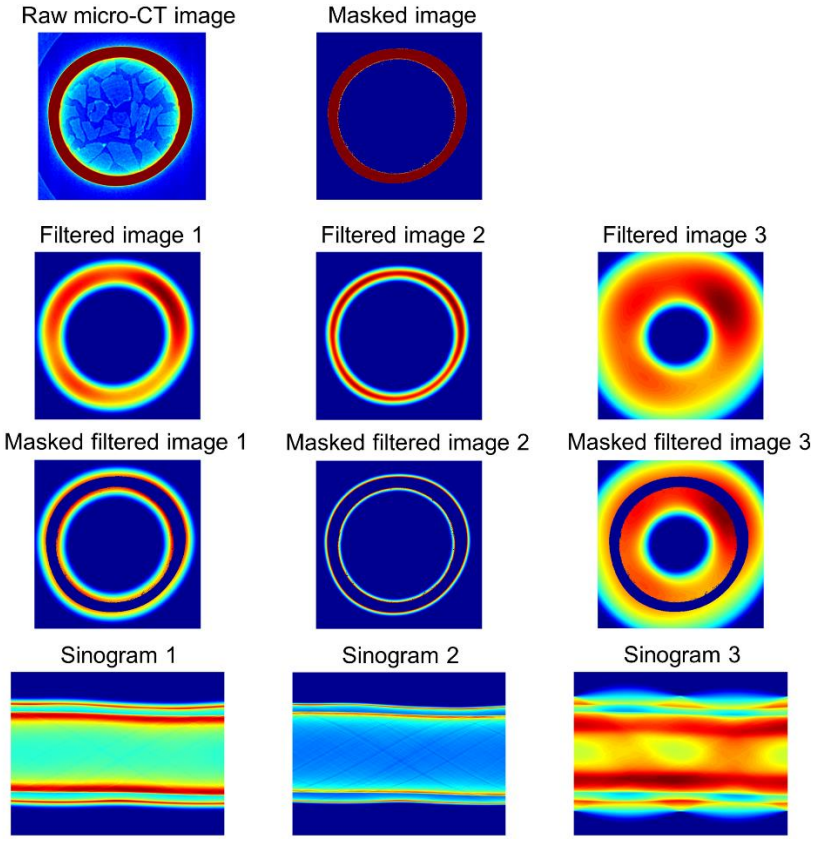

Figure 10: First row: Raw reconstructed micro-CT image and the corresponding masked one maintaining only the membrane. Second row: Three filtered images generated by blurring the masked image. Third row: The three filtered images multiplied by the inverse mask. Fourth row: Sinograms generated by the three masked filtered images.

First, the micro-CT data were segmented by thresholding and everything was masked out apart from the membrane. This was a trivial step due to the heavily absorbing nature of BCFZ compared to the other materials present in the CMR. Then three different images were obtained by blurring (using the *imfilter* function in MATLAB)

these masked images (second row in Figure 10).[49] As it is implied, this step needs to be done manually and the application of the blurring filters depend on the user's choice (no global solution). The filtered images were then multiplied by the inverse mask created during the first step and then these masked filtered images were forward projected (radon transform) yielding three sinograms. Finally, the three sinograms were subtracted from the raw micro-CT sinogram and the artefact-free image was obtained upon reconstruction. For comparison reasons, both the raw and the new, artefact-free reconstructed micro-CT image are presented in Figure 11 using the same colour axis. It can be also observed that the size of the membrane was not altered after the correction. This strategy was followed for all CMR micro-CT data.

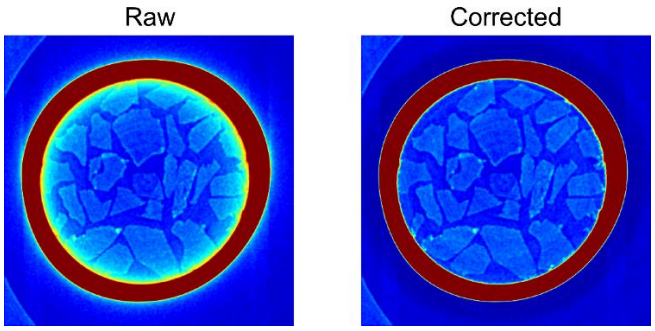

Figure 11: Left: Raw reconstructed micro-CT image, Right: Reconstructed artefact-free micro-CT image. The same colour axis is used for both images.

The next step involves finding the artefact-free micro-CT image that corresponds to the XRD-CT which is then cropped and aligned to the XRD-CT images (MATLAB scripts are provided in the Appendix). The micro-CT image is then forward projected in order to create the desired sinogram. The XRD-CT sinogram data volume is then divided by this micro-CT sinogram and then the XRD-CT absorption corrected images are reconstructed using a reconstruction algorithm (filtered back projection was used in this study).

Regarding the CMR XRD-CT data, the absorption correction mainly influences, as expected, the diffraction patterns generated by the BCFZ phase. This is clearly shown in Figure 12 where two BCFZ XRD-CT images before (left) and after (right) the absorption correction are presented. These XRD-CT images correspond to the highest intensity diffraction peak of BCFZ (reflection (011)). In order to compare them, each BCFZ image was first normalised with respect to its maximum value. As mentioned

previously, the uncorrected XRD-CT data yield reconstructed images where the shape and size of the BCFZ membrane is not well-defined (left in Figure 12). On the other hand, it can be clearly seen that the absorption corrected XRD-CT data lead to images where the intensity of the BCFZ map is homogeneous and the membrane has well-defined boundaries. It was therefore considered wise to follow this absorption correction strategy for all collected CMR XRD-CT data (*operando* experiments).

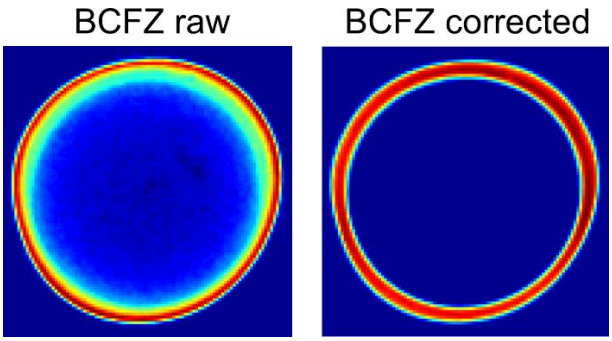

Figure 12: XRD-CT images corresponding to the highest intensity peak of BCFZ (reflection (011)) before (left) and after (right) the absorption correction.

It should be finally mentioned that MATLAB code was also developed for the first order approximation method. This code is not optimized and as a result is computationally expensive but it is a first step towards the design of new algorithms for the absorption correction of XRD-CT data. Unfortunately, there is a lack of such algorithms in literature and even in cases where it is mentioned that self-absorption correction of scattering/spectroscopic-CT data has been performed (typically in XRF-CT studies), the actual code is only described and not provided in the papers. It should be emphasized that the development of new, fast and robust algorithms for the absorption correction of XRD-CT data is not just a necessity but also crucial to the future of X-ray scattering/spectroscopic CT techniques in general.

In the simple code developed in this study, ray tracing was avoided and a simpler approach was chosen to calculate the attenuation along the X-ray beam paths. A schematic illustration is provided in Figure 13. On the left side of Figure 13, the sample, the incident X-ray beam, the transmitted X-rays through the sample and the scattered X-rays from a specific sample voxel (Cartesian coordinates (x_0, y_0)) are shown. In order to perform the absorption correction, the total attenuation along the various X-ray beam paths needs to be measured.

There are three possible scenarios depending on the experimental setup. More specifically, the calculation process depends on the detector position with respect to the sample. In XRD-CT experiments performed at synchrotrons, area detectors are used to collect two dimensional powder diffraction data. These powder diffraction images contain, given that there are crystalline components present in the sample, powder diffraction "rings". However, the detector centre and the sample centre are not necessarily positioned on an axis parallel to the beam axis. This means that in many cases the detector is placed at an offset, as shown in Figure 13 (sample and detector size are obviously not to scale). This offset is applied when the detector is not large enough to collect a wide *Q* range (for a given X-ray energy). This results in probing only a part of the full powder diffraction "rings". The two possible offset geometries are illustrated in Figure 13 as Detector 1 and Detector 2.

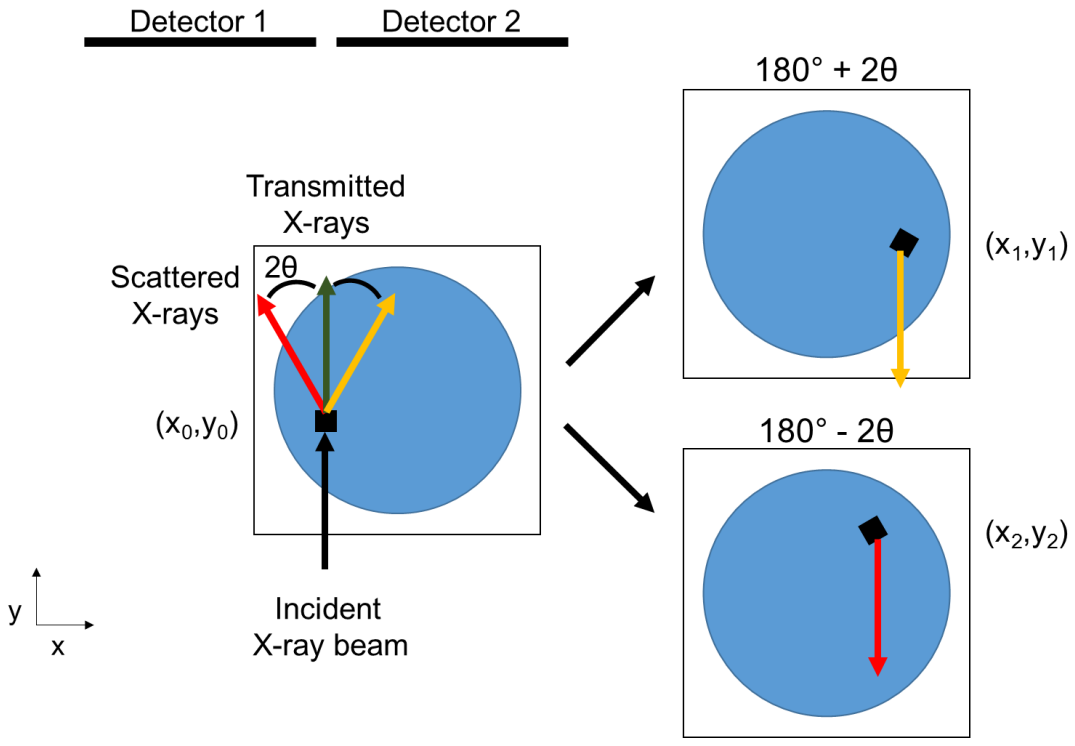

Figure 13: Schematic illustration showing how the code calculates the total attenuation along two different X-ray beam paths (path indicated by the black and yellow arrow and the black and red arrow).

If the experimental setup resembles the one shown in Figure 13 involving the Detector 1 geometry, then the total attenuation along the path indicated by the black and the red arrow needs to be calculated. On the other hand, if the experimental setup resembles the one shown in Figure 13 involving the Detector 2 geometry, then

the total attenuation along the path indicated by the black and the yellow arrow needs to be calculated. The MATLAB code first calculates the cumulative sum up to the point of interest (x_0, y_0) and then the sample is rotated. If the Detector 1 geometry is used, then the sample is rotated by 180 ° - 2θ, where 2θ is the scattering angle. The cumulative sum up to the new point of interest (x_1, y_1) in then calculated and the two values are summed to give the total attenuation along the original beam path. If the Detector 2 geometry is used, then the sample is rotated by 180 ° + 2θ and the same calculations are performed (point of interest is now (x_2, y_2)). Of course, this calculation has to be performed for every column, for every row (of the absorption-CT image), for every tomographic angle and for every scattering angle 2θ. This implies that the code involves four nested loops which is what makes is computationally expensive. Future work will focus on to improving the efficiency of the code.

BCFZ crystal structure

BCFZ perovskite

It is generally accepted that the chemical stability of the perovskite structure is improved when the B site is partially substituted by a metal cation with a single valence state (e.g. Zr^{4+}).[3] Tong *et al*. were the first to synthesize and test the performance of a $BaCo_xFe_yZr_zO_{3-\delta}$ (BCFZ) perovskite for oxygen separation.[51] $BaCo_{0.4}Fe_{0.6-x}Zr_xO_{3-\delta}$ (x = 0-0.4) samples were prepared and tested with oxygen temperature programmed oxidation (O_2-TPO). XRD analysis of the samples before and after the O_2-TPO experiment showed that the $BaCo_{0.4}Fe_{0.4}Zr_{0.2}O_{3-\delta}$ was the only sample that could maintain the cubic perovskite crystal structure. It was suggested that the O_2-TPO profiles show that the Co remains as Co^{3+} and is not further reduced to Co^{2+} but this is not clear from the figures presented in that study. XRD measurements at 800 °C under air, He, pure O_2 and 1 % O_2 in Ar showed that the $BaCo_{0.4}Fe_{0.4}Zr_{0.2}O_{3-\delta}$ can retain the perovskite structure under these conditions. It is also mentioned that the $BaCo_{0.4}Fe_{0.4}Zr_{0.2}O_{3-\delta}$ was tested under different oxygen partial pressures but the diffraction patterns are not presented in the paper. H_2-TPR and XRD tests revealed that the $BaCo_{0.4}Fe_{0.4}Zr_{0.2}O_{3-\delta}$ can regain the perovskite structure after treatment with 1 vol. % O_2 and 99 vol. % Ar. $BaCo_{0.4}Fe_{0.4}Zr_{0.2}O_{3-\delta}$ showed stable performance during the oxygen permeation test at 800 °C for 200 h.

The $BaCo_{0.4}Fe_{0.4}Zr_{0.2}O_{3-\delta}$ lost the perovskite structure under pure CO_2 atmosphere but it regained it after being treated with 1 vol. % O_2 and 99 vol. % Ar at 800 °C for 1 h which shows the good structural reversibility of this material. It should be noted that it is repeatedly mentioned in the paper that the $BaCo_{0.4}Fe_{0.4}Zr_{0.2}O_{3-\delta}$ has a pure perovskite-type crystal structure. However, there are two more peaks (22-25° and 32-35° 2θ respectively) present at the diffraction pattern collected at room temperature which are not identified and not discussed in the paper.

Yang *et al*. used two different methods to prepare the BCFZ perovskite: the solid state reaction (SSR) and the modified citrate (MC) method.[52] The $BaZrO_3$ (BZO) phase appears (BCFZ-BZO dual perovskite) when the SSR method is used. This phase is not present in the paper by Tong *et al*.[51] High temperature XRD measurements of the BCFZ samples calcined under different temperatures revealed that the formation of the perovskite structure takes place at approximately 800 °C. At temperatures higher than 900 °C, the $BaCoO_3$, $BaCO_3$ and BaO phases disappeared. For the MC method, the perovskite structure was formed at about 950 °C. There are some peaks at lower temperatures which were not identified in the paper. XRD patterns of the BCFZ powder were collected after being annealed in a H_2 containing atmosphere (the exact conditions are not mentioned in the paper). There is a new peak appearing for the SSR prepared sample but it was not identified in the paper.

Tablet *et al*. showed that the BCFZ hollow-fibre membranes can provide both stable and high values for oxygen permeation flux at high temperatures (850 °C).[53] However, the XRD data show that there is another phase present which was not identified. It seems to be the $BaZrO_3$ phase that Yang *et al*. mentioned in their paper.[52] In another study by the same group, the high oxygen permeation of BCFZ hollow-fibre membranes is shown but there are no XRD data that can prove the presence of the perovskite structure.[54] Wang *et al*. conducted high temperature XRD under air and showed that the BCFZ maintains its perovskite structure in the temperature range of 30-1000 °C.[55] The phase stability of BCFZ in different environments (i.e. in Ar, 2 % O_2 in Ar and in air) was also proved by XRD measurements performed at 900 °C. It is interesting to note that the preparation method for the BCFZ powder in this study was the same as in the paper by Tong *et*

al. but the previously mentioned unidentified peaks were not present in these diffraction patterns.[51]

Wang *et al*. prepared asymmetric hollow-fibre BCFZ membranes and conducted oxygen permeation experiments at 850 °C.[56] The oxygen permeation flux was decreased from 6 to 5 ml min^{-1} cm^{-2} in the first 60 h and then remained steady for the rest of the experiment. It was claimed that the presence of sulfur in the air led to this decrease. Also, an enrichment of Ba at the membrane side exposed to air is mentioned. Unfortunately, the EDX data are not presented in the paper and XRD measurements of the BCFZ sample were not performed in that study. Wang *et al*. tested these asymmetric hollow-fibre BCFZ membranes at low temperatures (400-500 °C) and showed that although there is a decrease in the oxygen permeation flux with time, the performance of the BCFZ can be restored by heating the membrane to 925 °C for 1 h in air.[57] EDX analysis revealed that the concentration of Ba is increased at the membrane surface exposed to the air stream and the concentration of Zr is increased at the membrane surface exposed to the He stream. Czuprat *et al*. investigated the influence of CO_2 on the oxygen permeation performance of BCFZ hollow-fibre membranes.[58] It was shown that the BCFZ membranes deactivated within 30 min when 10 % CO_2 in He was used on the outer side (air was used at the inner side) although high temperatures were applied (i.e. 800, 850 and 900 °C). SEM images revealed that a new layer with a thickness of about 5 µm was formed at the membrane surface exposed to CO_2. EDX analysis showed that there was an enrichment of Ba in this area. However, there was also an enrichment of Zr which was not discussed in the paper. High temperature XRD showed that $BaCO_3$ formed but there are many other peaks that were not identified. Also, it has to be noted that it is claimed that a pure perovskite-structure is present in the BCFZ samples before exposure to CO_2 and after regeneration but a closer look at the diffraction patterns shows that there is another phase present. This phase is probably $BaZrO_3$ which has been previously observed by Yang *et al*.[52] It was suggested that this dense layer acts as a protective layer that prevents the further formation of $BaCO_3$ by not allowing the diffusion of CO_2 to the inner layer of BCFZ. However, the thickness of this layer increased to 10 µm when a 50-50 % mixture of CO_2 and He was applied and the

exposure time was longer (5 h). A second Ba-depleted layer between the $BaCO_3$ and the inner BCFZ layer was present in both cases. It has to be noted that the changes in the concentration of Zr in these two layers was not discussed in the paper.

Efimov *et al*. conducted high temperature XRD experiments to study the effect of CO_2 in the crystal structure of BCFZ. XRD analysis showed that there is a dual perovskite phase present in their samples (i.e. the BCFZ and the $BaZrO_3$ phases).[59] It is mentioned that quantitative Rietveld analysis showed that their powder samples contained 16 wt. % cubic $BaZrO_3$. However, the results from the Rietveld analysis are not provided in the paper (not even the fits) and to the author's knowledge no BCFZ crystal structure model is available in any crystallographic database. Therefore, the aforementioned results (quantitative Rietveld refinement) are under question. The XRD experiments performed in an atmosphere containing 50 vol. % CO_2 and 50 vol. % N_2 showed that $BaCO_3$ is formed. There are other peaks that were not identified. It was suggested that the CoO phase is also present but this claim is based on TEM/EDX data. It should be noted that the concentration of BCFZ had decreased while the concentration $BaZrO_3$ phase remained almost constant during the CO_2 experiment. *In situ* high temperature XRD measurements performed in an atmosphere containing CO_2 revealed the formation of orthorhombic $BaCO_3$ and CoO at 600 °C, the phase transformation of orthorhombic $BaCO_3$ to rhombohedral at 800 °C and to the cubic phase at 1000 °C. After cooling to room temperature, a new phase appeared but it was not identified. It is mentioned that this phase is possibly related to a tetragonal perovskite phase. TEM/EDX data suggested that the $BaCO_3$ phase did not form a uniform layer around the BCFZ in contrast to the previous studies with BCFZ hollow-fibre membranes.[58] CoO and a Co-depleted BCFZ were also suggested to be present.

BCFZ crystal structure solution

High resolution neutron powder diffraction data of a (ground) $BaCo_{0.4}Fe_{0.4}Zr_{0.2}O_{3-\delta}$ membrane were collected at the ISIS pulsed neutron source at the Rutherford Appleton Laboratory. The measurements were performed with the High Resolution Powder Diffractometer (HRPD) which is the highest resolution neutron powder diffractometer of its type in the world. Two powder diffraction datasets were

collected at ambient conditions, probing two different *Q* regions (ca. *Q* = 2.5-9.5 $Å^{-1}$ and *Q* = 1.8-7 $Å^{-1}$ respectively). The analysis of the neutron powder diffraction data was performed with the GSASII software.[60]

Initially, peak indexing was performed with GSASII using the powder diffraction pattern with the longer *Q* range (ca. *Q* = 2.5-9.5 $Å^{-1}$) and the best result corresponded to space group Pm-3m (221). This is to be expected as the Pm-3m space group is the most common for cubic perovskite crystal structures and the BCFZ powder diffraction patterns indicated that the BCFZ unit cell exhibits high symmetry. Furthermore, similar to $BaCo_{0.4}Fe_{0.4}Zr_{0.2}O_{3-\delta}$ crystal structures, like $BaCoO_{2.2}$, $BaCo_{0.2}Fe_{0.8}O_{2.6}$ and $BaCo_{0.5}Fe_{0.5}O_{2.16}$ all correspond to cubic unit cells (space group 221).[61, 62] All the diffraction peaks present in the BCFZ powder diffraction data are predicted by this unit cell. The various BCFZ reflections are listed in the Appendix. The various atoms present in the $BaCo_{0.4}Fe_{0.4}Zr_{0.2}O_{3-\delta}$ unit cell are placed in special positions as shown in Table 1.

Table 1: Positions of the Ba, Co, Fe, Zr and O in the BCFZ unit cell

Atom	x	y	z
Ba	0	0	0
Fe	0.5	0.5	0.5
Co	0.5	0.5	0.5
Zr	0.5	0.5	0.5
O	0	0.5	0

An illustration of the $BaCo_{0.4}Fe_{0.4}Zr_{0.2}O_{3-\delta}$ unit cell is presented in Figure 14. The BCFZ is an $AB_xC_yD_zO_{3-\delta}$ ($x + y + z = 1$) type of perovskite. The large Ba atoms are placed in the A site of the perovskite (12-fold coordinated with the oxygen anions) and the Co, Fe and Zr atoms share the B site of the perovskite (6-fold coordinated).

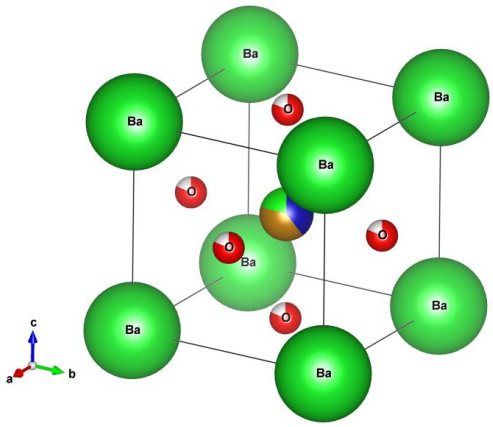

Figure 14: Illustration of the $BaCo_{0.4}Fe_{0.4}Zr_{0.2}O_{3-\delta}$ unit cell. The Ba atoms are placed in the A site of the perovskite and the Co, Fe and Zr at the B site of the perovskite.

Simultaneous Rietveld refinement was performed using both neutron powder diffraction patterns (i.e. both banks as shown in Figure 15). The following strategy was used for the Rietveld refinement of the BCFZ structure model:

1. Initially a hard constraint was applied and the thermal (isotropic) parameters (U_{iso}) of Co, Fe and Zr were set to be equal.
2. The thermal parameters of Ba, Fe/Co/Zr and O were refined sequentially in order to obtain good starting values before refining them all simultaneously.
3. The O occupancy was refined and this sequential refinement approach was then repeated (thermal parameters of Ba, Fe/Co/Zr and O and O occupancy) till the values of the various parameters stabilised.
4. The previous hard constraint was removed and a new one was applied setting the thermal parameter of Fe equal to the thermal parameter of Co (not Zr).
5. The thermal parameters of Ba, Co/Fe, O and O occupancies were refined simultaneously. The thermal parameter of Zr was then refined by itself. This refinement strategy was repeated till the various parameters stabilised.

At this point it should be emphasized that the same final result can be reached by following different strategies but this was the one requiring the minimum number of steps. It should also be pointed out the refinement becomes unstable if the thermal parameters (or occupancies) of Co, Fe and Zr are refined simultaneously (regardless of the constraints applied). The results of the Rietveld refinement are shown in Figure 15. The quality of the fit can be observed by inspecting the difference plot (cyan

colour line). It should be mentioned that there were minor peaks of CoO present in the diffraction data (only two CoO peaks can be observed). This is consistent with what has been previously observed in Ba-Co based perovskites.[62]

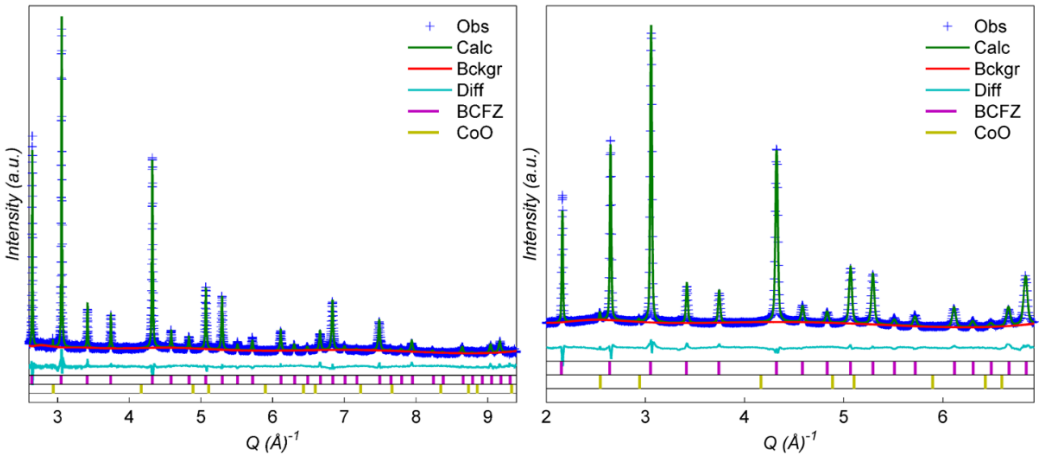

Figure 15: Results from the Rietveld analysis of the neutron powder diffraction data.

The results from the Rietveld analysis of the neutron powder diffraction data are summarised in Table 2.

Table 2: Results from the Rietveld refinement of the BCFZ structure

Crystal data	
Formula	$BaCo_{0.4}Fe_{0.4}Zr_{0.2}O_{2.46}$
Formula weight	240.84
Crystal system	Cubic
Space group	Pm-3m (no. 221)
α [Å]	4.10954
V [Å^3]	69.403
Z	1
D(calc.) [g cm^{-3}]	5.762
Refinement	
No. of observations	6176
No. of parameters	31
wR	3.84%

It can be seen that the O occupancies in the BCFZ unit cell are significantly lower than the theoretical value of 3 (no O vacancies). However, as mentioned previously, this phenomenon has been observed numerous times before in similar perovskites. For example, Mentre *et al*. recently solved the crystal structure of $BaCoO_{2.2}$ which is the most oxygen deficient perovskite.[62] Another example is the $BaCo_{0.2}Fe_{0.8}O_{2.6}$ structure reported by Bartłomiej *et al*. were the O occupancies are also very low.[61] It should finally be noted that the low O occupancies in all these crystal structures imply that the oxidation states of Co and Fe are significantly below 4 (in order to maintain the charge neutrality of the system). As it will be shown in the following sections, the BCFZ crystal structure was then used to analyze the XRD-CT data obtained from CMRs using this membrane. The BCFZ CIF is provided in the Appendix.

Operando XRD-CT measurements of CMRs during OCM

The results from the *operando* experiments using three different CMRs are presented in this section.

BCFZ membrane with Mn-Na-W/SiO_2 catalyst

A schematic representation of the experimental protocol followed for the OCM experiment with the BCFZ – 2 % Mn – 1.6 % Na – 3.1 % W/SiO_2 CMR is shown in Figure 16. XRD-CT measurements were made at nominal temperatures, ambient, 800, 900 and 1000 °C equating to actual temperatures (i.e. after temperature calibration) of ca. ambient, 660, 720 and 780 °C. The temperature of the system was increased with a ramp rate of 5 °C min^{-1} under the flow of He. More specifically, 30 ml min^{-1} He flow rate was used at the inner side of the membrane through the catalyst bed and 30 ml min^{-1} air flow at the outer side of the membrane. After reaching the required temperature for the OCM experiment (i.e. 780 °C), air was used from both sides of the BCFZ membrane as an activation step before switching to OCM conditions (i.e. flow rate of 50 ml min^{-1}). Next, different OCM reaction mixtures were used by varying the concentration of CH_4 in He (i.e. 5, 20, 50 and 100 % CH_4 in He). 3D-XRD-CT was then performed by collecting 11 XRD-CT 'slices' at different positions along the reactor (i.e. 25 µm apart) while keeping the reaction mixture the same (i.e. 100 ml min^{-1} of CH_4 at the inner side of the membrane through the catalyst bed and 100 ml

min^{-1} air at the outer side of the membrane). The system was then cooled to room temperature and a final XRD-CT dataset was collected.

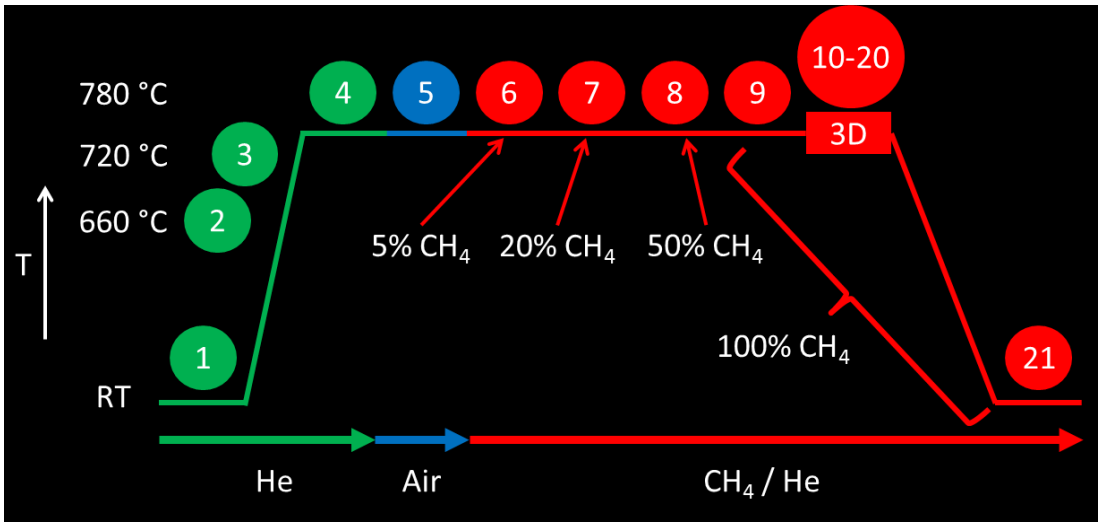

Figure 16: Schematic representation of the protocol followed during the OCM experiment with the BCFZ – 2%Mn-1.6%Na-3.1%W/SiO_2 CMR.

Initially, an XRD-CT scan of the CMR was performed at room temperature. As expected, the main crystalline phases present in the catalyst particles were cristobalite-low (ICSD: 9327), tridymite-low (ICSD: 413210), Mn_2O_3/Mn_7SiO_{12} (ISCD: 159865 and 71793 respectively) and Na_2WO_4 (ICSD: 2133). The phase distribution maps shown in Figure 17 represent the (normalised) values of the scale factors of these crystalline phases as obtained from the Rietveld analysis of the CMR XRD-CT data collected at room temperature. It can be seen that the two main crystalline SiO_2 phases, cristobalite and tridymite, are homogeneously distributed over the catalyst particles and define well their size and shape. On the other hand, it can be seen that there are certain areas where there is high concentration of Mn_2O_3/Mn_7SiO_{12}. The Na_2WO_4 phase which is present in all catalyst particles but there are areas of high concentration of this phase too (i.e. hotspots). Finally, the phase distribution map of BCFZ demonstrates that the membrane wall thickness is fairly uniform (ca. 200 μm) and that there are no macropores present.

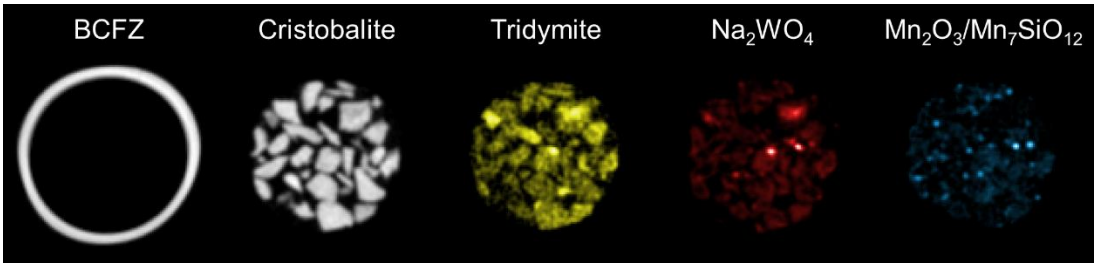

Figure 17: Phase distribution maps created based on the values of the scale factors of the crystalline phases present in the CMR as obtained from the Rietveld analysis of the XRD-CT data collected at room temperature before the OCM experiment.

The next XRD-CT scan was performed at 660 °C. Careful inspection of the reconstructed XRD-CT data revealed that the high temperature tomographic scans were performed at a different position compared to the room temperature scan due to thermal expansion/movement of the CMR during heating. It was feasible to identify this vertical change of the probing position after the OCM experiment by comparing the phase distribution maps of cristobalite. As mentioned previously, the phase distribution maps of cristobalite define well the catalyst particles and can be used to correlate different tomographic datasets. As a result, the data of the high temperature XRD-CT scans cannot be directly compared with the room temperature XRD-CT scans. In Figure 18, the results from the high temperature XRD-CT scans are presented which are all at the same position (i.e. XRD-CT 'slices' at a constant position of the CMR). The relative change of each phase, as determined from the integrated intensities (scale factors) for each XRD-CT dataset, is presented at the right side of Figure 18.

The support of the catalyst particles is seen to evolve at high temperatures which is in full agreement with the results obtained from the *operando* XRD-CT experiments of the fixed bed reactor with the same catalyst (Chapter 5). The diffraction peaks generated by Na_2WO_4 have disappeared completely at 660 °C although its melting point is 695 °C in 1 bar pressure.[63, 64] The mobile Na^+ species are incorporated into the SiO_2 framework and lead to the crystallisation of the remaining amorphous SiO_2 to the crystalline cristobalite phase. It can be seen though that after the initial spike, the signal from the diffraction signal corresponding to the cristobalite phase starts to decrease in favour of the transformation to the tridymite and quartz phases.

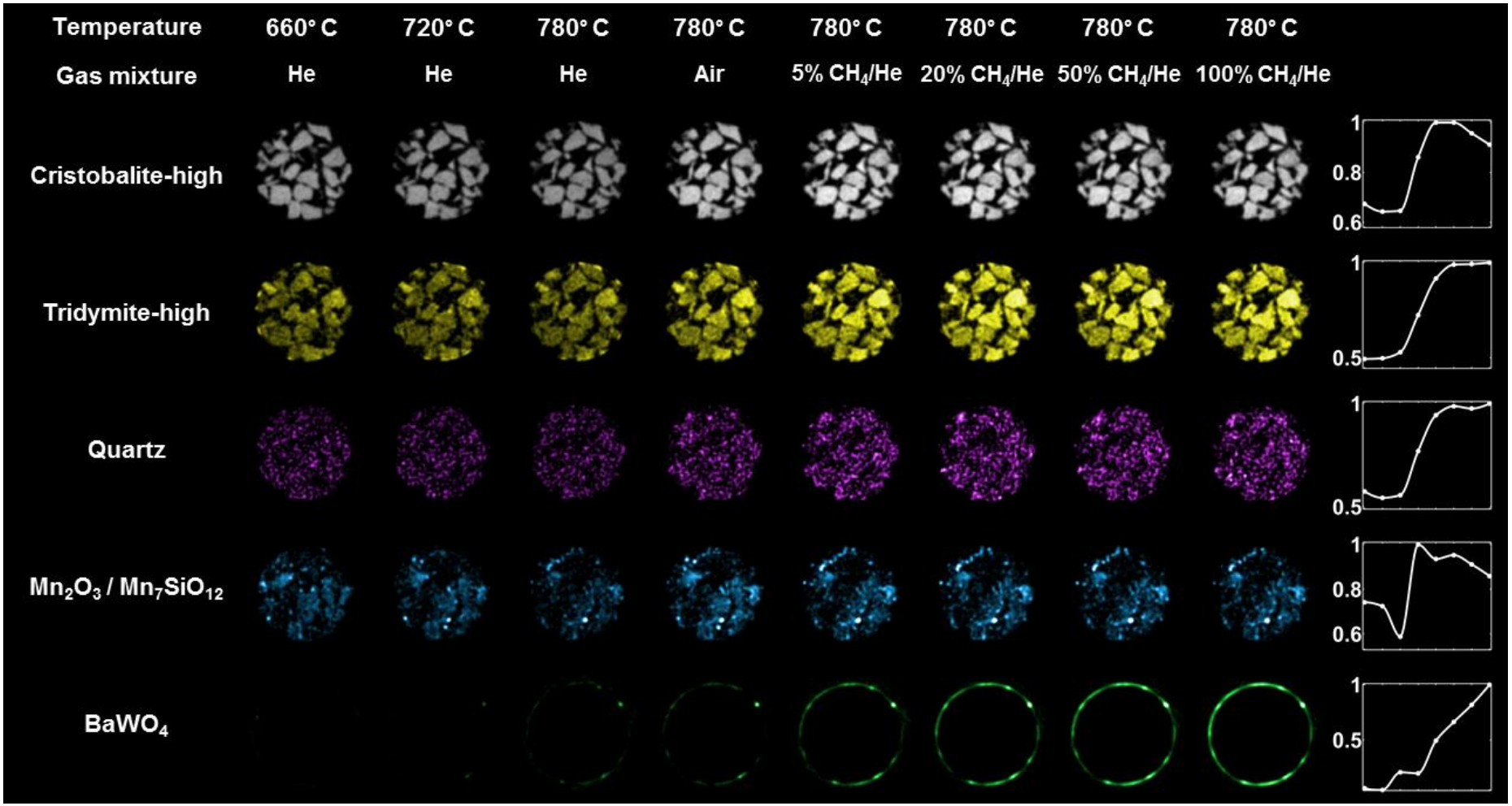

Figure 18: Phase distribution maps of Cristobalite, Tridymite, Quartz, Mn_2O_3/Mn_7SiO_{12} and $BaWO_4$ at high temperatures during the OCM experiment. At the right side, the relative change of each phase, as determined from the integrated intensities for each XRD-CT 'slice', is presented.

The results from the *in situ* XRD-CT experiments presented in the previous section (Figure 6) showed that the crystalline Mn_2O_3/Mn_7SiO_{12} phase decreased with time at high temperatures when a gas mixture of 5% CH_4/He is used. However, it is shown in Figure 18 that letting air pass through the catalyst bed leads to a significant increase of the crystalline Mn_2O_3/Mn_7SiO_{12} phase under OCM operating temperatures (780 °C). This is important as, if Mn_2O_3/Mn_7SiO_{12} needs to be present under OCM conditions to yield an active and C_2 selective catalyst then an activation step by using air at high temperatures is necessary; an issue which has been raised before in literature.[65] In the past, the Mn-Na-W/SiO_2 catalysts have shown great stability in terms of CH_4 conversion but the selectivity towards C_2 molecules has been shown to decrease with time.[66-68] Therefore, it might be also necessary to switch the inlet gases from reaction mixture to air after many hours of operation at high temperatures as a regeneration step for the catalyst. For example, Hou *et al*. showed that treating the Mn-Na-W/SiO_2 catalyst with O_2 for 2 h at 800 °C led to the reappearance of Na_2WO_4 and Mn_2O_3/Mn_7SiO_{12} and the disappearance of $MnWO_4$.[69]

It should be emphasized though that such (regeneration) treatments may not be needed in CMRs containing Mn-Na-W/SiO_2 catalysts. In the *operando* XRD-CT experiments of the Mn-Na-W/SiO_2 fixed bed reactor (Chapter 5), it was shown that the concentration of the Mn_2O_3/Mn_7SiO_{12} phase is diminished under very reducing environments (CH_4:Air molar ratio of 10:1) leading to the formation and growth of the $MnWO_4$ phase (reduction of Mn^{3+} to Mn^{2+} species). In the BCFZ – 2 % Mn – 1.6 % Na – 3.1 % W/SiO_2 CMR (Figure 18), the diffraction signal generated by the Mn_2O_3/Mn_7SiO_{12} phase is seen to decrease under OCM reaction conditions (i.e. gas mixtures of CH_4/He) but the Mn_2O_3/Mn_7SiO_{12} to $MnWO_4$ phase transformation was not observed for the duration of the experiment. This is crucial as the catalyst bed was exposed to 100 % CH_4 for almost 10 h and the Mn_2O_3/Mn_7SiO_{12} phases remained present till the end of the OCM experiment. This indicates that the O_2 transferred through the BCFZ ceramic membrane was enough to maintain the Mn_2O_3/Mn_7SiO_{12} phases and prevent the bulk reduction of the Mn species (from Mn^{3+} to Mn^{2+}).

However, another crystalline WO_4-containing phase appears as a result of the chemical interaction between the catalyst particles and the BCFZ ceramic membrane.

This new phase is $BaWO_4$ and it is seen to form/grow at the inner side of the BCFZ membrane where the catalyst particles are in direct contact with the membrane. As it is shown in Figure 18, $BaWO_4$ continuously grows during the OCM experiment regardless of the gases used (chemical environment present), proving that this is a purely temperature driven phenomenon. The formation and growth of the $BaWO_4$ phase show that the results obtained from the *in situ* XRD-CT experiment presented previously are directly reproducible.

3D-XRD-CT was also performed under OCM reaction conditions by collecting 11 XRD-CT 'slices' at different positions along the reactor (i.e. 25 μm apart) at 780 °C (flow rate of 100 ml min^1 of 100 % CH_4 at the inner side of the BCFZ membrane, through the catalyst bed). The phase distribution maps of cristobalite, tridymite, quartz, Mn_2O_3/Mn_7SiO_{12} and $BaWO_4$, as obtained from the Rietveld analysis of the 3D-XRD-CT data (scale factors normalised to the maximum value), are presented in Figure 19. In principle, these data should not be directly compared as they correspond to different sample volumes. However, it can be seen that there is clear trend regarding the crystalline SiO_2 phases. There is a decrease of cristobalite and an increase of tridymite and quartz. More importantly, there is a continuous growth of the $BaWO_4$ phase. These results suggest that these changes are a function of time as they are independent of the sample probing position.

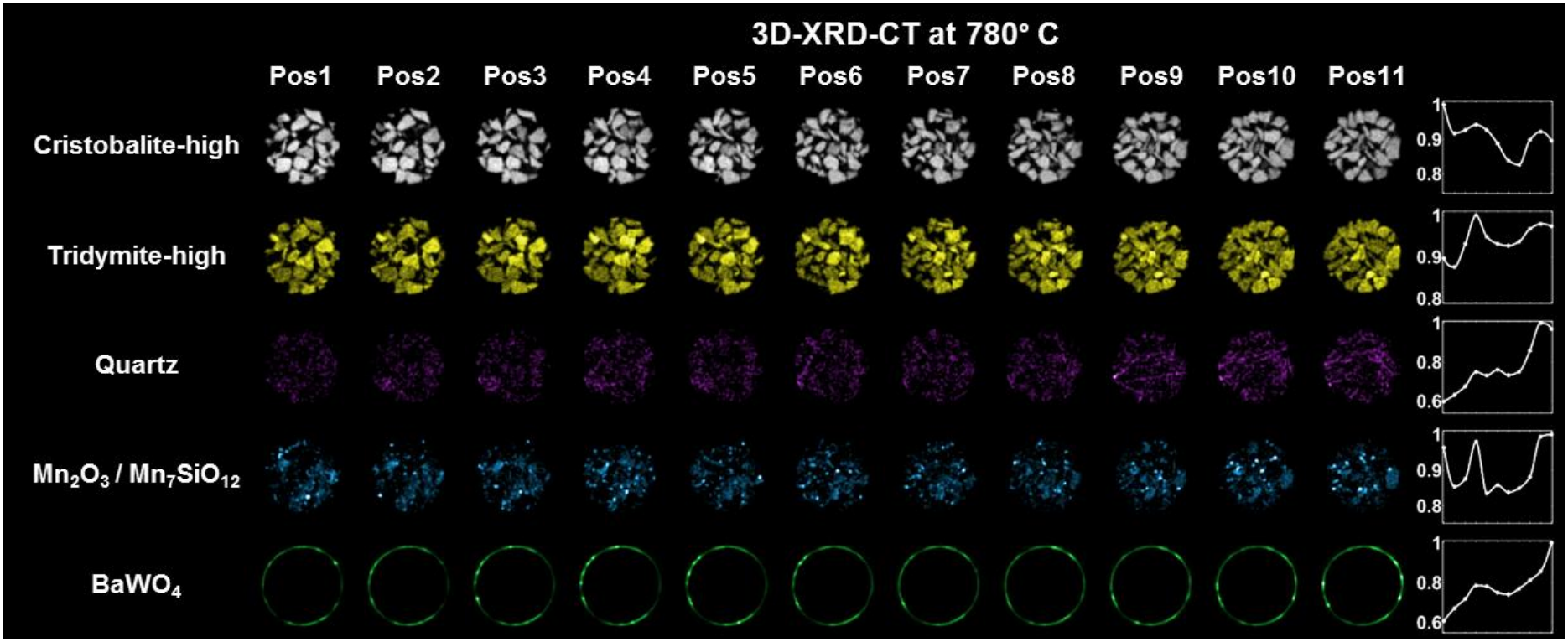

Figure 19: Phase distribution maps of Cristobalite, Tridymite, Quartz, Mn_2O_3/Mn_7SiO_{12} and $BaWO_4$ as obtained from the Rietveld analysis of the 3D-XRD-CT data (each XRD-CT "slice" is 25 µm apart from the next). 100 ml min^{-1} of 100 % CH4 was used at the inner side of the membrane through the catalyst bed and 100 ml min^{-1} air at the outer side of the BCFZ membrane

In Figure 20, the results from the volume rendering of the scale factors data volume (phase distribution volumes) are presented. The scale factors were normalised with respect to the maximum value for each data volume and the colour axes were scaled accordingly in order to improve the contrast of the respective figures.

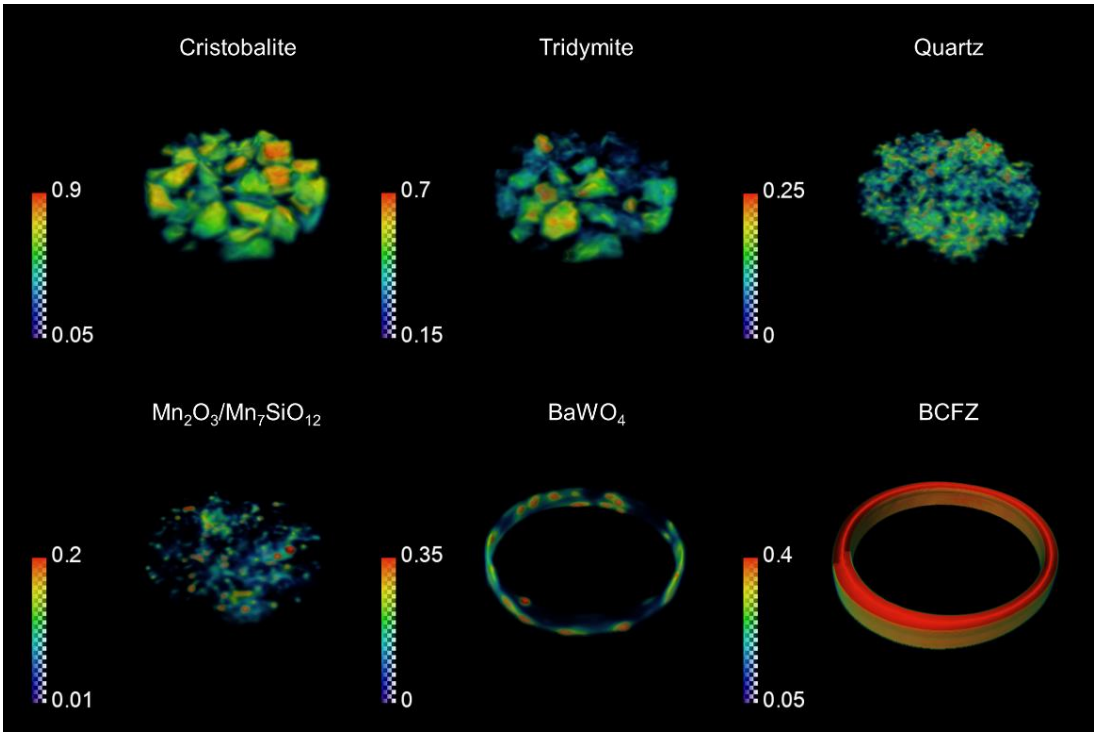

Figure 20: Volume rendering of the scale factors data volume (phase distribution volumes) obtained from the Rietveld analysis of the 3D-XRD-CT data.

The cristobalite phase distribution volume clearly describes the catalyst particles in terms of both size and shape. This is expected as cristobalite, it being the main crystalline phase of the SiO_2 catalyst support, is homogeneously distributed (uniform distribution) over the particles. Tridymite is present in most catalyst particles but it can also be seen that the sample regions showing high tridymite concentration also correspond to low cristobalite concentration. Similarly to cristobalite, quartz is seen to be present in all catalyst particles.

The results obtained from the XRD-CT data collected at room temperature before the OCM experiment indicated that Mn_2O_3/Mn_7SiO_{12} is not homogeneously distributed over the catalyst particles but is only present at specific regions with very high concentration, mainly near the surface of the catalyst particles (Figure 17). The Mn_2O_3/Mn_7SiO_{12} phase distribution volume (Figure 20) serves to verify this result and

also to show that the Mn_2O_3/Mn_7SiO_{12} distribution does not alter significantly under OCM reaction conditions.

The BCFZ membrane maintained its size and shape for the duration of the OCM experiment and no cracks were formed. This is also implied by the BCFZ phase distribution volume which clearly demonstrates the dense ceramic hollow-fibre design. Finally, the $BaWO_4$ phase distribution volume reveals that there are regions of high concentration of this phase at the inner side of the BCFZ membrane (hotspots of material) which, as it will be shown later, are mainly located at the catalyst-membrane interface. This is attributed to the W containing species, originating from the molten Na_2WO_4 phase, being both mobile and volatile.

As mentioned previously, the outflow gases from the CMR were analysed with mass spectrometry. The analysis of the gas products with mass spectrometry serves to illustrate that the integrated reactor system was captured in its active state. The mass spectrometry data from the OCM experiment are presented in Figure 21. Five regions are shown corresponding to air and different mixtures of CH_4 diluted in He (i.e. 5, 20, 50 and 100 vol. % CH_4 in He).

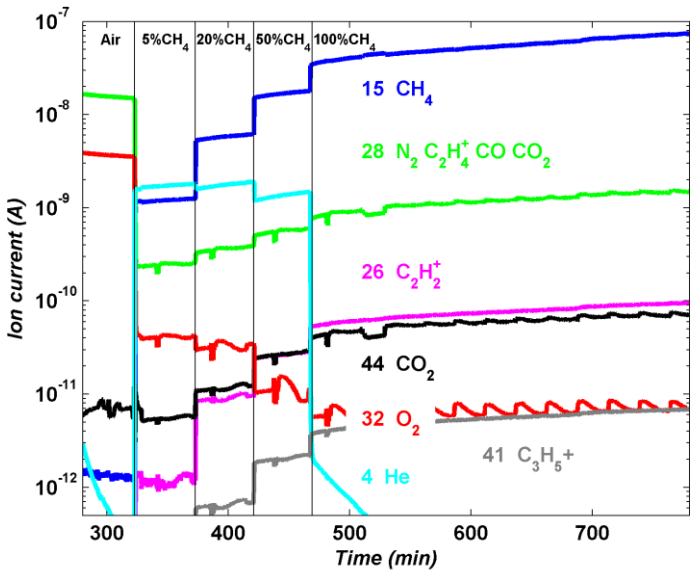

Figure 21 Mass spectrometry data corresponding to the following m/z ratios (possible species and respective line colour in parentheses): 4 (He - cyan), 15 (CH_4^+ - blue), 28 (N_2, CO, $C_2H_4^+$ - green), 32 (O_2 - red), 44 (CO_2 - black), 26 ($C_2H_2^+$ - magenta) and 41 ($C_3H_5^+$ - grey).

The signal from mass 26, which corresponds to $C_2H_2^+$ fractions, appears when the reaction mixture is used (i.e. 5 % CH_4 in He). The intensity of this signal increases with increasing CH_4 concentration (i.e. 20, 50 and 100 vol. % CH_4 in He). This phenomenon is expected as it is known from literature that the selectivity for C_2 molecules increases with increasing CH_4 concentration.[45] It also should also be noted that a signal from mass 41, which corresponds to $C_3H_5^+$ fractions, appears when a mixture of 20 % CH_4 in He is used and its intensity follows the same trend as the signal from mass 26. More importantly, the intensity of the signals corresponding to higher hydrocarbon molecules than CH_4 (i.e. C_2 and C_3 fractions) did not decrease throughout the experiment, although the $BaWO_4$ phase formed at the inner BCFZ membrane wall. The mass spectrometry data of the other two CMRs can be found in the Appendix (Figures A14 and A15) as they also only serve to show that the CMRs were captured in their active state (qualitative analysis only).

Finally, it was feasible to directly compare the state of the catalyst before, during and after the OCM reaction. As mentioned previously, the CMR slightly moved during temperature ramping but fortunately one of the 3D-XRD-CT scans was at the same position as the one at ambient conditions before the OCM experiment. More importantly, the XRD-CT scan at room temperature after the OCM experiment is also at the same position allowing the direct comparison of these three datasets. The phase distribution maps presented Figure 22 correspond to the respective (normalised) phase scale factors obtained from the Rietveld analysis of the XRD-CT data.

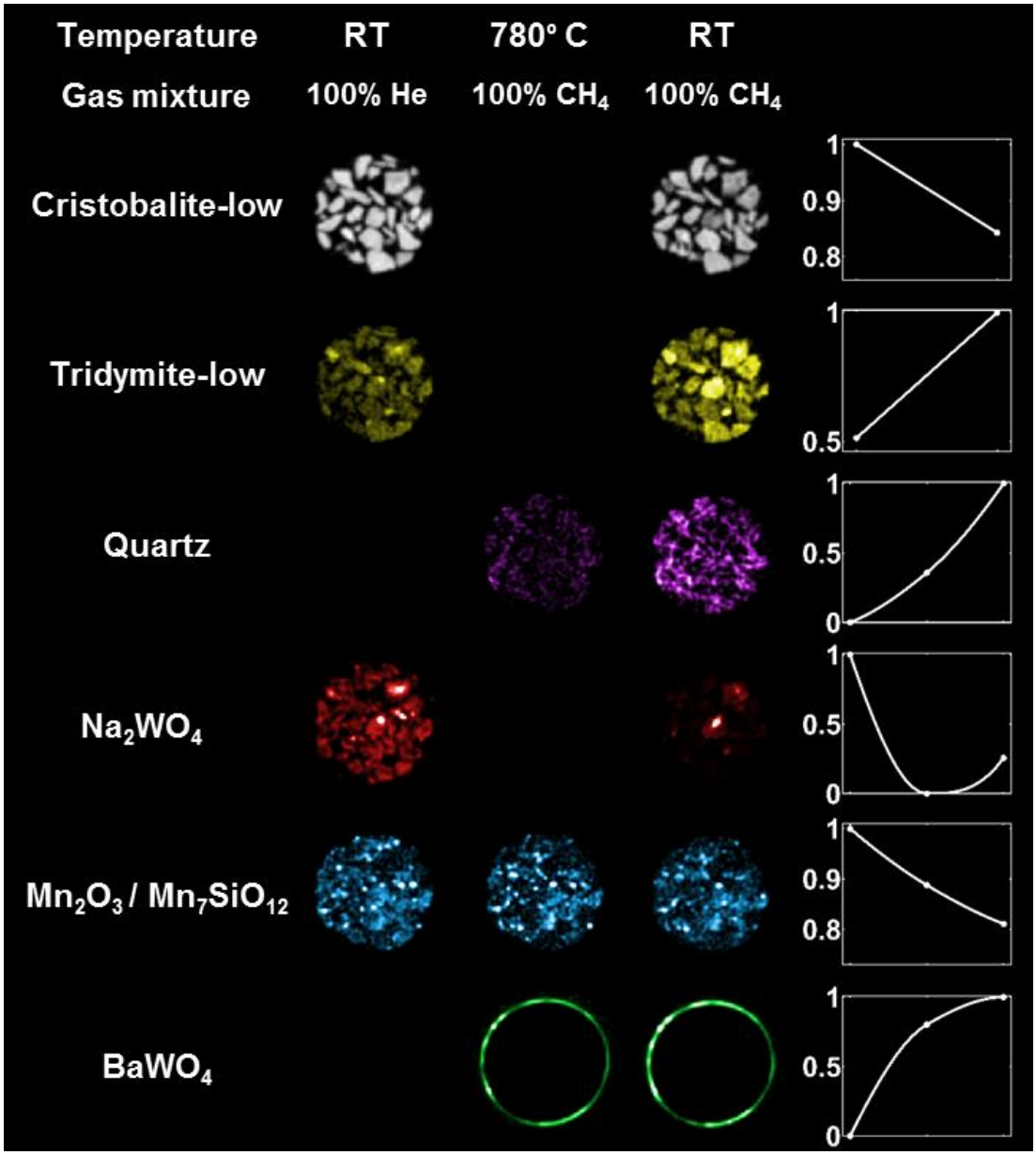

Figure 22: Phase distribution maps of Cristobalite, Tridymite, Quartz, Na_2WO_4, Mn_2O_3/Mn_7SiO_{12} and $BaWO_4$ at room temperature before the OCM experiment, at high temperatures during the OCM experiment and at room temperature after the OCM experiment. At the right side, the relative change of each phase, as determined from the integrated intensities for each XRD-CT 'slice', is presented.

The comparison of these three XRD-CT datasets reveals that by the end of the OCM experiment, cristobalite has been partially consumed in favour of the growth of the tridymite and quartz phases. The evolution of the SiO_2 support observed in this experiment is in full agreement with the results obtained from the Mn-Na-W/SiO_2 fixed bed reactor *operando* XRD-CT experiments presented previously in Chapter 5 further supporting the claim that the evolution of the SiO_2 support is a temperature driven phenomenon. The Mn_2O_3/Mn_7SiO_{12} phase is also seen to decrease during this

OCM experiment but, as mentioned previously, in contrast to the fixed bed reactor experiments, the formation of the $MnWO_4$ phase was not observed. The Na_2WO_4 phase is seen to reform after cooling to room temperature albeit at a lesser extent. This is to be expected as $BaWO_4$ formed and continuously grew during the OCM experiment which was not present in the initial materials (i.e. catalyst and membrane) composing the CMR.

In Figure 23, two coloured images are presented where the phase distribution maps of Na_2WO_4, $BaWO_4$ and Mn_2O_3/Mn_7SiO_{12} (red colour for Na_2WO_4, green colour for $BaWO_4$ and blue for Mn_2O_3/Mn_7SiO_{12}) have been overlaid on top of two grayscale images derived from the phase distribution maps of cristobalite and BCFZ. These two images correspond to the CMR XRD-CT data collected at room temperature before and after the OCM experiment. The XRD-CT data collected at room temperature before the OCM experiment (left side of Figure 23) indicate that the sample regions corresponding to high Mn_2O_3/Mn_7SiO_{12} concentration (blue hotspots) are mainly located near the surface of the catalyst particles. It can be seen that this is also the case at XRD-CT data collected at the end of the experiment (right side of Figure 23).

On the other hand, the phase distribution map of Na_2WO_4 significantly changes before and after the OCM experiment. As mentioned previously (Figure 17), the Na_2WO_4 phase is initially seen to be present in all catalyst particles but by the end of the OCM experiment it is located at specific regions of the sample (red hotspots). This result is of no surprise as the $BaWO_4$ formed/grew during the OCM experiment. The image on the right side of Figure 23, clearly shows that the areas of high concentration of $BaWO_4$ (green hotspots) are located at the interface between the catalyst particles and the BCFZ membrane. As expected, the Na_2WO_4 signal in these catalyst particles is absent/very weak.

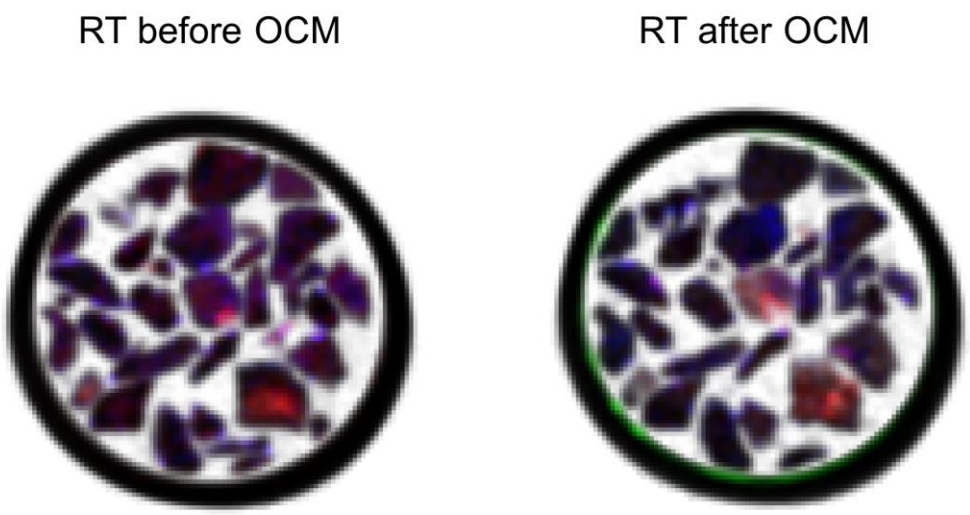

Figure 23: In these RGB images, the phase distribution maps of Na_2WO_4, Mn_2O_3/Mn_7SiO_{12} and $BaWO_4$ (red colour for Na_2WO_4, green colour for $BaWO_4$ and blue colour for Mn_2O_3/Mn_7SiO_{12}) have been overlaid on top of a grayscale image derived from the phase distribution maps of cristobalite and BCFZ.

As mentioned in a previous section, micro-CT measurements of the CMR were also performed in order to perform the self-absorption correction of the XRD-CT data. However, the micro-CT data of this CMR offered some indirect chemical information about this reactor system. This was possible due to the presence of W in the catalyst particles; a heavily absorbing material compared to the other catalyst components. The mobility/volatility of the W containing species is clearly illustrated in Figure 24. Micro-CT measurements of the CMR were performed at room temperature, before and after the OCM experiment. As shown in the top row of Figure 24, there was a catalyst particle rich in W containing species before the OCM experiment but this is not the case at the end of the experiment (as indicated by the red circles in Figure 24). The regions of high W concentration in this particle are absent after the OCM experiment. The migration of W is more apparent in the two images shown at the bottom row of Figure 24. These images correspond to the volume rendering of micro-CT data from a small region of interest (120 × 120 × 57 data volume) that includes the aforementioned catalyst particle. It can be clearly seen that the distribution of the W containing species significantly changes during the OCM experiment and that these species are mobile under the OCM reaction operating conditions.

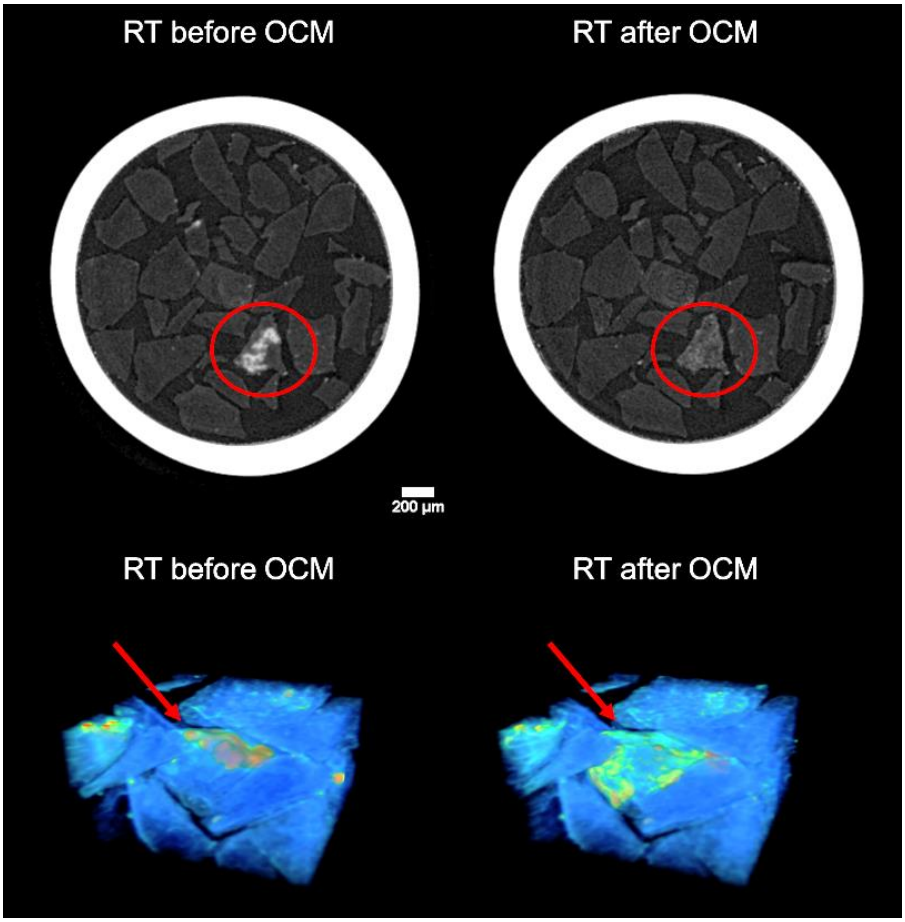

Figure 24: Micro-CT data of the CMR collected at room temperature before and after the OCM experiment. Top row: Comparable micro-CT images from the CMR indicating the migration of W containing species. Bottom row: Volume rendering of micro-CT data from a region of interest showing the migration of W

Additionally, the cross-sectioned CMR samples were imaged and analysed using SEM/WDS. The results from the SEM/WDS measurements for the BCFZ with 2 % Mn-1.6 % Na-3.1 % W/SiO_2 CMR after the OCM experiment are shown in Figure 25. Two different scans were performed in the same area of the sample, taken at different magnification levels. The area of interest is highlighted (blue colour) at the top left section of Figure 25. The elemental maps of W show clearly that it has migrated from the catalyst particles to the inner side of the BCFZ membrane which is consistent with the XRD-CT observations that portion of the W-containing species is migrating and depositing as $BaWO_4$ at the inner wall of the BCFZ membrane. It should also be noted that none of the other components of the catalyst seem to migrate to the BCFZ membrane.

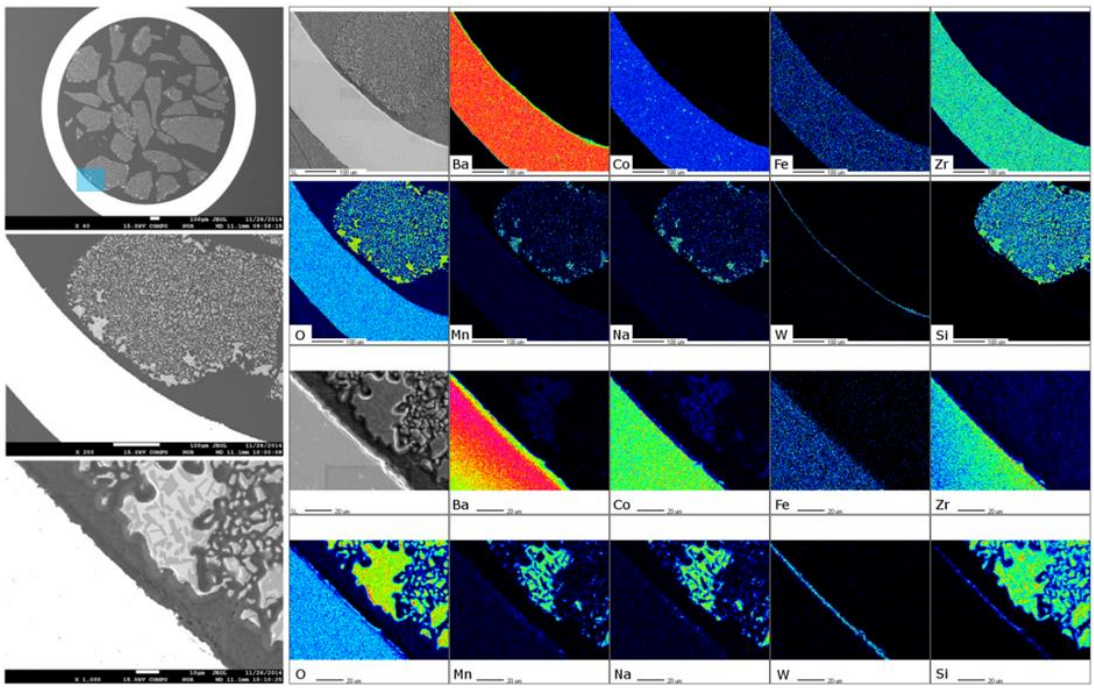

Figure 25: SEM images and WDS mapping of the cross section of BCFZ with 2 % Mn-1.6 % Na-3.1 % W/SiO_2 CMR. Top left: SEM image the cross section of the CMR and highlighted area of interest. Middle and bottom left: SEM images of the two areas of interest. Right: The SEM images and the corresponding elemental maps of Ba, Co, Fe, Zr, O, Mn, Na, W and Si from the respective areas of interest.

The BCFZ structure model obtained from the analysis of the neutron powder diffraction data was used for the Rietveld analysis of the CMR XRD-CT data. In Figure 26, the result from the Rietveld refinement of the BCFZ structure using the summed diffraction pattern (BCFZ membrane region only) of the XRD-CT data collected at room temperature before the OCM experiment is shown.

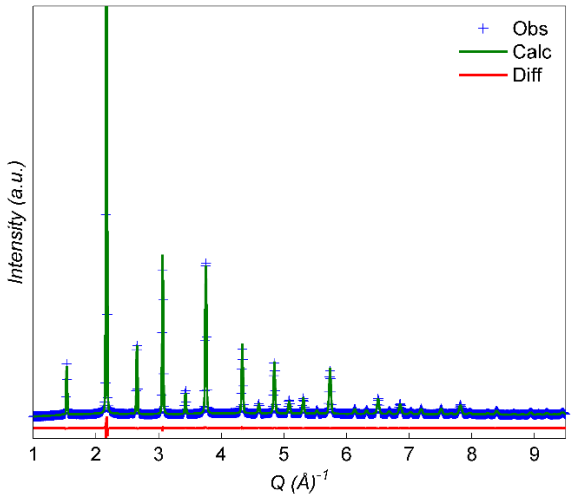

Figure 26: Rietveld refinement of the BCFZ structure using the summed diffraction pattern (BCFZ membrane region only) of the XRD-CT data collected at room temperature before the OCM experiment.

Of course, the quality of the spatially-resolved XRD patterns obtained from the XRD-CT data cannot be compared to the high resolution neutron powder diffraction data used to create/refine the BCFZ structure model. This becomes more apparent when it is taken into account that that the acquisition time per point was very short (50 ms) and the area detector was relatively small (300K pixels) leading to worse statistics (signal to noise ratio). Furthermore, a 10 % trimmed mean filter was applied to the XRD-CT data in order to remove any outliers. Despite these issues, the lattice parameters (unit cell parameter *a*), thermal parameters and oxygen occupancies of the BCFZ structure were refined during the Rietveld analysis of the CMR XRD-CT data. The results are presented in Figure 27 and should be treated as qualitative analysis only.

As mentioned previously, the BCFZ membrane retained its shape and size for the duration of the OCM experiment. However, as it is shown in Figure 27, Co is seen to gradually leave the BCFZ unit cell and be present as the crystalline CoO phase. It is still present as a minor phase in the CMR XRD-CT data collected at room temperature after the OCM experiment but it raises questions regarding the long-term chemical stability of the BCFZ membrane under OCM reaction conditions and reducing chemical environments in general.

The spatially-resolved diffraction patterns were not of high quality enough to allow the simultaneous refinement of the Fe, Co, Zr and O occupancies and the thermal parameters of Ba, Co, Fe, Zr and O. This is to be expected as such operations were not feasible even the high resolution neutron powder diffraction data (i.e. simultaneous refinement of the aforementioned parameters). Therefore, a more conservative approach was used for the Rietveld analysis of the CMR XRD-CT data. For every XRD-CT dataset, Rietveld analysis was performed using the summed diffraction pattern (pixels corresponding to BCFZ membrane only) in order to have a good starting model before performing the Rietveld analysis of the XRD-CT data. The occupancy of Ba, Co, Fe and Zr was kept constant to 1, 0.4, 0.4 and 0.2 respectively (i.e. as in the initial BCFZ structure model). Also, the thermal parameter of Fe was tied to Co (i.e. hard constraint). Consequently, the number of parameters being

refined decreased and this strategy led to a relatively stable refinement, as implied from the results presented in Figure 27.

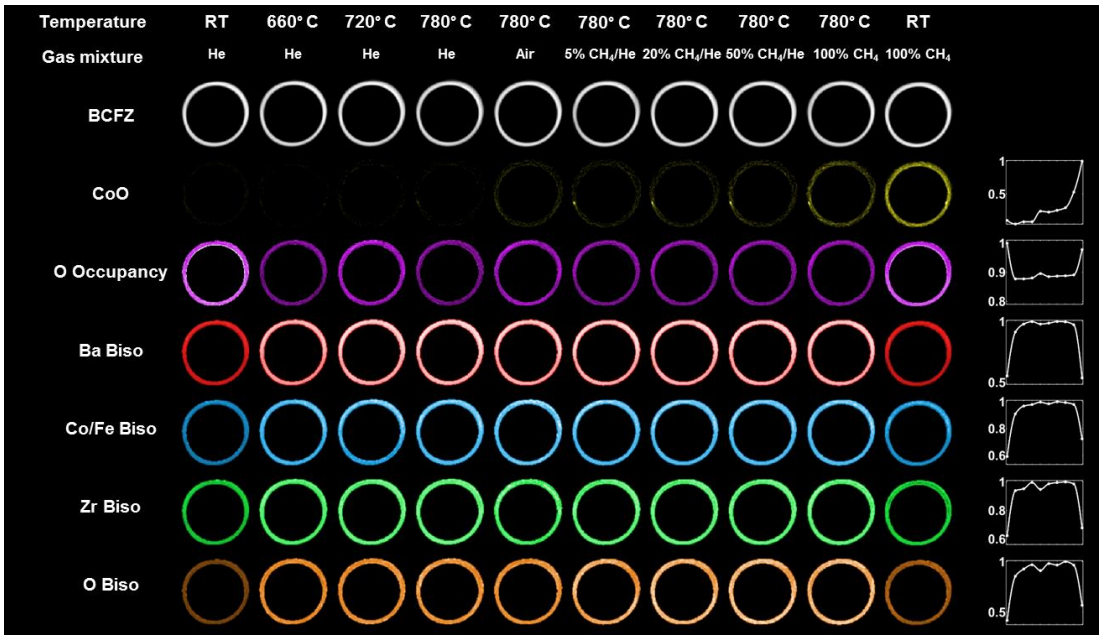

Figure 27: First and second row: Phase distribution maps of BCFZ and CoO, Third row: Oxygen occupancies in the BCFZ unit cell, Fourth to seventh row: Maps corresponding to the thermal parameters of Ba, Co/Fe, Zr and O of the BCFZ unit cell.

The relative change of each parameter, as determined from the integrated intensities for each XRD-CT 'slice', is shown at the right side of Figure 27. As mentioned previously, there were changes observed in the BCFZ relative peak intensities during the *in situ* XRD-CT experiment (Figure 8). However, these changes can now be rationalised using the BCFZ structure model. As shown in Figure 27, not only the thermal parameters of Ba, Fe/Co, Zr and O increase with increasing temperature but also the oxygen vacancies (oxygen occupancies are decreased). More importantly though, the values of these various parameters are seen to be homogeneous for every XRD-CT dataset. This is clearly shown in the maps corresponding to the aforementioned parameters (Ba, Fe/Co, Zr and O Biso and O occupancy) presented in Figure 27. Identical is the case of the BCFZ unit cell parameter as shown in Figure 28.

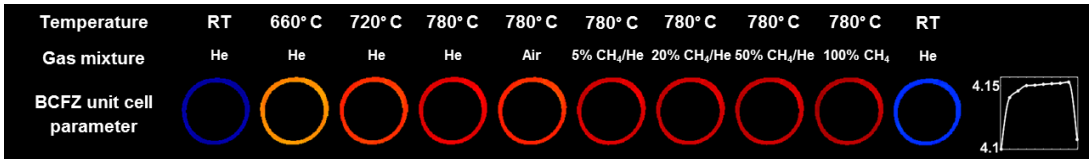

Figure 28: Maps corresponding to the BCFZ unit cell parameter under during the OCM experiment.

This means that there are not significant variations in the values of these parameters spatially but only when different operating conditions are applied. The changes as a function of temperature were already mentioned. Unfortunately, the changes when different chemical environments were applied while maintaining the temperature constant were not statistically significant to mention (the BCFZ diffraction patterns are essentially identical). However, the author is convinced that such changes can potentially be tracked by applying longer acquisition times and collecting higher quality XRD-CT data.

BCFZ membrane with La-Mn-Na-W/SiO_2 catalyst

As mentioned previously, the same experimental protocol was followed for all the *operando* CMR XRD-CT experiments. Initially, an XRD-CT scan of the BCFZ – 2 % La-2 % Mn-1.6 % Na-3.1 % W/SiO_2 CMR was performed at ambient conditions. The phase distribution maps of the various crystalline phases, as obtained from the Rietveld analysis (scale factors) of the XRD-CT data, are presented in Figure 29. As expected, the two crystalline SiO_2 phases, cristobalite and tridymite, follow a uniform distribution over the catalyst particles. The Na_2WO_4 phase is also present in all catalyst particles but mainly concentrated near the surface of the particles. On the contrary, the Mn_2O_3/Mn_7SiO_{12} phase is seen to be homogeneously. As expected, these results are in full agreement with the XRD-CT results of the 2 % La-2 % Mn-1.6 % Na-3.1 % W/SiO_2 fixed bed reactor experiments presented in the previous chapter (Figures 20 and 21 in Chapter 5). Unfortunately, the $La_4Mn_5O_{22}Si_4$ phase could not be observed in the CMR XRD-CT data as the signal-to-noise ratio was worse compared to the fixed bed reactor experiments. However, it was previously shown that this is only a minor phase which disappears with time under the high temperatures required for the OCM reaction.

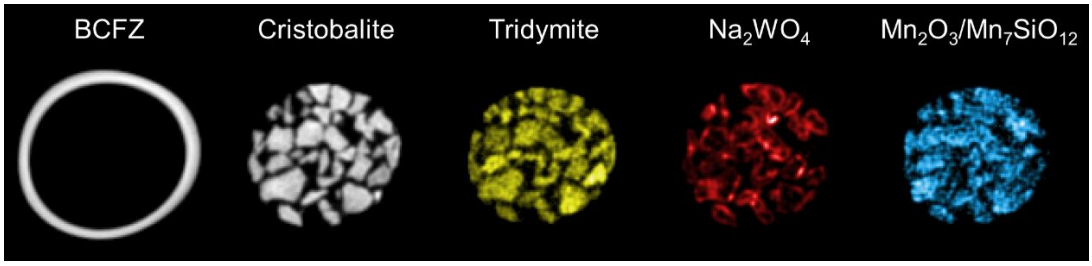

Figure 29: Phase distribution maps created based on the values of the scale factors of the crystalline phases present in the CMR (CMR XRD-CT data collected at room temperature)

The next three XRD-CT scans were performed at 660, 720 and 780 °C respectively. As in the case of the previous CMR experiment, inspection of the reconstructed XRD-CT data (cristobalite XRD-CT images) revealed that the high temperature XRD-CT scans were performed at a different position compared to the room temperature scan due to thermal expansion/movement of the CMR during heating. As a result, the XRD-CT data collected at high temperatures cannot/should not be directly compared with the XRD-CT data acquired at room temperature. The results from the Rietveld analysis of the high temperature XRD-CT data collected at the same position (i.e. XRD-CT 'slices' at a constant position of the CMR) are presented in Figure 30. These phase distribution maps correspond to the values of the corresponding (normalized) scale factors, as obtained from the Rietveld analysis of the XRD-CT data. The relative change of each phase, as determined from the integrated intensities for each XRD-CT dataset, is presented at the right side of Figure 30.

As expected, in accordance to the *operando* XRD-CT experiments of the fixed bed reactor with the same catalyst (Chapter 5), there is an evolution of SiO_2 support at high temperatures. This phenomenon was thoroughly discussed previously and it was attributed to the presence of mobile Na^+ species. The unexpected high concentrations of cristobalite and tridymite at 660 °C (compared to the other high temperature XRD-CT datasets) is explained by the fact that the CMR did not fully stabilize before reaching 780 °C. This can be seen after inspecting the cristobalite phase distribution maps presented in Figure 30 which suggest that the XRD-CT scan performed at 660 and 720 °C probed different positions of the CMR (i.e. with respect to all the XRD-CT data collected at 780 °C). The results obtained from the XRD-CT scans performed at the same position are though consistent with that which has been observed previously; namely that there is an initial increase in the presence of

cristobalite at 780 °C but that this is gradually consumed under OCM operating conditions while the tridymite and quartz phases increase as a function of time.

The Mn_2O_3/Mn_7SiO_{12} phase is seen to increase in the presence of air which is also consistent with was observed in the BCFZ – 2 % Mn-1.6 % Na-3.1 % W/SiO_2 CMR. The concentration of the Mn_2O_3/Mn_7SiO_{12} phase is though seen to decrease with time under OCM reaction conditions, especially when CH_4 rich (i.e. > 20 % CH_4/He) reaction mixtures are used. This result is in full agreement with what was observed in the *operando* 2 % La-2 % Mn-1.6 % Na-3.1 % W/SiO_2 fixed bed reactor XRD-CT experiments presented in the previous chapter (Figure 20 in Chapter 5). In these experiments, the Mn_2O_3/Mn_7SiO_{12} and $La_4Mn_5Si_4O_{22}$ phases were seen to decrease with time under OCM reaction conditions in favour of the formation and growth of the $NaLa(WO_4)_2$ phase.

However, in the CMR, there is a delay in the formation and growth of the $NaLa(WO_4)_2$ phase and this is attributed to the direct chemical interaction between the catalyst particles and the BCFZ membrane (formation of $BaWO_4$) and the subsequent loss of WO_4^{-2} species. It should be emphasized though that there is a delay in the growth of the $BaWO_4$ phase too when compared to the BCFZ – 2 % Mn-1.6 % Na-3.1 % W/SiO_2 CMR (Figure 18). $BaWO_4$ is seen to be present only at specific regions (hotspots in Figure 30) for several hours at high temperatures (each XRD-CT lasted approximately 45 min) before forming a uniform “ring” at the inner BCFZ membrane wall. This delay could be attributed to the presence of the La species in the catalyst particles. The aforementioned results are more apparent in the 3D-XRD-CT data presented in Figure 31.

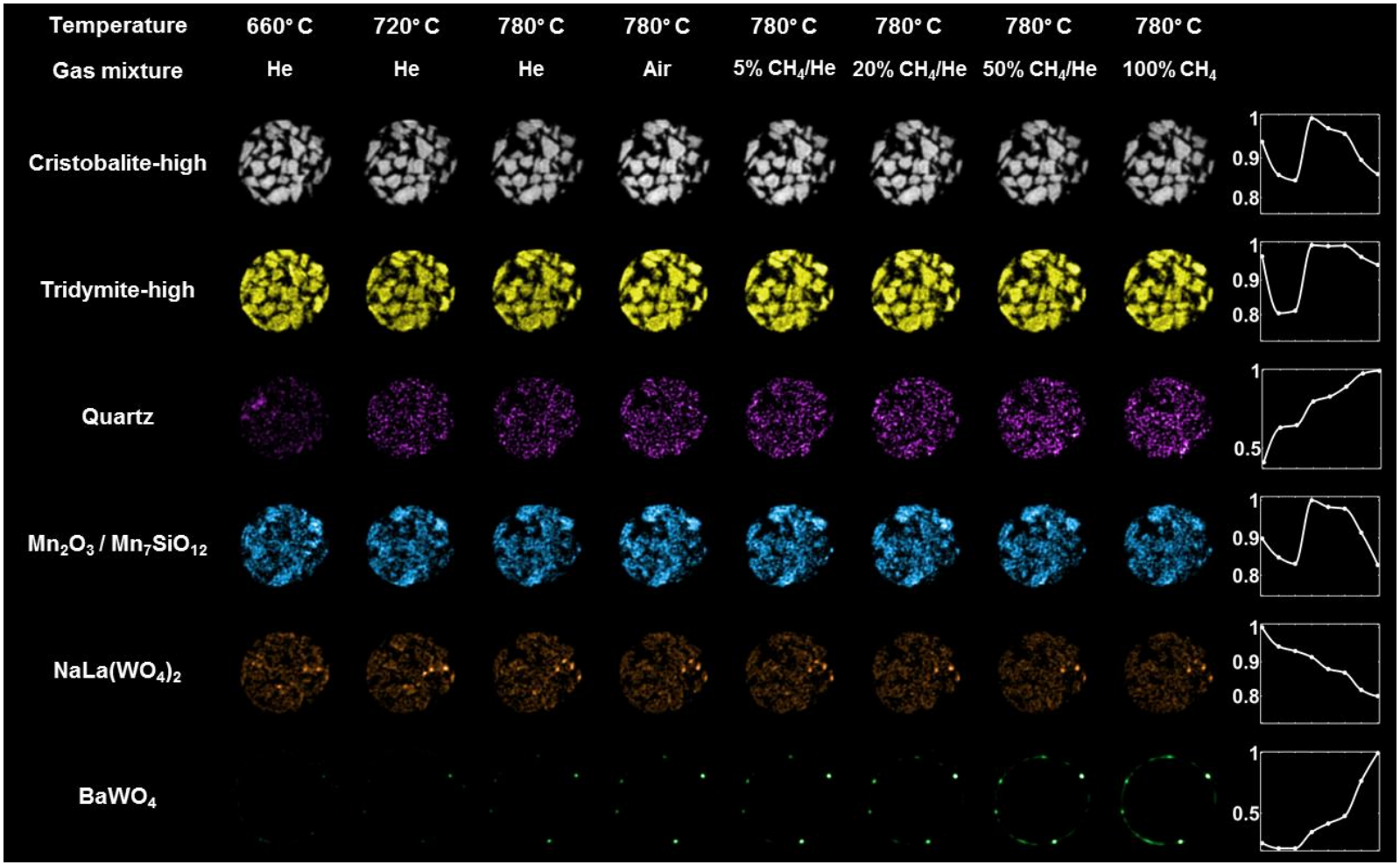

Figure 30: Phase distribution maps of Cristobalite, Tridymite, Quartz, Mn_2O_3/Mn_7SiO_{12}, $NaLa(WO_4)_2$ and $BaWO_4$ at high temperatures during the OCM experiment. At the right side, the relative change of each phase, as determined from the integrated intensities for each XRD-CT 'slice', is presented.

As in the previous CMR experiment, 3D-XRD-CT was performed under OCM reaction conditions by collecting 10 XRD-CT 'slices' at different positions along the reactor (i.e. 25 µm apart) at 780 °C (flow rate of 100 ml min^{-1} of 100 % CH_4 at the inner side of the BCFZ membrane, through the catalyst bed). The phase distribution maps presented in Figure 31 correspond to the scale factors (normalised to the maximum value) as obtained from the Rietveld analysis of the 3D-XRD-CT data.

As mentioned previously, these XRD-CT data should not be directly compared it as they correspond to different sample volumes. If the solid state changes taking place in the CMR were only a function of position (spatial dependence only), then the observation points shown on the right side of Figure 31 should not follow any specific trend. These plots correspond to the summed intensity of the various scale factors (normalised to the maximum value) as obtained from the Rietveld analysis of the 3D-XRD-CT data. However, for some crystalline phases there is a clear trend (even linear in some cases) indicating that some of the solid state changes can be tracked as a function of time (temporal dependence). For example, it can be clearly seen that cristobalite decreases with time while tridymite and quartz increase. More importantly though, there is a continuous growth of both the $NaLaWO_4$ and $BaWO_4$ phases. This indicates that the formation/growth of $NaLaWO_4$ is not completely prevented by the formation/growth of $BaWO_4$. This is a key result as it implies that if the catalyst is thermally treated (e.g. extended calcination periods) prior to its insertion in the CMR in order to convert the Na_2WO_4 to $NaLa(WO_4)_2$, then the formation/growth of $BaWO_4$ could be potentially supressed.

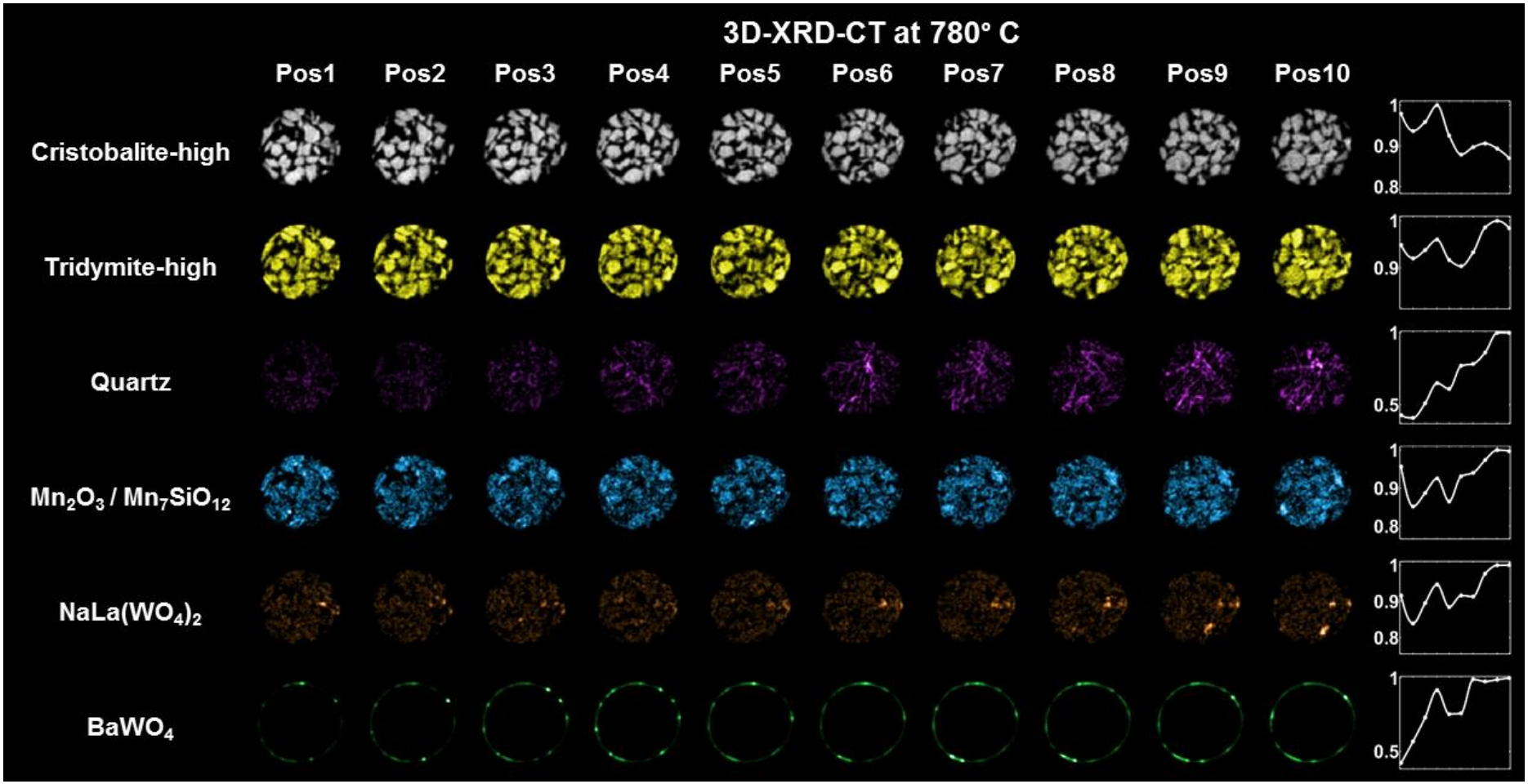

Figure 31: Phase distribution maps of Cristobalite, Tridymite, Quartz, Mn_2O_3/Mn_7SiO_{12}, $NaLa(WO_4)_2$ and $BaWO_4$ as obtained from the Rietveld analysis of the 3D-XRD-CT data (each XRD-CT "slice" is 25 µm apart from the next). 100 ml min^{-1} of 100 % CH4 was used at the inner side of the membrane through the catalyst bed and 100 ml min^{-1} air at the outer side of the BCFZ membrane

The results from the volume rendering of the scale factors data volume (phase distribution volumes) are presented in Figure 32. The scale factors were normalised with respect to the maximum value for each data volume and the colour axes were scaled accordingly in order to improve the contrast of the respective figures. As expected, the various crystalline SiO_2 phases are present in all catalyst particles.

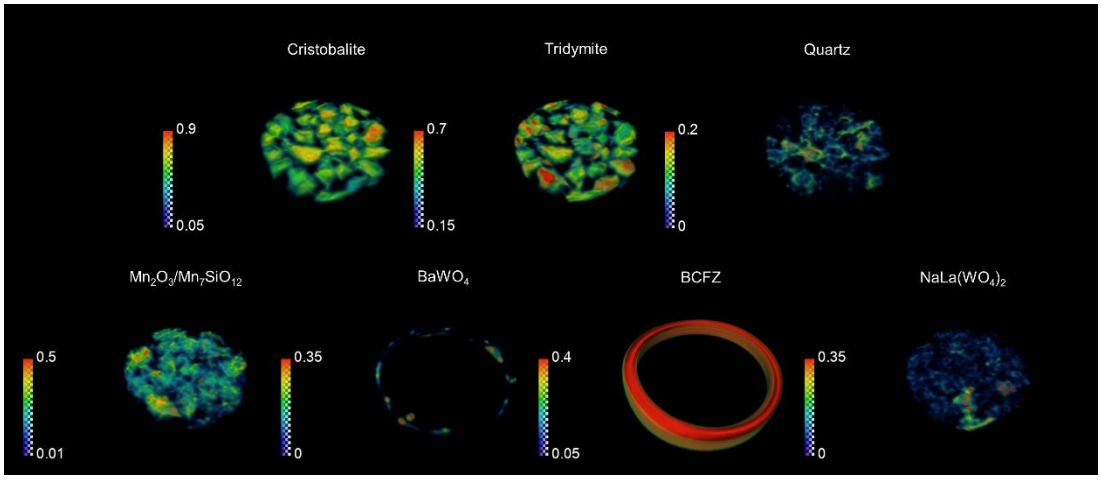

Figure 32: Volume rendering of the scale factors data volume (phase distribution volumes) obtained from the Rietveld analysis of the 3D-XRD-CT data

As expected, in contrast to the unpromoted catalyst (Figure 20), the Mn_2O_3/Mn_7SiO_{12} phase in the La-promoted catalyst is seen to be homogeneously distributed over all catalyst particles probed during the 3D-XRD-CT scan. The $BaWO_4$ phase is present in all XRD-CT datasets but it can also be observed that there are regions of high $BaWO_4$ concentration (hotspots). These hotspots are located at the interface between the catalyst particles and the inner BCFZ membrane wall. This is more apparent in the coloured image shown in Figure 33 where the phase distribution maps of Na_2WO_4, $BaWO_4$ and $NaLa(WO_4)_2$ (red colour for Na_2WO_4, green colour for $BaWO_4$ and blue colour for $NaLa(WO_4)_2$) have been overlaid on top of a grayscale image derived from the phase distribution maps of cristobalite and BCFZ. These phase distribution maps were derived from the Rietveld analysis of the XRD-CT data collected at room temperature after the OCM experiment. The $NaLa(WO_4)_2$ phase is seen to be present in all catalyst particles but the fact that the Na_2WO_4 phase is seen to partially reform upon cooling to room temperature after the OCM experiment proves that it was not fully converted to the $NaLa(WO_4)_2$ phase at high temperatures.

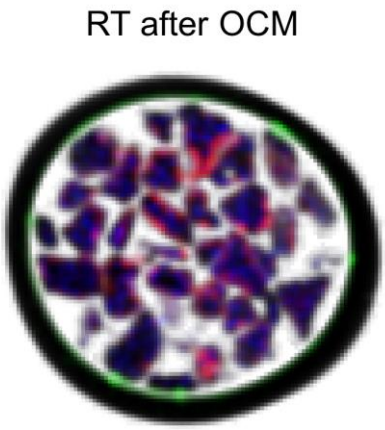

Figure 33: In this RGB image, the phase distribution maps of Na_2WO_4, $BaWO_4$ and $NaLa(WO_4)_2$ (red colour for Na_2WO_4, green colour for $BaWO_4$ and blue colour for $NaLa(WO_4)_2$) have been overlaid on top of a grayscale image derived from the phase distribution maps of cristobalite and BCFZ.

In contrast to the previous CMR experiment, the XRD-CT data acquired at room temperature after the OCM experiment did not probe the same sample volume as the XRD-CT data before the experiment (different position in the CMR). This means that these two datasets should not be directly compared in terms of quantitative analysis but can provide a good indication of the solid-state changes that took place in the CMR during the OCM experiment.

In Figure 34, the phase distribution maps of various crystalline phases from the XRD-CT datasets are presented. These datasets correspond to the following XRD-CT scans: room temperature before the OCM experiment, at 780 °C under 100 % CH_4 flow (inner side of BCFZ membrane) and room temperature scan after the OCM experiment. It should be noted that the high temperature XRD-CT scan was performed at the same CMR position as the room temperature XRD-CT scan before the OCM experiment.

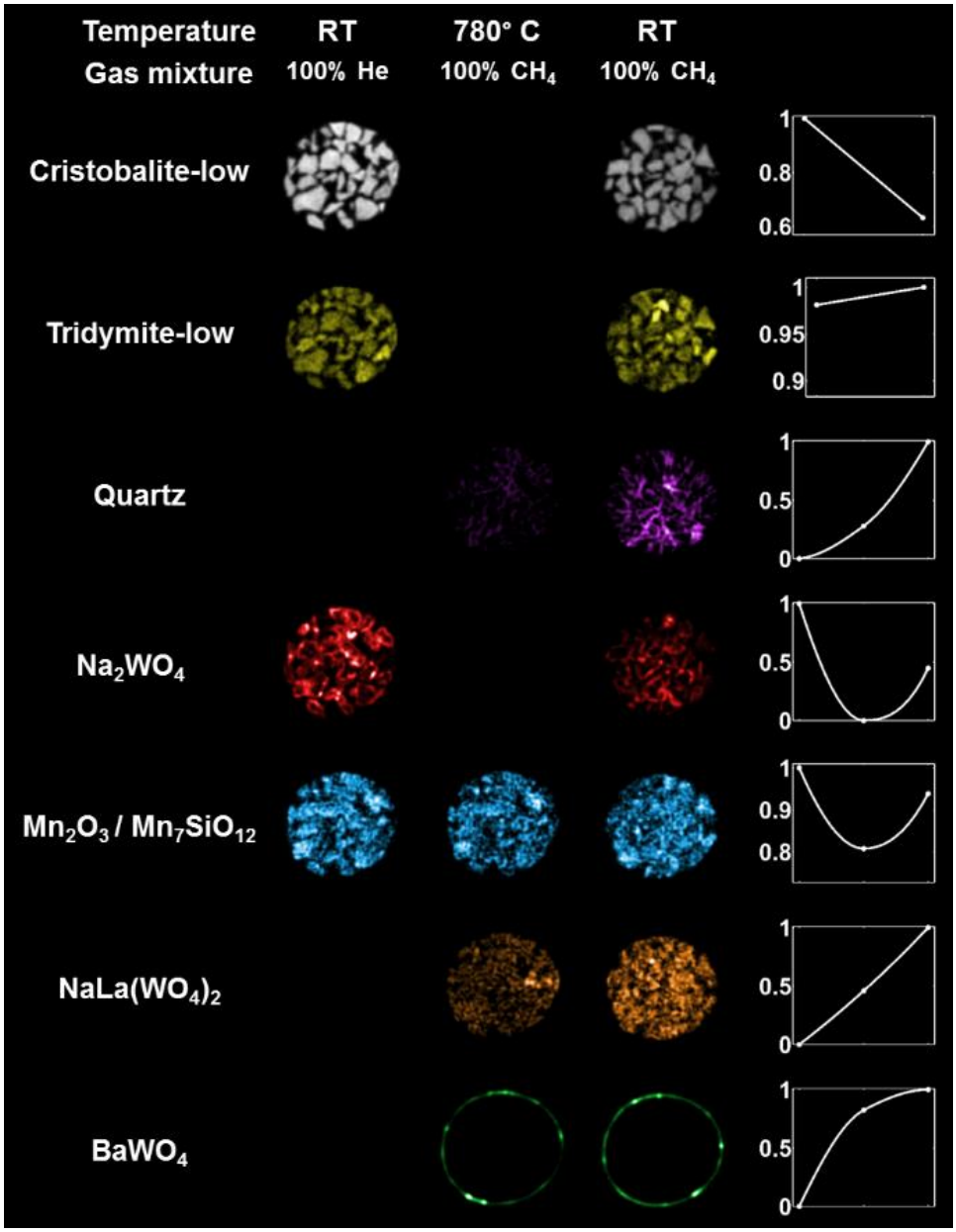

Figure 34: Phase distribution maps of Cristobalite, Tridymite, Quartz, Na_2WO_4, Mn_2O_3/Mn_7SiO_{12}, $NaLa(WO_4)_2$ and $BaWO_4$ at room temperature before the OCM experiment, at high temperatures during the OCM experiment and at room temperature after the OCM experiment. At the right side, the relative change of each phase, as determined from the integrated intensities for each XRD-CT 'slice', is presented.

It can be seen that the evolution of the SiO_2 support is consistent with what has been observed in the previous CMR experiment (consumption of cristobalite and consequent growth of tridymite and quartz). As it was also shown in Figure 33, Na_2WO_4 reforms upon cooling to room temperature after the OCM experiment. Of course, the concentration of Na_2WO_4 is lower compared to the fresh catalyst as both $NaLa(WO_4)_2$ and $BaWO_4$ formed/grew during the operation of the CMR. The fact that the $NaLa(WO_4)_2$ phase was seen not only to form but also to increase at high

temperatures in this CMR (Figure 31 and Figure 34) suggests that the $NaLa(WO_4)_2$ is chemically stable under these conditions. This means that not only the La species can stabilise the mobile WO_4^{-2} species but it is also implied that if $NaLa(WO_4)_2$ is the only Na-W containing phase in the fresh catalyst (no Na_2WO_4) then the catalyst may be stable the formation/growth of $BaWO_4$ can be supressed and maybe even completely prevented.

As in the case of the previous CMR, the BCFZ structure was also added to the Rietveld refinement and the results are presented in Figure 35. As previously, the parameters refined were the following: a) BCFZ lattice parameter, b) thermal parameters of Ba, Co/Fe (hard constraint), Zr and O and c) O occupancies. As expected, the summed diffraction patterns at 780 °C exported from the BCFZ membrane pixels are essentially identical (as in the previous CMR). This means that the BCFZ structure related changes as a function of time/chemical environment at 780 °C are statistically insignificant.

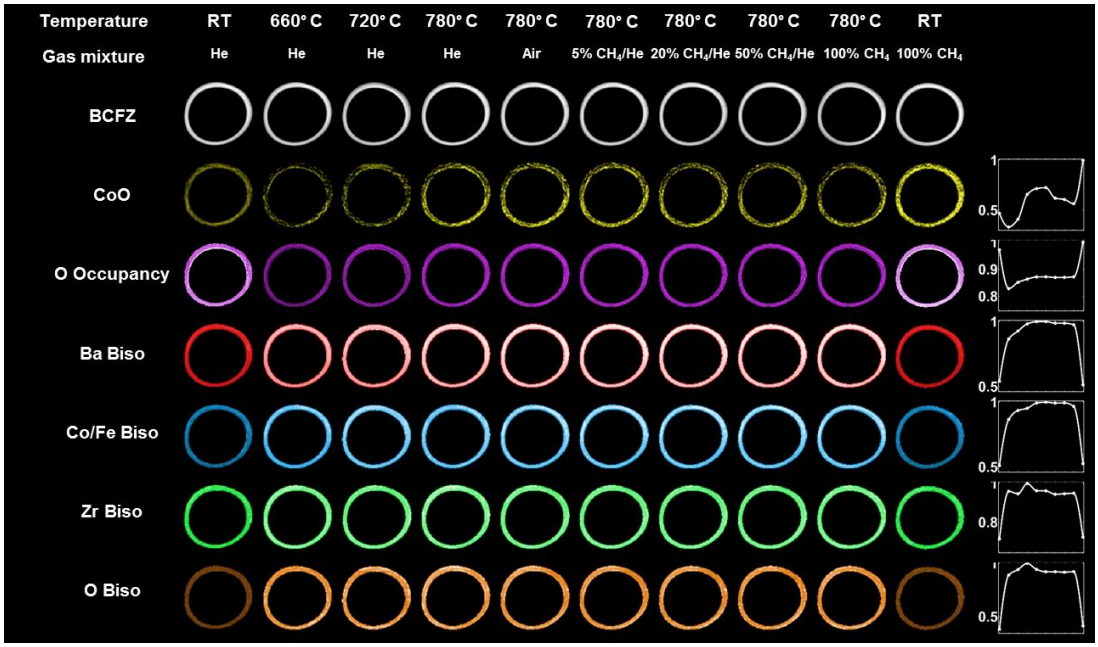

Figure 35: First and second row: Phase distribution maps of BCFZ and CoO, Third row: Oxygen occupancies in the BCFZ unit cell, Fourth to seventh row: Maps corresponding to the thermal parameters of Ba, Co/Fe, Zr and O of the BCFZ unit cell.

However, it can be clearly seen in Figure 35 that the distribution of all the aforementioned parameters is homogeneous in the BCFZ membrane which is consistent with was observed in the previous CMR experiment (Figure 27). The

relative change of each parameter, as determined from the integrated intensities for each XRD-CT 'slice', is shown at the right side of Figure 35. The thermal parameters of the various atoms present in the BCFZ structure are seen to increase with increasing temperature and the O occupancies decrease (more O vacancies present at high temperatures). The maps shown in Figure 36 correspond to the BCFZ unit cell parameter and it can be seen that they are also homogeneous and change only as a function of temperature.

It should also be pointed out that shape and size of the BCFZ membrane did not change during the OCM experiment and no cracks were formed. However, the formation and growth of CoO is observed again showing that the results obtained from the previous CMR experiment are directly reproducible (Figure 27). The CoO is only a minor phase present in the diffraction patterns (which could have been easily neglected) but it suggests there may be issues regarding the long term chemical stability of BCFZ under OCM operating conditions.

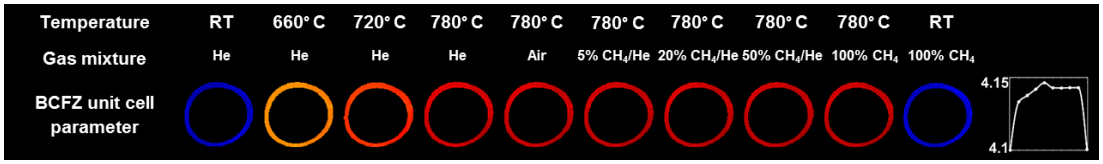

Figure 36: Maps corresponding to the BCFZ unit cell parameter under during the OCM experiment.

LSCF membrane with La-Mn-Na-W/SiO_2 catalyst

The last CMR experiment was performed using a $La_{0.6}Sr_{0.4}Co_{0.2}Fe_{0.8}O_3$ (LSCF) membrane and the 2 % La-2 % Mn-1.6 % Na-3.1 % W/SiO_2 catalyst. The same experimental protocol was followed as in the other CMR experiments. Unfortunately, the quality of the LSCF – 2 % La-2 % Mn-1.6 % Na-3.1 % W/SiO_2 CMR data was significantly inferior compared to the other CMR data. More specifically, the raw diffraction data suffered from saturation. This is clearly shown in Figure 37 where a summed 2D diffraction pattern derived from a line scan of the LSCF CMR XRD-CT data collected at room temperature is shown. For comparison reasons, also shown is a corresponding 2D diffraction pattern derived from a line scan of the BCFZ CMR XRD-CT data collected at room temperature (same colour axis for both images).

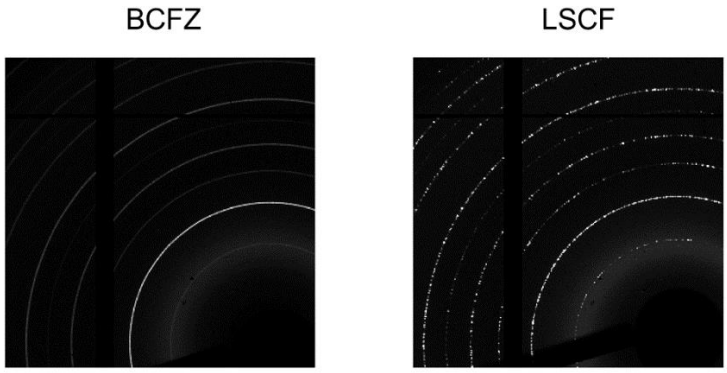

Figure 37: Summed 2D diffraction patterns derived from a line scan of the CMR XRD-CT data collected at room temperature. Left: BCFZ – 2%La-2%Mn-1.6%Na-3.1%W/SiO_2 CMR, Right: LSCF – 2%La-2%Mn-1.6%Na-3.1%W/SiO_2 CMR

Apart from the presence of large grains in the LSCF membrane that led to the formation of spots (single-crystal diffraction) on top of the powder diffraction data (Figure 37), the LSCF – La-Mn-Na-W/SiO_2 XRD-CT data severely suffered from self-absorption problems too. The LSCF membrane wall thickness used in this experiment was significantly larger compared to the BCFZ membranes (180-200 µm for the BCFZ membrane and 180-300 µm for the LSCF membrane). This is apparent on the left side of Figure 38 where the summed image from the channels (ca. Q = 2.28-2.95 $Å^{-1}$) corresponding to the highest LSCF intensity peak is shown (reflections (110) and (104)). For comparison reasons, also shown is the LSCF map corresponding to the respective scale factor as obtained from the Rietveld analysis of the filtered (10% trimmed mean) and self-absorption corrected XRD-CT data. It can be clearly seen that without the aforementioned corrections, the size and shape of the LSCF membrane cannot be defined.

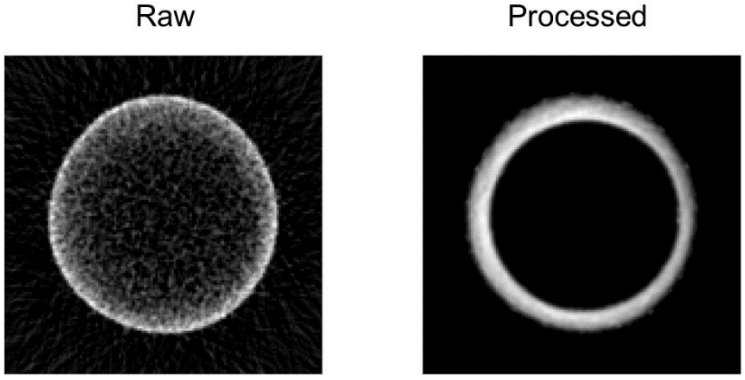

Figure 38: Left: Summed image from XRD-CT reconstructed data corresponding to the highest intensity LSCF peak (reflections (110) and (104)). Right: LSCF map corresponding to the respective scale factor as obtained from the Rietveld analysis of the filtered (10% trimmed mean) and self-absorption corrected XRD-CT data. Both images are derived from the same XRD-CT dataset.

It should be noted though that the relative intensities of the LSCF peaks change significantly from pixel to pixel. This is due to the very spotty 2D diffraction patterns and no filter can completely eradicate these artefacts. The only way to overcome this problem would have been to increase the size of the focused X-ray beam but this would also have also led to lower spatial resolution XRD-CT images. It should also be noted that the simple peak fitting (for the LSCF peaks) can also not provide homogeneous (in terms of intensity) LSCF maps. However, the Rietveld analysis (ICSD: 186173 for LSCF CIF) of the XRD-CT data overcame this issue and provided clear LSCF phase distribution maps where the LSCF membrane is well defined in both size and shape.

In Figure 39, the phase distribution maps of the various crystalline phases present in the CMR are shown. These maps correspond to the corresponding (normalised) scale factors as obtained from the Rietveld analysis of the XRD-CT data collected at room temperature. In accordance to what was been observed before, the cristobalite and tridymite phases are present in all catalyst particles. Similar is the case for the Na_2WO_4 phase which is mainly present near the surface of the catalyst particles while the Mn_2O_3/Mn_7SiO_{12} phase is homogenously distributed over the catalyst particles.

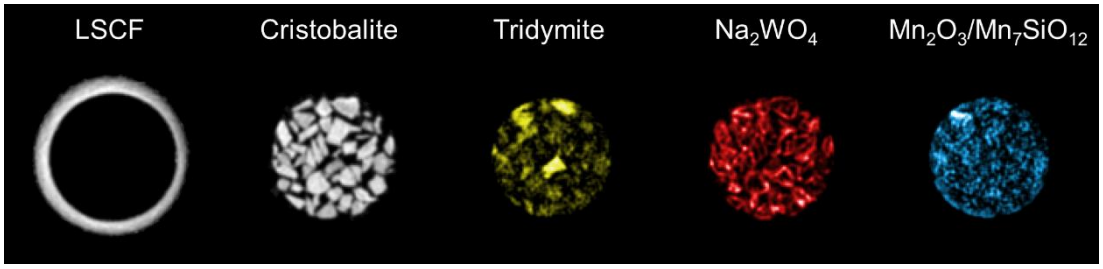

Figure 39: Phase distribution maps created based on the values of the scale factors of the crystalline phases present in the CMR (CMR XRD-CT data collected at room temperature)

As in the previous two CMR experiments, the thermal expansion of the LSCF membrane resulted in probing different sample volumes at high temperatures compared to the room temperature XRD-CT scan. The results from the high temperature XRD-CT data, collected at the same position, are presented in Figure 40. The phase distribution maps shown in Figure 40 correspond to the values of the corresponding scale factors, normalised with respect to the maximum value, as

obtained from the Rietveld analysis of these XRD-CT datasets. The relative change of each phase is plotted on the right side of Figure 40.

As expected, the cristobalite phase decreases with time at the high temperatures applied for the OCM experiment while tridymite is seen to be fairly stable and quartz significantly increases. As shown previously, the Mn_2O_3/Mn_7SiO_{12} phase is seen to increase when air is used as the inlet gas mixture through the catalyst bed but then decreases with time under OCM reaction conditions. There is again a delay in the formation/growth of the $NaLa(WO_4)_2$ phase and in this case it is attributed to the formation and growth of a new phase that was identified as $SrWO_4$ (Figure A16 in the Appendix). As in the case of the BCFZ CMRs, the mobile/volatile species are seen to chemically interact with the ceramic membrane. It can be seen that the $SrWO_4$ phase increases with time at high temperatures, eventually forming a uniform layer at the inner LSCF membrane wall, as in the case of the $BaWO_4$ phase in the BCFZ CMRs. This is the key result of this experiment as it proves that the main drawback of the three CMRs is related to the unstable W containing species present at the catalyst at high temperatures.

As in the previous two CMR experiments, 3D-XRD-CT was also performed at 780 °C while maintaining the OCM reaction mixtures constant (100 ml min^{-1} of 100 % CH_4 at the inner side of the membrane through the catalyst bed and 100 ml min^{-1} air at the outer side of the LSCF membrane). The results from the Rietveld refinement of the 3D-XRD-CT data are presented in Figure 41. It can be seen that there is a continuous consumption of cristobalite and growth of quartz which in full agreement with what has been observed in the previous experiments. It should also be noted that the $SrWO_4$ phase is also seen to continuously grow as a function of time which is identical to the behaviour of the $BaWO_4$ phase in the BCFZ CMRs.

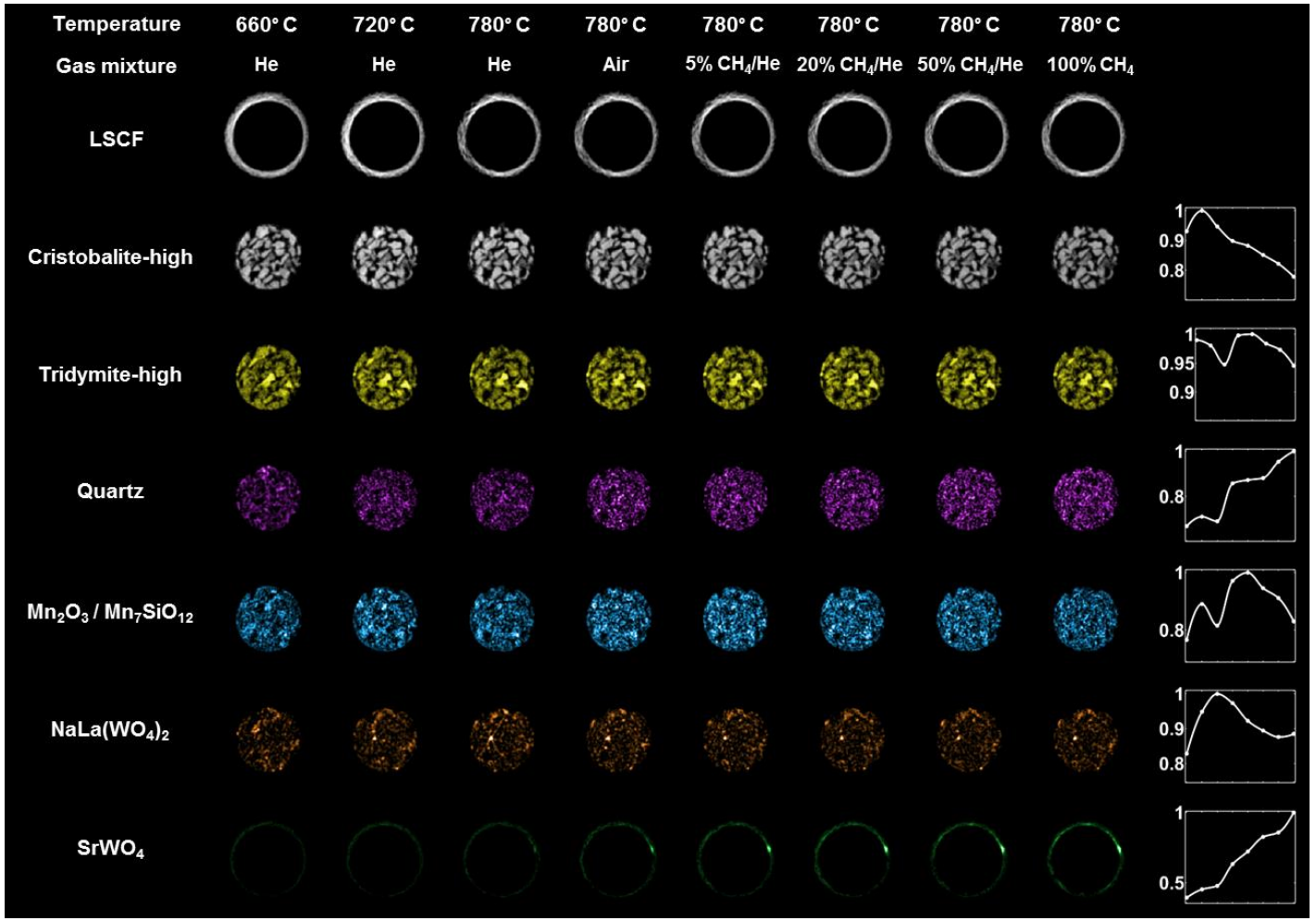

Figure 40: Phase distribution maps of LSCF, Cristobalite, Tridymite, Quartz, Mn_2O_3/Mn_7SiO_{12}, $NaLa(WO_4)_2$ and $BaWO_4$ at high temperatures during the OCM experiment. At the right side, the relative change of each phase, as determined from the integrated intensities for each XRD-CT 'slice', is presented.

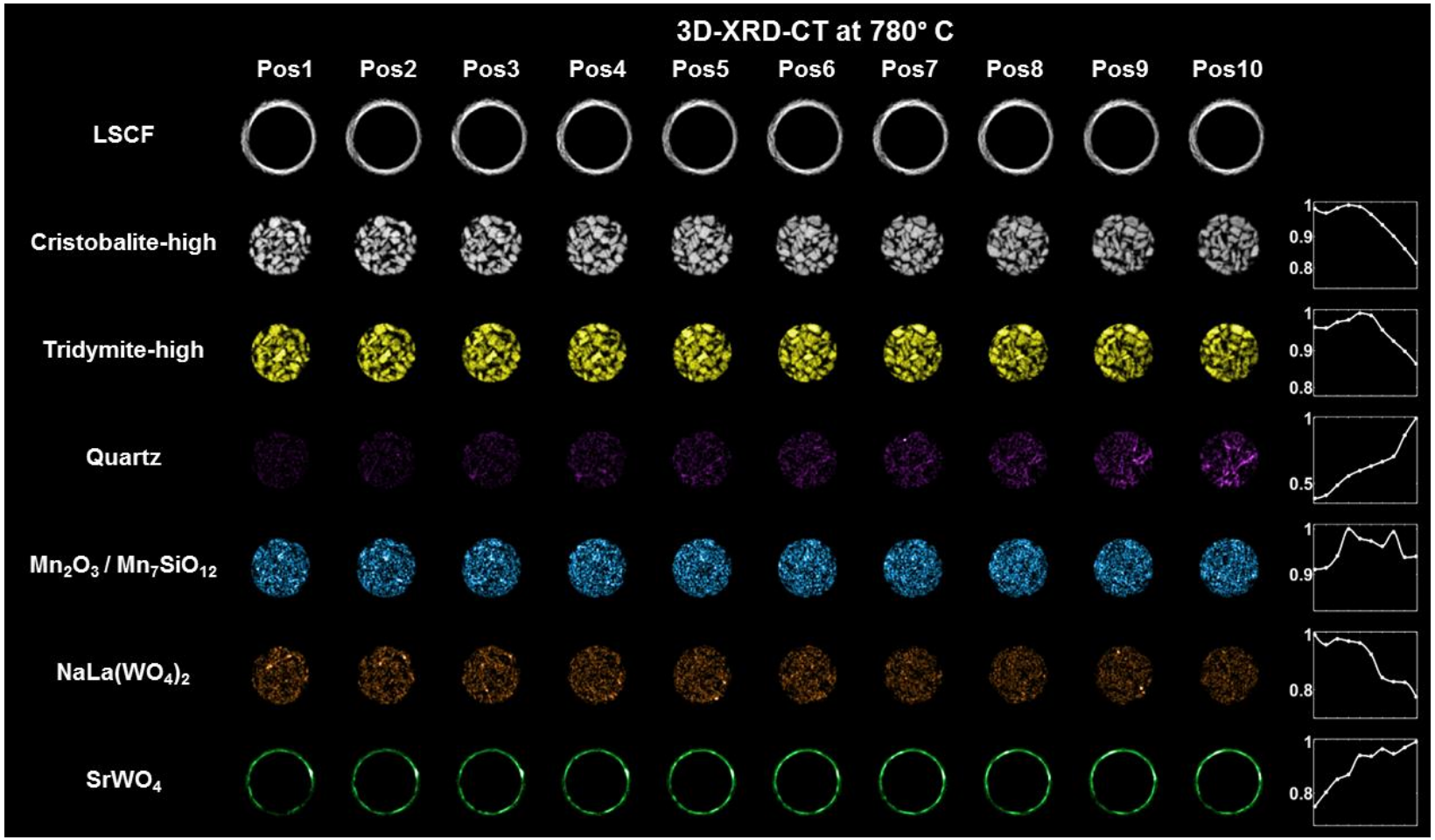

Figure 41: Phase distribution maps of LSCF, Cristobalite, Tridymite, Quartz, Mn_2O_3/Mn_7SiO_{12}, $NaLa(WO_4)_2$ and $BaWO_4$ as obtained from the Rietveld analysis of the 3D-XRD-CT data (each XRD-CT "slice" is 25 µm apart from the next). Flow rate of 100 ml min^{-1} of 100 % CH4 was used at the inner side of the membrane through the catalyst bed and 100 ml min^{-1} air at the outer side of the BCFZ membrane.

The results from the volume rendering of the 3D-XRD-CT data are presented in Figure 42. As expected, the three crystalline SiO_2 phases (cristobalite, tridymite and quartz) are homogeneously distributed over the catalyst particles. Similar is the case for the Mn_2O_3/Mn_7SiO_{12} phase which is in full agreement with the results obtained from BCFZ CMR containing the same catalyst. The $NaLa(WO_4)_2$ phase is seen to be present in most catalyst particles indicating that the formation/growth of the $SrWO_4$ phase only delays but does not prevent its evolution.

It should be noted though that no cracks formed in the LSCF membrane and no other La, Sr, Co or Fe containing phases were observed during the OCM experiment (apart from the $SrWO_4$ phase). This is in contrast to what was observed in the BCFZ CMRs where the Co was seen to leave the BCFZ unit cell and form CoO. This result indicates that the LSCF membrane is more chemically stable under OCM reaction conditions compared to the BCFZ membrane.

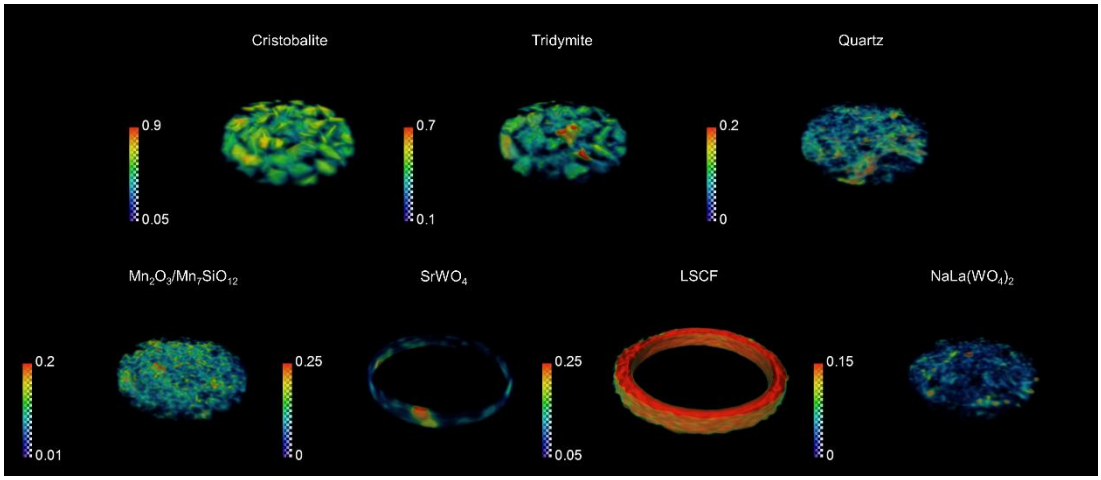

Figure 42: Volume rendering of the scale factors data volume (phase distribution volumes) obtained from the Rietveld analysis of the 3D-XRD-CT data

Finally, the results from the Rietveld analysis of three XRD-CT datasets collected at the same position are presented in Figure 43. These datasets correspond to XRD-CT data collected at room temperature before the OCM experiment, at 780 °C under 100 % CH_4 flow and at room temperature after the OCM experiment.

In accordance to what was previously observed, cristobalite is seen to have been partially consumed by the end of the OCM experiment while tridymite and quartz have grown. The Mn_2O_3/Mn_7SiO_{12} phase is seen to decrease with time under OCM

reaction conditions which in agreement with what has been previously observed (behaviour of the La-promoted catalyst under OCM reaction conditions). The Na_2WO_4 is seen to be present at the room temperature XRD-CT scan after the OCM experiment. However, its concentration is significantly lower as both $SrWO_4$ and $NaLa(WO_4)_2$ formed and grew during the operation of the CMR.

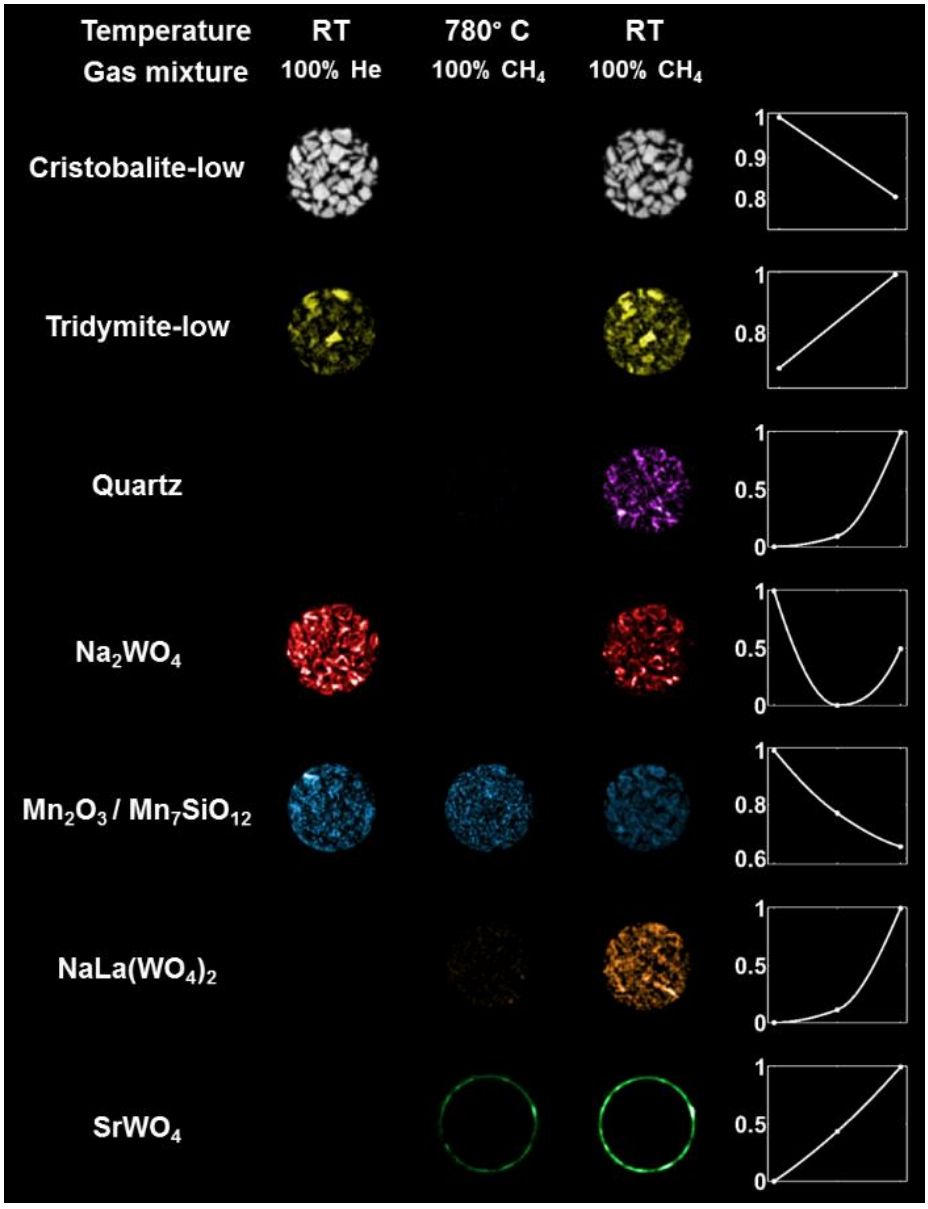

Figure 43 Phase distribution maps of Cristobalite, Tridymite, Quartz, Na_2WO_4, Mn_2O_3/Mn_7SiO_{12}, $NaLa(WO_4)_2$ and $SrWO_4$ at room temperature before the OCM experiment, at high temperatures during the OCM experiment and at room temperature after the OCM experiment. At the right side, the relative change of each phase, as determined from the integrated intensities for each XRD-CT 'slice', is presented.

The replacement of Na_2WO_4 by the $NaLa(WO_4)_2$ phase is also illustrated in Figure 44 where two RGB images have been overlaid on top of two grayscale image derived

from the phase distribution maps of cristobalite and LSCF (XRD-CT scans collected at room temperature before and after the OCM experiment). In most of the sample regions where the Na_2WO_4 phase was present in the fresh catalyst (red colour in Figure 44), the $NaLa(WO_4)_2$ phase is present in the spent catalyst (blue colour). It can finally be clearly seen that regions of high $SrWO_4$ concentration (green hotspots) are located at the interface between the LSCF membrane and the catalyst particles. This result is identical to what was observed in the BCFZ CMRs and the corresponding $BaWO_4$ phase.

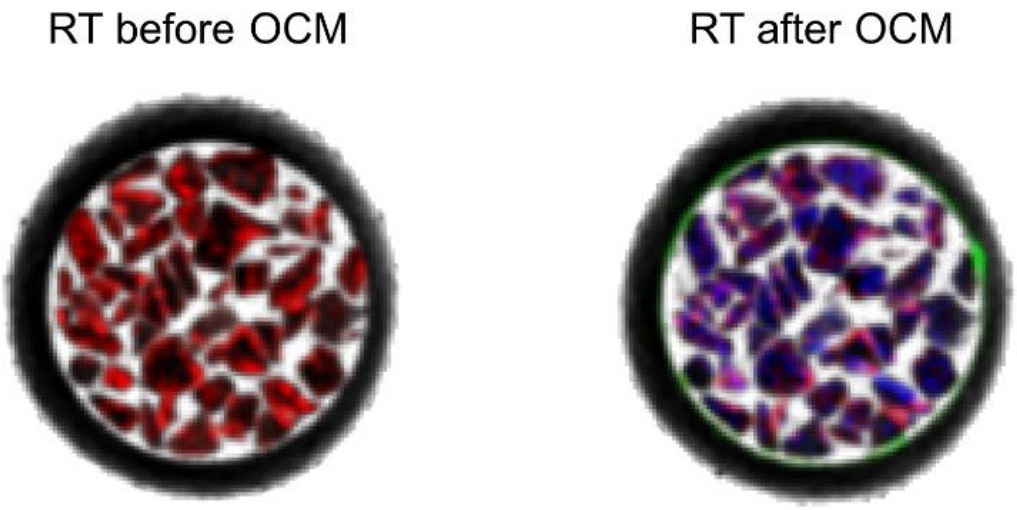

Figure 44: In these RGB images, the phase distribution maps of Na_2WO_4, $SrWO_4$ and $NaLa(WO_4)_2$ (red colour for Na_2WO_4, green colour for $SrWO_4$ and blue colour for $NaLa(WO_4)_2$) have been overlaid on top of a grayscale image derived from the phase distribution maps of cristobalite and LSCF.

Summary and Conclusions

Catalytic membrane reactors have the potential to render the process of oxidative coupling of methane to produce ethylene economically viable. For example, two of the highest values for C_2 yield (>35%) ever reported in literature have been achieved using catalytic membrane reactors.[70, 71] However, a number of questions regarding the true state of the active catalyst/membrane and their stability over time remain unanswered. These integrated reactor systems are typically characterised *ex situ* with electron microscopy techniques (SEM/TEM/EDX) and bulk powder diffraction.

Herein, three different catalytic membrane reactor systems have been studied, for the first time, under real OCM reaction conditions with XRD-CT. The *operando* XRD-

CT measurements allowed to spatially resolve the pertinent changes in the chemical/physical state within all working CMRs. Despite the challenging nature of these experiments it has been shown that spatially-resolved diffraction information can be gleaned from within the confines of working catalytic membrane reactors and that the results are reproducible. Indeed the state of the catalyst was captured prior to, under and after OCM *operando* conditions.

The three CMRs investigated under OCM operating conditions were a BCFZ – 2 % Mn-1.6 % Na-3.1 % W/SiO_2 CMR, a BCFZ – 2 % La-2 % Mn-1.6 % Na-3.1 % W/SiO_2 CMR and an LSCF – 2 % La-2 % Mn-1.6 % Na-3.1 % W/SiO_2 CMR. In all experiments, the Na_2WO_4 phase, present in the fresh catalysts, is seen to melt before reaching the required high temperatures for the OCM reaction (780 °C) and coincident to this event the formation of a new phase is observed. In the BCFZ CMRs, this phase was identifies as $BaWO_4$ while in the LSCF CMR the new phase was identified as $SrWO_4$. These new phases are seen to initially form at the interface between the catalyst particles and the inner side of the membranes. The mobility of W containing species was independently confirmed by micro-CT and ex situ SEM/WDS measurements. These phases are seen to continuously grow under the high temperatures used for the OCM reaction and regardless of the chemical environment present (reaction mixtures used) indicating that their formation and subsequent growth is a purely temperature driven phenomenon. The growth of stable the $BaWO_4$ phase in the BCFZ CMRs and the $SrWO_4$ phase in the LSCF CMR is extremely important as:

(1) loss of W is expected to have an impact on the stability of the catalyst (loss of one of the main catalyst components),
(2) it might lead to the deactivation of the membrane (BCFZ/LSCF) after many hours of operation by forming an inner layer at the membrane and therefore blocking the flow of oxygen to the catalyst bed

At this point it should be emphasized that in the La-promoted catalysts, the loss of WO_4^{-2} species and the formation/growth of $BaWO_4$/$SrWO_4$ did not prevent the formation of $NaLa(WO_4)_2$ in the catalyst particles. In fact, the $NaLa(WO_4)_2$ phase was seen to grow with time under OCM operating conditions (although with a delay compared to the respective fixed bed reactor experiments). This is important as the

formation and subsequent growth of $NaLa(WO_4)_2$ suggests that if the catalyst if pre-treated before it is inserted in the CMR (e.g. extensive catalyst calcination periods), then the formation/growth of the $BaWO_4$/$SrWO_4$ can be supressed if not completely prevented during the operation of the CMRs.

The SiO_2 support of both catalysts is also seen to evolve with time under OCM operating conditions and the results are in full agreement with the ones obtained from the *operando* XRD-CT fixed bed reactor experiments (using the same catalysts) presented in Chapter 5. More specifically, cristobalite is seen to gradually transform to tridymite and then to quartz at high temperatures (780 °C). This phenomenon was attributed to the presence of mobile Na^+ species and their incorporation to the SiO_2 framework.

In contrast to what was observed in the fixed bed reactor experiments, the Mn_2O_3/Mn_7SiO_{12} phase remains present for the duration of the OCM experiments. More specifically, the transformation of the Mn_2O_3/Mn_7SiO_{12} phase to the $MnWO_4$ phase was not observed in the Mn-Na-W/SiO_2 catalyst. This result suggests that the bulk reduction of the Mn species (Mn^{+3} to Mn^{+2}) was prevented in the CMRs. This observation becomes more important when it is taken into account that the 100 % CH_4 was used as the inlet gas to the catalyst bed for more than 8 h at 780 °C. This result implies that the oxygen permeation flux through the dense ceramic membranes was enough to prevent the bulk reduction of the Mn species present in the catalysts.

Last but not least, the crystal structure of BCFZ was solved using high resolution neutron powder diffraction data collected at the ISIS neutron source. The model provided an opportunity to extract more information on the nature of the BCFZ membrane's performance in operation. The BCFZ structure was added to the Rietveld refinement model and it was shown that not only the thermal parameters of the various atoms present in the BCFZ unit cell increase with increasing temperature but the O vacancies too (O occupancies decrease). It was also shown that the values of the aforementioned parameters do not vary significantly spatially, yielding uniform images (homogeneous distributions).

Beyond the findings for the various CMRs and their use for the OCM reaction, the work presented in this chapter also illustrates the value of these types of measurements in evaluating the performance of a reactor system for a chemical reactor engineering-based problem. Finally, it should be pointed out that the results of these CMR experiments clearly show that it possible to conduct *operando* XRD-CT systems of other functional devices too. For example, one can envision the use of XRD-CT to study batteries and micro-tubular solid oxide fuel cells under real operating conditions.

References

1. Wei, C.C. and K. Li, *Yttria-Stabilized Zirconia (YSZ)-Based Hollow Fiber Solid Oxide Fuel Cells.* Industrial & Engineering Chemistry Research, 2008. **47**(5): p. 1506-1512.
2. Vernoux, P., et al., *Ionically Conducting Ceramics as Active Catalyst Supports.* Chemical Reviews, 2013. **113**(10): p. 8192−8260.
3. Hashim, S.M., A.R. Mohamed, and S. Bhatia, *Current status of ceramic-based membranes for oxygen separation from air.* Advances in Colloid and Interface Science, 2010. **160**(1-2): p. 88-100.
4. Suranso, J., et al., *Mixed ionic-electronic conducting (MIEC) ceramic-based membranes for oxygen separation.* Journal of Membrane Science, 2008. **320**(1-2): p. 13-41.
5. Dong, X., et al., *Dense ceramic catalytic membranes and membrane reactors for energy and environmental applications.* Chemical Communications, 2011. **47**(39): p. 10886-10902.
6. Wei, Y., et al., *Dense ceramic oxygen permeable membranes and catalytic membrane reactors.* Chemical Engineering Journal, 2013. **220**: p. 185-203.
7. Pena, M.A. and J.L.G. Fierro, *Chemical Structures and Performance of Perovskite Oxides.* Chemical Reviews, 2001. **101**(7): p. 1981-2017.
8. Goldschmidt, V.M. and V.A. Skrifter Norske, Math. Naturwiss. Kl., 1926. **7**: p. 8.
9. Travis, W., et al., *On the application of the tolerance factor to inorganic and hybrid halide perovskites: a revised system.* Chemical Science, 2016. **7**(7): p. 4548-4556.
10. Thursfield, A. and I.S. Metcalfe, *The use of dense mixed ionic and electronic conducting membranes for chemical production.* Journal of Materials Chemistry, 2004. **14**(16): p. 2475.
11. Teraoka, Y., et al., *Oxygen permeation through perovskite-type oxides.* Chemistry Letters, 1985: p. 1743-1746.
12. Liu, Y., X. Tan, and K. Li, *Mixed Conducting Ceramics for Catalytic Membrane Processing.* Catalysis Reviews, 2006. **48**(2): p. 145-198.
13. Cousin, P. and R.A. Ross, *Preparation of mixed oxides: a review.* Materials Science and Engineering: A, 1990. **130**(1): p. 119–125.
14. Tan, X., S. Liu, and K. Li, *Preparation and characterization of inorganic hollow fiber membranes.* Journal of Membrane Science, 2001. **188**(1): p. 87-95.
15. Liu, S., et al., *Preparation and characterisation of SrCe0.95Yb0.05O2.975 hollow fibre membranes.* Journal of Membrane Science, 2001. **193**(2): p. 249-260.
16. Van Noyen, J., et al., *Fabrication of perovskite capillary membranes for high temperature gas separation.* Catalysis Today, 2012. **193**(1): p. 172-178.

17. Buysse, C., et al., *Development, performance and stability of sulfur-free, macrovoid-free BSCF capillaries for high temperature oxygen separation from air.* Journal of Membrane Science, 2011. **372**(1-2): p. 239-248.
18. Luyten, J., et al., *Preparation of LaSrCoFeO3-x membranes.* Solid State Ionics, 2000. **135**(1-4): p. 637-642.
19. Otsuka, K., S. Yokoyama, and A. Morikawa, *Catalytic activity and selectivity control for oxidative coupling of methane by oxygen-pumping through yttria-stabilized zirconia.* Chemistry Letters, 1985. **14**(3): p. 319-322.
20. Nagamoto, H., K. Hayashi, and H. Inoue, *Methane oxidation by oxygen transported through solid electrolyte.* Journal of Catalysis, 1990. **126**(2): p. 671-673.
21. Vayenas, C.G. and S. Bebelis, *Electrochemical promotion of heterogeneous catalysis.* Catalysis Today, 1999. **51**(3-4): p. 581–594.
22. Vayenas, C.G., *Catalytic and electrocatalytic reactions in solid oxide fuel cells.* Solid State Ionics, 1988. **28**: p. 1521-1539.
23. Vayenas, C.G., S. Bebelis, and S. Neophytides, *Non-Faradaic Electrochemical Modification of Catalytic Activity.* Journal of Physical Chemistry, 1988. **92**(18): p. 5083-5085.
24. Vayenas, C.G., S. Bebelis, and S. Ladas, *Dependence of catalytic rates on catalyst work function.* Nature, 1990. **343**(6259): p. 625 - 627.
25. Ladas, S., et al., *Origin of non-Faradaic electrochemical modification of catalytic activity.* Journal of Physical Chemistry, 1993. **97**(35): p. 8845-8848.
26. Vayenas, C.G. and C.G. Koutsodontis, *Non-Faradaic electrochemical activation of catalysis.* The Journal of Chemical Physics, 2008. **128**(18).
27. Liu, S., et al., *Methane coupling using catalytic membrane reactors.* Catalysis Reviews: Science and Engineering, 2001. **43**(1-2): p. 147-198.
28. ten Elshof, J.E., B.A. van Hassel, and H.J.M. Bouwmeester, *Activation of methane using solid oxide membranes.* Catalysis Today, 1995. **25**(3-4): p. 397-402.
29. ten Elshof, J.E., H.J.M. Bouwmeester, and H. Verweij, *Oxidative coupling of methane in a mixed-conducting perovskite membrane reactor.* Applied Catalysis A: General, 1995. **130**(2): p. 195-212.
30. Xu, S.J. and W.J. Thomson, *Perovskite-Type Oxide Membranes for the Oxidative Coupling of Methane.* Ceramics Processing, 1997 **43**(11A): p. 2731-2740.
31. Xu, S.J. and W.J. Thomson, *Stability of La0.6Sr0.4Co0.2Fe0.8O 3-δ Perovskite Membranes in Reducing and Nonreducing Environments.* Industrial and Engineering Chemistry Research, 1998. **37**(4): p. 1290-1299.
32. Zeng, Y., Y.S. Lin, and S.L. Swartz, *Perovskite-type ceramic membrane: Synthesis, oxygen permeation and membrane reactor performance for oxidative coupling of methane.* Journal of Membrane Science, 1998. **150**(1): p. 87-98.
33. Wang, W. and Y.S. Lin, *Analysis of oxidative coupling of methane in dense oxide membrane reactors.* Journal of Membrane Science, 1995. **103**(3): p. 219-233.
34. Tan, X. and K. Li, *Oxidative Coupling of Methane in a Perovskite Hollow-Fiber Membrane Reactor.* Industrial and Engineering Chemistry Research, 2006. **45**(1): p. 142-149.
35. Teraoka, Y., et al., *Mixed ionic-electronic conductivity of La1-xSrxCo1-yFeyO3-δ perovskite-type oxides.* Materials Research Bulletin, 1988. **23**(1): p. 51-58.
36. Petric, A., P. Huangb, and F. Tietzc, *Evaluation of La–Sr–Co–Fe–O perovskites for solid oxide fuel cells and gas separation membranes.* Solid State Ionics, 2000. **135**(1-4): p. 719–725.
37. Chang, X., et al., *A comparative study of the performance of symmetric and asymmetric mixed-conducting membranes.* Chinese Journal of Chemical Engineering, 2009. **17**(4): p. 562-570.

38. Jin, W., et al., *Preparation of an asymmetric perovskite-typemembrane and its oxygen permeability.* Journal of Membrane Science, 2001. **185**(2): p. 237–243.
39. Tiemersma, T.P., et al., *A kinetics study for the oxidative coupling of methane on a Mn/Na2WO4/SiO2 catalyst.* Applied Catalysis A: General, 2012. **433-434**: p. 96-108.
40. Czuprat, O., et al., *Oxidative Coupling of Methane in a BCFZ Perovskite Hollow Fiber Membrane Reactor.* Industrial & Engineering Chemistry Research, 2010. **49**(21): p. 10230-10236.
41. Czuprat, O., *Oxidative activation of light hydrocarbons in a perovskite hollow fiber membrane reactor*. 2010, Gottfried Wilhelm Leibniz Universitat Hannover: Hannover.
42. Olivier, L., et al., *Oxidative coupling of methane using catalyst modified dense perovskite membrane reactors.* Catalysis Today, 2009. **142**(1-2): p. 34-41.
43. Tan, X. and K. Li, *Inorganic hollow fiber membranes in catalytic processing.* Current Opinion in Chemical Engineering, 2011. **1**(1): p. 69-76.
44. Tan, X., et al., *Catalytic perovskite hollow fibre membrane reactors for methane oxidative coupling.* Journal of Membrane Science, 2007. **302**(1-2): p. 109-114.
45. Czuprat, O., et al., *Oxidative Coupling of Methane in a BCFZ Perovskite Hollow Fiber Membrane Reactor.* Industrial and Engineering Chemistry Research, 2010. **49**(21): p. 10230-10236.
46. Middelkoop, V., et al., *Development and characterisation of dense lanthanum-based perovskite oxygen-separation capillary membranes for high-temperature applications.* Journal of Membrane Science, 2014. **468**: p. 250-258.
47. Vamvakeros, A., et al., *Removing multiple outliers and single-crystal artefacts from X-ray diffraction computed tomography data.* Journal of Applied Crystallography, 2015. **48**(6): p. 1943-1955.
48. *TOPAS Version 5.0*. Bruker AXS: Karlsruhe, Germany.
49. *MATLAB*. 2010, The MathWorks Inc.: Natick, Massachusetts.
50. Kleuker, U., et al., *Feasibility study of x-ray diffraction computed tomography for medical imaging.* Physics in Medicine and Biology, 1998. **43**(10): p. 2911-2923.
51. Tong, J., et al., *Investigation of ideal zirconium-doped perovskite-type ceramic membrane materials for oxygen separation.* Journal of Membrane Science, 2002. **203**(1–2): p. 175-189.
52. Yang, L., et al., *Structure and oxygen permeability of BaCo0.4Fe0.6-xZrxO3-δ oxide: effect of the synthesis method.* Industrial and Engineering Chemistry Research, 2004. **43**(11): p. 2747-2752.
53. Tablet, C., et al., *Oxygen permeation study of perovskite hollow fiber membranes.* Catalysis Today, 2005. **104**(2-4): p. 126-130.
54. Schiestel, T., et al., *Hollow fiber perovskite membranes for oxygen separation.* Journal of Membrane Science, 2005. **258**(1-2): p. 1-4.
55. Wang, H., et al., *In situ high temperature X-ray diffraction studies of mixed ionic and electronic conducting perovskite-type membranes.* Materials Letters, 2005. **59**(28): p. 3750-3755.
56. Wang, H., et al., *Mixed oxygen ion and electron conducting hollow fiber membranes for oxygen separation.* Solid State Ionics, 2006. **177**(26-32): p. 2255-2259.
57. Wang, H., C. Tablet, and J. Caro, *Oxygen production at low temperature using dense perovskite hollow fiber membranes.* Journal of Membrane Science, 2008. **322**(1): p. 214-217.
58. Czuprat, O., et al., *Influence of CO2 on the oxygen permeation performance of perovskite-type BaCoxFeyZrzO3-δ hollow fiber membranes.* Journal of Membrane Science, 2010. **364**(1-2): p. 132-137.

59. Efimov, K., O. Czuprat, and A. Feldhoff, *In-situ X-ray diffraction study of carbonate formation and decomposition in perovskite-type BCFZ.* Journal of Solid State Chemistry, 2011. **184**: p. 1085-1089.
60. Toby, B.H. and R.B. Von Dreele, *GSAS-II: The genesis of a modern open-source all purpose crystallography software package.* Journal of Applied Crystallography, 2013. **46**(2): p. 544-549.
61. Gędziorowski, B., K. Świerczek, and J. Molenda, *La1 − xBaxCo0.2Fe0.8O3 − δ perovskites for application in intermediate temperature SOFCs.* Solid State Ionics, 2012. **225**: p. 437-442.
62. Mentre, O., et al., *BaCoO2.22: the most oxygen-deficient certified cubic perovskite.* Dalton Transactions, 2015. **44**(23): p. 10728-10737.
63. Haynes, W.M., *CRC Handbook of Chemistry and Physics, 95th Edition*. 2014: CRC Press.
64. Goranson, R.W. and F.C. Kracek, *An experimental investigation of the effect of pressure on phase equilibria of sodium tungstate and of related thermodynamic properties.* The Journal of Chemical Physics, 1935. **3**(2): p. 107-115.
65. Tiemersma, T.P., et al., *A kinetics study for the oxidative coupling of methane on a Mn/Na 2WO 4/SiO 2 catalyst.* Applied Catalysis A: General, 2012. **433-434**: p. 96-108.
66. Wang, D.J., M.P. Rosynek, and J.H. Lunsford, *Oxidative Coupling of Methane over Oxide-Supported Sodium-Manganese Catalysts.* Journal of Catalysis, 1995. **155**(2): p. 390-402.
67. Pak, S. and J.H. Lunsford, *Thermal effects during the oxidative coupling of methane over Mn/Na2WO4/SiO2 and Mn/Na2WO4/MgO catalysts.* Applied Catalysis A: General, 1998. **168**(1): p. 131-137.
68. Kou, Y., et al., *Amorphous features of working catalysts: XAFS and XPS characterization of Mn/Na2WO4/SiO2 as used for the oxidative coupling of methane.* Journal of Catalysis, 1998. **173**(2): p. 399-408.
69. Hou, S., et al., *Site requirements for the oxidative coupling of methane on SiO 2-supported Mn catalysts.* Industrial and Engineering Chemistry Research, 2006. **45**(21): p. 7077-7083.
70. Bhatia, S., C.Y. Thien, and A.R. Mohamed, *Oxidative coupling of methane (OCM) in a catalytic membrane reactor and comparison of its performance with other catalytic reactors.* Chemical Engineering Journal, 2009. **148**(2-3): p. 525-532.
71. Othman, N.H., Z. Wu, and K. Li, *An oxygen permeable membrane microreactor with an in-situ deposited Bi1.5Y0.3Sm0.2O3-δ catalyst for oxidative coupling of methane.* Journal of Membrane Science, 2015. **488**: p. 182-193.

CHAPTER 7: Arriving at five dimensional tomographic diffraction imaging with sub-minute XRD-CT

Abstract

Herein, we present the results from three XRD-CT experiments performed with a 10 wt. % Ni – 0.5 wt. % Pd/ 10 wt. % CeO_2 – ZrO_2/ Al_2O_3 catalyst used for methane reforming reactions. A new data collection strategy is introduced which allows both tomographic stages to move simultaneously (i.e. rotation and translation) leading to ultra-fast XRD-CT scans. As shown in the first part of this work, this new fast data collection strategy allowed us to perform a five dimensional (5D) tomographic diffraction imaging experiment by collecting 3D-XRD-CT scans during a redox experiment of the aforementioned catalyst. It should be emphasized that the analysis of the reconstructed data (> 10^6 diffraction patterns) was a challenging task but it is shown here that it is not only possible to perform Rietveld analysis of such large datasets at reasonable timescales but also to obtain unprecedented physico-chemical information about the sample under investigation. For example, the Rietveld analysis of the reconstructed XRD-CT data allowed us to differentiate between several $Ce_xZr_yO_2$ phases present in the sample. The results from an *operando* XRD-CT experiment of the same catalyst during the partial oxidation (POX) of methane to CO and H_2 are also presented in this Chapter. It is shown that XRD-CT can efficiently track the changes taking place in the catalyst under POX reaction conditions with characteristic examples being the continuous growth of the Ni crystallite size and the formation/growth of graphite as a function of time. The results from the *ex situ* characterisation of a spent catalyst, post POX, with sub-minute XRD-CT measurements are presented in the last part of this chapter. These results serve to illustrate the importance of making representative measurements and the value of whole catalyst bed chemical imaging under real process conditions.

Literature Review

Introduction

The catalytic partial oxidation of methane (POX) is considered to be a very promising alternative to the highly energy-demanding steam reforming of methane (highly endothermic reaction) to produce synthesis gas (CO and H_2) at gas-to-liquids (GTL) industrial plants (Fischer-Tropsch synthesis). The POX reaction is only mildly exothermic and it leads to a H_2/CO molar ratio of 2 which is suitable for the Fischer-Tropsch reaction. The methane reforming reactions (i.e. partial oxidation, steam and dry reforming of methane) along with the complete oxidation of methane as a reference are shown below (the autothermal reforming reaction is a combination of steam reforming and partial oxidation of methane):[1]

$CH_4 + 2\ O_2 \rightarrow CO_2 + 2H_2O$ $\Delta H°_{298K}$ = -802.3 kJ mol^{-1} (complete oxidation of methane)

$CH_4 + H_2O \rightarrow CO + 3H_2$ $\Delta H°_{298K}$ = +226 kJ mol^{-1} (steam reforming of methane)

$CH_4 + CO_2 \rightarrow 2CO + 2H_2$ $\Delta H°_{298K}$ = +261 kJ mol^{-1} (dry reforming of methane)

$CH_4 + 1/2\ O_2 \rightarrow CO + 2H_2$ $\Delta H°_{298K}$ = -35.7 kJ mol^{-1} (partial oxidation of methane)

$CO + H_2O \rightarrow CO_2 + H_2$ $\Delta H°_{298K}$ = -41.2 kJ mol^{-1} (water gas shift reaction)

Two different POX reaction mechanisms have been proposed in literature: (1) the "combustion-reforming mechanism" where methane is first completely oxidized to CO_2 and H_2O and the synthesis gas is produced from the steam and dry reforming of the residual CH_4; (2) the "pyrolysis mechanism" or "direct mechanism" where methane is pyrolyzed over the catalyst to produce CO and H_2 directly (i.e. without the preformation of CO_2).[2] Ni-based catalysts have been the most widely studied POX catalysts mainly due to the fact that Ni is a cheap material compared to the expensive noble metals (e.g. Pd, Pt, Rh and Ru). However, Ni-based catalysts are usually prone to deactivation with time under POX reaction conditions for a variety of reasons; the most often reported in literature being carbon deposition on active Ni sites (metallic Ni being the active catalyst component), sintering of Ni particles and solid-state reactions involving Ni (e.g. the formation of $NiAl_2O_4$ in Ni/Al_2O_3

catalysts).[2, 3] Al_2O_3 is traditionally chosen as the support material for the Ni catalysts mainly due to its stability at high temperatures and its low cost. This is clearly indicated in a review paper by Enger *et al*. where the catalyst development for the POX reaction (both noble and none-noble metal catalysts) was thoroughly discussed.[4] However, it is generally accepted that Ni/Al_2O_3 catalysts are unstable under POX reaction conditions as it has been shown that Ni can react with the Al_2O_3 support to form a $NiAl_2O_4$ phase which is considered to be inactive for the POX reaction and carbon deposition/ coke formation is unavoidable due to the acidic nature of Al_2O_3.[2, 4, 5] As a result, research has focused on investigating the effects of promoters (i.e. low loadings of noble metals) on Ni-based catalyst and also modifying the Al_2O_3 support with alkali earth and rare earth metal oxides (e.g. BaO, MgO, CaO, CeO_2, La_2O_3, Sm_2O_3, Y_2O_3).[4]

Ni/ CeO_2 – ZrO_2/ Al_2O_3 catalysts

CeO_2 is considered to be a good candidate as a support (or part of the support) for POX catalysts as it can supress the carbon deposition/ coke formation by releasing lattice oxygen (the lattice oxygen can be replenished by the gas-phase oxygen – redox behaviour of CeO_2).[6, 7] After the early work of Choudhary *et al*. who showed that Ni/CeO_2 is an active POX catalyst, Otsuka *et al*. were the first to demonstrate that CeO_2 can also produce CO and H_2 without any other components, further supporting CeO_2 as a promising support for POX catalysts.[8, 9] Indeed, it was later shown that Ni/Al_2O_3 promoted by CeO_2 catalysts exhibited improved performance compared to the unpromoted ones.[10, 11] However, CeO_2 is not the ideal support for a stable POX catalyst as it has poor thermal stability and resistance at high temperatures. On the other hand, it has been shown in several studies that the addition of ZrO_2 to CeO_2 leads not only to higher thermal resistance and improved oxygen storage capacity and redox properties but also to better catalytic performance at lower temperatures.[12-16] Therefore, it is of no surprise that Ni/CeO_2-ZrO_2 catalysts show higher performance compared to the Ni/CeO_2 catalysts; a phenomenon supported by numerous studies in literature.[6, 17-22] Unfortunately, from a practical point of view, CeO_2-ZrO_2 is an expensive material to be used as the support for industrial POX Ni-based catalysts especially when compared to Al_2O_3. On the other hand, Ni/Al_2O_3

catalysts where the Al_2O_3 support is modified with CeO_2-ZrO_2 can potentially get the best of both worlds and consequently such catalysts have gained a lot of attention in the past decade.[23-25] It should also be noted that the Ni/CeO_2-ZrO_2/Al_2O_3 catalysts have attracted interest as promising catalysts also for steam, autothermal and dry (CO_2) reforming of methane as Ni/Al_2O_3 catalysts have been shown to suffer from similar problems under these reaction conditions (sintering, carbon deposition/ coke formation and solid-state reactions involving Ni species).[26-34] It is also generally accepted that small amounts of noble metals (Pd, Pt, Rh and Ru) can be beneficial to Ni/Al_2O_3 catalysts as the reduction of the Ni species can be greatly enhanced (preventing/supressing the formation/growth of $NiAl_2O_4$) through a hydrogen spillover mechanism from the noble metal to the Ni species.[35-39]

Herein, the solid-state chemistry of a state-of-the-art 10 wt. % Ni – 0.5 wt. % Pd/ 10 wt. % CeO_2 – ZrO_2/ Al_2O_3 catalyst is investigated during POX with XRD-CT. Apart from this *operando* XRD-CT experiment, a five dimensional (5D) tomographic diffraction imaging experiment using this catalyst during redox has been also performed. This experiment has been made possible by using a new data collection strategy that allowed ultra-fast XRD-CT "slice" acquisition. As it will be shown in the last section of this chapter, *ex situ* 3D chemical imaging of a spent catalyst (i.e. post POX) has been also performed by acquiring successive XRD-CT scans, each lasting less than 1 minute.

Ultra-fast XRD-CT

In 1987, Harding *et al.* were the first to introduce a new materials characterisation technique termed X-ray diffraction computed tomography (XRD-CT).[40] XRD-CT couples traditional powder X-ray diffraction with first generation (i.e. pencil beam approach) computed tomography (CT). It was first demonstrated using a lab diffractometer and more than a decade later, in 1998, Kleuker *et al.* were the first to implement XRD-CT using synchrotron light for medical imaging applications (soft tissue).[41] The total acquisition time of that XRD-CT scan (using an 80 keV monochromatic pencil beam) was 2 h for 100 × 100 pixels reconstructed images using an area detector (900 × 900 μm^2 beam size using slit systems). XRD-CT was re-introduced a decade later, in 2008, by Stock *et al.* and Bleuet *et al*.[42, 43] Stock *et al.* also used a ca. 80 keV monochromatic pencil beam but with a smaller beam size of

100 × 100 μm^2 acquiring in total 714 powder diffraction images. It should be mentioned that the acquisition time per point (exposure plus readout time) was 10 s. Bleuet *et al*. used an 18 keV monochromatic pencil beam with a beam size of 1.6 × 2.3 μm^2 (vertical × horizontal) but the experimental details regarding the tomographic scan (i.e. number of translations and projections) and the acquisition time per point were omitted in the paper (it was only claimed that a 100 × 100 × 100 μm^3 data volume with a voxel size of 3 µm could be achieved in 6 h). Since then, XRD-CT has gained a lot of attention as a chemical imaging technique and has been used to study numerous different systems including biological samples, automotive paints, cement, radioactive samples and batteries among others.[44-58] In the aforementioned studies, XRD-CT was employed either to study static samples or for *ex situ* characterisation of functional materials (e.g. catalysts and batteries). However, it is generally accepted in literature that functional materials can change under working conditions; there are several review papers emphasizing the need for *in situ/ operando* techniques to characterize catalytic and electrochemical systems under real working conditions in order to gain a proper understanding of structure-activity relationships.[59-70] XRD-CT has recently been exploited as a chemical imaging tool to study several catalytic systems under real process conditions and in all cases new physico-chemical information was revealed due to the spatially-resolved signals obtained from such measurements; information that is/can be lost in bulk measurements.[71-75] However, the temporal resolution of the XRD-CT technique has been always considered to be its main drawback. This is clearly implied in Table 1 where the experimental details of most XRD-CT studies conducted in the past decade are presented (i.e. from papers where information available). It can be seen that in most studies, the total acquisition time of an XRD-CT scan is in the order of several hours which is far from ideal for dynamic experiments.

Table 1: Experimental details of XRD-CT studies performed during the 2008-2016 period. CS: Current Study

Energy (keV)	Beam size (μm × μm)	Number of diffraction patterns	Acquisition time per point (ms)	Total acquisition time (min)	Year	Ref
80.715	100 × 100	714	10000	660-720	2008	[42]
30	15 × 15	4941	10000	-	2009	[44]
18	2 × 4	7500	-	480	2010	[45]
18	2 × 4	6480	800	480	2010	[46]
86.88	100 × 100	1290	400	10	2011	[71]
29	0.3 × 0.3	8000	5000	720	2011	[47]
69.77	50 × 100	4800	-	17	2012	[72]
65	15 × 150	8190	1200-1300	-	2012	[49]
17	2 × 5	13189	1000	540	2012	[58]
86.7	150 × 150	8000	150	25	2013	[51]
86.88	100 × 100	1290	400	10	2014	[73]
29.6	0.2 × 0.11	22806	1000	-	2014	[52]
13	2 × 2	1517	2000	120	2015	[74]
89.965	100 × 100	2500	1000	420	2015	[54]
93	25 × 25	14700	50	40	2015	[75]
65	25 × 25	25200	1000	540	2016	[56]
75	30 × 30	7200	7.5	<1	2016	CS

The chosen acquisition time per point (ATPP) during an XRD-CT scan is based on the quality of the powder diffraction images obtained (i.e. user's decision during the experiment). This means that the ATPP does not depend only on the number of photons arriving at the sample per unit of time (synchrotron/beamline specific and X-ray optics dependant) but also on the detector capabilities. Nowadays, state-of-the-art single photon counting detectors (e.g. PILATUS CdTe series) are considered to be "noise-free" allowing very fast acquisition times. For example, it is now considered trivial to perform XRD-CT experiments at the high energy beamlines of

the ESRF (e.g. ID11, ID15, ID31) with ATPP of 10s of ms which is orders of magnitude faster compared to what was feasible till recently (i.e. ATPP of 100s of ms or several s).[75, 76] However, there is also another equally important factor which contributes to the time required to perform an XRD-CT scan and it is has not been investigated/discussed in literature in the past. This is the "dead time" of the measurement which depends not only on the motors' capabilities (fast motors are essential for fast XRD-CT scans) but also on the chosen data collection strategy. We recently provided a short review on the available data collection strategies and also introduced a new one, termed as interlaced XRD-CT, which allows, post experiment, choice between temporal and spatial resolution.[76] Herein, we present a new data collection strategy which minimizes the "dead time" during an XRD-CT scan. In fact, the total acquisition time of such an XRD-CT measurement can be calculated by just multiplying the ATPP with the total number of diffraction patterns collected. The breakthrough in this ultra-fast XRD-CT data collection strategy lies on the fact that both the rotation and the translation axis are continuously moving during the acquisition of the tomographic scan.

In Figure 1, the two traditional XRD-CT data collection strategies are demonstrated (i.e. how the sampling is performed in the frequency domain). In Panel A of Figure 1, the fast axis is the translation axis and the slow axis is the rotation axis (most common XRD-CT data collection strategy). The sample is continuously traversed across the beam and diffraction patterns are collected at fixed interval (positions t_n, t_{n+1}, etc) with the process then repeated at a number of fixed sample angular rotations (θ angular step size). On the contrary, in Panel B of Figure 1, the fast axis is the rotation axis and the slow axis is the translation axis. The sample is continuously rotated and diffraction patterns are collected at fixed interval (θ angular step size) with the process then repeated at a number of fixed sample traverse steps (positions t_n, t_{n+1}, etc). In both cases, even if a zig-zag approach is implemented, there is "dead time" present due to the stepped sample movement in one direction (rotation and translation respectively).

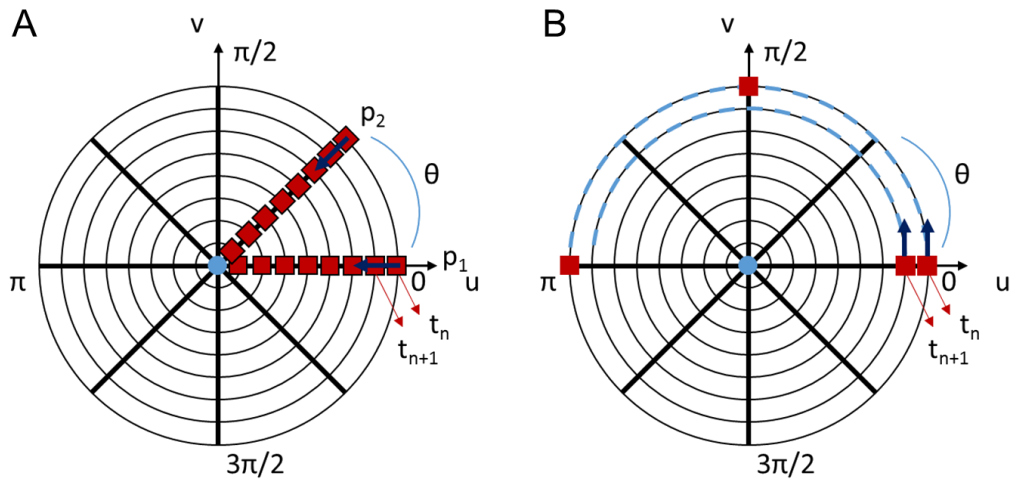

Figure 1: Demonstration of the two most common XRD-CT data collection strategies - how the sampling is performed in the frequency domain (θ: angles used for the CT scan, t_n: translation steps). Panel A: continuous traverse and stepped angular scan, Panel B: continuous angular and stepped traverse scan.

The fast XRD-CT approach is demonstrated in Figure 2. As in the case of a typical XRD-CT scan, the user specifies the number of translation and rotation steps prior to the measurement. For example, 100 translations and 72 angles (projections) were chosen for the fast XRD-CT experiments presented in the first and last section of this Chapter. The ATPP consists of the exposure time plus the readout time (and a short safety time when the ATPP is less than 10 ms). In our first attempt to perform the fast XRD-CT scan at beamline ID31 of the ESRF, the ATPP was 15 ms (11 ms exposure time and 4 ms readout time). When these fast XRD-CT experiments were performed, the newly purchased Pilatus3 X CdTe 2M detector had not been fully integrated with the beamline hardware. More specifically, there was a limitation associated with writing and transferring data from the detector PC to the beamline PCs (i.e. network limitation). However, even with these limitations, the total acquisition time of each XRD-CT scan was less than 2 min (108 s to collect 7200 images) which is a technical breakthrough when compared to what was feasible in the past (Table 1).

Once the ATPP is decided by the users, the velocity of the two motors (i.e. translation and rotation) is calculated by a simple script. As it is implied in panel A of Figure 2, the fast axis is the rotation axis in this data collection strategy. The sample is traversed from position t_n to position t_{n+1} while being continuously rotated. This means there is 180 ° difference between positions t_n and t_{n+1} and 360 ° difference

between positions t_n and t_{n+2}. This angular offset is clearly demonstrated in panel B of Figure 2.

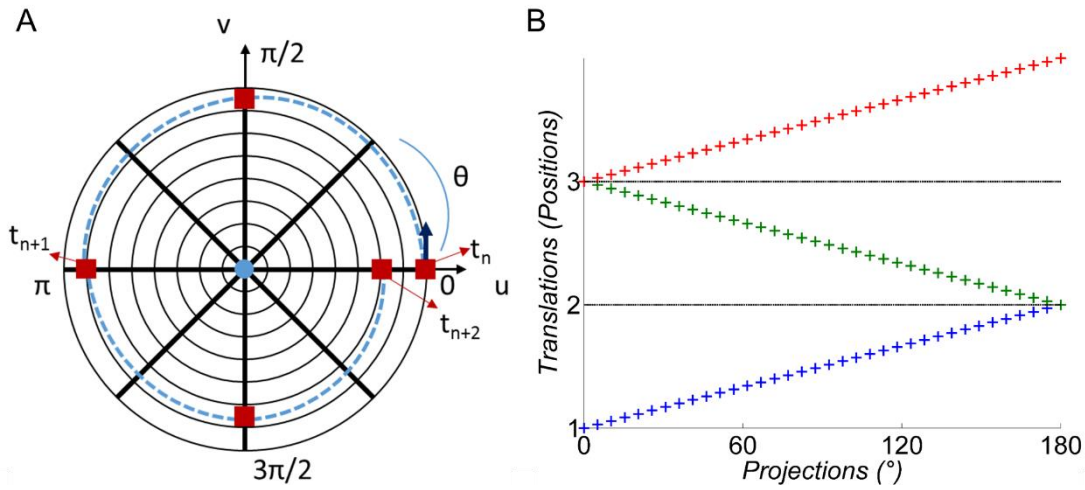

Figure 2: Left: Demonstration of the fast XRD-CT data collection strategy - how the sampling is performed in the frequency domain. Right: Demonstration of the angular offset between two adjacent positions (translation steps) during in a fast XTD-CT scan.

However, when this new data collection strategy is employed, it is not only this angular offset that needs to be taken into account before reconstructing the XRD-CT data but also the fact that the sample is being continuously traversed too. The necessary processing steps of the raw sinograms are illustrated in Figure 3 using a global sinogram from a fast XRD-CT scan. First, the raw sinogram is split into two sinograms (one of them needs to be flipped vertically due to the angular offset issue). A new sinogram is created after aligning the two parts of the raw sinogram (if the raw sinogram is not well centred - a simple offset can be applied) and recombining them (Figure 3). This pre-processing step corrects the angular offset described previously (0 – 180 ° for position t_n, 180 – 360 ° for position t_{n+1}). However, this is not enough as this sinogram leads to a reconstructed image full of ring artefacts (Figure 3). The next and final pre-processing step takes into account the continuous translation of the sample. As it is implied in Figure 2, this issue can be easily solved by simple interpolation. If the number of projections is n_p, then the offset for every projection p_i (where i = 1, 2… n_p) is p_i/n_p. This means that every column in the recombined sinogram (when the columns correspond to the tomographic angles used in the CT scan - projections) needs to be linearly interpolated after applying the

correct offset. These simple pre-processing steps are not computationally heavy and lead to high quality and artefact-free reconstructed images (Figure 3).

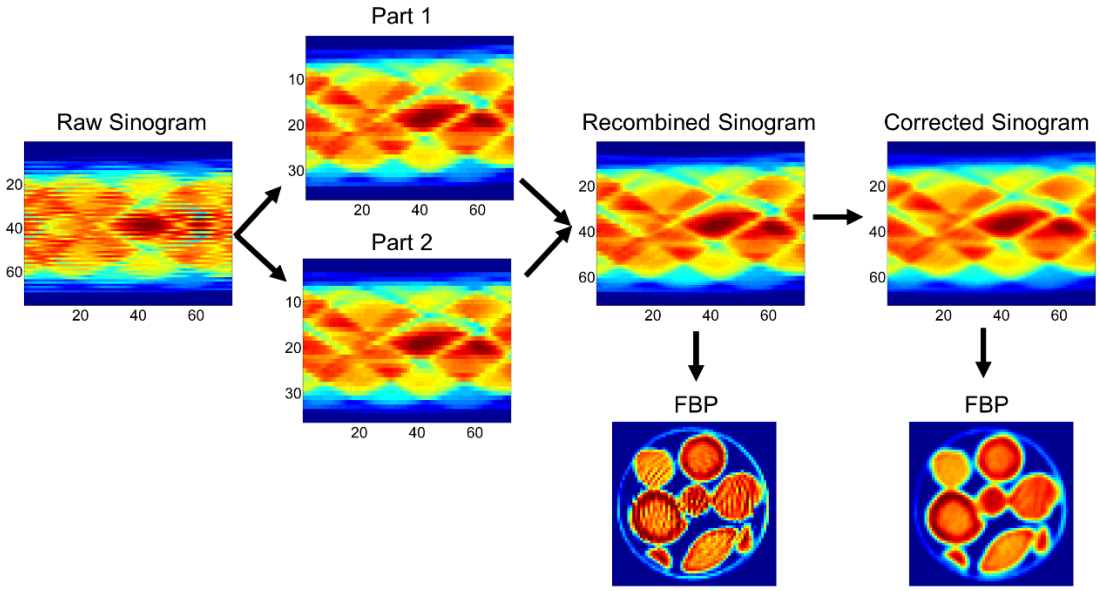

Figure 3: Demonstration of the required steps to process the raw sinograms prior to reconstruction when the fast data collection strategy is employed.

Materials and Methods

Catalyst preparation

The 10 wt. % Ni – 0.5 wt. Pd/ 10 wt. % CeO_2 – ZrO_2/ Al_2O_3 catalyst was prepared by sequential impregnation method. The CeO_2 – ZrO_2/ Al_2O_3 support was prepared by the co-impregnation method. Approximately 500 μm of (γ+δ)-Al_2O_3 was impregnated by aqueous solution of salts (cerium nitrate $Ce(NO)_3 \cdot 6H_2O$ and oxychloride of zirconium $ZrOCl \cdot 8H_2O$) at the required ratio. The CeO_2 – ZrO_2/ Al_2O_3 was dried at 120 °C for 6 h and calcined under air at 850 °C for 6 h with a heating rate of 2 °C min^{-1}. The 10 wt. % CeO_2 – ZrO_2/ Al_2O_3 support was impregnated by aqueous solution of nickel nitrate salt $Ni(NO_3)_2 \cdot 6H_2O$ of the appropriate concentration. Then, Ni/ CeO_2 – ZrO_2 / Al_2O_3 was dried at 120 °C for 6 h and calcined in air at 500 °C for 4 h with a heating rate of 2 °C min^{-1}. The Ni/ CeO_2 – ZrO_2/ Al_2O_3 was impregnated by aqueous solution of palladium nitrate $Pd(NO_3)_2$ salt of the appropriate concentration. The catalyst were then dried at 120 °C for 6 h and calcined in air at 500 °C for 4 h with a heating rate of 2 °C min^{-1}. The catalyst samples used in this study were kindly provided by the Boreskov Institute of Catalysis (BIC).

5D tomograhic diffraction imaging measurements at ID31, ESRF

XRD-CT measurements were made at beamline station ID31 of the ESRF using a 70 keV monochromatic X-ray beam focused to have a spot size of 25 µm x 25 µm. 2D powder diffraction patterns were collected using the state-of-the-art Pilatus3 X CdTe 2M (1475 × 1679 pixels, pixel size of 172 µm) hybrid photon counting area detector which uses cadmium telluride (CdTe) as the semiconducting direct conversion layer. The total acquisition time per point was 15 ms (exposure time of 11 ms and readout time of 4 ms). Four 3D-XRD-CT scans of the Ni – Pd/CeO_2 – ZrO_2/Al_2O_3 catalyst were acquired at different operating conditions: 1) at room temperature, 2) at 800 °C under He flow, 3) at 800 °C under 20 % H_2/He flow (reduction step) and 4) at 800 °C under 20 % O_2/He flow (reoxidation step). Each 3D-XRD-CT scan composed of 30 XRD-CT scans, each one collected at a different vertical position (i.e. 25 µm step size along the catalyst bed). Each XRD-CT scan lasted approximately 2 min. The tomographic measurements were made with 100 translation steps (translation step size of 25 µm) covering 0 – 180 ° angular range, in steps of 2.5 ° (i.e. 72 line scans). The detector calibration was performed using a CeO_2 NIST standard. Every 2D diffraction image was converted to a 1D powder diffraction pattern after applying an appropriate filter (i.e. 1 % trimmed mean filter) to remove outliers using in-house developed MATLAB scripts.[77] The final XRD-CT images (i.e. reconstructed data volume) were reconstructed using the filtered back projection algorithm.

Operando XRD-CT measurements at ID31, ESRF

XRD-CT measurements were made at beamline station ID31 of the ESRF using a 70 keV monochromatic X-ray beam focused to have a spot size of 20 µm x 20 µm. Here, the total acquisition time per point was 20 ms. Tomographic measurements were made with 225 translation steps (translation step size of 20 µm) covering 0 – 180 ° angular range, in steps of 1.125 ° (i.e. 160 line scans). Calibration and processing was carried as described in the section above (Fast XRD-CT measurements at ID31, ESRF) with X-ray detection again using the Pilatus 3X detector.

Ex situ sub-minute XRD-CT measurements at ID15, ESRF

XRD-CT measurements were made at beamline station ID15 of the ESRF using a 78.5 keV monochromatic X-ray beam focused to have a spot size of 30 µm x 30 µm. Again,

the Pilatus 3X detector was used. The total acquisition time per point was 7.5 ms (exposure time of 6 ms, readout time of 1 ms and safety time of 0.5 ms). The tomographic measurements were made with 100 translation steps covering 0 – 180 ° angular range, in steps of 2.5 ° (i.e. 72 line scans). 99 XRD-CT scans were performed it total, each one collected at a different vertical position (i.e. 30 μm step size along the 3rd dimension). Calibration was performed as described in the previous section. Here 2D diffraction patterns were radially integrated using the pyFAI software package.[78] The final XRD-CT images (i.e. reconstructed data volume) were reconstructed using the filtered back projection algorithm.

Reactor Cells

The three catalytic reactors investigated in this study consisted of 10 wt. % Ni – 0.5 wt. Pd/ 10 wt. % CeO_2 – ZrO_2/ Al_2O_3 catalysts (i.e. quartz capillary fixed bed reactors supported by glass wool); the catalyst loading was 35 mg for the *operando* experiment (4 mm outer diameter quartz capillary for the *operando* experiment, 2 mm for the 3D-XRD-CT scans). In each case, the reactor was mounted into a gas delivery stub, itself mounted to a standard goniometer (to enable alignment). The goniometer was fixed to a rotation stage set upon a translation stage to facilitate the movements required for the CT measurement. Heating was achieved by virtue of two Eurotherm hot air blowers heating each side of the catalytic reactor. During the *operando* XRD-CT measurements, the outflow gasses were monitored by mass spectrometry using an Ecosys portable mass spectrometer. The mass spec line was inserted inside the capillary from the top.

Rietveld analysis of the XRD-CT data

As in Chapter 6, quantitative Rietveld refinement was performed using the reconstructed diffraction patterns using the TOPAS software, on a voxel by voxel basis.[79] The results from the refinements were imported into MALTAB in order to create the various figures presented in this Chapter (e.g. phase distribution maps based on the scale factors or weight percentages, lattice parameters etc.). Unless stated otherwise, the Rietveld analysis of the XRD-CT data presented in this Chapter was based on the intensity of the scale factors and should be treated as a semi-quantitative analysis. As mentioned in the previous Chapters, quantitative Rietveld

refinement was performed using the summed diffraction pattern of each XRD-CT dataset prior to the Rietveld analysis of the XRD-CT data.

Ex situ X-ray micro-CT measurements at ID15, ESRF

The μ-absorption-CT (μ-CT) measurements were performed at beamline ID15 of the ESRF using a 92.8 keV monochromatic X-ray beam. Radiographs were recorded with an X-ray imaging camera (CCD) and the pixel resolution was 3.2 μm. Each micro-CT scan consisted of 800 projections (radiographs) covering an angular range of 0 – 180 ° (i.e. angular step size of 0.225 °). Flat-field and dark current images were also collected prior to the micro-CT measurements and were used to normalize the acquired radiographs before the tomographic reconstruction. The tomographic data were reconstructed using the filtered back projection algorithm.

Results & Discussion

5D tomographic diffraction imaging during redox

In this section, the results from a 5D tomographic diffraction imaging experiment using the 10 wt. % Ni – 0.5 wt. Pd/ 10 wt. % CeO_2 – ZrO_2/ Al_2O_3 catalyst are presented. This was achieved by performing a redox experiment of this catalyst and acquiring 3D-XRD-CT scans at four different operating conditions: 1) at room temperature, 2) at 800 °C under He flow, 3) at 800 °C under 20 % H_2/He flow (reduction/activation step) and 4) at 800 °C under 20 % O_2/He flow (reoxidation step). First, the results from the room temperature 3D-XRD-CT scan are presented.

3D-XRD-CT at room temperature

As stated previously, each 3D-XRD-CT dataset composed of 30 XRD-CT scans performed at different positions along the catalyst bed (step size of 25 μm). The phase identification was performed using the summed diffraction pattern from the XRD-CT scan collected at the middle of the 3D stack (XRD-CT scan 15). The crystalline phases identified were: CeO_2 (ICSD: 72155), ZrO_2 (ICSD: 66781), NiO (ICSD: 9866), PdO (ICSD: 24692) and theta-Al_2O_3.[80] The results of the phase identification are presented in Figure 4 where a region of interest of the summed diffraction pattern is shown. In the interest of clarity, only the high intensity peaks of Al_2O_3 are presented (theta-Al_2O_3 corresponds to a low symmetry, monoclinic unit cell generating

numerous diffraction peaks). It should be noted that $NiAl_2O_4$ was not detected on the fresh catalyst.

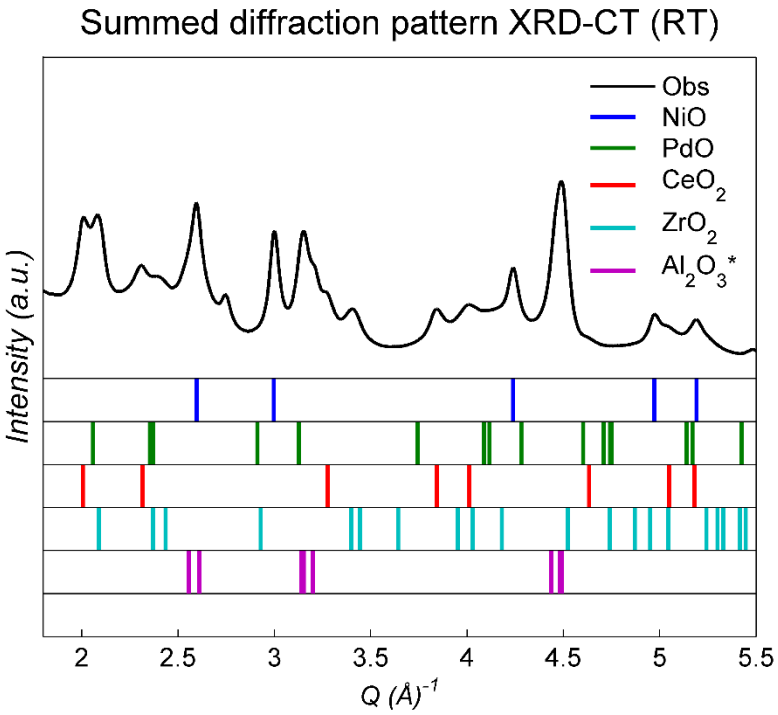

Figure 4: *Phase identification of the 10 % Ni-0.5 % Pd/10 % CeO_2-ZrO_2/Al_2O_3 catalyst. Black line: the summed diffraction pattern from the room temperature XRD-CT scan (i.e. after applying a binary mask to the reconstructed data in order to extract the diffraction patterns generated only by the sample), Blue ticks: NiO, Green ticks: PdO, Red ticks: CeO_2, Cyan ticks: ZrO_2, Magenta ticks: Al_2O_3 (high intensity peaks only)*

An instrument parameter file was created from information derived from Rietveld analysis of CeO_2 diffraction data collected during the beamtime. A Chebyshev polynomial was used to fit the background and a pseudo-Voigt profile function to fit the diffraction peaks.[81] A CeO_2 CIF file was obtained from the ICSD database to be used for the Rietveld refinement (ICSD: 72155). This instrument parameter file was then used for the Rietveld analysis of the XRD-CT data. The same data processing protocol was followed for all the XRD-CT data mentioned in this chapter. The results from the quantitative Rietveld refinement using the summed diffraction pattern of the XRD-CT data collected at room temperature are shown in Figure 5 (Rw = 0.026 on 1500 observations).

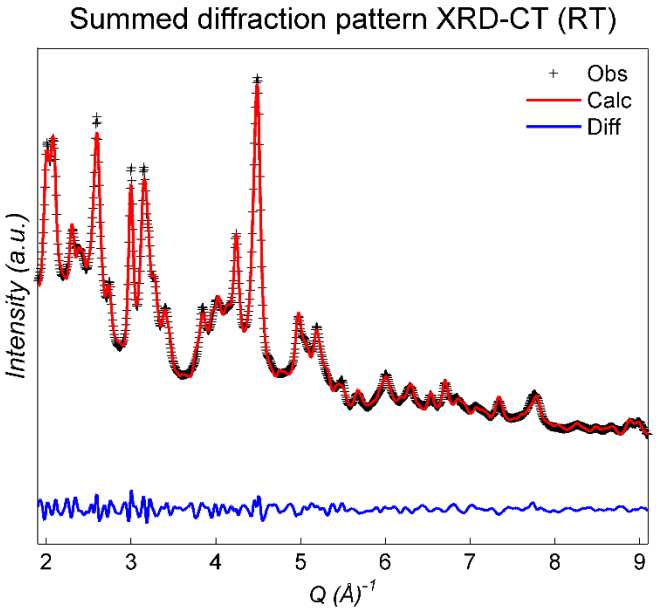

Figure 5: Quantitative Rietveld refinement using the summed diffraction pattern of a room temperature XRD-CT dataset (XRD-CT scan 15).

Prior to the Rietveld analysis of the reconstructed data (4D matrix in the case of 3D-XRD-CT data), the reconstructed XRD-CT images were processed using the images corresponding to the high intensity peak/peaks of Al_2O_3 (ca. Q = 4.5 $Å^{-1}$). More specifically, masks (binary images) were created after performing image segmentation of the Al_2O_3 images by thresholding, in order to mask out the SiO_2 capillary (reactor vessel) and the empty space between the catalyst particles. The Rietveld analysis of the acquired XRD-CT data was then performed, after cropping appropriately the reconstructed data, on a line-by-line basis using the TOPAS software (all the powder diffraction patterns present in each row of each XRD-CT dataset were processed simultaneously).[79] These pre-processing steps were performed in order to minimize the required time for the Rietveld analysis of the XRD-CT data (i.e. number of diffraction patterns to be processed). Apart from refining the background and the scale factors of all crystalline phases, the crystallite size of each phase was calculated too. Finally, the unit cell parameters of NiO, CeO_2 and ZrO_2 were added to the refinement as a crude inspection of the reconstructed data prior to the Rietveld analysis revealed that there were significant variations in the unit cell parameters of CeO_2 and ZrO_2 over the sample (spatial variations). That was not the case for the PdO and the Al_2O_3 unit cell parameters which were not refined. From a materials chemistry perspective, there are not expected to be significant variations

in the unit cell parameters of the Al_2O_3 it being the support of the catalyst. Additionally, refining the low symmetry Al_2O_3 unit cell parameters (lattice parameters a, b, c and β angle) does not only significantly increase the required computational time to perform the Rietveld analysis but can also lead to a less stable refinement (higher number of parameters being refined simultaneously). Regarding the PdO, only the high intensity diffraction peak (ca. Q = 2.35 $Å^{-1}$ corresponding to (002) and (011) reflections) is observed in some regions of the sample and as it is shown in Figure 4 there are other crystalline phases generating diffraction peaks in that Q region (i.e. CeO_2, ZrO_2 and Al_2O_3). Of course, it is also expected that there should not be significant variations in the PdO unit cell parameters as the 3D-XRD-CT measurement was performed at room temperature. For example, as it will be shown in the next section, the unit cell parameter of NiO does not vary significantly either. As a result, it was considered prudent to not refine the lattice parameters of PdO and Al_2O_3.

The results from the Rietveld analysis of the XRD-CT data collected from the fresh catalyst at room temperature are presented in Figures 6 to 10 (XRD-CT scan 15 and 3D-XRD-CT). In Figure 6, the phase distribution maps of all the crystalline phases present in the catalyst particles are shown (XRD-CT scan 15). These phase distribution maps correspond to the (normalised) values of the scale factors of each phase (Rietveld analysis). The Al_2O_3 distribution map shows that the Al_2O_3 is homogeneously distributed over the catalyst particles and clearly describes them in terms of both size and shape.

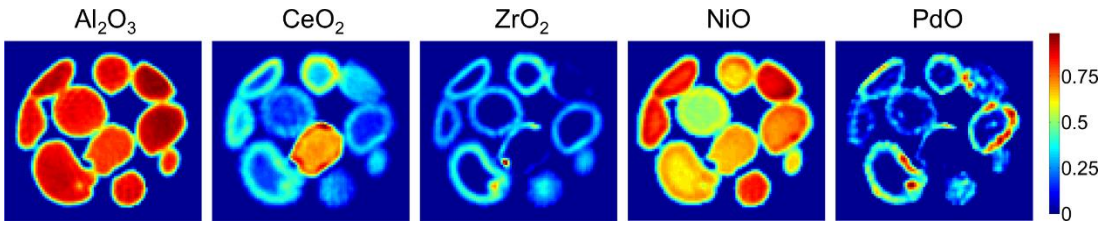

Figure 6: Phase distribution maps created based on the values of the scale factors of each crystalline phase derived from the Rietveld analysis of the XRD-CT data collected at the middle of the catalyst bed. Color bar indicate intensity in arbitrary units.

Interestingly, the NiO distribution map reveals that NiO is present in all catalyst particles, as expected due to the high loading (10 wt. %), but the distribution of the

NiO is not the same in all particles. Of course, there is a lack of information when traditional XRD-CT scans (2D slices) are performed. More specifically, it is unknown whether the bottom, middle or top of each catalyst particle is probed during the tomographic scan. However, as it is shown in Figure 7, such a problem is avoided when 3D-XRD-CT is performed. The results from the Rietveld analysis of the 30 XRD-CT measurements (3D-XRD-CT) were stored as data volumes, each one corresponding to a specific refined parameter. In Figure 7, the results from the volume rendering of the scale factors data volume (phase distribution volumes) are presented. The scale factors were normalised with respect to the maximum value for each data volume and the colour axes were scaled accordingly in order to improve the contrast of the respective figures. For example, the maximum value is 0.3 (instead of 1) in the ZrO_2 and PdO distribution volumes (Figure 7) as there some hotspots of these phases in the probed sample volume.

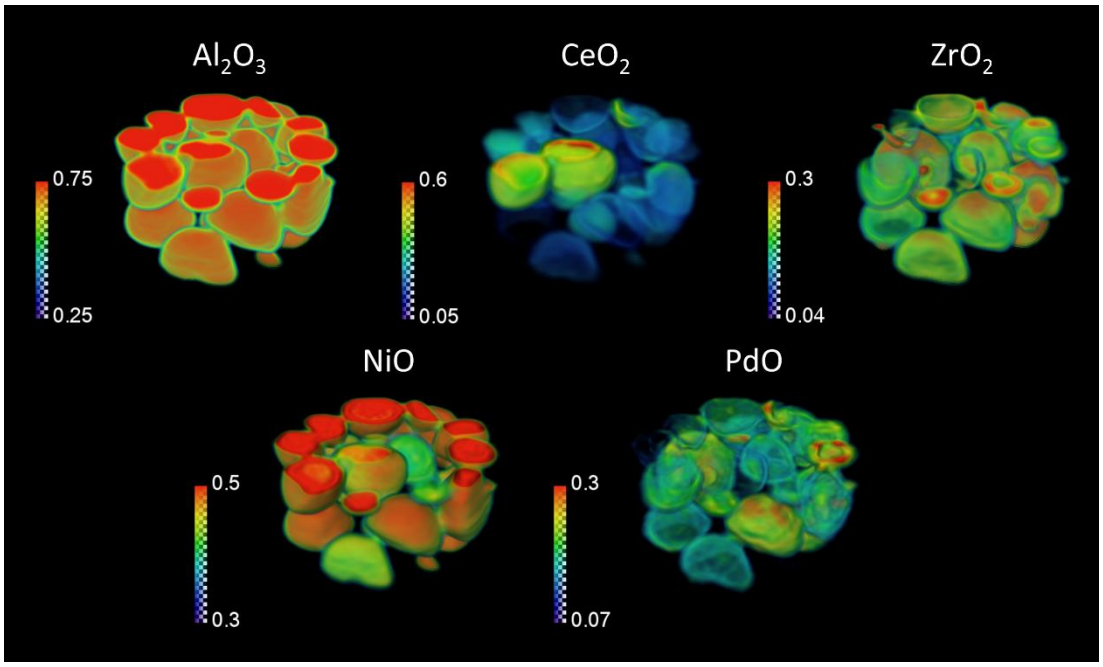

Figure 7: Volume rendering of the scale factors data volume (phase distribution volumes) obtained from the Rietveld analysis of the 3D-XRD-CT data collected at room temperature.

NiO is found in higher concentration close to the surface of the catalyst particles. PdO is also seen to be mainly present at/near the surface of the catalyst particles (Figure 6) which is a direct outcome of the preparation method (impregnation) and the low loading Pd (0.5 wt. %) used. The PdO distribution volume shown in Figure 7, shows that indeed the majority of the PdO is placed close to the surface of all catalyst

particles probed during the 3D-XRD-CT measurement. However, it should be mentioned that the PdO results should be treated with care due to the peak overlap and the absence of more than one high intensity PdO peaks problem.

The most interesting results obtained from the Rietveld analysis of the XRD-CT data are related to the CeO_2 and ZrO_2 phases. As it is clearly shown in Figure 6, the ZrO_2 map corresponds to an egg-shell distribution. It is only present at/close to the surface of the catalyst particles. Although one might have expected the same distribution for the CeO_2 phase (co-impregnation method used for the preparation of the $CeO_2 – ZrO_2$ / Al_2O_3 support), that is not the case. There is a strong signal generated by CeO_2 in the regions where ZrO_2 is present but it does not diminish closer to the centre of the catalyst particles (like the ZrO_2 signal does). Furthermore, it is clearly shown in Figure 6 that there is a catalyst particle where there is high concentration (strong signal) of CeO_2 but not of ZrO_2. As shown in Figure 7, the observations regarding the CeO_2/ZrO_2 distributions are in full agreement with the rest of the XRD-CT data (3D-XRD-CT).

As mentioned previously, the crystallite size of each crystalline phase was also calculated during the Rietveld analysis of the acquired XRD-CT data. In Figure 8, maps of the crystallite sizes of Al_2O_3, CeO_2, ZrO_2, NiO and PdO as obtained from the Rietveld analysis of the data corresponding to XRD-CT scan 15 are presented. In Figure 9, the results from the volume rendering of the data volume corresponding to the crystallite size of the various phases are shown (3D-XRD-CT). Although one might point out that the absolute values should be treated with care, it is in fact the changes of these values as a function of position in space (spatial variations of the crystallite size values of each phase) that provide the important physicochemical information about the system under study. For example, in Figure 9, it can be seen that the range of the crystallite size values of PdO and Al_2O_3 is very narrow. The results from the Rietveld analysis of the 3D-XRD-CT data also indicate this narrow distribution regarding the crystallite sizes of PdO and Al_2O_3 being present is all catalyst particles. However, this is not the case for the other crystalline phases present in the sample.

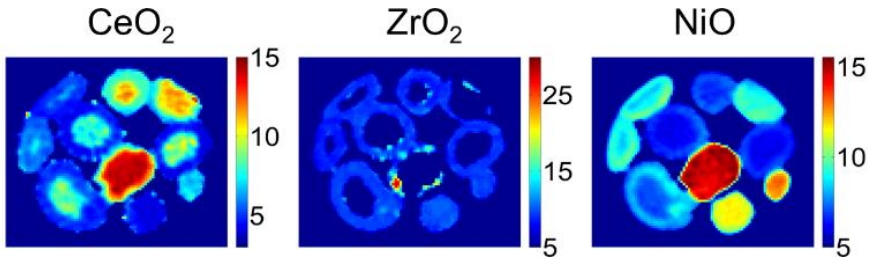

Figure 8: Maps of crystallite sizes of CeO_2, ZrO_2 and NiO as obtained from the Rietveld analysis of the XRD-CT data corresponding to XRD-CT scan 15 (units in nm).

A characteristic example is provided from the results obtained from XRD-CT scan 15 by comparing the ZrO_2 maps of Figures 6 and 8. The ZrO_2 crystallite size is generally seen to be very narrow too (8-10 nm) but in the regions where there are hotspots (areas of high concentration) of ZrO_2 (Figure 6) the average crystallite size increases up to 30 nm (Figure 8). The same conclusion is reached by comparing the ZrO_2 volumes shown in Figures 7 and 9, as the regions of high ZrO_2 concentration correspond to higher crystallite sizes. At first glance, one might think that the case of the CeO_2 phase is identical. The catalyst particle rich in CeO_2, shown in Figure 6 (approximately formed in the middle of the CeO_2 map), also corresponds to highly crystalline CeO_2 (highly crystalline in comparison to other regions of the sample). However, the range of CeO_2 crystallite sizes is anything but narrow in the other catalyst particles. In fact, the values of the crystallite sizes seem to follow an egg-yolk distribution. It can be seen in Figure 8 that in the core of most particles, where there is no ZrO_2, the CeO_2 crystallite size varies between 4-6 nm while at/close to the catalyst surface, where there is ZrO_2, the CeO_2 crystallite size is double (i.e. between 8-10 nm). This phenomenon is more apparent when the CeO_2 results presented in Figure 9 are observed. It can be readily seen that the CeO_2 crystallite size follows an egg-yolk distribution in all catalyst particles (3D-XRD-CT data).

Finally, the NiO crystallite size results are seen to be similar to the ones obtained regarding the ZrO_2 phase. As mentioned previously, although the NiO phase is present in all regions of every catalyst particle probed during the 3D-XRD-CT measurement, its concentration seems to be relatively higher close to the surface of the catalyst particles. It is no wonder then that in these regions, the average NiO crystallite size is also higher compared to the inner core of the catalyst particles (Figure 8). However, it should be noted that there is also a peculiar case too. The

highest values of the NiO crystallite size correspond to the catalyst particle reported previously (catalyst particle in the middle of the catalyst bed in Figure 6) although the NiO concentration is not higher compared to other catalyst particles. It seems that the chemistry of this specific particle may differ from the rest of the sample under investigation as there is also high concentration of highly crystalline CeO_2 (highly with respect to the other catalyst particles). This may imply that there is a different chemical interaction between the various components (NiO, CeO_2 and Al_2O_3). It should be noted that no other crystalline phases were identified to be present in this catalyst particle (i.e. apart from the ones mentioned throughout this section).

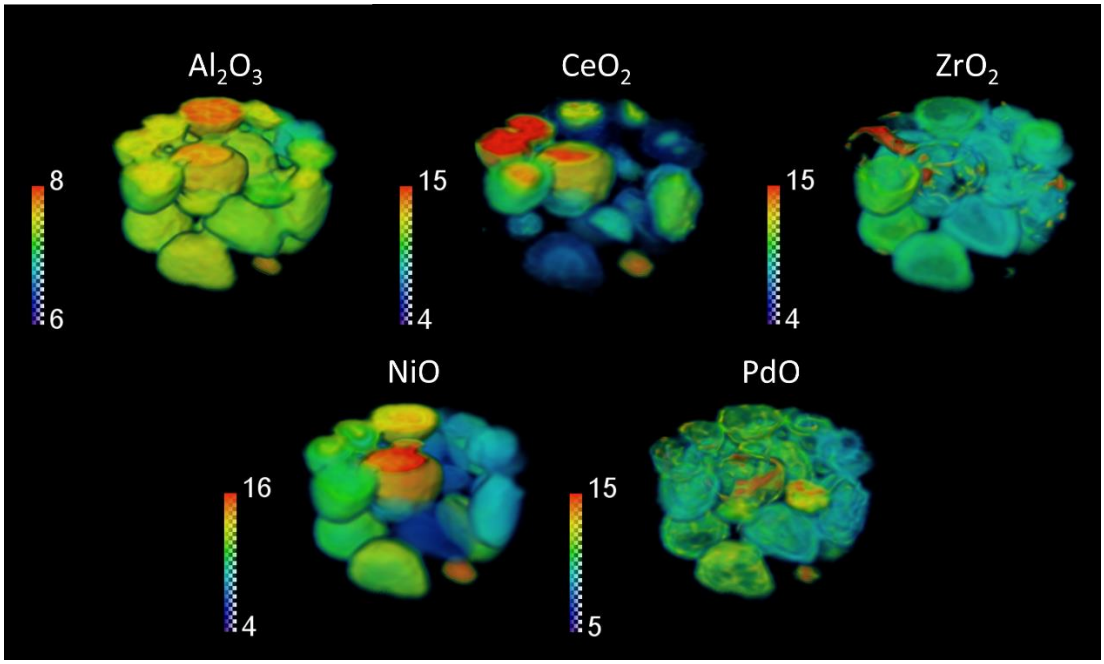

Figure 9: Volume rendering of the data volume corresponding to crystallite size of Al_2O_3, CeO_2, ZrO_2, NiO and PdO as obtained from the Rietveld analysis of the 3D-XRD-CT data collected at room temperature. Color bars indicate intensity in arbitrary units.

As previously stated, the unit cell parameters of CeO_2, ZrO_2 and NiO were also refined during the Rietveld analysis of the XRD-CT data. The unit cells of NiO and CeO_2 are cubic so there was only lattice parameter *a* being refined. The ZrO_2 unit cell is tetragonal so both lattice parameters *a* and *b* were added to the refinement. However, in the interest of brevity, the results obtained from lattice parameter *b* of ZrO_2 are not presented as they do not offer any new/extra information compared to the ones obtained lattice parameter *a*. The maps shown in Figure 10 correspond to the refined values of lattice parameter *a* of CeO_2, ZrO_2 and NiO (Rietveld analysis of

the data corresponding to XRD-CT scan 15). In Figure 11, the results from the volume rendering of the data volume corresponding to the lattice parameter *a* of the same phases are shown (3D-XRD-CT).

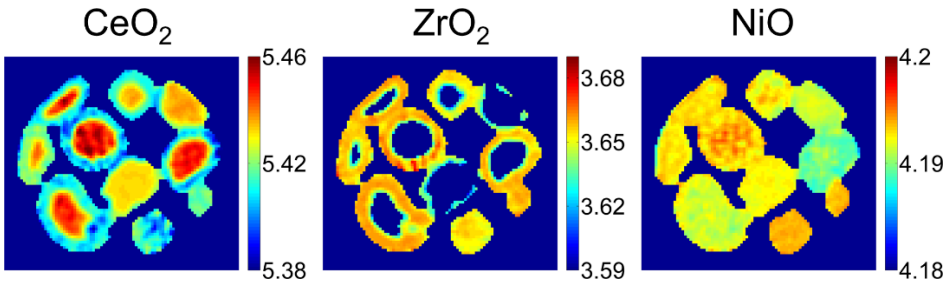

Figure 10: Maps of unit cell parameters (lattice parameter a) of CeO_2, ZrO_2 and NiO as obtained from the Rietveld analysis of the XRD-CT data corresponding to XRD-CT scan 15 (units in Å).

As expected, the unit cell size of NiO is fairly uniform in all regions in all catalyst particles (0.01 Å difference between minimum and maximum value for lattice parameter *a*, typically in the range 4.185-4.195 Å as shown in Figure 11). On the contrary, there seem to be two distinct ranges regarding the values of the ZrO_2 lattice parameter *a*. More specifically, as shown in Figures 10 and 11, in the regions of the sample where there are high concentrations of ZrO_2 (hotspots in Figure 6 and regions of high intensity in Figure 7), the values of lattice parameter *a* are low (3.63 - 3.64 Å). In all other regions, where CeO_2 is present too, the ZrO_2 lattice parameter *a* corresponds to higher values (3.65 - 3.66 Å). This implies that there are actually two different ZrO_2 phases present in the sample: 1) a high purity ZrO_2 present in areas of high concentration of ZrO_2 and 2) a Zr rich $Ce_xZr_yO_2$ phase (Ce incorporation in the ZrO_2 unit cell leads to larger unit cell). This is a rational result as $Ce_xZr_yO_2$ phases could form during the preparation of the catalyst. More importantly, two different CeO_2 crystalline species seem to be present in the catalyst too. As shown in Figures 10 and 11, the CeO_2 lattice parameter near the centre of the catalyst particles is significantly higher (5.44 - 5.46 Å) compared to closer to the surface of the catalyst (5.40 - 5.42 Å), where ZrO_2 is present too. This implies that there is incorporation of a Zr atom to the CeO_2 unit cell in the regions where both CeO_2 and ZrO_2 are present leading to Ce rich $Ce_xZr_yO_2$ phase (smaller unit cell compared to pure CeO_2).

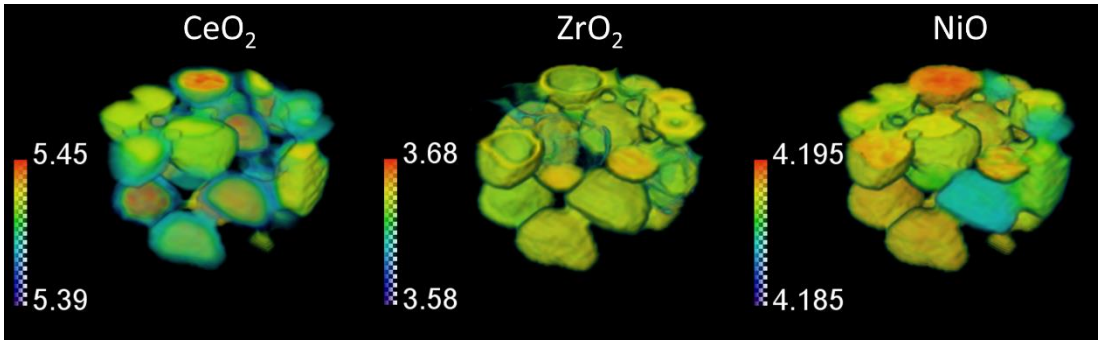

Figure 11: Volume rendering of the data volume corresponding to unit cell parameters of CeO_2, ZrO_2 and NiO as obtained from the Rietveld analysis of the 3D-XRD-CT data collected at room temperature (units in Å).

Summarising the CeO_2-ZrO_2 results derived from the Rietveld analysis of the 3D-XRD-CT data, it can be concluded that there are four distinct crystalline CeO_2-ZrO_2 species present in the catalyst:

1. Small crystallites of a Ce rich $Ce_xZr_yO_2$ (x>>y) phase near the surface of the catalyst particles
2. Larger crystallites of a higher purity CeO_2 phase closer to the core of the catalyst particles
3. Small crystallites of a Zr rich $Ce_xZr_yO_2$ (x<<y) phase near the catalyst surface
4. Larger crystallites of a higher purity ZrO_2 phase where there is high concentration of ZrO_2 (near the surface of the catalyst particles – hotspots of this material)

In order to verify the existence of these four distinct crystalline CeO_2-ZrO_2-$Ce_xZr_yO_2$ species, three summed diffraction patterns were exported from selected regions of interest. As it is shown in Figure 12, three masks were created based on the results from the Rietveld analysis results presented in Figure 6 and these masks correspond to a CeO_2 rich region, a ZrO_2 rich region and another region where both phases are present ($Ce_xZr_yO_2$). The three masks were applied to the reconstructed data volume (one at a time) and in each case the summed diffraction pattern was exported. These three diffraction patterns are plotted at the right side of Figure 12 where a specific *Q* region is chosen (i.e. where the highest intensity CeO_2 and ZrO_2 peaks lie). It can be clearly seen that there is a peak shift to larger *Q* values for the ZrO_2 (green line in Figure 12) in the ZrO_2 rich areas corresponding to a smaller unit cell (with respect to

the $Ce_xZr_yO_2$ - blue line in Figure 12). Similarly, there is a peak shift to smaller *Q* values for the CeO_2 (red line in Figure 12) in the CeO_2 rich areas corresponding to a larger unit cell (with respect to the $Ce_xZr_yO_2$ - blue line in Figure 12). Finally, it can also be readily observed that the broadening of the diffraction peaks (both for CeO_2 and ZrO_2) is higher in the region where both phases are present, implying the presence of smaller crystallites.

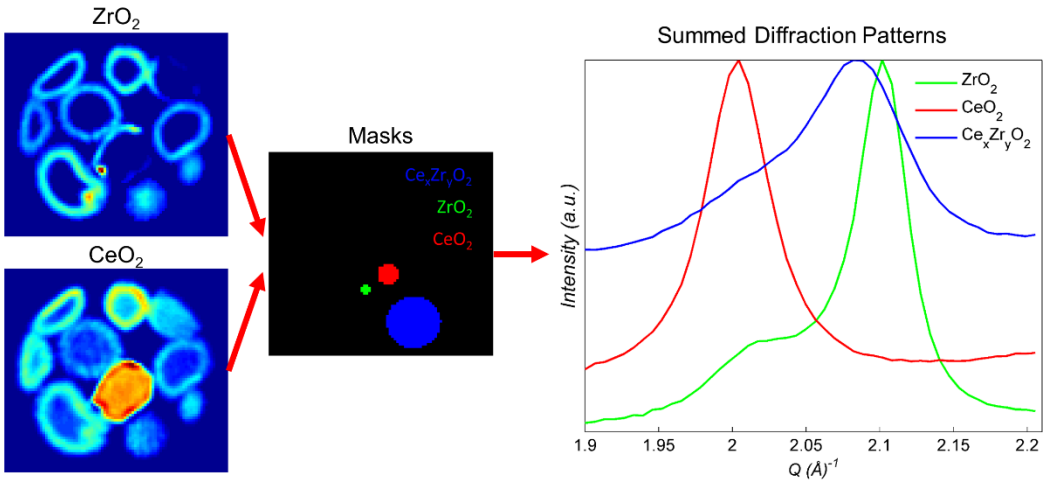

Figure 12: Regions of interest of three summed diffraction patterns exported from selected regions of interest after applying the respective masks (green, red and blue regions) to the XRD-CT data corresponding to XRD-CT scan 15. For comparison reasons, the diffraction patterns were normalised with respect to the highest intensity diffraction peak.

3D-XRD-CT at high temperature under He flow

After the 3D-XRD-CT measurement was performed at ambient conditions, the temperature of the system was increased to 800 °C (temperature ramp rate of 20 °C min^{-1}) under the flow of He (volumetric flow rate of 100 ml min^{-1}). The 10 wt. % Ni – 0.5 wt. Pd/ 10 wt. % CeO_2 – ZrO_2/ Al_2O_3 catalyst remained at 800 °C under He flow (volumetric flow rate of 100 ml min^{-1}) for 1 h while collecting a 3D-XRD-CT scan (30 XRD-CT scans). The gas mixture was then switched to a 20 % H_2/He (total flow rate of 100 ml min^{-1}). Another 3D-XRD-CT measurement was then performed under these reducing conditions in an attempt to capture the state of an activated 10 wt. % Ni – 0.5 wt. Pd/ 10 wt. % CeO_2 – ZrO_2/ Al_2O_3 catalyst. Finally, the gas mixture was switched to 20 % O_2/He (total flow rate of 100 ml min^{-1}) and a last 3D-XRD-CT scan was performed (catalyst re-oxidation experiment).

As explained previously, the fast XRD-CT data collection strategy involves continuous rotation of the sample under study. Unfortunately, this has implications when catalytic experiments are performed which require continuous flow of chemicals (reactants/products). Currently this means that traditional reactor cells for catalytic experiments cannot be used for fast XRD-CT measurements as the presence of gas lines (e.g. in heterogeneous catalysis experiments involving solid catalysts) typically limit the available angular range to 0 – 180 ° or best case scenario to 0 – 360 ° (i.e. for CT measurements). As a result, new reactor cells need to be designed that allow both free rotation of the sample and continuous flow of chemicals. In this experiment, this problem was overcome indirectly by inserting the gas line into the top of the cell but with no gas seal. This setup allowed both free rotation of the sample and the continuous flow of gases through the catalyst bed. This is far from ideal. From a safety perspective, this approach is only suitable for non- toxic / non- harmful gases. There is also the additional concern that the gas may not flow adequately through the bed though we tested that this was not an issue by testing flow at the bottom of the cell using a mass spectrometer. Future experiments using this continuous rotation data collection strategy should make use of gas delivery through rotational slip rings.

The summed diffraction patterns of the 3D-XRD-CT data (30 XRD-CT scans) collected at 800 °C under He flow are shown at the right side of Figure 13. For comparison reasons, the summed diffraction patterns of the 3D-XRD-CT data (30 XRD-CT scans) collected at room temperature are also presented at the left side of Figure 13. It can be clearly seen that the intensity of main NiO diffraction peak (reflection (002)) has significantly decreased while the diffraction peak at ca. Q = 2.55 – 2.65 $Å^{-1}$ has not. Since there is a NiO diffraction peak in this Q region (reflection (111)), one would expect that the intensity of this peak would decrease too. However, this is not the case and this phenomenon was attributed to the formation and growth of the undesired $NiAl_2O_4$ phase. It has been previously reported in literature that crystalline $NiAl_2O_4$ can be observed in Ni/Al_2O_3 catalysts calcined at temperatures above 600 °C.[82] It is no wonder then that the $NiAl_2O_4$ phase is seen to be present in the 10 wt. % Ni – 0.5 wt. Pd/ 10 wt. % CeO_2 – ZrO_2/ Al_2O_3 catalyst at 800 °C. The high intensity

peak of the $NiAl_2O_4$ phase lies in the aforementioned *Q* region (reflection (311)). It should also be noted that no metallic crystalline Ni or Pd was observed in the 3D-XRD-CT data collected at 800 °C under He flow. This indicates that a reducing chemical environment (e.g. H_2) is essential in order to avoid the NiO to $NiAl_2O_4$ transition and reduce the NiO to the desired Ni phase as the formation and growth of the $NiAl_2O_4$ phase is a thermal effect and takes place even under inert chemical environment (He flow).

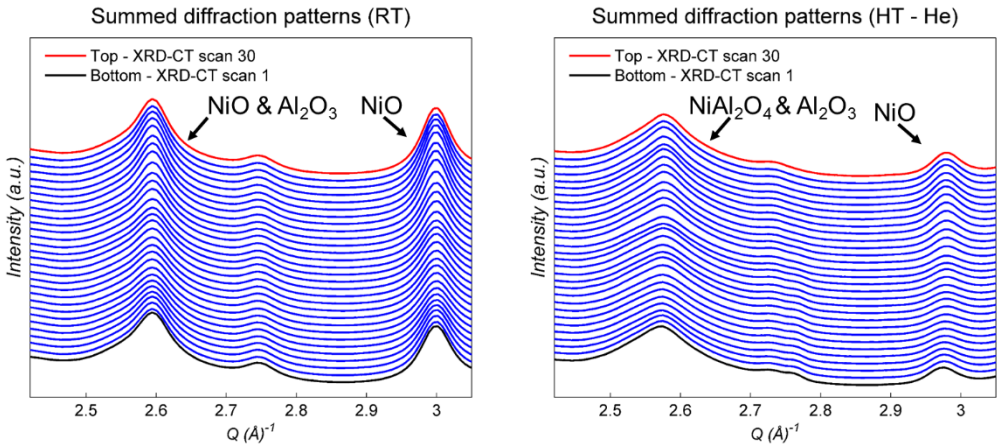

Figure 13: Left: The summed diffraction patterns of the 3D-XRD-CT data (30 XRD-CT scans) collected at room temperature. Right: The summed diffraction patterns of the 3D-XRD-CT data (30 XRD-CT scans) collected at 800 °C under He flow.

The phase distribution maps of certain crystalline phases of interest as obtained from the Rietveld analysis of the XRD-CT data collected at the bottom, middle and top of the sample (XRD-CT scans 1, 15 and 30 respectively) are presented in Figure 14. As discussed previously, the $NiAl_2O_4$ phase was also added to the model for the Rietveld analysis. The phase distribution maps shown in Figure 14 correspond to the values of the scale factors as obtained from the Rietveld analysis of the respective XRD-CT data. These scale factors were then normalised with respect to the maximum value of each phase. These results show that there are not significant changes axially (i.e. as a function of z position) during the collection of this 3D-XRD-CT scan (ca. 1 h total acquisition time). A closer inspection of the results shown in Figure 14 reveals that in the regions of the sample where the NiO signal is strong, the $NiAl_2O_4$ signal is weak and vice versa. More importantly though, the NiO phase is seen to be mainly present closer to the surface of the catalyst where the ZrO_2 phase (or Zr rich $Ce_xZr_yO_2$ phase to be more precise) is located. Such a characteristic example is provided in Figure 14

(as indicated by the arrows) where two distinct regions are seen to be present in a catalyst particle: a) a NiO - Zr rich $Ce_xZr_yO_2$ layer near the surface of the catalyst and b) a $NiAl_2O_4$ rich core. In general, the $NiAl_2O_4$ phase is seen to predominantly form where the Zr rich $Ce_xZr_yO_2$ phase is absent. This is an important result as it provides indirect evidence that the role of the Zr rich $Ce_xZr_yO_2$ phase is to stabilize the NiO phase and suppress the formation of $NiAl_2O_4$ phase.

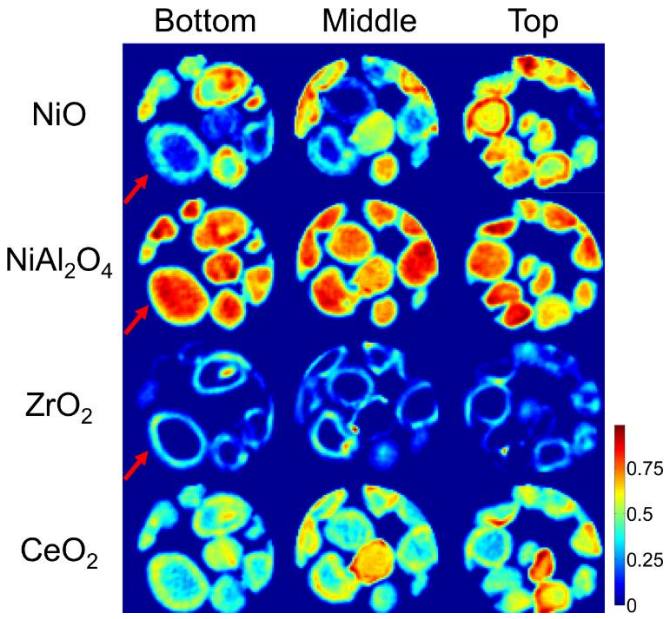

Figure 14: Phase distribution maps obtained from the Rietveld analysis of the XRD-CT data collected at the bottom, middle and top of the sample (XRD-CT scans 1, 15 and 30 respectively), Color bar indicates intensity in arbitrary units.

3D-XRD-CT at high temperature during reduction

The most interesting results were obtained from the 3D-XRD-CT scan performed under H_2 flow (20 % H_2/He, 100 ml min^{-1}). The summed diffraction patterns of the 3D-XRD-CT data (30 XRD-CT scans) collected at 800 °C under reducing environment are presented in Figure 15. In contrast to the results obtained under He flow, there are significant differences between the 30 summed diffraction patterns. The new diffraction peak that appears at ca. Q = 3.04 $Å^{-1}$ corresponds to the metallic Ni phase (reflection (111)). At the right side of Figure 15, the summed diffraction patterns from the top, middle and bottom (XRD-CT scans 30, 15 and 1 respectively) of the sample volume probed during the 3D-XRD-CT measurement under reducing conditions are presented. It is observed that the crystalline metallic Ni phase forms quickly and the

characteristic Ni peak (reflection (111)) is present even at the first XRD-CT data collected under H_2 flow (bottom of the sample volume probed – XRD-CT scan 1). However, the continuous growth of the Ni diffraction signal and decrease of the NiO and $NiAl_2O_4$ peaks (ca. Q = 3 $Å^{-1}$ and Q = 2.55 – 2.65 $Å^{-1}$ respectively) imply that NiO and $NiAl_2O_4$ were still present during the acquisition of this 3D-XRD-CT measurement (i.e. in several XRD-CT scans).

At this point it should be reminded that the gases were inserted from the top of the reactor cell and it should also be mentioned that the first XRD-CT scan (1) was performed at the bottom of the sample volume probed (3D-XRD-CT). This is an important detail as one could argue that it is not possible to reach a conclusion whether the observed gradient regarding the concentration of metallic Ni along the catalyst bed is a temporal phenomenon (time effect) or not. More specifically, the water vapour (steam) produced from the reduction of Ni-O species closer to the top of the reactor cell (inlet of gases) is likely to have an impact on the Ni-containing species further down the catalyst bed by delaying the reduction process. Since the bottom of the sample was probed first (showing relatively small Ni content) one could argue that, during the same time period, this would not be the case closer to the top of the sample.

However, it seems more likely that this is not the case here as the distance between the bottom and the top of the sample volume probed during the 3D-XRD-CT scan (i.e. XRD-CT scan 1 and 30) is ca. 750 μm; a relatively short distance to observe such major differences in solid-state chemistry. This suggests that the solid-state changes of the catalyst observed during the ca. 1 h it took to perform this 3D-XRD-CT measurement (acquisition time of each XRD-CT scan was ca. 2 min) were probably the same in the sample volume probed. Regardless of whether, the changes observed can be tracked as a function of time (uniform changes in the sample volume) or space (changes along the length of the reactor bed), the fact remains that the reduction process of the Ni-O and Ni-Al-O species is seen to be relatively slow in some regions of the sample and this can be attributed to the presence of water produced further closer to the reactor inlet. More importantly, the results obtained from this 3D-XRD-CT scan actually highlight the necessity for 3D chemical imaging of reactor beds rather than choosing

only one (z) position as vital information regarding the chemistry of the system under study can be missed. It should be also noted that at the time of writing it was realised that such dynamic 3D-XRD-CT measurements should be in fact performed using the interlaced approach. More specifically, the interlaced data collection strategy can be applied in the z direction (positions along the catalyst bed). For example, an interlaced 3D-XRD-CT scan would have provided a definite answer to the question raised regarding the observed Ni gradient along the catalyst bed.

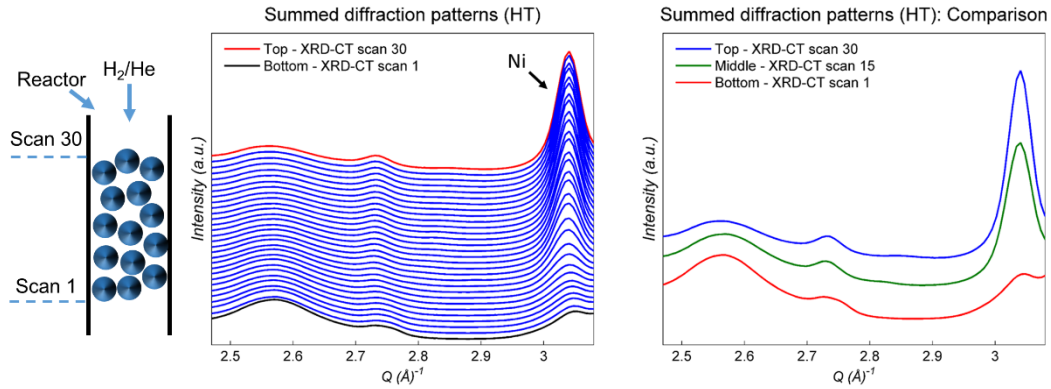

Figure 15: Left: Schematic representation illustrating the initial and final probing position during the 3D-XRD-CT at 800 °C under 20 % H_2/He flow. Middle: The summed diffraction patterns of the 3D-XRD-CT data (30 XRD-CT scans). Right: Summed diffraction patterns from the top, middle and bottom (XRD-CT scans 30, 15 and 1 respectively) of the sample volume probed during the high temperature 3D-XRD-CT measurement under 20 % H_2/He flow.

The results from the volume rendering of the scale factors data volume of the Ni, NiO, $Ni_2Al_2O_4$, CeO_2, ZrO_2 and Pd (phase distribution volumes) as obtained from the Rietveld analysis of the 3D-XRD-CT data are presented in Figure 16. These results clearly demonstrate the Ni concentration gradient along the length of the catalyst bed discussed previously. Similarly, the reduction of the NiO and the $NiAl_2O_4$ phases along the catalyst bed can also be readily observed. A closer inspection of the results also reveals that the $NiAl_2O_4$ phase, which is known to be more difficult to reduce compared to the NiO phase, remains present at positions of the catalyst bed where the NiO diffraction signal has already diminished. Of course, as also shown previously in Figure 15, only metallic Ni can be observed close to the top of the catalyst bed.

It should also pointed out that the areas of high NiO concentration are seen to correspond to the regions of the sample where the Zr rich $Ce_xZr_yO_2$ phase is present (as in the previous 3D-XRD-CT data collected under He flow). Furthermore, the

$Ce_xZr_yO_2$ oxides (i.e. the Ce and the Zr rich ones) seem to be the predominant phases compared to the respective high purity ones at high temperatures. This is implied from the CeO_2 phase distribution volume shown in Figure 16 where CeO_2 is seen to be mainly present near the surface of the catalyst similar to the ZrO_2 phase distribution volume.

Finally, it should be mentioned that metallic Pd is observed at the 3D-XRD-CT data collected under reducing conditions. The phase distribution volume of Pd shown in Figure 16 is perfectly correlated with the PdO distribution presented previously in Figure 7. This also suggests that the PdO results obtained from the Rietveld analysis of the 3D-XRD-CT data are reliable and also that not refining the unit cell parameters (lattice parameter *a*) did not lead to doubtful or contradictory results regarding the Pd/PdO phases. It is also important to note that the metallic Pd peak (reflection (111)) is observed at larger *Q* values than expected (ca. Q = 2.85 $Å^{-1}$) corresponding to a smaller unit cell than a pure Pd one. This results implies that Ni is incorporated in the Pd unit cell (shift of diffraction peak to larger *Q* values) and that Pd exists as a Ni_xPd_y phase (alloy) rather than a high purity Pd phase.

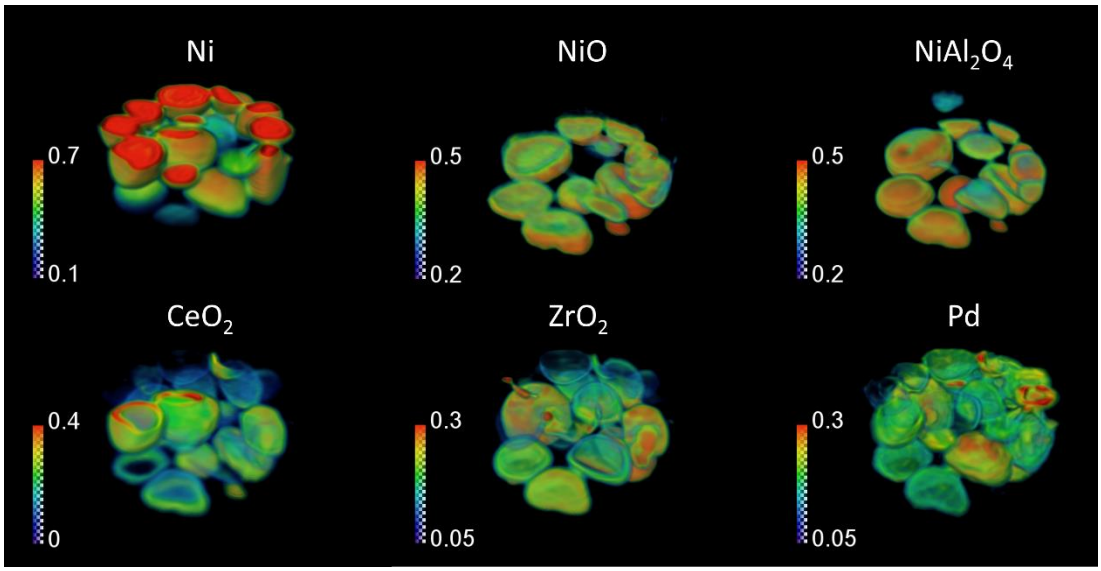

Figure 16: Volume rendering of the scale factors data volume of Ni, NiO, $Ni_2Al_2O_4$, CeO_2, ZrO_2 and Pd (phase distribution volumes) as obtained from the Rietveld analysis of the 3D-XRD-CT data collected at 800 °C under 20 % H_2/He flow. Color bars indicate intensity in arbitrary units.

3D-XRD-CT at high temperature during reoxidation

A re-oxidation step was then performed by exposing the catalyst sample to a 20 % O_2/He gas mixture (total flow rate of 100 ml min^{-1}) and a final 3D-XRD-CT dataset was acquired. At the left side of Figure 17, the summed diffraction patterns of the 3D-XRD-CT data (30 XRD-CT scans) are shown. It can be seen that the metallic Ni peak is absent in all datasets and that only the NiO and $NiAl_2O_4$ phases can be observed. At the right side of Figure 17, the summed diffraction patterns from the top, middle and bottom (XRD-CT scans 30, 15 and 1 respectively) of the sample volume probed during the high temperature 3D-XRD-CT measurement under 20 % O_2/He flow are shown. It can be observed that the intensity of the NiO peak decreases during the 3D-XRD-CT scan as it is gradually converted to $NiAl_2O_4$.

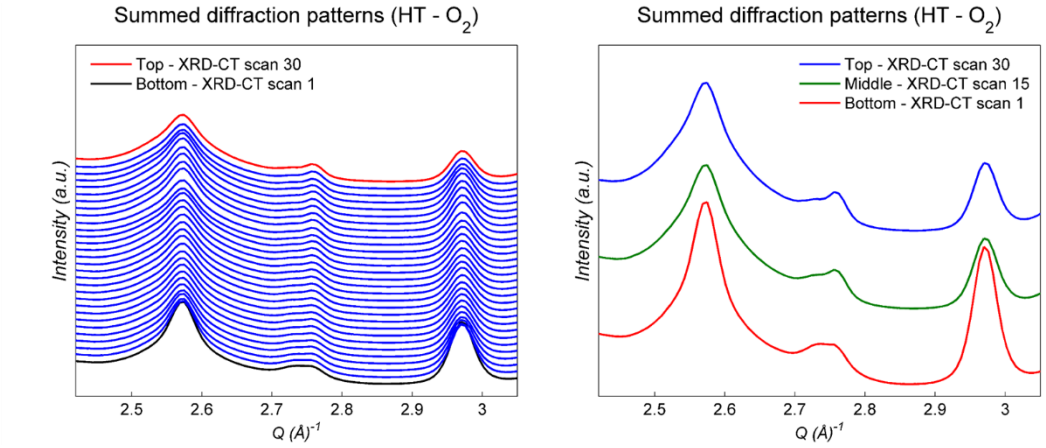

Figure 17: Left: The summed diffraction patterns of the 3D-XRD-CT data (30 XRD-CT scans) collected at 800 °C under 20 % O_2/He flow. Right: Summed diffraction patterns from the top, middle and bottom (XRD-CT scans 30, 15 and 1 respectively) of the sample volume probed during the high temperature 3D-XRD-CT measurement under 20 % O_2/He flow.

This gradual conversion of NiO to $NiAl_2O_4$ is more apparent in Figure 18 where the phase distribution maps of NiO, $NiAl_2O_4$, ZrO_2 and CeO_2 as obtained from the Rietveld analysis of the XRD-CT data collected at the bottom, middle and top of the sample (XRD-CT scans 1, 15 and 30 respectively) are presented. The results from the re-oxidation experiment show that the Ni to NiO is, as expected, a very fast process but the NiO to $NiAl_2O_4$ is a relatively slow one. Interestingly though the results presented in Figures 17 and 18 prove that this process can be studied with the fast XRD-CT data collection strategy with ease. For example, the effect of different promoters of the

Al_2O_3 support on the NiO to $NiAl_2O_4$ transformation could be investigated. However, such a study is beyond the scope of this work.

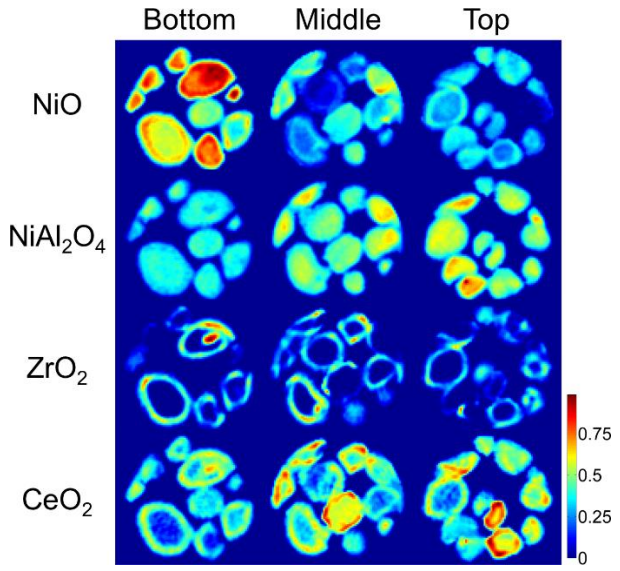

Figure 18: Phase distribution maps obtained from the Rietveld analysis of the XRD-CT data collected at the bottom, middle and top of the sample (XRD-CT scans 1, 15 and 30 respectively). Color bar indicates intensity in arbitrary units.

In Figure 19, the maps corresponding to the crystallite size of NiO as obtained from the Rietveld analysis of the XRD-CT data collected at the bottom, middle and top of the sample (XRD-CT scans 1, 15 and 30 respectively) under He and under 20 % O_2/He flow are compared. It can be readily observed that the re-oxidation step at 800 °C led to a substantial increase in the crystallite size of the NiO phase, implying that sintering of the NiO species took place. In many regions of the sample, the NiO crystallite size more than doubled from ca. 5-15 nm to ca. 20-35 nm. The increase of the NiO crystallite size was not avoided even in the regions where the various CeO_2/ZrO_2/$Ce_xZr_yO_2$ promoters are present indicating that careful consideration must be given to the catalyst pre-treatment before switching to real reaction conditions.

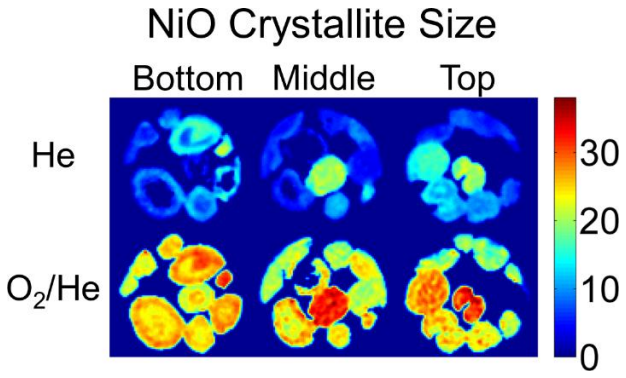

Figure 19: Maps of crystallite sizes of NiO (units in nm) as obtained from the Rietveld analysis of the XRD-CT data collected at the bottom, middle and top of the sample (XRD-CT scans 1, 15 and 30 respectively). Top row: Catalyst under He flow, Bottom row: Catalyst under 20 % O_2/He flow.

Operando XRD-CT measurements during POX

The results obtained from the 5D tomographic diffraction imaging experiment presented in the previous section showed that not only the chemistry of this Ni – Pd/ CeO_2 – ZrO_2/ Al_2O_3 catalyst is complex but also that the use of spatially-resolved scattering/ spectroscopic techniques is essential in order to gain a proper insight into the physico-chemical properties of such catalytic materials. Therefore, it was considered important to study the behaviour of this catalyst under real reaction conditions with XRD-CT and attempt to track the evolving solid-state chemistry taking place in this system. In this experiment, the XRD-CT scans were all performed at the same position (ca. middle) of the catalyst bed (i.e. same sample volume probed during the whole experiment) as the aim of this experiment was to obtain higher resolution reconstructed images compared to the 3D-XRD-CT data presented in the previous section (225 × 225 pixels images compared to 100 × 100 pixels images) which, of course, resulted to longer acquisition times (ca. 25 min per XRD-CT scan).

XRD-CT scan at room temperature

The results from the Rietveld analysis of the XRD-CT data of the fresh catalyst collected at room temperature are presented in Figures 20-22. In Figure 20, the phase distribution maps of all the crystalline phases present in the catalyst particles are shown. These phase distribution maps correspond to the values of the scale factors of each phase (Rietveld analysis) normalised with respect to the maximum values. As expected, these results are in full agreement with the ones obtained from

the Rietveld analysis of the 3D-XRD-CT data presented in the previous section (Figures 6-7).

As expected, the Al_2O_3 phase distribution map shows that the Al_2O_3 is homogeneously distributed over the catalyst particles (Al_2O_3 is the main support of the catalyst) and clearly describes them in terms of both size and shape. The advantage of the higher resolution XRD-CT measurements is quickly realized after inspecting the phase distribution maps of the other crystalline phases present in the sample. For example, the egg-shell distribution of the ZrO_2 phase, suggested in the previous section, is clearly shown in Figure 20. A closer look at the phase distribution maps presented in Figure 20 also reveals that there are two catalyst particles rich in CeO_2 where the ZrO_2 phase is essentially absent. Furthermore, the NiO distribution in these two particles is seen to be uniform which is in contrast to what is observed in the other catalyst particles. As mentioned previously, the NiO is present in all particles but in general it is seen to be predominantly located near the surface of the catalyst particles. This is an interesting result as it supports the corresponding results presented in Figure 6 and 7 and it implies that some of the particles might have been exposed to different conditions during the preparation of this catalyst. The results obtained from the Rietveld analysis of XRD-CT data (both 3D-XRD-CT and high resolution XRD-CT) suggest that the XRD-CT technique can potentially prove to be a very powerful tool to study such complex catalysts during their preparation (e.g. during the calcination step). Finally, the PdO map presented in Figure 20 shows that PdO possesses an egg-shell distribution which is also in agreement with the results derived from the 3D-XRD-CT data shown in the previous section (Figures 6-7).

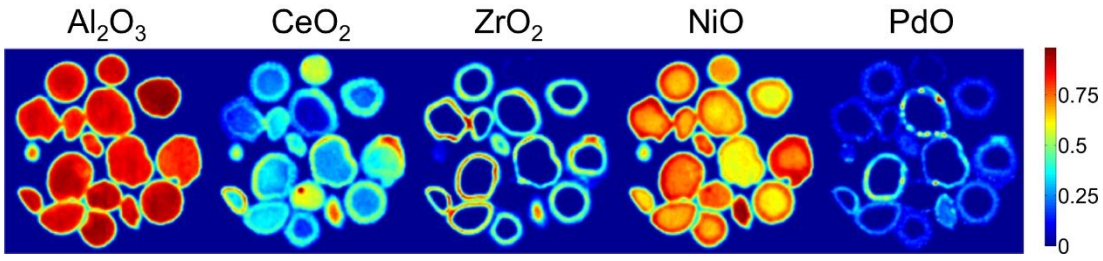

Figure 20: Phase distribution maps of Al_2O_3, CeO_2, ZrO_2, NiO and PdO as obtained from the Rietveld analysis of the XRD-CT data collected at room temperature. Color bar indicates intensity in arbitrary units.

The maps presented in Figure 21 correspond to the crystallite sizes of Al_2O_3, CeO_2, ZrO_2, NiO and PdO as obtained from the Rietveld analysis of the XRD-CT data collected at room temperature. It should be noted that the range of the values of the crystallite sizes is very similar to the ones obtained from the analysis of the 3D-XRD-CT data also collected at room temperature showing that the results presented in the previous section are reproducible (Figures 8-9). However, as mentioned previously, it is not the absolute values of the crystallite sizes that contain the important information about this system but the spatial distribution of these values (the spatial variations of the crystallite size of each phase).

In accordance with the 3D-XRD-CT results, the range of the crystallite size values of the PdO (9-11 nm) and Al_2O_3 (6-9 nm) phases is very narrow. Similar is the case for the ZrO_2 phase (9-12nm) in regions of the sample where the CeO_2 phase is also present. In regions of the sample where there is relatively high purity ZrO_2 (no CeO_2), the values of the crystallite sizes increase above 15 nm. The most important results are related to the CeO_2 phase as the egg-yolk distribution is observed again. It can be clearly seen in the high resolution images presented in Figure 21 that the size of the CeO_2 crystallites near the surface of the catalyst particles is less than 7 nm (4-7 nm) while closer to the core of the particles the value rises to more than 9 nm (9-16 nm). Finally, the range of the NiO crystallite size values is anything but narrow; as in Figure 7, it is shown that the values vary between 5-20 nm. It can also be seen that in most catalyst particles the size of the NiO crystallites is higher near the surface of the particles (Figure 21); where the NiO concentration is higher (Figure 20). However, the fact that there are four catalyst particles present where the average NiO crystallite size is almost double (16-20 nm) compared to the rest (8-12 nm) probably implies that not all catalyst particles were exposed to the same conditions during preparation of the catalyst (e.g. temperature gradients during the calcination step could affect the NiO crystallite size).

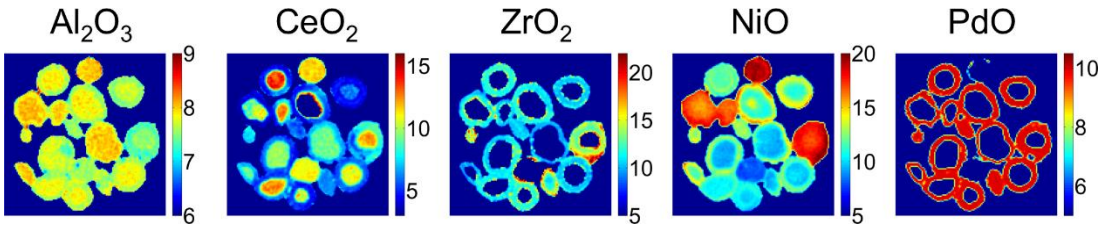

Figure 21: Maps of crystallite sizes of Al_2O_3, CeO_2, ZrO_2, NiO and PdO as obtained from the Rietveld analysis of the XRD-CT data collected at room temperature (units in nm).

The maps shown in Figure 22 correspond to the refined values of lattice parameter *a* of the CeO_2, ZrO_2 and NiO unit cells as obtained from the Rietveld analysis of the XRD-CT data collected at room temperature. As expected, there are not significant variations of the NiO unit cell parameter in the sample volume probed but the case of the ZrO_2 and CeO_2 phases is quite different. The areas of high concentration of ZrO_2 shown in Figure 20 seem to correspond to a smaller unit cell (implying the presence of relatively high purity ZrO_2) compared to other regions of the sample (Zr rich $Ce_xZr_yO_2$). A characteristic example is the region of interest highlighted in Figure 22 (as indicated by the red circle and arrow) which corresponds to a hotspot of ZrO_2 (Figure 20). Finally, the values of the CeO_2 unit cell parameter *a* are seen to follow an egg-yolk distribution which is in full agreement with the results obtained from the 3D-XRD-CT data collected at room temperature. This result suggests that there is a Ce rich $Ce_xZr_yO_2$ near the surface of the catalyst particles and a higher purity CeO_2 closer to the core of the particles. In conclusion, the higher resolution XRD-CT results presented in this section seem to validate the 3D-XRD-CT results regarding the existence of four different CeO_2-ZrO_2 species: 1) high purity CeO_2, 2) Ce rich $Ce_xZr_yO_2$, 3) Zr rich $Ce_xZr_yO_2$ and 4) high purity ZrO_2 species.

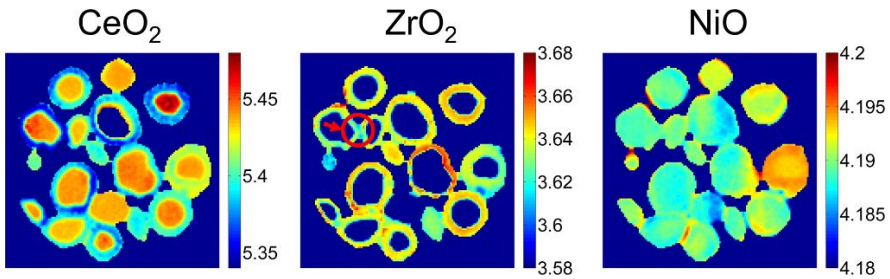

Figure 22: Maps of unit cell parameters (lattice parameter a) of CeO_2, ZrO_2 and NiO as obtained from the Rietveld analysis of the XRD-CT data collected at room temperature (units in Å).

XRD-CT scans during temperature ramping and catalyst activation

A schematic representation of the experimental protocol followed for the POX experiment with the 10 wt. % Ni – 0.5 wt. % Pd/ 10% CeO_2 – ZrO_2/Al_2O_3 catalyst is shown in Figure 23. Initially, an XRD-CT scan (1) of the fresh catalyst was collected at room temperature as mentioned previously. The temperature of the reactor was then increased to 800 °C with a ramp rate of 20 °C min^{-1} under the flow of He (i.e. 30 ml min^{-1}). Two Interlaced XRD-CT (IXRD-CT) scans were collected during temperature ramping (2-3).[76] Once the required temperature was reached, another XRD-CT scan was performed (4). The inlet gas was then switched to a 10% H_2/He gas mixture (total flow rate of 100 ml min^{-1}) and two XRD-CT scans were collected (5-6). The catalyst bed was then exposed to a POX reaction mixture (i.e. 90 ml min^{-1} of pure He, 12 ml min^{-1} of pure CH_4 and 3 ml min^{-1} of pure O_2 - CH_4/O_2 molar ratio of 4:1) which was kept constant for the duration of the experiment and seven XRD-CT scans were collected in total (7-13). The mass spectrometry data are presented in a following section and serve to illustrate that the catalyst was active under the imposed conditions (i.e. temperature and reaction mixtures).

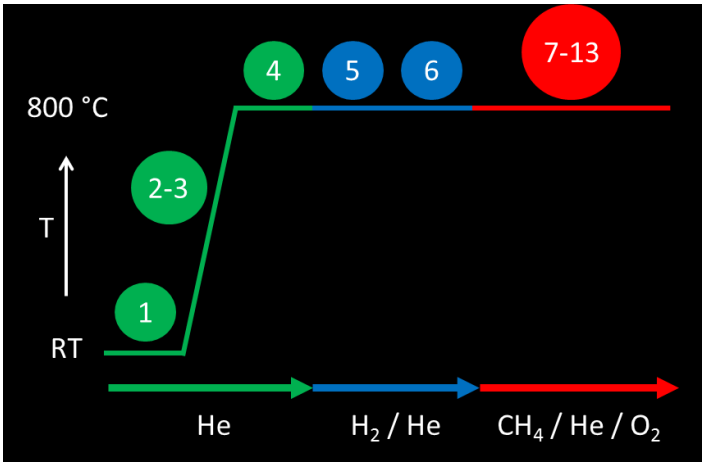

Figure 23: Schematic representation of the protocol followed during the POX experiment with the 10 wt. % Ni – 0.5 wt. % Pd / 10% CeO_2 – ZrO_2/Al_2O_3 catalyst.

The data acquired from the two IXRD-CT scans during temperature ramping from room temperature to 800 °C (ramp rate of 20 °C min^{-1}) were treated as a series of line scans. The air and glass scattering signal was supressed following the data process strategy described in Chapter 5. In Figure 24, the new diffraction patterns are plotted as a function of temperature and the results are shown from two

different points of view. These 320 diffraction patterns correspond to the summed diffraction patterns per line scan. It can be seen that the high intensity peak of NiO (ca. Q = 3 Å^{-1}, reflection (002)) starts decreasing above 700 °C. This result is in full agreement with the results obtained from the 3D-XRD-CT data collected at 800 °C under He flow which suggested that NiO gradually converts to the $NiAl_2O_4$ phase.

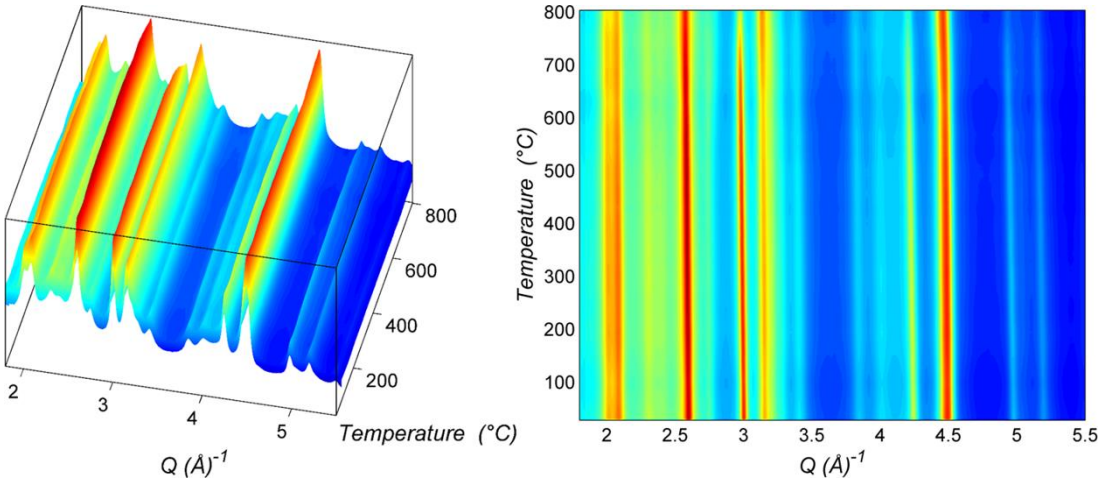

Figure 24: The 320 summed diffraction patterns per line scan acquired during the temperature ramping from room temperature to 800 °C (two IXRD-CT scans) are plotted as a function of temperature.

In Figure 25, the summed diffraction patterns derived from the XRD-CT data collected at room temperature, at 800 °C under He flow and at 800 °C under 20 % H_2/He flow, are shown. By comparing the summed diffraction patterns from the XRD-CT data collected at room temperature and at 800 °C under He flow, it can be clearly seen that the NiO diffraction signal (ca. Q = 3 Å^{-1}, reflection (002)) significantly decreases and the diffraction peak at ca. Q = 2.55 – 2.65 Å^{-1} is broadened implying the formation of the $NiAl_2O_4$ phase (generation of more diffraction peaks in the same Q region). However, the summed diffraction pattern from the XRD-CT data collected under 20 % H_2/He flow shows that the diffraction signal from both the NiO and $NiAl_2O_4$ phases has diminished and crystalline Ni-containing species mainly be found in the Ni metallic form. Also observed is the reduction of the diffraction signal generated by the CeO_2-ZrO_2-$Ce_xZ_yO_2$ phases (diffraction peaks in the region of Q = 2.0 – 2.1 Å^{-1}). It should be noted though that no new Ce or Zr phases were observed under the reducing conditions (no new diffraction peaks appear in the XRD-CT data).

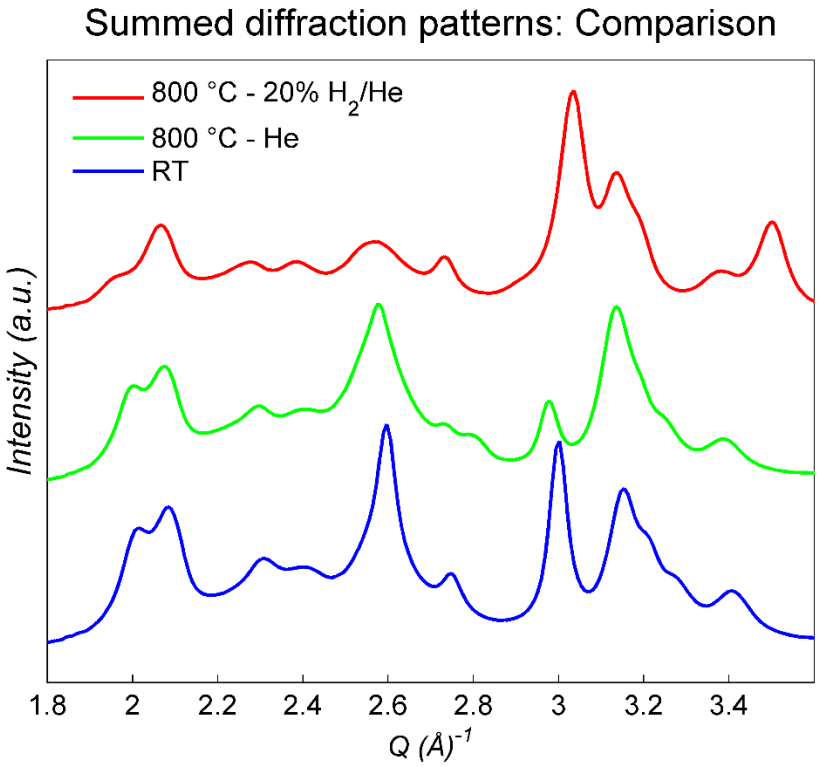

Figure 25: The summed diffraction patterns derived from the XRD-CT data collected at room temperature, 800 °C under He flow and 800 °C under 20 % H_2/He flow.

All the aforementioned solid-state changes are easier to track by inspecting the respective phase distribution maps derived from the XRD-CT data. In Figure 26, the phase distribution maps of the Ni, NiO, $NiAl_2O_4$, CeO_2, ZrO_2, Pd, PdO and Al_2O_3 phases, as obtained from the Rietveld analysis of the XRD-CT data collected at room temperature, at 800 °C under He flow and at 800 °C under 20 % H_2/He flow, are presented. These phase distribution maps correspond to the values of the scale factors of each phase (Rietveld analysis) normalised with respect to the maximum values.

It can be clearly seen from the XRD-CT data collected at 800 °C under He flow that the diffraction signal of the NiO phase has radically decreased and that crystalline Ni-containing species mainly exist in the $NiAl_2O_4$ form. The $NiAl_2O_4$ phase is seen to be predominantly located closer to the core of the catalyst particles rather than their surface. It is of no surprise that almost a reverse map is generated by the Al_2O_3 phase as a direct outcome of the formation and growth of the $NiAl_2O_4$ phase. The NiO phase is seen to be mainly present closer to the surface of the catalyst particles suggesting that the $Ce_xZr_yO_2$ phases serve to stabilize the Ni species and supress the

formation/growth of $NiAl_2O_4$. It should also be noted that the diffraction signal of the CeO_2-ZrO_2-$Ce_xZr_yO_2$ phases is also seen to decrease and there are also small amounts of metallic Pd present (no crystalline PdO is observed).

The results from the two successive XRD-CT scans acquired at 800 °C under 20 % H_2/He flow clearly show that the signal from both NiO and $NiAl_2O_4$ phases has diminished and that crystalline Ni species are found as metallic Ni. It should also be noted that Ni is still seen to grow during the acquisition of these two XRD-CT scans. At this point it should be reminded that the total acquisition time of each XRD-CT scan lasted approximately 25 min. The Ni results presented here serve also to support the previous claim that the Ni concentration gradient along the bed observed with the 3D-XRD-CT data was a time effect (acquisition time of each XRD-CT scan was less than 2 min) and that the reduction process of the NiO and $NiAl_2O_4$ phases is observed to be relatively slow (i.e. to achieve complete reduction of the Ni containing species).

Furthermore, the Al_2O_3 diffraction signal is seen to revert to its initial values (room temperature XRD-CT data) which is an outcome of the disappearance (reduction) of the $NiAl_2O_4$ phase. The diffraction signal generated by the CeO_2-ZrO_2-$Ce_xZr_yO_2$ phases is seen to decrease regardless of the chemical environment present and one could argue that it decreases as a function of time at high temperatures. It should be emphasized though that by the end of the reduction process the higher purity CeO_2 phase is essentially absent. As mentioned previously, this phase was located closer to the core of the catalyst particles. The only crystalline Ce-O species that remain present in the catalyst are in the form of a Ce rich $Ce_xZr_yO_2$ phase which is located close to the surface of the catalyst particles. It is therefore suggested that in the activated catalyst, the two crystalline Ce-O and Zr-O containing phases are actually a Ce rich $Ce_xZr_yO_2$ phase ($x>>y$) and a Zr rich $Ce_xZr_yO_2$ phase ($x<<y$). It is no wonder that these phases are perfectly co-located (i.e. near the surface of the catalyst) following an egg-shell distribution. Finally, it can be seen that metallic Pd is seen to grow under the reducing conditions and that there are some regions of high concentration (hotspots in Figure 26) at the surface of various catalyst particles.

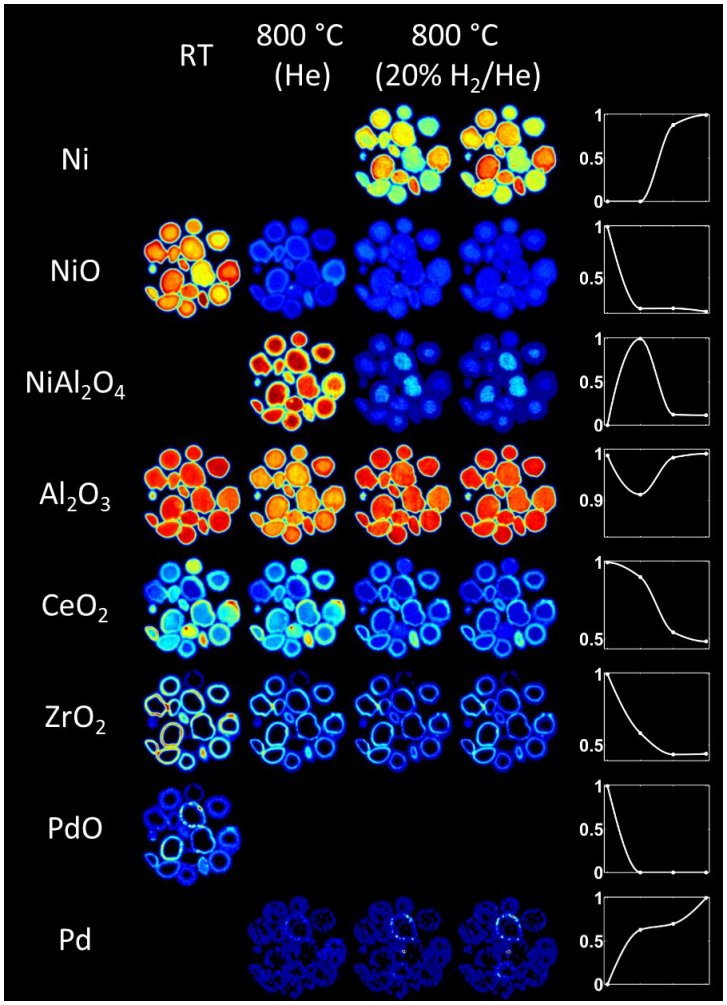

Figure 26: Phase distribution maps of all crystalline phases as obtained from the Rietveld analysis of the XRD-CT data collected at room temperature, at 800 °C under He flow and at 800 °C under 20 % H_2/He flow.

XRD-CT scans during POX

In Figure 27, the phase distribution maps of all crystalline phases, as obtained from the Rietveld analysis of the XRD-CT data collected at 800 °C under POX reaction conditions, are presented. As mentioned previously, these phase distribution maps correspond to the values of the scale factors of each phase (Rietveld analysis) normalised with respect to the maximum values. This is an important detail as it might be implied from Figure 27 that the NiO and $NiAl_2O_4$ phases are present in large amounts under POX reaction conditions but this is not the case here.

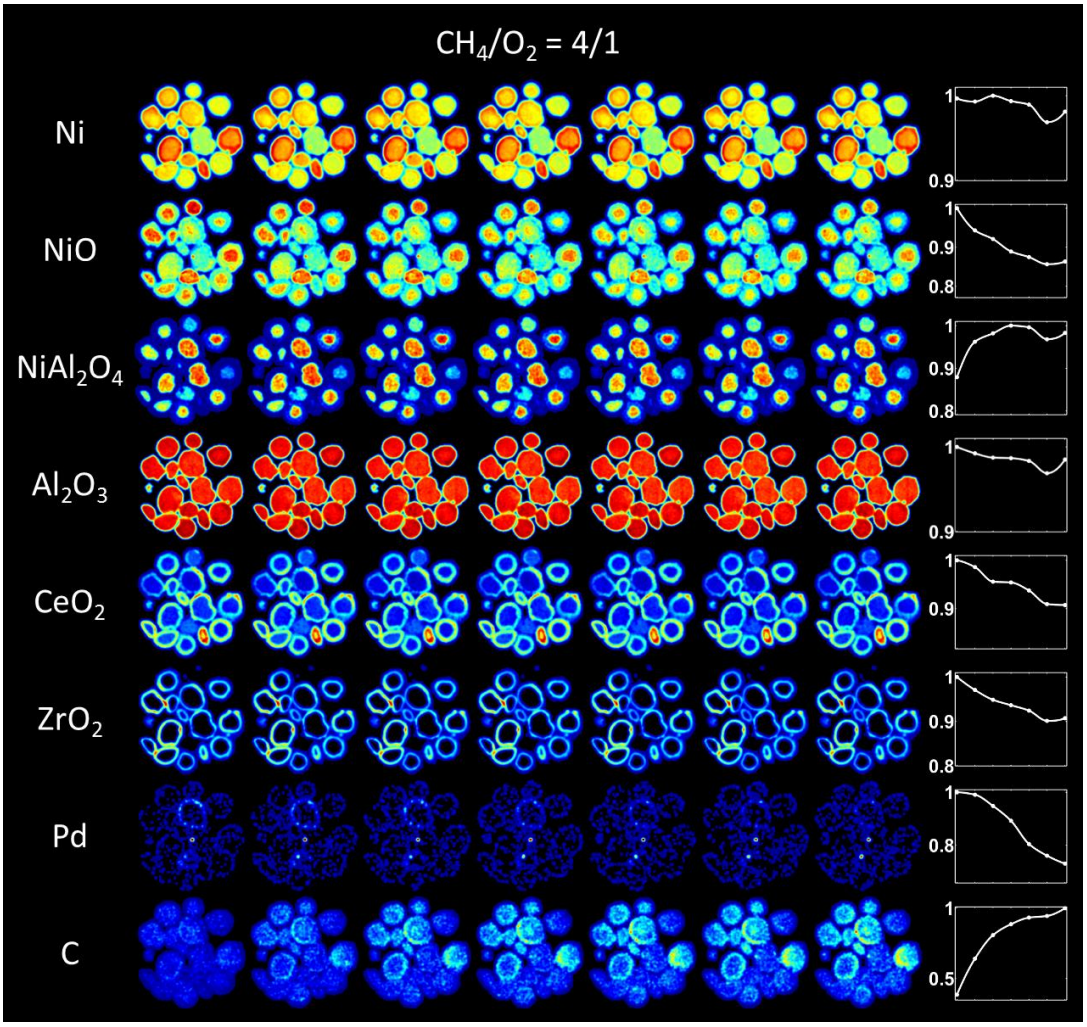

Figure 27: Phase distribution maps of all crystalline phases as obtained from the Rietveld analysis of the XRD-CT data collected under POX reaction conditions.

After inspecting the results presented in Figure 26, it was considered wise to keep both the NiO and $NiAl_2O_4$ phases in the model used for the Rietveld analysis of the XRD-CT data collected under reaction conditions in case any of these phases re-grow during the rest of the experiment. However, the results presented in Figure 27 actually serve to demonstrate that both these phases remain only as traces under reaction conditions and that crystalline Ni-containing species are found in the metallic Ni form. This can be clearly seen in Figure 28 where the summed diffraction patterns of all the XRD-CT data collected during POX experiment are presented.

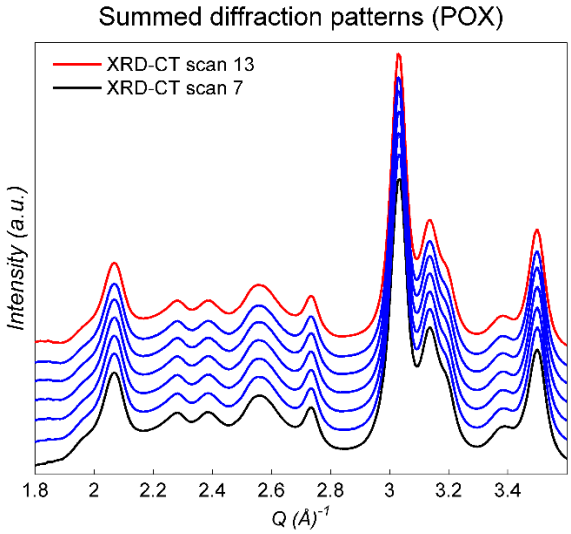

Figure 28: The summed diffraction patterns of the XRD-CT data collected at 800 °C under POX reaction conditions.

More importantly, the crystalline Ni phase is seen to be very stable for the duration of the POX experiment (ca. 3 h). It is impressive that Ni remains in a metallic form when one considers the harsh conditions of the rich methane mix, a CH_4/O_2 molar ratio of 4:1 compared to a ratio of 2:1 used in previous studies.[23-25] A methane rich stream was used to force a faster deactivation of the catalyst in order to capture its behaviour. For clarity, we state that no other crystalline Ni containing phases observed beyond trace amounts (e.g. NiO or $NiAl_2O_4$). However, as is shown in Figure 29, sintering of metallic Ni is seen to take place as a function of time during the POX experiment.

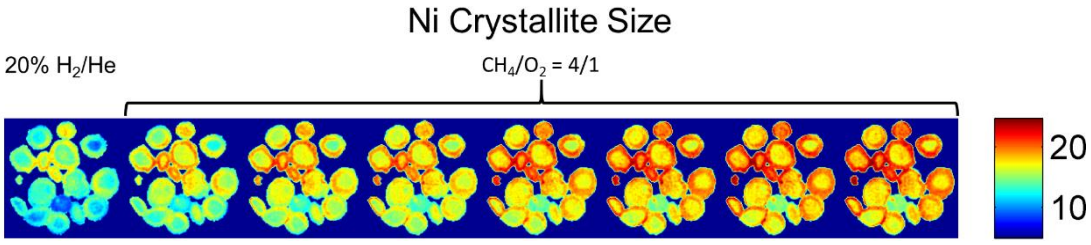

Figure 29: Maps of crystallite sizes of Ni as obtained from the Rietveld analysis of the XRD-CT data collected under reduction and under POX reaction conditions (units in nm).

The typical reaction mixture used to test the performance of POX catalysts is a gas mixture where the CH_4/O_2 molar ratio is 2:1 (stoichiometric ratio for the POX reaction). However, in this study the applied CH_4/O_2 molar ratio was 4:1 as it was attempted to force the catalyst to deactivate faster and capture the corresponding solid-state changes with the XRD-CT technique.

The mass spectrometry data acquired during the POX experiment are presented in Figure 30, where the signals from specific masses of interest are shown and serve to prove that the catalyst was captured in its active state during the POX reaction. It can be clearly seen that upon switching to POX reaction conditions (i.e. region 1 in Figure 30), the signal from masses 2 and 28 increase which correspond to fractions from the POX reaction products (i.e. H_2 and CO respectively). It can also be seen that the signal from masses 15, 17 and 44 (corresponding to CH_4, H_2O and CO_2 respectively) also increase and are present for the duration of the POX experiment. This means not only that CH_4 is not fully consumed (which is expected from the CH_4/O_2 molar ratio used) but that other side reactions take place too resulting in the formation of H_2O and CO_2. It can be clearly seen that the signal from all masses is stable for the duration of the POX experiment and no apparent deactivation of the catalyst was observed.

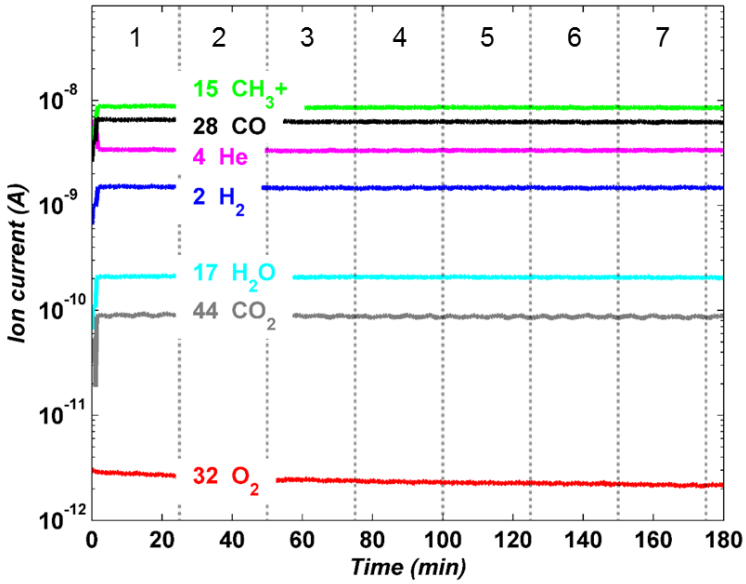

Figure 30: Mass spectrometry data corresponding to the following m/z ratios (possible species and respective line colour in parentheses): 2 (H_2 - blue), 4 (He - magenta), 15 (CH_4+ - green), 17 (H_2O - cyan), 28 (CO – black), 32 (O_2 - red) and 44 (CO_2 - gray). The different regions (1-7) indicated correspond to the seven XRD-CT data collected under POX reaction conditions.

However, as it is shown in Figure 27, upon switching to the POX reaction mixture a new phase formed which was identified as graphite (ICSD: 76767). Only one diffraction peak is observed at approximately Q = 1.81 $Å^{-1}$ (left side of Figure 31) which corresponds to the highest intensity peak of graphite (reflection (002)). This new phase is seen to continuously grow during the POX reaction experiment. As mentioned previously, the POX reaction experiment lasted for approximately 3 h and

it can be seen that the diffraction signal from this phase doubled during this time period. Although no apparent deactivation of the catalyst was observed (mass spectrometry data in Figure 30), it is reasonable to expect that the growth of graphite at the catalyst particles will become detrimental to its long-term performance (i.e. by blocking the active Ni/Pd sites).

Figure 27 also tells us that the Al_2O_3 remains stable for the duration of the POX experiment and no apparent growth of $NiAl_2O_4$ was observed. The diffraction signal from both $Ce_xZr_yO_2$ phases is seen to decrease with time under reaction conditions although one may argue that the decrease is not very significant (ca. 10 % decrease after 3 h). The Pd phase is also seen to decrease as a function of time under the POX reaction conditions. However, this should phenomenon should be expected as the Pd species are part of the active catalyst components (along with the metallic Ni species) and the reaction conditions are considered harsh. It should be emphasize that although this crystalline phase is mentioned as Pd throughout the text and Figures, it is not entirely true. As shown at the right side of Figure 31, the high intensity diffraction peak of this phase (and the only one) is found at ca. Q = 2.83 $Å^{-1}$ which is a high value for metallic Pd. This phase probably corresponds to Pd rich Ni_xPd_y (x<<y) alloy as the incorporation of Ni atom in the Pd unit cell will lead to a smaller unit cell which will generate the respective diffraction peak at higher Q values. It should be noted though that no other crystalline Pd-containing species were observed in the XRD-CT data collected during the POX experiment.

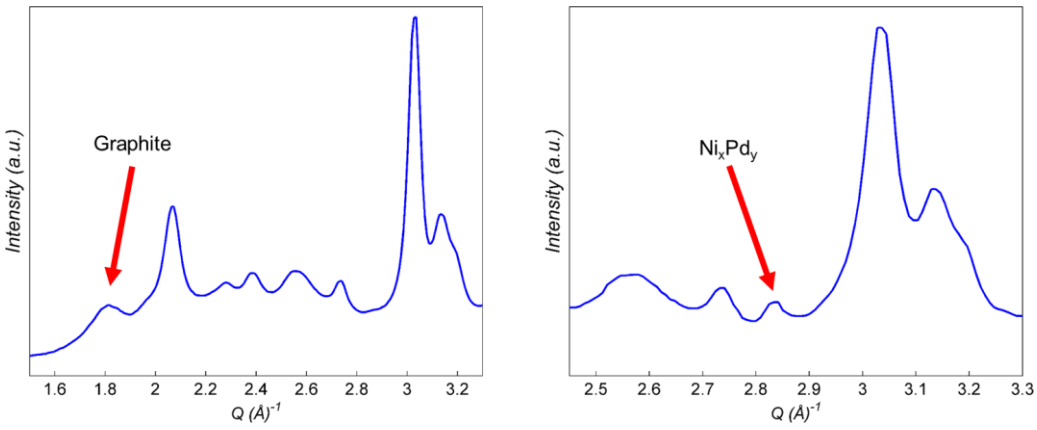

Figure 31: Left: Summed diffraction pattern from a region of interest of the last XRD-CT dataset (XRD-CT scan 13) demonstrating the high intensity graphite peak. Right: Summed diffraction pattern from a region of interest of the second XRD-CT dataset collected under 20 % H_2/He flow (XRD-CT scan 4) demonstrating the high intensity Pd peak.

Ex situ 3D chemical imaging with sub-minute XRD-CT measurements

In our first attempt to apply the fast XRD-CT data collection strategy, the total acquisition time per point was 15 ms as previously stated. These measurements were performed at beamline ID31 of the ESRF and allowed us to collect an XRD-CT scan in approximately 2 min (108 s) and perform the first five dimensional tomographic diffraction imaging experiment reported in literature. It should be mentioned though that at the time of this 5D experiment, the lower limit for the acquisition time per point was actually 15 ms as the then newly purchased Pilatus3 X CdTe 2M area detector had not been fully integrated with the ID31 beamline and there were network related limitations (how many images per second could be transferred from the detector dedication PC to beamline PCs). Once these technical obstacles were overcome, it was considered essential to attempt a sub-minute XRD-CT. This important technical achievement in the XRD-CT method was performed at beamline ID15 of the ESRF. The total acquisition time per point used was 7.5 ms (exposure time of 6 ms, readout time of 1 ms and safety time of 0.5 ms) which allowed us, for the first time, to collect an XRD-CT scan (7200 diffraction images) in less than a minute (54 s).

This acquisition time to perform an XRD-CT scan is several orders of magnitude shorter compared to what has been previously reported in literature. An extreme example in the work of Stock *et al.* from 2008 where the data acquisition rate was ca. 1 image min^{-1} while in the present study the rate was 8000 images min^{-1} (8000 times and more than four orders faster).[42] At the other end of the spectrum, in our recent study, we used 50 ms acquisition time for the XRD-CT scans (fastest reported value in literature at the time of writing) and the data collection rate was ca. 365 images min^{-1}. The data collection rate reported here is 20 times faster than that (again more than one order of magnitude faster). As it can be easily appreciated, this new fast XRD-CT data collection strategy coupled with the recent advances in detector and synchrotron technologies (e.g. X-ray optics) marks the beginning of a new era in diffraction imaging for materials characterisation.

The sample used for the ultra-fast XRD-CT measurements was a 10 wt. % Ni – 0.5 wt. Pd / 10 wt. % CeO_2 – ZrO_2 / Al_2O_3 catalyst taken from a fixed bed reactor after a POX

reaction experiment was performed (*ex situ* characterisation). In addition to these measurements being the fastest XRD-CT scans ever recorded, the XRDC-CT data collected during this beamtime experiment consist, to the author's knowledge, the largest 3D-XRDC-CT data volume ever acquired too. More specifically, the 3D-XRDC-CT data measured correspond to a 100×72×99×2000 raw (pre-reconstruction) diffraction data volume. This POX experiment was performed at the Research Complex at Harwell (RCaH) and the spent catalyst was brought to the ESRF for *ex situ* characterisation with 3D-XRD-CT. The setup used for the laboratory POX experiment is shown in Figure 32. At the right side of Figure 32, the gas delivery system used in the test rig is shown while at the left side, the reactor furnace can be observed. A k-type thermocouple was used to test and control temperature of the catalyst bed.

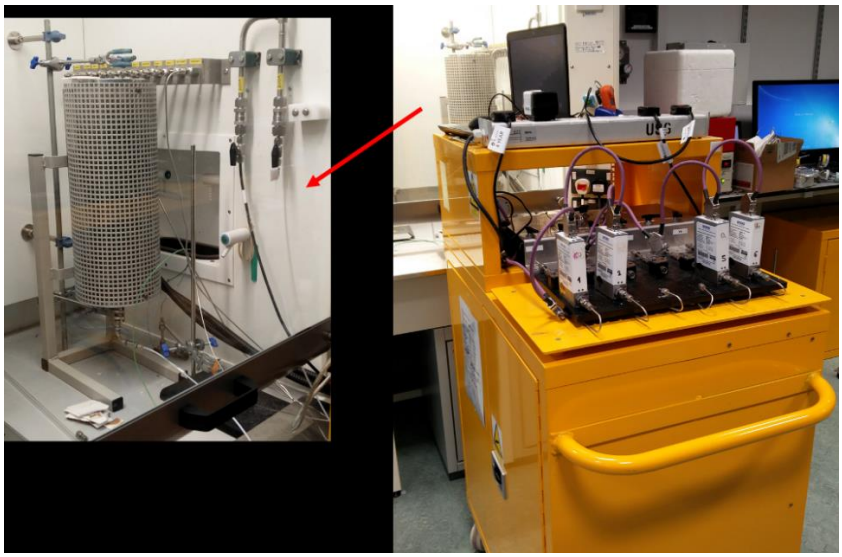

Figure 32: Photographs of the test rig used for the POX reaction experiments at the RCaH. Left: The furnace used for the fixed bed reactor experiments, Right: The gas delivery system.

In Figure 33, a simplified process flow diagram regarding the POX reaction experiment performed with the 10 wt. % Ni – 0.5 wt. Pd/ 10 wt. % CeO_2 – ZrO_2/ Al_2O_3 catalyst is shown. Three gas bottles were used containing the following gas mixtures: 1) 50 % CH_4/Ar, 2) 20 % O_2/He and 3) 100 % Ar (sweep gas). The gas flow rate was controlled by three mass flow controllers (Bronkhorst MFCs) operated by a dedicated PC. The catalyst (350 mg catalyst loading) was mounted in a quartz tube (diameter of 7 mm) and was supported by glass wool. The outflow gasses were monitored by mass spectrometry using an Ecosys portable mass spectrometer.

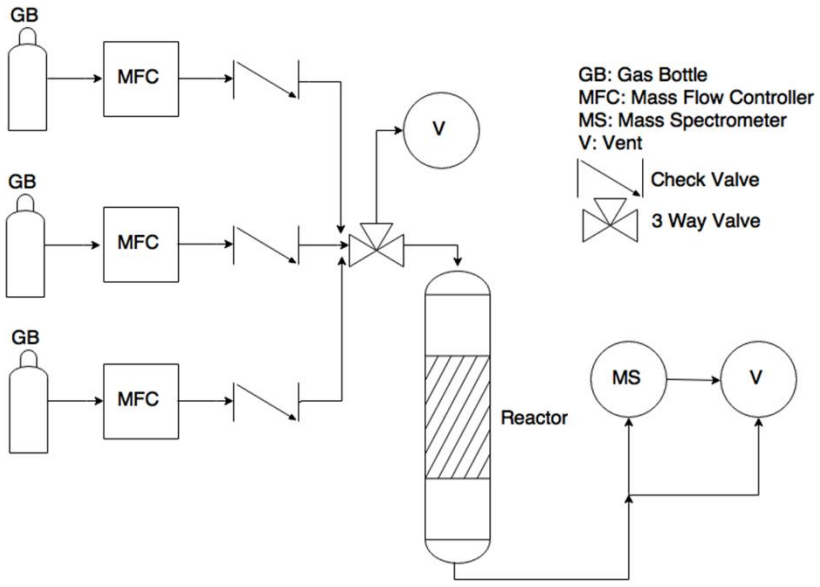

Figure 33: Process flow diagram regarding the POX reaction experiments performed in the laboratory at the Research Complex at Harwell.

The mass spectrometry data acquired during the POX experiment are presented in Figures 34 and 35, where the signals from specific masses of interest are shown. The temperature ramp rate was 10 °C min^{-1} and the operating (final) temperature for the POX experiment was 800 °C. The temperature of the catalyst was increased under the flow of a POX reaction mixture (100 ml min^{-1} of 50 % CH_4/Ar and 83.3 ml min^{-1} of 20 % O_2/He, equating to CH_4/O_2 molar ratio of 3:1). There are three distinct regions present in Figure 34. The beginning of region 1 corresponds to an operating temperature of 400 °C showing that the CH_4 (m/z ratio 15, green line in Figure 34) starts to react when this catalyst is present at very low temperatures. As expected, at the same time a radical decrease of the O_2 signal is observed. At the end of region 1, the system reached the operational temperature of 800 °C and the POX experiment was performed using different gas reaction mixtures (shown in region 2 in Figure 34). The duration of the POX experiment was ca. 105 min and then the temperature of the system was decreased to room temperature. A POX reaction gas mixture was kept till 615 °C was reached (region 3 in Figure 34) and then the reactor inlet gas mixture was switched to pure Ar (end of region 3 in Figure 34).

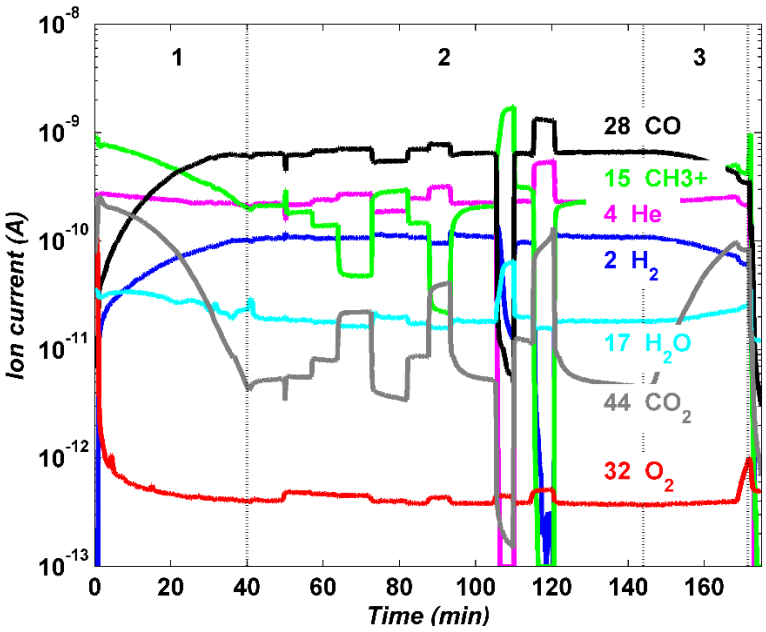

Figure 34 Mass spectrometry data corresponding to the following m/z ratios (possible species and respective line colour in parentheses): 2 (H_2 - blue), 4 (He - magenta), 15 (CH_4+ - green), 17 (H_2O - cyan), 28 (CO – black), 32 (O_2 - red) and 44 (CO_2 - grey). Region 1: Temperature ramping from 400 °C to 800 °C, Region 2: POX reaction conditions using different reaction mixtures, Region 3: Decreasing the temperature to 615 °C while keeping the last reaction gas mixture and then switching to pure Ar and cooling to room temperature.

A magnified version of region 2 in Figure 34 is presented in Figure 35 where the mass spectrometry data collected at 800 °C under POX reaction conditions are shown. The different regions indicated (1-12) correspond to the POX reaction mixtures presented in Table 2.

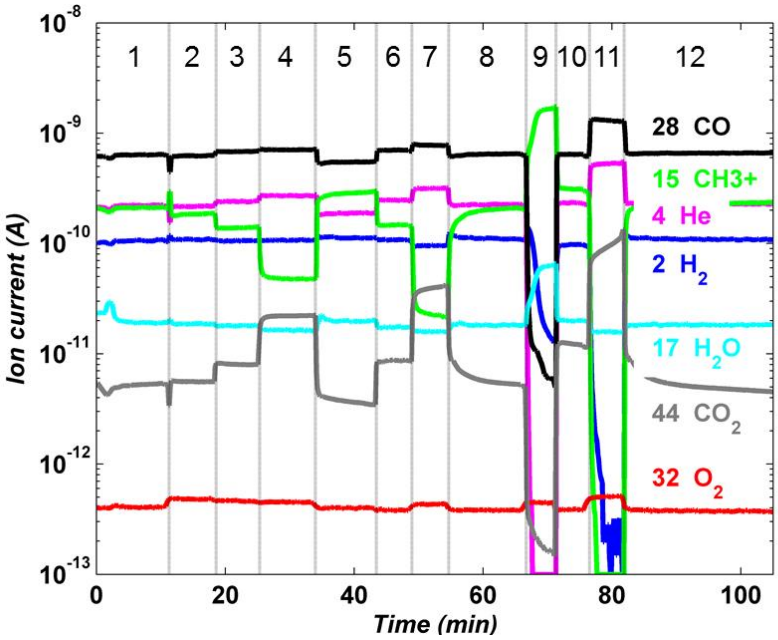

Figure 35 A magnified version of region 2 of Figure 34. The different regions indicated correspond to the POX reaction mixtures presented in Table 2.

Table 2: Summary of reaction mixtures tested during the POX experiment with the 10 wt. % Ni – 0.5 wt. % Pd / 10 wt. % $CeO_2 – ZrO_2 / Al_2O_3$ catalyst

	Reaction mixtures											
	1	**2**	**3**	**4**	**5**	**6**	**7**	**8**	**9**	**10**	**11**	**12**
50 % CH_4 / Ar ($ml\ min^{-1}$)	**100**	**50**	**50**	**50**	**50**	**100**	**100**	**100**	**100**	**100**	**0**	**100**
20 % O_2 / He ($ml\ min^{-1}$)	**83.3**	**41.6**	**50**	**62.5**	**31.25**	**62.5**	**100**	**83.3**	**0**	**83.3**	**83.3**	**83.3**
CH_4 / O_2 ratio	**3.0**	**3.0**	**2.5**	**2.0**	**4.0**	**4.0**	**2.5**	**3.0**	**-**	**3.0**	**0.0**	**3.0**
GHSV ($ml\ min^{-1}\ g^{-1}$)	**524**	**262**	**286**	**321**	**232**	**464**	**571**	**524**	**286**	**524**	**238**	**524**

As it is shown in Table 2, numerous reaction mixtures were used by varying not only the CH_4/O_2 molar ratio but also the GHSV (by changing the total volumetric flow rate of the inlet gas mixture). The mass spectrometry data collected under reaction conditions, presented in Figure 35, serve to illustrate that the catalyst was active under all the applied conditions (regions 1-8, 10 and 11 in Figure 35). The different reaction mixtures used in the regions 2-7 are summarized in Table 2 but what is important is that the activity of the catalyst is seen to be the same in regions 1 and 8, where the same conditions were applies (intensity of all signals is essentially identical). This result probably implies that the state of the catalyst did not change radically during this time period. The catalyst was then exposed, for ca. 5 min, to an O_2-free gas mixture (100 ml min^{-1} flow rate of 50 % CH_4/Ar gas mixture) before switching back to the POX reaction mixture (regions 9 and 10 respectively) used in regions 1 and 8 (100 ml min^{-1} of 50 % CH_4/Ar and 83.3 ml min^{-1} of 20 % O_2/He, equating to CH_4/O_2 molar ratio of 3:1). The mass spectrometry data suggest that the state of the catalyst did change during this CH_4 treatment (region 9) as the CH_4 signal is seen to be higher in region 10 compared to region 8 implying that the activity of the catalyst decreased (less CH_4 conversion). The catalyst was then exposed, for ca. 5 min, to a CH_4-free gas mixture (83.3 ml min^{-1} flow rate of 20 % CH_4/He gas mixture) in an attempt to regenerate the catalyst by burning the coke and other carbonic species possibly formed on the catalyst particles. The catalyst was then exposed to

the POX reaction mixture used in the previous step and the signals of all masses are observed to return to the values before the CH_4 treatment.

As mentioned previously, this POX reaction gas mixture was kept till 615 °C was reached (region 3 in Figure 34) at which point the reactor inlet gas mixture was switched to pure Ar (end of region 3 in Figure 34) and the system was cooled to room temperature. The spent catalyst was characterised with 3D-XRD-CT at beamline ID15 of the ESRF. It is important to note that the catalyst was retrieved from the laboratory reactor and a small portion was reloaded into a quartz tube for the XRD-CT measurement. This has the implication that particles from different parts of the reactor bed are blended though they remaining intact. Also of importance is that in both this experiment and the synchrotron experiment there was significant colour changes of the sample. Fresh calcined catalyst appeared green, whereas post POX, the catalyst appears black. The 3D-XRD-CT consisted of 99 XRD-CT datasets and lasted less than 2 hours. The Rietveld analysis took considerably longer with each reconstructed XRD-CT data volume requiring ca. 1 hour computational time (thus ca. 100 h for all slices). Although such a number may give the impression that this is a very slow process, it is actually not. To elucidate, the analysis of ca. 10^6 diffraction patterns was achieved in only four days using modern desktop PC.

The results from the volume rendering of the scale factors data volume (phase distribution volumes) are presented in Figure 36. The scale factors were normalised with respect to the maximum value for each data volume and the colour axes were scaled accordingly in order to improve the contrast of the respective figures. It should be noted that no crystalline-Pd containing phases were observed in the 3D-XRD-CT data. One would anticipate this though as the results from the *operando* XRD-CT experiment suggested that crystalline Pd (Ni_xPd_y) is formed under H_2 flow and then it gradually disappears under reaction conditions.

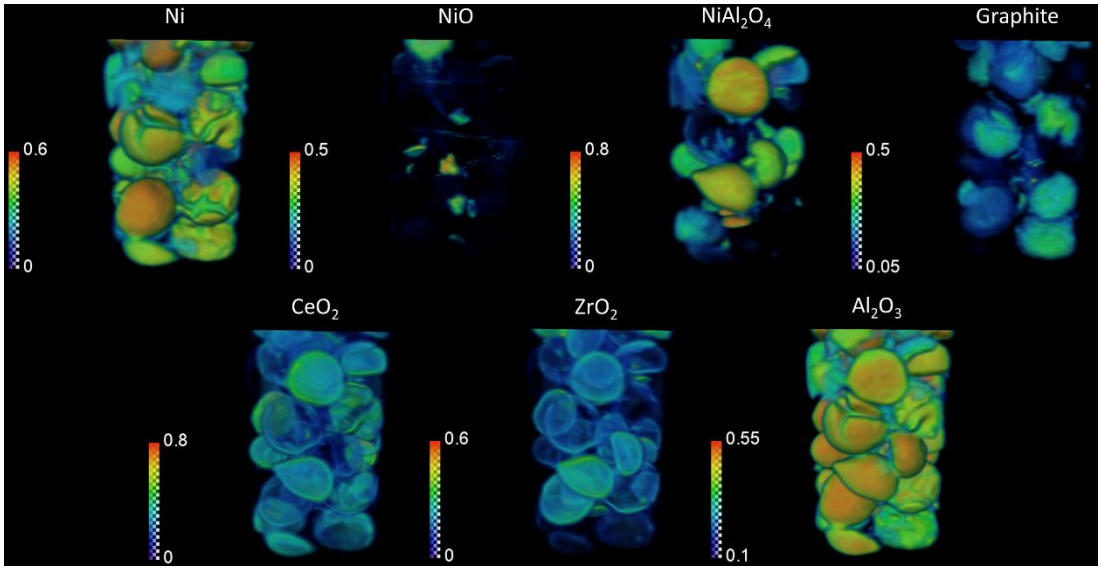

Figure 36: Volume rendering of the scale factors data volume of Ni, NiO, $Ni_2Al_2O_4$, Graphite, CeO_2, ZrO_2 and Al_2O_3 (phase distribution volumes) as obtained from the Rietveld analysis of the spent catalyst 3D-XRD-CT data collected at room temperature. Color bars indicate intensity in arbitrary units.

The most interesting result is, unexpectedly, derived from the Al_2O_3 phase. Since the Al_2O_3 is the main support of the catalyst, the Al_2O_3 phase distribution volume describes accurately the catalyst particles in terms of shape and size. It can be clearly seen that there are numerous particles that have cracks which implies that they suffered from thermal explosion at some point during the POX experiment. In order to verify this result (formation of cracks), traditional μ-absorption-CT (μ-CT) measurements of the spent catalyst were also performed at beamline ID15. Four successive μ-CT scans were acquired at different positions along the catalyst bed and the data were recombined to form a 565×595×1298 data volume (i.e. after appropriate cropping). At the left side of Figure 37, the results from the volume rendering of the reconstructed data (after masking out the background and the reactor vessel) are shown. Indeed, in accordance with the XRD-CT data, there are many catalyst particles containing cracks. Selected μ-CT images are presented at the right side of Figure 37 clearly showing that cracks are also present in the core of numerous catalyst particles implying that this was a result of uncontrolled rise in temperature (i.e. heat transfer limitations). It is interesting that there is high density regions (indicated by bright regions) at the crack surfaces in many but not all of the cracks, though we are not able to rationalize this at this time.

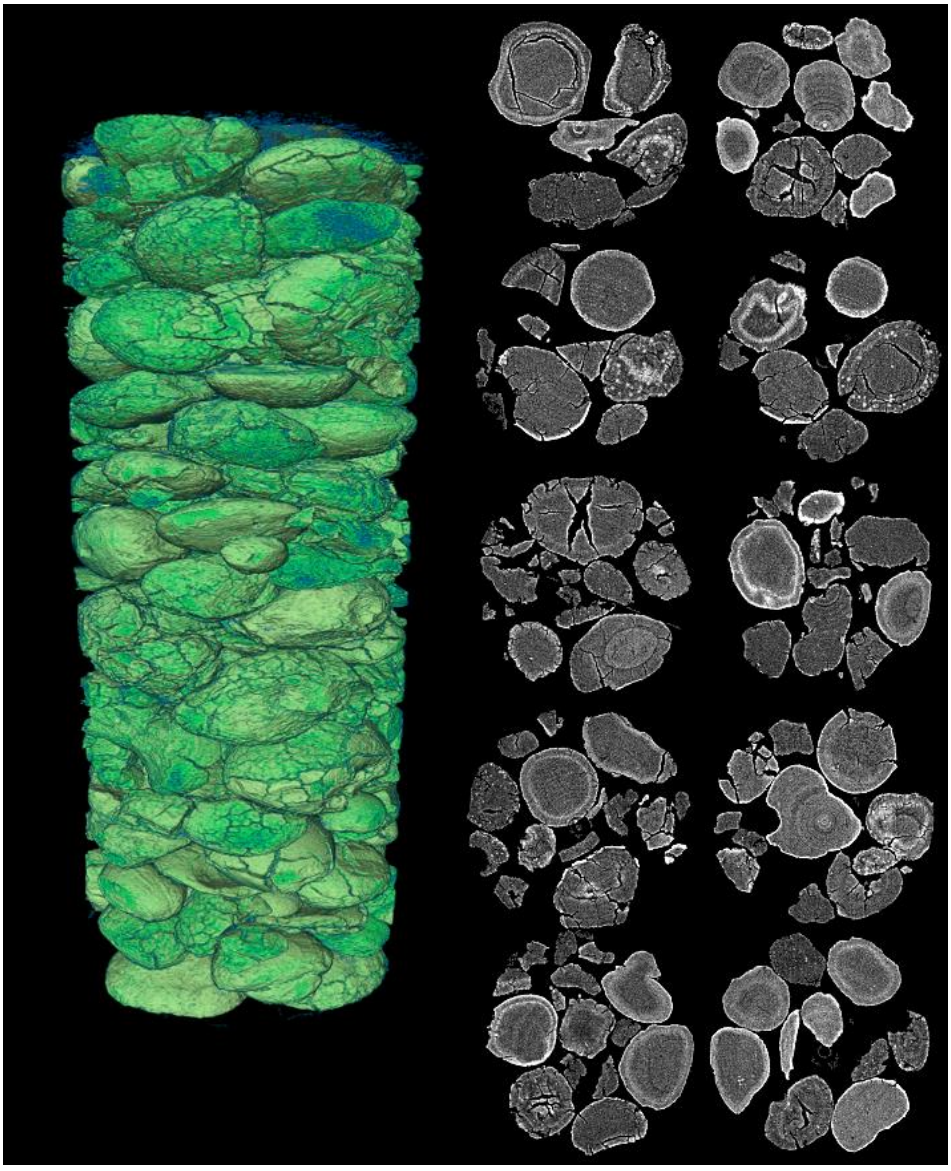

Figure 37: Left: Volume rendering of reconstructed µ-CT data (after masking out the background and the reactor vessel) corresponding to a 565×595×1298 matrix. Right: Selected µ-CT images.

Looking back at the protocol followed during the POX experiment performed in the laboratory (Figure 35), one could argue that this phenomenon took place during the catalyst regeneration step (region 11 in Figure 35). It was previously shown that crystalline graphite forms under POX reaction conditions and one cannot reject the idea that other non-crystalline carbonic species form and grow at the catalyst particles when considering that the whole sample and not just selected particles appear black in colour. Such species would not be visible in the XRD-CT data as they do not give rise to diffraction peaks. The catalyst particles could have exploded when the 20 % O_2/He gas mixture was used (regeneration step) as a result of heat generated by the exothermic oxidation reactions taking place at the catalyst particles.

This could also be supported from the fact that such cracks were not observed in the *operando* XRD-CT experiment where a catalyst regeneration step was not performed. However, this still remains an assumption which cannot be proved or disproved with these data. In fact, the results presented in this sub-section set a perfect example where *ex situ* characterisation can provide limited information regarding the sample under study and highlight the need for *in situ* or preferably *operando* characterisation of functional materials in order to gain a proper insight into the structure-activity relationships.

As it is shown at the right side of Figure 37, the μ-CT images suggest that there are significant differences (spatially) in the X-ray absorption signal from catalyst particle to catalyst particle. Depending on the particle under investigation, the intensity of the μ-CT images is seen to follow an egg-shell, egg-yolk or even uniform distribution. Of course, in this complex materials system involving several elements (Ni, Pd, Al, Zr and Ce) such differences cannot be resolved with traditional X-ray imaging (μ-CT data). On the other hand, as demonstrated in Figure 36, the 3D-XRD-CT technique can resolve these differences.

The CeO_2 phase distribution volume shown in Figure 36 suggests that the CeO_2 phase follows an egg-shell distribution in all catalyst particles. This result is in full agreement with what was observed in the *operando* XRD-CT experiment. More specifically, it was seen that at high temperatures (800 °C), the CeO_2 phase distribution map changes with time and once stabilized it is found to be present only near the surface of the catalyst particles, co-located with the ZrO_2 phase. As discussed in the previous sections, these CeO_2-ZrO_2 phases actually correspond to a Ce rich and a Zr rich $Ce_xZr_yO_2$ phase respectively. It is no wonder then that the CeO_2 phase distribution volume of the spent catalyst is very well correlated with the ZrO_2 one.

Additionally, it is also implied in Figure 36 that crystalline graphite formed during the POX experiment performed in the laboratory, which is in full agreement with what was observed in the *operando* XRD-CT experiment presented in the previous section. Furthermore, it can also be seen that the metallic Ni phase is present in all catalyst particles; a result also in agreement with what was observed in the *operando* XRD-

CT experiment. However, it is also implied that the $NiAl_2O_4$ and NiO phases are present in some particles (not just as traces as in the *operando* XRD-CT experiment).

In order to better demonstrate these differences in solid-state chemistry, the summed diffraction patterns from four catalyst particles of interest were extracted from the 3D-XRD-CT data and compared. These catalyst particles are shown at the left side of Figure 38 and at the right side, the summed diffraction patterns from the corresponding particles are displayed. The choice of these four catalyst particles was based on the results from the Rietveld analysis of the XRD-CT data shown in Figure 36: 1) a catalyst particle rich in NiO (red), 2) a cracked catalyst particle rich in Ni, 3) a catalyst particle rich in $NiAl_2O_4$ (blue) and 4) a cracked catalyst particle rich in graphite. As expected, there are major differences in the respective summed diffraction patterns. For example, the characteristic diffraction peak of graphite (ca. Q = 1.85 $Å^{-1}$) is seen to be really strong in the two catalyst particles that have cracks (i.e. green and gray particles).

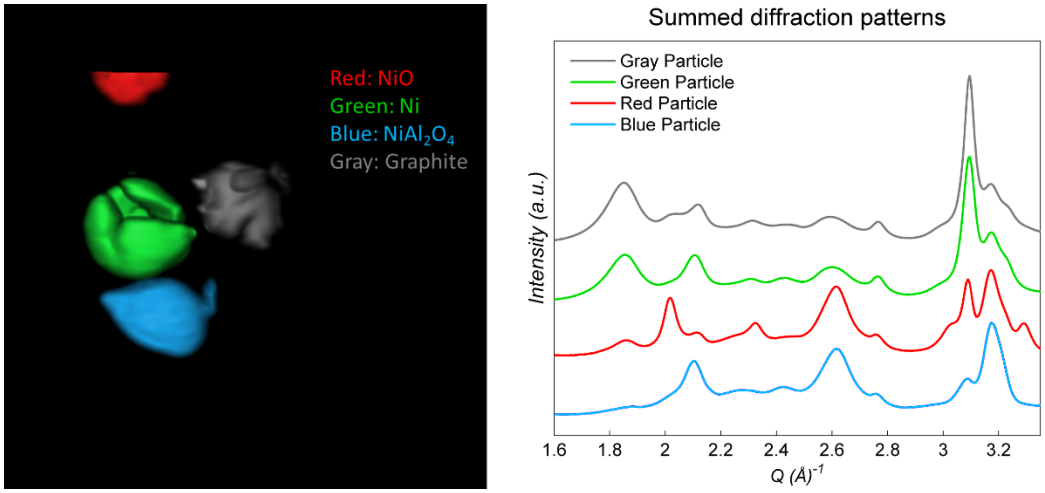

Figure 38: Left: Four catalyst particles of interest and the respective masks. Right: Regions of interest of the four summed diffraction patterns exported from the 3D-XRD-CT data after applying the masks shown on the left side.

Additionally, in the summed diffraction pattern extracted from the red particle, a diffraction peak at ca. Q = 3 $Å^{-1}$ can be observed which is the high intensity peak of NiO (reflection (002)). At the same particle, it can be seen that the diffraction peak at ca. Q = 2.55 – 2.65 $Å^{-1}$ is relatively high, implying that the $NiAl_2O_4$ phase is also present (reflection (311)). Of course, this also the case in the summed diffraction pattern extracted from the blue particle. It should be noted that the blue particle is

rich in Ni-O phases and the graphite peak is essentially absent. This is another indication that during the POX experiment, there were major chemical (solid-state) gradients along the catalyst bed. The results presented in this section clearly demonstrate that it is essential to characterize such complex materials *in situ* and preferably under *operando* conditions as they are chemically altered under reaction conditions and *ex situ* characterisation cannot provide the required information to understand the structure-activity relationships. This experiment also serves to illustrate how the chemistry of particles from different parts of a catalytic bed can be radically different, and furthermore that local probing of selective particles retrieved from a reactor may not be representative (i.e. whole bed imaging is highly desirable).

Summary

The results from three separate XRD-CT experiments performed with a 10 wt. % Ni – 0.5 wt. % Pd/ 10 wt. % CeO_2 – ZrO_2/ Al_2O_3 catalyst were presented in this chapter. A new XRD-CT data collection strategy was also introduced which allows for ultra-fast XRD-CT scans. The breakthrough in this data collection strategy lies on the fact that both tomographic stages (i.e. translation and rotation stages) continuously move during the data acquisition and as a result the "dead time" of the measurement is essentially minimized. This new data collection strategy coupled with a state-of-the-art area detector and the high brilliance hard X-ray beamlines ID15 and ID31 of the ESRF allowed the acquisition of sub-minute XRD-CT scans. This is orders of magnitude faster in comparison to what has been reported in literature in the past. Furthermore, this data collection approach can be in principle applied to all pencil beam tomographic techniques, like X-ray fluorescence computed tomography (XRF-CT), X-ray Absorption Fine Structure computed tomography (XAFS-CT) and tomographic Scanning Transmission X-ray Microscopy (STXM).

This new fast data collection strategy allowed us to perform a 5D tomographic diffraction imaging experiment and investigate the behaviour of the 10 wt. % Ni – 0.5 wt. % Pd/ 10 wt. % CeO_2 – ZrO_2/ Al_2O_3 catalyst during redox. This was achieved by collecting 3D-XRD-CT scans of the catalyst at four different operating conditions: 1) at room temperature (i.e. the fresh catalyst after calcination), 2) at 800 °C under He

flow, 3) at 800 °C under 20 % H_2/He flow investigating the catalyst during its activation and 4) at 800 °C under 20 % O_2/He flow examining how a re-oxidation step can impact the state of the catalyst. The results from the room temperature 3D-XRD-CT showed that the following crystalline phases can be found in the fresh catalyst (i.e. after calcination): NiO, PdO, CeO_2, ZrO_2 and Al_2O_3. The Rietveld analysis of the XRD-CT data also revealed that four distinct crystalline CeO_2-ZrO_2 phases exist in the fresh catalyst:

1. Small crystallites of a Ce rich $Ce_xZr_yO_2$ phase near the surface of the catalyst particles (egg-shell distribution)
2. Larger crystallites of a higher purity CeO_2 phase closer to the core of the catalyst particles (egg-yolk distribution)
3. Small crystallites of a Zr rich $Ce_xZr_yO_2$ phase near the surface of the catalyst particles (egg-shell distribution)
4. Large crystallites of a higher purity ZrO_2 phase where there is high concentration of ZrO_2 (near the surface of the catalyst particles)

NiO was the only crystalline Ni-containing phase present in the fresh catalyst but it was shown that if the catalyst is not exposed to a reducing environment, the NiO gradually transforms to the difficult-to-reduce $NiAl_2O_4$ phase at high temperatures (3D-XRD-CT data at 800 °C under 20 % H_2/He flow). Furthermore, the 3D-XRD-CT data collected during reduction and reoxidation revealed that the reduction process is slower compared to the reoxidation. Specifically, significant Ni/ NiO/ $NiAl_2O_4$ concentration gradients were observed along the catalyst bed during reduction but not during reoxidation. This phenomenon was attributed to the water formation during the reduction of the NiO/ $NiAl_2O_4$ species to metallic Ni. It was also shown that the reoxidation of the catalyst at 800 °C under 20 % O_2/He flow can have a strong impact on the Ni crystallite size (the NiO crystallite size more than doubled from ca. 5-15 nm to ca. 20-35 nm).

The second experiment involved investigating the catalyst under harsh POX reaction conditions (CH_4:O_2 molar ratio double compared to the POX reaction stoichiometric ratio) with high resolution XRD-CT scans. The XRD-CT data collected at high temperature (800 °C) revealed that only the $Ce_xZr_yO_2$ mixed oxides continue to exist

on the catalyst (the higher purity CeO_2 and ZrO_2 gradually disappear). Specifically, the $Ce_xZr_yO_2$ phases close to the surface of the catalyst (egg-shell distribution) are the ones to remain present in the catalyst. Furthermore, metallic Ni was seen to be the main crystalline Ni-containing phase of the catalyst under POX reaction conditions but sintering of the Ni crystallites was not avoided under reaction conditions. More importantly though, crystalline graphite was seen to form and continuously grow under POX reaction conditions. However, there is no indication in the mass spectrometry data collected during the POX experiment that the catalyst deactivated. This is probably the most significant result as it shows that this catalyst is not prone to deactivation even under harsh POX reaction mixtures. This was later verified after performing a separate POX experiment in the laboratory and subsequent *ex situ* characterisation with 3D-XRD-CT at beamline ID15 of the ESRF (third experiment). It was not feasible to observe the crystalline Pd-containing phases in all XRD-CT measurements due to the low Pd loading in the catalyst. However, it was seen that metallic crystalline Pd forms (present as a Ni_xPd_y phase) when the catalyst is activated under H_2 flow but then the diffraction signal generated by this phase decreases as a function of time at high temperatures under POX reaction conditions.

The third experiment was an *ex situ* characterisation experiment of a spent POX catalyst. More specifically, catalyst particles were randomly selected from a fixed bed reactor tested in the laboratory and were characterised with 3D-XRD-CT at the synchrotron. The 3D-XRD-CT was performed by collecting 99 XRD-CT scans; each one lasted less than 1 minute. At the time of writing, this is both the fastest acquisition time reported to acquire a single XRD-CT dataset and the largest 3D-XRD-CT data volume. The Rietveld analysis of this large 3D-XRD-CT dataset ($>10^6$ diffraction patterns) revealed that there were several particles exhibiting different solid-state chemistry. This means that the state of the catalyst during the POX experiment performed in the lab was not same over the whole catalyst bed. As a result, this experiment serves as a perfect example to demonstrate the need for both *in situ* spatially-resolved characterisation of functional materials and whole catalyst bed/ functional device chemical imaging.

Conclusions

The work presented in this Chapter represents a major technical advance towards real-time 3D chemical imaging of functional materials under *operando* conditions. Until now, the XRD-CT technique was considered to be a low temporal resolution technique in many cases making it difficult to track relatively fast solid-state changes taking place in the sample under study. Herein, we showed that the newly developed XRD-CT fast data collection strategy allowed us to perform 3D chemical imaging of a catalyst bed and extract unprecedented physico-chemical information regarding the state of the catalyst under different operating conditions. It should also emphasized that it was the Rietveld analysis of these very large XRD-CT datasets that allowed us to extract this information. With the advancements in synchrotron brightness, detector performance, sample environment (e.g. new reactor cells) and data analysis (e.g. Rietveld analysis of XRD-CT data), 3D chemical imaging experiments are bound to become increasingly easier to perform and one can readily foresee that they will replace conventional *in situ* XRD, and indeed conventional X-ray imaging, as the preferred method for characterising functional materials and devices (e.g. catalysts, batteries and fuel cells).

References

1. Berrocal, G.P., et al., *Novel supports for nickel-based catalysts for the partial oxidation of methane.* Catalysis Today, 2010. **149**(3–4): p. 240-247.
2. Al-Sayari, S.A., *Recent developments in the partial oxidation of methane to syngas.* Open Catalysis Journal, 2013. **6**(1): p. 17-28.
3. Dissanayake, D., et al., *Partial oxidation of methane to carbon monoxide and hydrogen over a Ni/Al2O3 catalyst.* Journal of Catalysis, 1991. **132**(1): p. 117-127.
4. Christian Enger, B., R. Lødeng, and A. Holmen, *A review of catalytic partial oxidation of methane to synthesis gas with emphasis on reaction mechanisms over transition metal catalysts.* Applied Catalysis A: General, 2008. **346**(1–2): p. 1-27.
5. Liu, H. and D. He, *Recent Progress on Ni-Based Catalysts in Partial Oxidation of Methane to Syngas.* Catalysis Surveys from Asia, 2012. **16**(2): p. 53-61.
6. Dong, W.-S., et al., *Comparative Study on Partial Oxidation of Methane over Ni/ZrO2, Ni/CeO2 and Ni/Ce–ZrO2 Catalysts.* Catalysis Letters, 2002. **78**(1): p. 215-222.
7. Shan, W., et al., *Syngas production from partial oxidation of methane over Ce1−XNiXOY catalysts prepared by complexation–combustion method.* Applied Catalysis A: General, 2006. **311**: p. 24-33.
8. Choudhary, V.R., V.H. Rane, and A.M. Rajput, *Selective oxidation of methane to CO and H2 over unreduced NiO-rare earth oxide catalysts.* Catalysis Letters, 1993. **22**(4): p. 289-297.

9. Otsuka, K., et al., *Direct Partial Oxidation of Methane to Synthesis Gas by Cerium Oxide.* Journal of Catalysis, 1998. **175**(2): p. 152-160.
10. Wang, H.-t., Z.-h. Li, and S.-x. Tian, *Effect of promoters on the catalytic performance of Ni/Al2O3 catalyst for partial oxidation of methane to syngas.* Reaction Kinetics and Catalysis Letters, 2004. **83**(2): p. 245-252.
11. Yu, C., et al., *Novel Ni/CeO2-Al2O3 composite catalysts synthesized by one-step citric acid complex and their performance in catalytic partial oxidation of methane.* Journal of Energy Chemistry, 2014. **23**(2): p. 235-243.
12. Fornasiero, P., et al., *Rh-Loaded CeO2-ZrO2 Solid-Solutions as Highly Efficient Oxygen Exchangers: Dependence of the Reduction Behavior and the Oxygen Storage Capacity on the Structural-Properties.* Journal of Catalysis, 1995. **151**(1): p. 168-177.
13. Fornasiero, P., et al., *Modification of the Redox Behaviour of CeO2Induced by Structural Doping with ZrO2.* Journal of Catalysis, 1996. **164**(1): p. 173-183.
14. Hori, C.E., et al., *Thermal stability of oxygen storage properties in a mixed CeO2-ZrO2 system.* Applied Catalysis B: Environmental, 1998. **16**(2): p. 105-117.
15. Pengpanich, S., et al., *Catalytic oxidation of methane over CeO2-ZrO2 mixed oxide solid solution catalysts prepared via urea hydrolysis.* Applied Catalysis A: General, 2002. **234**(1–2): p. 221-233.
16. Esteves, P., et al., *Ceria–zirconia mixed oxides as thermal resistant catalysts for the decomposition of nitrous oxide at high temperature.* Catalysis Today, 2011. **176**(1): p. 453-457.
17. Takeguchi, T., S.-n. Furukawa, and M. Inoue, *Hydrogen Spillover from NiO to the Large Surface Area CeO2–ZrO2 Solid Solutions and Activity of the NiO/CeO2–ZrO2 Catalysts for Partial Oxidation of Methane.* Journal of Catalysis, 2001. **202**(1): p. 14-24.
18. Pengpanich, S., V. Meeyoo, and T. Rirksomboon, *Methane partial oxidation over Ni/CeO2–ZrO2 mixed oxide solid solution catalysts.* Catalysis Today, 2004. **93–95**: p. 95-105.
19. Xu, S. and X. Wang, *Highly active and coking resistant Ni/CeO2–ZrO2 catalyst for partial oxidation of methane.* Fuel, 2005. **84**(5): p. 563-567.
20. Li, Y., et al., *Partial oxidation of methane to syngas over nickel monolithic catalysts.* AIChE Journal, 2006. **52**(12): p. 4276-4279.
21. Jalowiecki-Duhamel, L., H. Zarrou, and A. D'Huysser, *Low temperature hydrogen production from methane on cerium nickel- and zirconium-based oxyhydrides.* Catalysis Today, 2008. **138**(3–4): p. 124-129.
22. Salazar-Villalpando, M.D. and B. Reyes, *Hydrogen production over Ni/ceria-supported catalysts by partial oxidation of methane.* International Journal of Hydrogen Energy, 2009. **34**(24): p. 9723-9729.
23. Liu, Z.W., et al., *Partial oxidation of methane over Ni/Ce-ZrO2/ϑ-Al 2O3.* Korean Journal of Chemical Engineering, 2002. **19**(5): p. 742-748.
24. Dajiang, M., et al., *Catalytic Partial Oxidation of Methane over Ni/CeO2 -ZrO2 - Al2O3.* Journal of Rare Earths, 2007. **25**(3): p. 311-315.
25. Zhang, Q., et al., *Partial oxidation of methane on Ni/CeO2-ZrO2/γ-Al2O3 prepared using different processes.* Journal of Rare Earths, 2008. **26**(3): p. 347-351.
26. Li, H., H. Xu, and J. Wang, *Methane reforming with CO2 to syngas over CeO2-promoted Ni/Al2O3-ZrO2 catalysts prepared via a direct sol-gel process.* Journal of Natural Gas Chemistry, 2011. **20**(1): p. 1-8.
27. Oh, Y.-S., et al., *A highly active catalyst, Ni/Ce–ZrO2/ϑ-Al2O3, for on-site H2 generation by steam methane reforming: pretreatment effect.* International Journal of Hydrogen Energy, 2003. **28**(12): p. 1387-1392.

28. Roh, H.-S., K.-W. Jun, and S.-E. Park, *Methane-reforming reactions over Ni/Ce-ZrO2/ϑ-Al2O3 catalysts.* Applied Catalysis A: General, 2003. **251**(2): p. 275-283.
29. Cai, X., Y. Cai, and W. Lin, *Autothermal reforming of methane over Ni catalysts supported over ZrO2-CeO2-Al2O3.* Journal of Natural Gas Chemistry, 2008. **17**(2): p. 201-207.
30. Lisboa, J.S., et al., *Investigation of Ni/Ce-ZrO 2 catalysts in the autothermal reforming of methane.* Fuel Processing Technology, 2011. **92**(10): p. 2075-2082.
31. de Abreu, A.J., A.F. Lucrédio, and E.M. Assaf, *Ni catalyst on mixed support of CeO2–ZrO2 and Al2O3: Effect of composition of CeO2–ZrO2 solid solution on the methane steam reforming reaction.* Fuel Processing Technology, 2012. **102**: p. 140-145.
32. Ismagilov, I.Z., et al., *Hydrogen production by autothermal reforming of methane over NiPd catalysts: Effect of support composition and preparation mode.* International Journal of Hydrogen Energy, 2014. **39**(36): p. 20992-21006.
33. Ismagilov, I.Z., et al., *Effect of support modification on the physicochemical properties of a NiPd/Al2O3 catalyst for the autothermal reforming of methane.* Kinetics and Catalysis, 2015. **56**(3): p. 394-402.
34. de Freitas Silva, T., et al., *Ni/Al2O3 catalysts: effects of the promoters Ce, La and Zr on the methane steam and oxidative reforming reactions.* Catalysis Science & Technology, 2013. **3**(3): p. 635-643.
35. Choudhary, V.R., B. Prabhakar, and A.M. Rajput, *Beneficial Effects of Noble Metal Addition to Ni/Al2O3 Catalyst for Oxidative Methane-to-Syngas Conversion.* Journal of Catalysis, 1995. **157**(2): p. 752-754.
36. Ji, Y., et al., *A study on the ignition process for the catalytic partial oxidation of methane to synthesis gas by MS-TPSR technique.* Catalysis Letters, 2001. **71**(1): p. 45-48.
37. Dias, J.A.C. and J.M. Assaf, *Autothermal reforming of methane over Ni/γ-Al2O3 catalysts: the enhancement effect of small quantities of noble metals.* Journal of Power Sources, 2004. **130**(1–2): p. 106-110.
38. Li, B., et al., *Temperature profile of catalyst bed during oxidative steam reforming of methane over Pt-Ni bimetallic catalysts.* Applied Catalysis A: General, 2006. **304**: p. 62-71.
39. Basile, F., et al., *Rh–Ni synergy in the catalytic partial oxidation of methane: surface phenomena and catalyst stability.* Catalysis Today, 2002. **77**(3): p. 215-223.
40. Harding, G., J. Kosanetzky, and U. Neitzel, *X-ray diffraction computed tomography.* Medical Physics, 1987. **14**(4): p. 515-525.
41. Kleuker, U., et al., *Feasibility study of x-ray diffraction computed tomography for medical imaging.* Physics in Medicine and Biology, 1998. **43**(10): p. 2911-2923.
42. Stock, S.R., F. De Carlo, and J.D. Almer, *High energy X-ray scattering tomography applied to bone.* J Struct Biol, 2008. **161**(2): p. 144-50.
43. Bleuet, P., et al., *Probing the structure of heterogeneous diluted materials by diffraction tomography.* Nature Materials, 2008. **7**(6): p. 468-472.
44. De Nolf, W. and K. Janssens, *Micro X-ray diffraction and fluorescence tomography for the study of multilayered automotive paints.* Surface and Interface Analysis, 2010. **42**(5): p. 411-418.
45. Valentini, L., et al., *Towards three-dimensional quantitative reconstruction of cement microstructure by X-ray diffraction microtomography.* Journal of Applied Crystallography, 2011. **44**(2): p. 272-280.
46. Artioli, G., et al., *X-ray diffraction microtomography (XRD-CT), a novel tool for non-invasive mapping of phase development in cement materials.* Analytical and Bioanalytical Chemistry, 2010. **397**(6): p. 2131-2136.

47. Palancher, H., et al., *Hard X-ray diffraction scanning tomography with sub-micrometre spatial resolution: application to an annealed γ-U0.85Mo0.15particle.* Journal of Applied Crystallography, 2011. **44**(5): p. 1111-1119.
48. Álvarez-Murga, M., et al., *Microstructural mapping of C60 phase transformation into disordered graphite at high pressure, using X-ray diffraction microtomography.* Journal of Applied Crystallography, 2010. **44**(1): p. 163-171.
49. Stock, S.R. and J.D. Almer, *Diffraction microcomputed tomography of an Al-matrix SiC-monofilament composite.* Journal of Applied Crystallography, 2012. **45**(6): p. 1077-1083.
50. Valentini, L., et al., *Multifractal Analysis of Calcium Silicate Hydrate (C-S-H) Mapped by X-ray Diffraction Microtomography.* Journal of the American Ceramic Society, 2012. **95**(8): p. 2647-2652.
51. Egan, C.K., et al., *Non-invasive imaging of the crystalline structure within a human tooth.* Acta Biomaterialia, 2013. **9**(9): p. 8337-8345.
52. Bonnin, A., et al., *Impurity precipitation in atomized particles evidenced by nano x-ray diffraction computed tomography.* Applied Physics Letters, 2014. **105**(8): p. 084103.
53. Vanmeert, F., G. Van der Snickt, and K. Janssens, *Plumbonacrite identified by X-ray powder diffraction tomography as a missing link during degradation of red lead in a Van Gogh painting.* Angew Chem Int Ed Engl, 2015. **54**(12): p. 3607-10.
54. Wragg, D.S., et al., *Rietveld analysis of computed tomography and its application to methanol to olefin reactor beds.* Journal of Applied Crystallography, 2015. **48**(6): p. 1719-1728.
55. Jensen, K.M.O., et al., *X-Ray Diffraction Computed Tomography for Structural Analysis of Electrode Materials in Batteries.* Journal of the Electrochemical Society, 2015. **162**(7): p. A1310-A1314.
56. Frolich, S., et al., *Diffraction tomography and Rietveld refinement of a hydroxyapatite bone phantom.* Journal of Applied Crystallography, 2016. **49**(1): p. 103-109.
57. Basile, F., et al., *Combined Use of Synchrotron-Radiation-Based Imaging Techniques for the Characterization of Structured Catalysts.* Advanced Functional Materials, 2010. **20**(23): p. 4117-4126.
58. Voltolini, M., et al., *Understanding cement hydration at the microscale: new opportunities from `pencil-beam' synchrotron X-ray diffraction tomography.* Journal of Applied Crystallography, 2013. **46**(1): p. 142-152.
59. Beale, A.M., S.D. Jacques, and B.M. Weckhuysen, *Chemical imaging of catalytic solids with synchrotron radiation.* Chem Soc Rev, 2010. **39**(12): p. 4656-72.
60. Grunwaldt, J.D. and C.G. Schroer, *Hard and soft X-ray microscopy and tomography in catalysis: bridging the different time and length scales.* Chem Soc Rev, 2010. **39**(12): p. 4741-53.
61. Frenkel, A.I., J.A. Rodriguez, and J.G. Chen, *Synchrotron Techniques for In Situ Catalytic Studies: Capabilities, Challenges, and Opportunities.* ACS Catalysis, 2012. **2**(11): p. 2269-2280.
62. de Groot, F.M.F., et al., *In-situ scanning transmission X-ray microscopy of catalytic solids and related nanomaterials.* ChemPhysChem, 2010. **11**(5): p. 951-962.
63. Andrews, J.C. and B.M. Weckhuysen, *Hard X-ray spectroscopic nano-imaging of hierarchical functional materials at work.* ChemPhysChem, 2013. **14**(16): p. 3655-3666.
64. Grunwaldt, J.-D., J.B. Wagner, and R.E. Dunin-Borkowski, *Imaging Catalysts at Work: A Hierarchical Approach from the Macro- to the Meso- and Nano-scale.* ChemCatChem, 2013. **5**(1): p. 62-80.

65. Urakawa, A., *Trends and advances in Operando methodology.* Current Opinion in Chemical Engineering, 2016. **12**: p. 31-36.
66. Wang, H. and F. Wang, *In situ, operando measurements of rechargeable batteries.* Current Opinion in Chemical Engineering, 2016. **13**: p. 170-178.
67. Crumlin, E.J., et al., *X-ray spectroscopy of energy materials under in situ/operando conditions.* Journal of Electron Spectroscopy and Related Phenomena, 2015. **200**: p. 264-273.
68. Harks, P.P.R.M.L., F.M. Mulder, and P.H.L. Notten, *In situ methods for Li-ion battery research: A review of recent developments.* Journal of Power Sources, 2015. **288**: p. 92-105.
69. Deabate, S., et al., *3 In situ and operando determination of the water content distribution in proton conducting membranes for fuel cells: a critical review.* Energy & Environmental Science, 2012. **5**(10): p. 8824-8847.
70. Grey, C.P. and J.M. Tarascon, *Sustainability and in situ monitoring in battery development.* Nat Mater, 2017. **16**(1): p. 45-56.
71. Jacques, S.D., et al., *Dynamic X-ray diffraction computed tomography reveals real-time insight into catalyst active phase evolution.* Angew Chem Int Ed Engl, 2011. **50**(43): p. 10148-52.
72. O'Brien, M.G., et al., *Active phase evolution in single Ni/Al2O3 methanation catalyst bodies studied in real time using combined μ-XRD-CT and μ-absorption-CT.* Chemical Science, 2012. **3**(2): p. 509.
73. Beale, A.M., et al., *Chemical imaging of the sulfur-induced deactivation of Cu/ZnO catalyst bodies.* Journal of Catalysis, 2014. **314**: p. 94-100.
74. Price, S.W.T., et al., *In Situ Microfocus Chemical Computed Tomography of the Composition of a Single Catalyst Particle During Hydrogenation of Nitrobenzene in the Liquid Phase.* Angewandte Chemie, 2015. **127**(34): p. 10024-10027.
75. Vamvakeros, A., et al., *Real time chemical imaging of a working catalytic membrane reactor during oxidative coupling of methane.* Chemical Communications, 2015. **51**(64): p. 12752-12755.
76. Vamvakeros, A., et al., *Interlaced X-ray diffraction computed tomography.* Journal of Applied Crystallography, 2016. **49**(2): p. 485-496.
77. Vamvakeros, A., et al., *Removing multiple outliers and single-crystal artefacts from X-ray diffraction computed tomography data.* Journal of Applied Crystallography, 2015. **48**(6): p. 1943-1955.
78. Ashiotis, G., et al., *The fast azimuthal integration Python library: PyFAI.* Journal of Applied Crystallography, 2015. **48**: p. 510-519.
79. *TOPAS Version 5.0*. Bruker AXS: Karlsruhe, Germany.
80. Kovarik, L., et al., *Unraveling the Origin of Structural Disorder in High Temperature Transition Al2O3: Structure of ϑ-Al2O3.* Chemistry of Materials, 2015. **27**(20): p. 7042-7049.
81. Thompson, P., D.E. Cox, and J.B. Hastings, *Rietveld refinement of Debye-Scherrer synchrotron X-ray data from Al2O3.* Journal of Applied Crystallography, 1987. **20**(2): p. 79-83.
82. Li, G., L. Hu, and J.M. Hill, *Comparison of reducibility and stability of alumina-supported Ni catalysts prepared by impregnation and co-precipitation.* Applied Catalysis A: General, 2006. **301**(1): p. 16-24.

Conclusions & Future Work

This thesis focuses on the development and application of synchrotron X-ray scattering and spectroscopic CT techniques with application to image the operando chemistry occurring inside the confines of various reactors. This included studying working catalytic dense ceramic hollow-fibre membrane reactors, where prior to this work, there had been no studies at all of such integrated reactors under operation. Synchrotron-based XRD-CT was the principal technique used to characterise and investigate the heterogeneous solid materials under study. The past decade has seen significant interest and development of this technique as a tool investigate heterogeneous functional materials both under static (*ex situ*) and under working conditions (*in situ*/ *operando*).

The challenging nature of these studies required new approaches to both data collection and analysis which are summarised below. This includes new data filtering, novel approaches to self-absorption correction, the development of interlaced and fast XRD-CT collection and high throughput data processing. These technical advances are not limited to XRD-CT and are expected to have impact to other techniques and fields. Following from this, the new insights on the material systems studied have also been summarised and discussed. This includes the study of unpromoted and La-promoted Mn-Na-W-O/ SiO_2 catalysts within traditional packed beds and catalytic membrane reactors under operando conditions explicitly for the oxidative coupling of methane (OCM) reaction. The crystal structure solution of one of the membrane types investigated allowed, for the first time, the direct measurement of oxygen transport through imaging the oxygen occupancy of the membrane in various states of activity. Finally, a Ni-Pd/CeO_2-ZrO_2/Al_2O_3 reforming catalyst was also investigated under redox and partial oxidation (POX) of methane reaction conditions. The work presented in this thesis represents a substantial data processing achievement with the Rietveld analysis of ca. three million diffraction patterns.

Technical advances

As shown in Chapters 3 and 4 and in parts of Chapters 6 and 7, several technical advances have been achieved during this project; in some cases, these advances are not limited to XRD-CT but are applicable to all pencil /narrow beam scanning CT techniques (e.g. XRF/XAFS/PDF/STXM-CT).

Removal of single-crystal artefacts

One of the most common artefacts encountered in XRD-CT experiments is the presence of line or "streak" artefacts in the reconstructed data (XRD-CT images). Such artefacts arise when there are large crystallites present in the sample under study (large with respect to the size of the illuminating focused X-ray beam). The presence of such crystallites can lead to single crystal diffraction contribution to the powder diffraction data collected during an XRD-CT scan (i.e. spots on top of the powder diffraction rings). These spots lead to the presence of hotspots in the sinograms and the formation of line or "streak" artefacts in the reconstructed images. As presented in Chapter 3, a new data filtering approach was developed during this project that allows the suppression/removal of such artefacts; importantly the best of the filters developed is computationally efficient and does not lead to loss of information.

In this new approach, the filters are not applied to the raw 2D diffraction patterns (images) or to the sinograms (projection space) or to the reconstructed data (real space). In contrast to what has been previously attempted, the filters are applied to the polar transformed 2D diffraction patterns prior to integration. The effect of several filters was investigated, with the trimmed mean filter yielding the best results. To clarify, an ideal filter should change the intensities of the diffraction peaks generated by the phase(s) with large crystallites (i.e. decreasing the intensities) while maintaining the intensities of the rest the diffraction peaks (i.e. compared to unfiltered data). The trimmed mean filter does not do this; it performs the same operation (i.e. trimming) to all diffraction peaks.

A possible filter that can perform the desired task could be one that would trim different numbers of values per row in the polar transformed images (rows

corresponding to the distance from the beam centre (2θ/d/Q)). For example, the standard deviation-based filter also presented in Chapter 3 operates this way. However, it was shown that its performance is worse compared to the trimmed mean filter. This was attributed to the fact that the value of the standard deviation is different in every row. As a result, the threshold value (i.e. defined as multiple of the standard deviation) used to trim the outliers should not be constant (i.e. specified by the user) but should change per row in the polar transformed images. A superior filter then, would be one based on iterative calculation of the standard deviation which avoids sorting the values (which is computationally expensive) and requires no (arbitrary) user input. Here, the threshold value per row would be calculated by the filter algorithm. Although not presented in this thesis, such a filter was also developed during this project but requires further optimisation. It should finally be emphasized that this filtering process is not limited to XRD-CT data but can be used in general to treat single crystal artefacts in 2D powder diffraction data (i.e. in all other conventional powder diffraction where a 2D detector is used).

Self-absorption correction

Another commonly encountered problem in XRD-CT is related to self-absorption artefacts. From an experimental perspective, such artefacts are usually avoided/mitigated indirectly by using hard (high energy) X-rays. However, as it is shown in the XRD-CT data presented in Chapter 6, such an approach cannot always be taken. The catalytic membrane reactors (CMRs) investigated in this study composed of heavily absorbing dense ceramic membranes (BCFZ and LSCF) leading to self-absorption artefacts in the reconstructed XRD-CT data despite the use of hard X-rays (ca. 93 keV). In order to remove these artefacts, micro-CT (X-ray absorption contrast CT) of the same samples were used to correct the XRD-CT data for self-absorption. The self-absorption correction process is discussed in detail in Chapter 6. There are three types of self-absorption corrections that can be applied (i.e. zero, first and second order approximations). In this work, the simplest approach (zero order approximation) was used to improve the quality of the CMR XRD-CT data and indeed it had a major impact in the quality of the reconstructed XRD-CT images (especially in the case of the LSCF membrane). More specifically, in contrast to the

uncorrected XRD-CT data, the shape and size of the ceramic membranes was well-defined. It should also be noted that a simple algorithm for the first order approximation method was also developed during this project. However, this could be further improved by ray tracing. Finally, it should be emphasised that these algorithms can potentially be used to correct other scanning X-ray scattering/spectroscopic CT data (e.g. PDF-CT and XRF-CT).

New data collection strategies

In Chapter 4, the various previously available XRD-CT data collection strategies were discussed in detail and importantly a new collection strategy, termed Interlaced XRD-CT, was introduced. The new approach allows, post experiment, choice between temporal and spatial resolution. The temporal resolution in traditional scanning CT scans is equal to the total acquisition time to perform the CT scan. The interlaced approach provides increased temporal resolution (by *n* times where *n* is an integer, preferably power of 2) by performing successive lower spatial resolution XRD-CT scans (*1/n* spatial resolution). This is done by increasing the tomographic angular step size by *n* times and applying an appropriate angular offset for each XRD-CT scan (each one covering a 0-180 ° angular range). As a result, post experiment, each XRD-CT dataset can be treated independently providing the maximum temporal and minimum spatial resolution, or the various datasets can be recombined to yield lower temporal and higher spatial resolution. This data collection strategy is especially useful to study materials that are evolving during an experiment (e.g. functional materials under operating conditions). For example, in Chapter 4, it was shown that successive interlaced XRD-CT scans collected during temperature ramping from ambient to 800 °C allowed us to image a metastable orthorhombic Na_2WO_4 phase in the Mn-Na-W/SiO_2 catalyst that exists only over a short temperature range (cubic Na_2WO_4 phase present in the fresh Mn-Na-W/SiO_2 catalyst). Of particular note, is that different scattering angles can be treated independently. This can mean that if a phase is not changing during a fixed period it can be reconstructed with the highest spatial resolution even when other phases which are contributing to the diffraction patterns are changing. The interlaced approach is not limited to XRD-CT but can be applied to all 1st generation scanning CT experiments (e.g. XRF-CT, PDF-CT, XAFS-CT

and STXM-CT). The method is not expected to be supplanted by the fast method described below, since it should have application where there is low or limited photon fluxes as in the case of laboratory instruments and relatively low flux synchrotron beam lines.

The infinite continuous rotation data collection strategy, first conceptually introduced in Chapter 4, was implemented. This data collection strategy allows both tomographic stages to move simultaneously (i.e. rotation and translation) leading to ultra-fast XRD-CT scans as it essentially minimises the dead time of the measurement. Again, as in the case of the interlaced approach, the infinite continuous rotation method is applicable to all 1st generation scanning CT experiments. This method allowed us to collect the first ever reported sub-minute XRD-CT scans. This represents a major advance as till now the XRD-CT technique was considered a very slow technique (low temporal resolution), unable to track relatively fast solid state changes. As discussed in the short review presented in Chapter 7, the acquisition time of an XRD-CT scan in most cases requires 30 min to several hr. This new data collection strategy allowed us to collect not only the fastest XRD-CT scan ever reported in literature but also the largest 3D-XRD-CT scan too. It was also realised that this fast approach should ideally be coupled with the interlaced approach when performing 3D-XRD-CT scan under dynamic conditions. Here, the interlaced approach is applied in the *z* direction; the coupling of these two methods though still remains to be demonstrated.

Catalytic systems

Multi-length scale imaging of working solid catalysts

As discussed thoroughly in Chapter 5, the Mn-Na-W/SiO_2 based catalysts are considered to be one of the most promising materials for the oxidative coupling of methane (OCM) to ethane and ethylene due to their high performance under reaction conditions (i.e. in terms of both activity and selectivity to C_2 molecules). These catalysts have been studied extensively in the past 25 years but there is still ongoing debate regarding the state of the active catalysts and the reasons behind their deactivation. In this work various X-ray scattering/spectroscopic CT techniques

were, for the first time, employed to study a Mn-Na-W/SiO_2 and a La-promoted Mn-Na-W/SiO_2 catalyst under OCM reaction conditions. Specifically, XRD-CT was used to study the two catalysts at the reactor level and multimodal μ-XRD/XRF/absorption-CT was employed to investigate the behavior of the two catalysts at the single particle level (multi-length scale imaging). Both studies revealed that these materials not only evolve under the high temperatures required for the OCM reaction (typically >750 °C) as a function of time, but also during temperature ramping and cooling (e.g. the evolution of the Na_2WO_4 phase). It is no wonder then that the lack of *in situ* studies of these catalysts in literature (with most studies focusing on *ex situ* characterisation of these materials) is directly related to our limited understanding of the state of these catalysts under real reaction conditions. The spatially-resolved signals obtained from the chemical tomographic techniques applied, allowed us to resolve several discrepancies in the literature and gain new insight and understanding into the behavior of these catalysts under OCM operating conditions. For example, it was shown that neither crystalline Mn_2O_3/Mn_7SiO_{12} nor $MnWO_4$ phases are required components to yield an active OCM catalyst. Furthermore, the melting of the Na_2WO_4 phase during temperature ramping yields Na^+ and WO_4^{2-} species which are observed to be both mobile and volatile. The volatility of the Na^+ ions was indirectly observed through the formation of a crystalline SiO_2 cristobalite layer at the inner side of the amorphous SiO_2 tube (reactor vessel). The crystallization of amorphous SiO_2 to the crystalline cristobalite form at these temperatures can only be achieved by incorporating Na^+ species in the SiO_2 framework. The SiO_2 support of the catalysts was also seen to evolve under the high temperatures required for the OCM regardless of the imposed chemical environment. Specifically, gradual conversion of the cristobalite phase to the tridymite and quartz phases was observed. Most importantly, it was seen that the La can improve the chemical stability of the Mn-Na-W/SiO_2 catalyst by immobilising the Na^+ and WO_4^{2-} species and forming a new crystalline phase, identified as $NaLa(WO_4)_2$. As a result, the information obtained from these *in situ* experiments is expected to open new pathways to rationally designing improved OCM catalysts. Future *in situ* chemical tomographic experiments should focus on the effect of other promoters (e.g. Ce) to the performance of the Mn-Na-W/SiO_2 based catalysts.

Chemical imaging of working catalytic membrane reactors

In the past decade, dense perovskite-type ceramic membranes have attracted a lot of attention as functional materials for both pure oxygen production and chemical synthesis. These materials activate at high temperatures (typically above 650 °C) allowing only oxygen ions to diffuse through them. This is achieved by applying a oxygen concentration gradient (by virtue of oxygen partial pressure difference) between the two sides of the membrane. There are various types and designs of CMRs but the ones investigated in this study are integrated reactor systems consisting of a dense hollow-fibre ceramic membrane in combination with a catalyst bed. Unfortunately, such complex materials systems are typically characterised *ex situ*, fresh or post-mortem, with techniques like SEM/TEM/EDX and powder diffraction. In this work, we used high energy synchrotron X-rays (ca. 93 keV) to probe the interior of the dense ceramic membrane, and performed the first ever *in situ* experiments of working CMRs. Indeed, it was shown that spatially-resolved diffraction information can be gleaned from within the confines of working CMRs and that solid-state evolution of the various CMR components could be followed. This represents a major characterisation advance; advancing from the situation of no *in situ* insight to having spatio-temporal resolved chemical information.

The XRD-CT results showed that the mobile/volatile Na^{+} and WO_4^{2-} species, originating from the catalyst bed, chemically interact with the ceramic membranes forming new stable crystalline phases. In the case of the BCFZ membrane, the formation of a $BaWO_4$ layer at the inner membrane wall was observed while in the case of the LSCF membrane the new phase was $SrWO_4$. The continuous growth of these phases under OCM reaction conditions is expected to have a negative impact on the long-term stability of the CMRs; the formation of inner BaWO4/SrWO4 layers can block the oxygen flow to the catalyst bed deactivating the CMRs.

The crystal structure of BCFZ was solved using high resolution neutron powder diffraction data and this structure model was then added to the model used during the Rietveld analysis of the CMR XRD-CT data. The Rietveld analysis allowed the refinement of the BCFZ structure model and the creation of maps corresponding to the unit cell parameters, thermal parameters and oxygen occupancies. The most

important aspect of this work is that it demonstrates that XRD-CT experiments of such complex systems are not only feasible but the Rietveld analysis of the XRD-CT data can provide unprecedented spatially-resolved physico-chemical information about these systems. This study is expected to have an impact not only on the scientific community working on CMRs but on the fuel cell community as well. For example, one can easily foresee the application of XRD-CT to study micro-tubular SOFCs under operating conditions and to track the (evolving) solid state chemistry taking place at the electrodes (or possible electrode/electrolyte chemical interaction) as a function of potential.

5D diffraction imaging and Rietveld analysis of large datasets

In Chapter 7, the results from three XRD-CT experiments using a methane reforming Ni-Pd/CeO_2-ZrO_2/Al_2O_3 catalyst were presented. We implemented the fast data collection strategy to conduct a 5D tomographic diffraction imaging experiment by collecting 3D-XRD-CT scans (<2 min per XRD-CT scan) under different operating conditions. The Rietveld analysis of the 3D XRD-CT datasets (>10^6 diffraction patterns) yielded 3D maps of various parameters including phase distributions, unit cell parameters and crystallite sizes. It should be emphasised that it was the combination of spatially resolved diffraction signals and the Rietveld analysis approach that allowed us to discriminate between four different $Ce_xZr_yO_2$ phases present in the fresh catalyst. The redox experiment showed that the reduction process (under H_2/He flow) is slower compared to re-oxidation. The 3D-XRD-CT collected during the reduction revealed a gradient in the concentrations of NiO, $NiAl_2O_4$ and metallic Ni along the length of the catalyst bed. This was attributed to the formation of water during the reduction (NiO and $NiAl_2O_4$ being the Ni-containing phases in the catalyst prior to reduction).

The same catalyst was also investigated during the partial oxidation of methane (POX) to CO and H_2 using XRD-CT. After reduction, almost all Ni is found in metallic form and remains in this state for the duration of the POX experiment though the Ni crystallites are seen to continuously sinter. Under POX conditions crystalline graphite forms and gradually increases in concentration with time.

Ex situ characterisation of a spent POX catalyst using sub-minute XRD-CT scans led to the largest 3D-XRD-CT data volume reported to date (100×72×99×2000). Rietveld analysis of this large data volume revealed that catalyst particles from different positions in the bed exhibit substantially different solid state chemistry. Importantly, these results illustrate *ex situ* characterisation, especially single-point and indeed bulk measurements can readily yield misleading information regarding the state and the inferred behaviour of the catalysts. Indeed, the results demonstrate not only the need for *in situ*/ *operando* characterisation but also whole-bed imaging.

Final Remarks

In addition to the specific material insight that has been gained, the work presented in thesis has led to significant advances in collection, processing and analysis of XRD-CT data which also have application to other techniques. It was clearly demonstrated that XRD-CT can be used to obtain spatio-temporal chemical information of functioning catalysts from within the confines of different working catalytic reactor types. It was shown that the coupling of spatially-resolved diffraction signals with Rietveld analysis approach can provide unprecedented physico-chemical insight. XRD-CT can have application to a range of material systems and is particularly appealing as it allows materials to be studied intact and under imposed environmental conditions. As such, it is expected to replace conventional in situ XRD, and indeed conventional X-ray imaging, as the preferred method for characterising materials and devices. In cases where the wt. % loading of the material of interest is low (e.g. << 1 wt. %) or the average crystallite size is too small (nanomaterials) for XRD signals, other chemical tomographic techniques can be employed, like XRF-CT and PDF-CT.

Appendix

Removing multiple outliers and single crystal artefacts from X-ray diffraction computed tomography data

Summed diffraction pattern

The summed diffraction pattern of the XRD-CT dataset is shown at the left side of Figure A1. The cristobalite (green), $BaWO_4$ (red), Mn_2O_3 (cyan) and BCFZ (magenta) peaks presented at the right side of Figure S2 correspond to the sinograms used in this work.

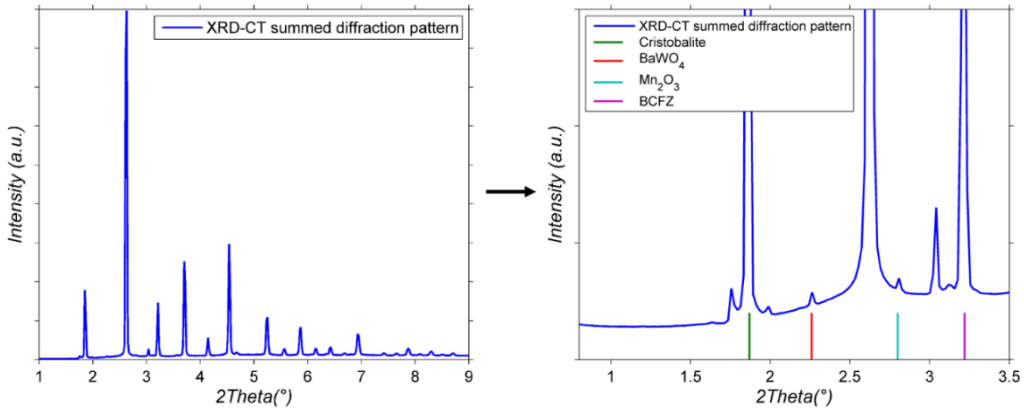

Figure A1: Left: The summed diffraction pattern from the XRD-CT dataset presented in the main paper. Right: A region of interest (ROI) of that diffraction pattern, showing four peaks corresponding to cristobalite (green), $BaWO_4$ (red), Mn_2O_3 (cyan) and BCFZ (magenta) phases.

Tomographic reconstruction algorithms

The effect of different reconstruction algorithms to deal with spotty sinograms is presented in Figure A2. The sinogram used corresponds to $BaWO_4$ also shown in Figure 3 in Chapter 3. The XRDUA software program was used to implement the various tomographic algorithms. Initially, the CeO_2 (NIST) diffraction pattern was used for calibration and then the XRD-CT data were processed (i.e. azimuthal integration of the raw 2D diffraction images and creation of the sinograms). As expected (see first row in Figure S8), the $BaWO_4$ sinogram and reconstructed XRD-CT image (i.e. using the filtered back projection algorithm) are identical with the ones generated using the MATLAB script used in this work. Different tomographic

algorithms were implemented to reconstruct the spotty BaWO4 sinogram using the XRDUA software. More specifically, the algebraic reconstruction technique (ART), the simultaneous algebraic reconstruction technique (SART), the simultaneous iterative reconstruction technique (SIRT), the ordered subset expectation minimization (OSEM) and the maximum likelihood expectation maximization (MLEM) algorithms were tested. As it is shown in Figure S8, the reconstructed images are full of line artefacts regardless of the algorithm used (or how many iterations are used).

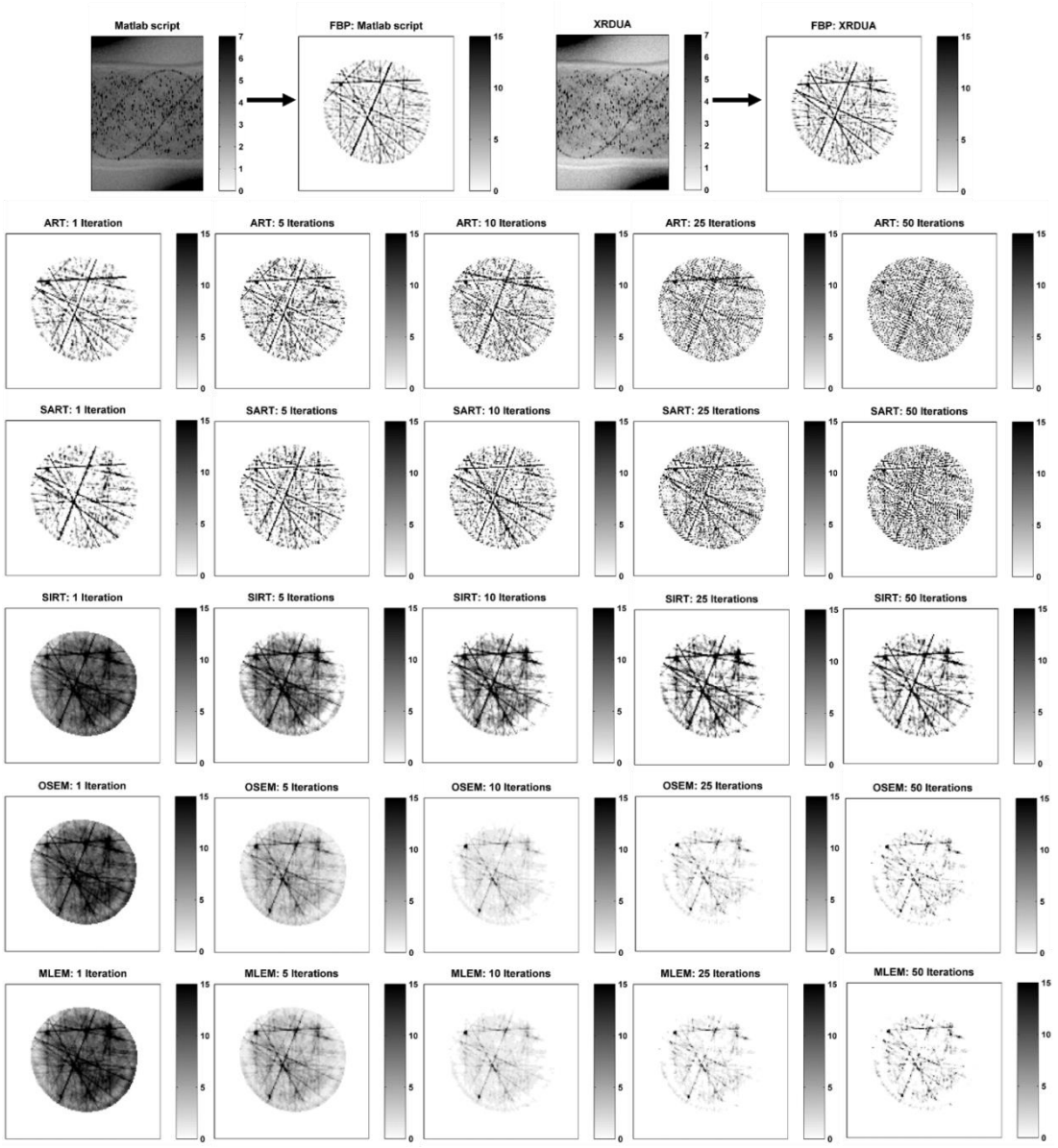

Figure A2: Top row: BaWO¬4 sinograms and reconstructed images (FBP) using the MATLAB script provided in the ESI and the XRDUA software program. The reconstructed images when ART, SART, SIRT, OSEM, MLEM are used is also shown.

Alpha-trimmed mean filter

In Figure A3, the derived 1D diffraction patterns for the CeO_2 standard using different values for the alpha-trimmed mean are shown (i.e. 0, 1, 2, 3, 5, 10, 25, 50 and 75% respectively). The 2D diffraction image shown in Panel A of Figure 2 in Chapter 3 is used as the benchmark tool. As it is shown in Figure A3, there are no obvious changes in the 1D diffraction patterns using the different filters.

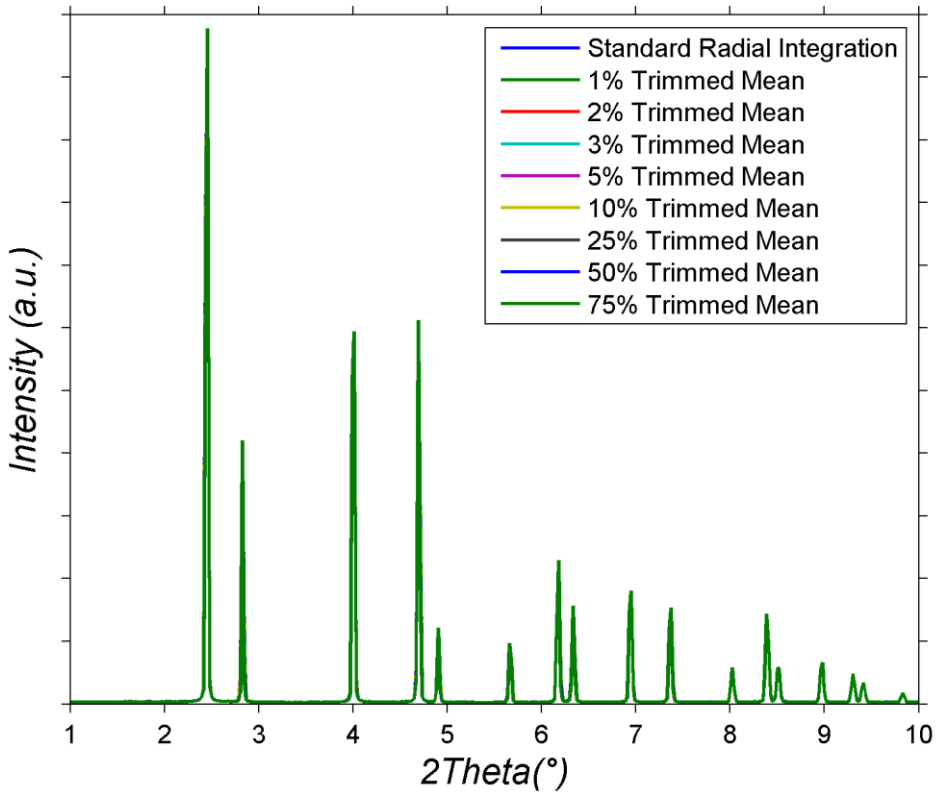

Figure A3: The 1D diffraction patterns for the CeO_2 standard are shown using different values for the alpha-trimmed mean filter.

In Figure A4, the relative difference between the 1D diffraction pattern calculated with standard radial integration and 1, 2 and 3% alpha-trimmed mean filter is presented. It can be seen that the values remain less than 10% even for the 3% alpha-trimmed mean filter.

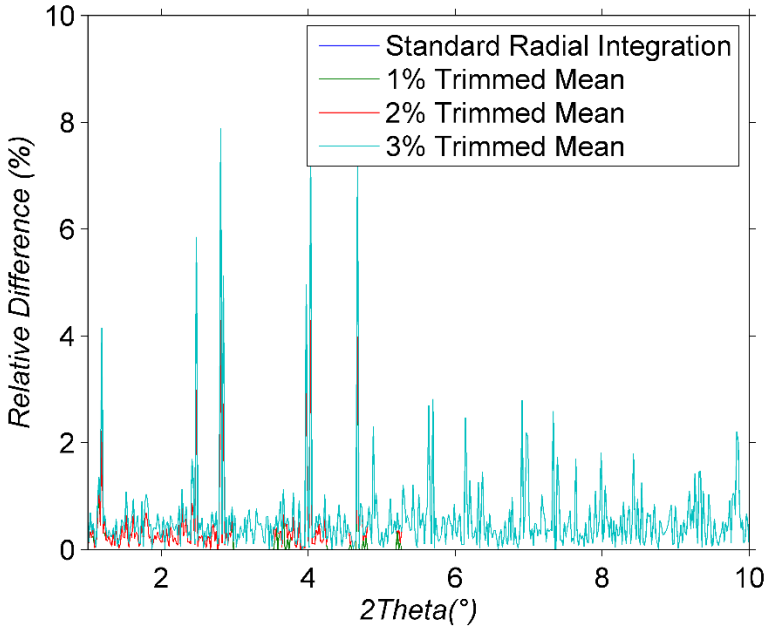

Figure A4: The relative difference between the 1D diffraction pattern calculated with standard radial integration and 1, 2 and 3% alpha-trimmed mean filter for the CeO_2 is shown.

In Figure A5, the relative difference between the 1D diffraction pattern calculated with standard radial integration and 10, 25, 50 and 75% alpha-trimmed mean filter is presented. As expected, the values increase and there are differences more than 50% for the 75% alpha-trimmed mean filter at certain scattering angles 2θ.

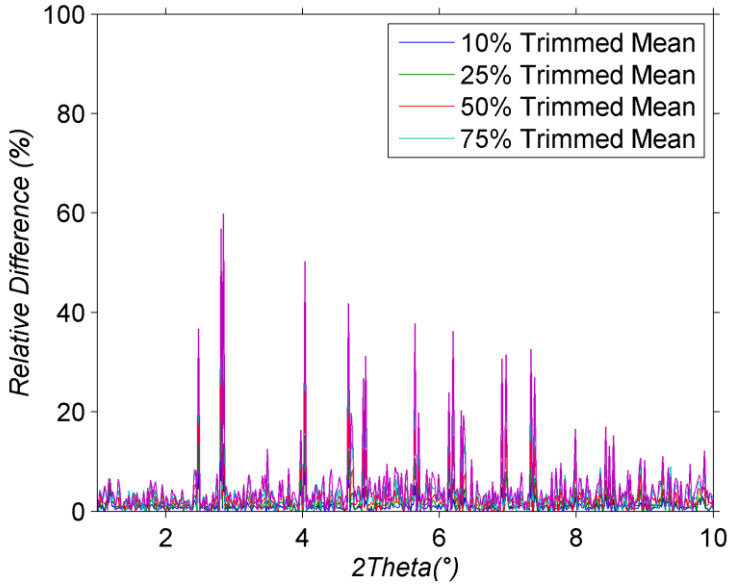

Figure A5: The relative difference between the 1D diffraction pattern calculated with standard radial integration and 1, 2 and 3% alpha-trimmed mean filter for the CeO_2 is shown

The maximum values of the relative difference between the 1D diffraction pattern calculated with standard radial integration and 1, 2, 3, 5, 10, 25, 50 and 75% alpha-trimmed mean filter for the CeO_2 are presented in Figure A6.

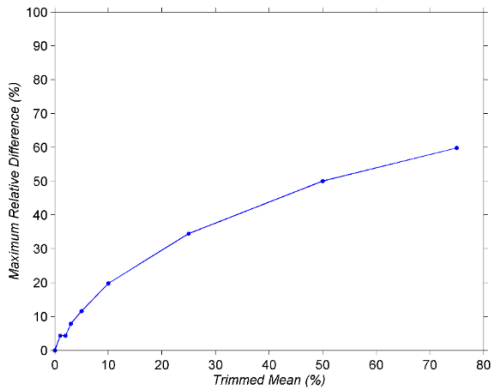

Figure A6: The maximum values of the relative difference between the 1D diffraction pattern calculated with standard radial integration and 1, 2, 3, 5, 10, 25, 50 and 75% alpha-trimmed mean filter for the CeO_2 is shown.

However, as it was shown also in Figure A3, even for the extreme case of the 75% trimmed mean filter, the changes are not radical. The maximum intensities of the diffraction peaks are maintained and the main changes are observed at the tails of the Bragg peaks. This is clearly shown in Figure A7 where the 1D diffraction pattern calculated with standard radial integration and the one calculated with 75% trimmed mean filter are presented.

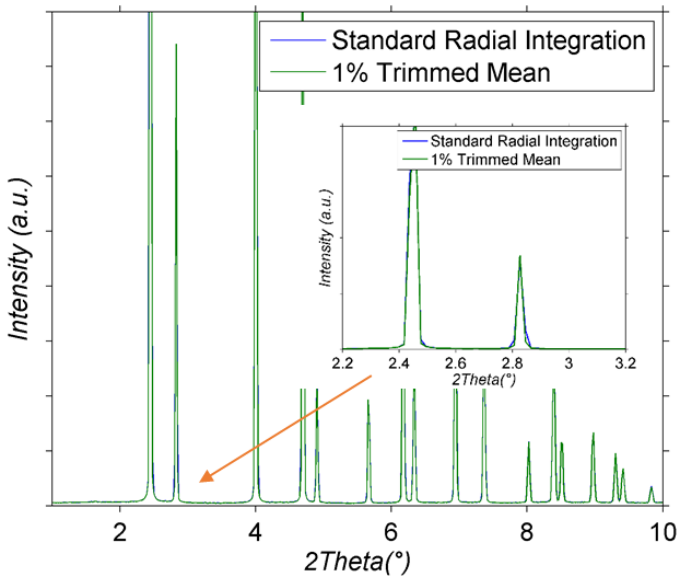

Figure A7: The 1D diffraction patterns for the CeO_2 standard is shown using standard radial integration and 75% alpha-trimmed mean filter. Also shown is a 2ϑ region of interest where the maximum relative difference between the two diffraction patterns is observed (i.e. scattering angle 2.85° 2ϑ.

Scripts for removing outliers from XRD-CT data

The main MATLAB in-house functions used in this work are provided below.

```
function [rBin,phiBin,ibad] = binning(image,cnt_x,cnt_y)
% The function binning is used to set up the polar transformation.
It
% requires a raw 2D diffraction image and the coordinates of the
beam
% centre after the calibration i.e. (cnt_x,cnt_y)

nox = size(image,1);
noy = size(image,2);
X = cumsum(ones(nox,noy),2) - cnt_x  ;
Y = cumsum(ones(nox,noy),1) - cnt_y  ;
rh = sqrt(X.^2 + Y.^2);
phi = atan2d(Y,X)+180;
phiBinSize = 1;
phiBin = round(phi/phiBinSize);
rBinSize = 1;
rBin = round(rh/rBinSize);
ibad = sub2ind(size(phiBin),cnt_y,cnt_x);


function T = image2pol(a,rBin,phiBin,ibad)
% The image2pol function transforms an image from Cartesian to polar
% coordinates

T = zeros(max(rBin(:)),max(phiBin(:)));
for i = 1: length(rBin(:))
    if i == ibad;
        continue
    end
    T(rBin(i),phiBin(i)+1) = a(i);
end


function M = masknan(a)
% The masknan function creates a binary mask (i.e. NaN and 1 values
only)
% and requires as an input the original 2D diffraction image.

a(find(a == 0)) = 0.01;
a(find(a < 0)) = 0;
M = image2pol(a,rBin,phiBin,ibad);
M(find(M==0)) = NaN;
M(find(M>0)) = 1;


function F = tnans(T,z)
% The tnans function is used to transfer the NaN values in each row
of a 2
% dimensional matrix (T) to the end of each row. The user can choose
if the
% NaN values are converted to zeros at the end of the operation.
% T is the 2D matrix (e.g. grayscale image)
% if z == 1 then the nan values are going to be zeros
```

```
F = zeros(size(T));
for i = 1:size(T,1)
    F(i,1:length(find(~isnan(T(i,:))))) = T(i,~isnan(T(i,:)));
    if z == 1
        F(i,length(find(~isnan(T(i,:))))+1:end) = 0;
    else
        F(i,length(find(~isnan(T(i,:))))+1:end) = NaN;
    end
end

function MN = masknan2(M)
% The masknan2 function creates a binary mask (i.e. 0 and 1 values
only)
% and requires as an input the binary mask created with the masknan
% function. This process is necessary if the user wants to apply the
% ordfilt2 function.
MN = tnans(M,0);

function A = filterextrv(B,sd)
% The filterextrv function applies the Standard Deviation based
Trimmed
% Mean filter to the polar transformed images.
% B is the polar transformed image
% sd: how many times the standard deviation should be applied as the
% threshold value. The user should input 10 times the desired value.

for i = 1: size(B,1)
    B(i,find(abs(B(i,:)-nanmean(B(i,:)))>(sd/10)*nanstd(B(i,:)))) =
nan;
end
A(1:size(B,1)) = nanmean(B,2);
```

Below is provided, for the interested reader, a simplified example of the MATLAB code used to apply different filter in the XRD-CT data presented in this work.

```
%% XRD-CT reconstruction example
% Parameters from the tomographic scan
nFastAxisSteps = 140;
slowAxisStart = -94.5;
slowAxisEnd = 94.5;
nSlowAxisSteps = 105;
angleStep = abs(slowAxisEnd-slowAxisStart)/nSlowAxisSteps;
theta = angleStep:angleStep:abs(slowAxisEnd-slowAxisStart);
theta = theta(find(theta<=180));

% Directory name
xrdct_datasets = {'test'};
% Domains for ordfilt2
fm1 = [1 1 1 1 1]; % Row Median filter
fm2 = ones(3,3); % Median filter
fm3 = [0 1 0 ; 1 1 1;0 1 0]; % Cross Median filter
sdtm = 10*[1,1.5,2,3]; % Standard Deviatioan based Trimmed Mean
Filter

mm = 1;
XRDCT_filters(mm).name = char(xrdct_datasets(mm));
% specify the directory where the images have been stored
```

```
mypath = sprintf('/data/%s/',char(xrdct_datasets(mm)));
mystem = sprintf('%s_',char(xrdct_datasets(mm)));
% n is the number of images in the xrd-ct scan
n = 20000;

% Generate the names and allocate zeros
clear RAW
vnames = {'r','fm', 'f','atm'};
tth = size(T,1);
for ii = 1:length(sdtm)
    RAW.(sprintf('%s%s',char(vnames(4)),num2str(sdtm(ii)))) =
zeros(n,length(tth));
end
for ii = [0,1,2,3,5,10,25,50]
    RAW.(sprintf('%s%s',char(vnames(1)),num2str(ii))) =
zeros(n,length(tth));
    if (ii < 10)

RAW.(sprintf('%s%s%s1',char(vnames(1)),num2str(ii),char(vnames(2))))
= zeros(n,length(tth));

RAW.(sprintf('%s%s%s2',char(vnames(1)),num2str(ii),char(vnames(2))))
= zeros(n,length(tth));

RAW.(sprintf('%s%s%s3',char(vnames(1)),num2str(ii),char(vnames(2))))
= zeros(n,length(tth));
    end
end

for jj = 0 : n
    % Directory for the raw images
    fn = sprintf('%s%s%.jpg',mypath,mystem,jj);
    % Read the raw images
    I = imread(fn);
    % Transform the raw I image from Cartesian to polar coordinates
    T = image2pol(I,rBin,phiBin).*masknan;
    % The different nth rank-order filters
    F1 = ordfilt2(tnans(T,1),3,fm1).*maskn;
    F2 = ordfilt2(tnans(T,1),5,fm2).*maskn;
    F3 = ordfilt2(tnans(T,1),3,fm3).*maskn;
    % The SDTM filter
    for ii = 1:1:length(sdtm)

RAW.(sprintf('%s%s',char(vnames(4)),num2str(sdtm(ii))))(jj+1,:) =
filterextrv(T,length(tth),sdtm(ii));
    end
    % The alpha-trimmed mean filters
    for ii = [0,1,2,3,5,10,25,50]
        RAW.(sprintf('%s%s',char(vnames(1)),num2str(ii)))(jj+1,:) =
trimmean(T(1:length(tth),:),ii,2)';
        if (ii < 10)

RAW.(sprintf('%s%s%s1',char(vnames(1)),num2str(ii),char(vnames(2))))
(jj+1,:) = trimmean(F1(1:length(tth),:),ii,2)';

RAW.(sprintf('%s%s%s2',char(vnames(1)),num2str(ii),char(vnames(2))))
(jj+1,:) = trimmean(F2(1:length(tth),:),ii,2)';

RAW.(sprintf('%s%s%s3',char(vnames(1)),num2str(ii),char(vnames(2))))
(jj+1,:) = trimmean(F3(1:length(tth),:),ii,2)';
        end
```

```
    end

    fprintf('\r---> %.4d',jj);
end

% Store the projection data
for ii = 1:1:length(sdtm)

XRDCT_filters(mm).(sprintf('%s%s_projectiondata',char(vnames(4)),num
2str(sdtm(ii)))) =
reshape(RAW.(sprintf('%s%s',char(vnames(4)),num2str(sdtm(ii)))),nFas
tAxisSteps,nSlowAxisSteps+1,size(T,1));
end
for ii = [0,1,2,3,5,10,25,50]

XRDCT_filters(mm).(sprintf('%s%s_projectiondata',char(vnames(1)),num
2str(ii))) =
reshape(RAW.(sprintf('%s%s',char(vnames(1)),num2str(ii))),nFastAxisS
teps,nSlowAxisSteps+1, size(T,1));
    if (ii < 10)

XRDCT_filters(mm).(sprintf('%s%s%s1_projectiondata',char(vnames(1)),
num2str(ii),char(vnames(2)))) =
reshape(RAW.(sprintf('%s%s%s1',char(vnames(1)),num2str(ii),char(vnam
es(2)))),nFastAxisSteps,nSlowAxisSteps+1, size(T,1));

XRDCT_filters(mm).(sprintf('%s%s%s2_projectiondata',char(vnames(1)),
num2str(ii),char(vnames(2)))) =
reshape(RAW.(sprintf('%s%s%s2',char(vnames(1)),num2str(ii),char(vnam
es(2)))),nFastAxisSteps,nSlowAxisSteps+1, size(T,1));

XRDCT_filters(mm).(sprintf('%s%s%s3_projectiondata',char(vnames(1)),
num2str(ii),char(vnames(2)))) =
reshape(RAW.(sprintf('%s%s%s3',char(vnames(1)),num2str(ii),char(vnam
es(2)))),nFastAxisSteps,nSlowAxisSteps+1, size(T,1));
    end
end

% Centre the sinograms
for ii = 1:1:length(sdtm)

XRDCT_filters(mm).(sprintf('%s%s_centredsino',char(vnames(4)),num2st
r(sdtm(ii)))) =
XRDCT_filters(mm).(sprintf('%s%s_projectiondata',char(vnames(4)),num
2str(sdtm(ii))))(:,1:length(theta),:);
end
for ii = [0,1,2,3,5,10,25,50]

XRDCT_filters(mm).(sprintf('%s%s_centredsino',char(vnames(1)),num2st
r(ii))) =
XRDCT_filters(mm).(sprintf('%s%s_projectiondata',char(vnames(1)),num
2str(ii)))(:,1:length(theta),:);
    if (ii < 10)

XRDCT_filters(mm).(sprintf('%s%s%s1_centredsino',char(vnames(1)),num
2str(ii),char(vnames(2)))) =
XRDCT_filters(mm).(sprintf('%s%s%s1_projectiondata',char(vnames(1)),
num2str(ii),char(vnames(2))))(:,1:length(theta),:);

XRDCT_filters(mm).(sprintf('%s%s%s2_centredsino',char(vnames(1)),num
2str(ii),char(vnames(2)))) =
```

```
XRDCT_filters(mm).(sprintf('%s%s%s2_projectiondata',char(vnames(1)),
num2str(ii),char(vnames(2))))(:,1:length(theta),:);

XRDCT_filters(mm).(sprintf('%s%s%s3_centredsino',char(vnames(1)),num
2str(ii),char(vnames(2)))) =
XRDCT_filters(mm).(sprintf('%s%s%s3_projectiondata',char(vnames(1)),
num2str(ii),char(vnames(2))))(:,1:length(theta),:);
    end
end

% Filtered back projection
ii = 0;
[finalSize,NAng,NCh] =
size(XRDCT_filters(mm).(sprintf('%s%s_centredsino',char(vnames(1)),n
um2str(ii))));
clear s0
for kk = 1 : NCh
    for ii = 1:1:length(sdtm)

XRDCT_filters(mm).(sprintf('%s%s_fbp',char(vnames(4)),num2str(sdtm(i
i))))(:,:,kk) =
iradon(XRDCT_filters(mm).(sprintf('%s%s_centredsino',char(vnames(4))
,num2str(sdtm(ii))))(:,:,kk),theta,'linear','Shepp-
Logan',0.9,finalSize);
    end

    for ii = [0,1,2,3,5,10,25,50]

XRDCT_filters(mm).(sprintf('%s%s_fbp',char(vnames(1)),num2str(ii)))(
:,:,kk) =
iradon(XRDCT_filters(mm).(sprintf('%s%s_centredsino',char(vnames(1))
,num2str(ii)))(:,:,kk),theta,'linear','Shepp-Logan',0.9,finalSize);
        if (ii < 10)

XRDCT_filters(mm).(sprintf('%s%s%s1_fbp',char(vnames(1)),num2str(ii)
,char(vnames(2))))(:,:,kk) =
iradon(XRDCT_filters(mm).(sprintf('%s%s%s1_centredsino',char(vnames(
1)),num2str(ii),char(vnames(2))))(:,:,kk),theta,'linear','Shepp-
Logan',0.9,finalSize);

XRDCT_filters(mm).(sprintf('%s%s%s2_fbp',char(vnames(1)),num2str(ii)
,char(vnames(2))))(:,:,kk) =
iradon(XRDCT_filters(mm).(sprintf('%s%s%s2_centredsino',char(vnames(
1)),num2str(ii),char(vnames(2))))(:,:,kk),theta,'linear','Shepp-
Logan',0.9,finalSize);

XRDCT_filters(mm).(sprintf('%s%s%s3_fbp',char(vnames(1)),num2str(ii)
,char(vnames(2))))(:,:,kk) =
iradon(XRDCT_filters(mm).(sprintf('%s%s%s3_centredsino',char(vnames(
1)),num2str(ii),char(vnames(2))))(:,:,kk),theta,'linear','Shepp-
Logan',0.9,finalSize);
        end
    end
end


save XRDCT_effectfilters.mat -v7.3 XRDCT_filters
```

Interlaced X-ray Diffraction Computed Tomography

Sampling in the frequency domain

As discussed in Chapter 4, the artefacts shown in Figure 5 are a result of undersampling during the tomographic scan. An illustration of this problem for traditional X-ray CT using a parallel X-ray beam is provided in Figure A8. If the number of projections is small, then the θ angle in the Fourier space will be large, which will lead to aliasing distortions in the reconstructed images. This phenomenon is thoroughly discussed in the work of Pan and Kak.[1]

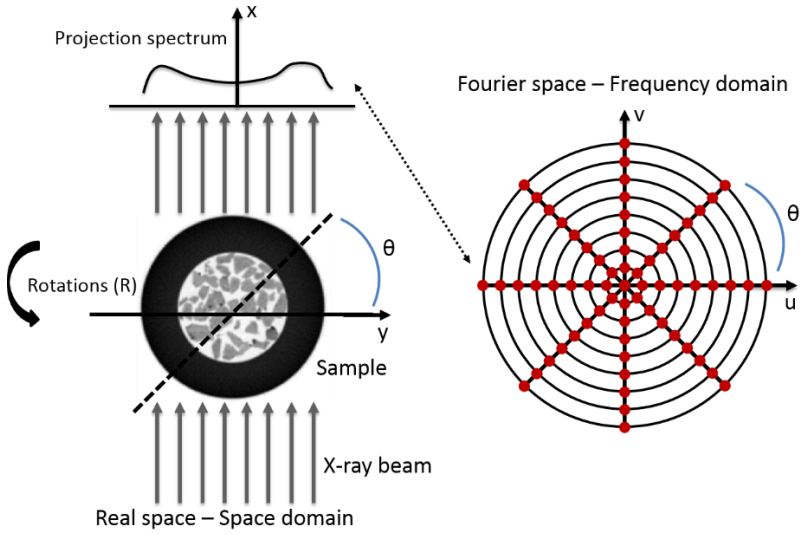

Figure A8: The sampling in the real space and frequency domain during a tomographic scan.

Comparison of different reconstruction algorithms

In Figure A9, the reconstructed images of the sinograms presented in Figure 5 of the Chapter 4 are shown. For comparison, both the filtered back projection (FBP) and the SART algorithm have been implemented to reconstruct the images.[2, 3] The built-in function *iradon* of MATLAB (The MathWorks Inc., Natick, MA, USA) was used for the FBP algorithm and the AIR Tools package (i.e. a MATLAB package with implementations of several algebraic iterative reconstruction methods) was used for the SART algorithm [4]. The FBP reconstructed image was used for the first iteration (instead of a zeros matrix) in order to reduce the computational time for the SART algorithm (i.e. achieving the same final reconstructed images with less iterations). In Figure A9, it can be clearly seen that the quality of the reconstructed images

corresponding to spatial resolution *2x*, *4x* and *8x* does not improve further when the SART algorithm is used regardless how many iterations are applied. In the case of the spatial resolution *1x* sinogram (angular step size of 12 °), the SART algorithm seems to supress the aliasing artefacts but in expense of spatial information. For example, small catalyst particles disappear with increasing number of iterations (as indicated by the arrows in Figure A9).

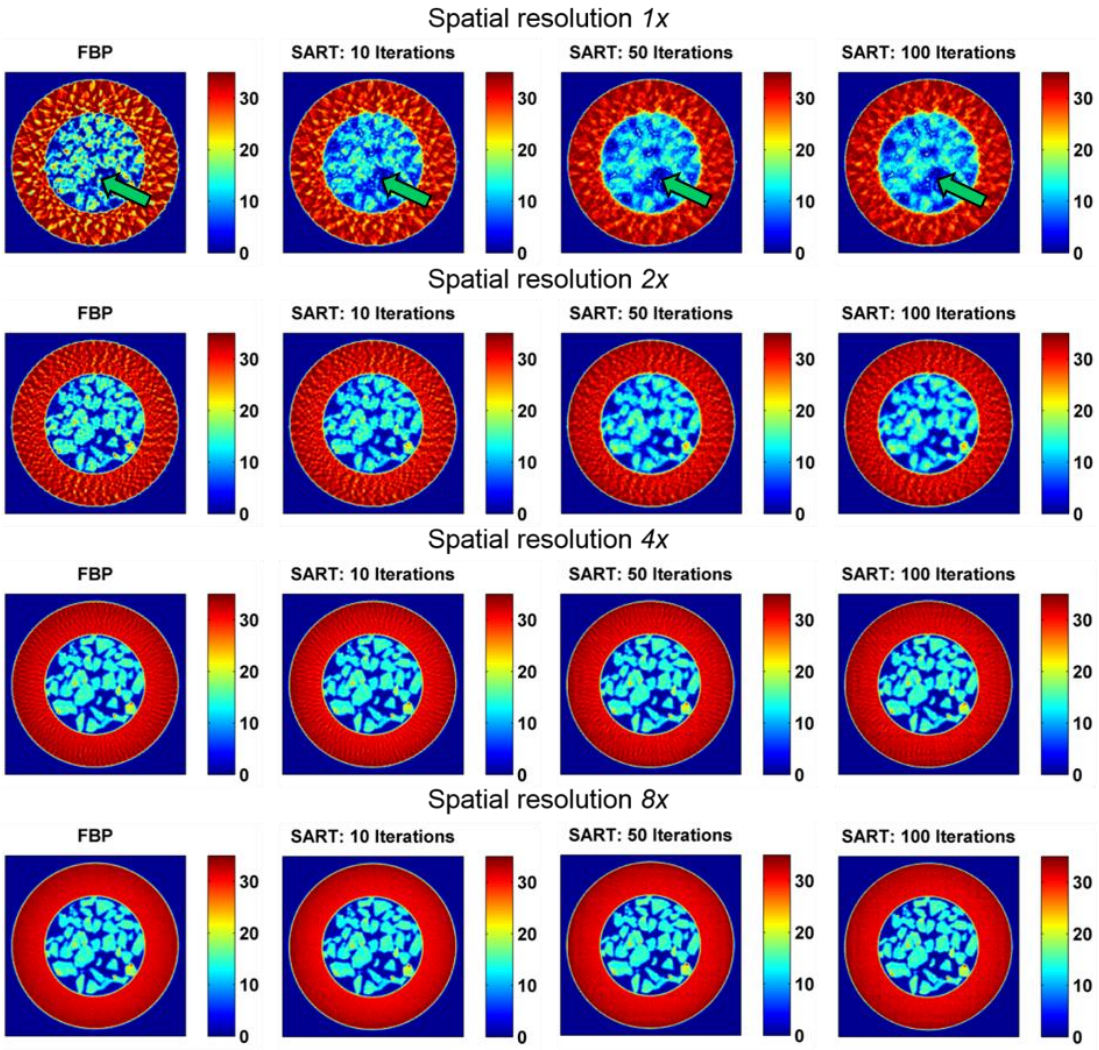

Figure A9: Reconstructed images of the sinograms presented in Figure 5 of the main paper using the filtered back projection (FBP) and the SART algorithms (10, 50 and 100 iterations).

Numerous algebraic iterative reconstruction techniques were tested for the spatial resolution *1x* sinogram and the results are presented in Figure A10. More specifically, the SART algorithm, the diagonally relaxed orthogonal projections (DROP) method, Landweber's method, Cimmino's method and the Component Averaging (CAV) method were tested as provided by the AIR Tools package [3, 5-8]. It can be seen that

these reconstruction algorithms yield almost identical images. As a result, in this study it was chosen to convolute the sinograms with an appropriate window function and use the FBP for reconstruction.

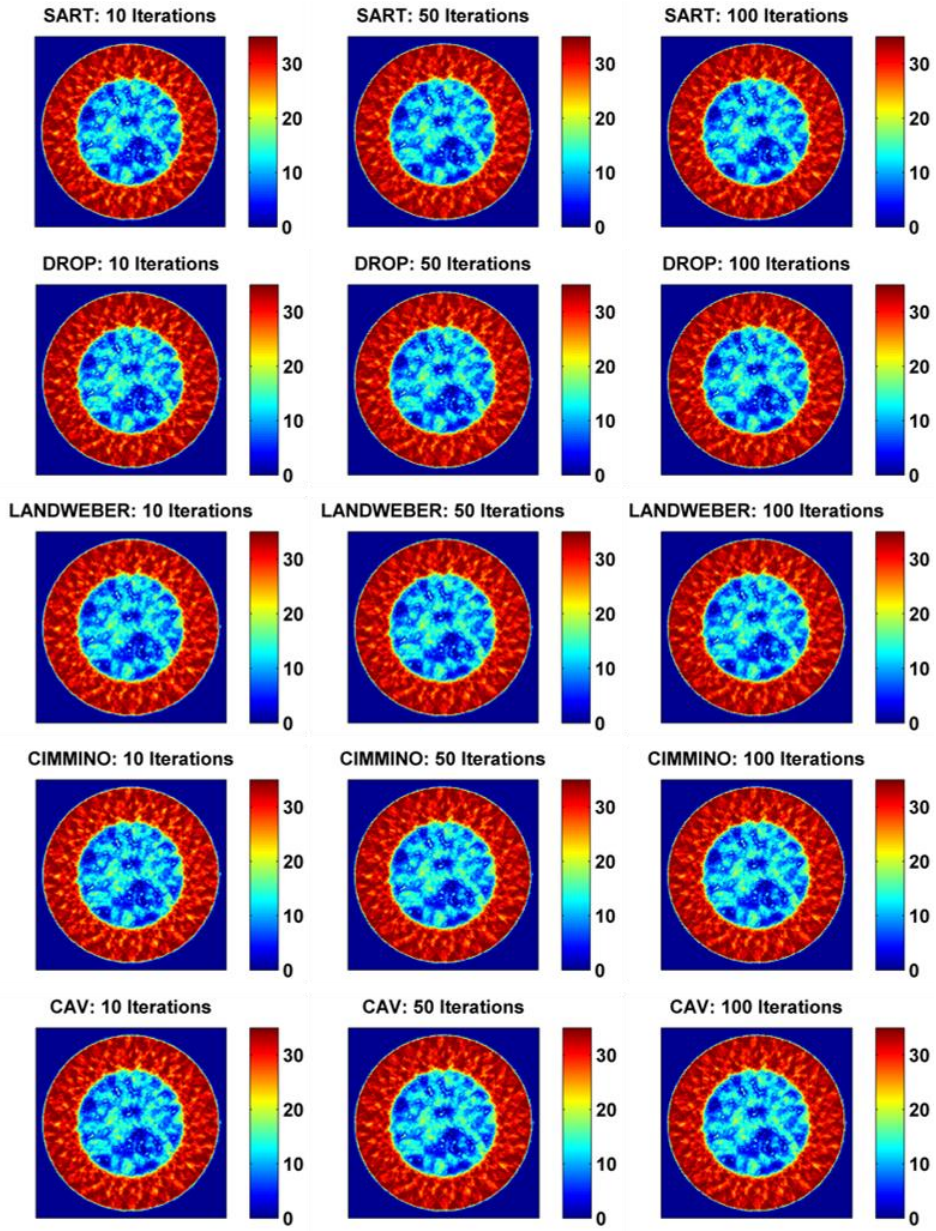

Figure A10: Reconstructed images of the sinogram corresponding to spatial resolution 1x presented in Figure 5 of the main paper using the SART, DROP, Lanweber, Cimmino and CAV algorithms (10, 50 and 100 iterations).

Solid state changes as a function of temperature

The summed diffraction patterns for every translational (line) scan for the two IXRD-CT scans are plotted in Figure A11. In total, 240 diffraction patterns have been plotted (i.e. 120 per IXRD-CT scan). As expected, the signal from the capillary contributes to

the formation of a high intensity background. An appropriate polynomial was fitted with MATLAB and the background was subtracted as shown in Figure A11.

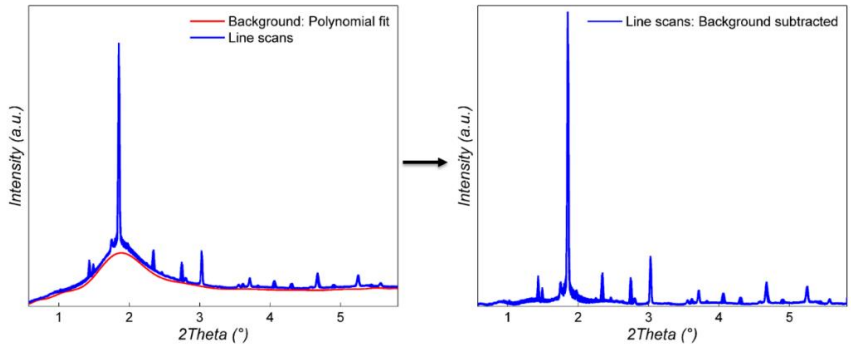

Figure A11: Left: The summed diffraction patterns for every translational scan for the two IXRD-CT scan (240 in total) and the polynomial created for background subtraction are presented. Right: The 240 diffraction patterns after the background subtraction are shown.

The 240 diffraction patterns after the background subtraction are plotted as a function of temperature in Figure A12. It can be seen that the peaks corresponding to cubic (Fd-3m) Na_2WO_4 (e.g. 1.42 ° 2θ) disappear at approximately 600 °C.

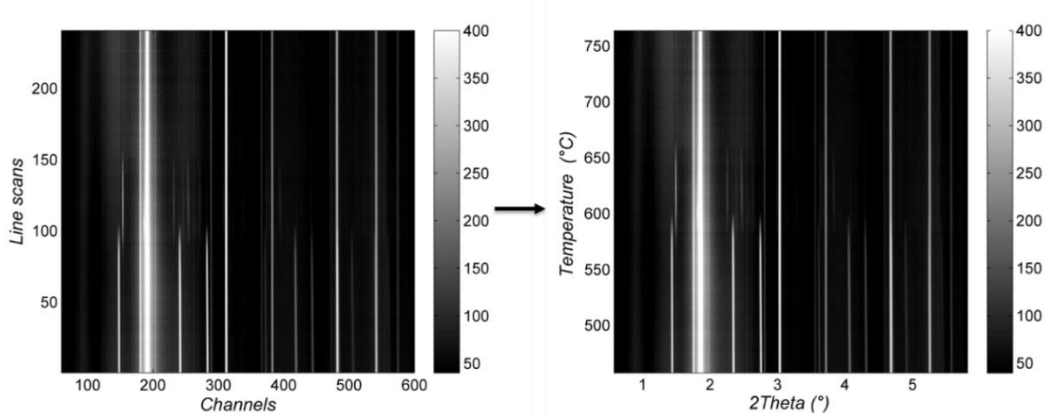

Figure A12: Left: The 240 diffraction patterns after the background subtraction are plotted. Right: These diffraction patterns are plotted as a function of temperature.

Pawley whole powder pattern fitting

As mentioned in the main paper, the main crystalline phases present in the catalyst, in the temperature range of 620 to 640 °C, are cristobalite, tridymite, Na_2WO_4, and Mn_2O_3. There are also minor peaks of quartz and $Na_2Si_2O_5$ (as a result of the excess of Na during the catalyst preparation). As recently reported by Sadjadi *et al.*, it is not trivial to decide whether the Mn_2O_3 and/or the Mn_7SiO_{12} phases are present in the catalyst as both generate similar diffraction patterns.[9] As a result, all the previously

mentioned phases were used for the whole powder pattern fitting. Pawley analysis was performed with the GSASII software using the appropriate unit cells: tetragonal I-42d for cristobalite (ICSD ref: 44095), hexagonal $P6_3/mmc$ for tridymite (ICSD ref: 200479), cubic Ia-3 for Mn_2O_3 (ICSD ref: 187263), $P6_222$ for quartz (ICSD ref: 89287), $I4_1/acd$ for Mn_7SiO_{12} (ICSD ref: 12123), monoclinic $P2_1/n$ for $Na_2Si_2O_5$ (ICSD ref: 88662) and orthorhombic Fddd for the low symmetry Na_2WO_4 phase. The summed diffraction from tomo scan 1 of IXRD-CT scan 2 was used for the Pawley analysis, corresponding to a temperature range of 620 to 640 °C, as there is only the low symmetry Na_2WO_4 phase present and no cubic Na_2WO_4. The results are presented in Figure A13 where it can be seen that all the peaks present in the diffractogram have been fitted.

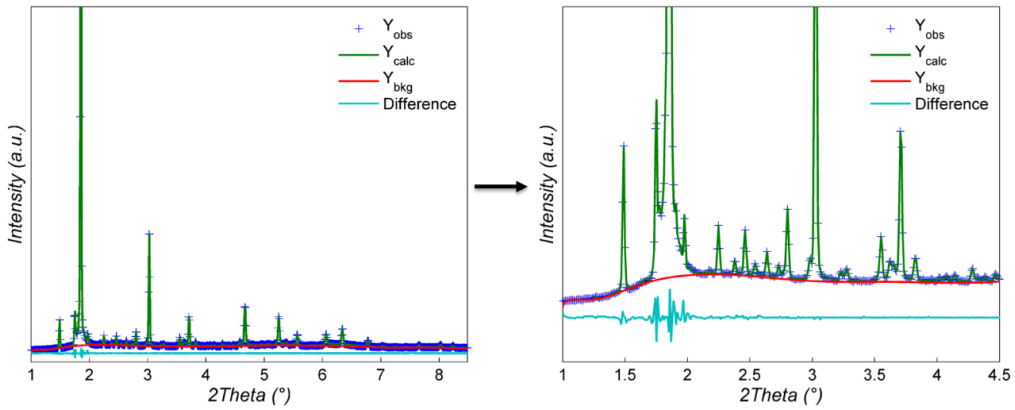

Figure A13: Left: Pawley whole powder pattern profile fitting using the summed diffraction pattern of tomo scan 1 of IXRD-CT scan 2. Right: A region of interest showing that even the minor peaks present in the diffractogram have been fitted appropriately.

Operando studies of catalytic membrane reactors for the oxidative coupling of methane

Self-absorption correction scirpts

Zero order approximation code

This simple MATLAB code requires as an input the following: a micro-CT image, the sinogram data volume of an XRD-CT dataset (projection data) and the tomographic angles used during the XRD-CT scan. It provides absorption corrected reconstructed XRD-CT images. The script

```
function bp = abscor(sn,theta,bpa)
% The abscor function requires also the centreSino, sinocentering,
fbprec,
% maskmembrane and imoixrdctim functions
% sn is the sinogram data volume sn(translations,rotations,spectral
% channels), theta are the tomographic angles and bpa is the micro-
CT image
% Author: A Vamvakeros 2016

% Take the global xrd-ct sinogram and centre it
sn(isnan(sn))=0;
ss = sum(sn,3);
ss = centreSino(ss,theta);
ss = sinocentering(ss,'normal',0.3);

% Recontruct the global xrd-ct image
bp = fbprec(ss(1:end-0,:),theta);bp(bp<0)=0;
% Remove the ring artefact generated by the FBP
sz = floor(size(bp,1)/1);
x = 1:sz;
x = repmat(x,sz,1);
y = x';

xc = round(sz/2);
yc = round(sz/2);
r = sqrt(((x-xc).^2 + (y-yc) .^2));
bpn = bp;
bpn(r>floor(sz/2)-10)=0;

% The user decides the values for the various filters
mskx = maskmembrane(bpn,max(bpn(:))/3,0);
se = strel('disk',1);
mskx = imdilate(mskx,se);
vx = mskx(:,round(size(mskx,2)/2));

mska = maskmembrane(bpa,2,0);
mska = bwareaopen(mska,30);
mska = imdilate(mska,se);
va = mska(:,round(size(mska,2)/2));

% The following part of the code attempts to align the micro-CT
image and
% the global xrd-ct image
inx = find(vx>0);
ina = find(va>0);
dx = inx(end)-inx(1);
da = ina(end)-ina(1);
r = dx/da;

imr = imresize(mska,r,'bilinear');
ima = zeros(size(bpn));
of = round((size(ima,1)-size(imr,1))/2);
kk = 1;
for ii = -10:10
    for jj = -10:10
        ima = zeros(size(bpn));
        if mod(of,2)==0
            ima(1+of+ii:end-of+(ii+0),1+of+jj:end-of+(jj+0)) = imr;
        else
            ima(1+of+ii:end-of+(ii+1),1+of+jj:end-of+(jj+1)) = imr;
```

```
        end
        di(kk) = mean(mean(abs(ima-mskx)));
        ind(kk,:) = [ii,jj];
        kk = kk +1;
    end

end

m = find(di==min(di));
ii = ind(m,1); jj = ind(m,2);

imr = imresize(bpa,r,'bilinear');
ima = zeros(size(bpn));
if mod(of,2)==0
    ima(1+of+ii:end-of+(ii+0),1+of+jj:end-of+(jj+0)) = imr;
else
    ima(1+of+ii:end-of+(ii+1),1+of+jj:end-of+(jj+1)) = imr;
end

mskout = imoixrdctim(ima);
ima = ima.*mskout;

theta = 0:1.8:180-1.8;
fpa = radon(ima,theta);
ofs = round(size(fpa,1)-size(ss,1))/2;
fpa = fpa(1+ofs:end-ofs,:);

kk = 1;
for ii = -10:0.1:10
    thetan = theta + ii;
    bpanew = fbprec(fpa,thetan);
    dibp(kk) = mean(mean((bpn-bpanew)));
    ang(kk) = ii;
    kk = kk +1;
end
m = find(dibp==min(dibp));
thetan = theta + ang(m);

% Forward project the aligned micro-CT image, align the absorption
and
% diffraction ct sinograms and perform the absorption correction
bpanew = fbprec(fpa,thetan);
fpa = radon(bpanew,theta);
fpa = fpa(1+ofs:end-ofs,:);
%
fpaf = exp(-fpa.*0.0058);
snew = ss./fpaf;
bpf = fbprec(snew,theta);

% Now do it for all sinograms (xrd-ct projection data volume)
sn = s(:,1:length(theta),:);sn(isnan(sn))=0;
sn = centreSino(sn,theta);
sn = sinocentering(sn,'normal',0.3);

for ii = 1:size(sn,3);
    sn(:,:,ii) = sn(:,:,ii)./fpaf;
end

% Reconstruct the absorption corrected xrd-ct data volume
```

```
bp = fbprec(sn,theta);
bp(bp<0)=0;


function SC = centreSino(S,theta,range)
% Aligns sinogram to centre of rotation (Parallel beam only)
% INPUTS:    S,      Sinogram data to be aligned
%            theta,  projection angles (e.g. 0:3:177)
%            range,  spectral range over which to consider (e.g. [20
400])
% OUTPUT:    SC,     aligned sinogram data set
%
%
% See: Azevedo et al. IEEE trans. Nucl. Sci. 37 (1990) 1525
% Author: CK EGAN March 2012
%-------------------------------------------------------

% preallocate
if ndims(S) >1 && ndims(S) < 4
    [m,n,e]=size(S);   % n is number of projection angles
    SC=zeros(m,n,e);
elseif ndims(S) == 4
    [l,m,n,e]=size(S);   % n is number of projection angles
    SC=zeros(l,m,n,e);
end

% if angles not specified assume projections taken over 180 degrees
if nargin < 2
    theta = 0:180/n:180-(180/n);
    range(1) = round(e/4);
    range(2) = round(e/1.33);
end

if nargin < 3
    range(1) = round(e/4);
    range(2) = round(e/1.33);
end

% integrate over the spectral domain (if it has one)
if (ndims(S)>2)
    SS = squeeze(sum(S(:,:,range(1):range(2)),3));
else
    SS = S;
end

% calculate projection centre-of-mass for each projection
s1=zeros(1,n);
s2=zeros(1,n);

if ndims(S) >1 && ndims(S) < 4  % ----------------------
conventional sinogram -----------

    for i=1:m % sum over image dimension
        s1 = double(i-ceil(m./2)).*squeeze(SS(i,:)) + s1;
        s2 = squeeze(SS(i,:)) + s2;
    end

    sr = s1./s2;
    d = (n./2).*(n^2/2 - 1 - (cot(pi./(2.*n)))^2);
```

```
    h11 = (n^2)./(4.*d);
    h12 = -n./(2.*d);
    h13 = h12.*cot(pi./(2.*n));

    % calculate centre of rotation
    cs = sum(sr.*(h11+h12.*cosd(theta)+h13.*sind(theta)));

    % display rotation offset to user
    disp(['Centre of rotation is off by ' num2str(cs) ' pixels'])

    % correct for offset centre of rotation for each channel
    for k=1:e
        extrapval = S(m,n,k);
        [xx yy]=meshgrid(1:n,1:m); %xx,yy are both outputs of
meshgrid (so called plaid matrices).

SC(:,:,k)=interp2(xx,yy,squeeze(S(:,:,k)),xx,yy+cs,'*spline',extrapv
al);
    end

elseif ndims(S)==4 % ------------------------  for 3D arrays ------
-------

    for ii=1:l   % loop over each sinogram slice

        for i=1:m % sum over image dimension
            s1 = double(i-ceil(m./2)).*squeeze(SS(ii,i,:)) + s1;
            s2 = squeeze(SS(ii,i,:)) + s2;
        end

        sr = s1./s2;
        d = (n./2).*(n^2/2 - 1 - (cot(pi./(2.*n)))^2);
        h11 = (n^2)./(4.*d);
        h12 = -n./(2.*d);
        h13 = h12.*cot(pi./(2.*n));

        % calculate centre of rotation
        cs = sum(sr.*(h11+h12.*cosd(theta)+h13.*sind(theta)));

        % display rotation offset to user
        disp(['Centre of rotation is off by ' num2str(cs) '
pixels'])

        % correct for offset centre of rotation for each channel
        for k=1:e
            extrapval = S(m,n,k);
            [xx yy]=meshgrid(1:n,1:m); %xx,yy are both outputs of
meshgrid (so called plaid matrices).

SC(ii,:,:,k)=interp2(xx,yy,squeeze(S(ii,:,:,k)),xx,yy+cs,'*spline',e
xtrapval);
        end

    end
end

function Sn = sinocentering(sino,method,o)
% Interpolates the data so that the number of rows is an odd number
```

```
% sino is the sinogram, method is either normal or interlaced
depending on
% how the xrd-ct was performed and o is a constant used to
interpolate the
% data (if needed - otherwise should be removed).
% Author A Vamvakeros 2016

% For interlaced scans - needs to be changes accorinding to the
experiment
m=1;
for i = 1:8;
    m(i+1)=1+16*i;
end;

% Calculate all the angles for the space series
for i = 1:8;
    anglesoi(1:15,i) = m(i):m(i+1)-2;
end
anglesall = reshape(anglesoi,[],1); % all the angles in one row -
120 columns

if nargin<3
    o = .55 ;
end

Sn = zeros(size(sino,1)-1,size(sino,2),size(sino,3));
for ii = 1:size(sino,3)
    if strcmp(method,'normal')
        Sn(:,:,ii) = interp1(sino(:,:,ii),[1:size(sino,1)-
1]+o,'spline') ;
    elseif strcmp(method,'interlaced')
        Sn(:,:,ii) = interp1(sino(:,anglesall,ii),[1:size(sino,1)-
1]+o,'spline') ; % For interlaced
    end
end

function FBP = fbprec(s,theta,sz)
% The fbprec function reconstructs the images using the FBP
algorithm
% s: The sinogram (2D or 3D) matrix
% theta: The tomographic angles
% sz: Size of the reconstructed image
% Author A Vamvakeros 2015

if nargin<3
    FBP = zeros(size(s,1),size(s,1),size(s,3));
else
    FBP = zeros(sz,sz,size(s,3));
end

for ii = 1 : size(s,3)
    FBP(:,:,ii) = iradon(s(:,:,ii),theta,'linear','Shepp-
Logan',1,size(FBP,1));
    %t = imrotate(t,-90); % after baking
    %subplot(2,1,1)
    %imagesc(s);axis image
    %title(num2str(ii));
    %subplot(2,1,2)
    %imagesc(t);axis image
    %drawnow;
```

```
    %pause(0.1);
    %pause;
end

function maskmem = maskmembrane(imoi,threshold,showfig)
% A simple function for image segmentation based on thresholding
% Requires an image of interest (imoi) and a threshold value
% Autor A Vamvakeros 2014
maskmem = imoi;
maskmem(maskmem<threshold) = 0;
maskmem(maskmem>0) = 1;

if showfig == 1
    figure(1);

    subplot(1,2,1)
    imagesc(imoi);colorbar;
    title('Raw image');
    axis off;
    axis image;

    subplot(1,2,2)
    imagesc(maskmem);colorbar;
    title('Mask');
    axis off;
    axis image;
end

function A = imoixrdctim(imoi,~)
% This function creates a circular binary mask interactively using
an image
% Requires imoi: image of interest
% Author A Vamvakeros 2014

figure;
h_im = imagesc(imoi);
axis image;
colorbar;
impixelinfo;
p = imellipse;
indices = wait(p);
%Winsize = get(gcf,'outerposition');
Roi = createMask(p,h_im);
%Roipos = [min(indices(:,1)),min(indices(:,2)),...
%    max(indices(:,1))-min(indices(:,1)),...
%    max(indices(:,2))-min(indices(:,2))];
close;
if nargin > 1
    figure;imagesc(Roi);axis image;colorbar;
end
A = Roi;
```

BCFZ reflections

The list of the observed and calculated BCFZ reflections.

h	k	l	TOF	F_obs	F_calc	phase	mult	sig	gam	FWHM
1	1	1	114587.4	1.654	1.557	0	8	1316.442	358.658	3292.234
2	0	0	99233.06	5.227	5.324	0	6	831.933	298.921	2119.816
2	1	0	88755.37	0.249	0.255	180	24	590.955	267.17	1536.033
2	1	1	81021.39	0.258	0.27	0	24	451.022	248.088	1197.131
2	2	0	70165.84	4.627	4.342	0	12	299.417	210.947	821.392
2	2	1	66152.81	0.186	0.199	180	24	254.637	201.06	711.35
3	0	0	66152.81	0.186	0.199	180	6	254.637	198.827	710.02
3	1	0	62757.96	0.163	0.199	0	24	220.886	188.58	625.566
3	1	1	59837.32	1.231	1.171	0	24	194.641	181.371	560.488
2	2	2	57289.87	3.804	3.545	0	8	173.711	175.367	508.56
3	2	0	55042.34	0.202	0.156	180	24	156.671	165.308	463.136
3	2	1	53040.17	0.17	0.146	0	48	142.553	160.345	427.673
4	0	0	49614.64	2.712	2.896	0	6	120.571	148.951	370.273
3	2	2	48133.34	0.092	0.122	180	24	111.866	146.373	348.859
4	1	0	48133.34	0.092	0.122	180	24	111.866	144.489	347.628
3	3	0	46777.27	0.091	0.107	0	12	104.297	140.405	327.837
4	1	1	46777.27	0.091	0.107	0	24	104.297	141.107	328.299
3	3	1	45529.73	0.861	0.873	0	24	97.659	137.288	310.82
4	2	0	44376.97	2.693	2.369	0	24	91.795	133.177	294.908
4	2	1	43307.57	0.116	0.096	180	48	86.578	130.498	281.426
3	3	2	42311.95	0.051	0.078	0	24	81.909	128.207	269.455
4	2	2	40510.77	2.1	1.939	0	24	73.906	122.623	247.865
4	3	0	39692.37	0.101	0.076	180	24	70.452	119.079	237.785
5	0	0	39692.37	0.101	0.076	180	6	70.452	119.079	237.785
4	3	1	38921.66	0.061	0.057	0	48	67.301	117.134	229.486
5	1	0	38921.66	0.061	0.057	0	24	67.301	116.76	229.227
3	3	3	38194.17	0.492	0.645	0	8	64.415	116.031	222.369
5	1	1	38194.17	0.491	0.645	0	24	64.415	114.922	221.597
4	3	2	36853.76	0.042	0.06	180	48	59.316	111.336	207.911
5	2	0	36853.76	0.042	0.06	180	24	59.316	110.54	207.352
5	2	1	36234.41	0.022	0.041	0	48	57.053	108.97	201.305
4	4	0	35083.97	1.774	1.302	0	12	53.001	105.219	189.835
4	4	1	34548.39	0.123	0.048	180	24	51.181	103.855	184.92
5	2	2	34548.39	0.123	0.048	180	24	51.181	104.252	185.203
4	3	3	34036.61	0.08	0.03	0	24	49.48	103.081	180.692
5	3	0	34036.61	0.08	0.03	0	24	49.48	102.07	179.966
5	3	1	33546.92	0.556	0.474	0	48	47.887	100.82	175.636
4	4	2	33077.79	1.167	1.068	0	24	46.393	99.745	171.648
6	0	0	33077.79	1.166	1.068	0	6	46.393	99.187	171.245
6	1	0	32627.8	0.026	0.038	180	24	44.988	97.835	167.253
5	3	2	32195.7	0.006	0.021	0	48	43.664	97.046	163.849
6	1	1	32195.7	0.006	0.021	0	24	43.664	96.729	163.618

BCFZ CIF

The BCFZ CIF created using the neutron powder diffraction data is provided below:

```
##########################################################################
BCFZ
# phase info for bcfz_cubic follows
_pd_phase_name  bcfz_cubic
_cell_length_a  4.109539
_cell_length_b  4.109539
_cell_length_c  4.109539
_cell_angle_alpha  90
_cell_angle_beta   90
_cell_angle_gamma  90
_cell_volume  69.403
_symmetry_cell_setting  cubic
_symmetry_space_group_name_H-M  "P m 3 m"
loop_
   _space_group_symop_id
   _space_group_symop_operation_xyz
    1  x,y,z
    2  z,x,y
    3  y,z,x
    4  x,y,-z
    5  -z,x,y
    6  y,-z,x
    7  -z,x,-y
```

8 -y,-z,x

9 y,-z,-x

10 -x,y,-z

11 -z,-x,y

12 x,-y,-z

13 y,x,z

14 z,y,x

15 x,z,y

16 y,x,-z

17 -z,y,x

18 x,-z,y

19 -z,y,-x

20 -x,-z,y

21 x,-z,-y

22 -y,x,-z

23 -z,-y,x

24 y,-x,-z

25 -x,-y,-z

26 -z,-x,-y

27 -y,-z,-x

28 -x,-y,z

29 z,-x,-y

30 -y,z,-x

31 z,-x,y

32 y,z,-x

33 -y,z,x

34 x,-y,z

35 z,x,-y

36 -x,y,z

37 -y,-x,-z

38 -z,-y,-x

39 -x,-z,-y

40 -y,-x,z

41 z,-y,-x

42 -x,z,-y

43 z,-y,x

44 x,z,-y

45 -x,z,y

46 y,-x,z

47 z,y,-x

48 -y,x,z

ATOMIC COORDINATES AND DISPLACEMENT PARAMETERS

loop_

_atom_site_label

_atom_site_type_symbol

_atom_site_fract_x

```
  _atom_site_fract_y

  _atom_site_fract_z

  _atom_site_occupancy

  _atom_site_adp_type

  _atom_site_U_iso_or_equiv

  _atom_site_symmetry_multiplicity

Ba1    Ba   0.00000     0.00000     0.00000     1.000      Uiso 0.022      1

Co2    Co   0.50000     0.50000     0.50000     0.400000   Uiso 0.029      1

Fe3    Fe   0.50000     0.50000     0.50000     0.400000   Uiso 0.029      1

Zr4    Zr   0.50000     0.50000     0.50000     0.200      Uiso 0.033      1

O5     O    0.50000     0.50000     0.00000     0.820      Uiso 0.018      3


loop_  _atom_type_symbol _atom_type_number_in_cell

  Ba   1

  Co   0.4

  Fe   0.4

  O    2.46

  Zr   0.2


# Note that Z affects _cell_formula_sum and _weight

_cell_formula_units_Z  1

_chemical_formula_sum  "Ba Co0.4 Fe0.4 O2.46 Zr0.2"

_chemical_formula_weight  240.84
```

Mass spectrometry data

As mentioned in Chapter 6, the outflow gases from the various CMRs were analysed with mass spectrometry. The analysis of the gas products with mass spectrometry serves to illustrate that the CMRs were captured in their active state (qualitative analysis only). The mass spectrometry data from the OCM experiment with the BCFZ – La-Mn-Na-W/SiO_2 CMR are presented in Figure A14. Five regions (1-5) are shown which correspond to air and different mixtures of CH_4 diluted in He (i.e. 5, 20, 50 and 100 vol. % CH_4 in He) respectively. To clarify, these gas mixtures were used from the inner side of the ceramic membrane, through the catalyst bed.

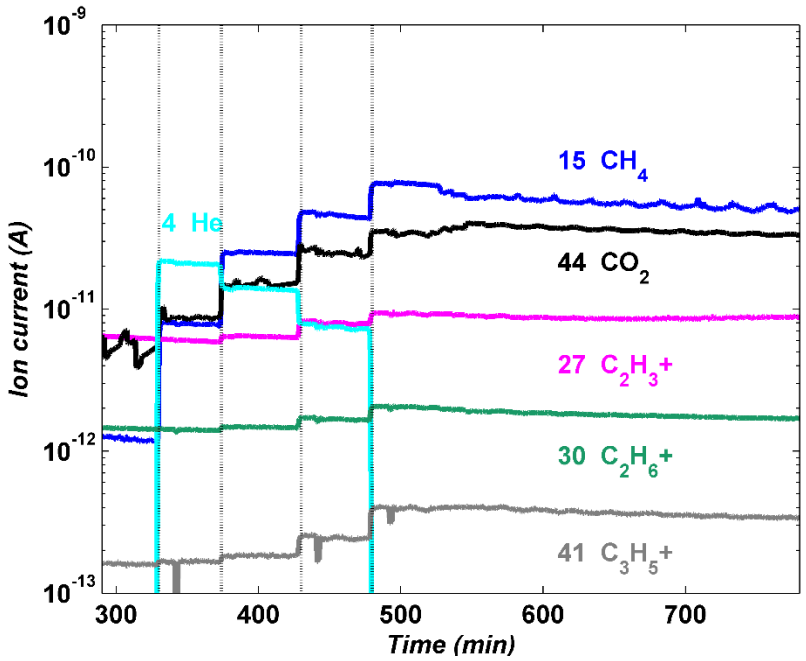

Figure A14: Mass spectrometry data corresponding to the following m/z ratios (possible species and respective line colour in parentheses): 4 (He - cyan), 15 (CH_4+ - blue), 27 (C_2H_2+ - magenta), 30 (C_2H_6+ dark green), 41 (C_3H_5+ - grey) and 44 (CO_2 - black). The five regions (1-5) shown correspond to air (1) and different mixtures of CH_4 diluted in He (i.e. 5, 20, 50 and 100 vol. % CH_4 in He in regions 2-5 respectively).

The signal from mass 27, which corresponds to higher than methane hydrocarbon molecules ($C_2H_3^+$ fractions), appears when the reaction mixture is used (i.e. 5 % CH_4 in He) and the intensity of this signal increases with increasing CH_4 concentration (i.e. 20, 50 and 100 vol. % CH_4 in He). It also should also be noted that a signal from mass 41, which corresponds to $C_3H_5^+$ fractions, appears under OCM reaction conditions and its intensity follows the same trend as the signal from mass 27.

The mass spectrometry data from the OCM experiment with the LSCF – La-Mn-Na-W/SiO_2 CMR are presented in Figure A15 where the indicated five regions correspond to the same gas mixtures as in the BCFZ – La-Mn-Na-W/SiO_2 CMR experiment (i.e. the same experimental protocol was followed in both CMR experiments). It can be clearly seen that the same trend is observed for all masses. Importantly though, the intensity of the signals corresponding to $C_2H_3^+$ and $C_3H_5^+$ fractions is seen to remain stable during both OCM experiments, although $BaWO_4$ formed at the inner BCFZ membrane wall in the BCFZ – La-Mn-Na-W/SiO_2 CMR and $SrWO_4$ at the inner LSCF membrane wall in the LSCF – La-Mn-Na-W/SiO_2 CMR. However, the continuous growth of these phases under OCM reaction conditions is expected to be detrimental to the long-term stability of these CMRs. If a uniform layer of $BaWO_4$/$SrWO_4$ forms at the inner BCFZ/LSCF membrane wall, then the CMR is expected to deactivate (i.e. by preventing the oxygen flow to the catalyst bed).

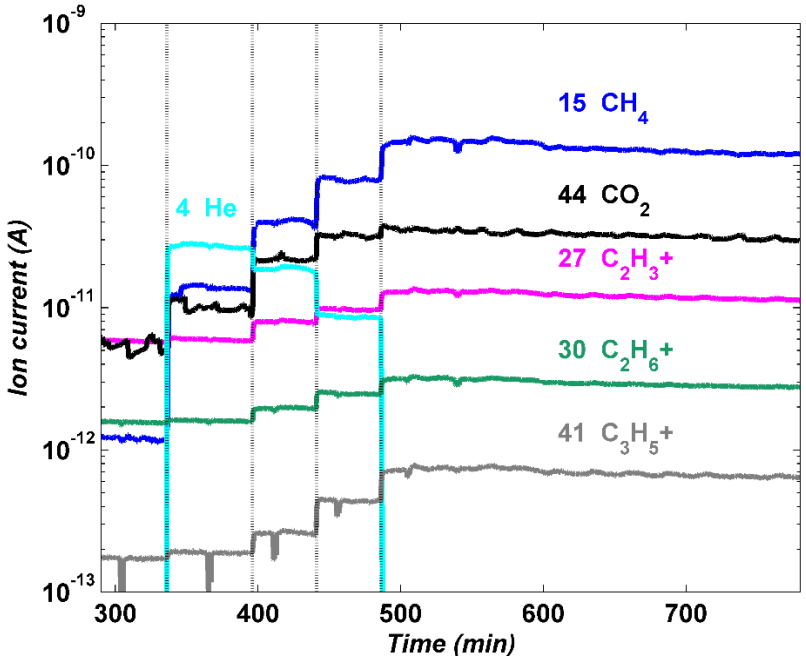

Figure A15: Mass spectrometry data corresponding to the following m/z ratios (possible species and respective line colour in parentheses): 4 (He - cyan), 15 (CH_4+ - blue), 27 (C_2H_2+ - magenta), 30 (C_2H_6+ dark green), 41 (C_3H_5+ - grey) and 44 (CO_2 - black). The five regions (1-5) shown correspond to air (1) and different mixtures of CH_4 diluted in He (i.e. 5, 20, 50 and 100 vol. % CH_4 in He in regions 2-5 respectively).

$SrWO_4$ Phase Identification

The phase identification of the $SrWO_4$ phase, formed during the OCM experiment with the LSCF – La-Mn-Na-W/SiO_2 CMR, is shown in Figure A16. The diffraction

pattern shown in Figure A16 corresponds to the summed diffraction pattern from the LSCF membrane only pixels. The highest intensity peak of the $SrWO_4$ phase is at ca. Q = 1.96 $Å^{-1}$ corresponding to the (112) and (013) reflections (ca. Q = 1.958 and 1.969 respectively). The diffraction pattern was exported from the CMR XRD-CT data collected at room temperature after the OCM experiment.

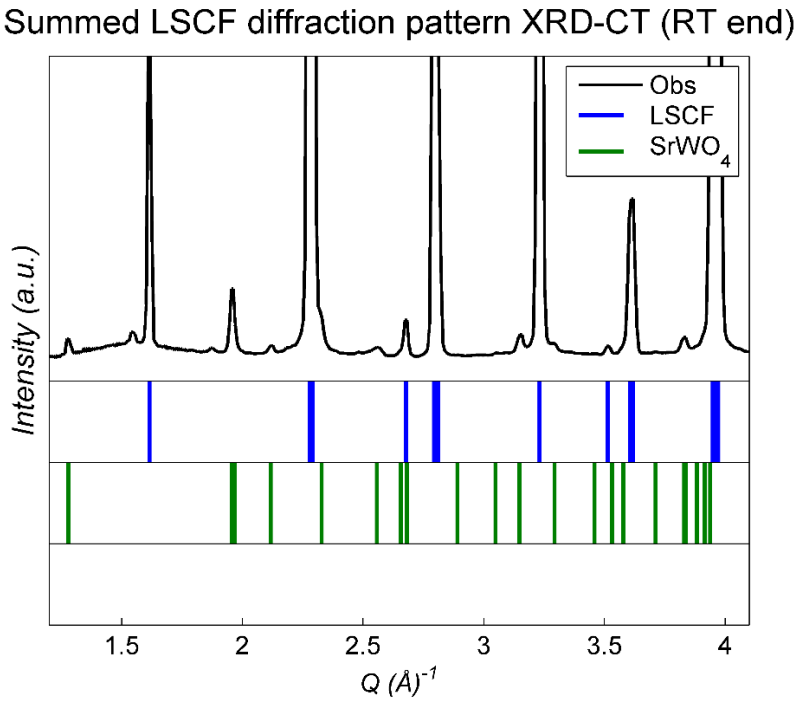

Figure A16: Phase identification of a summed diffraction pattern from pixels of interest (i.e. after applying a mask and taking into account only the pixels corresponding to the LSCF membrane) at room temperature after the OCM experiment.

References

1. Pan, S.X. and A.C. Kak, *A computational study of reconstruction algorithms for diffraction tomography: Interpolation versus filtered-backpropagation.* Acoustics, Speech and Signal Processing, IEEE Transactions on, 1983. **31**(5): p. 1262-1275.
2. Kak, A.C., *Computerized tomography with X-ray, emission, and ultrasound sources.* Proceedings of the IEEE, 1979. **67**(9): p. 1245-1272.
3. Andersen, A.H. and A.C. Kak, *Simultaneous Algebraic Reconstruction Technique (SART): A superior implementation of the ART algorithm.* Ultrasonic Imaging, 1984. **6**(1): p. 81-94.
4. Hansen, P.C. and M. Saxild-Hansen, *AIR Tools — A MATLAB package of algebraic iterative reconstruction methods.* Journal of Computational and Applied Mathematics, 2012. **236**(8): p. 2167-2178.
5. Censor, Y., et al., *On diagonally relaxed orthogonal projection methods.* SIAM Journal on Scientific Computing, 2007. **30**(1): p. 473-504.
6. Landweber, L., *An Iteration Formula for Fredholm Integral Equations of the First Kind.* American Journal of Mathematics, 1951. **73**(3): p. 615-624.

7. Cimmino, G., *Calcolo approssimato per le soluzioni dei sistemi di equazioni lineari, XVI (9) (1938) 326–333.* La Ricerca Scientifica, 1938. **16**(9): p. 326-333.
8. Censor, Y., D. Gordon, and R. Gordon, *Component averaging: An efficient iterative parallel algorithm for large and sparse unstructured problems.* Parallel Computing, 2001. **27**(6): p. 777-808.
9. Sadjadi, S., et al., *Feasibility study of the Mn-Na2WO4/SiO2 catalytic system for the oxidative coupling of methane in a fluidized-bed reactor.* Catalysis Science and Technology, 2015. **5**(2): p. 942-952.